antioxidants

Special Issue Reprint

Applications of Antioxidant Nanoparticles, 2nd Edition

Edited by
Rita Cortesi and Maddalena Sguizzato

mdpi.com/journal/antioxidants

MDPI

Applications of Antioxidant Nanoparticles, 2nd Edition

Applications of Antioxidant Nanoparticles, 2nd Edition

Guest Editors

Rita Cortesi
Maddalena Sguizzato

MDPI

Basel • Beijing • Wuhan • Barcelona • Belgrade • Novi Sad • Cluj • Manchester

Guest Editors

Rita Cortesi
Department of Chemical Pharmaceutical and Agricultural Sciences (DoCPAS)
University of Ferrara
Ferrara
Italy

Maddalena Sguizzato
Department of Chemical Pharmaceutical and Agricultural Sciences (DoCPAS)
University of Ferrara
Ferrara
Italy

Editorial Office

MDPI AG
Grosspeteranlage 5
4052 Basel, Switzerland

This is a reprint of the Special Issue, published open access by the journal *Antioxidants* (ISSN 2076-3921), freely accessible at: https://www.mdpi.com/journal/antioxidants/special_issues/nanoparticles_2.

For citation purposes, cite each article independently as indicated on the article page online and as indicated below:

Lastname, A.A.; Lastname, B.B. Article Title. *Journal Name* **Year**, *Volume Number*, Page Range.

ISBN 978-3-7258-7332-6 (Hbk)
ISBN 978-3-7258-7333-3 (PDF)
https://doi.org/10.3390/books978-3-7258-7333-3

© 2026 by the authors. Articles in this reprint are Open Access and distributed under the Creative Commons Attribution (CC BY) license. The reprint as a whole is distributed by MDPI under the terms and conditions of the Creative Commons Attribution-NonCommercial-NoDerivs (CC BY-NC-ND) license (https://creativecommons.org/licenses/by-nc-nd/4.0/).

Contents

About the Editors . . . . . **vii**

Rita Cortesi and Maddalena Sguizzato
Applications of Antioxidant Nanoparticles, 2nd Edition
Reprinted from: *Antioxidants* **2026**, *15*, 340, https://doi.org/10.3390/antiox15030340 . . . . . **1**

Francesca Baldassarre, Chiara Boncristiani, Michela Ottolini, Concetta Nobile, Maryam Shahzad Shirazi, Giuseppe E. De Benedetto, et al.
Shaping Lycopene Nanoparticles Performance: How Surfactants Influence Stability, Antioxidant Activity, and Uptake in Human Skin Spheroids
Reprinted from: *Antioxidants* **2026**, *15*, 136, https://doi.org/10.3390/antiox15010136 . . . . . **5**

M. Alfawaz, Ekramy M. Elmorsy, Ahmad Najem Alshammari, Noor A. Hakim, Najlaa M. M. Jawad, Soha A. Hassan, et al.
Carvacrol-Loaded Chitosan Nanoparticles as a Multifunctional Nanotherapeutic Strategy Targeting Oxidative Stress, Inflammation, Apoptosis, and Genotoxicity in Nonalcoholic Fatty Liver Disease
Reprinted from: *Antioxidants* **2025**, *14*, 1432, https://doi.org/10.3390/antiox14121432 . . . . . **31**

Xiangyu Mao, Wenyuan Li, Yuanyuan Li, Xuemei Jiang, Ruinan Zhang, Lianqiang Che, et al.
Effect of Nano-Selenium on Intestinal Oxidative Stress Induced by H_2O_2 in Mice
Reprinted from: *Antioxidants* **2025**, *14*, 1073, https://doi.org/10.3390/antiox14091073 . . . . . **59**

Enrique Gutierrez-Albanchez, Elena Fuente-González, Svitlana Plokhovska, Francisco Javier Gutierrez-Mañero and Beatriz Ramos-Solano
Enhanced Anti-Inflammatory Effects of Rosemary (*Salvia rosmarinus*) Extracts Modified with *Pseudomonas shirazensis* Nanoparticles
Reprinted from: *Antioxidants* **2025**, *14*, 931, https://doi.org/10.3390/antiox14080931 . . . . . **89**

Aarthi Jeganathan, Karuppusamy Arunachalam, Anju Byju, Anju Rani George, Sradha Sajeev, Kavimani Thangasamy and Geetha Natesan
Chitosan Nanoparticle-Mediated Delivery of *Alstonia venenata* R.Br. Root Methanolic Extract: A Promising Strategy for Breast Cancer Therapy in DMBA-Induced Breast Cancer in Sprague Dawley Rats
Reprinted from: *Antioxidants* **2024**, *13*, 1513, https://doi.org/10.3390/antiox13121513 . . . . . **104**

Cornelia-Ioana Ilie, Angela Spoiala, Cristina Chircov, Georgiana Dolete, Ovidiu-Cristian Oprea, Bogdan-Stefan Vasile, et al.
Antioxidant, Antitumoral, Antimicrobial, and Prebiotic Activity of Magnetite Nanoparticles Loaded with Bee Pollen/Bee Bread Extracts and 5-Fluorouracil
Reprinted from: *Antioxidants* **2024**, *13*, 895, https://doi.org/10.3390/antiox13080895 . . . . . **137**

Xiuan Zhu, Wenjie Wen, Jingjing Yan, Yuran Wang, Rumeng Wang, Xiang Ma, et al.
Rod-Shaped Mesoporous Zinc-Containing Bioactive Glass Nanoparticles: Structural, Physico-Chemical, Antioxidant, and Immuno-Regulation Properties
Reprinted from: *Antioxidants* **2024**, *13*, 875, https://doi.org/10.3390/antiox13070875 . . . . . **166**

Hong-Wei Shi, Bo-Cheng Yang, Yun-Qing Ren and Yi Xue
Applications of Antioxidant Nanoparticles in Immune-Mediated Inflammatory Diseases
Reprinted from: *Antioxidants* **2025**, *14*, 1128, https://doi.org/10.3390/antiox14091128 . . . . . **182**

Supandeep Singh Hallan, Francesca Ferrara, Maddalena Sguizzato and Rita Cortesi
Cyclodextrin-Based Nanotransporters as a Versatile Tool to Manage Oxidative Stress-Induced Lung Diseases
Reprinted from: *Antioxidants* **2025**, *14*, 1007, https://doi.org/10.3390/antiox14081007 . . . . . **215**

Chiara Bellini, Fabrizio Mancin, Emanuele Papini and Regina Tavano
Nanotechnological Approaches to Enhance the Potential of α-Lipoic Acid for Application in the Clinic
Reprinted from: *Antioxidants* **2024**, *13*, 706, https://doi.org/10.3390/antiox13060706 . . . . . **248**

About the Editors

Rita Cortesi

Rita Cortesi works at the Department of Chemical, Pharmaceutical and Agricultural Sciences of Ferrara University (Italy). After graduation, she earned a PhD in Pharmaceutical Sciences and attended an HMC postdoctoral fellowship at Nottingham University (UK). As a Pharmaceutical Technologist, she works on the nanotechnology formulation and development of nanosystems for the controlled release of bioactive molecules and drug delivery systems for gene therapy. Her other interests are in the field of cosmetics. Her studies are conducted in collaboration with prestigious international research groups throughout the world.

Maddalena Sguizzato

Maddalena Sguizzato is currently a Tenure Track Researcher at the University of Ferrara, Department of Chemical, Pharmaceutical and Agricultural Sciences. She earned her PhD in Chemical Sciences, and she was a Visiting PhD Student at NC State University (NC, USA) and Visiting Researcher at the University of Oslo (Norway) and at the University of Geneva (Switzerland). Her research focuses on the formulation of lipid-based nanosystems for the targeted delivery of poorly soluble molecules as well as for cosmetic use. She is the co-author of several publications in the field of drug delivery and antioxidant application. Her main interests are related to natural and synthetic antioxidants and their relevance to plant, animal and human health and disease, the evaluation of in vitro and in vivo antioxidant capacity, pharmacodynamics and pharmacokinetics of natural antioxidants, redox modulation in biological systems by pro- and antioxidants, innovative techniques of antioxidant delivery, and protocols for the extraction, isolation, and structural characterization of new natural antioxidants, dietary antioxidants, food supplements, and subproducts.

antioxidants

MDPI

Editorial

Applications of Antioxidant Nanoparticles, 2nd Edition

Rita Cortesi * and Maddalena Sguizzato

Department of Chemical, Pharmaceutical and Agricultural Sciences (DoCPAS), University of Ferrara, 44100 Ferrara, Italy; sgzmdl@unife.it

* Correspondence: crt@unife.it

It is known that the overproduction of reactive oxygen species (ROS), which regulate numerous physiological processes, can generate oxidative stress, responsible for the onset of several pathologies [1]. Therefore, a useful therapeutic approach to reducing or neutralizing oxidative stress is the administration of antioxidants. This has been addressed in several fields (i.e., pharmaceuticals, cosmetics, and food) with different types of formulations, including the use of nanoparticles, which have transformed the field of antioxidant therapeutics through enabling specialized nano-delivery systems. In our previous Special Issue "Applications of Antioxidant Nanoparticles", we summarized and published recent advances in the design, production, characterization, use, and effects of antioxidant nanoparticles.

In this Special Issue of *Antioxidants* entitled "Applications of Antioxidant Nanoparticles, 2nd Edition", we continue to compile the latest breakthroughs in the design, production, characterization, and utilization of antioxidant nanoparticles in the biomedical, pharmaceutical, cosmetic, and food sectors. The merging of antioxidant therapy and nanomedicine marks a major advancement in the treatment of oxidative disorders, offering more accurate, efficient, and biocompatible approaches.

In this second edition, seven research articles and three reviews have been collected. Specifically, the seven research articles can be divided into two main groups depending on the organic (contributions 1, 2, and 5) or inorganic (contributions 3, 4, 6, and 7) nature of the studied nanoparticle system.

In drug delivery, organic nanoparticles are biocompatible carriers encapsulating therapeutic agents able to improve solubility, protect against degradation, and enable targeted and/or sustained release. They enhance efficacy in treating diseases like cancer by reducing toxicity and promoting controlled, site-specific drug accumulation [2–5].

Among the contributions of the first group, the research by Baldassarre and colleagues (contribution 1) evaluates the influence of some excipients on the performance of nanoparticle formulations. Indeed, the effect of two different nonionic surfactants, polyvinyl alcohol (PVA) and Tween 20, on the production of organic polymer-based nanoparticles (i.e., polylactic-co-glycolic acid) is described and a thorough discussion is given, in which potential applications in skincare are proposed. Different parameters were investigated in this research, and the results revealed that the type of surfactant affects the stability of nanoparticles and their retention and cellular uptake, neutralizing oxidative stress in skin cells. Contributions 2 and 5 investigate the organic polymer chitosan as a good candidate for the potential treatment of human pathologies, such as nonalcoholic fatty liver disease (NAFLD) and breast cancer. Notably, Alfawaz and colleagues propose loaded chitosan nanoparticles for enhanced bioavailability, solubility, and sustained release, and support their potential as an advanced nanotherapeutic strategy for NAFLD management, specifically acting on inflammation. Similarly, Aarthi Jeganathan's group demonstrate that loaded

chitosan nanoparticles enable the sustained release of active compounds, supporting improvements in various biochemical, enzymatic, and histopathological parameters relating to breast cancer pathology, such as tumor volume and lipid peroxidation.

The remaining contributions (3, 4, 6, and 7) describe the employment of inorganic nanoparticles. Compared to organic materials, inorganic nanoparticles are versatile, stable, and biocompatible drug delivery vehicles; therefore, they are proposed for different purposes, such as targeted therapy, gene delivery, and imaging. Key types include gold, silica, iron oxide, and ceramic, offering advantages like controlled release, high payload capacity, and protection against enzymatic degradation [6].

In fact, inorganic nanoparticles exhibit unique physicochemical properties that allow them to be functionalized with various specific ligands to enhance their affinity for target cells or molecules, making them particularly effective in cancer treatment through improving tumor imaging and drug penetration [7–10]. In this context, Mao and colleagues (contribution 3) demonstrate that selenium supplementation mitigates the damage caused by H_2O_2 to the intestinal morphology of mice jejunum and restores the level of related inflammatory factors. Along these lines, Gutierrez-Albanches' group (contribution 4) investigated the potential of silver nanoparticles to deliver *Pseudomonas shirazensis* metabolites, with the aim of enhancing the bioactivity of rosemary extracts in postharvest applications. Moreover, the use of magnetite nanoparticles is proposed by Ilie and colleagues (contribution 6) as a drug delivery system for the dual encapsulation of bioactive compounds to treat the gut microbiota dysbiosis that occurs in cancer therapy, demonstrating synergistic antioxidant and antibacterial effects. In addition, the zinc-containing bioactive glass nanoparticles designed and developed by Zhu's group (contribution 7) are proposed to improve antioxidant and anti-inflammatory effects, facilitating bone and tissue regeneration through exploiting free radical scavenging activity and immunomodulation.

Finally, the reviews by Shi and Hallan's groups (contribution 8 and 9) offer an overview of the applications of nanoparticle systems in the treatment of autoimmune and lung diseases. Shi and colleagues specifically addressed immune-mediated inflammatory diseases, such as alopecia areata and multiple sclerosis, in which oxidative stress plays a key role in onset and progression, and highlighted the potential of nano-antioxidants as a promising therapeutic approach, primarily due to their stability and their capability for targeted delivery (contribution 8). Hallan's review, on the other hand, considers the use of organic nanostructures such as cyclodextrins in the treatment of oxidative stress-driven lung diseases such as cystic fibrosis, pulmonary hypertension, chronic airway diseases, and lung cancer (contribution 9). The third review offers an overview of the nanoformulation of a natural compound, alpha-lipoic acid, with potent antioxidant properties that protect cells and tissues from oxidative stress. Specifically, it describes the engineering of the molecule of interest as a novel, innovative formulation strategy, which promises to be an effective drug delivery system (contribution 10).

Overall, all of the reviews emphasize that nanoparticulate systems can overcome the problems of poor solubility, stability in aqueous solutions, and bioavailability after administration, which hinder their clinical utility. However, in some cases, the lack of physiological models for assessing the efficacy of tissue-oriented drug targeting and subsequent clinical studies remains an open issue.

In summary, through this second edition, we have attempted to expand the awareness of researchers regarding the different applications of nanoparticles in counteracting or regulating the effect of oxidative stress in different diseases, either through topical or systemic treatments. The combination of green production methods and natural molecules has also been explored in this second edition, demonstrating multifunctional hybrid approaches that mitigate oxidative stress, inflammation, and microbial potential. Finally, the studies

https://doi.org/10.3390/antiox15030340

collected in this Special Issue emphasize the potential of nanotechnological systems in modulating the activity of the molecules being carried—such as antioxidant actives—after administration, enhancing their therapeutic activity, stability, and targeted uptake and delivery across different biomedical applications characterized by redox environments.

Author Contributions: Conceptualization, writing—original draft, review, and editing: R.C. and M.S. All authors have read and agreed to the published version of the manuscript.

Acknowledgments: We thank all the authors included in this Special Issue for contributing their high-quality work. We also acknowledge the reviewers who critically evaluated the articles and the Section Managing Editor for his kind help.

Conflicts of Interest: The authors declare no conflicts of interest.

List of Contributions:

1. Baldassarre, F.; Boncristiani, C.; Ottolini, M.; Nobile, C.; Shahzad Shirazi, M.; De Benedetto, G.E.; Colangelo, G.; Vergaro, V.; Valli, L.; Ciccarella, C. Shaping Lycopene Nanoparticles Performance: How Surfactants Influence Stability, Antioxidant Activity, and Uptake in Human Skin Spheroids. *Antioxidants* **2026**, *15*, 136. https://doi.org/10.3390/antiox15010136.
2. Alfawaz, M.; Elmorsy, E.M.; Alshammari, A.N.; Hakim, N.A.; Jawad, N.M.M.; Hassan, S.A.; Fawzy, M.S.; Esmaeel, S.E. Carvacrol-Loaded Chitosan Nanoparticles as a Multifunctional Nanotherapeutic Strategy Targeting Oxidative Stress, Inflammation, Apoptosis, and Genotoxicity in Nonalcoholic Fatty Liver Disease. *Antioxidants* **2025**, *14*, 1432. https://doi.org/10.3390/antiox14121432.
3. Mao, X.; Li, W.; Li, Y.; Jiang, X.; Zhang, R.; Che, L.; Zhuo, Y.; Sun, M.; Wang, X.; Wu, D.; et al. Effect of Nano-Selenium on Intestinal Oxidative Stress Induced by H_2O_2 in Mice. *Antioxidants* **2025**, *14*, 1073. https://doi.org/10.3390/antiox14091073.
4. Gutierrez-Albanchez, E.; Fuente-González, E.; Plokhovska, S.; Gutierrez-Mañero, F.J., Ramos-Solano B. Enhanced Anti-Inflammatory Effects of Rosemary (*Salvia rosmarinus*) Extracts Modified with Pseudomonas shirazensis Nanoparticles. *Antioxidants* **2025**, *14*, 931. https://doi.org/10.3390/antiox14080931.
5. Jeganathan, A.; Arunachalam, K.; Byju, A.; George, A.R.; Sajeev, S.; Thangasamy, K.; Natesan, G. Chitosan Nanoparticle-Mediated Delivery of *Alstonia venenata* R.Br. Root Methanolic Extract: A Promising Strategy for Breast Cancer Therapy in DMBA-Induced Breast Cancer in Sprague Dawley Rats. *Antioxidants* **2024**, *13*, 1513. https://doi.org/10.3390/antiox13121513.
6. Ilie, C.-I.; Spoiala, A.; Chircov, C.; Dolete, G.; Oprea, O.-C.; Vasile, B.-S.; Crainiceanu, S.A.; Nicoara, A.-I.; Marinas, I.C.; Stan, M.S.; et al. Antioxidant, Antitumoral, Antimicrobial, and Prebiotic Activity of Magnetite Nanoparticles Loaded with Bee Pollen/Bee Bread Extracts and 5-Fluorouracil. *Antioxidants* **2024**, *13*, 895. https://doi.org/10.3390/antiox13080895.
7. Zhu, X.; Wen, W.; Yan, J.; Wang, Y.; Wang, R.; Ma, X.; Ren, D.; Zheng, K.; Deng, C.; Zhang, J. Rod-Shaped Mesoporous Zinc-Containing Bioactive Glass Nanoparticles: Structural, Physico-Chemical, Antioxidant, and Immuno-Regulation Properties. *Antioxidants* **2024**, *13*, 875. https://doi.org/10.3390/antiox13070875.
8. Shi, H.-W.; Yang, B.-C.; Ren, Y.-Q.; Xue, Y. Applications of Antioxidant Nanoparticles in Immune-Mediated Inflammatory Diseases. *Antioxidants* **2025**, *14*, 1128. https://doi.org/10.3390/antiox14091128.
9. Hallan, S.S.; Ferrara, F.; Sguizzato, M.; Cortesi, R. Cyclodextrin-Based Nanotransporters as a Versatile Tool to Manage Oxidative Stress-Induced Lung Diseases. *Antioxidants* **2025**, *14*, 1007. https://doi.org/10.3390/antiox14081007.
10. Bellini, C.; Mancin, F.; Papini, E.; Tavano, R. Nanotechnological Approaches to Enhance the Potential of α-Lipoic Acid for Application in the Clinic. *Antioxidants* **2024**, *13*, 706. https://doi.org/10.3390/antiox13060706.

References

1. Dizdaroglu, M.; Jaruga, P.; Birincioglu, M.; Rodriguez, H. Free Radical-Induced Damage to DNA: Mechanisms and Measurement 1,2 1This Article Is Part of a Series of Reviews on "Oxidative DNA Damage and Repair." The Full List of Papers May Be Found on the Homepage of the Journal. 2Guest Editor: Miral Dizdaroglu. *Free Radic. Biol. Med.* **2002**, *32*, 1102–1115. [CrossRef] [PubMed]
2. Mitchell, M.J.; Billingsley, M.M.; Haley, R.M.; Wechsler, M.E.; Peppas, N.A.; Langer, R. Engineering Precision Nanoparticles for Drug Delivery. *Nat. Rev. Drug Discov.* **2021**, *20*, 101–124. [CrossRef] [PubMed]
3. Hussein Kamareddine, M.; Ghosn, Y.; Tawk, A.; Elia, C.; Alam, W.; Makdessi, J.; Farhat, S. Organic Nanoparticles as Drug Delivery Systems and Their Potential Role in the Treatment of Chronic Myeloid Leukemia. *Technol. Cancer Res. Treat.* **2019**, *18*, 1533033819879902. [CrossRef] [PubMed]
4. Calzoni, E.; Cesaretti, A.; Polchi, A.; Di Michele, A.; Tancini, B.; Emiliani, C. Biocompatible Polymer Nanoparticles for Drug Delivery Applications in Cancer and Neurodegenerative Disorder Therapies. *JFB* **2019**, *10*, 4. [CrossRef] [PubMed]
5. Lee, B.K.; Yun, Y.H.; Park, K. Smart Nanoparticles for Drug Delivery: Boundaries and Opportunities. *Chem. Eng. Sci.* **2015**, *125*, 158–164. [CrossRef] [PubMed]
6. Unnikrishnan, G.; Joy, A.; Megha, M.; Kolanthai, E.; Senthilkumar, M. Exploration of Inorganic Nanoparticles for Revolutionary Drug Delivery Applications: A Critical Review. *Discov. Nano* **2023**, *18*, 157. [CrossRef] [PubMed]
7. Paul, W.; Sharma, C.P. Inorganic Nanoparticles for Targeted Drug Delivery. In *Biointegration of Medical Implant Materials*; Elsevier: Amsterdam, The Netherlands, 2020; pp. 333–373, ISBN 978-0-08-102680-9.
8. Liu, H.; Gou, X.; Tan, Y.; Fan, Q.; Chen, J. Immunotherapy and Delivery Systems for Melanoma. *Hum. Vaccines Immunother.* **2024**, *20*, 2394252. [CrossRef] [PubMed]
9. Inorganic Nanoparticles for Transdermal Drug Delivery and Topical Application. In *Nanoscience in Dermatology*; Academic Press: Cambridge, MA, USA, 2016; pp. 57–72.
10. Verma, C.; Berdimurodov, E.; Verma, D.K.; Berdimuradov, K.; Alfantazi, A.; Hussain, C.M. 3D Nanomaterials: The Future of Industrial, Biological, and Environmental Applications. *Inorg. Chem. Commun.* **2023**, *156*, 111163. [CrossRef]

Disclaimer/Publisher's Note: The statements, opinions and data contained in all publications are solely those of the individual author(s) and contributor(s) and not of MDPI and/or the editor(s). MDPI and/or the editor(s) disclaim responsibility for any injury to people or property resulting from any ideas, methods, instructions or products referred to in the content.

antioxidants

MDPI

Article

Shaping Lycopene Nanoparticles Performance: How Surfactants Influence Stability, Antioxidant Activity, and Uptake in Human Skin Spheroids

Francesca Baldassarre [1,2,*], Chiara Boncristiani [3], Michela Ottolini [1], Concetta Nobile [4], Maryam Shahzad Shirazi [1], Giuseppe E. De Benedetto [5], Gianpiero Colangelo [6], Viviana Vergaro [3,*], Ludovico Valli [1,2] and Giuseppe Ciccarella [1,2,4]

[1] Department of Biological and Environmental Sciences and Technologies (DiSTeBA), University of Salento, S. P. 6 Lecce-Monteroni SNC, 73100 Lecce, Italy; michela.ottolini@unisalento.it (M.O.); maryam.shahzadshirazi@unisalento.it (M.S.S.); ludovico.valli@unisalento.it (L.V.); giuseppe.ciccarella@unisalento.it (G.C.)
[2] UdR INSTM, Salento, 73100 Lecce, Italy
[3] Department of Experimental Medicine, University of Salento, S. P. 6 Lecce-Monteroni SNC, 73100 Lecce, Italy; chiara.boncristiani@unisalento.it
[4] Institute of Nanotechnology, CNR NANOTEC, Consiglio Nazionale delle Ricerche, S. P. 6 Lecce-Monteroni SNC, 73100 Lecce, Italy; concetta.nobile@nanotec.cnr.it
[5] Department of Cultural Heritage, University of Salento, Via D. Birago 64, 73100 Lecce, Italy; giuseppe.debenedetto@unisalento.it
[6] Department of Engineering for Innovation, University of Salento, S. P. 6 Lecce-Monteroni SNC, 73100 Lecce, Italy; gianpiero.colangelo@unisalento.it
* Correspondence: francesca.baldassarre@unisalento.it (F.B.); viviana.vergaro@unisalento.it (V.V.)

Abstract

There is a growing demand for plant-derived antioxidants to replace synthetic ones in skincare applications. Phytochemicals are characterized by certain limitations, including poor bioavailability and chemical instability, which affect their industrial exploitation. Tomato peel extract has been used as a source of lycopene, which is renowned for its antioxidant properties. To improve the bioavailability of extracted lycopene, polymeric (poly-lactic-co-glycolic acid) nano-carriers were synthesized by comparing two non-ionic surfactants, polyvinyl alcohol (PVA) and Tween 20. The impact of surfactants has been studied by evaluating: (i) colloidal stability determined by dynamic light scattering; (ii) lycopene retention and bioactivity over time, as measured by spectrophotometric assays; (iii) biological interactions on 2D and 3D keratinocyte and melanocyte cell cultures. It was found that both surfactants enable the formation of stable lycopene-loaded nanoparticles suspensions; however, greater colloidal stability was exhibited by nanoparticles prepared with Tween 20. PVA, on the other hand, provided greater nanoparticle stability in terms of loaded lycopene retention and antioxidant activity. Tween 20 surfactant improves the internalization of lycopene-loaded nanoparticles in human skin spheroids. It was demonstrated that both surfactants provided excellent intracellular antioxidant activity of lycopene. This was observed in keratinocytes, melanocytes, adherent cells, and spheroids, suggesting potential skincare applications.

Keywords: lycopene; PLGA nanoparticles; non-ionic surfactants; human skin spheroids

1. Introduction

Significant advancements have been made over the past few decades in enhancing the bioavailability of bioactive ingredients for the food, cosmetics, and pharmaceutical industries [1,2]. Lycopene (Lyc) is one of the most widely commercialized carotenoids thanks to its high antioxidant capacity among natural, plant-derived active compounds (e.g., vitamins, anthocyanins, and phenolic compounds) [3,4]. In addition, among various carotenoids, Lyc is the second most potent antioxidant after astaxanthin. It is a significant inhibitor of reactive oxygen species (ROS); it has been demonstrated to remove singlet oxygen at a rate that is two and ten times higher than that of beta-carotene and alpha-tocopherol, respectively [5]. Lycopene is also recognized for its potential anti-inflammatory properties, and antidiabetic, antithrombotic, and antimicrobial effects, as well as for its protective effects on the cardiovascular system, its ability to mitigate oxidative damage, and prevent cancer [6,7]. Recent epidemiological studies have provided insights into the health benefits of dietary Lyc, which has been shown to decrease the risk and complications associated with several chronic diseases, including cardiovascular diseases, obesity, type 2 diabetes, cancer, and neurodegenerative disorders. The etiology of these chronic diseases is principally associated with oxidative stress-induced systemic and low-grade chronic inflammation. Lyc has been demonstrated to attenuate elevated levels of proinflammatory mediators (e.g., proinflammatory cytokines and oxidized phospholipids) by modulating oxidative stress, a property that is attributable to its potent antioxidant characteristics. The available evidence suggests that this combination has the capacity to act as a safeguard against the development of chronic inflammatory disorders [8]. As demonstrated in approximately 200 articles and reviews, Lyc has been shown to have anti-obesity and anti-diabetic properties in a variety of organs and tissues, including but not limited to adipose tissue and the liver, kidneys, pancreas, brain, ovaries, intestines, and eyes. The underlying mechanism of these effects can be attributed to the substance's antioxidant and anti-inflammatory properties, as well as its ability to regulate specific signalling pathways [9]. Concerning cancer prevention, it has been demonstrated that a higher dietary intake and circulating concentration of Lyc have protective effects against prostate cancer, in a dose-dependent way [10]. Lycopene has also shown an inhibitory effect on the proliferation and progression of colorectal cancer cells [5]. Lycopene's nutraceutical impact involves benefits for cardiovascular and neurodegenerative diseases; it can improve vascular and endothelial function, reduce atherosclerotic plaque size, and contribute to cognitive longevity and the treatment of several neuronal diseases (Parkinson's and Alzheimer's diseases) [11,12].

Lycopene cannot be produced by the human body and thus must be obtained through dietary intake. It is the pigment responsible for the red colouring of foods such as tomatoes, watermelons, papayas, pink grapefruits, and guavas.

Although Lyc and carotenoids can be obtained through chemical synthesis, these processes usually involve complicated, low-yield reactions that are not economically or environmentally favourable. Other strategies include extraction from plant sources and, more recently, microbial synthesis. Extraction from plants, especially tomatoes, is a conventional method that is widely performed; however, it tends to result in low yields, requires large areas of land for cultivation, and suffers from seasonality. Using microorganisms for carotenoid production is appealing because of their rapid growth, high yields, and year-round availability. However, the cost of growth media undermines the viability of this method. In this context, producing Lyc using waste products offers a dual benefit: generating sustainable, high-value products, while providing an alternative waste management solution [13,14]. In the interest of conserving resources and reducing the considerable expenses associated with waste disposal, there has emerged a novel trend of utilizing waste

https://doi.org/10.3390/antiox15010136

recovery processing residues as prospective sources of compounds with active properties, such as nutraceuticals and functional ingredients [15].

Tomatoes represent the most significant source of Lyc. Italy, along with Spain and Portugal, is one of Europe's biggest producers of tomatoes. Every year, more than 10 million tons of these fruits are turned into peeled tomatoes, juices, and other products. This process creates a lot of waste (millions of tons each year and about 4% of the weight of the processed tomatoes). This is both an inconvenience for the producers and a resource. As Lyc is predominantly present in the skin of the fruit, tomato peel (TP) has the potential to serve as an alternative, cost-effective source of carotenoids [16]. Lycopene derived from tomato waste is generally considered safe and is gaining regulatory interest for use in food and supplements. Bodies such as the European Food Safety Authority (EFSA) have established an acceptable daily intake (ADI) of 0.5 mg/kg body weight per day. Extracts from tomato by-products are considered novel foods (EFSA's Novel Foods Regulation), requiring specific safety assessments, especially regarding other carotenoids present. The EFSA scrutinizes new products also for the presence of phytoene and phytofluene (precursor carotenoids of Lyc) and ensures that overall intake does not exceed the ADI [17]. Specific bodies are responsible for regulating and certifying natural, organic, and naturally derived ingredients for use in cosmetics and cosmeceuticals (such as CosMOS and NATRUE). These bodies' ultimate goal is to promote sustainable cosmetics throughout their entire production cycle, from sourcing raw materials to packaging and communication (https://www.cosmos-standard.org; https://natrue.org/it/, accessed on 7 January 2026). They also promote sustainable circular economy practices to add value to waste products. However, the safety of Lyc depends on the extraction method used.

Methods of Lyc extraction include organic solvent extraction (conventional, such as liquid–liquid, Soxhlet, microwave, and ultrasound-assisted extraction), and green techniques (alternative). In the food, cosmetic, and pharmaceutical industries, an environmentally friendly carotenoid extraction process with minimal loss of bioactivity is desirable. Supercritical CO_2 (SC-CO_2) extraction is a more environmentally friendly alternative to organic solvent extraction and is already used in the food industry to produce solvent-free extracts [3,18].

However, due to the high degree of unsaturation exhibited by Lyc, a highly significant propensity for chemical degradation and cis–trans isomerization is exhibited under conditions of extreme temperature and pH value, exposure to oxygen, and to light. The observed phenomenon of colour fading in the compound is primarily attributable to chemical instability. This, in turn, results in a concomitant loss of both bioavailability and bioactivity [19,20]. The exploitation of Lyc biological properties is also impeded by its hydrophobic nature and insolubility in aqueous solvents, as well as in many other solvents, which affect its efficient delivery. These limitations considerably restrict its commercial applications [21,22]. Additionally, the high degree of lipophilicity could impact its permeation through the stratum corneum (the outermost layer of the epidermis) in dermatological applications. This phenomenon can be attributed to the substance's propensity to interact with the components of stratum corneum, resulting in its prolonged retention within this initial layer [23–25].

To improve the delivery of Lyc to the deeper layers of the skin, several formulation strategies have been suggested, including the use of surfactants, permeation enhancers, cyclodextrin complexes, and various nanoscale delivery systems [19,20,22]. Delivery systems such as nanoemulsions, liposomes, niosomes, nanogels, and polymeric and inorganic nanoparticles improve the stability, permeability, and targeted delivery of bioactive compounds and plant extracts [26–29]. The utilization of biopolymeric and lipid-based nanostructures as effective carriers has been demonstrated to be a promising approach

for the protection of Lycopene throughout the digestive system, with the potential for incorporation into functional foods or nutraceutical products [19,20]. To enhance the delivery of Lyc to the deeper layers of the skin, vesicular nanocarriers such as liposomes and more deformable variants, including transfersomes, ethosomes and niosomes, and nanoemulsions have been proposed [24,25,30,31].

It has been established that Lyc is more efficient than β-carotene in preventing oxidative damage when applied in skincare formulations. This has been demonstrated to provide beneficial results in terms of protection against photodamage and indicates its potential as an anti-ageing ingredient [32–34]. Lycopene-rich products, including tomato extract obtained by SC-CO_2, have demonstrated protective effects against UVB/UVA irradiation, and anti-inflammatory and anti-apoptosis responses on different cell lines (e.g., fibroblasts and keratinocytes) [31,35]. Previous studies have also reported anti-tyrosinase and anti-melanogenesis properties, which support the great potential of these natural extracts in dermatology [35]. In detail, the protective effects of Lyc-rich products have been demonstrated through the inhibition of NF-κB [33] and UVB-induced ornithine decarboxylase (ODC) activity, along with the prevention of inflammatory responses [34]. As was indicated in previous in vitro studies, tomato extracts have also been reported to greatly inhibit tyrosinase (73%) [36]. Furthermore, carotenoids have been demonstrated to offer protection against melanogenic intermediates and exogenous DNA damage [37], and a protective effect on the skin by preventing the apoptosis of fibroblast cells [38]. Specifically, various anti-ageing treatments, facial moisturizers, and eye creams now contain Lyc due to their great ability to protect the skin from potential UV radiation damage and prolong a tan [39,40].

In this study, Lyc, starting from TP extract in the oil form and obtained with SC-CO_2 (provided by Licofarma s.r.l., Galatina, Lecce, Italy), has been nonencapsulated using polylactic-co-glycolic acid (PLGA), a copolymer that has been approved by the U.S. Food and Drug Administration, synthesizing Lyc-loaded nanoparticles for delivery in skin cells. The suitability of PLGA for bioactive encapsulation, as flavonoids and carotenoids, has been widely investigated [41,42]. Recent studies have demonstrated enhanced stability and protection against the chemical degradation of Lyc, even when subjected to simulated in vitro gastrointestinal conditions, through the utilization of nanoencapsulation by PLGA [43,44].

The objective of the study was to optimize the physicochemical and biological properties of Lyc-loaded PLGA nanoparticles (Lyc@PLGA NPs) by manipulating their stabilization phase using two distinct surfactants, namely polyvinyl alcohol (PVA) and Tween 20. Surfactants have been shown to play a pivotal role in the stabilization process during the synthesis of polymeric NPs. The impact of surfactants on the synthesis process is such that they have the capacity to affect a number of key factors, including the size of the particles, the zeta potential, the surface morphology, the drug loading and, ultimately, the biological interactions [45–49].

SC-CO_2 TP extract has been compared to a Lyc standard, analyzing UV and HPLC spectra. The produced nanoparticles were characterized by electron microscopy, spectrophotometry, FT-IR, and dynamic light scattering to study their morphology, Lyc retention, and colloidal stability over time. The antioxidant capacity of TP extract and Lyc@PLGA NPs have been assessed with DPPH inhibition testing. Biological interactions have been studied in a spontaneously immortalized human keratinocyte cell line, HaCaT, and melanoma cell line, SK-MEL-2. Two-dimensional and three-dimensional cell cultures have been treated to verify the surfactant impact on cell viability, uptake, and intracellular antioxidant activity. A cellular uptake study was performed to provide direct visualization and quantification of NP internalization in human skin spheroids. This has been achieved through the utilization of confocal imaging, which involves the analysis of the intrinsic fluorescence of Lyc, thereby

https://doi.org/10.3390/antiox15010136

circumventing the necessity for additional NP chemical modifications. This approach has been applied as preliminary screening to in vitro permeation (e.g., Franz diffusion cells) and ex vivo assays on animal or human skin sections, thereby addressing methodological and ethical concerns. It has been demonstrated that 3D cell culture systems, including skin cell models, have the capacity to overcome the limitations of 2D cultures. This is due to their ability to replicate the complex phenotypical heterogeneity that occurs during cell growth [50].

Stable nanosuspensions have been produced, providing better colloidal stability with Tween 20 and higher Lyc stability over time with PVA. Cellular assays demonstrated that the internalization of Lyc@PLGA NPs in HaCaT and SK-MEL-2 spheroids was particularly affected by surfactant, rather than the antioxidant activity that is high in any case, thus contributing to the potential Lyc exploitation in skincare applications.

2. Materials and Methods

2.1. Materials

Tomato peel extract in oil form, obtained with SC-CO_2, has been kindly provided by the cosmetics farmer Licofarma s.r.l. (Galatina, Lecce, Italy). Lycopene $\geq$ 98%(HPLC) from tomato, PLGA, RESOMER RG 501, polyvinyl alcohol (PVA) Mw 31,000–50,000, 98–99% hydrolyzed, Tween 20, 2,2-Diphenyl-1-picrylhydrazyl (DPPH), 2′,7′-dichlorofluorescein diacetate (DCFDA, $\geq$97% HPLC, powder, cell-permeable non-fluorescent probe), and thiazolyl blue tetrazolium bromide (MTT) were purchased from Merck Life Science S.r.l. (Milan, Italy). DAPI was purchased from Thermo Scientific (Rockford, IL, USA). Dulbecco's Modified Eagle Medium (DMEM) (4.5 mg/L glucose) was purchased from Biowest (Nuaillé, France).

2.2. High-Performance Liquid Chromatography Analysis of Lyc in the TP Extract

For high-performance liquid chromatography (HPLC) analysis, an Agilent 1100 HPLC system (Santa Clara, CA, USA) consisting of a solvent tray, a vacuum degasser G1322A, a binary pump G1312A, an autosampler G1329A, a thermostatted column compartment G1316, and a diode array UV-vis detector G1315B was used. The system was controlled by Chemstation software (version number A.08.01 [783], Agilent).

Chromatographic separations were performed in isocratic mode at 30 °C using a Thermo Scientific Accucore C18 reversed phase column (2.6 μm, 10 cm × 2.1 mm). The detection wavelength was 472 nm. The mobile phase consisted of methanol and acetonitrile (50/50 *v*/*v*) at a flow rate of 0.3 mL/min.

2.3. Preparation of Lyc-Loaded PLGA Nanoparticles

Lyc@PLGA NPs were prepared modifying the emulsification solvent diffusion method described in the literature [51,52]. Briefly, 100 mg of PLGA (RESOMER RG 501, Merck Life Science S.r.l., Milan, Italy) was dissolved in 8 mL of ethyl acetate and solubilized for 2 h under agitation. Then, 12.5 mg of TP extract (measured density of 0.8 g/mL) was dissolved in 2 mL of PLGA solution to obtain a polymer (mg)/extract (mg) ratio of 2/1. This organic phase was mixed with 0.5 mL of filtered deionized water (0.45 μm filter) at 3.000 rpm for 30 min at RT. Afterwards, this first water-in-oil (*w*/*o*) emulsion was poured drop by drop using a syringe with a thin needle, into 10 mL of a 0.5% (*w*/*v*) surfactant solution, which was homogenized at 8000 rpm for 3 min, using an Ultra-Turrax blender model IKA T25 (IKA Werke, Staufen, Germany) in an ice bath. Two emulsifiers were used to compare different colloid stabilization actions, in detail: PVA (Mw 31,000–50,000, 98–99% hydrolyzed) obtaining Lyc@PLGA@PVA NPs and Tween 20 obtaining Lyc@PLGA@Tween 20 NPs. The resulting water-in-oil-in-water (*w*/*o*/*w*) emulsions were stirred overnight on a magnetic

stirring plate at 500 rpm to remove the organic solvent through evaporation. The produced nanoparticles were centrifuged at 15,000 rpm for 15 min at 4 °C and washed (with deionized water) three times to remove emulsifiers. The suspension was finally suspended in filtered deionized water, freeze-dried, and stored at 4 °C for the subsequent characterizations and biological studies.

2.4. Characterization of Lyc-Loaded PLGA Nanoparticles

2.4.1. Scanning Electron Microscopy

Morphological characterization of PLGA NPs has been performed by scanning electron microscopy, under a FESEM (MERLIN, Carl Zeiss GmbH, Oberkochen, Germany) operating at an accelerating voltage of 20 kV. A sample solution drop (10 μL) was placed on a standard TEM carbon-coated Cu grid and dried at room temperature.

2.4.2. Dynamic Light Scattering Analysis

Lyc@PLGA NPs' colloidal stability and size distribution were investigated by average hydrodynamic diameter, polydispersity index, and ζ-potential measurements through dynamic light scattering (DLS). Samples were analyzed with a Nano ZS90 (Malvern Instruments, Malvern, UK) instrument. The ζ-potential analysis was carried out by laser doppler velocimetry (LDV). Measurements were performed at 25 °C, in filtered distilled water (0.45 μm), at a concentration of 0.05 mg/mL, setting the refractive index of PLGA (1.33). The ζ-potential values are reported as the mean of 5 measurements; each of them was derived from 20 different runs to establish measurement repeatability. Particle size distribution data are reported as the mean of 3 measurements (each of them derived from 12 different runs) to warrant repeatability. Lyc@PLGA@PVA NPs and Lyc@PLGA@Tween 20 NPs were analyzed after synthesis and after 25 days of storage in aqueous solution at 4 °C.

2.4.3. UV–Vis Assay

Lycopene content in TP extract and PLGA NPs was determined by UV-vis spectrophotometry, scanning from 350 to 550 nm by a Jasco V-530 spectrophotometer (JASCO EUROPE s.r.l., Cremella, Italy). The samples were prepared in ethyl acetate. TP extract has been dissolved in the solvent at the concentration of 0.3 mg/mL. The Lyc loaded into PLGA NPs was extracted under NP dissolution by vortexing 2 mg of each sample in 1 mL of ethyl acetate for 3 min and sonicating in an ice bath for 30 min. The resulting solutions were then centrifuged at 15,000 rpm for 10 min at 4 °C before UV-vis analysis. The quantification has been performed referring to a standard curve using a Lyc standard from tomato (Merck Life Science S.r.l.) at known concentrations in the range 1.5–25 μg/mL in ethyl acetate; measurements of Abs values at λ_{max} 485 nm were chosen, and the line fitting has been performed through Origin software (version 93E) [31,53].

2.4.4. Fourier-Transform Infrared Spectroscopy

The vibrational features of the samples were analyzed by FT-IR spectroscopy. The direct analysis on Lyc@PLGA@PVA NPs and Lyc@PLGA@Tween 20 NPs was performed comparing PLGA (as a blank control) and Lyc@PLGA NPs in their freeze-dried form, whereas the TP extract was measured as a solution in ethyl acetate. A small aliquot of each sample was deposited onto the ATR element of an FT-IR spectrometer (PerkinElmer Spectrum One); the TP extract was allowed to evaporate completely prior to acquisition, while the freeze-dried nanoparticle powders were analyzed directly. The analysis on Lyc released by PLGA NPs was performed following NP dissolution as described in the previous Section 2.4.3. For each measurement, 64 scans were collected in the spectral

range 4000–600 cm^{-1}. All spectra were recorded under identical instrumental conditions to enable qualitative comparison.

2.5. Determination of Free Radical Scavenging Activity

Free radical scavenging activity has been determined by quantifying the inhibition of the DPPH reagent. TP extract was dissolved in ethyl acetate at a concentration of 6 mg/mL and then diluted in the working solutions to analyze DPPH inhibition to achieve the selected quantities of 0.25–0.5–1–2 mg. The scavenging activity of Lyc loaded into PLGA NPs was determined following NP dissolution as described in the previous Section 2.4.3. Briefly, 0.5 mL of the produced samples (TP extract and Lyc solution released by PLGA NPs) was added to 2.5 mL of 0.1 mM DPPH-methanolic solution and vigorously shaken in the dark at room temperature. The absorbance of samples at 515 nm was measured after 30 min. Ascorbic acid and methanol were used as positive and negative controls, respectively. Ascorbic acid (2 mg in 0.5 mL of water) was added to 2.5 mL of a 0.1 mM methanolic DPPH solution, in the same way as for the extract. The scavenging activity was calculated using Equation (1):

$$SA\% = \left[\frac{Abs\ control - Abs\ sample}{Abs\ control}\right] \times 100 \quad (1)$$

where *control* is the DPPH-methanolic solution.

2.6. Stability of Lyc-Loaded PLGA NPs

For the storage stability study, the powders of Lyc@PLGA@PVA NPs and Lyc@PLGA @Tween 20 NPs were kept at 4 °C for 5 months and analyzed for any change in Lyc content and percent residual scavenging activity [54]. Lyc content has been quantified at each time interval (0–2–3–5 months) using the procedure just described in Section 2.4.3. The retention index percentage has been calculated using the following Equation (2):

$$Retention\ index\ (\%) = \frac{C1}{C0} \times 100 \quad (2)$$

where C1 represents the Lyc content after storage (2–3–5 months), and C0 is the Lyc content before storage, at time 0 (after freeze-drying).

The retentional antioxidant was calculated using the following Equation (3):

$$Scavenging\ activity\ retention\ rate\ (\%) = \frac{D1}{D0} \times 100 \quad (3)$$

where D1 is the DPPH radical scavenging activity of the sample at different intervals of storage (2–3–5 months), and D0 is the DPPH radical scavenging activity of the sample before storage, at time 0 (after freeze-drying). Sample preparation and scavenging activity were performed as described in Section 2.5.

2.7. In Vitro Biological Studies of Lyc-Loaded PLGA NPs

2.7.1. Cell Culture and Spheroids Formation

HaCaT (obtained from CLS Cell Lines Service GmbH (Eppelheim, Baden-Wurttemberg, Germany) and SK-MEL-2 cell lines (ATCC (Manassas, VA, USA; HTB-72)) were maintained in Dulbecco's modified Eagle's medium (DMEM) supplemented with fetal bovine serum (FBS) (10%), penicillin (100 $U \cdot mL^{-1}$ culture medium), streptomycin (100 $mg \cdot mL^{-1}$ culture medium), and glutamine (5%). Cells were grown in a humidified incubator at 37 °C, 5% CO_2, and 95% relative humidity.

For the spheroid formation, HaCaT and SK-MEL-2 were trypsinized and seeded into each well of an ultra-low attachment U-shaped 96-well plate (Corning Costar 7007, Merck Life Science S.r.l., Milan, Italy) in 80 µL complete medium at cell densities of 12×10^4 cells/well and 8×10^4 cells/well, respectively. The U-plates were centrifuged at 3000 rpm for 20 min at 4 °C, and then the plates were transferred in the humidified incubator for at least 24 h to allow the spheroid formation and growth. The morphological characteristics of the spheroids, including their diameter and shape, were determined by microscopic optical analysis using an inverted EVOS XL Cell Imaging System microscope (Thermo Fisher, Waltham, MA, USA).

2.7.2. Cell Viability Test by MTT Assay

Cells were added to 24-well culture plates at 1 mL per well, and incubated at 37 °C, 5% CO_2, and 95% relative humidity for 24, 48, and 72 h with Lyc@PLGA@PVA NPs and Lyc@PLGA@Tween 20 NPs (50–100–200 µg/mL). The control was a complete culture medium. After the incubation period, cultures were removed from the incubator, and MTT solution (5 mg/mL) was aseptically added. Cultures were returned to the incubator and incubated for 3 h. Afterwards, the cultures were removed from the incubator, and the resulting MTT formazan crystals were dissolved in DMSO. The plates were ready within 15 min after adding DMSO. After the incubation time, pipetting up and down was required to completely dissolve the MTT formazan crystals. Absorbance at a wavelength of 570 nm was measured using a Microplate Reader CLARIOstar PLUS (BMG LABTECH, Ortenberg, Germany). Calculate the percentage of cell viability using Equation (4):

$$Cells\ Viability\ (\%) = \frac{Abs\ (t)}{Abs\ (nt)} \times 100 \quad (4)$$

where Abs (t) is the absorbance of treated cells and Abs (nt) is the absorbance of non-treated cells. The results are expressed as mean ± SD of three separate experiments.

Spheroid viability upon incubation with Lyc@PLGA@PVA NPs and Lyc@PLGA@Tween 20 NPs was measured by MTT assay, as described by Bresciani et al., 2019 [55]. Briefly, on the third day, spheroids covered by 80 µL of medium were incubated with NP suspensions at different concentrations (50, 100, and 200 µg/mL). After 24 h of incubation, the medium was removed, the spheroids were washed with PBS, and 100 µL of 5 mg/mL MTT solution was added to each well. After 3 h of incubation, the MTT solution was removed, the insoluble formazan crystals were dissolved with 100 µL of dimethyl sulfoxide, and the absorbance at 570 nm was measured in a Microplate Reader CLARIOstar PLUS. Cell viability percentage was calculated using Equation (4). The results are expressed as mean ± SD of three separate experiments, in which four spheroids were used for each condition.

2.7.3. Cellular Uptake of Lyc-Loaded PLGA Nanoparticles by Confocal Imaging

HaCaT (12×10^4 cells) and SK-MEL-2 (8×10^4 cells) spheroids were seeded as explained above and treated with nanoparticle suspension with a concentration of 100 µg/mL. After rinsing with phosphate-buffered saline (PBS) twice, spheroids were fixed with PFA 4% for 20 min at RT, followed by three washes with PBS, then stained with DAPI for 1 h. The stained spheroids were stored in PBS at 4 °C until imaging. The spheroids were imaged as z stacks with a Zeiss LSM700 confocal microscope (Zeiss, Oberkochen, Germany) equipped with a Zeiss Axio Observer Z1 inverted microscope using a 10× and 20× objective with a 1.46 numerical aperture for imaging using the same settings between repeats. Laser beams with 405 nm and 488 nm excitation wavelengths were used for DAPI and FITC for lycopene imaging, respectively. Spheroid volume was calculated using ImageJ v1.51n software with the 3D Object Counter v2.0 plugin. The threshold for background and object

voxels was manually adjusted for each image in order to capture the whole volume of each spheroid [56,57].

2.7.4. Intracellular Reactive Oxygen Species Measurement by DCFDA Assay

A total of 3×10^5 HaCaT cells and 2×10^5 SK-MEL-2 cells were seeded into 6-well culture plates with 2 mL of media per well and incubated for 72 h in order to reach a final confluence of 80%. Both cell lines were first treated for 24 h at 37 °C with the PLGA NP suspensions and, simultaneously, with H_2O_2 to induce exogenous stress (1 mM). Twenty-four hours later, the cells were exposed to a 10 µM DCFDA solution for 30 min. After that, period cells were collected, washed twice with PBS, and subjected to centrifugation at 1200× *g* for 5 min at room temperature. Subsequently, the cell pellet was resuspended in PBS supplemented with 1% FBS and the cells were analyzed. The results are expressed as mean ± SD of three separate experiments.

Three-day-old 3D spheroids of HaCaT (12×10^4 cells/well) and SK-MEL-2 (8×10^4 cells/well) were selected for reactive oxygen species (ROS) analysis. These spheroids were exposed for 24 h at 37 °C to PLGA NP suspensions supplemented with 1 mM H_2O_2. After the incubation period, all spheroids were rinsed with 10 mL of PBS and were collected in a 15 mL tube. After centrifugation (5 min, 400× *g*), spheroids were incubated for 30 min with DCFDA solution (10 µM), washed twice with PBS, and subjected to centrifugation at 1200× *g* for 5 min at room temperature. Subsequently, the cell pellet was resuspended in PBS supplemented with 1% FBS and the cells were analyzed. The results are expressed as mean ± SD of three separate experiments, in which 12 spheroids were used for each condition.

Flow cytometry was performed on a flow cytometer (BD Biosciences, San Jose, CA, USA) equipped with Cytexpert software (version 2.6).

3. Results

3.1. Characterization of TP Extract

TP extract (Licofarma s.r.l., Galatina, Italy) and Lyc standard, both in ethyl acetate, have been analyzed by HPLC. As illustrated in Figure 1, the chromatogram of TP extract shows a peak at retention time (Rt) of 9.91 min, in line with the peak at Rt 9.94 min of the Lyc standard.

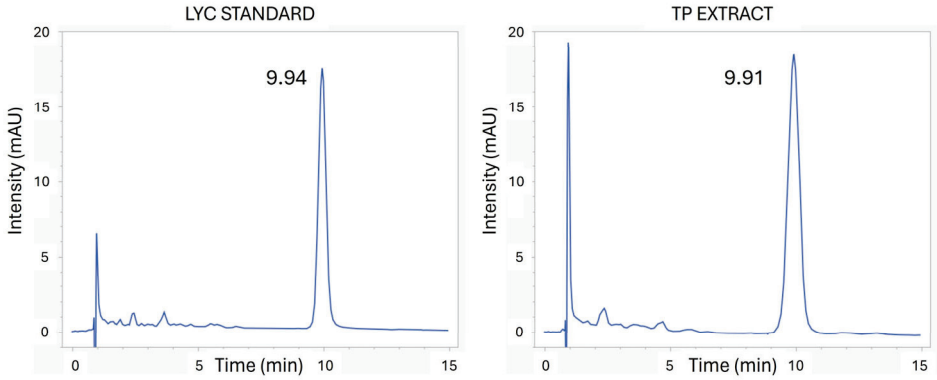


Figure 1. HPLC chromatograms (λ = 472 nm) of Lyc standard and TP extract in ethyl acetate.

This comparison has also been made with UV-vis. As we can observe in Figure 2, the absorption spectrum of Lyc has been recorded in the extract solubilized in the same solvent.

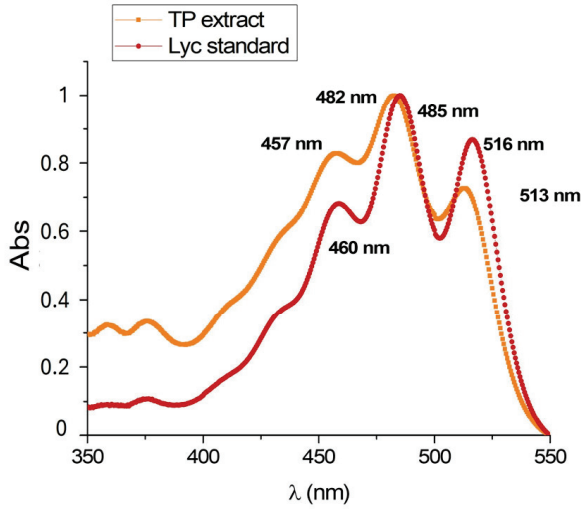


Figure 2. UV-vis spectrum of TP extract and Lyc standard in ethyl acetate.

Lycopene from TP extract obatained with SC-CO_2 (Licofarma s.r.l.) showed three absorbance peaks (λ_{max}) at 457, 482, and 513 nm, consistent with those obtained for the Lyc standard from tomato (Merck Life Science S.r.l.) (460 nm, 485 nm, and 516 nm).

Bioactivity in terms of free radical scavenging activity has been determined by DPPH inhibition test, testing TP extract solubilized in ethyl acetate. As demonstrated in Figure S1, the antioxidant activity increases linearly with an increasing amount of dissolved extract. At 2 mg, a percentage of 96 is achieved, which is equivalent to the activity observed for the same amount of ascorbic acid, which was utilized as a positive control.

3.2. Charaterization of Lyc@PLGA NPs

3.2.1. Influence of Surfactants on NP Physicochemical Properties

DLS analysis has been used to study the surfactant influence on particle size, zeta potential, and colloidal stability of Lyc@PLGA NP aqueous suspensions. Table 1 reports the ζ-potential, average hydrodynamic diameter (Z-average), and polydispersity index (PdI) of Lyc@PLGA@PVA NPs and Lyc@PLGA@Tween 20 NPdiluted suspensions.

Table 1. DLS parameters measured on diluted Lyc@PLGA NP suspensions in filtered distilled water (0.45 μm).

Sample	ζ-Potential (mV) [1]	Z-Average (nm) [2]	PdI [3]
Lyc@PLGA@PVA NPs	−28.6 ± 1.15	393.5 ± 25.19	0.44 ± 0.021
Lyc@PLGA@Tween 20 NPs	−43.6 ± 1.47	177.6 ± 8	0.4 ± 0.016

[1] ζ-potential values are reported as the mean (±standard deviation) of 5 measurements; each of them is derived from 20 different runs; [2] Z-average (±standard deviation) is the average hydrodynamic diameter of 3 distribution size measurements, and each one consists of 12 runs; [3] polydispersity Index (PdI) is reported as the mean (±standard deviation) of 3 distribution size measurements, and each one consists of 12 runs.

The ζ-potential values $\geq$ |20 mV| and PDI $\leq$ 0.5 indicated stable colloidal suspensions for both the used surfactant. The utilization of Tween 20 produced particles with a more negative charge and a lower average hydrodynamic size compared to PVA. The improved size distribution due to Tween 20 is evident in the intensity plot shown in Figure S2. No difference was measured between the PDIs, indicating that both suspensions have good homogeneity. A higher negative charge is also found in particles produced with Tween 20 when empty particles are produced under the same conditions without the addition of the extract, as shown in Table S1. However, the PLGA@Tween 20 NPs' |ζ-potential| is lower than the |ζ-potential| of Lyc@PLGA@Tween 20 NPs ($\cong$−30 vs. $\cong$−44 mV). No

differences in terms of average size and polydispersity have been registered for empty NPs. Furthermore, the colloidal stability is maintained for 25 days in an aqueous suspension, as indicated by the unaltered DLS parameters reported in Table S2.

Morphological analysis by SEM confirmed the formation of spherical particles with real dimensions in the range 100–200 nm, as can be observed in representative SEM images in Figures 3 and S3.

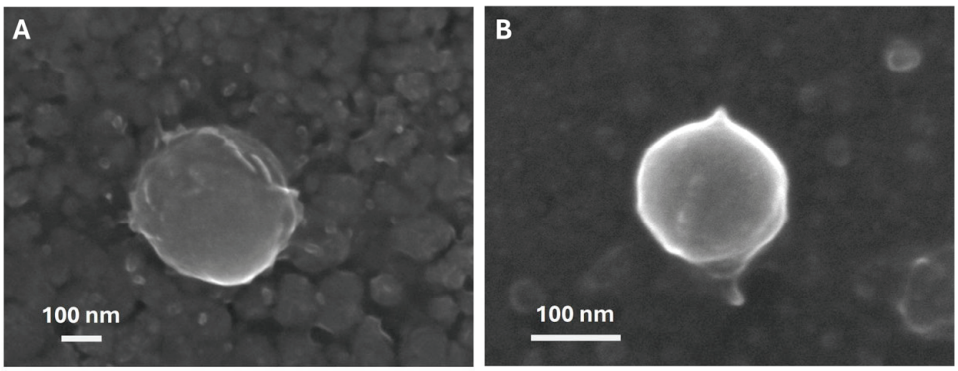


Figure 3. Representative SEM images at different magnifications of a single particle, for (**A**) Lyc@PLGA@PVA NPs and (**B**) Lyc@PLGA@Tween 20 NPs.

3.2.2. Influence of Surfactants on Lyc Encapsulation and Stability

The qualitative verification of Lyc encapsulation was obtained through FT-IR analysis conducted on Lyc@PLGA NPs, blank PLGA, and the TP extract. In Figure 4, organized into four single-spectrum panels (Figure 4A–D), the vibrational profiles are presented separately in order to clearly highlight the spectral regions associated with Lyc. Panels A and B show the spectra of freeze-dried NPs, Lyc@PLGA@PVA NPs (red line), and Lyc@PLGA@Tween 20 NPs (green line), respectively, whereas panels C and D report the FT-IR spectra of PLGA (black line) and the TP extract analyzed in ethyl acetate (blue line). In panels A and B, the blue dashed rectangles mark the aliphatic C–H stretching region (3000–2800 cm^{-1}) associated with (C–H) groups typical of carotenoids and clearly visible in the TP extract (panel Figure 4D). The red arrows indicate the conjugated C=C stretching vibrations (1600–1500 cm^{-1}), which represent the fundamental signature of the polyene chain of Lyc. The blue arrows highlight the region between 850 and 750 cm^{-1}, where Lyc exhibits characteristic out-of-plane C–H bending and torsional vibrations of the polyene backbone—features that are not observed in blank PLGA. These Lyc-associated bands appear in both nanoparticle formulations but are absent in the blank PLGA (panel Figure 4C), which display only the typical polymer-related vibrations, including the strong ester C=O stretching band at 1750 cm^{-1} and the C–O–C stretching region between 1300 and 1100 cm^{-1}.

The integrity of Lyc after release from the nanoparticles was further evaluated by analyzing the spectra of the formulations dissolved in ethyl acetate, as shown in Figure S4. The spectra of the dissolved NPs exhibited the full set of Lyc-associated features, including the aliphatic C–H stretching (3000–2800 cm^{-1}), the conjugated C=C stretching modes (1600–1500 cm^{-1}) and, notably, the characteristic band at 960 cm^{-1}, attributed to the out-of-plane =C–H bending of all-trans Lyc (see Figure S4).

FT-IR spectra features have also been verified by UV-vis analysis. In Figure S5, UV-vis spectra of Lyc solution following NP dissolution at time 0 are reported. By comparing these spectra with those shown in Figure 2, we can confirm that the molecule has not been modified after being encapsulated and released from the produced nanoparticles. The UV-vis calibration curve (λ_{max} 485 nm) has been used for the quantification of encapsulated Lyc following dissolution of the same quantity of NPs. The Lyc@PLGA@PVA

https://doi.org/10.3390/antiox15010136

NPs and Lyc@PLGA@Tween 20 NPs have been loaded with 3.2 ± 0.29 µg/mg NPs and 2.1 ± 0.36 µg/mg NPs of Lyc, respectively. These data are obtained as the average of three independent synthesis batches. The PVA stabilization protocol results in a higher load of Lyc from the feeding TP extract.

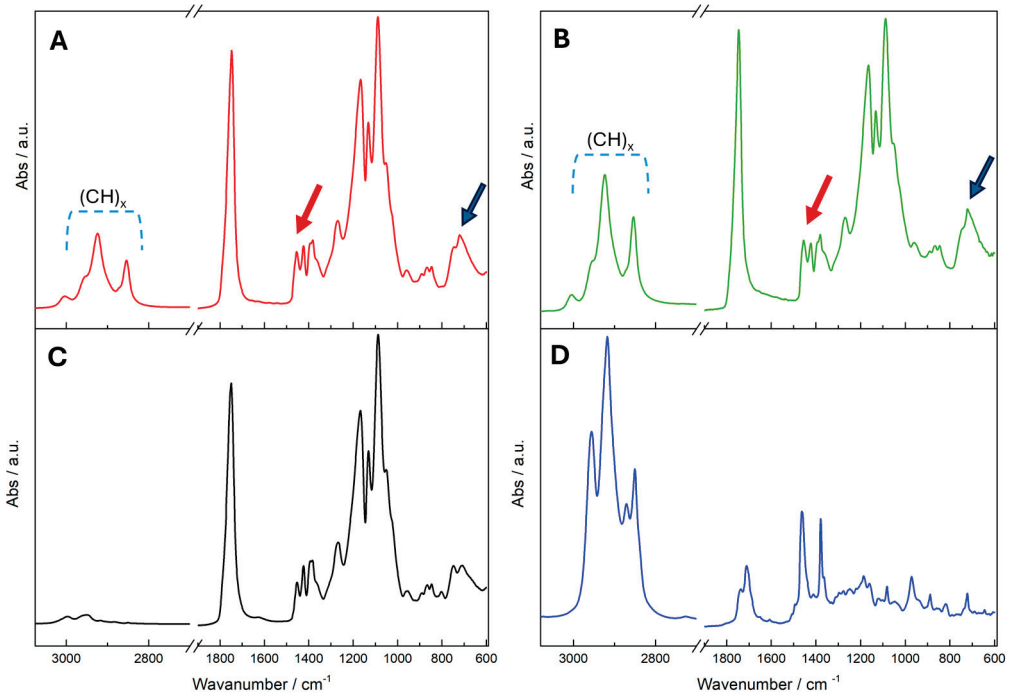


Figure 4. FT-IR spectra of Lyc@PLGA@PVA-NPs (**A**), Lyc@PLGA@Tween20-NPs (**B**), PLGA (**C**) and TP extract in ethyl acetate (**D**). Dashed rectangles indicate the aliphatic C–H stretching region (3000–2800 cm^{-1}). Red arrows denote the conjugated C=C stretching vibrations of lycopene (1600–1500 cm^{-1}), while blue arrows highlight the characteristic out-of-plane C–H bending modes of the lycopene polyene chain in the 850–750 cm^{-1} region.

A UV-vis quantification assay has also been used to measure the Lyc retention index over time from Lyc@PLGA NP powder (at 4 °C). As we can observe in the plot of Figure 5A, PVA emulsifier provided a higher stability in terms of Lyc retention than Tween 20.

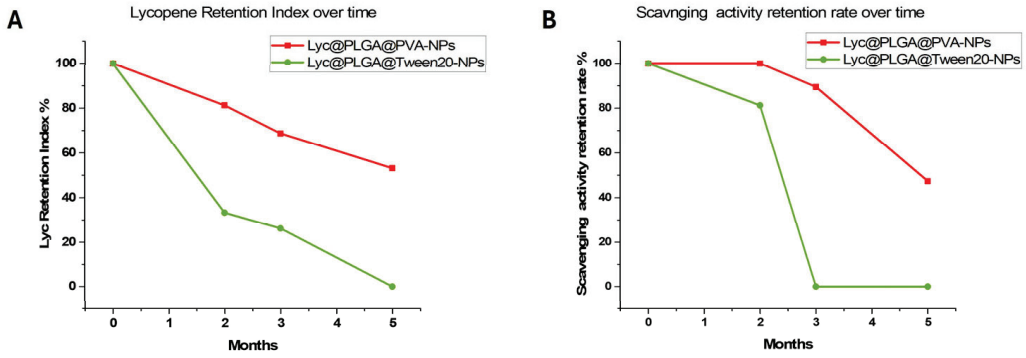


Figure 5. (**A**) Lyc retention index % and (**B**) scavenging activity retention rate % of freeze-dried Lyc@PLGA@PVA NPs and Lyc@PLGA@Tween 20 NPs over time, stored at 4 °C.

The Lyc@PLGA@PVA NP particles lose 40% of the encapsulated Lyc after 5 months of storage; on the other hand, the Lyc@PLGA@Tween 20 NPs lose all their content due to greater degradation of the compound during storage.

https://doi.org/10.3390/antiox15010136

The stability of Lyc loaded into PLGA@PVA NPs has also been confirmed by a DPPH assay measuring the antioxidant activity retention percentage of Lyc solutions after Lyc@PLGA NP dissolution. In the plot of Figure 5B, we can observe a low loss of antioxidant activity after 5 months of storage for PLGA@PVA NPs. For the Lyc@PLGA@Tween 20 NPs, scavenging activity has been maintained after 2 months of storage despite the loss of ≅80% of Lyc retention. After three months of storage, the retained Lyc in the Tween 20 NPs was inactive under the investigated conditions.

Considering the measured Lyc retention over time by UV adsorption, samples that are more than one month old are not ideal for internalization studies using fluorescence, whether for PVA or Tween 20. Then, to facilitate the study of surfactants' influence on Lyc@PLGA NPs' interaction with spheroids, the nanoparticles used for biological testing were no older than one month.

3.3. Influence of Surfactants on Lyc@PLGA NPs' Interaction with HaCaT and SK-MEL-2 Spheroids

3.3.1. Cell Viability and Uptake of Lyc@PLGA NPs

MTT data, reported in Figure S6, indicated a low reduction in cell viability of HaCaT adherent cells after treatment with Lyc@PLGA@Tween 20 NPs at 200 μg/mL, that does not change over time (Figure S6A). SK-MEL-2 adherent cell viability has been affected by both NPs, with a linear decrease in percentages increasing Lyc@PLGA@Tween 20 NP concentrations over time (Figure S6B). Concerning Lyc@PLGA@PVA NPs, the toxic effect, revealed at 200 μg/mL after 48 h of treatment, does not persist after 72 h, suggesting a slowdown in cell proliferation (Figure S6B). MTT data on HaCaT and SK-MEL-2 spheroids have shown that both the produced NPs do not affect cell viability after 24 h of treatment at 100–200 μg/mL (Figure S6C,D). These NP concentrations have been selected for the subsequent biological assays.

The normalized fluorescence intensities by confocal microscopy analysis of the treated spheroids are reported in Figure 6. Fluorescence intensity referred to Lyc excitation at 488 nm. Normalization was performed with respect to the volume of the spheroid that was analyzed. In Figure 6A–D, representative images of HaCaT and SK-MEL-2 spheroids after 24 h of treatment are reported.

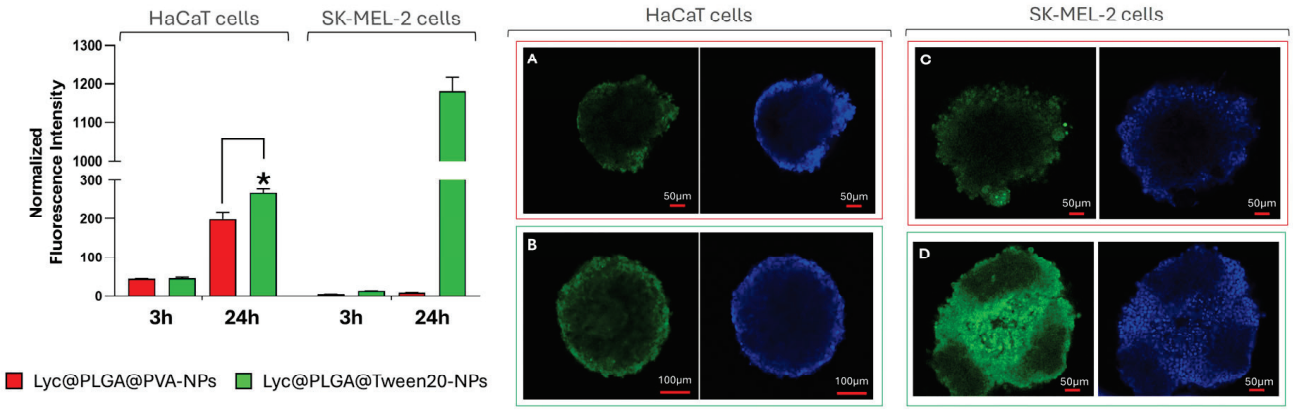


Figure 6. Uptake of Lyc@PLGA@PVA NPs and Lyc@PLGA@Tween 20 NPs in HaCaT and SK-MEL-2 spheroids by confocal imaging. On the left, intensity fluorescence (normalized for spheroid volume) measured after 3 and 24 h of treatment. Data have been reported as mean ± SD of 3 spheroids for each condition, analyzing 30 z stacks. Statistically significant value (*) $p \leq 0.05$ versus Lyc@PLGA@PVA NP 24 h treatment, from the *t*-test. On the right, representative images of HaCaT and SK-MEL-2 spheroids after 24 h of treatment with Lyc@PLGA@PVA NPs (**A**,**C**) and Lyc@PLGA@Tween 20 NPs (**B**,**D**); in green, emitted fluorescence of Lyc ($\lambda_{exc.}$ = 488 nm), and in blue, cell nuclei stained with DAPI ($\lambda_{exc.}$ = 405 nm).

HaCaT spheroids showed an increase in Lyc@PLGA NP internalization over time. As a function of time, there is a marked increase in normalized intensity, with a 4.5-fold rise observed for Lyc@PLGA@PVA NPs and with a ≅6-fold rise for Lyc@PLGA@Tween 20 NPs, from 3 to 24 h of treatment. The significant difference between Lyc@PLGA@PVA NPs and Lyc@PLGA@Tween 20 NPs at 24 h indicated an impact of surfactant on NP uptake in HaCaT spheroids.

SK-MEL-2 spheroids showed very low internalization for both investigated NPs after 3 h of incubation. Instead, a clear difference between the two surfactants has been observed after 24 h of incubation. Lyc@PLGA@PVA NP internalization remained at the low value that had been recorded at 3 h, instead of Lyc@PLGA@Tween 20 NP internalization, which considerably increased from 14.3 ± 0.26 to 1182 ± 34.4.

The gallery images reported in Figure S7 show the penetration of NPs across spheroids after 24 h of incubation. Concerning HaCaT spheroids, we observe that Lyc@PLGA@Tween 20 NPs were internalized more than Lyc@PLGA@PVA NPs, as measured by fluorescence quantitative analysis. Clearly, there is a greater accumulation of all particles along the periphery of the spheroid on the top, compared to a more homogeneous distribution on the bottom. Greater uniformity is observed for Lyc@PLGA@Tween 20 NPs penetration than Lyc@PLGA@PVA NPs (see Figure S7).

3.3.2. Antioxidant Activity of Lyc@PLGA NPs

ROS production percentages measured with DCFDA assay are reported in Figure 7. HaCaT and SK-MEL-2 adherent cells and spheroids have been treated with 200 μg/mL of Lyc@PLGA@PVA NPs and Lyc@PLGA@Tween 20 NPs and H_2O_2 (1 mM) for 24 h. Representative flow cytometric spectra of intracellular ROS analysis are reported in Figure S8. The negative control is defined as the condition that has not been subjected to any treatment, while the positive control is defined as the condition that has been subjected to treatment with only H_2O_2.

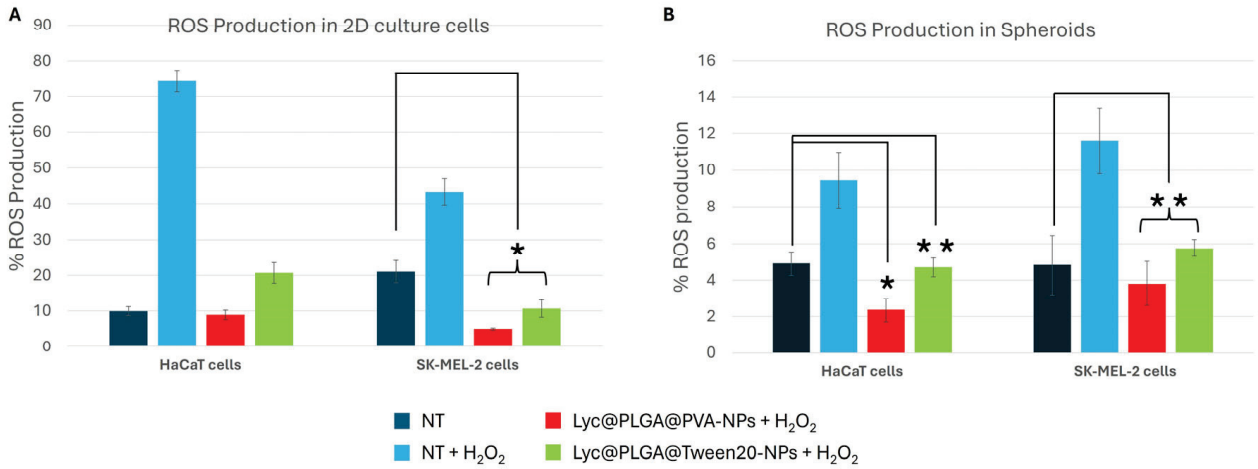


Figure 7. ROS production percentages in HaCaT and SK-MEL-2 2D culture (**A**) and HaCaT and SK-MEL-2 spheroids (**B**), reporting the negative control as the untreated condition (blue histograms), the positive control as treatment with only H_2O_2 (light blue histograms), and treated conditions as treatment with NPs and H_2O_2 (red and green histograms). (**A**) Data have been reported as the mean ± SD of 3 experiments; (**B**) data have been reported as the mean ± SD of 3 experiments, in which 12 spheroids were used for each condition. Statistically significant value (*) $p \leq 0.05$ and (**) $p \leq 0.5$ are versus the non-treated condition (blue histograms), from the *t*-test.

The ROS inhibition effect of Lyc-loaded NPs is evident for both investigated samples, in 2D as well as in spheroids. Lycopene delivered by PLGA NPs restores ROS levels

to those of the control condition, despite the oxidative stimulus of hydrogen peroxide. This effect has been detected both in 2D and spheroids. In SK-MEL-2 adherent cells, a significative ROS reduction with respect to the non-treated condition has been detected, following Lyc@PLGA@PVA NP and Lyc@PLGA@Twen 20 NP incubation (Figure 7A). This ROS reduction with respect to the non-treated condition has also been found in HaCaT and SK-MEL-2 spheroids (Figure 7B).

4. Discussion

The TP extract, obtained with SC-CO_2, has been kindly provided by Licofarma s.r.l. (Galatina, Lecce, Italy) in the oil form. Many analytical methods have been used to assess Lyc isomers in food or extracts, such as UV–vis spectrophotometry and HPLC [21]. Solubilization of Lyc is quite difficult due to its high hydrophobic index. Here, we dissolved both commercial and TP extract in ethyl acetate, taking advantage of Lyc's high solubility in this solvent (145.3 mg/mL), which is also used to synthesize PLGA nanoparticles. The chromatographic profile of TP extract corresponds to that of the standard in the same solvent (ethyl acetate) and HPLC conditions. The compounds are separated by their Rt values, which, for the all-trans-lycopene standard and its isomers, are in the range of 8–20 min, using C18 and C30 columns [21]. The major compound identified in the extract was Lyc at Rt 9.91 min, consistent with the identified peak of commercial Lyc (see Figure 1).

UV–vis spectrophotometry has been employed for the simple and rapid detection of Lyc in TP extract, comparing with the commercial standard. The UV-vis spectrum of Lyc samples in organic solvents reported different maximum absorption wavelengths depending on the different solubilization methods [21]. Scanning the region 350–550 nm, three maximum absorbance bands have been revealed at λ_{max} 457, 482, and 513 nm [31,53], similar to those obtained for the tomato Lyc standard (λ_{max} 460, 485, and 516 nm); see Figure 2. The measured Abs at λ_{max} 485 nm has been chosen for the quantification experiments on Lyc@PLGA NPs.

The DPPH assay has confirmed the great antioxidant activity of TP extract thanks to the comparison with the same quantity of ascorbic acid, used as a positive control (96% of inhibition for both samples). The chemical nature of these compounds is different; Lyc is a hydrophobic molecule, and ascorbic acid is a water-soluble vitamin. Despite this difference, they are important nutrients found in fruit and vegetables (particularly tomatoes), and they work together to promote cellular health, reducing inflammation, supporting the immune system, and protecting skin from oxidative stresses. Lipid-soluble Lyc acts within cell membranes, while water-soluble ascorbic acid acts within the cytoplasm, although they work together to neutralize ROS and regenerate other antioxidants, such as vitamin E. The dose-dependence assay enabled us to evaluate the effect of extract concentration on the DPPH protocol and determine the concentration at which almost 100% inhibition was achieved. The high scavenging activity of TP extract resulted in dose dependence; this data is important given that the TP extract is in oil form. The linearity of in vitro antioxidant activity excludes that the solubilization of a given amount of Lyc contained in the extract can be affected by heterogeneity of lipid matrix.

Having verified the presence of Lyc in the initial extract and determined the optimal conditions for its characterization and quantification, we proceeded to focus on its efficient encapsulation.

PLGA is a copolymer approved by the U.S. FDA and is currently used in a broad range of biomedical applications thanks to its biocompatibility, biodegradability, and capacity to preserve loaded drug degradation [58]. Lyc@PLGA NPs have been fabricated through the double emulsion method using ethyl acetate as the organic solvent and a polymer/TP extract ratio of 2/1. The effects of polymer concentration, the type of organic

https://doi.org/10.3390/antiox15010136

solvent used, temperature, and the injection and agitation rates of the organic and aqueous phases were widely studied [59]. However, surfactants play a key role in the stabilization phase of polymeric NP emulsion formation, in their size, and finally, in biological interactions [45–47].

We have compared two non-ionic and biocompatible surfactants: Tween 20 and PVA. Tween 20 is the commercial name for polysorbate 20, a type of emulsifier utilized in food and pharmaceutical fields, as well as cosmetics, particularly in products for the skin, hair, and nails. PVA offers interesting versatility for a variety of industrial applications, including controlled drug delivery systems, tissue adhesion barriers, transdermal patches, and tissue engineering [48]. The deposition of non-ionic surfactants at the interface of emulsified w/o droplets affected their size, and therefore affected the final colloidal stability and PdI. The average hydrodynamic diameter (see Table 1) and the size distribution by intensity (see Figure S2) suggest that Tween 20 has a greater stabilizing effect. The smaller Z-average (Table 1) of the Lyc@PLGA@Tween 20 NPs means there is less aggregation of nanoparticles in solution than with PVA. Under SEM observation, the actual sizes of Lyc@PLGA@PVA NPs and Lyc@PLGA@Tween 20 NPs are very similar (see Figure 3 and Figure S3). The colloidal stability in water has also been confirmed by ζ-potential measurements, which differed between the two surfactants. Nanoparticles acquire a surface charge of $\cong -44$ mV with Tween 20, compared to $\cong -30$ mV with PVA (Table 1). Both NPs maintained this negative charge after 25 days in suspension (Table S2), suggesting a stabilization effect of carriers in liquid media over time. The more negative ζ-potential value of Lyc@PLGA@Tween 20 NPs confirmed their improved distribution in size, since this parameter is recognized as an indicator of colloidal stability. When the surface charge of NPs is homogeneous (i.e., either positive or negative), the Van der Waals and electrostatic forces are known to oppose each other, leading to the formation of a stable suspension, without flocculation or precipitation [60]. PLGA nanoparticles are typically negatively charged due to the carboxyl groups on the polymer surface, with a ζ-potential often around -20 mV, as confirmed by our measurements (see Table S1). As both PVA and Tween 20 are non-ionic, the interpretation of the ζ-potential in order to predict the stability of our colloidal nanosuspensions is linked to the resulting surfactants' steric effect [48]. Furthermore, considering the DLS parameters values for empty NPs, we can deduce that the adsorption of these hydrophilic emulsifiers on Lyc@PLGA NPs reduced their hydrophobicity and decreased the interfacial tension between Lyc and PLGA, leading to relatively homogeneous and stable nanosuspensions. Our data suggested that Tween 20's emulsification capability is superior to that of PVA, concerning Lyc-loaded NPs. This result is not in accordance with previous reports [61,62], suggesting that the interaction with the loaded compound could also play a crucial role. A previous study on Lyc-loaded polysaccharide NPs showed that PVA concentration significantly impacts colloidal stability and molecule loading [63]. The high hydrophilic–lipophilic balance and low critical micelle concentration of polysorbates give Tween 20, when used, high surface activity, even at low concentrations (the protocol provided for 0.5% w/v of both surfactants). Instead, PVA stabilizes emulsions by forming an interconnected network with the polymer at the interface (through hydrogen bond formation), resulting in a fraction of PVA remaining associated on the NPs [48,64]. This feature can be observed by comparing the morphological structure of the synthesized NPs. Thin ridges have been primarily observed on the surface of Lyc@PLGA@PVA NPs (see Figure 3), suggesting the presence of an emulsifier.

Material choice, including emulsifiers, affect particle size, zeta potential, surface morphology features, and also drug loading [48,49]. Lycopene loading has been verified through FT-IR analysis on freeze-dried NPs and on Lyc solution after NP dissolution. The FT-IR analysis offered a qualitative indication of Lyc encapsulation within the PLGA

nanoparticles. As shown in Figure 4, the spectra of the loaded formulations were dominated by the characteristic bands of the polymer matrix, and FT-IR therefore could not provide quantitative information on Lyc content. Although the overall spectral profile of both Lyc@PLGA NPs resembles that of blank PLGA due to the predominance of the polymer matrix, marked differences emerge in the highlighted regions, confirming the contribution of the encapsulated Lyc [65–67]. The attenuation and partial overlap of these signals can be attributed to matrix effects and to the solid-state nature of the formulations, a behaviour commonly observed for carotenoids embedded in polymeric carriers [68,69]. Despite these intrinsic limitations, the subtle yet reproducible spectral differences detected in the relevant regions of Figure 4 were sufficient to qualitatively confirm encapsulation. The analysis performed after NP dissolution (Figure S4) further reinforced these observations. Under homogeneous solvent conditions, the vibrational profile of the released Lyc matched that of the TP extract, suggesting that the encapsulation and release processes did not cause detectable alterations to the characteristic polyene structure. The persistence of the characteristic band at 960 cm^{-1} confirms that the polyene chain remained intact, and that the carotenoid preserved its structural configuration throughout the formulation and release processes [67,70]. Although qualitative, this agreement supports the conclusion that the molecule maintains its structural integrity throughout the process. Overall, FT-IR offered qualitative confirmation of Lyc encapsulation and complemented the quantitative loading values obtained through UV–vis analysis.

UV-vis analysis has been used to quantify loaded Lyc; the calculated value of μg Lyc/mg NPs indicates a higher compound content for Lyc@PLGA@PVA NPs. Larger particles commonly have a higher drug loading capacity; moreover, PVA has been widely demonstrated to be highly efficient in synthesizing carriers for the effective loading of different drugs [48,71].

In addition, emulsifiers, such as polysorbate and PVA, are also known to confer stability to NPs during storage in an aqueous medium and/or after freeze-drying. The colloidal stability of Lyc@PLGA NP aqueous suspensions has been discussed relating to DLS parameters. In view of the unstable nature of the compound, a series of tests were also carried out to assess the stability of loaded Lyc over time. These tests evaluated the retention and antioxidant activity of Lyc, following NP powder dissolution after storage. The protective effect of PLGA on Lyc has previously been demonstrated in a simulated gastrointestinal tract system [44]. Emulsifiers could also play a key role in retaining and stabilizing Lyc [72]. Retention index and scavenging activity percentages suggested a better capacity to protect Lyc toward degradation for Lyc@PLGA@PVA NPs with respect to Lyc@PLGA@Tween 20 NPs, in accordance with the known strong interaction of PVA with the NP surface [48]. There is a linear tendency between both measured indexes and storage time for Lyc@PLGA@PVA NPs. Regarding the Lyc@PLGA@Tween 20 NPs, the scavenging activity remained after two months of storage, despite a considerable loss of Lyc. This is probably due to isomers forming as a result of Lyc degradation; these isomers nevertheless remain bioactive [6,19]. Our results confirmed the strategic role of nanoparticles, comparing with microencapsulation and electrospinning techniques which provide a Lyc retention rate of 30–50% after ≅30 days of storage at room temperature, and ≅40% after 14 days at 4 °C [18,73]. The delayed degradation that has been observed, especially for Lyc@PLGA@PVA NPs, is comparable to that found for other nanocarriers [30,72,74].

Our primary objective was to compare the influence of two non-ionic surfactants (PVA and Tween 20) on NP performance. Crucially, we relied on Lyc's intrinsic emitted fluorescence to monitor internalization in human spheroids, deliberately avoiding external probes that could alter the physicochemical properties of the carriers. Considering the measured Lyc retention over time, samples older than one month exhibit reduced UV

absorption, rendering them unsuitable for accurate internalization studies. Consequently, to disentangle storage-related degradation from the surfactant's actual impact on cellular interaction, and to ensure comparable PLGA NPs properties, we performed biological assays using samples within a defined post-synthesis timeframe ($\leq$1 month).

Furthermore, the performed stability assays on NP aqueous suspensions and stored powder consist of a preliminary screening to support future dermatologic formulation and shelf-life validation.

In this context, the evaluation of surfactant-induced stability in an efficient biological environment represents a fundamental rational basis for the study. Indeed, ensuring that the Lyc remains encapsulated and protected from rapid degradation is a mandatory prerequisite; without proof of such foundational stability and antioxidant retention, further complex investigations, such as Franz diffusion cell experiments, would lack a scientifically sound starting point.

The biological interactions of NPs are contingent on their size and surface phenomena. Consequently, the cellular uptake and bioactivity of delivery systems are also dependent on the surfactants used [46,47]. Their hydrophilic nature promotes interaction with cells, ligands, and proteins, which may lead to benefits as well as potential toxic effects that need to be investigated [48].

First, we studied cell availability through MTT tests treating HaCaT and SKMEL-2, 2D and 3D cultures, with different concentrations of Lyc@PLGA@PVA NPs and Lyc@PLGA@Tween 20 NPs. MTT data (see Figure S6) suggested that 100 μg/mL and 200 μg/mL of Lyc@PLGA@ NPs could safely be used to treat cells for 24 h.

The skin is a complex organ composed of multiple layers. The most superficial layer is the epidermis, which represents the main physical and chemical barrier to permeation by bioactive agents and NPs. Keratinocytes are the most abundant cell type in the epidermis, accounting for 90% of cells. They are responsible for producing keratin, the organ's major physical barrier [75]. It has been established that NPs are able to penetrate the skin via the same pathways that have been described for other substances. However, it is important to note that the ability of NPs to penetrate varies according to their size, composition, and colloidal stability [75]. For example, negatively charged NPs cross the epidermis more easily than those with a positive charge [76]. Polymeric NPs can cross the epidermis by penetrating the stratum corneum, accumulating on the upper surface, and penetrating the hair follicle (where melanocytes are located) [75].

There are a few problems with using 2D human keratinocytes and melanocytes as a replacement for animal experiments. The main problems are that they do not replicate the in vivo complexity, the cellular architecture comprising the extracellular matrix microenvironment, and cell–cell interactions. Three-dimensional cell culture systems overcome many of these limitations, more closely mimicking the complex phenotypic heterogeneity produced during cell growth [50,77]. The merits of in vitro skin 3D models extend to the field of cosmetics development. Regarding skin applications, the utilization of animal models frequently proves to be suboptimal. It is a commonly held view that economically advantageous species, which include rodents, have a skin composition that is too dissimilar to human skin. Conversely, animals with more human-like skin, such as pigs, are too difficult to manage and too expensive for regular use. Moreover, ethical considerations further underscore the limitations of animal models in skin research.

We investigated the uptake and penetration of Lyc@PLGA NPs across spheroids of HaCaT and SK-MEL-2 cells, to ascertain the function of PLGA NPs and the impact of surfactants. The employment of spheroids is a very interesting tool due to their simplicity, low cost, and high reproducibility. Hence, they are suitable for high-throughput cell function and cytotoxicity analysis, biochemical analysis, and different imaging techniques, including

confocal microscopy [50]. Moreover, our analysis exploited the emitted fluorescence of Lyc. This avoids the limitations associated with fluorochrome labelling of NPs, which could interfere with their physicochemical properties and mask the impact of surfactants. This assay is a critical step that precedes time-consuming and costly ex vivo testing and justifies it.

The internalization of the Lyc@PLGA@Tween 20 NPs after a 24 h treatment period is observed to be greater in comparison to that of the other NPs. This phenomenon is probably attributable to the markedly negative ζ-potential exhibited by the Lyc@PLGA@Tween 20 NPs, in conjunction with their comparatively low average hydrodynamic diameter [75]. Furthermore, the greater colloidal stability of Lyc@PLGA@Tween 20 NPs in aqueous solution can encourage interaction with cells, promoting their internalization at the same treatment time and concentration. This difference is even greater when SKMEL-2 cells are compared to HaCaT cells; this is probably due to the increased phagocytic activity of the cancer cells. A comparatively low proportion of Lyc@PLGA@PVA NPs are internalized in SK-MEL-2 cells in comparison to Lyc@PLGA@Tween 20 NPs (see Figure 6). Thus, Tween 20 promotes the NPs' uptake by melanocytes, providing a potential exploitation of this surfactant for anticancer drug delivery, also considering the detected moderate toxic effect (see Figure S6). It has been demonstrated through in vitro studies that the chemical composition of nanocarriers, in conjunction with the presence of emulsifiers, exerts a significant influence on cell uptake and penetration [23,78]. However, the distinguishing feature of our study is the in vitro assay on cell spheroids with confocal analysis, which exploits the intrinsic fluorescence of the loaded compound. Furthermore, it can be deduced from the observation of the Z-stacks in Figure S7 that the NPs are capable of homogeneous penetration across HaCaT and SK-MEL-2 spheroids. This assay constitutes a proof-of-concept investigation into the role of the produced carriers in terms of their uptake by skin cells, which are organized in a 3D architecture that is useful in simulating the complex in vivo environment. It is anticipated that the results of the present study will be utilized in future transdermal studies, with a view to validating the Lyc penetration and distribution.

Despite the divergent internalization of the produced NPs by the surfactant employed, the loaded Lyc exhibited remarkable antioxidant activity, as evidenced by its capacity to inhibit intracellular ROS production following treatment with Lyc@PLGA NPs. As illustrated in Figure 7, both Lyc@PLGA@PVA NPs and Lyc@PLGA@Tween 20 NPs were found to restore the ROS levels to those of the non-treated cells, thereby avoiding the oxidative stimulus of H_2O_2 treatment. This outcome is in accordance with the findings of previous studies on Lyc-loaded carriers [79].

5. Limitations of the Study and Future Perspectives

We have developed a protocol for the nanoencapsulation of Lyc from tomato extract in PLGA nanoparticles, and have studied their antioxidant activity in human skin spheroids. We fully recognize the importance of ex vivo skin permeation data, such as those obtained via Franz diffusion cells, for the validation of dermatological formulations. However, the present study was specifically designed as a foundational proof-of-concept and a rational screening phase. Our primary objective was to elucidate how the choice of surfactants dictates the physicochemical stability, antioxidant retention, and biological performance of Lyc@PLGA NPs. The significance of surfactants and the wide range of their functions have been extensively debated. By employing 3D human skin spheroids, we have provided a significantly more sophisticated and physiologically relevant assessment of cellular uptake and ROS inhibition than traditional 2D cultures, as previously discussed. This approach serves as a necessary methodological bridge, establishing the essential biological safety and efficacy parameters before proceeding to costly ex vivo trials. The findings presented

here provide a rational basis for selecting Lyc@PLGA@PVA NPs as the lead candidate for advanced development. Future investigations will involve the integration of these optimized nanosystems into complete topical vehicles, followed by long-term stability protocols and quantitative permeation studies using ex vivo human skin to fully validate their translational and industrial potential.

Lycopene has been selected as a challenging model compound due to its interesting biological properties. However, Lyc is not among the most potent antioxidants currently available; there are several alternative compounds, both natural and synthetic, exhibiting significantly higher antioxidant capacity while also offering superior chemical stability. This choice was also influenced by selected sources for molecule extraction. The Lyc-rich extract has been supplied by Licofarma s.r.l. in oil form, which was obtained using a SC-CO_2 process on tomato peels. Licofarma s.r.l. holds a patent for extracting Lyc from tomatoes using SC-CO_2 and uses the resulting extract as an ingredient in different cosmetic/nutraceutical formulations. We worked to efficiently synthesize Lyc-loaded NPs as an alternative cosmetic ingredient to oily SC-CO_2 TP extract. The exploitation of tomato peel by Licofarma s.r.l. addressed the increasing trend of utilizing waste recovery as prospective sources of bioactive compounds. So, the choice of Lyc as a model compound is also motivated by the challenge of implementing sustainable, circular economy practices. Furthermore, the investigated protocols and analytical methods will be a platform for other bioactive molecule encapsulations with different industrial relevance, including the utilization of other natural or waste sources.

Concerning physicochemical stability, DLS measurements demonstrated that the tested surfactants were capable of yielding Lyc-loaded NPs that exhibited stability within an aqueous solution over a period of up to 25 days. However, the absence of a long-term stability assay on NP suspensions is a limit of the proposed investigation.

Once the NPs have been synthesized, they must be incorporated into a vehicle suitable for dermatologic use. Prior to being incorporated into a cosmetic formulation, NPs are usually characterized in terms of their morphology, size distribution, zeta potential, and encapsulation and/or loading efficiency. We have to consider that the physical stability of skincare formulations containing NPs depends not only on the nature of the interactions between nanoparticles, but also on their interaction with the dispersant and emulsifiers. In this scenario, our proof-of-concept study into the role of surfactants impact is pivotal, working as a screening tool.

Our main future focus is the development of suitable skincare formulations based on Lyc@PLGA NPs. Moreover, the selection of an appropriate vehicle is contingent upon the intended purpose of the cosmetic product. Therefore, we will prepare the potential skincare formulation by adding small volumes of nanosuspension directly to a gel, cream, or o/w emulsion, mixing them together to obtain the final product. Some precautions should be observed: the appropriate concentrations of surfactants or polymers must be determined to prevent the particles from growing and aggregating during storage; the use of ionized additives such as electrolytes should also be avoided to prevent nanocolloid agglomeration. Finally, the product's evaluation will include physical and chemical analysis, monitoring organoleptic properties, colour, odour, the presence of phase separation, pH, and viscosity. The potential Lyc release rate from the formulation will also be analyzed exploiting in vitro assays (e.g., systems like Franz cells).

The preliminary storage stability test indicated that surfactants play a critical role in maintaining the retention and activity of the encapsulated Lyc. Freeze-dried Lyc@PLGA@PVA NPs have a good stability up to 5 months of storage at 4 °C; instead, Lyc@PLGA@Tween 20 NPs remain fairly stable after 2 months of storage at 4 °C. This is a limitation that will be considered in future studies, which will need to take into account the

https://doi.org/10.3390/antiox15010136

storage time based on the surfactant used for the synthesis of the nanoparticles, the storage temperature, and the samples' state (suspended in water, wet, or dry).

Shelf lives of at least 12–24 months are generally required for cosmetic or pharmaceutical ingredients. Therefore, a shelf-life evaluation will be performed under different temperatures, extending the time beyond five months, to understand the stability of the skincare formulation based on Lyc@PLGA NPs.

Our proof-of-concept study has been preceded with biological assays verifying the cytocompatibility, cellular uptake efficiency, and antioxidant activity of Lyc-loaded NPs.

Transdermal penetration evaluation is crucial for potential active ingredients and carriers because, as previously discussed, the skin is a very selective organ.

We conducted a preliminary cellular uptake study to investigate the influence of surfactants on the efficient internalization of Lyc in human keratinocytes and melanocytes, which were selected as cellular models of the epidermis. We performed confocal microscopy to provide z-stack imaging and quantify fluorescence following the treatment of human skin spheroids with NPs. Furthermore, since Lyc is fluorescent, we were able to visualize its uptake directly in the acquired z-stacks, avoiding NP fluorochrome labelling. Our results suggest that Lyc@PLGA@Tween 20 NPs enhance Lyc uptake in spheroids, particularly in melanocytes. This indicates that Tween 20 plays a crucial role in promoting cell interaction.

It is evident that the available data is inadequate for the purpose of substantiating claims pertaining to the penetration, retention, and transport of Lyc across the skin layers.

The choice to prioritize the study of surfactant-cell interactions via 3D models serves to validate the performance of the formulation at the cellular level, bypassing the mentioned limits of 2D cell cultures. This screening is crucial: confirming that NPs are stable enough to deliver their cargo and exert a biological effect within a stratified cellular architecture provides the necessary justification for future, more resource-intensive ex vivo permeation trials. While the cellular spheroids provide valuable insights into cellular internalization and antioxidant protection within their 3D structure, it does not account for the barrier function of the stratum corneum. Future studies employing Franz diffusion cells and ex vivo skin models are already planned to quantify the actual permeation performance.

However, the spheroid uptake assay will be employed in future investigations involving new spheroids generated from co-cultures, which are designed to better mimic the human epidermis and provide a more efficient ex vivo model. We also plan to use commercially available human epidermis models to address the challenge of conducting animal-free studies.

Although, the antioxidant activity in terms of ROS inhibition following oxidative stress is great for both studied samples. This means that the surfactant affected NP internalization in spheroids without interfering with bioactivity, which remains high even at lower levels of internalized Lyc. This is undoubtedly due to Lyc's significant intrinsic antioxidant capacity and increased bioavailability from carriers.

Lyc@PLGA NP-enriched formulations will be tested for long-term and transdermal permeation, verifying the antioxidant activity in human spheroids as well as in a commercial reconstructed human epidermis. Proteomics and metabolomics will be performed to understand the biochemical pathways triggered by Lyc released in target cells (keratinocytes or melanocytes) to support the preliminary biological data on 2D and 3D cell cultures and to exclude toxicity and/or side effects of nano-formulations. The omics sciences offer technological advances that are well-integrated into the concept of "cosmeceuticals", which refers to cosmetics that have a scientifically proven preventive or curative effect.

These future perspectives will explore the data of the present proof-of-concept study and support the industrial relevance of potential skincare formulations based on Lyc@PLGA NPs.

https://doi.org/10.3390/antiox15010136

6. Conclusions

The present study is a proof-of-concept investigation into the effect of surfactants on the properties of PLGA NPs, using Lyc as a challenging model compound. We have compared PVA and Tween 20 as surfactants for colloid stabilization and efficient Lyc loading. Colloidal stability in aqueous medium is affected by the surfactant, as demonstrated by the better DLS parameters of Lyc@PLGA@Tween 20 NP suspensions with respect to Lyc@PLGA@PVA NPs. The stability of loaded Lyc retention and scavenging capacity over time was enhanced by Lyc@PLGA@PVA NPs, suggesting a protective effect from PVA. Chemical assays provide a controlled and reproducible means of monitoring the loss of radical scavenging capacity due to degradation during storage, which is a critical parameter for skincare formulation and shelf-life evaluation. The concentrations and treatment times were selected based on the stability and cytotoxicity data to investigate Lyc@PLGA NPs' effect on cell uptake and bioactivity. We performed a cell uptake assay on HaCaT and SK-MEL-2 spheroids, measuring the fluorescence of encapsulated Lyc directly using confocal imaging. This study emphasized the pivotal role of Tween 20 in facilitating the internalization of NPs by human melanocytes, thereby underscoring its potential for further applications. Despite the detected effect on cell uptake, the bioactivity of Lyc is enhanced by delivery via all Lyc@PLGA NPs. The substantial antioxidant capacity of Lyc@PLGA@PVA NPs and Lyc@PLGA@Tween 20 NPs in HaCaT and SK-MEL-2 spheroids could offer significant potential for skin protection. The data obtained on stability and bioactivity will be exploited for future performance research on effective skincare formulations containing the nanosized ingredients. Biological assays will be conducted to verify cytocompatibility, transdermal penetration/distribution, and ROS inhibition. Moreover, the stability of loaded Lyc in a cellular environment will be investigated by testing the final formulations.

Future perspectives provide long-term stability tests and sophisticate transdermal permeation studies to support the industrial relevance of Lyc@PLGA NP-based skincare formulations.

Supplementary Materials: The following supporting information can be downloaded at: https://www.mdpi.com/article/10.3390/antiox15010136/s1. Figure S1. Scavenging activity percentage by DPPH inhibition assay versus TP extract mg; Figure S2. Size distribution plot as Intensity (%) of diluted Lyc@PLGA NP suspensions; Table S1. DLS parameters measured on empty PLGA-NP suspensions; Table S2. DLS parameters measured on Lyc@PLGA NP suspensions after 25 days; Figure S3. Representative SEM images of Lyc@PLGA@PVA NPs and Lyc@PLGA@Tween 20 NPs; Figure S4. FT-IR of Lyc solution after Lyc@PLGA NP dissolution; Figure S5. UV-vis spectra of Lyc solution after Lyc@PLGA NP dissolution; Figure S6. Cell viability data on HaCaT and SK-MEL-2 2D and Spheroids; Figure S7. Confocal microscopy gallery images; Figure S8. Representative flow cytometric spectra of intracellular ROS analysis.

Author Contributions: Conceptualization, F.B., V.V., and G.C. (Giuseppe Ciccarella); methodology, F.B. and V.V.; validation, F.B. and C.B.; formal analysis, F.B., V.V., C.B., and M.O.; investigation, F.B., V.V., C.B., M.O., C.N., and G.E.D.B.; resources, C.N., G.E.D.B., G.C. (Gianpiero Colangelo), L.V., and G.C. (Giuseppe Ciccarella); writing—original draft preparation, F.B., C.B., and M.O.; writing—review and editing, V.V., G.C. (Gianpiero Colangelo), and M.S.S.; visualization, F.B., C.B., and M.O.; supervision, F.B., V.V., and L.V.; project administration, G.C. (Giuseppe Ciccarella); and funding acquisition, G.C. (Giuseppe Ciccarella). All authors have read and agreed to the published version of the manuscript.

Funding: This research was funded by Ministry of Enterprises and Made in Italy, Direzione generale per gli incentivi alle imprese, DECRETO MINISTERIALE, 31 December 2021, ACCORDI PER L'INNOVAZIONE, DECRETO DIRETTORIALE, 18 March 2022, Project "ANASTASIA-Applicazione delle NAnotecnologie per l'incremento Sostenibile della sTAbilità di prodotti del Settore cosmetica e Analitico", CUP: B89J23001360005. Supported in part by Bando a Cascata (CODBAN) 000608 denominato "SMART" (acronimo di "Advanced Screening Models for the preclinical testing of ALS RNA

Therapeutics"), CUP J53C24002150007, Spoke #3, nell'ambito del PNRR MUR—M4C2—Inv.1.4—Avviso "Centri Nazionali"—D.D. n. 3138 del 16 December 2021—Prog. CN00000041 "National Center for Gene Therapy and Drugs based on RNA Technology".

Institutional Review Board Statement: Not applicable.

Informed Consent Statement: Not applicable.

Data Availability Statement: The original contributions presented in this study are included in the article/Supplementary Materials. Further inquiries can be directed to the corresponding authors.

Acknowledgments: We thank the cosmetics farmer Licofarma s.r.l. (Galatina, Lecce, Italy) for providing the tomato peel extract.

Conflicts of Interest: The authors declare no conflicts of interest. We clarify that the main reagents used in the experiments were sourced from a company and that no potential conflict of interest exists.

Abbreviations

The following abbreviations are used in this manuscript:

Lyc	Lycopene
PLGA	Poly-lactic-co-glycolic acid
PLGA NPs	PLGA nanoparticles
PVA	Polyvinyl alcohol
Lyc@PLGA NPs	Lycopene loaded PLGA nanoparticles
Lyc@PLGA@PVA NPs	Lycopene loaded PLGA nanoparticles with PVA
Lyc@PLGA@Tween 20 NPs	Lycopene loaded PLGA nanoparticles with Tween 20
SC-CO_2	Supercritical CO_2
TP	Tomato peel

References

1. Rodríguez-Mena, A.; Ochoa-Martínez, L.A.; González-Herrera, S.M.; Rutiaga-Quiñones, O.M.; González-Laredo, R.F.; Olmedilla-Alonso, B. Natural Pigments of Plant Origin: Classification, Extraction and Application in Foods. *Food Chem.* **2023**, *398*, 133908. [CrossRef]
2. Brudzyńska, P.; Sionkowska, A.; Grisel, M. Plant-Derived Colorants for Food, Cosmetic and Textile Industries: A Review. *Materials* **2021**, *14*, 3484. [CrossRef] [PubMed]
3. Popescu, M.; Iancu, P.; Plesu, V.; Bildea, C.S. Carotenoids Recovery Enhancement by Supercritical CO2 Extraction from Tomato Using Seed Oils as Modifiers. *Processes* **2022**, *10*, 2656. [CrossRef]
4. Matei, F.; Zirra, D. (Eds.) *Introduction to Biotech Entrepreneurship: From Idea to Business: A European Perspective*; Springer International Publishing: Cham, Switzerland, 2019.
5. Przybylska, S. Lycopene—A Bioactive Carotenoid Offering Multiple Health Benefits: A Review. *Int. J. Food Sci. Tech.* **2020**, *55*, 11–32. [CrossRef]
6. Caseiro, M.; Ascenso, A.; Costa, A.; Creagh-Flynn, J.; Johnson, M.; Simões, S. Lycopene in Human Health. *LWT* **2020**, *127*, 109323. [CrossRef]
7. Ali, M.Y.; Sina, A.A.I.; Khandker, S.S.; Neesa, L.; Tanvir, E.M.; Kabir, A.; Khalil, M.I.; Gan, S.H. Nutritional Composition and Bioactive Compounds in Tomatoes and Their Impact on Human Health and Disease: A Review. *Foods* **2020**, *10*, 45. [CrossRef]
8. Saini, R.K.; Rengasamy, K.R.R.; Mahomoodally, F.M.; Keum, Y.-S. Protective Effects of Lycopene in Cancer, Cardiovascular, and Neurodegenerative Diseases: An Update on Epidemiological and Mechanistic Perspectives. *Pharmacol. Res.* **2020**, *155*, 104730. [CrossRef]
9. Zhu, R.; Chen, B.; Bai, Y.; Miao, T.; Rui, L.; Zhang, H.; Xia, B.; Li, Y.; Gao, S.; Wang, X.-D.; et al. Lycopene in Protection against Obesity and Diabetes: A Mechanistic Review. *Pharmacol. Res.* **2020**, *159*, 104966. [CrossRef]
10. Rowles, J.L.; Ranard, K.M.; Smith, J.W.; An, R.; Erdman, J.W. Increased Dietary and Circulating Lycopene Are Associated with Reduced Prostate Cancer Risk: A Systematic Review and Meta-Analysis. *Prostate Cancer Prostatic Dis.* **2017**, *20*, 361–377. [CrossRef]
11. Kwatra, B. A review on potential properties and therapeutic applications of lycopene. *Int. J. Med. Biomed. Stud.* **2020**, *4*, 33–44. [CrossRef]
12. Crowe-White, K.M.; Phillips, T.A.; Ellis, A.C. Lycopene and Cognitive Function. *J. Nutr. Sci.* **2019**, *8*, e20. [CrossRef]

13. Jing, Y.; Guo, F.; Zhang, S.; Dong, W.; Zhou, J.; Xin, F.; Zhang, W.; Jiang, M. Recent Advances on Biological Synthesis of Lycopene by Using Industrial Yeast. *Ind. Eng. Chem. Res.* **2021**, *60*, 3485–3494. [CrossRef]
14. Li, L.; Liu, Z.; Jiang, H.; Mao, X. Biotechnological Production of Lycopene by Microorganisms. *Appl. Microbiol. Biotechnol.* **2020**, *104*, 10307–10324. [CrossRef] [PubMed]
15. Baiano, A. Recovery of Biomolecules from Food Wastes—A Review. *Molecules* **2014**, *19*, 14821–14842. [CrossRef] [PubMed]
16. Squillace, P.; Adani, F.; Scaglia, B. Supercritical CO_2 Extraction of Tomato Pomace: Evaluation of the Solubility of Lycopene in Tomato Oil as Limiting Factor of the Process Performance. *Food Chem.* **2020**, *315*, 126224. [CrossRef] [PubMed]
17. European Food Safety Authority (EFSA). Use of Lycopene as a Food Colour—Scientific Opinion of the Panel on Food Additives, Flavourings, Processing Aids and Materials in Contact with Food. *Eur. Food Saf. Auth. J.* **2008**, *6*, 674. [CrossRef]
18. Mihalcea, L.; Crăciunescu, O.; Gheonea (Dima), I.; Prelipcean, A.-M.; Enachi, E.; Barbu, V.; Bahrim, G.E.; Râpeanu, G.; Oancea, A.; Stănciuc, N. Supercritical CO_2 Extraction and Microencapsulation of Lycopene-Enriched Oleoresins from Tomato Peels: Evidence on Antiproliferative and Cytocompatibility Activities. *Antioxidants* **2021**, *10*, 222. [CrossRef]
19. Falsafi, S.R.; Rostamabadi, H.; Babazadeh, A.; Tarhan, Ö.; Rashidinejad, A.; Boostani, S.; Khoshnoudi-Nia, S.; Akbari-Alavijeh, S.; Shaddel, R.; Jafari, S.M. Lycopene Nanodelivery Systems; Recent Advances. *Trends Food Sci. Technol.* **2022**, *119*, 378–399. [CrossRef]
20. Carvalho, G.C.; De Camargo, B.A.F.; De Araújo, J.T.C.; Chorilli, M. Lycopene: From Tomato to Its Nutraceutical Use and Its Association with Nanotechnology. *Trends Food Sci. Technol.* **2021**, *118*, 447–458. [CrossRef]
21. Amorim, A.D.G.N.; Vasconcelos, A.G.; Souza, J.; Oliveira, A.; Gullón, B.; De Souza De Almeida Leite, J.R.; Pintado, M. Bio-Availability, Anticancer Potential, and Chemical Data of Lycopene: An Overview and Technological Prospecting. *Antioxidants* **2022**, *11*, 360. [CrossRef]
22. Guerra, A.S.; Hoyos, C.G.; Molina-Ramírez, C.; Velásquez-Cock, J.; Vélez, L.; Gañán, P.; Eceiza, A.; Goff, H.D.; Zuluaga, R. Extraction and Preservation of Lycopene: A Review of the Advancements Offered by the Value Chain of Nanotechnology. *Trends Food Sci. Technol.* **2021**, *116*, 1120–1140. [CrossRef]
23. Ascenso, A.; Pinho, S.; Eleutério, C.; Praça, F.G.; Bentley, M.V.L.B.; Oliveira, H.; Santos, C.; Silva, O.; Simões, S. Lycopene from Tomatoes: Vesicular Nanocarrier Formulations for Dermal Delivery. *J. Agric. Food Chem.* **2013**, *61*, 7284–7293. [CrossRef] [PubMed]
24. Butnariu, M.V.; Giuchici, C.V. The Use of Some Nanoemulsions Based on Aqueous Propolis and Lycopene Extract in the Skin's Protective Mechanisms against UVA Radiation. *J. Nanobiotechnol.* **2011**, *9*, 3. [CrossRef] [PubMed]
25. Lopes, L.B.; VanDeWall, H.; Li, H.T.; Venugopal, V.; Li, H.K.; Naydin, S.; Hosmer, J.; Levendusky, M.; Zheng, H.; Bentley, M.V.L.B.; et al. Topical Delivery of Lycopene Using Microemulsions: Enhanced Skin Penetration and Tissue Antioxidant Activity. *J. Pharm. Sci.* **2010**, *99*, 1346–1357. [CrossRef]
26. Baldassarre, F.; Vergaro, V.; De Castro, F.; Biondo, F.; Suranna, G.P.; Papadia, P.; Fanizzi, F.P.; Rongai, D.; Ciccarella, G. Enhanced Bioactivity of Pomegranate Peel Extract Following Controlled Release from $CaCO_3$ Nanocrystals. *Bioinorg. Chem. Appl.* **2022**, *2022*, 6341298. [CrossRef]
27. Kyriakoudi, A.; Spanidi, E.; Mourtzinos, I.; Gardikis, K. Innovative Delivery Systems Loaded with Plant Bioactive Ingredients: Formulation Approaches and Applications. *Plants* **2021**, *10*, 1238. [CrossRef]
28. Baldassarre, F.; Schiavi, D.; Ciarroni, S.; Tagliavento, V.; De Stradis, A.; Vergaro, V.; Suranna, G.P.; Balestra, G.M.; Ciccarella, G. Thymol-Nanoparticles as Effective Biocides against the Quarantine Pathogen Xylella Fastidiosa. *Nanomaterials* **2023**, *13*, 1285. [CrossRef]
29. Baldassarre, F.; Schiavi, D.; Di Lorenzo, V.; Biondo, F.; Vergaro, V.; Colangelo, G.; Balestra, G.M.; Ciccarella, G. Cellulose Nanocrystal-Based Emulsion of Thyme Essential Oil: Preparation and Characterisation as Sustainable Crop Protection Tool. *Molecules* **2023**, *28*, 7884. [CrossRef]
30. Okonogi, S.; Riangjanapatee, P. Physicochemical Characterization of Lycopene-Loaded Nanostructured Lipid Carrier Formulations for Topical Administration. *Int. J. Pharm.* **2015**, *478*, 726–735. [CrossRef]
31. Kanpipit, N.; Mattariganont, S.; Janphuang, P.; Rongsak, J.; Daduang, S.; Chulikhit, Y.; Thapphasaraphong, S. Comparative Study of Lycopene-Loaded Niosomes Prepared by Microfluidic and Thin-Film Hydration Techniques for UVB Protection and Anti-Hyperpigmentation Activity. *Int. J. Mol. Sci.* **2024**, *25*, 11717. [CrossRef]
32. Ribaya-Mercado, J.D.; Garmyn, M.; Gilchrest, B.A.; Russell, R.M. Skin Lycopene Is Destroyed Preferentially over β-Carotene during Ultraviolet Irradiation in Humans. *J. Nutr.* **1995**, *125*, 1854–1859. [CrossRef] [PubMed]
33. Calniquer, G.; Khanin, M.; Ovadia, H.; Linnewiel-Hermoni, K.; Stepensky, D.; Trachtenberg, A.; Sedlov, T.; Braverman, O.; Levy, J.; Sharoni, Y. Combined Effects of Carotenoids and Polyphenols in Balancing the Response of Skin Cells to UV Irradiation. *Molecules* **2021**, *26*, 1931. [CrossRef] [PubMed]
34. Fazekas, Z.; Gao, D.; Saladi, R.N.; Lu, Y.; Lebwohl, M.; Wei, H. Protective Effects of Lycopene Against Ultraviolet B-Induced Photodamage. *Nutr. Cancer* **2003**, *47*, 181–187. [CrossRef] [PubMed]
35. Jamaleddine, A.; Urrutigoïty, M.; Bouajila, J.; Merah, O.; Evon, P.; De Caro, P. Ecodesigned Formulations with Tomato Pomace Extracts. *Cosmetics* **2022**, *10*, 7. [CrossRef]

36. Ambarwati, N.S.S.; Armandari, M.O.; Widayat, W.; Desmiaty, Y.; Elya, B.; Arifianti, A.E.; Ahmad, I. In Vitro Studies on the Cytotoxicity, Elastase, and Tyrosinase Inhibitory Activities of Tomato (*Solanum Lycopersicum* Mill.) Extract. *J. Adv. Pharm. Technol. Res.* **2022**, *13*, 182–186. [CrossRef]
37. Smit, N.; Vicanova, J.; Cramers, P.; Vrolijk, H.; Pavel, S. The Combined Effects of Extracts Containing Carotenoids and Vitamins E and C on Growth and Pigmentation of Cultured Human Melanocytes. *Skin Pharmacol. Physiol.* **2004**, *17*, 238–245. [CrossRef]
38. Satriyasa, B.K.; Widianti, I.G.A.; Manuaba, I.B.G.F. The Potential of Carrot Extract as a Sunscreen to Prevent Apoptosis in White Mice (Mus Musculus) Fibroblast Cell Cultures Exposed to UVB Light. *Bali Med. J.* **2022**, *11*, 527–530. [CrossRef]
39. Costa, A.; Marques, M.; Congiu, F.; Paiva, A.; Simões, P.; Ferreira, A.; Bronze, M.R.; Marto, J.; Ribeiro, H.M.; Simões, S. Evaluating the Presence of Lycopene-Enriched Extracts from Tomato on Topical Emulsions: Physico-Chemical Characterization and Sensory Analysis. *Appl. Sci.* **2021**, *11*, 5120. [CrossRef]
40. Ciriminna, R.; Fidalgo, A.; Meneguzzo, F.; Ilharco, L.M.; Pagliaro, M. Lycopene: Emerging Production Methods and Applications of a Valued Carotenoid. *ACS Sustain. Chem. Eng.* **2016**, *4*, 643–650. [CrossRef]
41. Pool, H.; Quintanar, D.; Figueroa, J.D.D.; Marinho Mano, C.; Bechara, J.E.H.; Godínez, L.A.; Mendoza, S. Antioxidant Effects of Quercetin and Catechin Encapsulated into PLGA Nanoparticles. *J. Nanomater.* **2012**, *2012*, 145380. [CrossRef]
42. Santos Assunção, L.; Quênia Muniz Bezerra, P.; Stahl Hermes Poletto, V.; De Oliveira Rios, A.; Graça Ramos, I.; Duarte Ferreira Ribeiro, C.; Aparecida Souza Machado, B.; Izabel Druzian, J.; Alberto Vieira Costa, J.; Larroza Nunes, I. Combination of Carotenoids from Spirulina and PLA/PLGA or PHB: New Options to Obtain Bioactive Nanoparticles. *Food Chem.* **2021**, *346*, 128742. [CrossRef]
43. Anwar Ul Alam, M.; Kassu, A.; Kassama, L. Effect of Surfactant and Sonication Time on Improving the Bio-Accessibility of Lycopene Synthesized in Poly-Lactic Co-Glycolic Acid Nanoparticles. In Proceedings of the 2022 American Society of Agricultural and Biological Engineers, Houston, TX, USA, 17–20 July 2022.
44. Misir, J.; Kassama, L. Nanoencapsulation of Lycopene by PLGA: Effect on Physicochemical Properties and Extended-Release Kinetics in a Simulated GIT System. *LWT* **2025**, *225*, 117747. [CrossRef]
45. Phan, H.T.; Haes, A.J. What Does Nanoparticle Stability Mean? *J. Phys. Chem. C* **2019**, *123*, 16495–16507. [CrossRef]
46. Kulkarni, S.A.; Feng, S.-S. Effects of Particle Size and Surface Modification on Cellular Uptake and Biodistribution of Polymeric Nanoparticles for Drug Delivery. *Pharm. Res.* **2013**, *30*, 2512–2522. [CrossRef] [PubMed]
47. Salatin, S.; Maleki Dizaj, S.; Yari Khosroushahi, A. Effect of the Surface Modification, Size, and Shape on Cellular Uptake of Nanoparticles. *Cell Biol. Int.* **2015**, *39*, 881–890. [CrossRef]
48. Cortés, H.; Hernández-Parra, H.; Bernal-Chávez, S.A.; Prado-Audelo, M.L.D.; Caballero-Florán, I.H.; Borbolla-Jiménez, F.V.; González-Torres, M.; Magaña, J.J.; Leyva-Gómez, G. Non-Ionic Surfactants for Stabilization of Polymeric Nanoparticles for Biomedical Uses. *Materials* **2021**, *14*, 3197. [CrossRef] [PubMed]
49. Beg, S.; Rahman, M.; Kohli, K. Quality-by-Design Approach as a Systematic Tool for the Development of Nanopharmaceutical Products. *Drug Discov. Today* **2019**, *24*, 717–725. [CrossRef]
50. Klicks, J.; Von Molitor, E.; Ertongur-Fauth, T.; Rudolf, R.; Hafner, M. In Vitro Skin Three-Dimensional Models and Their Applications. *J. Cell Biol.* **2017**, *3*, 21–39. [CrossRef]
51. Nkabinde, L.A.; Shoba-Zikhali, L.N.N.; Semete-Makokotlela, B.; Kalombo, L.; Swai, H.; Grobler, A.; Hamman, J.H. Poly (D,L-Lactide-Co-Glycolide) Nanoparticles: Uptake by Epithelial Cells and Cytotoxicity. *Express Polym. Lett.* **2014**, *8*, 197–206. [CrossRef]
52. Stevanović, M.; Radulović, A.; Jordović, B.; Uskoković, D. Poly(DL-lactide-*co*-glycolide) Nanospheres for the Sustained Release of Folic Acid. *J. Biomed. Nanotechnol.* **2008**, *4*, 349–358. [CrossRef]
53. Dos Santos, R.C.; Ombredane, A.S.; Souza, J.M.T.; Vasconcelos, A.G.; Plácido, A.; Amorim, A.D.G.N.; Barbosa, E.A.; Lima, F.C.D.A.; Ropke, C.D.; Alves, M.M.M.; et al. Lycopene-Rich Extract from Red Guava (*Psidium guajava* L.) Displays Cytotoxic Effect against Human Breast Adenocarcinoma Cell Line MCF-7 via an Apoptotic-like Pathway. *Food Res. Int.* **2018**, *105*, 184–196. [CrossRef]
54. Cao, S.; Li, S.; Zhang, Z.; Zhang, L.; Jiang, L. Preparation and Evaluation of Novel Agriophyllum Squarrosum Starch Nanoparticles for Encapsulation of Lycopene with Enhanced Retention Rate and Bioactivity during Simulated In-Vitro Digestion. *Int. J. Biol. Macromol.* **2025**, *288*, 138436. [CrossRef]
55. Bresciani, G.; Hofland, L.J.; Dogan, F.; Giamas, G.; Gagliano, T.; Zatelli, M.C. Evaluation of Spheroid 3D Culture Methods to Study a Pancreatic Neuroendocrine Neoplasm Cell Line. *Front. Endocrinol.* **2019**, *10*, 682. [CrossRef] [PubMed]
56. Bolte, S.; Cordelières, F.P. A Guided Tour into Subcellular Colocalization Analysis in Light Microscopy. *J. Microsc.* **2006**, *224*, 213–232. [CrossRef] [PubMed]
57. Joutsen, J.; Da Silva, A.J.; Luoto, J.C.; Budzynski, M.A.; Nylund, A.S.; De Thonel, A.; Concordet, J.-P.; Mezger, V.; Sabéran-Djoneidi, D.; Henriksson, E.; et al. Heat Shock Factor 2 Protects against Proteotoxicity by Maintaining Cell-Cell Adhesion. *Cell Rep.* **2020**, *30*, 583–597.e6. [CrossRef] [PubMed]
58. Lu, Y.; Cheng, D.; Niu, B.; Wang, X.; Wu, X.; Wang, A. Properties of Poly (Lactic-Co-Glycolic Acid) and Progress of Poly (Lactic-Co-Glycolic Acid)-Based Biodegradable Materials in Biomedical Research. *Pharmaceuticals* **2023**, *16*, 454. [CrossRef]

59. Huang, W.; Zhang, C. Tuning the Size of Poly(Lactic-co-glycolic Acid) (PLGA) Nanoparticles Fabricated by Nanoprecipitation. *Biotechnol. J.* **2018**, *13*, 1700203. [CrossRef]
60. Trefalt, G.; Ruiz-Cabello, F.J.M.; Borkovec, M. Interaction Forces, Heteroaggregation, and Deposition Involving Charged Colloidal Particles. *J. Phys. Chem. B* **2014**, *118*, 6346–6355. [CrossRef]
61. Geng, J.; Li, K.; Qin, W.; Ma, L.; Gurzadyan, G.G.; Tang, B.Z.; Liu, B. Eccentric Loading of Fluorogen with Aggregation-Induced Emission in PLGA Matrix Increases Nanoparticle Fluorescence Quantum Yield for Targeted Cellular Imaging. *Small* **2013**, *9*, 2012–2019. [CrossRef]
62. Wang, R.; Zou, L.; Yi, Z.; Zhang, Z.; Zhao, M.; Shi, S. PLGA Nanoparticles Loaded with Curcumin Produced Luminescence for Cell Bioimaging. *Int. J. Pharm.* **2023**, *639*, 122944. [CrossRef]
63. De Andrades, E.O.; Da Costa, J.M.A.R.; De Lima Neto, F.E.M.; De Araujo, A.R.; De Oliveira Silva Ribeiro, F.; Vasconcelos, A.G.; De Jesus Oliveira, A.C.; Sobrinho, J.L.S.; De Almeida, M.P.; Carvalho, A.P.; et al. Acetylated Cashew Gum and Fucan for Incorporation of Lycopene Rich Extract from Red Guava (*Psidium guajava* L.) in Nanostructured Systems: Antioxidant and Antitumor Capacity. *Int. J. Biol. Macromol.* **2021**, *191*, 1026–1037. [CrossRef] [PubMed]
64. Sharma, N.; Madan, P.; Lin, S. Effect of Process and Formulation Variables on the Preparation of Parenteral Paclitaxel-Loaded Biodegradable Polymeric Nanoparticles: A Co-Surfactant Study. *Asian J. Pharm. Sci.* **2016**, *11*, 404–416. [CrossRef]
65. Li, Y.; Su, J.; Liu, S.; Li, S.; Liu, S.; Zhang, H.; Ding, Z.; Wang, Z.; Liu, M.; Zhao, Y. Improved Stability and Biocompatibility of Lycopene Liposomes with Sodium Caseinate and PEG Coating. *Int. J. Biol. Macromol.* **2025**, *311*, 143685. [CrossRef] [PubMed]
66. Akhoond Zardini, A.; Mohebbi, M.; Farhoosh, R.; Bolurian, S. Production and Characterization of Nanostructured Lipid Carriers and Solid Lipid Nanoparticles Containing Lycopene for Food Fortification. *J. Food Sci. Technol.* **2018**, *55*, 287–298. [CrossRef]
67. De Nardo, T.; Shiroma-Kian, C.; Halim, Y.; Francis, D.; Rodriguez-Saona, L.E. Rapid and Simultaneous Determination of Lycopene and β-Carotene Contents in Tomato Juice by Infrared Spectroscopy. *J. Agric. Food Chem.* **2009**, *57*, 1105–1112. [CrossRef]
68. Rehman, A.; Tong, Q.; Jafari, S.M.; Assadpour, E.; Shehzad, Q.; Aadil, R.M.; Iqbal, M.W.; Rashed, M.M.A.; Mushtaq, B.S.; Ashraf, W. Carotenoid-Loaded Nanocarriers: A Comprehensive Review. *Adv. Colloid Interface Sci.* **2020**, *275*, 102048. [CrossRef]
69. Arshad, M.T.; Maqsood, S.; Ikram, A.; Khan, A.A.; Raza, A.; Ahmad, A.; Gnedeka, K.T. Encapsulation Techniques of Carotenoids and Their Multifunctional Applications in Food and Health: An Overview. *Food Sci. Nutr.* **2025**, *13*, e70310. [CrossRef]
70. Hamed, D.; Keddari, S.; Boufadi, M.Y.; Bessad, L. Lycopene Purification with DMSO Anti-Solvent: Optimization Using Box-Behnken's Experimental Design and Evaluation of the Synergic Effect between Lycopene and *Ammi visnaga* L. Essential Oil. *Chem. Pap.* **2022**, *76*, 6335–6347. [CrossRef]
71. Sukmawati, A.; Utami, W.; Yuliani, R.; Da'i, M.; Nafarin, A. Effect of Tween 80 on Nanoparticle Preparation of Modified Chitosan for Targeted Delivery of Combination Doxorubicin and Curcumin Analogue. *IOP Conf. Ser. Mater. Sci. Eng.* **2018**, *311*, 012024. [CrossRef]
72. Makou, N.B.; Javadi, A.; Anarjan, N.; Torbati, M. Simultaneous Extraction and Nanoemulsification of Lycopene from Tomato Waste: Optimization and Stability Studies of Lycopene Nanoemulsions in Selected Food System. *Food Meas.* **2024**, *18*, 9671–9683. [CrossRef]
73. İnanç Horuz, T.; Belibağlı, K.B. Nanoencapsulation by Electrospinning to Improve Stability and Water Solubility of Carotenoids Extracted from Tomato Peels. *Food Chem.* **2018**, *268*, 86–93. [CrossRef]
74. Wang, Y.; Lv, J.; Li, C.; Xu, Y.; Jin, F.; Wang, F. Walnut Protein Isolate-Epigallocatechin Gallate Nanoparticles: A Functional Carrier Enhanced Stability and Antioxidant Activity of Lycopene. *Food Res. Int.* **2024**, *189*, 114536. [CrossRef]
75. Salvioni, L.; Morelli, L.; Ochoa, E.; Labra, M.; Fiandra, L.; Palugan, L.; Prosperi, D.; Colombo, M. The Emerging Role of Nanotechnology in Skincare. *Adv. Colloid Interface Sci.* **2021**, *293*, 102437. [CrossRef]
76. Lee, O.; Jeong, S.H.; Shin, W.U.; Lee, G.; Oh, C.; Son, S.W. Influence of Surface Charge of Gold Nanorods on Skin Penetration. *Ski. Res. Technol.* **2013**, *19*, e390–e396. [CrossRef] [PubMed]
77. Punzo, A.; Porru, E.; Silla, A.; Simoni, P.; Galletti, P.; Roda, A.; Tagliavini, E.; Samorì, C.; Caliceti, C. Grape Pomace for Topical Application: Green NaDES Sustainable Extraction, Skin Permeation Studies, Antioxidant and Anti-Inflammatory Activities Characterization in 3D Human Keratinocytes. *Biomolecules* **2021**, *11*, 1181. [CrossRef]
78. Baldassarre, F.; Allegretti, C.; Tessaro, D.; Carata, E.; Citti, C.; Vergaro, V.; Nobile, C.; Cannazza, G.; D'Arrigo, P.; Mele, A.; et al. Biocatalytic Synthesis of Phospholipids and Their Application as Coating Agents for $CaCO_3$ Nano–Crystals: Characterization and Intracellular Localization Analysis. *ChemistrySelect* **2016**, *1*, 6507–6514. [CrossRef]
79. Zhang, D.; Jiang, Y.; Xiang, M.; Wu, F.; Sun, M.; Du, X.; Chen, L. Biocompatible Polyelectrolyte Complex Nanoparticles for Lycopene Encapsulation Attenuate Oxidative Stress-Induced Cell Damage. *Front. Nutr.* **2022**, *9*, 902208. [CrossRef] [PubMed]

Disclaimer/Publisher's Note: The statements, opinions and data contained in all publications are solely those of the individual author(s) and contributor(s) and not of MDPI and/or the editor(s). MDPI and/or the editor(s) disclaim responsibility for any injury to people or property resulting from any ideas, methods, instructions or products referred to in the content.

antioxidants

MDPI

Article

Carvacrol-Loaded Chitosan Nanoparticles as a Multifunctional Nanotherapeutic Strategy Targeting Oxidative Stress, Inflammation, Apoptosis, and Genotoxicity in Nonalcoholic Fatty Liver Disease

M. Alfawaz [1], Ekramy M. Elmorsy [2,3], Ahmad Najem Alshammari [1], Noor A. Hakim [4], Najlaa M. M. Jawad [4], Soha A. Hassan [5], Manal S. Fawzy [2,*]and Safya E. Esmaeel [6,7]

[1] Department of Medical Laboratory Technology, College of Applied Medical Sciences, Northern Border University, Arar 91431, Saudi Arabia; mohammed.alfawaz@nbu.edu.sa (M.A.); ahmad.alshammari2@nbu.edu.sa (A.N.A.)
[2] Center for Health Research, Northern Border University, Arar 73213, Saudi Arabia; ekramy.elmorsy@nbu.edu.sa
[3] Department of Forensic Medicine and Clinical Toxicology, Faculty of Medicine, Mansoura University, Mansoura 35516, Egypt
[4] Department of Clinical Nutrition, Faculty of Applied Medical Sciences, King Abdulaziz University, Jeddah 21589, Saudi Arabia; ohakim@kau.edu.sa (N.A.H.); nalsini@kau.edu.sa (N.M.M.J.)
[5] Department of Biotechnology, Faculty of Applied Health Sciences Technology, October 6 University, 6th of October 12585, Egypt; soha.ahmed.dent@o6u.edu.eg
[6] Department of Physiology, Faculty of Medicine, Zagazig University, Zagazig 44519, Egypt
[7] Department of Physiology, College of Medicine, Northern Border University, Arar 91431, Saudi Arabia; safya.ebraheem@nbu.edu.sa
* Correspondence: manal.darwish@nbu.edu.sa

Abstract

Nonalcoholic fatty liver disease (NAFLD) associated with high-fat diet (HFD) intake involves oxidative stress, inflammation, apoptosis, and genotoxicity. Carvacrol, a natural monoterpenoid phenol, exhibits potent antioxidant, anti-inflammatory, and cytoprotective properties, but its clinical application is limited by poor solubility and bioavailability. Chitosan nanoparticles, known for their biocompatibility and ability to enhance drug delivery, offer a promising nanotherapeutic platform for carvacrol delivery in NAFLD. Given the limited therapeutic options for NAFLD, there is a growing interest in nanotherapeutic strategies to enhance the delivery and efficacy of natural antioxidants. This study examined carvacrol-loaded chitosan nanoparticles (CRV-CNPs) in HFD-induced NAFLD. Sixty rats were assigned to six groups: control, CRV-treated (100 mg/kg), CRV-CNP-treated (100 mg/kg), HFD-fed, and two combination groups receiving HFD with either CRV or CRV-CNPs (100 mg/kg) for six weeks after 14 weeks on HFD. Liver function, metabolic markers, oxidative stress parameters, antioxidant enzyme levels, inflammatory and fibrotic mediators, apoptotic gene expression, genotoxicity indices, and histopathological changes were evaluated. CRV-CNPs showed greater efficacy than free carvacrol in ameliorating hepatic dysfunction and metabolic disturbances in HFD-fed rats. CRV-CNPs significantly reduced malondialdehyde, upregulated Nrf2, and elevated hepatic glutathione peroxidase, superoxide dismutase, catalase, and reduced glutathione. Inflammatory markers (NF-κB, iNOS, IL-1β, CRP) and transforming growth factor-beta were suppressed. Pro-apoptotic genes (*Bax*, *Caspase-3*) were downregulated, while antiapoptotic Bcl-2 was upregulated. CRV-CNPs also reduced DNA fragmentation and 8-hydroxy-2′-deoxyguanosine levels, indicating strong antigenotoxic effects. Histopathological and ultrastructural assessments revealed mitigated steatosis, preserved hepatic architecture, and maintained mitochondrial integrity. In conclusion, CRV-CNPs provide potent hepatoprotection by targeting

oxidative stress, inflammation, apoptosis, and genotoxicity in NAFLD, demonstrating enhanced bioavailability, solubility, and sustained release, which support their potential as an advanced nanotherapeutic strategy for NAFLD management.

Keywords: high-fat diet; hepatic dysfunction; carvacrol; chitosan nanoparticles; antioxidants; anti-inflammatory effects

1. Introduction

Nonalcoholic fatty liver disease (NAFLD) is one of the most prevalent chronic liver disorders globally, affecting nearly 30% of the population [1]. Often regarded as the hepatic manifestation of metabolic syndrome, its severity correlates closely with obesity, hypertension, insulin resistance, and dyslipidemia [2]. Hepatic lipid accumulation in NAFLD acts not only as a marker of metabolic stress but also as a driver of pathological changes, ranging from simple steatosis to advanced cirrhosis [3]. NAFLD encompasses a spectrum of hepatic disorders, primarily classified as nonalcoholic fatty liver (NAFL) and nonalcoholic steatohepatitis (NASH). NAFL is characterized by a mild, reversible accumulation of lipids within hepatocytes, whereas NASH represents a more severe and progressive variant, often evolving into fibrosis, cirrhosis, and ultimately hepatocellular carcinoma [4,5] (Figure 1).

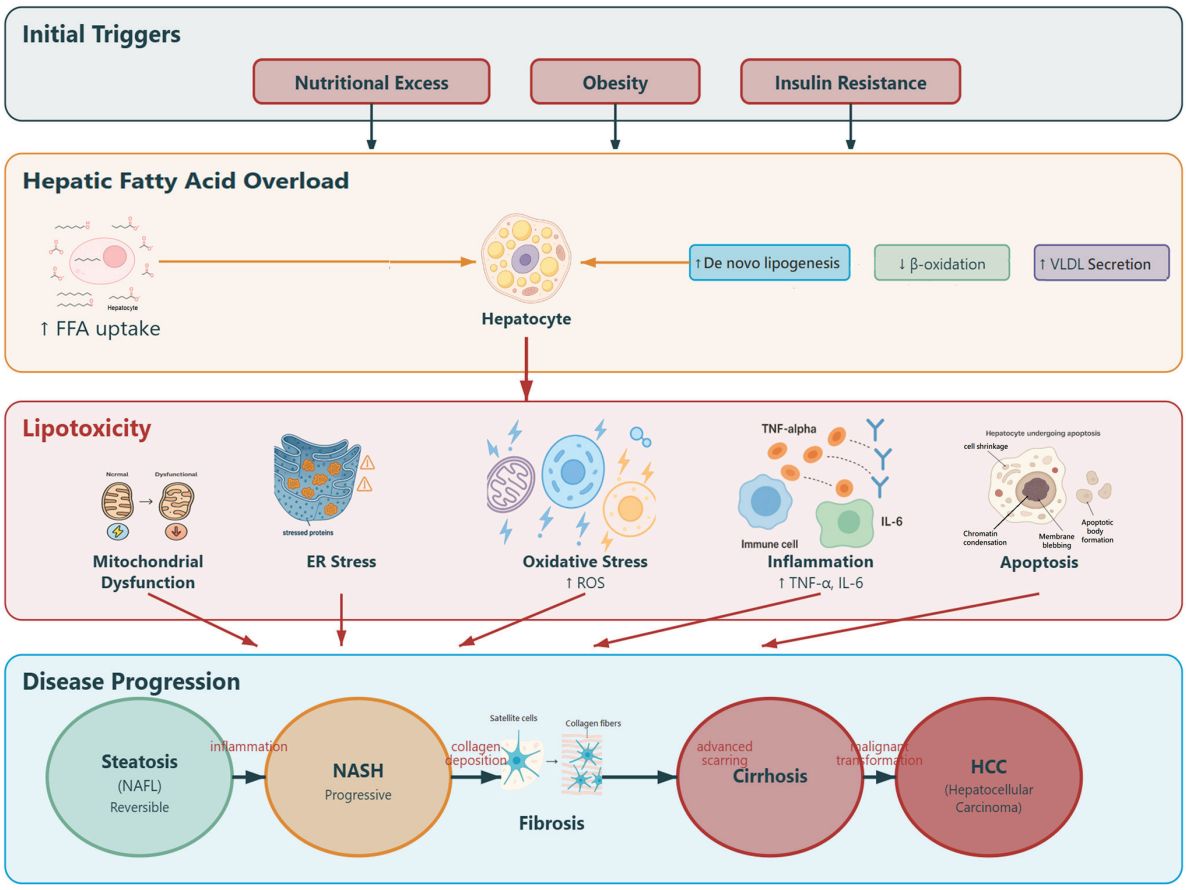


Figure 1. Schematic representation of the main biochemical mechanisms underlying nonalcoholic fatty liver disease (NAFLD) development and progression, highlighting key molecular pathways and targets of antioxidant/anti-inflammatory therapy, and biochemical pathways and progression of nonalcoholic steatohepatitis (NASH) to hepatocellular carcinoma (HCC). VLDL: Very low density lipoprotein, ER: Endoplasmic Reticulum.

Lifestyle modification remains the first-line therapy for NAFLD management. Sustained weight loss of at least 5% can reduce hepatic steatosis and liver injury, while reductions over 7% are associated with histological improvement in NASH [6]. Additionally, regular physical activity enhances glucose and lipid metabolism, reduces steatosis, lowers liver enzymes, and supports the structural integrity of mitochondria and the liver [7]. Current pharmacological interventions for metabolic syndrome employ combinations of agents targeting associated comorbidities, yet no single therapy has consistently demonstrated efficacy for NAFLD treatment [8]. Accordingly, there is an urgent need to develop novel therapies targeting key pathogenic pathways, particularly those involving oxidative stress, apoptosis, and inflammatory signaling. In this context, natural products have attracted considerable attention for their antioxidant, antiapoptotic, and anti-inflammatory properties, which may help counter hepatic oxidative stress and inflammation in NAFLD [9].

Carvacrol (CRV; 5-Isopropyl-2-methylphenol) with a molecular formula: $C_{10}H_{14}O$, found in mountain thyme and oregano essential oils, has notable antioxidant, antiapoptotic, anti-inflammatory, and anticancer activities that often exceed those of synthetic antioxidants [10–12]. It is recognized as safe by the FDA and classified as a chemical flavoring by the European Commission [13]. Several experimental investigations have examined carvacrol's hepatoprotective effects in NAFLD and related models. For example, Mohseni et al. showed that carvacrol administration ameliorated oxidative stress and inflammation in rats with diet-induced fatty liver, leading to significant reductions in serum ALT/AST and improved histological profiles [11]. Likewise, Cho et al. reported that carvacrol modulated lipid metabolism and reduced hepatic steatosis, partly by influencing gene expression involved in adipogenesis and inflammation [14]. Although these studies highlight carvacrol's therapeutic promise in NAFLD, limitations in solubility, bioavailability, and sustained hepatic delivery remain significant barriers to clinical translation [15], and high doses may carry cytotoxic risks [16]. Therefore, nanoformulation strategies have thus been employed to enhance CRV's stability, solubility, and bioavailability while minimizing toxicity [17].

Chitosan (CH), derived from chitin by deacetylation, is widely used as a nanomicrodelivery vehicle due to its biodegradability, biocompatibility, hydrophilicity, low toxicity, and straightforward nanoparticle fabrication [18,19]. Its versatility allows for production in various forms, including films, gels, membranes, fibers, and beads. It also promotes the transport of a wide range of molecules across mucosal barriers by temporarily modifying tight junctions [15]. CH is available in various molecular weights, allowing for precise control of nanoparticle or microparticle size [20]. Lower molecular weight CH is preferable for water solubility and nanoparticle production [21]. Moreover, the presence of free amino groups enables further functionalization for targeted delivery [15]. Importantly, nanoscale drug delivery systems offer several advantages over conventional formulations, including enhanced dissolution rates, increased solubility, and improved in vivo therapeutic outcomes, primarily due to their small particle size [22]. In this sense, the present study is distinguished by its novel integration of carvacrol with chitosan nanoparticles (CRV-CHNPs), designed to enhance solubility, stability, and bioefficacy. This nanotherapeutic approach specifically targets key biochemical mechanisms underlying HFD-induced NAFLD, including oxidative stress, inflammation, and apoptosis. By leveraging nanoparticle-mediated delivery, our strategy targets critical pathogenic pathways central to disease progression. Moreover, this study evaluates the hepatoprotective effects of CRV-CHNPs versus free carvacrol in a high-fat diet (HFD)-induced rat model, offering new insights into the therapeutic advantages and potential translational relevance of advanced nanodelivery systems in fatty liver disease.

Based on existing evidence that carvacrol exerts hepatoprotective effects and that chitosan nanoencapsulation improves bioavailability and cellular delivery, we hypothesized

that CRV-CHNPs would provide superior protection against HFD-induced NAFLD in rats by more effectively ameliorating hepatic oxidative stress, inflammation, apoptosis, and genotoxicity compared to free carvacrol.

2. Materials and Methods

An overview of the experimental workflow, including molecular docking, nanoparticle preparation, in vivo interventions, and analytical endpoints, is summarized in Figure 2.

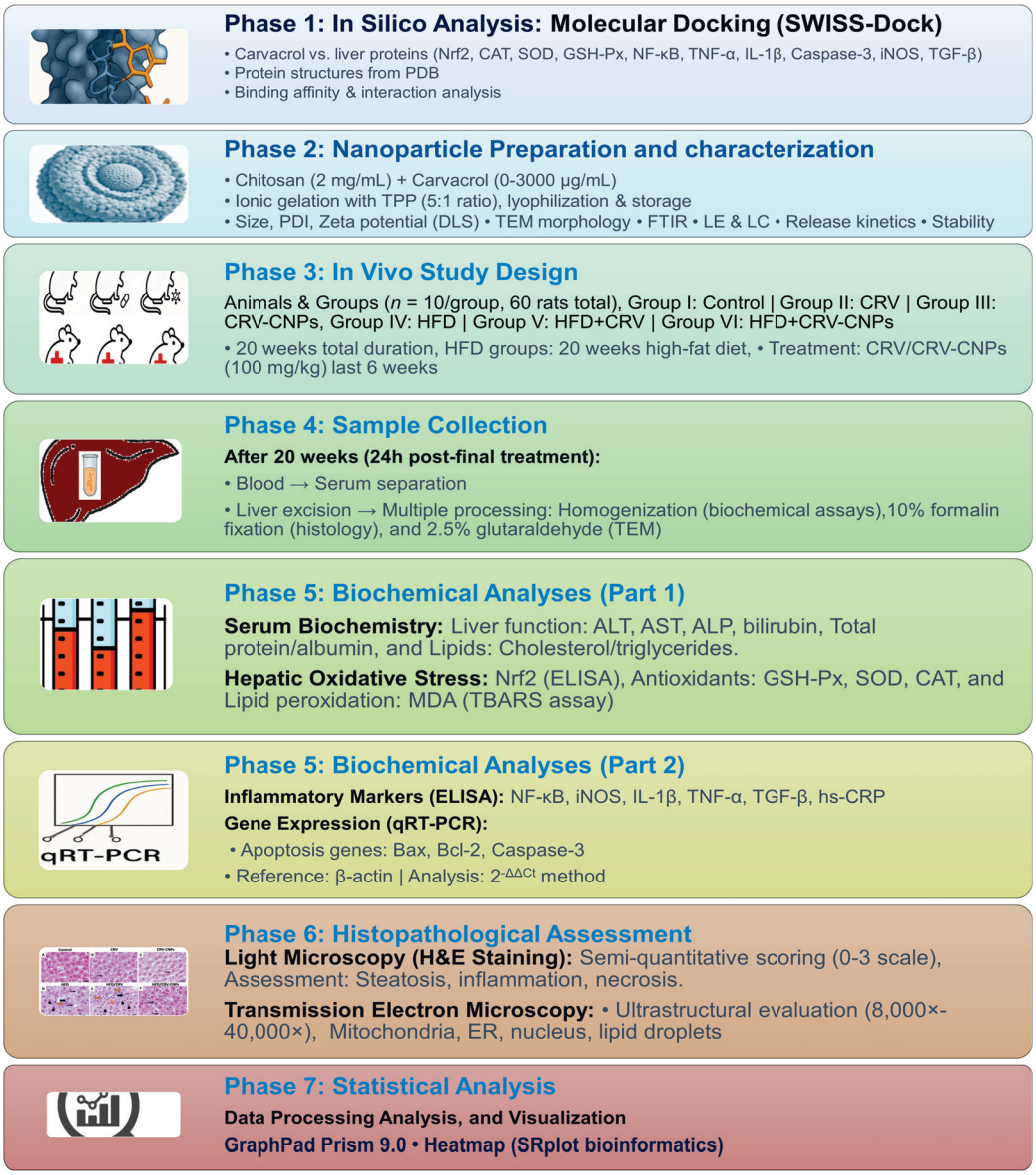


Figure 2. An overview of the experimental workflow in this study.

2.1. Molecular Docking

The SWISS-Dock server employed the EADock DSS engine and CHARMM force field to predict ligand–protein interactions involving Carvacrol and key liver molecules, including Nrf2, catalase (CAT), superoxide dismutase (SOD), glutathione peroxidase (GSH-Px), NF-κB, TNF-α, IL-1β, caspase-3, iNOS, and TGF-β. Crystal structures for all proteins were obtained from the Protein Data Bank. Subsequently, water molecules were removed, polar hydrogens were introduced, and standard energy minimization techniques were applied. Before docking, the 3D structure of carvacrol was optimized for energy efficiency. FullFitness and estimated binding free energy values were utilized to select the optimal

binding poses. The SWISS-Dock and the Vienna model for analyzing and illustrating protein–ligand interactions, including hydrogen bonding and hydrophobic contacts, in high-resolution structural representations.

2.2. Preparation of Carvacrol (CRV)-Loaded Chitosan Nanoparticles (CRV-CHNPs)

Carvacrol (purity ≥ 99%) was purchased from AB Chem Company (Mansoura, Egypt). The chemical structures of chitosan and carvacrol, and their proposed interaction within the CRV-loaded chitosan nanoparticle system, are illustrated in Figure 3.

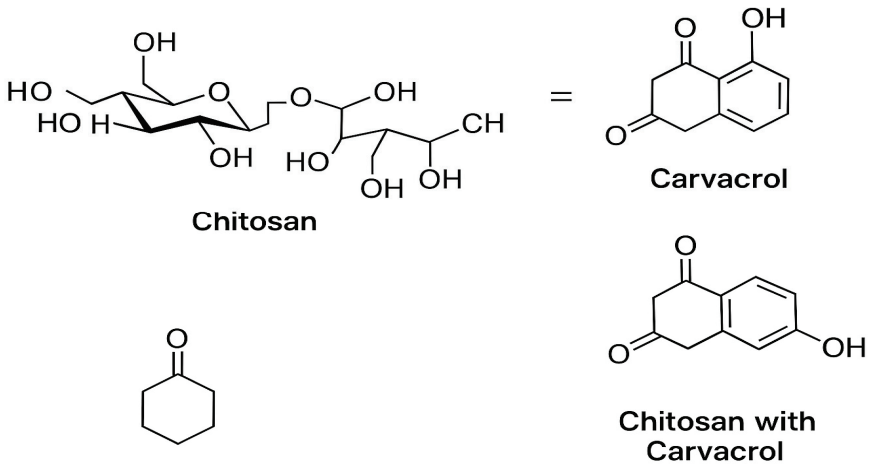


Figure 3. Chemical structures of chitosan and carvacrol, and schematic representation of their interaction within the carvacrol-loaded chitosan nanoparticle system.

To prepare CRV-loaded chitosan nanoparticles (CRV-CHNPs), chitosan (2 mg/mL) was dissolved in 1% acetic acid, supplemented with 1% Tween 80, and sonicated for 15 min. The pH was adjusted to 5 with 2 NaOH, after which carvacrol (0–3000 μg/mL) was added, and the mixture was sonicated for 5 min. A solution of sodium tripolyphosphate in deionized water was gradually introduced to the chitosan solution while stirring continuously, maintaining a 5:1 (*w*/*w*) chitosan-to-crosslinker ratio. The suspension was magnetically stirred for one hour to enable cross-linking and stabilization. Nanoparticles were separated by centrifugation at 12,000× *g* for 20 min at 4 °C, rinsed twice with deionized water to remove free CRV and excess TPP, and then frozen at −80 °C. They were subsequently subjected to lyophilization.

Key characterization parameters, including zeta potential, hydrodynamic mean diameter, and PDI, were evaluated using a Zetasizer Nano ZS (Malvern Panalytical, Malvern, Worcestershire, UK). Physicochemical properties were assessed by measuring zeta potential in triplicate, and the Z-average was determined from diluted samples. The morphology of the nanoparticles was characterized by transmission electron microscopy (TEM; JEOL 2100, Tokyo, Japan) operated at 160 kV. According to the manufacturer (Sigma-Aldrich, St. Louis, MO, USA), the chitosan used had a molecular weight of 190–310 kDa and a deacetylation degree of 85%. These structural features play a crucial role in determining the encapsulation efficiency and stability of the formulations.

Encapsulation performance was assessed by calculating the loading efficiency (LE) and loading content (LC) of CRV in the nanoparticles. The calibration curve was obtained by analyzing a series of CRV standard solutions at 334 nm. Residual CRV in the supernatant was measured spectrophotometrically at 334 nm, and LE and LC were calculated using the equations below:

LE (%) = [CRV in nanoparticles / CRV added] × 100
LC (%) = [CRV in nanoparticles / Nanoparticle weight] × 100

CRV release in vitro was evaluated by the dialysis bag technique (MWCO 12–14 kDa) employing PBS (pH 7.4, 0.5% Tween-80) at 37 °C. At scheduled intervals of up to 48 h, samples were withdrawn, examined at 334 nm, and the cumulative release was calculated. Stability testing of lyophilized CRV-CHNPs was conducted at −20 °C, 4 °C, and 25 °C (dark) for 6 months, with evaluations of zeta potential, particle size, PDI, and encapsulation efficiency.

FTIR analysis was performed using an ATR-FTIR spectrometer (PerkinElmer, Waltham, MA, USA) in the range of 4000–400 cm^{-1} with a resolution of 4 cm^{-1} and 32 scans. Spectra were obtained for pure CRV, pure chitosan, a physical mixture of CRV and chitosan, and CRV-CHNPs.

2.3. Animals, Diets, and Experimental Protocol

Sixty adult male albino rats (average weight 179.73 ± 8.23 g) were obtained from the Animal Facility of the Faculty of Medicine, Mansoura University, Egypt. All experimental procedures adhered to the National Institutes of Health (NIH) Guide for the Care and Use of Laboratory Animals and the International Guiding Principles for Biomedical Research Involving Animals (1985). All animal procedures were revised and approved by the "Research Ethics Committee of the October 6 University, Egypt (approval code: 20251207)".

Animals were acclimatized for two weeks before experimentation under standard laboratory conditions (temperature 21–25 °C, relative humidity 50–60%, and a 12 h light/dark cycle). All rats had unrestricted access to commercial rodent chow (Al Wadi Co., Giza, Egypt) and water throughout the study period. The standard rodent diet (Laboratory Rodent Diet 5001) contained 23% crude protein, 56% carbohydrates, 6% crude fiber, 8% ash, 4.5% crude fat, and 2.5% mineral mix, providing a caloric value of 3.36 kcal/g. The high-fat diet (HFD) was prepared by blending 35% beef tallow with 65% of the standard diet, yielding an energy density of 5.53 kcal/g. All diets were stored at 4 °C before use to preserve nutritional integrity. Rats were randomly allocated into six groups (n = 10 per group):

- Group I (Control): Received a standard laboratory rodent diet.
- Group II (CRV): Fed a standard diet and orally administered carvacrol (100 mg/kg body weight) for the final six weeks. The selected carvacrol dose was based on previous studies demonstrating its potent antioxidant and anti-inflammatory properties [23–25].
- Group III (CRV-CNPs): Received a standard diet and treated with carvacrol-loaded chitosan nanoparticles (100 mg/kg body weight) via oral gavage during the final six weeks.
- Group IV (HFD): Fed a high-fat diet (HFD) for 20 weeks according to the method described by Chang et al. [26].
- Group V (HFD + CRV): Fed an HFD for 20 weeks and co-administered carvacrol (100 mg/kg body weight) daily via oral gavage for the final six weeks.
- Group VI (HFD + CRV-CNPs): Fed an HFD for 20 weeks and co-administered CRV-loaded chitosan nanoparticles (100 mg/kg body weight) daily via oral gavage for the final six weeks.

The number of animals per group was determined according to current recommendations for preclinical in vivo studies using rodent models of metabolic and hepatic disorders [27]. Previous experimental reports and power analysis frameworks indicate that sample sizes of 8–12 rats per group are generally sufficient to detect biologically meaningful differences in biochemical and histopathological parameters with a statistical power of 0.8 and significance level of α = 0.05 [28]. This group size aligns with the ARRIVE 2.0 guidelines and internationally recognized ethical standards, ensuring appropriate statistical validity while adhering to the 3Rs principle (Reduction, Refinement, Replacement) of animal research [29]. The selected sample size also balanced ethical and practical considerations, allowing robust detection of treatment effects among six experimental groups

while minimizing unnecessary animal use. All enrolled animals completed the study protocol with no exclusions, mortality, or data attrition. This design ensured reliable one-way ANOVA comparisons across groups and adhered to established preclinical standards for rigor, reproducibility, and research practice.

2.4. Tissue Sample Collection and Homogenization

Following an overnight fast, rats were euthanized by cervical dislocation 24 h after the final treatment. Blood samples were withdrawn from the hepatic portal vein into non-heparinized tubes, allowed to clot at room temperature, and centrifuged at 3000× *g* for 10 min to obtain serum. The resulting serum was aliquoted into Eppendorf tubes and immediately analyzed biochemically. Liver tissues were carefully excised, rinsed with ice-cold 1.15% potassium chloride (KCl) solution to remove residual blood, and stored at −20 °C until further biochemical analysis. For histopathological evaluation, representative liver sections were fixed in 10% neutral buffered formalin. For homogenate preparation, weighed portions of liver tissue were homogenized in 50 mmol/L Tris–HCl buffer (pH 7.4) using a Teflon-glass homogenizer at cold conditions. The homogenates were centrifuged at 10,000× *g* for 15 min at 4 °C, and the resulting supernatants were collected and stored at −80 °C for subsequent biochemical and enzymatic assays.

2.5. Body Weight and Liver Index

The body weight of each rat was recorded at the start of the study and again at the end of the 20 weeks. At sacrifice, the liver was rapidly excised, weighed, and used to calculate the liver index (liver weight/body weight × 100%) [30].

2.6. Serum Biochemistry and Liver Redox Assessment

Serum total protein, albumin, and globulin concentrations were determined colorimetrically according to the method described by Krohn [31]. Hepatic function markers, including alanine aminotransferase (ALT), aspartate aminotransferase (AST), and alkaline phosphatase (ALP), were assessed following the protocol of Goodla et al. [32]. At the same time, total bilirubin levels were quantified using the procedure described by Rosenthal et al. [33]. Serum lipid profile parameters, including total cholesterol and triglycerides, were determined following established colorimetric methods [34]. The catalog numbers of all chemicals and the accession IDs of the kits used in this study have been included as follows. Nuclear factor erythroid 2-related factor 2 (Nrf2) concentrations were measured using a rat-specific ELISA kit (Cat. No. E-EL-R1052; Elabscience® Biotechnology Co., Ltd., Houston, TX, USA) in accordance with the manufacturer's protocol. The levels of key hepatic antioxidant enzymes—glutathione peroxidase (GSH-Px), superoxide dismutase (SOD), and catalase (CAT)—were determined using colorimetric assay kits from BioDiagnostic® (Giza, Egypt): GSH-Px (Cat. No. GSH-Px 2524), SOD (Cat. No. SOD 2521), and CAT (Cat. No. CA 2517).

Spectrophotometric readings were obtained using a BioTek® microplate reader (Winooski, VT, USA) at 340 nm for GSH-Px (NADPH oxidation), 560 nm for SOD (nitroblue tetrazolium inhibition), and 510 nm for CAT (hydrogen peroxide decomposition). Lipid peroxidation was quantified by measuring malondialdehyde (MDA) levels using a thiobarbituric acid reactive substances (TBARS) assay kit (Cat. No. MD 2529; BioDiagnostic, Giza, Egypt) according to the manufacturer's instructions.

2.7. Inflammatory Markers

Hepatic concentrations of key inflammatory mediators, including nuclear factor kappa B (NF-κB), inducible nitric oxide synthase (iNOS), interleukin-1β (IL-1β), and tumor necrosis factor-α (TNF-α), were quantified using rat-specific enzyme-linked immunosorbent

assay (ELISA) kits according to the manufacturers' protocols. The following kits were employed: NF-κB (Cat. No. E-EL-R0674) and iNOS (Cat. No. E-EL-R0520) from Elabscience® Biotechnology Co., Ltd. (Houston, TX, USA), IL-1β (Cat. No. MBS702717) from MyBioSource (San Diego, CA, USA), and TNF-α (Cat. No. CEK1115) from Bio-Med Diagnostics (Milton Keynes, UK). Hepatic transforming growth factor-β (TGF-β) levels were determined using a commercial ELISA kit (Cat. No. E-UNEL-R0054, Elabscience® Biotechnology Co., Ltd., Houston, TX, USA). In addition, high-sensitivity C-reactive protein (hs-CRP) concentrations were measured using a rat-specific CRP ELISA kit (eBioscience®, San Diego, CA, USA). All assays were performed in duplicate, and absorbance was measured at the appropriate wavelength using a microplate reader (BioTek Instruments, Winooski, VT, USA). The results were expressed as picograms or nanograms per milligram of protein in liver tissue homogenates.

2.8. RNA Isolation, cDNA Synthesis, and Quantitative Real-Time PCR

Liver tissue samples were homogenized in 1 mL of QIAzol Lysis Reagent (Qiagen, Hilden, Germany) using a TissueLyser II homogenizer (QIAGEN GmbH, Hilden, Germany). Chloroform was then added, and the mixture was centrifuged at 12,000× *g* for 15 min at 4 °C to achieve phase separation. The upper aqueous phase containing RNA was carefully collected into RNase-free microtubes. RNA was precipitated with isopropanol and recovered by centrifugation at 12,000× *g* for 10 min. The RNA pellet was subsequently washed with 75% ethanol, air-dried, and redissolved in nuclease-free water. Residual ethanol was removed by brief centrifugation at 7500× *g* for 5 min. The purity was evaluated based on the A260/A280 and A260/A230 absorbance ratios measured using a NanoDrop 2000 spectrophotometer (Thermo Fisher Scientific, Waltham, MA, USA). Values between 1.8 and 2.1 for A260/A280 and ≥1.8 for A260/A230 were considered acceptable, confirming minimal protein and solvent contamination. The integrity was verified by visualizing 28S and 18S rRNA bands on a 1% agarose gel. The concentration was calculated automatically from the absorbance at 260 nm, ensuring sufficient RNA yield for subsequent analysis.

Complementary DNA (cDNA) was synthesized from total RNA using the iScript™ cDNA Synthesis Kit (Bio-Rad, Hercules, CA, USA) following the manufacturer's protocol. Quantitative real-time PCR (qRT-PCR) was performed using the iTaq™ Universal SYBR® Green Supermix (Bio-Rad, Hercules, CA, USA, Cat. No. 172-5121) on a Rotor-Gene Q system (Qiagen, Hilden, Germany). Specific primers for apoptosis-related genes, Bax (Bcl-2-associated X), Bcl-2 (B-cell lymphoma-2), and Caspase-3 (cysteine–aspartic acid protease-3), were designed and synthesized by Macrogen (Seoul, South Korea) (Table 1). Primer stocks were reconstituted in RNase-free water and stored at −20 °C until use to preserve stability. The relative expression levels of the target genes were normalized to *β-actin* as the reference gene and calculated using the $2^{-\Delta\Delta Ct}$ method described by Livak and Schmittgen [35].

Table 1. Primer sequences for quantitative RT-PCR analysis of apoptosis-related genes in Wistar rat liver.

Gene	* NCBI Gene ID_Rattus Norvegicus	Forward (5′→3′)	Reverse (5′→3′)
Bax	24887	CGGCGAATTGGAGATGAACTGG	CTAGCAAAGTAGAAGAGGGCAACC
Bcl-2	24224	TGTGGATGACTGACTACCTGAACC	CAGCCAGGAGAAATCAAACAGAGG
Caspase-3	25402	GTGGAACTGACGATGATATGGC	CGCAAAGTGACTGGATGAACC
β-Actin	81822	AAGATCCTGACCGAGCGTGG	CAGCACTGTGTTGGCATAGAGG

* NCBI: National Center for Biotechnology Information available at (https://www.ncbi.nlm.nih.gov/) (last accessed 28 October 2025).

2.9. Histological Evaluation of Liver

Liver specimens designated for histological analysis were excised immediately after dissection and fixed in 10% neutral buffered formalin at a 20:1 fixative-to-tissue ratio (*v*/*v*) for 72 h. Fixed samples were dehydrated through graded ethanol solutions, cleared in xylene, and infiltrated with molten paraffin wax. Tissue blocks were embedded and sectioned using a rotary microtome at a thickness of 4–5 μm. Sections were mounted on glass slides, deparaffinized, rehydrated through a descending alcohol series, and stained with hematoxylin and eosin (H&E) for routine histological evaluation.

Histopathological examination was performed on three rats per group using a light microscope (Olympus BX53, Tokyo, Japan) at 400× magnification. For each animal, three representative slides were prepared, each containing three liver sections. Four non-overlapping fields were examined per section, yielding 12 microscopic fields per liver sample. The mean lesion score per rat was calculated by averaging the field scores for each animal. Semi-quantitative evaluation of hepatic steatosis followed the AASLD guidelines (Table 2). Lesions were scored semi-quantitatively from 0 (no lesion) to 3 (severe), and the mean score per rat was obtained by averaging all individual field scores. Tissue morphology was assessed by an experienced histopathologist blinded to the experimental groups to minimize bias. Semi-quantitative data were used to determine relative histological improvement across treatment groups.

Table 2. Scoring system for semi-quantitative liver lesion assessment.

Score	Composite Multi-Criteria Liver Assessment Score
0 (none)	No pathological changes
1 (mild)	The liver demonstrated sporadic to mild hepatocellular degeneration and necrosis, accompanied by little to no inflammatory cell infiltration and occasional vascular congestion.
2 (moderate)	The liver showed marked inflammatory cell infiltration, moderate vacuolar hepatocyte degeneration, mild vascular congestion, and multifocal necrotic lesions.
3 (severe)	The liver demonstrated extensive inflammatory infiltration and necrosis, along with severe degeneration of hepatocytes and moderate to severe vascular congestion.

2.10. Transmission Electron Microscopy (TEM)

For ultrastructural analysis, small liver specimens (~1 mm^3) were immediately fixed in 2.5% glutaraldehyde prepared in 0.1 M phosphate buffer (pH 7.4) at 4 °C for 24 h to preserve cellular architecture. After primary fixation, tissues were rinsed three times with phosphate buffer and subsequently post-fixed in 1% osmium tetroxide (OsO_4) for 2 h at 4 °C to enhance membrane contrast. Dehydration was performed using a graded ethanol series (50%, 70%, 90%, 95%, and 100%), followed by two rinses in acetone to ensure complete dehydration. Samples were infiltrated with a mixture of acetone and epoxy resin, embedded in pure epoxy resin (Epon 812 or equivalent), and polymerized at 60 °C for 48 h. Ultrathin sections (60–70 nm) were prepared using an ultramicrotome (Leica EM UC7, Vienna, Austria) equipped with a diamond knife. Sections were mounted on copper grids and counterstained sequentially with uranyl acetate (2%, 30 min) and lead citrate (10 min) to enhance structural contrast. The stained sections were examined using a JEOL JEM-2100 transmission electron microscope (JEOL Ltd., Tokyo, Japan) operated at an accelerating voltage of 160 kV. Digital micrographs were obtained at varying magnifications (8000×–40,000×) to evaluate hepatocellular ultrastructural changes, including mitochondrial morphology, endoplasmic reticulum integrity, nuclear condensation, and lipid droplet accumulation [36,37].

2.11. Statistical Analysis

All data were tested for normality using the Shapiro–Wilk test and for homogeneity of variances using Levene's test before parametric analysis. Statistical comparisons among groups were performed using one-way analysis of variance (ANOVA) followed by Tukey's post hoc multiple comparison test for pairwise group analysis (SAS software, version 9.4; SAS Institute Inc., Cary, NC, USA). Results are expressed as mean ± standard error of the mean (SEM), and differences were considered statistically significant at $p < 0.05$. Graphical representations were generated using GraphPad Prism 9.0 (GraphPad Software, San Diego, CA, USA). A hierarchical clustering heatmap was constructed to visualize comparative group relationships using the online bioinformatics platform SRplot—Science and Research Plotting Tool (https://www.bioinformatics.com.cn) (accessed on 12 October 2025) with the default visualization parameters.

3. Results

3.1. Molecular Docking Results

Molecular docking analysis revealed that Carvacrol exhibits a multifaceted interaction profile with antioxidant, inflammatory, and apoptotic signaling proteins relevant to hepatic protection. Carvacrol exhibited the highest binding affinity for GSH-Px (–6.0 kcal/mol) and Nrf2 (–5.7 kcal/mol) compared to other antioxidant targets. This was corroborated by several stabilizing interactions, including four hydrogen bonds with Nrf2 and significant hydrophobic contacts with critical residues such as Val606 and Gly367. Carvacrol exhibited moderate affinity for superoxide dismutase (SOD) (–5.4 kcal/mol) and catalase (CAT) (–5.0 kcal/mol), establishing limited hydrogen bonds while maintaining significant hydrophobic interactions with key catalytic residues, such as Val7 and His364. Carvacrol demonstrated a significant affinity for inflammatory mediators, particularly NF-κB (–6.3 kcal/mol), establishing eight hydrophobic interactions with key residues (Trp464, Arg432, Lys430). Docking with TNF-α (–5.6 kcal/mol) and IL-1β (–4.6 kcal/mol) supports the anti-inflammatory activity through interactions with critical aromatic and aliphatic residues. Carvacrol demonstrated moderate binding affinity for Caspase-3 (–4.1 kcal/mol) and TGF-β (–4.1 kcal/mol), primarily via hydrophobic interactions, suggesting a potential role in reducing apoptosis and profibrotic signaling (Figure 4 and Table 3).

3.2. Characterization of Carvacrol-Loaded Chitosan Nanoparticles (CRV-CNPs)

Transmission electron microscopy revealed that the synthesized CRV-CNPs exhibited spherical morphology with uniform dispersion and smooth surfaces (Figure 5A). The particle size distribution determined from TEM micrographs ranged between 70 and 131 nm (Figure 5B), confirming nanoscale formation. In contrast, dynamic light scattering (DLS) analysis yielded a hydrodynamic diameter of 192 nm, a value higher than the particle diameter, which is attributed to the hydration layer and the Brownian motion of nanoparticles in the colloidal suspension. The polydispersity index (PDI) was measured at 0.448 (Figure 5C), suggesting acceptable monodispersity and uniform particle size distribution. The zeta potential of +35.9 mV (Figure 5D) indicated strong electrostatic repulsion among particles, supporting good colloidal stability of the nanoparticle suspension.

The entrapment efficiency of the formulation was 83.36%, verifying successful encapsulation of carvacrol within the chitosan matrix and consistency with earlier reports on chitosan–carvacrol nanocomposites. The formation of positively charged, spherical nanoparticles with a narrow size distribution supports their potential for enhanced bioavailability, controlled drug release, and improved therapeutic performance.

ATR-FTIR spectra revealed distinct changes in functional group signals following nanoparticle formation. Specifically, a reduction in the intensity of the CRV phenolic band

(~3340 cm^{-1}) and a shift in the O–H/N–H stretching (~3400 cm^{-1}) were observed in CRV-CHNPs, indicating hydrogen bonding interactions between carvacrol and chitosan, and confirming successful encapsulation (Figure 6).

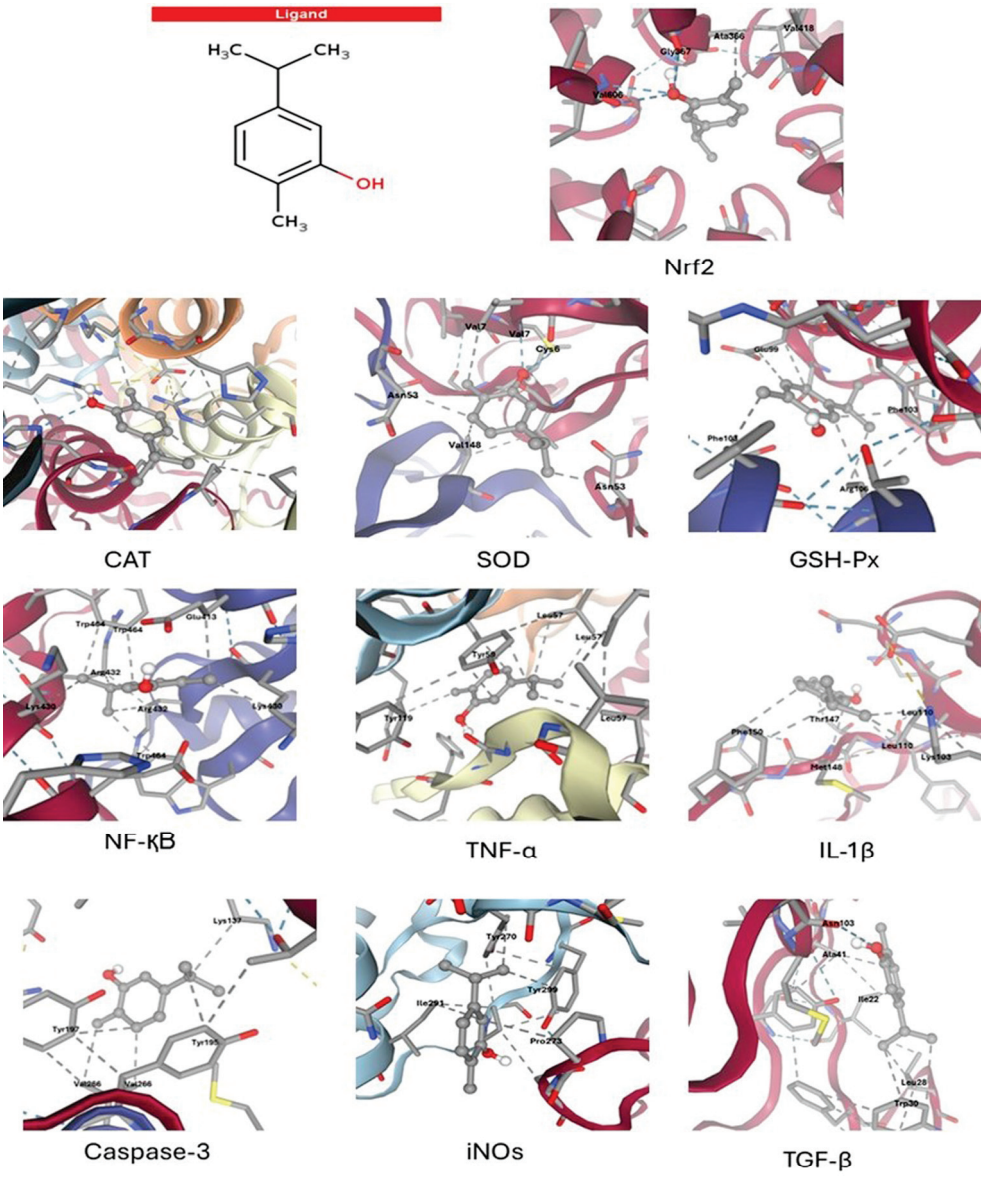


Figure 4. Molecular docking interactions of Carvacrol with key antioxidant, inflammatory, apoptotic, and fibrogenic targets involved in hepatic protection. The figure shows hydrogen bonds and hydrophobic interactions as dotted blue and gray lines, respectively. Also, major active-site residues contributing to ligand stabilization for each protein are shown. Nrf2: Nuclear factor erythroid 2–related factor 2; CAT: catalase; SOD: superoxide dismutase; GSH-Px: glutathione peroxidase; NF-κB: Nuclear Factor kappa-light-chain-enhancer of activated B cells; TNF-α: Tumor Necrosis Factor-alpha; IL-1β: Interleukin-1β; iNOs: inducible nitric oxide synthase; TGF-β: transforming growth factor-beta.

Table 3. Molecular docking interactions of Carvacrol with key antioxidant, inflammatory, apoptotic, and fibrogenic targets involved in hepatic protection.

Target	Affinity (kcal/mol)	Hydrogen Bonds	Hydrophobic Contacts	Active Residues
Nrf2	−5.7	4	2	Val606(2), Gly367(2), Ala366, Val418
CAT	−5	1	3	Arg363, His364(2), Pro368
SOD	−5.4	2	4	Val7(2), Cys6, Asn53(2), Val148
GSH-Px	−6	0	6	Glu88(2), Phe103(2), Arg106(2)
NF-κB	−6.3	0	8	Trp464(3), Arg432(2), Lys430(2), Glu413

Table 3. *Cont.*

Target	Affinity (kcal/mol)	Hydrogen Bonds	Hydrophobic Contacts	Active Residues
TNF-α	−5.6	0	7	Tyr119, Tyr59(3), Leu57(3)
Il-1β	−4.6	0	7	Phe150(2), Met148, Leu110(2), Lys103, Thr147
Caspase-3	−4.1	0	5	Lys137, Tyr195, Tyr197, Val266(2)
iNOS	−4.8	0	4	Tyr270, Ile291, Pro273, Tyr299
TGF-β	−4.1	1	5	Asn103, Ala41, Ile22, Leu28, Trp30(2)

The table summarizes binding affinity (kcal/mol), the number of hydrogen bonds and hydrophobic interactions, and the major active-site residues contributing to ligand stabilization for each protein. Nrf2: Nuclear factor erythroid 2–related factor 2; CAT: catalase; SOD: superoxide dismutase; GSH-Px: glutathione peroxidase; NF-κB: Nuclear Factor kappa-light-chain-enhancer of activated B cells; TNF-α: Tumor Necrosis Factor-alpha; IL-1β: Interleukin-1β; iNOs: inducible nitric oxide synthase; TGF-β: transforming growth factor-beta.

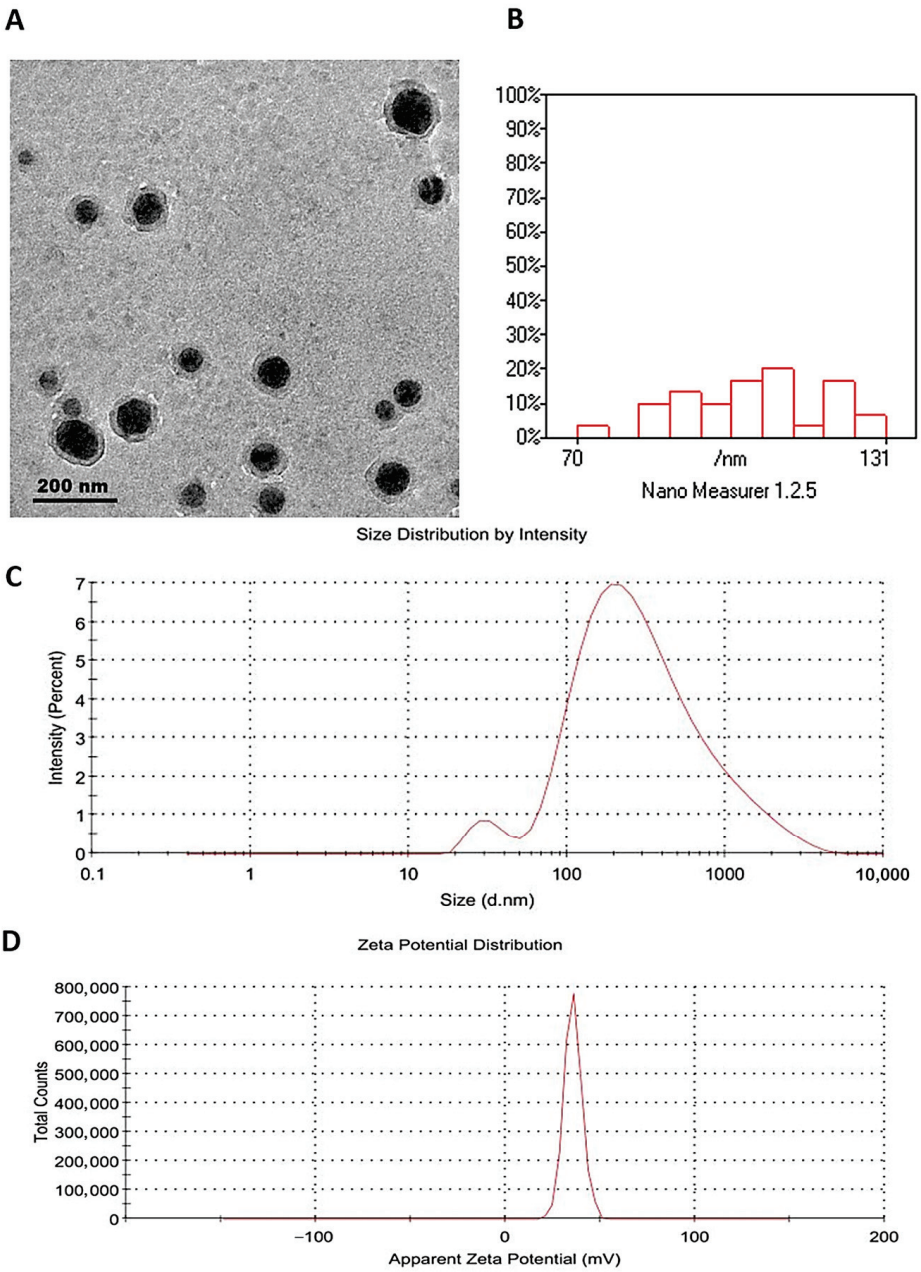


Figure 5. Characterization of Carvacrol-Loaded Chitosan Nanoparticles (CNPs): (**A**) TEM image showing nearly spherical particles; (**B**) particle size histogram indicating most particles range from 70 to 131 nm with good distribution; (**C**) size distribution by intensity; (**D**) zeta potential distribution. The nanoparticles exhibited a Z-average size of 192 nm, a PDI of 0.448, and a zeta potential of 35.9 mV.

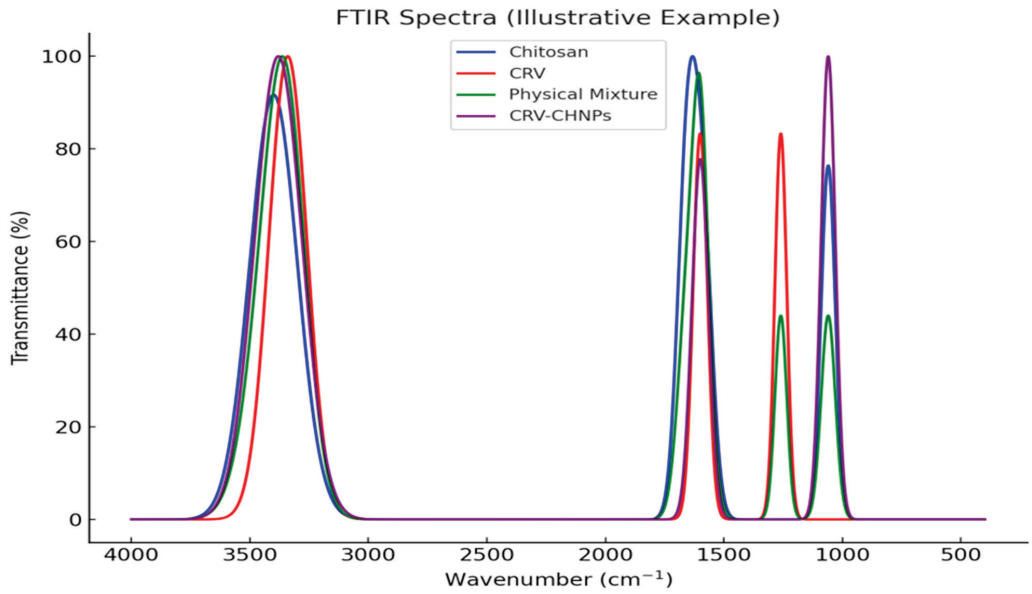


Figure 6. Attenuated Total Reflectance-Fourier Transform Infrared (ATR-FTIR) spectra of pure chitosan, carvacrol (CRV), their physical mixture, and CRV-CHNPs. Characteristic spectral shifts indicate the successful encapsulation of CRV.

3.3. Body Weight and Liver Index Results

As shown in Figure 7A, liver weight was significantly elevated in HFD-fed rats compared to animals receiving a normal diet or those treated with CRV or CRV-CNPs. Co-administration of CRV or CRV-CNPs slightly reduced liver weight; however, this reduction did not reach statistical significance compared to the HFD group.

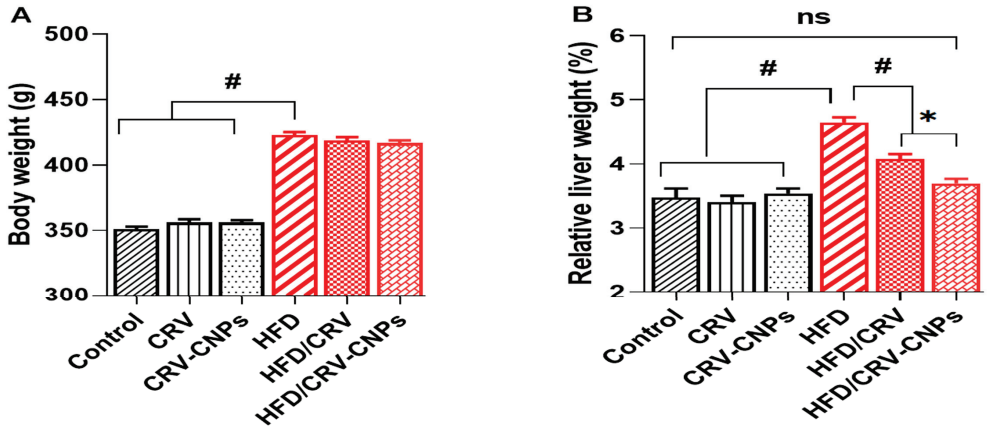


Figure 7. Effect of carvacrol (CRV) and CRV-loaded chitosan nanoparticles (CRV-CNPs) on body weight (**A**) and liver index (**B**) in rats receiving a high-fat diet. CRV: carvacrol (100 mg/kg body weight); CRV-CNPs: carvacrol-loaded chitosan nanoparticles (100 mg/kg body weight); HFD: high-fat diet; HFD/CRV: carvacrol (100 mg/kg body weight) + high-fat diet; HFD/CRV-CNPs: carvacrol-loaded chitosan nanoparticles (100 mg/kg body weight) + high-fat diet. Data are presented as mean ± standard deviation (SD) from $n = 10$ per group. Error bars depict both upper and lower limits of SD for each group. Significant group-wise differences are indicated by # ($p < 0.05$), * ($p < 0.01$), and ns (not significant).

In contrast, the liver index (ratio of liver weight to body weight) showed a more distinctive pattern. HFD-fed rats showed a significant increase in liver index compared with all control and treatment groups, consistent with hepatic lipid accumulation and steatosis commonly observed in HFD-induced NAFLD models. Co-treatment with CRV or CRV-CNPs markedly attenuated this increase, with CRV-CNPs exhibiting greater efficacy

than free CRV in restoring the liver index to near-control values, with nonsignificant differences observed (Figure 7B).

3.4. Hepatic Function and Lipid Metabolism

The effects of carvacrol (CRV) and carvacrol-loaded chitosan nanoparticles (CRV-CNPs) on hepatic function and lipid metabolism indices in high-fat diet (HFD)-induced rats are presented in Table 4. HFD-fed rats demonstrated a significant decline in total serum protein levels, including both albumin and globulin fractions, compared with the normal control and groups receiving CRV or CRV-CNPs alone. Co-administration of CRV or CRV-CNPs significantly restored these parameters, with the most notable improvements observed in the HFD + CRV-CNPs group, where protein levels approached normal values. Conversely, no significant recovery was detected in the HFD + CRV group compared to the untreated HFD group.

Table 4. Effects of carvacrol (CRV) and CRV-loaded chitosan nanoparticles (CRV-CNPs) on hepatic function and lipid metabolism indices in rats fed a high-fat diet.

Items	Control	CRV	CRV-CNPs	HFD	HFD/CRV	HFD/CRV-CNPs
TP (g/dL)	5.98 ± 0.38 $^{\#}$	6.01 ± 0.42 $^{\#}$	6.13 ± 0.41 $^{\#}$	3.22 ± 0.33	3.95 ± 0.29	4.72 ± 0.49 $^{\#,¥}$
Alb (g/dL)	3.17 ± 0.15 $^{\#}$	3.12 ± 0.11 $^{\#}$	3.19 ± 0.28 $^{\#}$	1.72 ± 0.09	2.01 ± 0.14	2.53 ± 0.13 $^{*,\#,¥}$
Glo (g/dL)	2.81 ± 0.16 $^{\#}$	2.89 ± 0.18 $^{\#}$	2.94 ± 0.20 $^{\#}$	1.53 ± 0.12	1.94 ± 0.09	2.19 ± 0.07 $^{\#,¥}$
ALT (U/L)	34.21 ± 3.55 $^{\#}$	31.20 ± 2.31 $^{\#}$	30.03 ± 3.59 $^{\#}$	88.21 ± 5.77	65.59 ± 4.16 $^{\#}$	41.07 ± 3.38 $^{*\#}$
AST (U/L)	71.13 ± 4.47 $^{\#}$	70.13 ± 5.18 $^{\#}$	68.52 ± 3.62 $^{\#}$	141.91 ± 8.11	112.70 ± 7.16 $^{\#}$	84.54 ± 4.25 $^{*\#}$
ALP (U/L)	153.21 ± 6.93 $^{\#}$	149.84 ± 5.08 $^{\#}$	147.61 ± 6.17 $^{\#}$	220.36 ± 10.37	184.16 ± 7.45 $^{\#}$	166.27 ± 5.20 $^{\#}$
GGT (U/L)	11.21 ± 1.12 $^{\#}$	10.41 ± 2.14 $^{\#}$	9.27 ± 1.40 $^{\#}$	22.17 ± 3.02	18.41 ± 1.76 $^{\#}$	14.33 ± 2.43 $^{\#}$
TB (g/dL)	0.41 ± 0.06 $^{\#}$	0.39 ± 0.08 $^{\#}$	0.38 ± 0.04 $^{\#}$	1.32 ± 0.12	0.87 ± 0.10 $^{\#}$	0.62 ± 0.09 $^{\#}$
TG (mg/dL)	57.12 ± 4.11 $^{\#}$	55.39 ± 3.23 $^{\#}$	52.28 ± 5.12 $^{\#}$	123.31 ± 6.18	105.58 ± 4.57 $^{\#}$	79.77 ± 3.62 $^{*,\#,¥}$
TC (mg/dL)	78.26 ± 5.42 $^{\#}$	74.12 ± 6.18 $^{\#}$	72.58 ± 4.77 $^{\#}$	131.22 ± 8.26	98.16 ± 4.11 $^{\#}$	86.27 ± 4.09 $^{\#}$

Data are expressed as mean ± SE. Abbreviations: "TG, triglycerides; TC, total cholesterol; ALT, alanine aminotransferase; AST, aspartate aminotransferase; ALP, alkaline phosphatase; GGT, gamma-glutamyltransferase; TB, Total bilirubin; TP, total protein; Alb, albumin; Glo, globulin." CRV: carvacrol (100 mg/kg body weight); CRV-CNPs: carvacrol-loaded chitosan nanoparticles (100 mg/kg body weight); HFD: high-fat diet; HFD/CRV: carvacrol (100 mg/kg body weight) + high-fat diet; HFD/CRV-CNPs: carvacrol-loaded chitosan nanoparticles (100 mg/kg body weight) + high-fat diet. $^{\#}$ indicates significant difference compared to the HFD group; * indicates significant difference compared to the HFD/CRV-CNPs group; $^{¥}$ indicates significant difference compared to the Control group.

Regarding hepatic enzyme activities, ALT, AST, ALP, and GGT were markedly elevated in HFD-fed rats relative to all control groups, reflecting hepatocellular injury. Both CRV and CRV-CNP supplementation significantly reduced these enzyme activities, with CRV-CNPs showing superior normalization, reaching levels that did not differ significantly from those of the normal control rats. Similarly, total bilirubin concentrations were elevated in the HFD group but significantly diminished following CRV-CNPs treatment, returning to baseline control levels.

3.5. Redox Status

As shown in Figure 7, Nrf2 activity (Figure 8A) was significantly reduced in HFD-fed rats compared with all control groups. Both CRV and CRV-CNP supplementation markedly restored Nrf2 levels, with the HFD + CRV-CNPs group exhibiting the greatest upregulation. This activation of Nrf2 was accompanied by parallel restoration of its downstream antioxidant system. Specifically, the levels of reduced glutathione (GSH) (Figure 8B) and the enzymatic activities of SOD, GSH-Px, and CAT (Figure 8C–E) were significantly decreased in the HFD group but notably increased after treatment with CRV or CRV-CNPs. Importantly, GSH and GSH-Px values in the nanoform-treated group were comparable to those of controls. Conversely, the HFD group exhibited a sharp rise in

malondialdehyde (MDA), an indicator of lipid peroxidation (Figure 8F). This elevation was significantly reduced by CRV, with greater attenuation observed in CRV-CNP-treated rats.

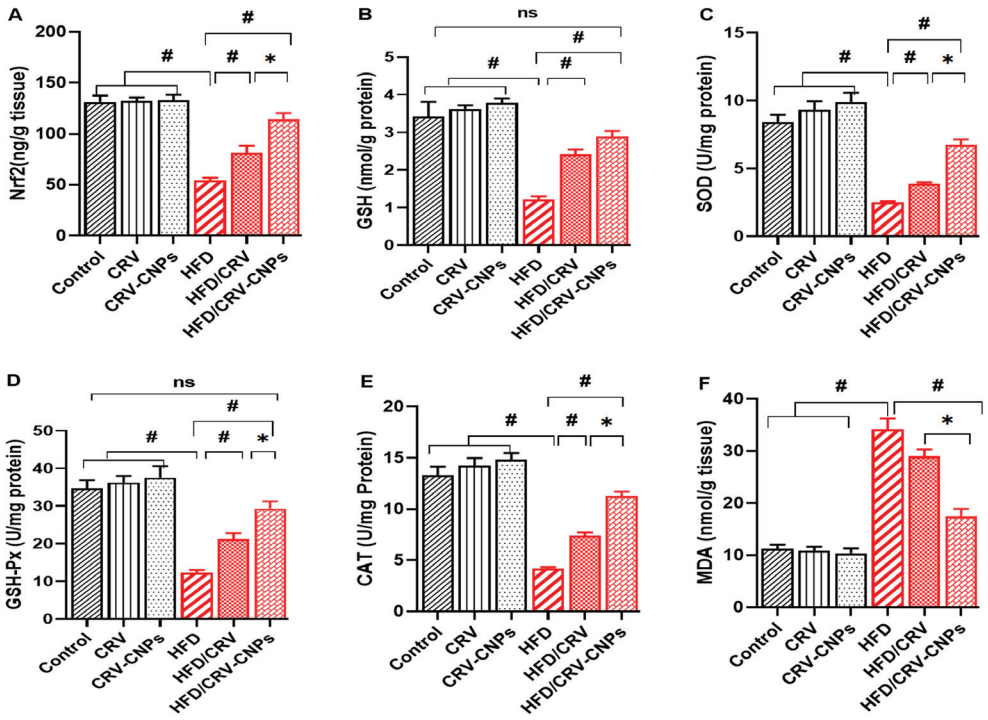


Figure 8. Effect of carvacrol (CRV) and CRV-loaded chitosan nanoparticles (CRV-CNPs) on hepatic redox status in rats receiving a high-fat diet (**A**–**F**). Nrf2: nuclear factor erythroid 2-related factor 2; GSH: glutathione; SOD: superoxide dismutase; GSH-Px: glutathione peroxidase; CAT: catalase; MDA: malondialdehyde. CRV: carvacrol (100 mg/kg body weight); CRV-CNPs: carvacrol-loaded chitosan nanoparticles (100 mg/kg body weight); HFD: high-fat diet; HFD/CRV: carvacrol (100 mg/kg body weight) + high-fat diet; HFD/CRV-CNPs: carvacrol-loaded chitosan nanoparticles (100 mg/kg body weight) + high-fat diet. # indicates significant difference compared to the HFD group; * indicates significant difference compared to the HFD/CRV-CNPs group; ns, nonsignificant.

3.6. Inflammation Response

As illustrated in Figure 9, hepatic inflammatory biomarkers were markedly elevated in HFD-fed rats. Levels of NF-κB (Figure 9A), iNOS (Figure 9B), IL-1β (Figure 9C), and TNF-α (Figure 9D) increased significantly compared with the normal control and groups receiving CRV or CRV-CNPs alone, indicating activation of hepatic inflammation caused by lipid overload. Treatment with CRV or CRV-CNPs significantly mitigated this response, with CRV-CNPs exhibiting superior efficacy. Notably, NF-κB, IL-1β, and TNF-α levels in the HFD + CRV-CNPs group were comparable to those in the normal control, demonstrating the nanoformulation's enhanced ability to suppress the NF-κB/iNOS/IL-1β axis more efficiently than free CRV. Regarding systemic inflammation, C-reactive protein levels (Figure 9E) were significantly increased in HFD-fed rats, consistent with aggravated hepatic inflammation. Both CRV and CRV-CNPs significantly reduced CRP levels, with the strongest reduction in the HFD + CRV-CNPs group, restoring values near those of the normal control. Similarly, transforming growth factor-β (TGF-β) (Figure 9F) was significantly elevated in HFD-fed rats, reflecting early fibrotic activation. Co-treatment with CRV or CRV-CNPs significantly reduced TGF-β levels, with the CRV-CNPs formulation producing the greatest decline, approaching control levels.

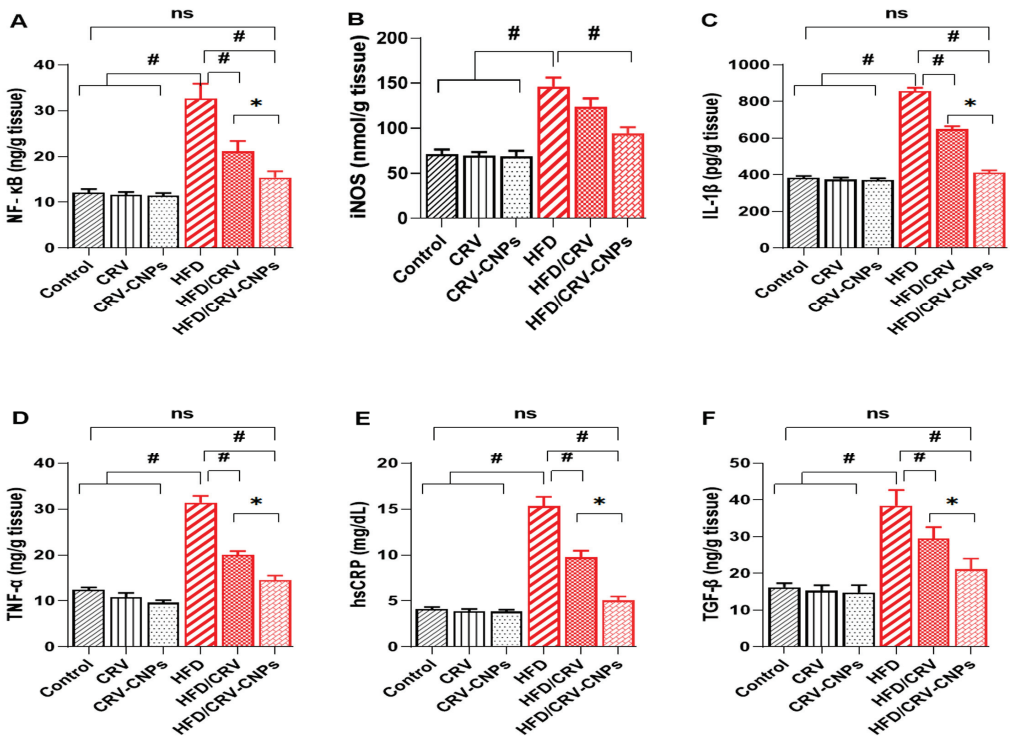


Figure 9. Effect of carvacrol (CRV) and CRV-loaded chitosan nanoparticles (CRV-CNPs) on hepatic inflammatory markers in rats receiving a high-fat diet (**A**–**F**). NF-kB, nuclear factor kappa B; iNOS, inducible nitric oxide synthase; IL-1β, interleukin-1β; TNF-α, tumor necrosis factor alpha; hs CRP, C-reactive protein; TGF-β, transforming growth factor-β. CRV: carvacrol (100 mg/kg body weight); CRV-CNPs: carvacrol-loaded chitosan nanoparticles (100 mg/kg body weight); HFD: high-fat diet; HFD/CRV: carvacrol (100 mg/kg body weight) + high-fat diet; HFD/CRV-CNPs: carvacrol-loaded chitosan nanoparticles (100 mg/kg body weight) + high-fat diet. # indicates significant difference compared to the HFD group; * indicates significant difference compared to the HFD/CRV-CNPs group; ns, nonsignificant.

3.7. Apoptosis-Related Genes

As shown in Figure 10, the expression of hepatic apoptosis-regulating genes was markedly altered in HFD-fed rats compared with the control groups. Specifically, *Bax* (Figure 10A) and *Caspase-3* (Figure 10C) mRNA levels were significantly upregulated, while *Bcl-2* expression (Figure 10B) was significantly downregulated, indicating enhanced pro-apoptotic signaling and compromised hepatocellular protection.

Treatment with CRV or CRV-CNPs substantially reversed the HFD-induced apoptotic imbalance, as evidenced by upregulation of *Bcl-2* and significant downregulation of *Bax* and *Caspase-3* expression relative to the HFD group. Notably, the CRV-CNP-treated rats exhibited a more pronounced modulation of apoptotic gene expression than those receiving free CRV, highlighting the nanoparticle formulation's superior antiapoptotic efficacy. Furthermore, rats administered CRV or CRV-CNPs alone showed no significant difference from the control group, confirming the safety and non-cytotoxic nature of the treatment.

3.8. Hepatic DNA Damage Biomarkers

As shown in Figure 11, HFD-fed rats exhibited a significant elevation in hepatic DNA fragmentation, demonstrating increased genomic instability caused by lipid overload. Co-treatment with CRV or CRV-CNPs significantly reduced DNA fragmentation, with CRV-CNPs showing the most pronounced protective effect (Figure 11A). Similarly, hepatic concentrations of 8-hydroxy-2′-deoxyguanosine (8-OHdG), a well-established biomarker of oxidative DNA damage, were markedly increased in HFD-fed rats compared with controls.

Treatment with CRV or CRV-CNPs significantly decreased 8-OHdG levels, with the lowest values observed in the HFD + CRV-CNPs group (Figure 11B).

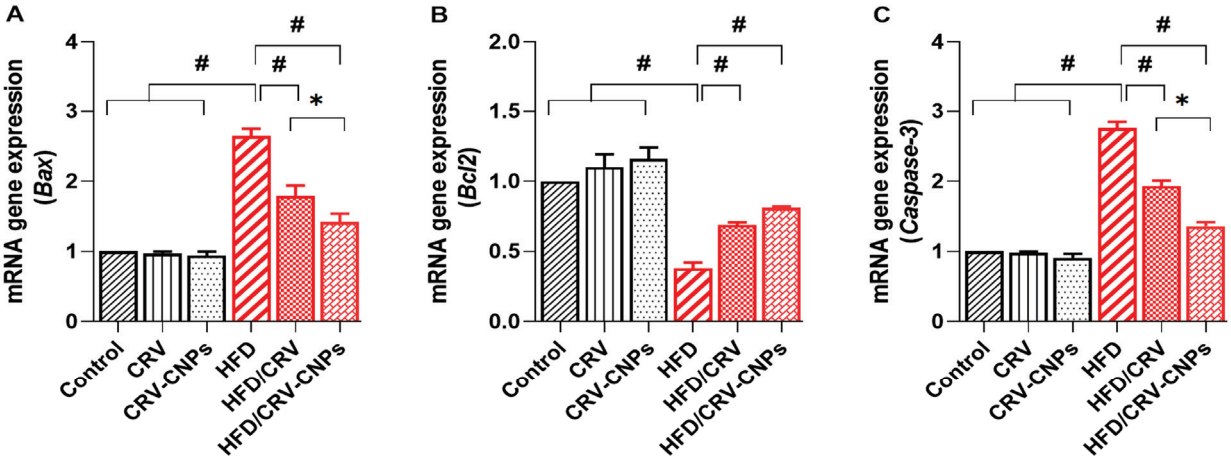


Figure 10. Effect of carvacrol (CRV) and CRV-loaded chitosan nanoparticles (CRV-CNPs) on Hepatic apoptotic gene expression in rats receiving a high-fat diet (**A**–**C**). *Bax*: Bcl-2-associated X protein; *Bcl2*:'B-cell lymphoma 2; *Caspase 3*: cysteine–aspartic acid protease-3. CRV: carvacrol (100 mg/kg body weight); CRV-CNPs: carvacrol-loaded chitosan nanoparticles (100 mg/kg body weight); HFD: high-fat diet; HFD/CRV: carvacrol (100 mg/kg body weight) + high-fat diet; HFD/CRV-CNPs: carvacrol-loaded chitosan nanoparticles (100 mg/kg body weight) + high-fat diet. # indicates significant difference compared to the HFD group; * indicates significant difference compared to the HFD/CRV-CNPs group.

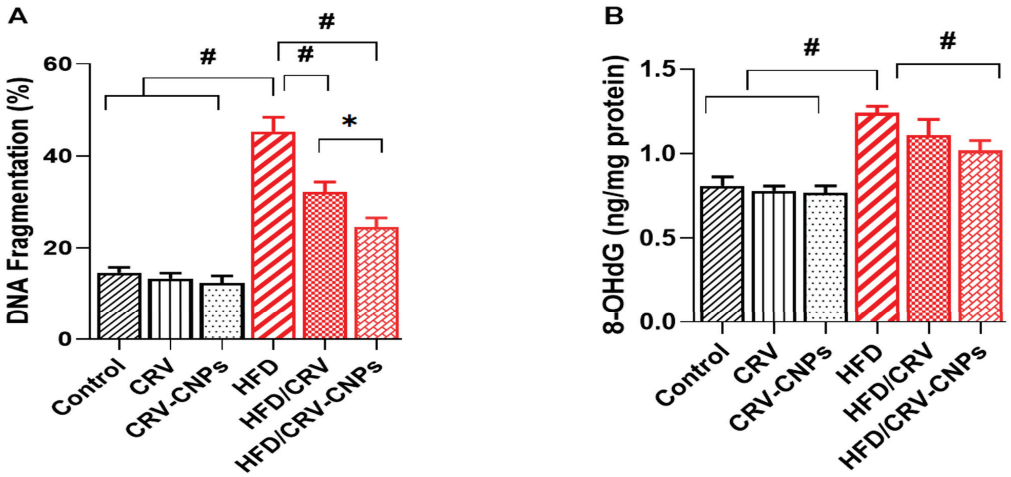


Figure 11. Effect of carvacrol (CRV) and CRV-loaded chitosan nanoparticles (CRV-CNPs) on Hepatic DNA fragmentation and 8-hydroxy-2′-deoxyguanosine (8-OHdG) levels in rats receiving a high-fat diet (**A**,**B**). CRV: carvacrol (100 mg/kg body weight); CRV-CNPs: carvacrol-loaded chitosan nanoparticles (100 mg/kg body weight); HFD: high-fat diet; HFD/CRV: carvacrol (100 mg/kg body weight) + high-fat diet; HFD/CRV-CNPs: carvacrol-loaded chitosan nanoparticles (100 mg/kg body weight) + high-fat diet. # indicates significant difference compared to the HFD group; * indicates significant difference compared to the HFD/CRV-CNPs group.

3.9. Histopathological Examination

Microscopic evaluation revealed that administration of CRV or CRV-CNPs did not induce any histopathological alterations in hepatic tissues. The lobular architecture remained intact, the central veins appeared normal, and hepatocytes were polygonal with centrally located nuclei and eosinophilic cytoplasm (Figure 12A–C). In contrast, HFD-fed rats exhibited severe diffuse steatosis, characterized by numerous intracellular lipid vacuoles of varying

sizes that displaced nuclei toward the cell periphery. Livers also showed scattered necrotic hepatocytes, diminished cellular detail, and mild perivascular inflammatory infiltration (Figure 12D). Liver sections from HFD + CRV-treated rats displayed mild-to-moderate hepatocellular dissociation, scattered necrotic cells, and focal to bridging portal fibrosis, accompanied by low inflammatory infiltrates and occasional hemorrhagic foci separating hepatic cords (Figure 12E). Conversely, the HFD + CRV-CNPs group exhibited only mild swelling and vacuolization of hepatocytes, with largely preserved hepatic cords and lobular organization (Figure 12F).

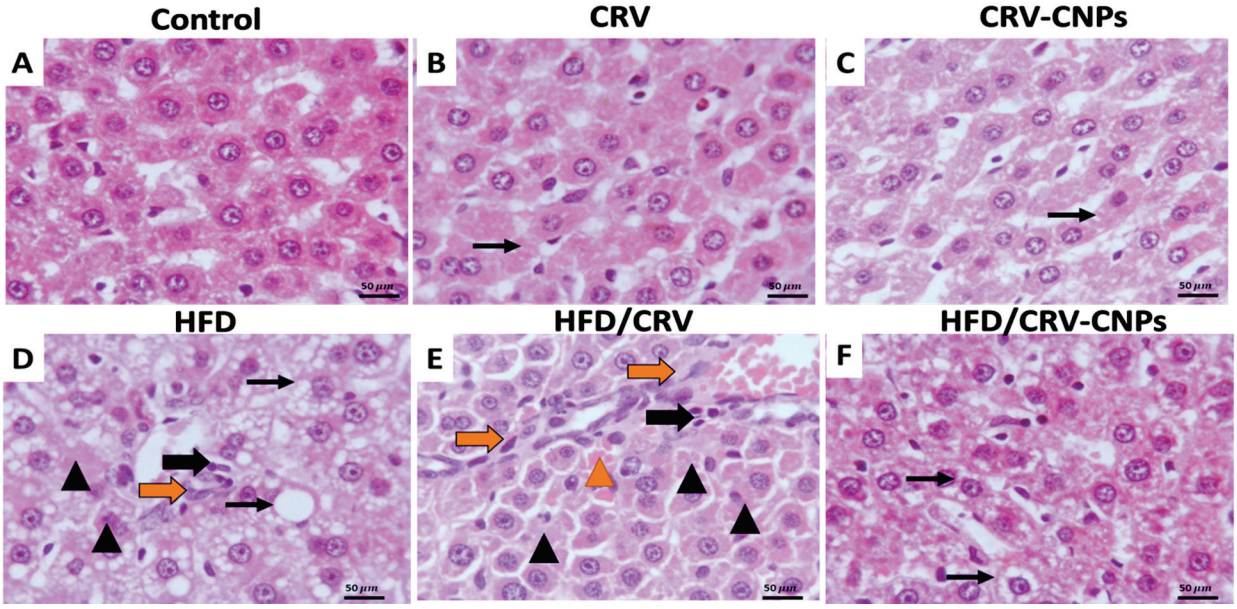


Figure 12. Representative photomicrograph of hepatic parenchyma of different treatment groups. (**A**) Control group; (**B**) CRV: carvacrol (100 mg/kg body weight); (**C**) CRV-CNPs: carvacrol-loaded chitosan nanoparticles (100 mg/kg body weight); (**D**) HFD: high-fat diet; (**E**) HFD/CRV: carvacrol (100 mg/kg body weight) + high-fat diet; and (**F**) HFD/ CRV-CNPs: carvacrol-loaded chitosan nanoparticles (100 mg/kg body weight) + high-fat diet. Thin arrows indicate hepatocellular swelling with vacuolation; black thick arrows indicate inflammation; orange thick arrow indicates fibrosis; arrowheads indicate hepatocellular necrosis; orange arrowhead indicates minor hemorrhage. magnification 400×; scale bar = 50 μm.

Quantitatively, histopathological severity scores were significantly higher in the HFD group compared with controls. In contrast, CRV or CRV-CNPs administration markedly reduced these scores, with the most substantial improvement observed in the CRV-CNPs-treated rats (Figure 13).

3.10. Ultrastructural Examination

As shown in Figure 14A–C, hepatocytes from the control, CRV-, and CRV-CNP-treated rats retained normal ultrastructural organization. Cells displayed well-preserved rough endoplasmic reticulum (rER), intact mitochondrial morphology, and spherical nuclei with distinct nucleoli, indicating maintained cellular homeostasis. In contrast, hepatocytes from HFD-fed rats showed severe ultrastructural alterations (Figure 14D). These included swollen mitochondria with disrupted cristae, dilated rER cisternae, cytoplasmic disintegration, chromatin condensation, irregular nuclear contours, and extensive cytoplasmic vacuolation, hallmarks of lipid-induced organelle stress and hepatocellular degeneration. Co-treatment with CRV (Figure 14E) or CRV-CNPs (Figure 14F) markedly alleviated these degenerative changes. Hepatocytes in the CRV-CNPs group exhibited largely preserved mi-

tochondria and rER, intact nuclear membranes, and only minimal cytoplasmic vacuolation, demonstrating superior ultrastructural preservation compared with free CRV treatment.

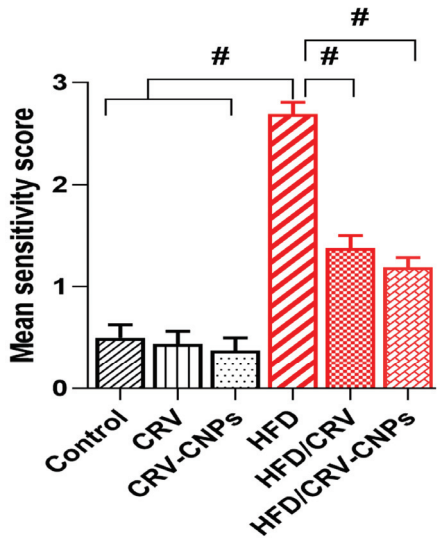


Figure 13. Histopathological severity scores of hepatic injury in control and experimental groups. CRV: carvacrol (100 mg/kg body weight); CRV-CNPs: carvacrol-loaded chitosan nanoparticles (100 mg/kg body weight); HFD: high-fat diet; HFD/CRV: carvacrol (100 mg/kg body weight) + high-fat diet; HFD/CRV-CNPs: carvacrol-loaded chitosan nanoparticles (100 mg/kg body weight) + high-fat diet. # indicates a significant difference compared to the HFD group.

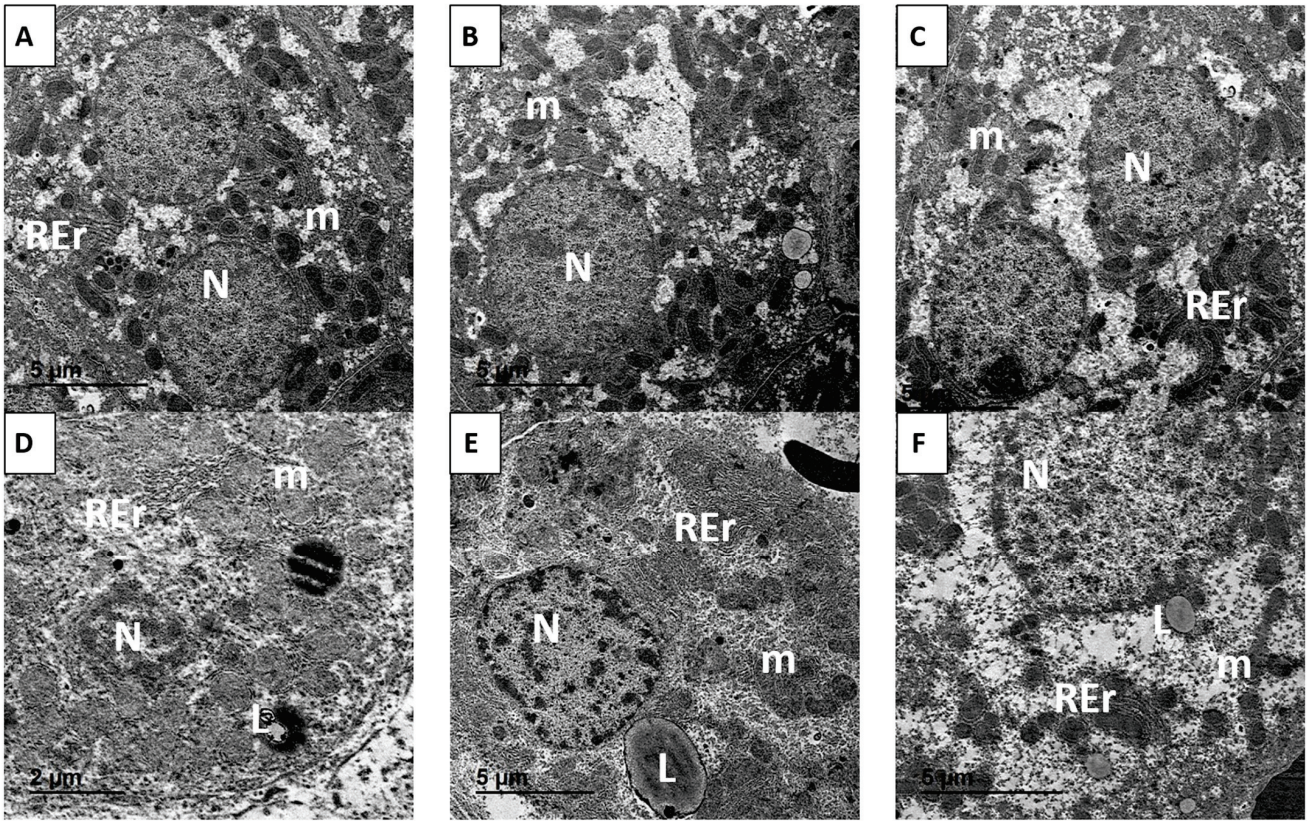


Figure 14. Representative photomicrograph of liver ultrastructure from control and different experimental groups. (**A**) control group; (**B**) CRV group; (**C**) CRV-CNPS; (**D**) HFD; (**E**) HFD/CRV; (**F**) HF/CRV-CPNPs (N) nucleus, (m) mitochondria, (REr) rough endoplasmic reticulum, (L) variable-sized lipid droplet.

3.11. Multivariable Analysis

A hierarchical clustering heatmap (Figure 15) was generated to visualize the relationships among biochemical and molecular variables across all experimental groups. The control, CRV, and CRV-CNPs groups formed a closely related cluster, reflecting similar profiles characterized by lower expression of proinflammatory, apoptotic, and oxidative stress markers (IL-1β, TNF-α, Caspase-3, MDA, iNOS) and higher levels of antioxidant indicators (GSH, SOD, CAT, and Nrf2). In contrast, the HFD group formed a distinct, isolated cluster with the highest concentrations of inflammatory mediators, oxidative stress markers, and hepatic injury enzymes (ALT, AST, ALP, GGT), concurrent with diminished antioxidant defenses. The HFD + CRV and HFD + CRV-CNPs groups occupied intermediate positions between the HFD and control clusters, indicating partial restoration of biochemical and molecular homeostasis. Notably, the HFD + CRV-CNPs group showed the greatest alignment with the control-related cluster, underscoring the superior modulatory efficacy of the nanoformulation in restoring the hepatic redox-inflammatory balance.

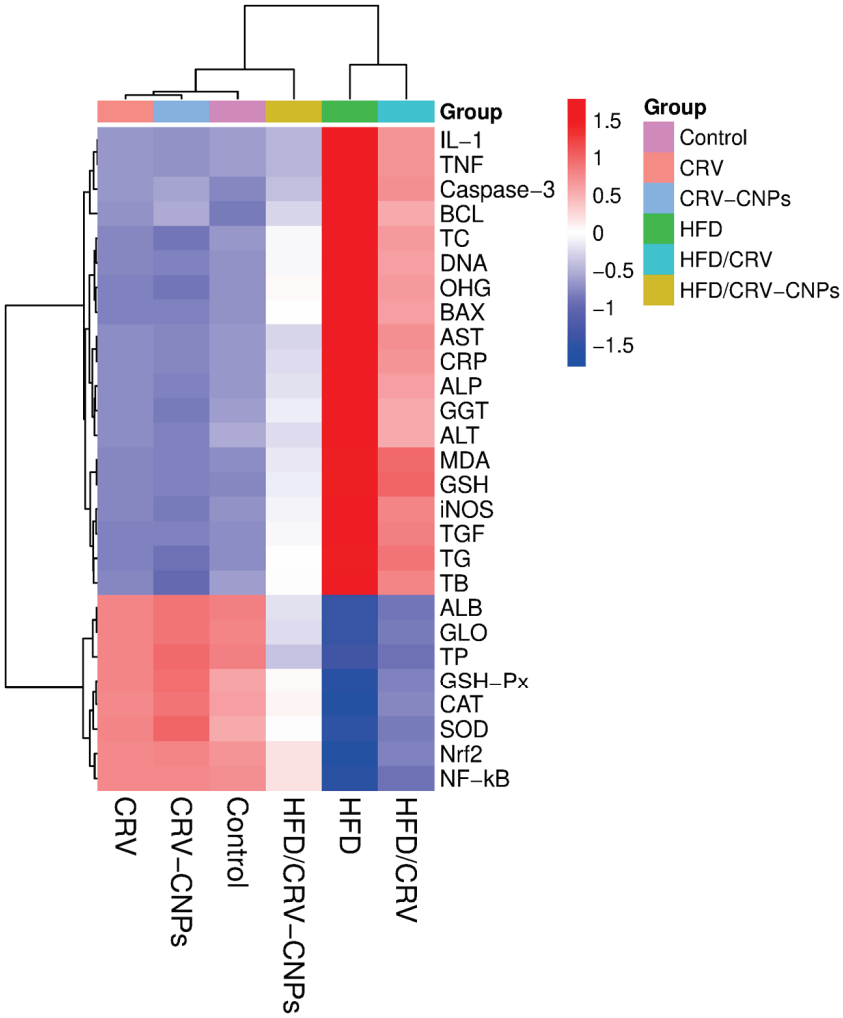


Figure 15. Hierarchical clustering heatmap of biochemical and molecular markers across experimental groups. Blue indicates lower levels; red indicates higher levels relative to the group mean. Key panels highlight proinflammatory cytokines (IL-1, TNF), apoptosis markers (Caspase-3, BAX, BCL), liver function enzymes (AST, ALT, ALP, GGT), oxidative stress markers (MDA, GSH), and regulatory proteins (Nrf2, NF-kB). CRV-CHNPs intervention notably reversed HFD-induced elevations in inflammatory and apoptotic markers, while restoring antioxidant defenses, as evidenced by marked color shifts in the corresponding clusters. These critical differences offer mechanistic insights into the therapeutic impact of CRV-CHNPs in NAFLD.

4. Discussion

The present study provides mechanistic and therapeutic evidence for the hepatoprotective efficacy of carvacrol-loaded chitosan nanoparticles (CRV-CNPs) against high-fat diet (HFD)-induced liver injury in rats. Unlike previous reports that focused primarily on free carvacrol or other phytocompounds, our data demonstrate that nanoencapsulation markedly enhances carvacrol's functional performance in mitigating hepatic steatosis, oxidative stress, inflammation, apoptosis, and genotoxicity.

4.1. Integration and Critical Comparison to Previous Work

Our molecular docking results elucidated specific interactions between carvacrol and antioxidant (Nrf2, SOD, CAT, GSH-Px), inflammatory (NF-κB, TNF-α, IL-1β, iNOS, TGF-β), and apoptotic (Bax, Bcl-2, caspase-3) pathways, providing a mechanistic rationale corroborated by comparable in silico studies for related monoterpenes and polyphenols [38,39]. However, prior work did not validate these computational predictions via direct in vivo assessment. Here, the alignment between docking and biological outcomes strengthens the translational value of our approach [40].

Long-term HFD feeding recapitulated key metabolic derangements seen in rodent NAFLD models, including weight gain, hyperlipidemia, and hepatic steatosis, consistent with previous studies [41,42]. The reduction in liver index and the restoration of ALT/AST observed following CRV-CNP administration closely match findings with silymarin, naringin, and curcumin-based nanoparticles in similar models, highlighting a common benefit of nanoencapsulation (i.e., enhanced hepatic protection) [43,44].

4.2. Lipid Metabolism and Antioxidant Restoration

CRV-CNPs normalized hepatic and serum lipid parameters and reduced histological steatosis. Previous work showed carvacrol could reduce lipid accumulation via AMPK-mediated β-oxidation and downregulation of SREBP-1c; our findings substantiate and extend these results by demonstrating that the nanocarrier formulation amplifies this effect and improves lipid export and antioxidant enzyme activity [12,14]. Comparable results were achieved with nanocarrier-formulated nutraceuticals, which significantly reduced lipid deposition and fibrosis in experimental NAFLD [45–47]. Thus, the metabolic normalization achieved by CRV-CNPs supports their translational potential as nano-nutraceuticals for NAFLD management [46].

Oxidative stress represents a central element in NAFLD pathogenesis, as hepatocyte fat overload increases mitochondrial ROS production, depleting endogenous antioxidant capacity [48]. Our data revealed elevated hepatic MDA levels and suppressed Nrf2 activation, SOD, CAT, and GSH-Px activities in HFD-fed rats, biochemical hallmarks of oxidative imbalance [49,50]. CRV-CNPs restored these parameters near baseline control values, confirming reactivation of the Nrf2-antioxidant axis, a key defense pathway also stimulated by other polyphenolic nanoparticles [51–53]. Recent nanobiomaterial studies are consistent with our findings, leading to reduced hepatic oxidative burden in NAFLD models [54].

4.3. Inflammation and Apoptosis

Hepatic inflammation driven by NF-κB activation is a major contributor to NAFLD progression [55]. Elevated levels of NF-κB, TNF-α, IL-1β, and iNOS observed in our HFD model confirmed amplification of this pathway. CRV-CNPs markedly suppressed these proinflammatory mediators, outperforming free CRV (Figure 16). This effect likely arises from improved cellular internalization and sustained CRV release from the chitosan matrix. Similar declines in inflammatory signaling have been documented in studies where

nanoparticle-encapsulated antioxidants, including curcumin-loaded PLGA and cerium oxide (CeO_2) nanostructures, reduced hepatic cytokine release [56,57]. Furthermore, CRV-CNP administration reduced systemic CRP and TGF-β1 levels, reflecting attenuation of profibrotic processes by inhibiting hepatic stellate cell activation. This observation aligns with findings that nanocarrier-based antifibrotic systems mitigate collagen deposition by targeting ROS-TGF-β signaling [58–61].

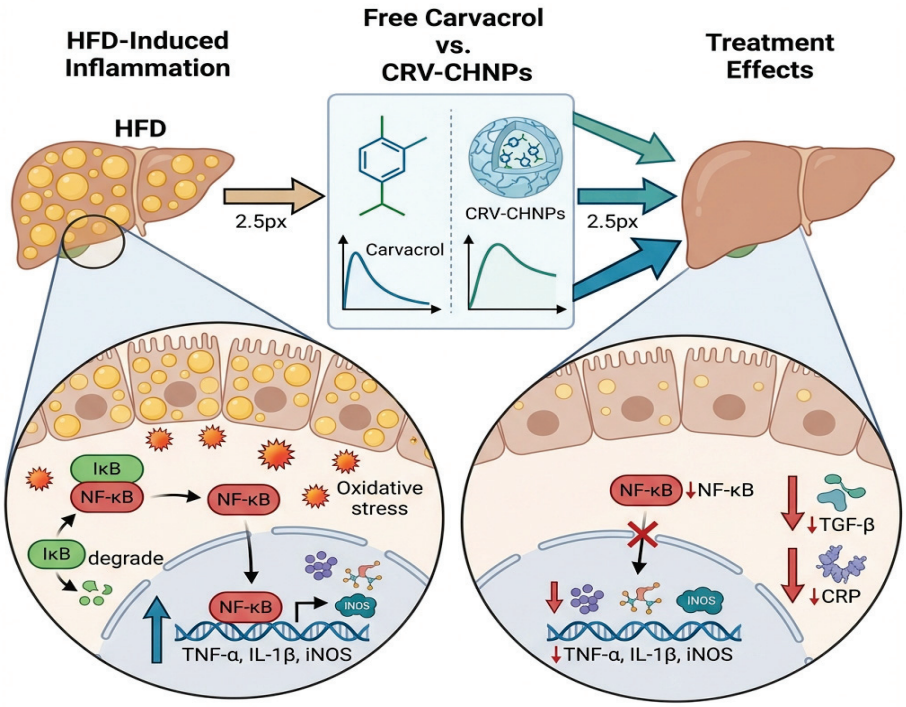


Figure 16. Molecular responses of inflammatory biomarkers to Carvacrol and CRV-CHNPs treatment in HFD-induced NAFLD Rat Model. Adapted from GRABSTRACT-Science, visualized (https://grabstract.io/) (accessed 20 November 2025).

NAFLD is also characterized by apoptosis and genotoxic stress resulting from lipotoxic metabolite accumulation and mitochondrial dysfunction. In this study, HFD significantly upregulated *Bax* and *Caspase-3*, while suppressing *Bcl-2*, leading to hepatocyte apoptosis. CRV-CNPs reversed this imbalance, restoring antiapoptotic signaling and reducing pro-apoptotic expression. These results concur with earlier studies where CRV modulated the Bcl-2/Bax ratio to prevent oxidative apoptosis [10,62]. In parallel, CRV-CNPs substantially decreased DNA fragmentation and 8-OHdG levels, confirming strong genomic protection. 8-OHdG is recognized as a reliable biomarker for oxidative DNA damage and NAFLD-associated carcinogenic risk [63,64]. Comparable reductions in 8-OHdG were reported with exosome-like, polyphenol-rich nanoparticles that enhanced Nrf2-mediated detoxifying enzyme expression and reduced hepatic vacuolation [65,66].

4.4. Histopathological and Ultrastructural Preservation

Histopathological and ultrastructural evaluations further supported these molecular findings. The HFD group displayed classical patterns of macrovesicular steatosis, lobular inflammation, and mitochondrial degeneration, consistent with previous reports linking lipid accumulation to mitochondrial cristae disruption and rER dilation [67,68]. Conversely, CRV-CNP administration largely preserved hepatocellular ultrastructure, maintaining intact mitochondria, organized rER, and normal nuclear morphology, confirming robust cytoprotective efficacy.

4.5. Multivariate Comparisons

The multivariate analysis, integrating biochemical, molecular, and histological parameters, underscored this effect, showing that the CRV-CNP treatment group clustered closest to the control, indicating near normalization of hepatic function and redox-inflammatory balance. This pattern mirrors previous multiscale omics-based clustering studies, demonstrating the restoration of transcriptional and metabolic signatures with targeted nanoformulations in NAFLD [69,70].

4.6. Innovative Mechanistic Insight

Collectively, the current data demonstrate that CRV-CNPs exert a comprehensive hepatoprotective effect through multi-mechanistic modulation of redox, inflammatory, apoptotic, and fibrotic pathways. By overcoming the solubility and stability limitations of free carvacrol, the chitosan nanoparticle matrix enables sustained therapeutic release, enhanced hepatocellular absorption, and improved pharmacodynamic efficacy.

The use of nanoparticles as carriers for carvacrol aims to enhance its hepatic bioavailability by protecting it from premature degradation in the gastrointestinal tract and facilitating its absorption. Upon oral administration, nanoparticles can enhance intestinal uptake via transcellular transport, paracellular diffusion, and endocytosis by enterocytes or M cells in Peyer's patches. Once absorbed, these nanoparticles are often transported via the portal vein directly to the liver, thereby increasing local hepatic concentrations of the encapsulated compound. Recent studies indicate that the physicochemical properties of nanoparticles, including size, surface charge, and hydrophobicity, critically influence their interaction with the intestinal epithelium and subsequent systemic distribution [71,72]. Thus, the oral delivery of carvacrol-loaded nanoparticles represents a strategic approach to overcome the compound's low intrinsic bioavailability, ensuring a more targeted and sustained release at the hepatic level. Integrating these findings with prior reports on nanocarrier-based antioxidants, such as silymarin-, curcumin-, and naringenin-loaded nanoparticles, suggests that polymeric nanoformulations represent a viable strategy for next-generation NAFLD therapeutics [40,73,74].

4.7. Study Limitations and Future Perspectives

Despite providing valuable mechanistic insights, this study has certain limitations that should be acknowledged. First, using a single animal model and dosage regimen may not fully recapitulate the metabolic heterogeneity observed in human NAFLD. Additional models incorporating genetic susceptibility or comorbidities, such as insulin resistance or obesity, would strengthen translational relevance. Second, although CRV-CNPs demonstrated favorable biochemical and histological outcomes, long-term pharmacokinetic, biodistribution, and toxicity profiles were not evaluated; these are crucial to establishing clinical safety, as prolonged nanoparticle accumulation could pose hepatic or immunological risks. While chitosan-based nanoparticles are generally considered biocompatible and biodegradable according to previous studies, comprehensive in vivo safety evaluations, including potential immunogenicity and long-term tissue accumulation, are essential before advancing to human use.

Third, the study did not include in-depth molecular or omics-based analyses to delineate global transcriptional or metabolic alterations downstream of Nrf2 or NF-κB signaling. As emphasized in recent nanotherapeutic reviews, multi-omics are essential for validating molecular targets and clarifying nanoparticle–cell interactions in liver tissue. Furthermore, it should be noted that all experimental methods carry inherent uncertainties, and the observed data may be influenced by technical variability or biological heterogeneity; therefore, interpretations should be made cautiously.

Future studies should, therefore, explore dose–response optimization, long-term safety under chronic exposure conditions, and combinatory approaches involving CRV-CNPs with other hepatoprotective nutraceuticals or metabolic modulators. Ultimately, translating these findings into clinical intervention will necessitate GMP-scale production, pharmacokinetic modeling, and targeted delivery validation to ensure reproducibility and patient safety in human NAFLD [75].

5. Conclusions

This study demonstrates that carvacrol-loaded chitosan nanoparticles (CRV-CNPs) provide potent hepatoprotection against HFD-induced nonalcoholic fatty liver disease by targeting multiple pathogenic mechanisms. CRV-CNPs effectively alleviated hepatic lipid accumulation, oxidative stress, inflammation, apoptosis, and DNA damage while maintaining normal liver architecture. The enhanced efficacy of CRV-CNPs is attributed to improved solubility, stability, and bioavailability, enabling sustained hepatic delivery. Mechanistically, CRV-CNPs upregulated hepatic Nrf2 and antioxidant enzymes, inhibited NF-κB signaling and downstream inflammatory cytokines (TNF-α, IL-1β, iNOS), attenuated pro-apoptotic gene expression (Bax, Caspase-3), and prevented oxidative DNA damage, thereby restoring biochemical balance and preserving cellular integrity more efficiently than free CRV. Together, these findings highlight CRV-CNPs as a promising nanotherapeutic platform for NAFLD management, integrating antioxidant, anti-inflammatory, and antiapoptotic properties within a safe, biocompatible design. Further studies should evaluate pharmacokinetics, long-term safety, and clinical translation.

Author Contributions: Conceptualization, E.M.E.; data curation, S.A.H.; formal analysis, E.M.E.; funding acquisition, M.S.F.; investigation, S.A.H.; methodology, S.A.H. and S.E.E.; resources, M.A., A.N.A., N.A.H., N.M.M.J., M.S.F. and S.E.E.; software, E.M.E. and M.S.F.; validation, M.A., E.M.E., A.N.A., N.A.H., N.M.M.J., M.S.F. and S.E.E.; visualization, E.M.E.; writing—original draft preparation, S.A.H.; writing—review and editing, M.A., E.M.E., A.N.A., N.A.H., N.M.M.J., M.S.F. and S.E.E. All authors have read and agreed to the published version of the manuscript.

Funding: The authors extend their appreciation to Northern Border University, Saudi Arabia, for supporting this work through project number (NBU-CRP-2025-1442).

Institutional Review Board Statement: The animal study protocol was approved by the Research Ethics Committee, October 6 University, Egypt, registration code number: 20251207, on 27 July 2025.

Informed Consent Statement: Not applicable.

Data Availability Statement: The original contributions presented in this study are included in the article. Further inquiries can be directed to the corresponding author.

Conflicts of Interest: The authors declare no conflicts of interest.

Abbreviations

The following abbreviations are used in this manuscript:

AASLD	American Association for the Study of Liver Diseases
ALB	Albumin
ALP	Alkaline phosphatase
ALT	Alanine aminotransferase
AMPK	AMP-activated protein kinase
AST	Aspartate aminotransferase
Bax	Bcl-2-associated X protein
Bcl-2	B-cell lymphoma 2
CAT	Catalase

Caspase-3	Cysteine–aspartic acid protease-3
CH	Chitosan
CRP	C-reactive protein
CRV	Carvacrol
CRV-CNPs	Carvacrol-loaded chitosan nanoparticles
DLS	Dynamic light scattering
DNA	Deoxyribonucleic acid
ELISA	Enzyme-linked immunosorbent assay
EMA	European Medicines Agency
FAO	Food and Agriculture Organization
GGT	Gamma-glutamyl transferase
GMP	Good Manufacturing Practice
GSH	Reduced glutathione
GSH-Px	Glutathione peroxidase
HDL	High-density lipoprotein
HFD	High-fat diet
HSCs	Hepatic stellate cells
H&E	Hematoxylin and eosin
IL-1β	Interleukin-1 beta
iNOS	Inducible nitric oxide synthase
LD	Lipid droplets
LC	Loading content
LE	Loading efficiency
LDL	Low-density lipoprotein
MDA	Malondialdehyde
NAFLD	Nonalcoholic fatty liver disease
NASH	Non-alcoholic steatohepatitis
NF-κB	Nuclear factor kappa B
NIH	National Institutes of Health
Nrf2	Nuclear factor erythroid 2–related factor 2
PDI	Polydispersity index
qRT-PCR	Quantitative real-time polymerase chain reaction
RNA	Ribonucleic acid
ROS	Reactive oxygen species
SOD	Superoxide dismutase
SRplot	Science and Research Plotting Tool
TB	Total bilirubin
TC	Total cholesterol
TEM	Transmission electron microscopy
TG	Triglycerides
TGF-β	Transforming growth factor-beta
TNF-α	Tumor necrosis factor-alpha

References

1. Han, S.K.; Baik, S.K.; Kim, M.Y. Non-alcoholic fatty liver disease: Definition and subtypes. *Clin. Mol. Hepatol.* **2023**, *29*, S5–S16. [CrossRef]
2. Kim, Y.; Chang, Y.; Cho, Y.K.; Ahn, J.; Shin, H.; Ryu, S. Metabolically healthy versus unhealthy obesity and risk of fibrosis progression in non-alcoholic fatty liver disease. *Liver Int. Off. J. Int. Assoc. Study Liver* **2019**, *39*, 1884–1894. [CrossRef] [PubMed]
3. Bence, K.K.; Birnbaum, M.J. Metabolic drivers of non-alcoholic fatty liver disease. *Mol. Metab.* **2021**, *50*, 101143. [CrossRef] [PubMed]
4. Pierantonelli, I.; Svegliati-Baroni, G. Nonalcoholic Fatty Liver Disease: Basic Pathogenetic Mechanisms in the Progression From NAFLD to NASH. *Transplantation* **2019**, *103*, e1–e13. [CrossRef] [PubMed]
5. Salvoza, N.; Giraudi, P.J.; Tiribelli, C.; Rosso, N. Natural Compounds for Counteracting Nonalcoholic Fatty Liver Disease (NAFLD): Advantages and Limitations of the Suggested Candidates. *Int. J. Mol. Sci.* **2022**, *23*, 2764. [CrossRef]

6. Hallsworth, K.; McPherson, S.; Anstee, Q.M.; Flynn, D.; Haigh, L.; Avery, L. Digital Intervention With Lifestyle Coach Support to Target Dietary and Physical Activity Behaviors of Adults With Nonalcoholic Fatty Liver Disease: Systematic Development Process of VITALISE Using Intervention Mapping. *J. Med. Internet Res.* **2021**, *23*, e20491. [CrossRef]
7. Nendouvhada, L.P.; Sibuyi, N.R.S.; Fadaka, A.O.; Meyer, S.; Madiehe, A.M.; Meyer, M.; Gabuza, K.B. Phytonanotherapy for the Treatment of Metabolic Dysfunction-Associated Steatotic Liver Disease. *Int. J. Mol. Sci.* **2024**, *25*, 5571. [CrossRef]
8. Wong, V.W.; Singal, A.K. Emerging medical therapies for non-alcoholic fatty liver disease and for alcoholic hepatitis. *Transl. Gastroenterol. Hepatol.* **2019**, *4*, 53. [CrossRef]
9. Wal, P.; Yadav, S.; Jha, S.K.; Singh, A.; Bhargavi, B.; Shivaram, R.; Imran, M.; Aziz, N. Role of natural compounds in non-alcoholic fatty liver diseases (NAFLD): A mechanistic approach. *Egypt. Liver J.* **2025**, *15*, 50. [CrossRef]
10. Sadeghzadeh, S.; Hejazian, S.H.; Jamhiri, M.; Hafizibarjin, Z.; Sadeghzadeh, S.; Safari, F. The effect of carvacrol on transcription levels of Bcl-2 family proteins in hypertrophied heart of rats. *Physiol. Pharmacol.* **2018**, *22*, 54–62.
11. Mohseni, R.; Karimi, J.; Tavilani, H.; Khodadadi, I.; Hashemnia, M. Carvacrol Downregulates Lysyl Oxidase Expression and Ameliorates Oxidative Stress in the Liver of Rats with Carbon Tetrachloride-Induced Liver Fibrosis. *Indian. J. Clin. Biochem.* **2020**, *35*, 458–464. [CrossRef] [PubMed]
12. Khazdair, M.R.; Moshtagh, M.; Anaeigoudari, A.; Jafari, S.; Kazemi, T. Protective effects of carvacrol on lipid profiles, oxidative stress, hypertension, and cardiac dysfunction–A comprehensive review. *Food Sci. Nutr.* **2024**, *12*, 3137–3149. [CrossRef]
13. Mączka, W.; Twardawska, M.; Grabarczyk, M.; Wińska, K. Carvacrol-A Natural Phenolic Compound with Antimicrobial Properties. *Antibiotics* **2023**, *12*, 824. [CrossRef] [PubMed]
14. Cho, S.; Choi, Y.; Park, S.; Park, T. Carvacrol prevents diet-induced obesity by modulating gene expressions involved in adipogenesis and inflammation in mice fed with high-fat diet. *J. Nutr. Biochem.* **2012**, *23*, 192–201. [CrossRef]
15. Vitali, A.; Stringaro, A.; Colone, M.; Muntiu, A.; Angiolella, L. Antifungal Carvacrol Loaded Chitosan Nanoparticles. *Antibiotics* **2021**, *11*, 11. [CrossRef]
16. Llana-Ruiz-Cabello, M.; Gutiérrez-Praena, D.; Pichardo, S.; Moreno, F.J.; Bermúdez, J.M.; Aucejo, S.; Cameán, A.M. Cytotoxicity and morphological effects induced by carvacrol and thymol on the human cell line Caco-2. *Food Chem. Toxicol.* **2014**, *64*, 281–290. [CrossRef]
17. Mauriello, E.; Ferrari, G.; Donsì, F. Effect of formulation on properties, stability, carvacrol release and antimicrobial activity of carvacrol emulsions. *Colloids Surf. B Biointerfaces* **2021**, *197*, 111424. [CrossRef]
18. Tripathy, A.; Pahal, S.; Mudakavi, R.J.; Raichur, A.M.; Varma, M.M.; Sen, P. Impact of Bioinspired Nanotopography on the Antibacterial and Antibiofilm Efficacy of Chitosan. *Biomacromolecules* **2018**, *19*, 1340–1346. [CrossRef]
19. Garg, U.; Chauhan, S.; Nagaich, U.; Jain, N. Current Advances in Chitosan Nanoparticles Based Drug Delivery and Targeting. *Adv. Pharm. Bull.* **2019**, *9*, 195–204. [CrossRef]
20. Barbosa, M.; Vale, N.; Costa, F.M.T.A.; Martins, M.C.L.; Gomes, P. Tethering antimicrobial peptides onto chitosan: Optimization of azide-alkyne "click" reaction conditions. *Carbohydr. Polym.* **2017**, *165*, 384–393. [CrossRef] [PubMed]
21. Layek, B.; Lipp, L.; Singh, J. Cell Penetrating Peptide Conjugated Chitosan for Enhanced Delivery of Nucleic Acid. *Int. J. Mol. Sci.* **2015**, *16*, 28912–28930. [CrossRef]
22. Ewii, U.E.; Attama, A.A.; Olorunsola, E.O.; Onugwu, A.L.; Nwakpa, F.U.; Anyiam, C.; Chijioke, C.; Ogbulie, T. Nanoparticles for drug delivery: Insight into in vitro and in vivo drug release from nanomedicines. *Nano TransMed* **2025**, *4*, 100083. [CrossRef]
23. Mortazavi, A.; Mohammad Pour Kargar, H.; Beheshti, F.; Anaeigoudari, A.; Vaezi, G.; Hosseini, M. The effects of carvacrol on oxidative stress, inflammation, and liver function indicators in a systemic inflammation model induced by lipopolysaccharide in rats. *Int. J. Vitam. Nutr. Res.* **2023**, *93*, 111–121. [CrossRef]
24. Badr, A.M.; El-Orabi, N.F.; Mahran, Y.F.; Badr, A.M.; Bayoumy, N.M.; Hagar, H.; Elmongy, E.I.; Atawia, R.T. In vivo and In silico evidence of the protective properties of carvacrol against experimentally-induced gastric ulcer: Implication of antioxidant, anti-inflammatory, and antiapoptotic mechanisms. *Chem. Biol. Interact.* **2023**, *382*, 110649. [CrossRef]
25. Hosseini, M.; Arab, Z.; Beheshti, F.; Anaeigoudari, A.; Shakeri, F.; Rajabian, A. Zataria multiflora and its constituent, carvacrol, counteract sepsis-induced aortic and cardiac toxicity in rat: Involvement of nitric oxide and oxidative stress. *Anim. Models Exp. Med.* **2023**, *6*, 221–229. [CrossRef]
26. Chang, K.-J.; Lin, J.-A.; Chen, S.-Y.; Weng, M.-H.; Yen, G.-C. Silymarin protects against high fat diet-evoked metabolic injury by induction of glucagon-like peptide 1 and sirtuin 1. *J. Funct. Foods* **2019**, *56*, 136–144. [CrossRef]
27. Cui, X.S.; Li, H.Z.; Li, L.; Xie, C.Z.; Gao, J.M.; Chen, Y.Y.; Zhang, H.Y.; Hao, W.; Fu, J.H.; Guo, H. Rodent model of metabolic dysfunction-associated fatty liver disease: A systematic review. *J. Gastroenterol. Hepatol.* **2025**, *40*, 48–66. [CrossRef] [PubMed]
28. Zhang, X.; Hartmann, P. How to calculate sample size in animal and human studies. *Front. Med.* **2023**, *10*, 1215927. [CrossRef] [PubMed]
29. Festing, M.F.W.; Altman, D.G. Guidelines for the Design and Statistical Analysis of Experiments Using Laboratory Animals. *ILAR J.* **2002**, *43*, 244–258. [CrossRef] [PubMed]

30. Xu, Z.J.; Fan, J.G.; Ding, X.D.; Qiao, L.; Wang, G.L. Characterization of high-fat, diet-induced, non-alcoholic steatohepatitis with fibrosis in rats. *Dig. Dis. Sci.* **2010**, *55*, 931–940. [CrossRef]
31. Krohn, R.I. The colorimetric detection and quantitation of total protein. *Curr. Protoc. Cell Biol.* **2011**. [CrossRef]
32. Goodla, L.; Manubolu, M.; Pathakoti, K.; Jayakumar, T.; Sheu, J.-R.; Fraker, M.; Tchounwou, P.B.; Poondamalli, P.R. Protective Effects of Ammannia baccifera Against CCl4-Induced Oxidative Stress in Rats. *Int. J. Environ. Res. Public Health* **2019**, *16*, 1440. [CrossRef]
33. Rosenthal, P.; Blanckaert, N.; Kabra, P.M.; Thaler, M.M. Liquid-chromatographic determination of bilirubin and its conjugates in rat serum and human amniotic fluid. *Clin. Chem.* **1981**, *27*, 1704–1707. [CrossRef]
34. Hadi, W.H.; Khudair, T.T.; Al-Fartosi, K.G. Level of lipid profile and liver enzyme of diabetic male rats induced by streptozotocin treated with forxiga. *3c Empresa Investig. Y Pensam. Crítico* **2023**, *12*, 273–288. [CrossRef]
35. Livak, K.J.; Schmittgen, T.D. Analysis of relative gene expression data using real-time quantitative PCR and the $2^{-\Delta\Delta CT}$ Method. *Methods* **2001**, *25*, 402–408. [CrossRef] [PubMed]
36. Graham, L.; Orenstein, J.M. Processing tissue and cells for transmission electron microscopy in diagnostic pathology and research. *Nat. Protoc.* **2007**, *2*, 2439–2450. [CrossRef] [PubMed]
37. Wisse, E.; Braet, F.; Duimel, H.; Vreuls, C.; Koek, G.; Olde Damink, S.W.; van den Broek, M.A.; De Geest, B.; Dejong, C.H.; Tateno, C.; et al. Fixation methods for electron microscopy of human and other liver. *World J. Gastroenterol.* **2010**, *16*, 2851–2866. [CrossRef] [PubMed]
38. Shinde, P.; Agraval, H.; Srivastav, A.K.; Yadav, U.C.S.; Kumar, U. Physico-chemical characterization of carvacrol loaded zein nanoparticles for enhanced anticancer activity and investigation of molecular interactions between them by molecular docking. *Int. J. Pharm.* **2020**, *588*, 119795. [CrossRef]
39. Olaokun, O. Computational identification of polyphenols from medicinal plant extracts with biological activity against oxidative stress-related diseases: An in silico anti-inflammatory study. *S. Afr. J. Bot.* **2025**, *183*, 62–73. [CrossRef]
40. Moghtadaie, A.; Mahboobi, H.; Fatemizadeh, S.; Kamal, M.A. Emerging role of nanotechnology in treatment of non-alcoholic fatty liver disease (NAFLD). *EXCLI J.* **2023**, *22*, 946–974. [CrossRef]
41. Lian, C.-Y.; Zhai, Z.-Z.; Li, Z.-F.; Wang, L. High fat diet-triggered non-alcoholic fatty liver disease: A review of proposed mechanisms. *Chem. Biol. Interact.* **2020**, *330*, 109199. [CrossRef]
42. Estévez-Vázquez, O.; Benedé-Ubieto, R.; Guo, F.; Gómez-Santos, B.; Aspichueta, P.; Reissing, J.; Bruns, T.; Sanz-García, C.; Sydor, S.; Bechmann, L.P.; et al. Fat: Quality, or Quantity? What Matters Most for the Progression of Metabolic Associated Fatty Liver Disease (MAFLD). *Biomedicines* **2021**, *9*, 1289. [CrossRef]
43. Bakır, M.; Geyikoglu, F.; Colak, S.; Turkez, H.; Bakır, T.O.; Hosseinigouzdagani, M. The carvacrol ameliorates acute pancreatitis-induced liver injury via antioxidant response. *Cytotechnology* **2016**, *68*, 1131–1146. [CrossRef] [PubMed]
44. Mohebbati, R.; Paseban, M.; Soukhtanloo, M.; Jalili-Nik, M.; Shafei, M.N.; Yazdi, A.J.; Rad, A.K. Effects of standardized Zataria multiflora extract and its major ingredient, Carvacrol, on Adriamycin-induced hepatotoxicity in rat. *Biomed. J.* **2018**, *41*, 340–347. [CrossRef]
45. Abou Assi, R.; Abdulbaqi, I.M.; Siok Yee, C. The Evaluation of Drug Delivery Nanocarrier Development and Pharmacological Briefing for Metabolic-Associated Fatty Liver Disease (MAFLD): An Update. *Pharmaceuticals* **2021**, *14*, 215. [CrossRef]
46. Moosavian, S.A.; Sathyapalan, T.; Jamialahmadi, T.; Sahebkar, A. The Emerging Role of Nanomedicine in the Management of Nonalcoholic Fatty Liver Disease: A State-of-the-Art Review. *Bioinorg. Chem. Appl.* **2021**, *2021*, 4041415. [CrossRef]
47. Li, S.; Duan, F.; Li, S.; Lu, B. Administration of silymarin in NAFLD/NASH: A systematic review and meta-analysis. *Ann. Hepatol.* **2024**, *29*, 101174. [CrossRef]
48. Arroyave-Ospina, J.C.; Wu, Z.; Geng, Y.; Moshage, H. Role of Oxidative Stress in the Pathogenesis of Non-Alcoholic Fatty Liver Disease: Implications for Prevention and Therapy. *Antioxidants* **2021**, *10*, 174. [CrossRef]
49. Li, S.; Tan, H.-Y.; Wang, N.; Zhang, Z.-J.; Lao, L.; Wong, C.-W.; Feng, Y. The role of oxidative stress and antioxidants in liver diseases. *Int. J. Mol. Sci.* **2015**, *16*, 26087–26124. [CrossRef] [PubMed]
50. Li, N.; Hao, L.; Li, S.; Deng, J.; Yu, F.; Zhang, J.; Nie, A.; Hu, X. The NRF-2/HO-1 Signaling Pathway: A Promising Therapeutic Target for Metabolic Dysfunction-Associated Steatotic Liver Disease. *J. Inflamm. Res.* **2024**, *17*, 8061–8083. [CrossRef]
51. Muriel, P.; Ramos-Tovar, E.; Montes-Páez, G.; Buendía-Montaño, L.D. *Experimental Models of Liver Damage Mediated by Oxidative Stress*; Academic Press: Oxford, UK, 2017; pp. 529–546.
52. Lebda, M.A.; Sadek, K.M.; Abouzed, T.K.; Tohamy, H.G.; El-Sayed, Y.S. Melatonin mitigates thioacetamide-induced hepatic fibrosis via antioxidant activity and modulation of proinflammatory cytokines and fibrogenic genes. *Life Sci.* **2018**, *192*, 136–143. [CrossRef]
53. Ngo, V.; Duennwald, M.L. Nrf2 and Oxidative Stress: A General Overview of Mechanisms and Implications in Human Disease. *Antioxidants* **2022**, *11*, 2345. [CrossRef]
54. Padmanaban, S.; Pully, D.; Samrot, A.V.; Gosu, V.; Sadasivam, N.; Park, I.K.; Radhakrishnan, K.; Kim, D.K. Rising Influence of Nanotechnology in Addressing Oxidative Stress-Related Liver Disorders. *Antioxidants* **2023**, *12*, 1405. [CrossRef]

55. Kumar, D.; Dwivedi, D.K.; Lahkar, M.; Jangra, A. Hepatoprotective potential of 7,8-Dihydroxyflavone against alcohol and high-fat diet induced liver toxicity via attenuation of oxido-nitrosative stress and NF-κB activation. *Pharmacol. Rep.* **2019**, *71*, 1235–1243. [CrossRef] [PubMed]
56. Karatayli, E.; Sadiq, S.C.; Schattenberg, J.M.; Grabbe, S.; Biersack, B.; Kaps, L. Curcumin and Its Derivatives in Hepatology: Therapeutic Potential and Advances in Nanoparticle Formulations. *Cancers* **2025**, *17*, 484. [CrossRef]
57. Casals, G.; Perramón, M.; Casals, E.; Portolés, I.; Fernández-Varo, G.; Morales-Ruiz, M.; Puntes, V.; Jiménez, W. Cerium Oxide Nanoparticles: A New Therapeutic Tool in Liver Diseases. *Antioxidants* **2021**, *10*, 660. [CrossRef]
58. Singh, S.; Sharma, N.; Shukla, S.; Behl, T.; Gupta, S.; Anwer, M.K.; Vargas-De-La-Cruz, C.; Bungau, S.G.; Brisc, C. Understanding the Potential Role of Nanotechnology in Liver Fibrosis: A Paradigm in Therapeutics. *Molecules* **2023**, *28*, 2811. [CrossRef] [PubMed]
59. Chen, Y.N.; Li, M.Q.; Zhang, H.J.; Xu, N.N.; Xu, Y.Q.; Liu, W.X.; Chen, T.T.; Li, N.; Wu, G.Y.; Zhao, J.M.; et al. Nanoparticle-based drug delivery systems: A promising approach for the treatment of liver fibrosis. *Int. J. Pharm X* **2025**, *10*, 100411. [CrossRef]
60. Du, X.; Niu, R.; Liu, X.; Wu, F.; Yang, X.; Ma, X.; Zhang, J.; Zhou, H.; Shao, L.; Wang, S. Nanomedicines in the Treatment of Liver Fibrosis: A Review. *Int. J. Nanomed.* **2025**, *20*, 9641–9665. [CrossRef] [PubMed]
61. Mostafa, S.; Shetab Boushehri, M.A.; Ezzat, A.A.; Weiskirchen, R.; Lamprecht, A.; Mansour, S.; Tammam, S.N. Targeted Delivery of Anti-TGF-β1-siRNA Using PDGFR-β Peptide-Modified Chitosan Nanoparticles for the Treatment of Liver Fibrosis. *Mol. Pharm.* **2025**, *22*, 6741–6758. [CrossRef]
62. Dariushnejad, H.; Roshanravan, N.; Wasman, H.M.; Cheraghi, M.; Pirzeh, L.; Ghorbanzadeh, V. Silibinin, Synergistically Enhances Vinblastine-Mediated Apoptosis in Triple Negative Breast Cancer Cell Line: Involvement of Bcl2/Bax Caspase-3 Pathway. *Int. J. Hematol. Oncol. Stem Cell Res.* **2024**, *18*, 174–182. [CrossRef] [PubMed]
63. Dwivedi, D.K.; Jena, G.B. NLRP3 inhibitor glibenclamide attenuates high-fat diet and streptozotocin-induced non-alcoholic fatty liver disease in rat: Studies on oxidative stress, inflammation, DNA damage and insulin signalling pathway. *Naunyn-Schmiedeberg's Arch. Pharmacol.* **2020**, *393*, 705–716. [CrossRef] [PubMed]
64. Omari Shekaftik, S.; Nasirzadeh, N. 8-Hydroxy-2'-deoxyguanosine (8-OHdG) as a biomarker of oxidative DNA damage induced by occupational exposure to nanomaterials: A systematic review. *Nanotoxicology* **2021**, *15*, 850–864. [CrossRef] [PubMed]
65. Ma-On, C.; Sanpavat, A.; Whongsiri, P.; Suwannasin, S.; Hirankarn, N.; Tangkijvanich, P.; Boonla, C. Oxidative stress indicated by elevated expression of Nrf2 and 8-OHdG promotes hepatocellular carcinoma progression. *Med. Oncol.* **2017**, *34*, 57. [CrossRef]
66. Subudhi, P.D.; Bihari, C.; Sarin, S.K.; Baweja, S. Emerging role of edible exosomes-like nanoparticles (ELNs) as hepatoprotective agents. *Nanotheranostics* **2022**, *6*, 365. [CrossRef]
67. Zheng, P.; Ma, W.; Gu, Y.; Wu, H.; Bian, Z.; Liu, N.; Yang, D.; Chen, X. High-fat diet causes mitochondrial damage and downregulation of mitofusin-2 and optic atrophy-1 in multiple organs. *J. Clin. Biochem. Nutr.* **2023**, *73*, 61–76. [CrossRef]
68. Xue, R.; Wu, Q.; Guo, L.; Ye, D.; Cao, Q.; Zhang, M.; Xian, Y.; Chen, M.; Yan, K.; Zheng, J. Pyridostigmine attenuated high-fat-diet induced liver injury by the reduction of mitochondrial damage and oxidative stress via α7nAChR and M3AChR. *J. Biochem. Mol. Toxicol.* **2024**, *38*, e23671. [CrossRef]
69. Ægidius, H.M.; Veidal, S.S.; Feigh, M.; Hallenborg, P.; Puglia, M.; Pers, T.H.; Vrang, N.; Jelsing, J.; Kornum, B.R.; Blagoev, B.; et al. Multi-omics characterization of a diet-induced obese model of non-alcoholic steatohepatitis. *Sci. Rep.* **2020**, *10*, 1148. [CrossRef]
70. Ramos-Lopez, O. Multi-Omics Nutritional Approaches Targeting Metabolic-Associated Fatty Liver Disease. *Genes* **2022**, *13*, 2142. [CrossRef]
71. Sabourian, P.; Yazdani, G.; Ashraf, S.S.; Frounchi, M.; Mashayekhan, S.; Kiani, S.; Kakkar, A. Effect of Physico-Chemical Properties of Nanoparticles on Their Intracellular Uptake. *Int. J. Mol. Sci.* **2020**, *21*, 8019. [CrossRef]
72. Zheng, Y.; Luo, S.; Xu, M.; He, Q.; Xie, J.; Wu, J.; Huang, Y. Transepithelial transport of nanoparticles in oral drug delivery: From the perspective of surface and holistic property modulation. *Acta Pharm. Sinica B* **2024**, *14*, 3876–3900. [CrossRef]
73. Hegazi, O.E.; Alalalmeh, S.O.; Alnuaimi, G.R.H.; Shahwan, M.; Jairoun, A.A.; Alorfi, N.M.; Majrashi, S.A.; Alkhanani, M.F.; Alkhattabi, A.; Alourfi, M.M.; et al. NAFLD and nutraceuticals: A review of completed phase III and IV clinical trials. *Front. Med.* **2023**, *10*, 1227046. [CrossRef] [PubMed]
74. Li, G.; Dai, Z.; Guo, J. Therapeutic Nanomaterials in NAFLD: Current Advances and Potential Applications in Patients with Concurrent HBV Infection. *Int. J. Nanomed.* **2025**, *20*, 3803–3823. [CrossRef] [PubMed]
75. Padmanaban, S.; Baek, J.-W.; Chamarthy, S.S.; Chandrasekaran, S.; Samrot, A.V.; Gosu, V.; Park, I.-K.; Radhakrishnan, K.; Kim, D.-K. Nanoparticle-based therapeutic strategies for chronic liver diseases: Advances and insights. *Liver Res.* **2025**, *9*, 104–117. [CrossRef] [PubMed]

Disclaimer/Publisher's Note: The statements, opinions and data contained in all publications are solely those of the individual author(s) and contributor(s) and not of MDPI and/or the editor(s). MDPI and/or the editor(s) disclaim responsibility for any injury to people or property resulting from any ideas, methods, instructions or products referred to in the content.

antioxidants

MDPI

Article

Effect of Nano-Selenium on Intestinal Oxidative Stress Induced by H_2O_2 in Mice

Xiangyu Mao [1], Wenyuan Li [1], Yuanyuan Li [1], Xuemei Jiang [1], Ruinan Zhang [1], Lianqiang Che [1], Yong Zhuo [1], Mengmeng Sun [2], Xianxiang Wang [3], De Wu [1] and Shengyu Xu [1,*]

[1] Animal Disease-Resistance Nutrition, Ministry of Education, Ministry of Agriculture and Rural Affairs, Key Laboratory of Sichuan Province, Animal Nutrition Institute, Sichuan Agricultural University, Chengdu 611130, China; mxy010117@163.com (X.M.); liwenyuan0106@163.com (W.L.); perseverance_bai@163.com (Y.L.); 71310@sicau.edu.cn (X.J.); 72022@sicau.edu.cn (R.Z.); che.lianqiang@sicau.edu.cn (L.C.); zhuoyong@sicau.edu.cn (Y.Z.); wude@sicau.edu.cn (D.W.)
[2] College of Science, Sichuan Agricultural University, Xin Kang Road, Yucheng District, Ya'an 625014, China; sunmeng14391@163.com
[3] College of Science, Sichuan Agricultural University, Chengdu 611130, China; xianxiangwang@hotmail.com
* Correspondence: shengyuxu@sicau.edu.cn or shengyu_x@hotmail.com; Tel.: +86-028-86290922

Abstract

Selenium is an important trace element with certain antioxidant effects. Nano-selenium, as a novel selenium source, has the advantages of strong biological activity, high absorption efficiency, and low toxicity. The aim of the present study was to compare the protective effects of sodium selenite and nano-selenium on intestinal oxidative stress induced by hydrogen peroxide (H_2O_2) in mice. A total of 60 female mice were randomly divided into 6 groups with 10 replicates per group and 1 mouse per replicate (n = 10). The first three groups were as follows: the Control group (C), fed with basal diet; the sodium selenite group (SS), basal diet + 0.3 mg·kg^{-1} sodium selenite; and the nano-selenium group (NS), basal diet + 0.3 mg·kg^{-1} nano-selenium. The latter three groups (CH, SSH, NSH) were fed the same diet as the former three groups, but the last 10 days of the experiment were fed with drinking water containing 0.3% H_2O_2 to induce oxidative stress. The results showed that under normal conditions, the supplementation with sodium selenite or nano-selenium decreased the spleen index of mice; sodium selenate up-regulates *GPX3* expression in the ileum, and increases T-SOD in the colon of mice; and nano-selenium up-regulated *GPX1* expression but decreased T-AOC in the jejunum. After drinking water treated with H_2O_2, H_2O_2 increased the expression of intestinal inflammatory factors and selenium proteins, such as *IL-1β* and *SOD* in jejunum, *IL-1β*, *NF-κB*, *IL-10*, *TXNRD1*, *TXNRD2*, *GPX1*, *GPX3*, *GPX4*, and *CAT* in ileum, and *IL-1β* and *SOD* in colon. At the antioxidant level, H_2O_2 decreased T-AOC in the jejunum. In the H_2O_2 treatment, sodium selenite and nano-selenium increased the ratio of VH to CD (VH/CD) in jejunum; sodium selenite up-regulated the expression of *TXNRD1* in jejunum, down-regulated the expression of *GPX3* in ileum, at the antioxidant level, decreased the T-SOD and T-AOC in colon, and increased the content of MDA in ileum; and nano-selenium down-regulated the expression of *TXNRD1* in colon. At the same time, the expression of *IL-1β*, *NF-κB*, *IL-10*, *TXNRD1*, *TXNRD2*, *GPX1*, *GPX4*, and *CAT* can be restored to normal levels by selenium supplementation. According to the results, drinking H_2O_2 induced intestinal oxidative stress in mice to a certain extent, and selenium supplementation mitigated the destructive effect of H_2O_2 on the intestinal morphology of mice jejunum and restored the level of related inflammatory factors, and had a positive effect on antioxidants.

Keywords: nano-selenium; intestine; oxidative stress; antioxidant capacity; selenoprotein

1. Introduction

The intestinal tract is essential for nutrient digestion and absorption in animals. It also serves as a primary immune barrier and a major site of reactive oxygen species (ROS) production. Small and moderate amounts of ROS contribute to killing invading pathogens, wound healing, and tissue repair, as excessive ROS can cause tissue oxidative damage [1]. Oxidative stress is defined as an imbalance between the amount of reactive oxygen species/nitrogen species (ROS/RNS) produced and the ability of cells to neutralize them through antioxidant defenses [2]. Therefore, the intestinal tract is susceptible to exogenous and metabolic oxidative free radical damage, inducing intestinal oxidative stress, which may lead to a variety of intestinal diseases and cause huge losses to animal husbandry.

Selenium is an essential trace mineral element for animals, and its organic form is mainly selenocystine. Selenoprotein is formed through this organic form and plays an important role in many biological functions, such as anti-oxidation in the body, the formation of thyroid hormones, DNA synthesis, and positive effects on fertility and reproduction [3]. At the same time, selenium also plays a positive role in anti-inflammation, improving immune function, and promoting animal growth [3,4]. Nanotechnology refers to a comprehensive technical system for the preparation and research of substances at the nanoscale. Compared with single atoms or other large particles, nanoparticles exhibit new characteristics, such as larger surface area and smaller particle size, large specific surface area, high catalytic activity, good uniformity, and good physical reaction [5,6]. The novel selenium source nano-selenium is a nano-scale pink powder, which has the properties of nanoparticles and shows the advantages of high biological activity, high bioavailability, high absorption rate, low toxicity, high safety, and chemical stability. It also has a variety of biological activities, such as immune system, antioxidant, antiviral, and anti-cancer activities [7,8].

Therefore, it is of great significance to study whether nano-selenium has a better protective effect in animals. At present, there have been many studies and applications of nano-selenium. In the rat model of L-arginine-induced acute pancreatitis, through the analysis of histopathology, related pancreatic enzymes, antioxidant enzymes, inflammatory factors, immune factors, apoptosis factors, NF-κB, and other factors, the supplementation of nano-selenium has a positive effect on the endocrine and exocrine functions of acute pancreatitis [9]. Kondaparthi et al. [10] used different doses of nano-selenium and sodium selenite to study the liver of mice, and found that low doses of nano-selenium had better antioxidant effects in the liver. As for the effect of nano-selenium on the animal digestive tract, it has been found that nano-selenium has positive effects on intestinal homeostasis and mucosal immune defense by regulating goblet cells in laying hens [11]. Liu et al. [12] studied the protective effect of nano-selenium on intestinal injury induced by a high-fat diet (HFD) in young grass fish. They analyzed intestinal morphology, tight junction, inflammation, antioxidants, and intestinal flora, and the results showed that nano-selenium supplementation reduces intestinal injury caused by HFD and maintains the integrity of the intestine. Meanwhile, relevant research has been conducted on the nano-selenium (SENP) used in the present study. They found that the nano-selenium alleviates the immune response and apoptosis of lipopolysaccharide (LPS)-induced yak testicular interstitial cells by regulating the expression of genes related to apoptosis and inflammation [13].

At present, there are few studies on the relationship between nano-selenium and the intestinal tract, and few studies on the prevention and protection of different selenium sources on mammalian intestinal oxidative damage. Therefore, in the present study, mice were fed with 0.3% H_2O_2 in drinking water to induce oxidative damage, and the related in-

dicators were measured to analyze the effects of nano-selenium on H_2O_2-induced intestinal oxidative stress.

2. Materials and Methods

2.1. Preparation of Chitosan Nano-Selenium Composites

Initially, chitosan nano-selenium (CS-SeNPs) was synthesized by dissolving 1.0 g of chitosan powder in a 1% (*w*/*w*) acetic acid solution. This mixture was stirred continuously at room temperature for 6–12 h to completely dissolve, yielding a clarified, slightly pale-yellow solution at a concentration of 10 mg/mL, which was set aside as a reserve liquid. Subsequently, 1 mL of a 50 mM Na_2SeO_3 solution and 0.08 mL of the earlier prepared chitosan reserve liquid were briskly transferred into a beaker and promptly diluted to 8 mL with distilled water. With continuous stirring and shaking, 2 mL of a 100 mM ascorbic acid (Vc) solution was gradually added dropwise. The color transition of the mixture from colorless to bright red indicated the formation of CS-SeNPs. Following formation, the colloidal mixture was loaded into a dialysis bag with a molecular weight cut-off of 3500 and subjected to dialysis for 24 h, with changes in distilled water every 5–8 h. This process yielded CS-SeNPs at a concentration of 5 mM. The nano-selenium composites were then stored at 4 °C for further use.

2.2. Mice and Management

Sixty 3-week-old specific pathogen-free (SPF) female mice (Institute of Cancer, ICR) were randomly divided into 6 groups with 10 replicates per group and 1 mouse per replicate (n = 10). The 6 groups were (1) Control (C): basal diet; (2) sodium selenite group (SS): basal diet + 0.3 mg·kg^{-1} sodium selenite; (3) nano-selenium group (NS): basal diet + 0.3 mg·kg^{-1} nano-selenium; (4) Control + H_2O_2 group (CH): basal diet + 0.3% H_2O_2 drinking water; (5) sodium selenite + H_2O_2 group (SSH): basal diet + 0.3 mg·kg^{-1} sodium selenite + 0.3% H_2O_2 drinking water; and (6) nano-selenium + H_2O_2 group (NSH): basal diet + 0.3 mg·kg^{-1} nano-selenium + 0.3% H_2O_2 drinking water. Sodium selenium was obtained from Chengdu Shuxing Feed Co., Ltd., Chengdu, China. Nano-selenium was graciously provided by Professor Xianxiang Wang at the College of Science, Sichuan Agricultural University. The nano-selenium exhibits a spherical morphology, with a uniform particle size distribution of approximately 50 nanometers (Figure 1). The powder X-ray diffraction (XRD) pattern of the nano-selenium reveals the presence of monoclinic Se8 crystalline domains; however, the crystallinity is not high enough to produce distinct peaks (Figure 2). The test period was 8 weeks and 10 days. The mice in groups 4, 5, and 6 were allowed to drink ad libitum with 0.3% H_2O_2 water for the last 10 days. During the experiment, the mice were provided with sufficient drinking water and feed every day, given free access to feed and water, the cages were changed every 5–7 days, and clean bedding was provided. The laboratory was ventilated, clean, and quiet; the ambient temperature was maintained at 23 °C, and the dark/light cycle was 12 h. The formula of the basic diet is shown in Table 1. In order to add selenium to the basic diet, the sodium selenite group and the selenium nanoparticles group were fully stirred in the prepared feed to ensure that all the ingredients in the feed were fully mixed.

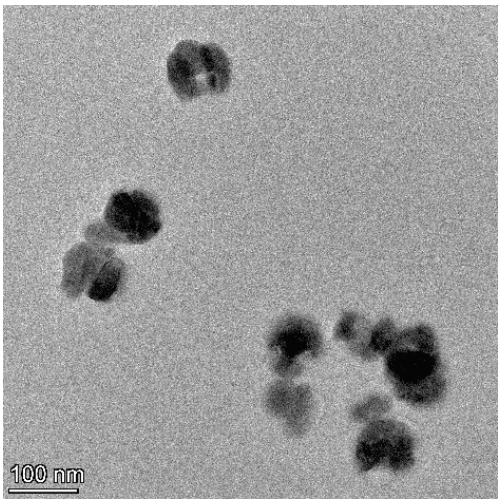


Figure 1. Transmission electron microscope image of nano-selenium.

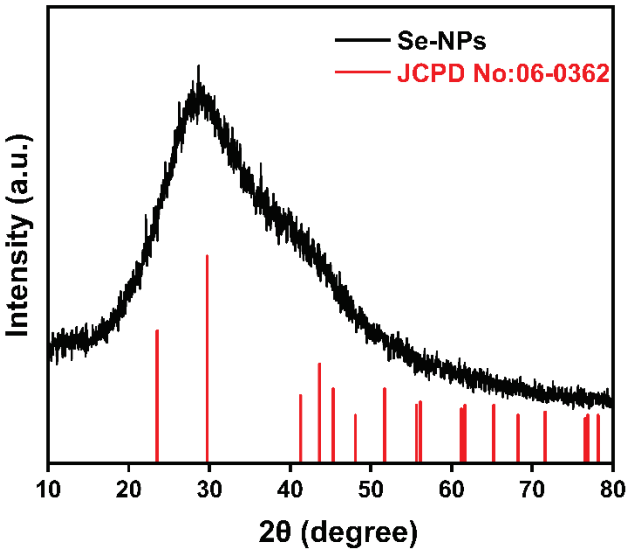


Figure 2. X-ray diffraction patterns of nano-selenium.

Table 1. Ingredient composition of basal diets (as-fed basis).

Composition	Ingredient (g·kg^{-1})
Casein	200
Maltodextrin	100
Corn starch	430.1
Sucrose	80
Fat powder 1-extruded corn type	100
Microcrystalline cellulose	50
L-cystine	3
Calcium carbonate	6
Calcium hydrogen phosphate	10
Potassium citrate	8
Choline chloride, 50%	2.6
Vitamin [1]	0.3
Mineral element [2]	10
Total	1000

[1] Per kilogram diet provided: vitamin A, 7200 IU; vitamin D_3, 1440 IU; vitamin E, 60 IU; vitamin K_3, 2.88 mg; vitamin B_1, 1.2 mg; vitamin B_2, 4.32 mg; vitamin B_6, 1.26 mg; vitamin B_{12}, 0.15 mg; D-biotin, 2.88 mg; D-pantothenic acid, 15 mg; folate, 2.4 mg; niacin, 24 mg. [2] Per kilogram diet provided: sodium, 1.022 g; calcium, 6.2626 g; phosphorus, 2.9932 g; chloride, 1.8119 g; zinc, 0.0273 g; copper, 0.0053 g; iodine, 0.005 g; potassium, 3.06 g; manganese, 0.065 g; iron, 0.0567 g; magnesium, 0.4781 g.

2.3. Determination of Selenium Content in Feed

According to the People's Republic of China National Standard GB/T 13883-2023 [14], the main steps include: (1) acid digestion, (2) dilution of the digestion fluid, (3) preparation of the standard curve, and (4) measurement. The specific operation was carried out according to GB/T 13883-2023.

The basal dietary selenium content was determined to be 0.042 $mg \cdot kg^{-1}$.

2.4. Sampling

On the last day of the experiment, the mice were fasted overnight and sacrificed by CO_2 after recording their living weight. The liver, spleen, kidney, heart, and pancreas were dissected and weighed, and the organ index was calculated according to the living weight. Organ index = organ weight/live weight.

After the mice were dissected, the whole jejunum, ileum, and colon tissues were collected and washed with normal saline. About 1 cm of the middle segment of the jejunum was taken and placed in 10% paraformaldehyde for intestinal morphological analysis. The remaining jejunum, ileum, and colon were placed in 2 mL cryotubes and snap-frozen in liquid nitrogen tanks, then stored at −80 °C for subsequent determination of antioxidant enzyme and related inflammatory factor gene expression and antioxidant indices.

2.5. Intestinal Histomorphology

The collected jejunal tissues were wrapped in paraffin. Paraffin sections were sectioned into 5–6 μm thick pieces using a microtome and stained with hematoxylin and eosin (H&E). The villi height (VH) and crypt depth (CD) of the jejunum were measured by NDP.view 2.9.22, and the ratio of VH to CD (VH/CD) was calculated. Ten complete and longest intestinal villi were selected from each section to measure their height, and the depth was determined by selecting the root of or near the crypt of the measured intestinal villi.

2.6. Measurement of Expression Levels of Antioxidant Enzymes and Inflammatory Factors in Intestinal Tissues

2.6.1. Total RNA Isolation

Trizol was added to the tissue samples to extract total RNA. Then, chloroform shaking and centrifugation were performed. Followed by isopropanol addition for RNA precipitation and washing. The RNA precipitate was completely dissolved in an appropriate amount of diethylpyrocarbonate water (DEPC water). After dissolution, the RNA concentration was determined, and then reverse transcription was performed immediately.

2.6.2. Reverse Transcription

RNA was reverse transcribed to cDNA using the Novizan Bio HiScript® III RT SuperMix for qPCR (+gDNA wiper) kit (R323-01, Novizan Biotech Co., Ltd., Nanjing, China). Methods and procedures were performed according to the instructions.

2.6.3. Real-Time Fluorescent Quantitative PCR

The ChamQ Universal SYBR qPCR Master Mix kit (Q711-02, Novizan Biotech Co., Ltd., Nanjing, China) was used for the assay. Amplification procedures and method steps were performed according to the instructions. Relative gene expression was calculated using the $2^{-\Delta\Delta Ct}$ method [15].

2.6.4. Measurement Indicators

Inflammatory factors in the jejunum, ileum, and colon included interleukin-1β (*IL-1β*), tumor necrosis factor (*TNF-α*), nuclear factor kappa B (*NF-κB*), and interleukin-10 (*IL-10*).

Selenoproteins and antioxidant enzymes in jejunum, ileum, and colon tissues included thioredoxin reductase 1 (*TXNRD1*), thioredoxin reductase 2 (*TXNRD2*), glutathione peroxidase 1 (*GPX1*), glutathione peroxidase 2 (*GPX2*), glutathione peroxidase 3 (*GPX3*), glutathione peroxidase 4 (*GPX4*), superoxide dismutase (*SOD*), and catalase (*CAT*).

The primer sequences used in the PCR experiments were retrieved from the National Center for Biotechnology Information website and synthesized at Beijing Tsingke Biotech Co., Ltd., Beijing, China. The primer sequences are shown in Table 2.

Table 2. Primer sequence.

Gene Name	Sequence	Base Pair	Accession No.
β-actin	F: GGCTGTATTCCCCTCCATCG R: CCAGTTGGTAACAATGCCATGT	154	NM_007393
IL-1β	F: GCAACTGTTCCTGAACTCAACT R: ATCTTTTGGGGTCCGTCAACT	89	NM_008361
TNF-α	F: CCCTCACACTCAGATCATCTTCT R: GCTACGACGTGGGCTACAG	61	NM_013693
NF-κB	F: ATGGCAGACGATGATCCCTAC R: TGTTGACAGTGGTATTTCTGGTG	111	NM_008689
IL-10	F: GCTCTTACTGACTGGCATGAG R: CGCAGCTCTAGGAGCATGTG	105	NM_010548
TXNRD1	F: CCCACTTGCCCCAACTGTT R: GGGAGTGTCTTGGAGGGAC	134	NM_001042523
TXNRD2	F: GATCCGGTGGCCTAGCTTG R: TCGGGGAGAAGGTTCCACAT	86	NM_013711
GPX1	F: AGTCCACCGTGTATGCCTTCT R: GAGACGCGACATTCTCAATGA	105	NM_008160
GPX2	F: GCCTCAAGTATGTCCGACCTG R: GGAGAACGGGTCATCATAAGGG	143	NM_030677
GPX3	F: CCTTTTAAGCAGTATGCAGGCA R: CAAGCCAAATGGCCCAAGTT	120	NM_008161
GPX4	F: GATGGAGCCCATTCCTGAACC R: CCCTGTACTTATCCAGGCAGA	185	NM_008162
SOD	F: CAGACCTGCCTTACGACTATGG R: CTCGGTGGCGTTGAGATTGTT	113	NM_013671
CAT	F: AGCGACCAGATGAAGCAGTG R: TCCGCTCTCTGTCAAAGTGTG	181	NM_009804

β-actin: beta-actin; *IL-1β*: interleukin-1β; *TNF-α*: tumor necrosis factor-α; *NF-κB*: nuclear factor kappa B; *IL-10*: interleukin-10; *TXNRD1*: thioredoxin reductase 1; *TXNRD2*: thioredoxin reductase 2; *GPX1*: glutathione peroxidase 1; *GPX2*: glutathione peroxidase 2; *GPX3*: glutathione peroxidase 3; *GPX4*: glutathione peroxidase 4; *SOD*: superoxide dismutase; *CAT*: catalase.

2.7. Measurement of Antioxidant Indicators

Appropriate amounts of jejunum, ileum, and colon tissue were weighed, washed, and homogenized in physiological saline. The samples were diluted 10 times with physiological saline according to the weight of the samples in a frozen storage tube and homogenized in a homogenizer by adding steel beads. We transferred the homogenate to a centrifuge tube. Centrifugation was performed at 3000 r·min^{-1} for 15 min. The supernatant was

collected, and the protein concentration was determined by Beyotime P0010 BCA Protein Concentration Assay kit (enhanced) (P0010S, Beyotime, Shanghai, China). According to the protein concentration, the activities of superoxide dismutase (SOD, A001-1-2), total antioxidant capacity (T-AOC, A015-2-1), catalase (CAT, A007-1-1), and malondialdehyde (MDA, A003-1-2) in the jejunum of mice were measured by antioxidant kits purchased from Nanjing Jiancheng Bioengineering Institute (Nanjing, China). T-AOC and MDA content in the ileum were measured. The contents of SOD, T-AOC, and MDA in the colon were measured. The method and steps of the determination were strictly in accordance with the instructions in the kit.

2.8. Statistical Analysis

All data were preliminarily sorted using Excel 2020, and then a *t*-test was performed between normal drinking water and H_2O_2 treatment using SAS 9.4 software. One-way ANOVA was used between C, SS, NS, and CH, SSH, NSH, and multiple comparisons were made by the Tukey method. Data were expressed as mean ± standard error, $p < 0.05$ as a significant level, $0.05 \leq p \leq 0.1$ as a trend. At the same time, SAS 9.4 software was used to calculate the effect size, and the effect size was calculated in one-way ANOVA: eta-squared (η^2), $\eta^2 < 0.06$ was a minor effect, $0.06 \leq \eta^2 < 0.14$ was a medium effect, and $\eta^2 \geq 0.14$ was a large effect. Effect sizes were calculated in the *t*-test as Hedges' g (g), with $|g| < 0.5$ as a minor effect, $0.5 \leq |g| < 0.8$ as a medium effect, and $|g| \geq 0.8$ as a large effect.

3. Results

3.1. Effect of Nano-Selenium on Organ Index

Under normal conditions, the group SS and group NS significantly reduced the spleen index of mice, and the effect size was large ($p < 0.05$, $\eta^2 = 0.219$, 95% CI [0.036,0.52], Table 3). However, for the kidney index, selenium supplementation was not significant, but the effect size was large ($p > 0.05$, $\eta^2 = 0.147$, 95% CI [0.016,0.50]). Compared with group NS, group NSH significantly increased the spleen index and the effect size was large ($p < 0.05$, $g = -1.011$, 95% CI [−2.00,−0.02]), and there was no significant difference in the kidney index between the two groups, but the effect size was large ($p = 0.05$, $g = 0.891$, 95% CI [−0.06,1.84]). However, there was no significant effect on the organ indices of liver, kidney, heart, and pancreas between nano-selenium and sodium selenite under normal conditions or H_2O_2 oxidative stress treatment, and the effect size is small or medium ($p > 0.05$, $\eta^2 < 0.14$, $|g| < 0.8$).

3.2. Effect of Nano-Selenium on the Morphology of Jejunum

Under normal conditions, the jejunal villi were arranged more neatly and completely after the addition of selenium (Figures 3B,C and 4B,C; as shown in the red box indicated by the arrow), and nano-selenium was the best (Figures 3C and 4C). After H_2O_2 stress, the jejunal villi of mice became disordered, incomplete, and almost incomplete, indicating that they were subjected to certain oxidative damage (Figures 3D and 4D). This phenomenon was reversed in the sodium selenite group (Figures 3E and 4E), while more complete and orderly villi were observed in the nano-selenium group (Figures 3F and 4F). These results indicated that nano-selenium had a positive protective effect on the oxidative damage of villi induced by H_2O_2.

Table 3. Effects of nano-selenium on organ index under normal conditions or H_2O_2 oxidative stress treatment.

Index	Treatments					
	C	**SS**	**NS**	**CH**	**SSH**	**NSH**
Liver	0.044 ± 0.001	0.042 ± 0.002	0.044 ± 0.001	0.044 ± 0.001	0.042 ± 0.001	0.044 ± 0.001
Spleen	0.0043 ± 0.0003 [a]	0.0035 ± 0.0002 [b]	0.0036 ± 0.0002 [b]	0.0042 ± 0.0002	0.0038 ± 0.0003	0.0042 ± 0.0002 *
Kidney	0.0066 ± 0.0002	0.0064 ± 0.0003	0.0071 ± 0.0002	0.0070 ± 0.0002	0.0067 ± 0.0002	0.0065 ± 0.0002
Heart	0.0050 ± 0.0001	0.0048 ± 0.0002	0.0050 ± 0.0002	0.0048 ± 0.0002	0.0047 ± 0.0002	0.0048 ± 0.0001
Pancreas	0.0050 ± 0.0002	0.0048 ± 0.0002	0.0053 ± 0.0002	0.0049 ± 0.0002	0.0053 ± 0.0002	0.0049 ± 0.0003

	C × SS × NS		**CH × SSH × NSH**		**C × CH**		**SS × SSH**		**NS × NSH**	
	p-value	η^2-value (95% CI)	*p*-value	η^2-value (95% CI)	*p*-value	*g*-value (95% CI)	*p*-value	*g*-value (95% CI)	*p*-value	*g*-value (95% CI)
Liver	0.33	0.083 [0.004,0.44]	0.67	0.031 [0.004,0.34]	0.71	0.161 [−0.74,1.06]	0.85	−0.082 [−1.01,0.84]	0.97	−0.016 [−0.94,0.91]
Spleen	0.04	0.219 [0.036,0.52]	0.38	0.070 [0.003,0.40]	0.80	0.111 [−0.79,1.01]	0.44	−0.340 [−1.25,0.57]	0.03	−1.011 [−2.00,−0.02]
Kidney	0.12	0.147 [0.016,0.50]	0.22	0.109 [0.011,0.44]	0.23	−0.533 [−1.45,0.38]	0.33	−0.443 [−1.38,0.50]	0.05	0.891 [−0.06,1.84]
Heart	0.76	0.021 [0.003,0.31]	0.76	0.021 [0.002,0.34]	0.62	0.223 [−0.71,1.15]	0.52	0.283 [−0.62,1.19]	0.27	0.497 [−0.44,1.44]
Pancreas	0.31	0.085 [0.008,0.37]	0.47	0.055 [0.004,0.32]	0.73	0.151 [−0.75,1.05]	0.13	−0.702 [−1.66,0.25]	0.28	0.479 [−0.43,1.39]

Note: In all results, tables and figures are the same: $n = 10$. Results are presented as mean ± SE. SE, standard error. C: Control, basal diet; SS: basal diet + 0.3 mg·kg^{-1} sodium selenium; NS: basal diet + 0.3 mg·kg^{-1} nano-selenium; CH: basal diet + 0.3% H_2O_2 drinking water; SSH: basal diet + 0.3 mg·kg^{-1} sodium selenium + 0.3% H_2O_2 drinking water; NSH: basal diet + 0.3 mg·kg^{-1} nano-selenium + 0.3% H_2O_2 drinking water. [a, b] Under normal conditions or H_2O_2 treatment, different letters indicate significant differences between the different Se source treatments ($p < 0.05$). * Indicates significant difference between H_2O_2 treatment and drinking water without H_2O_2 ($p < 0.05$). C × SS × NS: *p* value obtained by adding selenium under normal conditions (one-way ANOVA test was performed among the three groups of group C, group SS, and group NS); CH × SSH × NSH: *p* value obtained by adding selenium when feeding H_2O_2 drinking water was analyzed (one-way ANOVA test was performed among the three groups of group CH, group SSH, and group NSH); C × CH: the *p* value obtained by feeding H_2O_2 without selenium addition was analyzed (*t*-test was performed between the two groups of group C and group CH); SS × SSH: *p* value obtained by feeding H_2O_2 when sodium selenite was added (*t*-test was performed between the two groups of group SS and group SSH); NS × NSH: *p* value obtained by feeding H_2O_2 when nano-selenium was added (*t*-test was performed between the two groups of group NS and group NSH). η^2 is the effect size (eta-squared) of a single-factor variance analysis. *g* is the effect size (Hedges' g) of the *t*-test analysis. (95% CI) represents the 95% confidence interval of the effect size.

There were no significant differences in jejunum villus height and crypt depth among different selenium sources or between normal and H_2O_2-treated mice ($p > 0.05$, Figure 5). But the villus height has a relatively large effect size ($p > 0.05$, $\eta^2 = 0.191$, 95% CI [0.046,0.59]), nano-selenium is the most effective. Meanwhile, in the group SS and the group SSH, there was no significant difference between the two groups, but they had a relatively large effect size ($p > 0.05$, $g = 0.910$, 95% CI [−0.30,1.81]) for CD.

Under normal conditions, the group SS and group NS tended to increase the jejunal VH/CD one by one, and the effect size was large ($p = 0.08$, $\eta^2 = 0.250$, 95% CI [0.050,0.59]). However, in the presence of H_2O_2, the group SSH and group NSH significantly increased the VH/CD compared with the group CH, and the effect size was large ($p < 0.05$, $\eta^2 = 0.335$, 95% CI [0.102,0.69]).

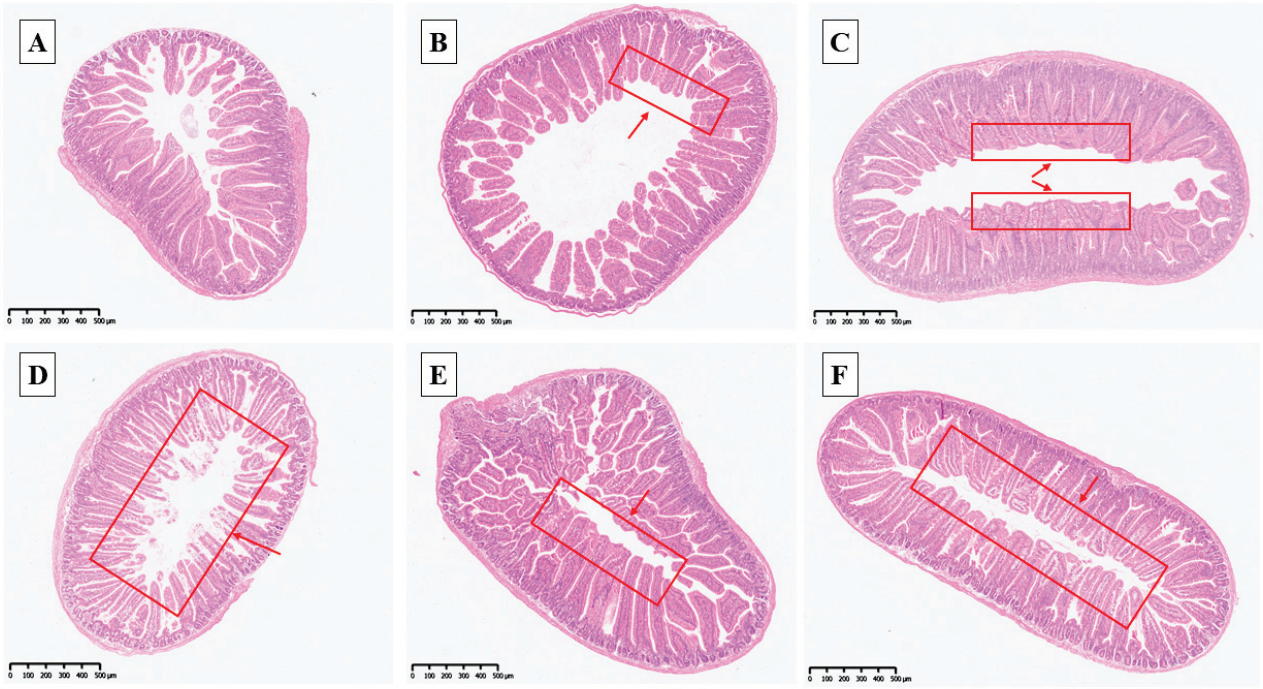


Figure 3. Diagram of jejunum sections in each group (HE staining, magnification: 50×). (**A**) Control: basal diet; (**B**) sodium selenite group: basal diet + 0.3 mg·kg^{-1} sodium selenium; (**C**) nano-selenium group: basal diet + 0.3 mg·kg^{-1} nano-selenium; (**D**) Control + H_2O_2 group: basal diet + 0.3% H_2O_2 drinking water; (**E**) sodium selenite + H_2O_2 group: basal diet + 0.3 mg·kg^{-1} sodium selenium + 0.3% H_2O_2 drinking water; (**F**) nano-selenium + H_2O_2 group: basal diet + 0.3 mg·kg^{-1} nano-selenium + 0.3% H_2O_2 drinking water.

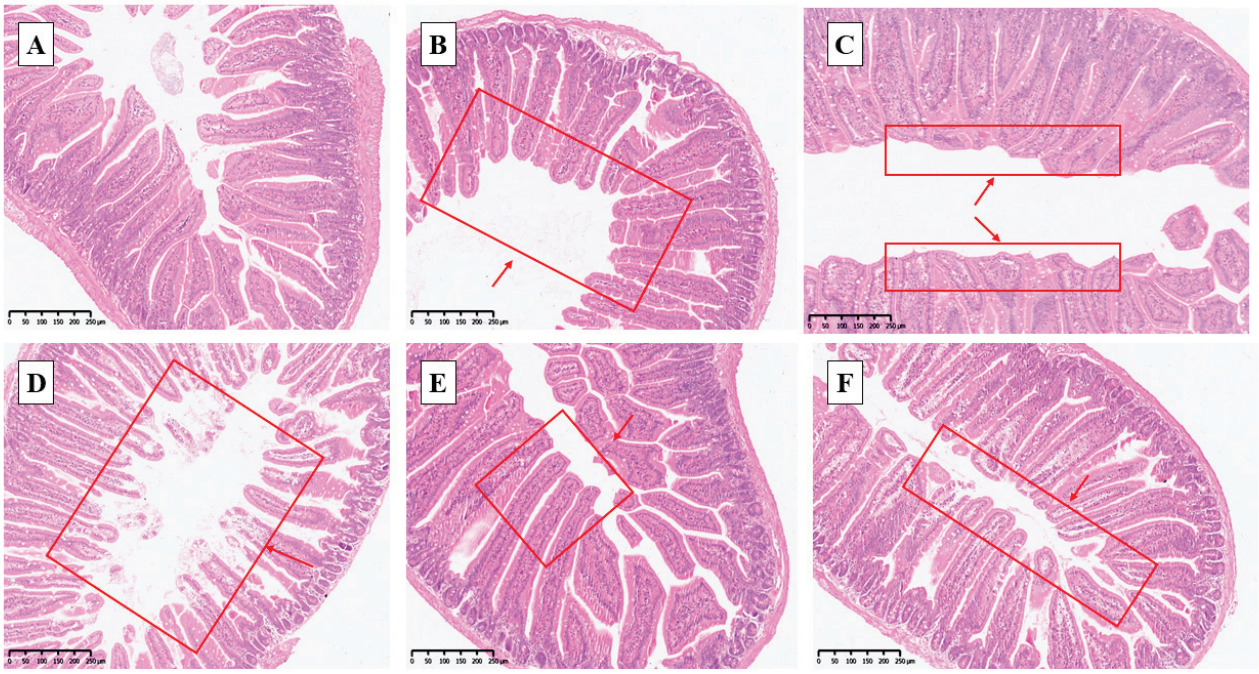


Figure 4. Diagram of jejunum sections in each group (HE staining, magnification: 100×). (**A**) Control: basal diet; (**B**) sodium selenite group: basal diet + 0.3 mg·kg^{-1} sodium selenium; (**C**) nano-selenium group: basal diet + 0.3 mg·kg^{-1} nano-selenium; (**D**) Control + H_2O_2 group: basal diet + 0.3% H_2O_2 drinking water; (**E**) sodium selenite + H_2O_2 group: basal diet + 0.3 mg·kg^{-1} sodium selenium + 0.3% H_2O_2 drinking water; (**F**) nano-selenium + H_2O_2 group: basal diet + 0.3 mg·kg^{-1} nano-selenium + 0.3% H_2O_2 drinking water.

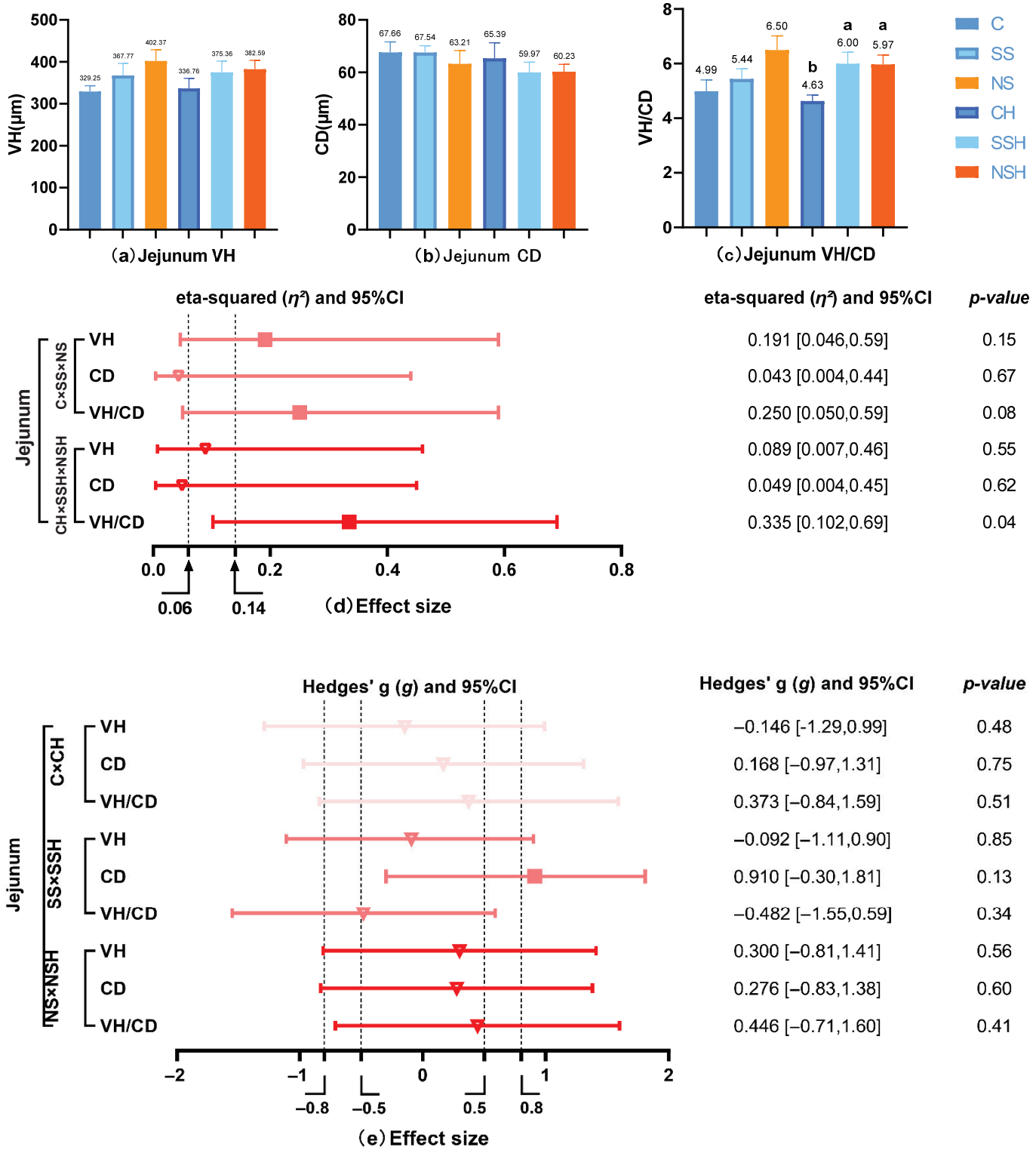


Figure 5. Effects of nano-selenium on jejunal tissue morphology under normal conditions or H_2O_2 oxidative stress treatment. (**a**) Bar graph of jejunal villus height index (VH), (**b**) bar graph of jejunal crypt depth index (CD), (**c**) bar graph of the ratio of VH to CD (VH/CD), (**d**) effect size forest plot of jejunum morphology [eta-squared (η^2)], (**e**) effect size forest plot of jejunum morphology [Hedges' g (g)]. Note: In all effect size forest plots, the squares and inverted triangles represent the effect size values. The squares indicate large effect sizes, and the lines on both sides represent their confidence intervals.

3.3. Effect of Nano-Selenium on the Expression of Anti-Inflammatory and Antioxidant-Related Genes in the Intestine

3.3.1. Gene Expression of Intestinal Inflammatory Factors

In the jejunum of mice, sodium selenite and nano-selenium had no significant effect on the expression of inflammatory factors under normal conditions and H_2O_2 treatment ($p > 0.05$, Figure 6a,d,e). However, in normal conditions, the addition of selenium did not show a significant difference in *IL-10* levels, but the effect size was large ($p > 0.05$, $\eta^2 = 0.169$, 95% CI [0.024,0.57]). And in group C and CH, there was no significant difference between the two groups of *IL-10*, but the effect size was large ($p > 0.05$, $g = -0.846$, 95% CI [−1.95,0.26]). Compared with group C, group CH significantly increased the expression of *IL-1β*, and the effect size was large ($p < 0.05$, $g = -1.311$, 95% CI [−2.37,−0.25]).

In the ileum of mice, compared with group C, group SS tended to increase the expression of *IL-1β*, while group NS tended to decrease the expression of *IL-1β*, and the effect size was large ($p = 0.09$, $\eta^2 = 0.190$, 95% CI [0.039,0.57], Figure 6b,d,e). Compared with the group C and group NS, group SS tended to increase the expression of *NF-κB*, and the effect size was large ($p = 0.05$, $\eta^2 = 0.317$, 95% CI [0.119,0.67]). Compared with group C, group CH significantly increased the expression of *NF-κB* and *IL-10*, and the effect size was large ($p < 0.05$, $|g| \geq 0.8$).

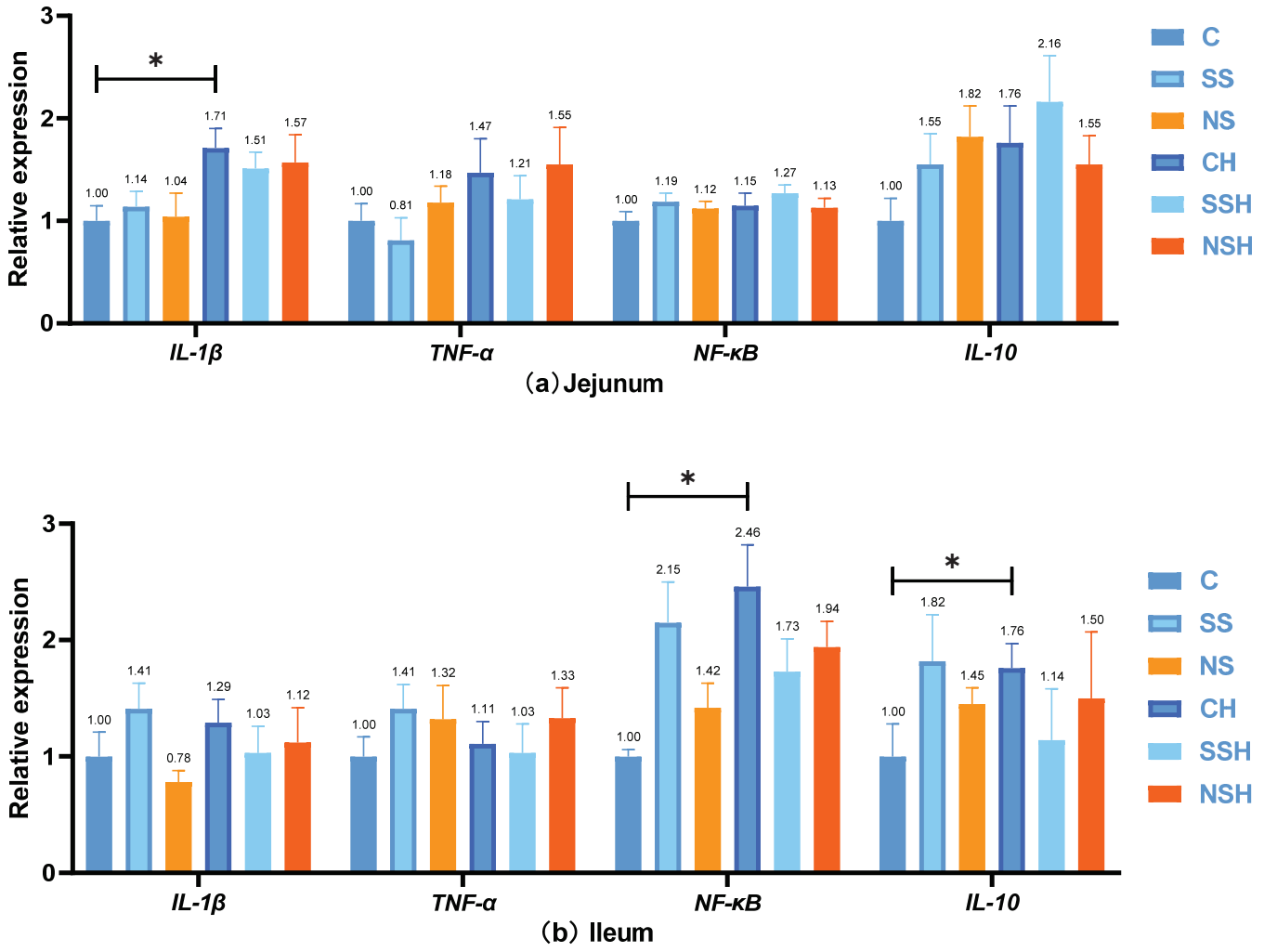
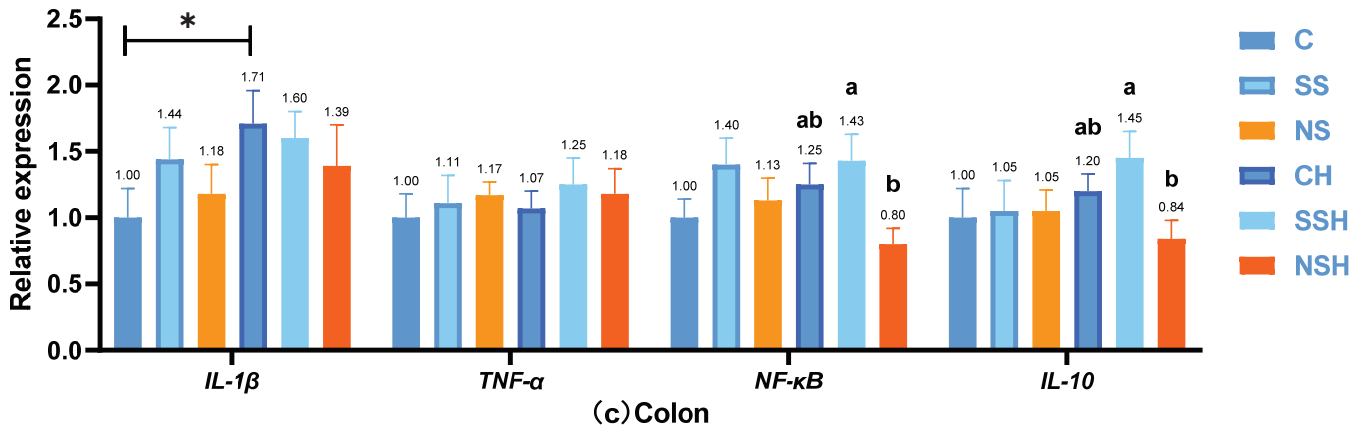


Figure 6. *Cont.*



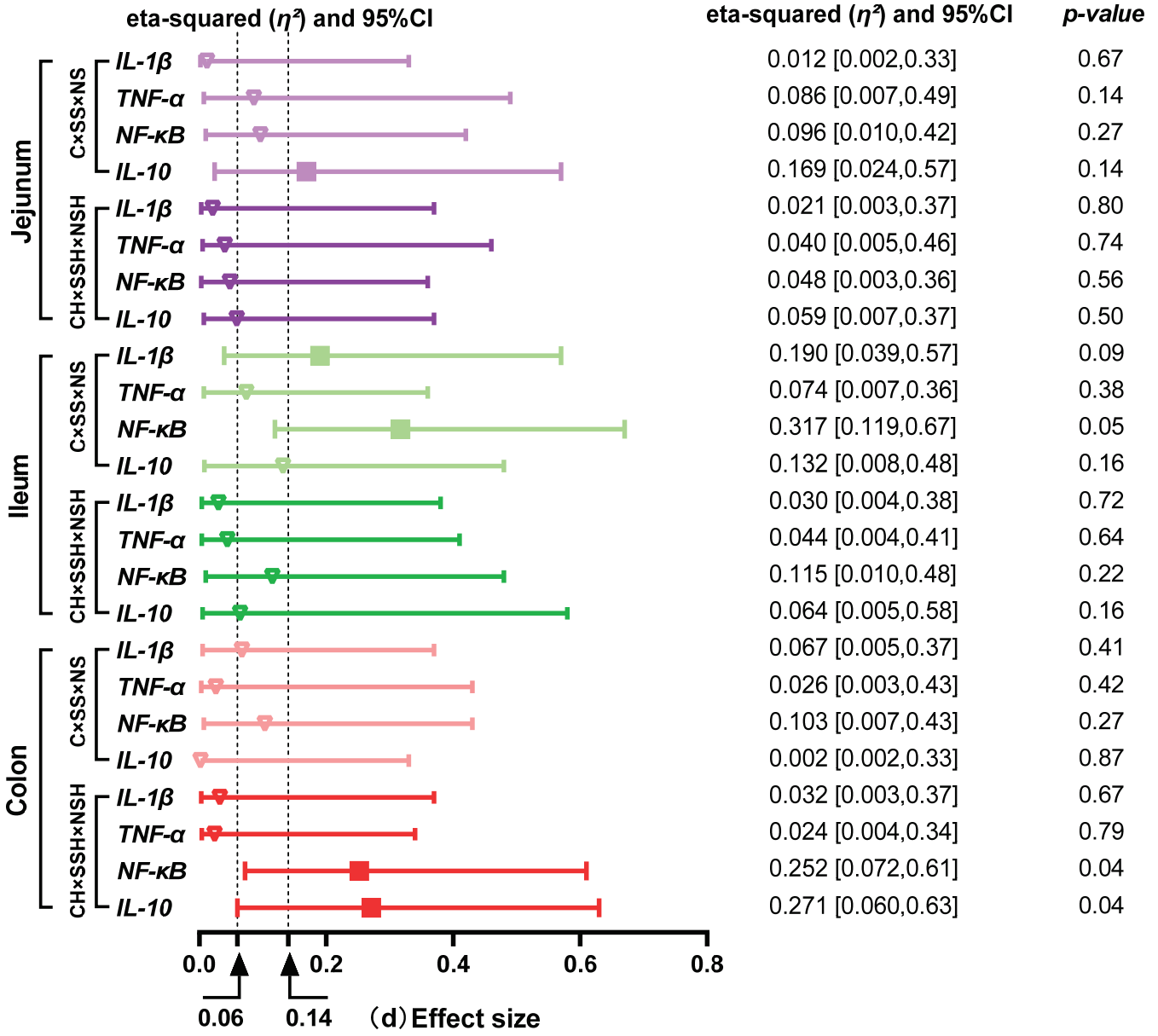


Figure 6. *Cont.*

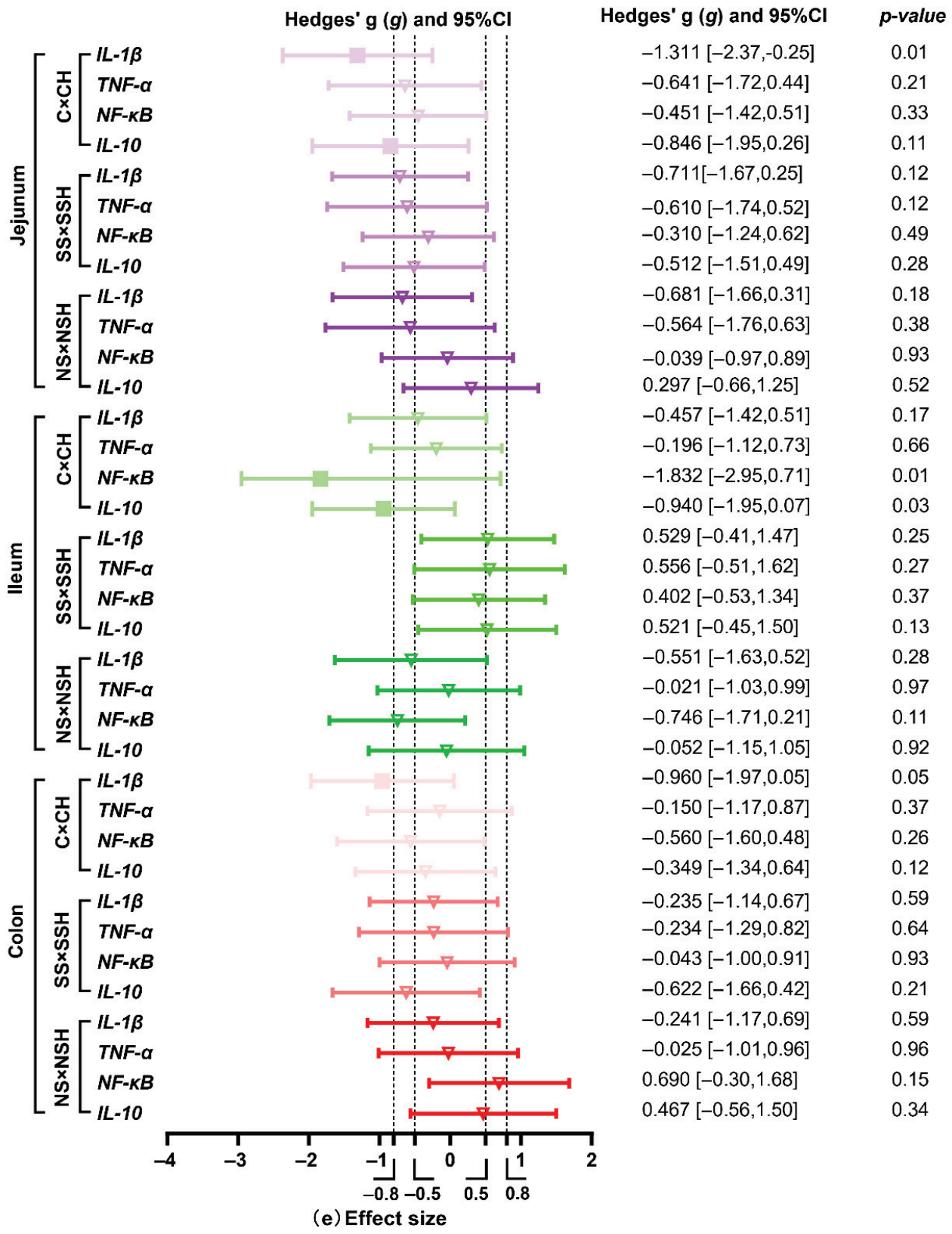


Figure 6. Effect of nano-selenium on gene expression levels of inflammatory factors in mouse gut under normal conditions or H_2O_2 oxidative stress treatment. (**a**) Bar graph of jejunal inflammatory factor gene expression, (**b**) bar graph of gene expression of inflammatory factors in the ileum, (**c**) bar graph of colonic inflammatory factor gene expression, (**d**) effect size forest plot of intestinal inflammatory factor gene expression [eta-squared (η^2)], (**e**) effect size forest plot of intestinal inflammatory factor gene expression [Hedges' g (g)].

In the colon of mice, under normal conditions, sodium selenite and nano-selenium had no significant effect on the expression of colonic inflammatory factors in mice, and the effect size is small or medium ($p > 0.05$, $\eta^2 < 0.14$, $|g| < 0.8$, Figure 6c,d,e). Compared with group C, group CH significantly increased the expression of *IL-1β*, and the effect size was large ($p < 0.05$, $g = -0.960$, 95% CI [−1.97,0.05]). Compared with group SS, group NS significantly reduced the expression of *NF-κB* and *IL-10*, and the effect size was large ($p < 0.05$, $\eta^2 \geq 0.14$).

3.3.2. Intestinal Antioxidant Gene Expression

In the jejunum of mice, sodium selenite and nano-selenium had no significant effect on gene expression of antioxidant enzymes under normal conditions ($p > 0.05$, Figure 7a,d,e). However, the addition of selenium did not show a significant difference in *GPX2* levels, but the effect size was large ($p > 0.05$, $\eta^2 = 0.157$, 95% CI [0.015,0.61]). Compared with group C, group CH significantly increased the expression of *SOD* and the effect size was large ($p < 0.05$, $g = -1.175$, 95% CI [−2.29,−0.06]); meanwhile, there was no significant difference in *GPX3* and *CAT* between the two groups, but the effect size was large ($p > 0.05$, $|g| \geq 0.8$). Compared with group SS, group SSH significantly increased the expression of *TXNRD1*, and the effect size was large ($p < 0.05$, $g = -1.282$, 95% CI [−2.27,−0.29]). Compared with group NS, group NSH significantly increased the expressions of *TXNRD2*, *GPX1*, *GPX3*, *GPX4*, and *CAT*, and the effect size was large ($p < 0.05$, $|g| \geq 0.8$). In the presence of H_2O_2, group SSH significantly increased the expression of *TXNRD1* and the effect size was large ($p = 0.05$, $\eta^2 = 0.200$, 95% CI [0.033,0.49]), and group NSH tended to increase the expression of *GPX1* and the effect size was large ($p = 0.09$, $\eta^2 = 0.201$, 95% CI [0.037,0.54]).

In the ileum of mice, under normal conditions, sodium selenite and nano-selenium had a tendency to increase the expression level of *TXNRD1* but the effect size was large ($p = 0.05$, $\eta^2 = 0.202$, 95% CI [0.073,0.51], Figure 7b,d,e), group NS significantly increased the expression level of *GPX1*, and the effect size was large compared with the group C ($p < 0.05$, $\eta^2 = 0.311$, 95% CI [0.091,0.63]). Compared with group C and group NS, group SS significantly increased *GPX3* expression level, and the effect size was large ($p < 0.05$, $\eta^2 = 0.338$, 95% CI [0.119,0.69]). However, the addition of selenium did not show a significant difference in *TXNRD2* levels, but the effect size was large ($p < 0.05$, $\eta^2 = 0.140$, 95% CI [0.015,0.49]). Compared with group C, group CH significantly increased the expression levels of *TXNRD1*, *TXNRD2*, *GPX1*, *GPX3*, *GPX4*, and *CAT*, and the effect size was large ($p < 0.05$, $|g| \geq 0.8$), and tended to increase the expression level of *SOD* but the effect size was large ($p = 0.08$, $g = -0.809$, 95% CI [−1.75,0.13]). Compared with group SS, group SSH significantly reduced the expression of *TXNRD1* and *GPX2*, and the effect size was large ($p < 0.05$, $|g| \geq 0.8$). Compared with group NS, group NSH tended to increase the expression of *GPX3* ($p = 0.09$), and significantly decreased the expression of *SOD*, and the effect size was large ($p < 0.05$, $g = 1.173$, 95% CI [0.19,2.15]). Compared with the group CH, group SSH tended to decrease *TXNRD1* and the effect size was large ($p = 0.07$, $\eta^2 = 0.192$, 95% CI [0.031,0.58]), and significantly decreased *GPX3* expression level and the effect size was large ($p < 0.05$, $\eta^2 = 0.253$, 95% CI [0.076,0.56]), and group NSH had a tendency to decrease *SOD* expression level and the effect size was large ($p = 0.07$, $\eta^2 = 0.192$, 95% CI [0.047,053]). However, in H_2O_2 treatment, the addition of selenium did not show a significant difference in *GPX2* level, but the effect size was large ($p > 0.05$, $\eta^2 = 0.168$, 95% CI [0.016,0.53]).

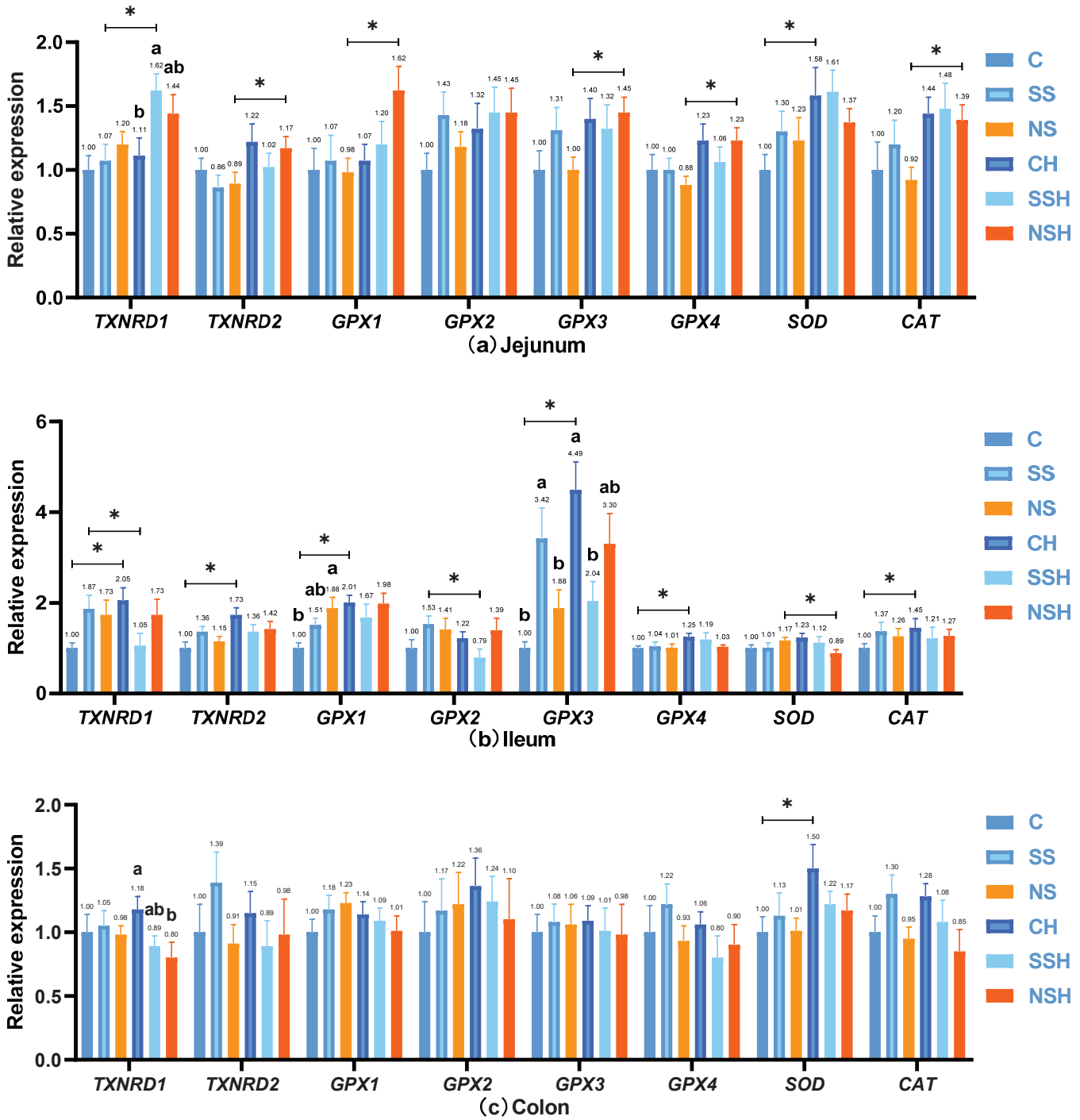


Figure 7. *Cont.*

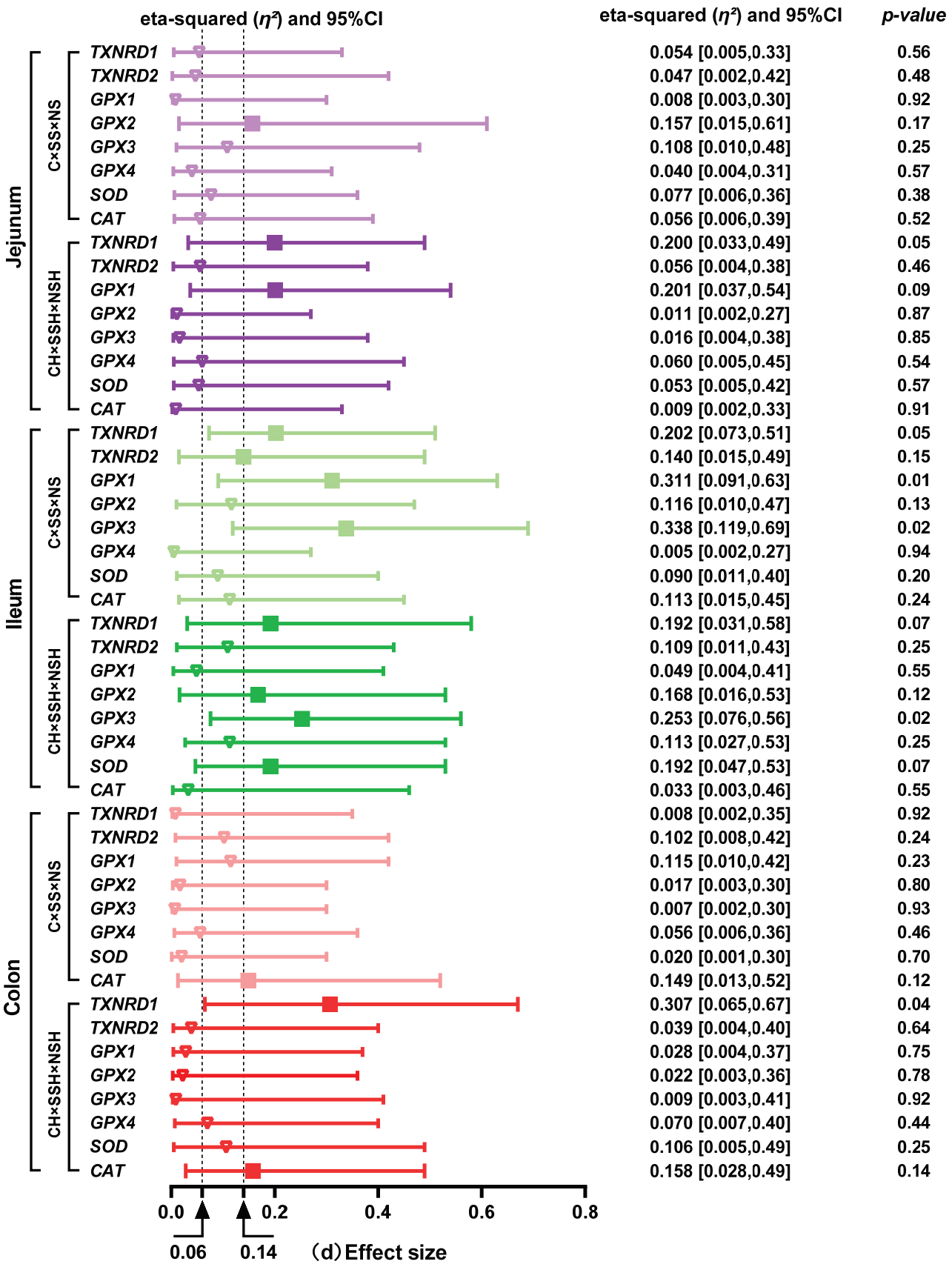


Figure 7. *Cont.*

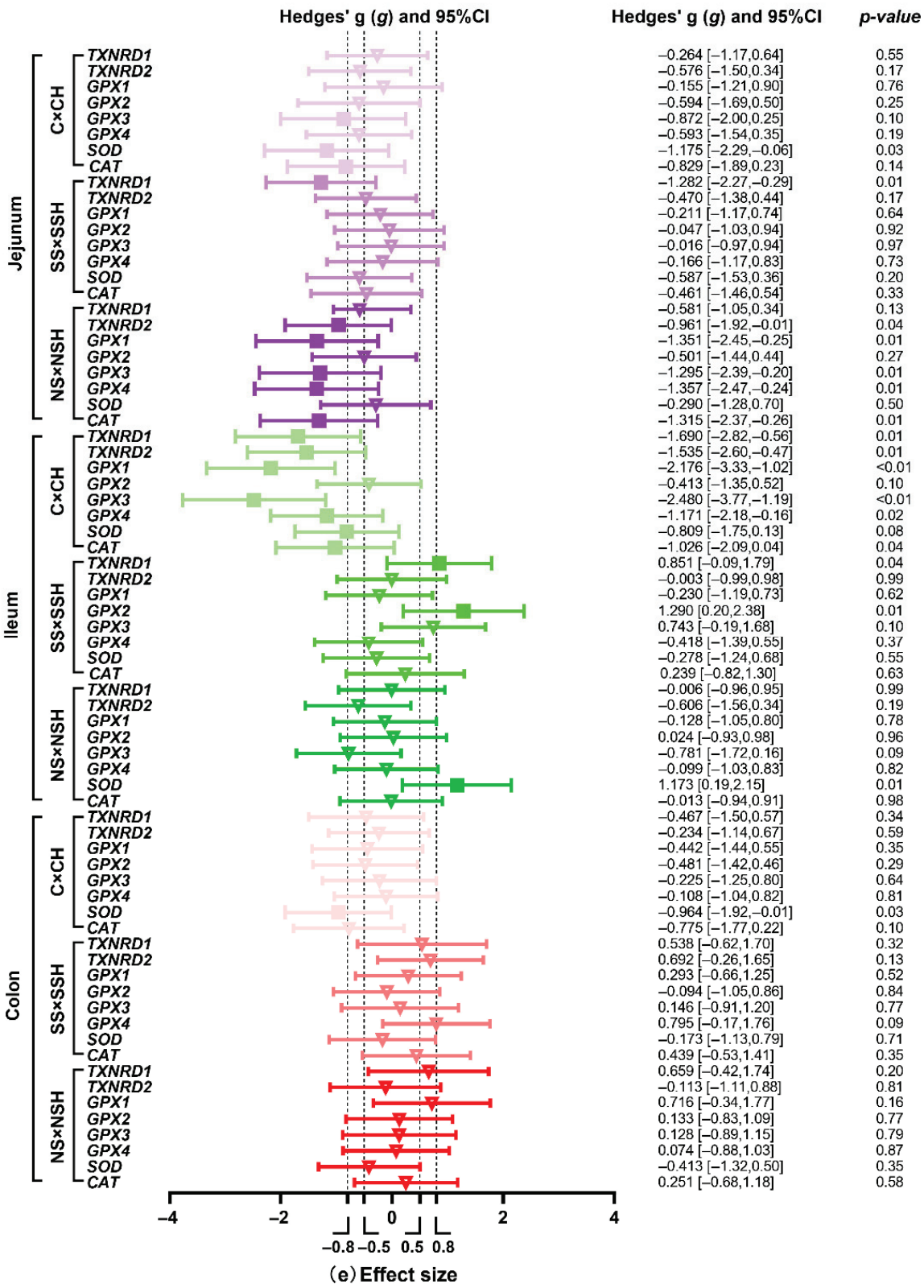


Figure 7. Effect of nano-selenium on gene expression levels of intestinal selenoprotein and antioxidant enzymes in mice under normal conditions or H_2O_2 oxidative stress treatment. (**a**) Bar graph of jejunal intestinal selenoprotein and antioxidant enzymes gene expression, (**b**) bar graph of gene expression of intestinal selenoprotein and antioxidant enzymes in the ileum, (**c**) bar graph of colonic intestinal selenoprotein and antioxidant enzymes gene expression, (**d**) effect size forest plot of intestinal selenoprotein and antioxidant enzymes gene expression [eta-squared (η^2)], (**e**) effect size forest plot of intestinal selenoprotein and antioxidant enzymes gene expression [Hedges' g (g)].

In the colon of mice, under normal conditions, sodium selenite and nano-selenium had no significant effect on the expression of antioxidant enzymes ($p > 0.05$, Figure 7c,d,e). However, the addition of selenium to the *CAT* did not show significant effects, but the effect size was large ($p > 0.05$, $\eta^2 = 0.149$, 95% CI [0.013,0.52]). Compared with group C, group CH significantly increased the expression of *SOD*, and the effect size was large ($p < 0.05$, $g = -0.964$, 95% CI [−1.92,−0.01]). Compared with group SS, group SSH tended to reduce the expression of *GPX4* ($p = 0.09$). In the H_2O_2 treatment, nano-selenium significantly reduced the expression of TXNRD1, with a large effect size ($p < 0.05$, $\eta^2 = 0.307$, 95% CI [0.065, 0.67]). However, the addition of selenium did not show a significant difference in *CAT* levels, but the effect size was large ($p > 0.05$, $\eta^2 = 0.158$, 95% CI [0.028,0.49]).

3.4. Effect of Nano-Selenium on the Antioxidant Capacity

In the jejunum of mice, group SS tended to increase T-SOD, and the effect size was large ($p = 0.07$, $\eta^2 = 0.181$, 95% CI [0.026,0.47], Table 4). Compared with group C and group SS, group NS significantly reduced T-AOC ($p < 0.05$, $\eta^2 = 0.308$, 95% CI [0.087,0.61]). However, in normal conditions, the addition of selenium did not show a significant difference in MDA levels, but the effect size was large ($p > 0.05$, $\eta^2 = 0.168$, 95% CI [0.019,0.50]), nano-selenium effectively reduced the content of MDA, but the sodium selenite group had a certain increase. Compared with group C, group CH significantly reduced T-AOC, and the effect size was large ($p < 0.05$, $g = 1.857$, 95% CI [0.77,2.95]). Compared with the group SS, group SSH tended to reduce T-AOC ($p = 0.06$). Compared with group SSH, group NSH significantly reduced CAT, and the effect size was large ($p < 0.05$, $\eta^2 = 0.249$, 95% CI [0.047,0.60]).

In the ileum of mice, sodium selenite and nano-selenium had no significant effect on the antioxidant capacity under normal conditions and H_2O_2 treatment ($p > 0.05$). Compared with the group SS, group SSH significantly increased MDA, and the effect size was large ($p < 0.05$, $g = -1.600$, 95% CI [−2.84,−0.36]). Compared with the group NS, group NSH tended to increase MDA, and the effect size was large ($p = 0.06$, $g = -1.103$, 95% CI [−2.18,−0.03]).

In the colon of mice, compared with group C, group SS significantly increased T-SOD, and the effect size was large ($p < 0.05$, $\eta^2 = 0.285$, 95% CI [0.064,0.66]). Compared with group SS, group SSH significantly reduced T-SOD and T-AOC, and the effect size was large ($p < 0.05$, $|g| \geq 0.8$). Compared with group NS, group NSH significantly reduced T-SOD, and the effect size was large ($p < 0.05$, $g = 0.967$, 95% CI [0.01,1.92]). Compared with group CH, group SSH significantly reduced T-SOD, and the effect size was large ($p < 0.05$, $\eta^2 = 0.242$, 95% CI [0.081,0.54]). Group SSH significantly reduced T-AOC compared with the group CH and group NSH, and the effect size was large ($p < 0.05$, $\eta^2 = 0.323$, 95% CI [0.122,0.63]).

Table 4. Effects of nano-selenium on intestinal antioxidation in mice under normal conditions or H_2O_2 oxidative stress treatment.

Intestinal Structure	Antioxidant Index	Treatments					
		C	SS	NS	CH	SSH	NSH
Jejunum	T-SOD (U/mgprot)	504.34 ± 20.92	546.17 ± 27.89	459.99 ± 26.23	490.07 ± 22.43	471.22 ± 35.11	451.84 ± 31.55
	T-AOC (mmol/g)	0.16 ± 0.01 ^{a}	0.17 ± 0.01 ^{a}	0.13 ± 0.01 ^{b}	0.13 ± 0.00 *	0.14 ± 0.01	0.13 ± 0.01
	CAT (U/mgprot)	14.00 ± 1.76	14.74 ± 2.30	11.84 ± 1.93	11.57 ± 1.05 ^{ab}	13.79 ± 1.84 ^{a}	8.56 ± 1.12 ^{b}
	MDA (nmol/mgprot)	0.84 ± 0.07	0.97 ± 0.08	0.71 ± 0.10	0.95 ± 0.08	1.01 ± 0.14	0.80 ± 0.05
Ileum	T-AOC (mmol/g)	0.15 ± 0.01	0.14 ± 0.01	0.15 ± 0.02	0.14 ± 0.01	0.13 ± 0.02	0.15 ± 0.01
	MDA (nmol/mgprot)	2.75 ± 0.61	2.62 ± 0.62	2.34 ± 0.36	4.05 ± 0.68	5.76 ± 0.74 *	4.76 ± 1.72
Colon	T-SOD (U/mgprot)	270.99 ± 9.87 ^{b}	333.01 ± 17.33 ^{a}	306.79 ± 11.94 ^{ab}	277.64 ± 15.22 ^{a}	202.51 ± 18.12 ^{b}*	251.76 ± 21.25 ^{ab}*
	T-AOC (mmol/g)	0.05 ± 0.00	0.05 ± 0.00	0.05 ± 0.01	0.06 ± 0.01 ^{a}	0.04 ± 0.00 ^{b}*	0.06 ± 0.00 ^{a}
	MDA (nmol/mgprot)	2.19 ± 0.54	2.78 ± 0.53	3.25 ± 0.89	2.35 ± 0.33	3.03 ± 0.75	2.13 ± 0.49

		C × SS × NS		CH × SSH × NSH		C × CH		SS × SSH		NS × NSH	
		p-value	η^2-value (95% CI)	*p*-value	η^2-value (95% CI)	*p*-value	*g*-value (95% CI)	*p*-value	*g*-value (95% CI)	*p*-value	*g*-value (95% CI)
Jejunum	T-SOD	0.07	0.181 [0.026,0.47]	0.67	0.031 [0.004,0.35]	0.65	0.204 [−0.72,1.13]	0.11	0.741 [−0.22,1.70]	0.85	0.086 [−0.84,1.01]
	T-AOC	0.01	0.308 [0.087,0.61]	0.80	0.051 [0.003,0.35]	0.01	1.857 [0.77,2.95]	0.06	0.668 [−0.29,1.62]	0.83	−0.096 [−1.02,0.83]
	CAT	0.58	0.040 [0.003,0.34]	0.03	0.249 [0.047,0.60]	0.25	0.509 [−0.41,1.42]	0.76	0.140 [−0.86,1.14]	0.16	0.628 [−0.30,1.55]
	MDA	0.10	0.168 [0.019,0.50]	0.31	0.128 [0.016,0.56]	0.28	−0.473 [−1.39,0.44]	0.78	−0.140 [−1.21,0.93]	0.29	−0.377 [−1.31,0.56]
Ileum	T-AOC	0.88	0.010 [0.002,0.29]	0.71	0.029 [0.002,0.33]	0.21	0.614 [−0.41,1.64]	0.74	0.210 [−0.72,1.14]	0.85	−0.083 [−1.01,0.84]
	MDA	0.96	0.011 [0.003,0.28]	0.41	0.095 [0.010,0.49]	0.16	−0.646 [−1.63,0.34]	0.01	−1.600 [−2.84,−0.36]	0.06	−1.103 [−2.18,−0.03]
Colon	T-SOD	0.02	0.285 [0.064,0.66]	0.02	0.242 [0.081,0.54]	0.88	−0.157 [−1.06,0.74]	<0.01	2.229 [1.06,3.39]	0.03	0.967 [0.01,1.92]
	T-AOC	0.75	0.024 [0.003,0.37]	0.01	0.323 [0.122,0.63]	0.14	−0.683 [−1.64,0.27]	0.03	1.093 [0.06,2.13]	0.41	−0.372 [−1.31,0.56]
	MDA	0.59	0.069 [0.006,0.52]	0.81	0.074 [0.004,0.56]	0.79	−0.147 [1.35,1.06]	0.79	−0.136 [−1.23,0.96]	0.28	0.593 [−0.57,1.76]

4. Discussion

4.1. The Role of Chitosan in Nano-Selenium Materials

The nano-selenium material used in the present study was synthesized using chitosan powder, so its components include selenium and chitosan. At present, chitosan has been widely applied in the field of nanomaterials [16]. Chitosan nano-selenium particles (CSNP), as nano-carriers, have good stability because they have a high positive charge, which can prevent the aggregation and sedimentation of nanoparticles; CSNP has a large specific surface area, which enables it to have a high loading capacity and encapsulation for substances. Meanwhile, CSNP has a high degree of biocompatibility, good tolerance to organisms, and does not cause obvious adverse reactions [17]. Therefore, chitosan has excellent capabilities in terms of solubility, biocompatibility, biodegradability, stability, and easy functionalization. Moreover, it has the advantages of being non-toxic, having a low-level immune response, mucosal adhesion, and high absorption [18,19]. However, due to its relatively weak mechanical properties and high degradation rate, it is usually used in combination with other substances or in composite materials [20]. So, from a biological activity point of view, chitosan mainly serves as a carrier in the form of nanoparticles to effectively transport and deliver substances in organisms, such as drugs in medicine and trace elements in nutrition.

4.2. Effect of Nano-Selenium on Organ Index

The organ index (organ-to-body weight ratio) is an important indicator of physiological status and toxicity in animals. Under normal conditions, organ indices remain stable; significant increases may indicate edema or hyperplasia, while decreases suggest atrophy [21–24]. In this study, there were no significant differences in the organ indices of liver, kidney, heart, and pancreas of mice among different treatments, indicating that the organ indices of mice were stable against selenium supplementation and H_2O_2 treatment, and were not affected by selenium or the toxic effects of H_2O_2. Although not statistically significant, a large effect size suggested potential influences of selenium and H_2O_2 on the kidney index. However, both sodium selenite and nano-selenium significantly reduced the spleen index in mice. Similar to the study by Attia et al. [25], selenium supplementation significantly reduced the organ index in the spleen of chickens, while other organ indices were not significantly affected by selenium level or selenium source. In the study results of Ali et al. [26], the spleen index was also reduced when chickens were given selenium. On the one hand, it may be related to the experimental time, experimental conditions, and individual animal differences. On the other hand, selenium may be present in the basal diet of mice, and additional supplementation of selenium may have an effect on their spleen. When nano-selenium was fed in the present study, H_2O_2 treatment significantly increased the spleen index of mice. As mentioned above, H_2O_2 may have caused edema or lesions in the spleen of mice, resulting in an increase in spleen index.

4.3. Effect of Nano-Selenium on the Morphology of Jejunum

The main function of the jejunum is to digest and absorb nutrients, which contributes to the normal operation of the body's metabolism and immune system [27]. The villus height (VH), crypt depth (CD), and the ratio of villus height to crypt depth (VH/CD) are key indicators of intestinal health and absorptive capacity [28,29]. Higher villus height indicates greater intestinal absorption area and better absorption ability [30]. Crypt depth was closely related to the proliferation rate of epithelial cells [31]. Shallow crypts suggest higher cell maturation, whereas deeper crypts indicate villus atrophy and reduced function [32]. The ratio of villus height to crypt depth (VH/CD) is a comprehensive reflection of intestinal function.

In this study, sodium selenite and nano-selenium had no significant effect on villus height and crypt depth in the jejunum of mice under normal conditions or H_2O_2 treatment. Similar to the results of this study, both sodium selenite and nano-selenium had no significant effect on jejunal villus height and crypt depth of broilers at 21 days. In addition, nano-selenium and sodium selenite also had no effect on jejunal villus height under stress [33]. Khajeh et al. [34] showed that nano-selenium had different effects on crypt depth at the height of jejunal villi in broilers at different days of age. Therefore, we speculate that this may be related to rearing duration. However, through the analysis of effect size, it was found that adding selenium had a large effect on the villus height, and the nano-selenium group had the highest villus height. This indicates that nano-selenium has certain effectiveness in improving the villus height in the jejunum of mice, but further proof is needed. We used H_2O_2 to induce oxidative stress, which had no effect on jejunum morphology in mice. Similar to the results of some studies, stress had no significant effect on the intestinal morphology of animals [33,35]. On the one hand, it may be related to the rapid epithelialization of intestinal mucosa [35]; on the other hand, when subjected to stress, the body will produce a self-protection mechanism to reduce the damage caused by stress. We found that supplementation of selenium under normal conditions tended to improve the jejunal VH/CD of mice, and the effect of nano-selenium was better. In the presence of H_2O_2, feeding sodium selenite and nano-selenium significantly increased the jejunal VH/CD. And the effect sizes are all considered to be large. Rehman et al. [33] also found that the addition of sodium selenite and nano-selenium significantly improved the VH/CD of the jejunum in broilers [34]. According to the comprehensive index of VH/CD, nano-selenium has a positive protective effect on jejunum morphology in mice.

From the analysis of results, selenium supplementation had no significant effect on villus height and crypt depth, but it had a certain effectiveness in improving the villus height, and significantly increased VH/CD. At the same time, from the numerical value and morphological diagram, H_2O_2 has a certain damage effect on the jejunum, and selenium supplementation can improve this phenomenon, and nano-selenium has a better effect. He et al. [36] pointed out that selenium deficiency in animals affects the structure of small intestinal mucosa and damages the functions of the small intestinal immune barrier and physical barrier. At the same time, selenium can also enhance the intestinal barrier by improving the intestinal immune status, oxidation status, and maintaining the integrity and normal function of the small intestine [37–39]. Therefore, nano-selenium has a positive effect on jejunum morphology in mice under stress.

4.4. Effect of Nano-Selenium on the Expression of Intestinal Inflammatory Factors

Intestinal immune cytokines are crucial in regulating gastrointestinal inflammation [40]. Key pro-inflammatory factors include *IL-1β*, which promotes neutrophil infiltration and T-cell activation [41], and *NF-κB*, a transcription factor that enhances multiple pro-inflammatory cytokines [42]. Conversely, the anti-inflammatory cytokine *IL-10*—produced by Th2 cells—alleviates inflammation by inhibiting pro-inflammatory cytokine production and plays a protective role in colitis models [41,43–45]. Reduced *IL-10* levels weaken anti-inflammatory capacity and exacerbate inflammation. Inflammatory pathways are often redox-sensitive; excess ROS induces oxidative stress, promoting inflammation and tissue apoptosis [46].

We measured inflammatory factor expression across intestinal segments in mice. Under normal conditions, selenium supplementation did not significantly alter expression levels; the expression of intestinal inflammatory factors was at normal levels and did not seem to be regulated by selenium. Nonetheless, large effect sizes were observed for certain indicators: nano-selenium increased *IL-10* expression in the jejunum, while in the ileum, it

reduced *IL-1β*—unlike sodium selenite, which elevated both *IL-1β* and *NF-κB*. These trends suggest a potential anti-inflammatory effect of nano-selenium that merits further study. H_2O_2 treatment up-regulates several inflammatory factors in all three intestinal segments. Similar to previous studies, H_2O_2 up-regulates the expression of some inflammatory factors in intestinal epithelial cells [47–49]. As an ROS, H_2O_2 disrupts redox balance, promotes oxidative stress, and contributes to intestinal diseases [50]. In this study, H_2O_2 up-regulated the expression of pro-inflammatory factors in different intestinal segments, which suggests that feeding H_2O_2 in drinking water induces an inflammatory response in the intestine of mice to a certain extent, and the intestine of mice is under stress. In the jejunum, although not significantly, H_2O_2 had a large effect size on increasing the expression of *IL-10*. In the ileum, H_2O_2 up-regulated the expression of anti-inflammatory factor *IL-10*, which may be a self-protective mechanism of the body to secrete anti-inflammatory cytokines by up-regulating the expression of anti-inflammatory factors, thereby slowing down the occurrence of inflammation. Through longitudinal comparison, we found that H_2O_2 had no significant effect on the expression of *IL-1β*, *NF-κB*, and *IL-10* in the treatment of selenium supplementation. Selenium supplementation appeared to normalize the expression of these inflammatory factors. At the same time, the expression levels of *NF-κB* and *IL-10* in the colon of mice in the nano-selenium group were the lowest in the presence of H_2O_2. From a signaling pathway perspective, the *NF-κB* pathway plays a key role in mediating immune and inflammatory responses. As a major regulator of inflammatory responses, its role is mainly to regulate the expression of hundreds of immune-related genes, especially those encoding pro-inflammatory cytokines and chemokines [51]. The *NF-κB* pathway mediates inflammatory responses via classical (e.g., TLR, TNFR) and non-classical (e.g., CD40, RANK) activation [52]. Its complex interaction with ROS may involve both activation and inhibition. This difference may be related to the specificity of different upstream pathways and cells [53]. Studies have found that ROS drives the *NF-κB* pathway in the duodenum of mice, thereby inducing inflammation [54]. Therefore, on the one hand, ROS directly regulates the *NF-κB* signaling pathway; on the other hand, some cytokines (such as *TNF-α* and *IL-1β*) activate *NF-κB*, and the activated *NF-κB* in turn drives the expression of pro-inflammatory factors to participate in the inflammatory process [52,55]. In this study, H_2O_2 increased *IL-1β* (jejunum/colon). In the ileum, *NF-κB* was also significantly elevated, accompanied by a numerical increase in *IL-1β* levels. These observations suggest that H_2O_2, as a reactive oxygen species (ROS), exerts pro-inflammatory effects through dual mechanisms: (1) up-regulating cytokine *IL-1β* to activate the *NF-κB* signaling pathway, and (2) directly stimulating *NF-κB* pathway activation. However, in the three groups fed with H_2O_2 drinking water, compared with sodium selenite, nano-selenium down-regulated the expression of *NF-κB*, and compared with the Control group fed with H_2O_2 drinking water, *IL-1β* and *NF-κB* were decreased numerically, indicating anti-inflammatory potential. This finding aligns with numerous studies demonstrating selenium's ability to mitigate intestinal stress-induced inflammation through modulation of inflammatory mediators [56–61]. For example, some studies have found that nano-selenium significantly down-regulate the expression levels of *IL-1β* and *TNF-α* [62,63].

Selenium exerts pivotal regulatory functions in intestinal inflammation. Accumulating evidence demonstrates that selenium deficiency in animals triggers oxidative stress, up-regulates the expression of corresponding inflammatory factors, and induces intestinal tissue inflammation [64–66]. This deficiency is also associated with reduced antimicrobial peptide production [67] and disrupted gut microbiota equilibrium [68]. Selenium exerts antioxidant and immunomodulatory effects via selenoproteins [69]. Notably, nano-selenium demonstrates enhanced bioavailability and biosafety profiles attributable to its unique nanostructure, thereby exhibiting modulatory effects on intestinal inflammatory markers.

4.5. Effect of Nano-Selenium on the Expression of Intestinal Selenoproteins and Antioxidant Enzymes

Selenium mainly exists in the form of selenocysteine (SeCys) in the body [70], and then selenocysteine is inserted into the nascent polypeptide chain in a co-translational manner by insertion elements, thereby synthesizing selenoproteins [71]. A total of 25 selenoprotein genes were identified by bioinformatics studies [72]. As antioxidant enzymes, selenoproteins such as glutathione peroxidase (*GPX*) family, such as *GPX1-4*, can effectively metabolize peroxides in cells and act as an antioxidant defense mechanism to prevent excessive reactive oxygen species/reactive nitrogen species. Thioredoxin reductase (*TXNRD1-3*) are oxidoreductases that regulate the redox state of proteins such as thioredoxin as well as small molecules such as thioctic tetrathionate [73]. These, along with enzymes like superoxide dismutase (*SOD*) and catalase (*CAT*), are essential in mitigating oxidative stress.

This study investigated the transcriptional regulation of antioxidant markers (selenoproteins and antioxidases). Under normal conditions, neither sodium selenite nor nano-selenium supplementation significantly modulated the expression of most antioxidant markers in the mouse intestine, consistent with previous findings demonstrating no alteration in *SOD* and *CAT* gene expression upon selenium supplementation [74]. We speculate that the regulation of antioxidant marker expression may be related to the dose level of selenium supplementation and the physiological status of the animals. Several studies have found that the regulation of selenoprotein expression may require a supertrophic dose of selenium [75,76]. Notably, selenium supplementation has been demonstrated to enhance the body's antioxidant defense system predominantly under oxidative stress conditions [77,78], potentially explaining the lack of significant effects observed under basal conditions. Although not statistically significant, large effect sizes were observed for certain indicators: selenium increased *GPX2* in the jejunum, *TXNRD1* and *TXNRD2* in the ileum, and *CAT* in the colon. Only in the ileum did nano-selenium significantly up-regulate *GPX1*, and sodium selenite increased *GPX3*, aligning with reports that selenium can up-regulate *GPX* family expression [79–81]. Selenoproteins have a unique and graded dependence on the trace element selenium [82]. H_2O_2 treatment in mice fed nano-selenium significantly increased the expression of antioxidant markers and concentrated in the jejunum. Labunskyy et al. pointed out that some selenoproteins are called stress-related selenoproteins [71], and these proteins are closely related to the stress state in the body [83]. Selenium supplementation was found to up-regulate selenoprotein expression under stress conditions [84–86]. These results indicate that selenium plays a positive role in the expression of selenoproteins and antioxidants in the body under stress. Due to its small volume, large specific surface area, and unique physicochemical properties, nano-selenium has higher antioxidant activity and better bioavailability [87,88], thus significantly improving the antioxidant status of mice intestinal tract. However, in the basal diet, H_2O_2 also up-regulated the expression of some antioxidant markers, mainly concentrated in the ileum of mice. From another point of view, we speculate that this is a part of the compensatory response to prevent oxidative damage, which is a kind of self-protection reaction of the body [3]. Te Velde et al. also pointed out that up-regulation of selenoproteins or antioxidant enzymes may be a defense mechanism against oxidative stress during inflammation [89]. Similarly, some studies have found that the expression of selenoproteins and antioxidant enzymes is up-regulated under stress, and the expression of selenoproteins and antioxidant enzymes is restored to normal level with the addition of selenium, such as nano-selenium [57,90,91]. So, in the ileum, H_2O_2 treatment had no effect on most of the antioxidant markers in mice fed nano-selenium.

Overall, there were differences in the expression of antioxidant markers in different intestinal segments of mice. The expression of selenoproteins is affected by many factors,

and the different expression may be related to the status of selenium, the catabolic pathways of selenium in different tissues, and the differences in its biosynthesis and utilization [69]. It is also regulated by differences in the availability of selenium [71]. In addition, intestinal microorganisms can also affect the expression of selenoproteins. Guevara et al. [81] pointed out that selenium affects the composition of microbes in different intestinal segments. Different microorganisms have different uptake, storage, utilization, and excretion abilities of selenium, which may lead to competition between microorganisms and the host for selenium, limiting the availability of selenium and affecting the expression of selenoproteins [92,93].

4.6. Effect of Nano-Selenium on Intestinal Antioxidation

T-SOD, T-AOC, CAT, and MDA are the main indices reflecting the antioxidant capacity and redox status of the body. T-SOD is the first line of antioxidant defense, which can convert superoxide anions into H_2O_2 and water [94]. T-AOC reflects the overall levels of enzymatic and non-enzymatic antioxidants in the body [95]. CAT, as its name implies, is an enzyme that decomposes H_2O_2. H_2O_2 produced by the body and superoxide can be degraded to water and oxygen by CAT [96]. One molecule of CAT can convert 6 million H_2O_2 grabs into water and oxygen per minute [97], thus playing a key role in antioxidant protection. Conversely, MDA—a product of lipid peroxidation induced by ROS—serves as a biomarker of oxidative stress and cellular membrane damage [98,99].

This study revealed that nano-selenium supplementation reduced the T-AOC of the jejunum under normal conditions, which may be related to the toxic effects of nano-selenium. Long-term study by Xiao et al. [100] demonstrated that nano-selenium can suppress both antioxidant enzyme activity and selenoprotein expression, thereby exacerbating oxidative stress, which leads to organ lesions and decreased antioxidant capacity. The toxicity of nano-selenium is critically dependent on the size and chemical properties of nanoparticles [101]. In addition, both sodium selenite and nano-selenium have pro-oxidative properties at high concentrations, leading to the generation of ROS [102]. Therefore, we speculate that the jejunum's anatomical position as the primary intestinal segment exposed to nano-selenium first, and may suffer from toxic effects to a certain extent, so the T-AOC is reduced; however, this might also be an accidental phenomenon. Although not statistically significant, sodium selenite increased MDA content in the jejunum, whereas nano-selenium reduced it, with a large effect size, warranting further investigation. Meanwhile, sodium selenite seems to be more toxic than nano-selenium, which was demonstrated in a short-term toxicity test [103]. It up-regulated ileal IL-1β and NF-κB expression, increased jejunal MDA, and reduced colonic T-SOD and T-AOC in H_2O_2-treated mice. Notably, sodium selenite increased colonic T-SOD under normal conditions but decreased it under oxidative stress, suggesting it may aggravate H_2O_2-induced damage.

Collectively, these findings indicate that selenium supplementation—particularly sodium selenite—may exert adverse effects on select intestinal antioxidant parameters, though the overall impact on systemic antioxidant capacity appears limited. Previous studies also reported no significant effects of organic selenium or nano-selenium glycinate on T-SOD, MDA, or T-AOC [104,105]. We propose that selenium supplementation effects may be modulated by three key factors: (1) treatment duration, (2) dosage levels, and (3) selenium bioavailability. Furthermore, as previously discussed, gut microbial selenium competition may represent an additional limiting factor for host selenium utilization, though this hypothesis requires experimental validation.

4.7. Limitations of This Study and Future Research Directions

This study has several limitations. Primarily, although the nano-selenium was synthesized using chitosan, no chitosan-only Control group was included. Therefore, the potential influence of chitosan itself on bioavailability and bioactivity remains unassessed. Furthermore, certain negative effects were observed in intestinal antioxidant indicators following selenium supplementation. Although we hypothesize that these may be related to selenium toxicity, this study did not include explicit toxicity assays or dose–response evaluations, which warrants further investigation.

In terms of statistical analysis, although all statistically significant results showed large effect sizes ($p < 0.05$, $\eta^2 \geq 0.14$, $|g| \geq 0.8$), several non-significant outcomes also exhibited large effect sizes. This indicates that it may have certain practical significance and some effect, but there is no significant evidence to support this effect. The wide confidence intervals of some effect estimates further reflect uncertainty in the true effect magnitude, likely resulting from the small sample size. Finally, due to limited tissue availability, only gene expression of selected inflammatory and antioxidant markers was measured; protein-level validation was not performed.

Based on these limitations, subsequent investigations should focus on the following aspects:

1. Include a chitosan-only experimental group to clarify its individual contribution to the effects of nano-selenium.

2. Perform toxicity and dose–response studies using graded concentrations of nano-selenium, combined with assays such as LDH and MTT, to establish its safety profile.

3. Increase sample size to enhance statistical power, reduce random error, and obtain more precise effect estimates.

4. Supplement gene expression data with Western blot analysis to corroborate findings at the protein level.

5. Conduct mechanistic studies using cell models to elucidate underlying signaling pathways.

5. Conclusions

Our results showed that 0.3% H_2O_2 drinking water induced intestinal oxidative stress in mice to a certain extent. The supplementation with sodium selenium and nano-selenium improved intestinal morphology, alleviated oxidative damage, and restored the expression of related inflammatory factors. At the same time, nano-selenium played a positive role in increasing the expression of selenoprotein in the jejunum under stress. However, it showed no significant effect on improving the antioxidant indicators in the intestinal tract. In the future, further research is needed from the perspectives of carriers, selenium dosage levels, protein levels, and increasing the sample size.

Author Contributions: Conceptualization and methodology, X.M.; software, X.J. and R.Z.; validation, D.W., X.W. and X.J.; formal analysis, X.M. and R.Z.; investigation, L.C. and Y.Z.; resources, D.W., S.X., X.W. and M.S.; data curation, X.M., W.L. and Y.L.; writing—original draft preparation, X.M.; writing—review and editing, S.X. and M.S.; visualization, W.L. and Y.L.; supervision, S.X., L.C. and Y.Z.; project administration and funding acquisition, S.X. All authors have read and agreed to the published version of the manuscript.

Funding: This work was supported by the National Key Research and Development Program (2023YFD1300803), Sichuan Province "145" Breeding Tackle Project (2021YFYZ0008), China Agriculture Research System (CARS-35), and Sichuan Innovation Team of China Agriculture System (SCCXTD-2024-8).

Institutional Review Board Statement: All experimental procedures followed current laws regarding animal protection and were approved by the Animal Care and Use Committee of Sichuan Agricultural University (ethical approval code: SICAU 2023214016, approval date: 15 October 2023).

Informed Consent Statement: Not applicable.

Data Availability Statement: None of the data were deposited in an official repository. The data that support the study findings are available from the authors upon request.

Conflicts of Interest: The authors declare no conflicts of interest.

References

1. Bhattacharyya, A.; Chattopadhyay, R.; Mitra, S.; Crowe, S.E. Oxidative stress: An essential factor in the pathogenesis of gastrointestinal mucosal diseases. *Physiol. Rev.* **2014**, *94*, 329–354. [CrossRef]
2. Persson, T.; Popescu, B.O.; Cedazo-Minguez, A. Oxidative stress in Alzheimer's disease: Why did antioxidant therapy fail? *Oxidative Med. Cell. Longev.* **2014**, *2014*, 427318. [CrossRef] [PubMed]
3. Kudva, A.K.; Shay, A.E.; Prabhu, K.S. Selenium and inflammatory bowel disease. *Am. J. Physiol.-Gastrointest. Liver Physiol.* **2015**, *309*, G71–G77. [CrossRef] [PubMed]
4. Mehdi, Y.; Hornick, J.L.; Istasse, L.; Dufrasne, I. Selenium in the environment, metabolism and involvement in body functions. *Molecules* **2013**, *18*, 3292–3311. [CrossRef] [PubMed]
5. Patra, A.; Lalhriatpuii, M. Progress and Prospect of Essential Mineral Nanoparticles in Poultry Nutrition and Feeding-a Review. *Biol. Trace Elem. Res.* **2020**, *197*, 233–253. [CrossRef]
6. Michalak, I.; Dziergowska, K.; Alagawany, M.; Farag, M.R.; El-Shall, N.A.; Tuli, H.S.; Emran, T.B.; Dhama, K. The effect of metal-containing nanoparticles on the health, performance and production of livestock animals and poultry. *Vet. Q.* **2022**, *42*, 68–94. [CrossRef]
7. Zhang, T.; Qi, M.; Wu, Q.; Xiang, P.; Tang, D.; Li, Q. Recent research progress on the synthesis and biological effects of selenium nanoparticles. *Front. Nutr.* **2023**, *10*, 1183487. [CrossRef]
8. Skalickova, S.; Milosavljevic, V.; Cihalova, K.; Horky, P.; Richtera, L.; Adam, V. Selenium nanoparticles as a nutritional supplement. *Nutrition* **2017**, *33*, 83–90. [CrossRef]
9. Abdel-Hakeem, E.A.; Abdel-Hamid, H.A.; Abdel Hafez, S.M.N. The possible protective effect of Nano-Selenium on the endocrine and exocrine pancreatic functions in a rat model of acute pancreatitis. *J. Trace Elem. Med. Biol.* **2020**, *60*, 126480. [CrossRef]
10. Kondaparthi, P.; Deore, M.; Naqvi, S.; Flora, S.J.S. Dose-dependent hepatic toxicity and oxidative stress on exposure to nano and bulk selenium in mice. *Environ. Sci. Pollut. Res. Int.* **2021**, *28*, 53034–53044. [CrossRef]
11. Yin, Y.; Ahmed, N.; Hassan, M.F.; Guo, K.; Shakir, Y.; Zang, J.; Lyu, J. Effect of Nano-selenium on Biological Mechanism of Goblet Cells of the Small Intestine Within Laying Hen. *Biol. Trace Elem. Res.* **2024**, *202*, 1699–1710. [CrossRef]
12. Liu, S.; Yu, H.; Li, P.; Wang, C.; Liu, G.; Zhang, X.; Zhang, C.; Qi, M.; Ji, H. Dietary nano-selenium alleviated intestinal damage of juvenile grass carp (Ctenopharyngodon idella) induced by high-fat diet: Insight from intestinal morphology, tight junction, inflammation, anti-oxidization and intestinal microbiota. *Anim. Nutr.* **2022**, *8*, 235–248. [CrossRef]
13. Li, H.; Tang, Y.; Wang, H.; Liu, X.; Zeng, Y.; Zhang, R.; Yang, C.; Khan, A.; Wu, B.; Wang, X.; et al. Nano-selenium alleviated immunoresponse, apoptosis and oxidative stress in Leydig cells of yak. *Colloids Surf. B Biointerfaces* **2025**, *252*, 114684. [CrossRef] [PubMed]
14. *GB 13883-2023*; Determination of selenium in feeds. State Administration for Market Regulation (SAMR) and Standardization Administration of China (SAC): Beijing, China, 2023.
15. Chang, J.; Pan, X.; Wei, W.; Jiang, X.; Che, L.; Lin, Y.; Zhuo, Y.; Feng, B.; Hua, L.; Li, J.; et al. Dietary inulin supplementation in early gestation regulates uterine fluid exosomes and angiogenesis to improve embryo implantation in sows. *J. Anim. Sci. Biotechnol.* **2025**, *16*, 111. [CrossRef]
16. Mushtaq, A.; Li, L.; Anitha, A.; Grøndahl, L. Chitosan Nanomedicine in Cancer Therapy: Targeted Delivery and Cellular Uptake. *Macromol. Biosci.* **2021**, *21*, e2100005. [CrossRef]
17. Pathak, R.; Bhatt, S.; Punetha, V.D.; Punetha, M. Chitosan nanoparticles and based composites as a biocompatible vehicle for drug delivery: A review. *Int. J. Biol. Macromol.* **2023**, *253*, 127369. [CrossRef]
18. Kankariya, Y.; Chatterjee, B. Biomedical Application of Chitosan and Chitosan Derivatives: A Comprehensive Review. *Curr. Pharm. Des.* **2023**, *29*, 1311–1325. [CrossRef] [PubMed]
19. Cohen, E.; Poverenov, E. Hydrophilic Chitosan Derivatives: Synthesis and Applications. *Chem. –A Eur. J.* **2022**, *28*, e202202156. [CrossRef]
20. Jafernik, K.; Ładniak, A.; Blicharska, E.; Czarnek, K.; Ekiert, H.; Wiącek, A.E.; Szopa, A. Chitosan-Based Nanoparticles as Effective Drug Delivery Systems-A review. *Molecules* **2023**, *28*, 1963. [CrossRef] [PubMed]

21. Li, L.; Lin, X.; Chen, T.; Liu, K.; Chen, Y.; Yang, Z.; Liu, D.; Xu, G.; Wang, X.; Lin, G. Systematic evaluation of CdSe/ZnS quantum dots toxicity on the reproduction and offspring health in male BALB/c mice. *Ecotoxicol. Environ. Saf.* **2021**, *211*, 111946. [CrossRef]
22. Song, Z.; Si, X.; Zhang, X.; Chen, J.; Jia, H.; He, Y.; Liu, H.; Kou, Z.; Dai, Z.; Wu, Z. Amuc Prevents Liver Inflammation and Oxidative Stress in Mice Challenged with Salmonella Typhimurium. *J. Nutr.* **2023**, *153*, 532–542. [CrossRef]
23. Li, Z.; Li, X.; Cai, Z.; Jin, G.; Ahn, D.U.; Huang, X. Immunomodulatory effects of chicken soups prepared with the native cage-free chickens and the commercial caged broilers. *Poult. Sci.* **2022**, *101*, 102053. [CrossRef]
24. Lu, X.; Guo, C.; Zhu, Y. Selenium-enriched crude polysaccharide from Rosa roxburghii Tratt ameliorates cadmium-induced acute kidney injury in mice by modulating intestinal microorganisms. *Heliyon* **2023**, *9*, e19678. [CrossRef]
25. Attia, Y.; Abdalah, A.; Zeweil, H.; Bovera, F.; El-Din, A.T.; Araft, M. Effect of inorganic or organic selenium supplementation on productive performance, egg quality and some physiological traits of dual-purpose breeding hens. *Czech J. Anim. Sci.* **2010**, *55*, 505–519. [CrossRef]
26. Ali, F.; Saeed, K.; Fatemeh, H. Nano-Bio Selenium Synthesized by Bacillus subtilis Modulates Broiler Performance, Intestinal Morphology and Microbiota, and Expression of Tight Junction's Proteins. *Biol. Trace Elem. Res.* **2022**, *200*, 1811–1825. [CrossRef]
27. Zhu, Y.; Shi, C.; Niu, Q.; Wang, J.; Zhu, W. Dynamic changes in morphology, gene expression and microbiome in the jejunum of compensatory-growth rats induced by protein restriction. *Microb. Biotechnol.* **2018**, *11*, 734–746. [CrossRef] [PubMed]
28. Khan, I.; Zaneb, H.; Masood, S.; Ashraf, S.; Rehman, H.F.; Tahir, S.K.; Rehman, H.U.; Khan, A.; Taj, R.; Rahman, S.U.; et al. Supplementation of Selenium Nanoparticles-Loaded Chitosan Improves Production Performance, Intestinal Morphology, and Gut Microflora in Broiler Chickens. *J. Poult. Sci.* **2022**, *59*, 272–281. [CrossRef] [PubMed]
29. Lu, D.; Yao, D.; Hu, G.; Zhou, J.; Shen, X.; Qian, L. Maternal docosahexaenoic acid supplementation during lactation improves exercise performance, enhances intestinal glucose absorption and modulates gut microbiota in weaning offspring mice. *Front. Nutr.* **2024**, *11*, 1423576. [CrossRef]
30. Xu, Z.R.; Hu, C.H.; Xia, M.S.; Zhan, X.A.; Wang, M.Q. Effects of dietary fructooligosaccharide on digestive enzyme activities, intestinal microflora and morphology of male broilers. *Poult. Sci.* **2003**, *82*, 1030–1036. [CrossRef] [PubMed]
31. Zhang, A.W.; Lee, B.D.; Lee, S.K.; Lee, K.W.; An, G.H.; Song, K.B.; Lee, C.H. Effects of yeast (*Saccharomyces cerevisiae*) cell components on growth performance, meat quality, and ileal mucosa development of broiler chicks. *Poult. Sci.* **2005**, *84*, 1015–1021. [CrossRef]
32. Li, R.; Liu, J.; Liu, M.; Liang, M.; Wang, Z.; Sha, Y.; Ma, H.; Lin, Y.; Li, B.; You, J.; et al. Effects of selenium-enriched yeast dietary supplementation on egg quality, gut morphology and caecal microflora of laying hens. *Anim. Biotechnol.* **2024**, *35*, 2258188. [CrossRef] [PubMed]
33. Rehman, H.F.u.; Zaneb, H.; Masood, S.; Yousaf, M.S.; Hayat, K.; Majeed, K.A.; Zeeshan, M.; Ashraf, S.; Khan, I.; Khan, A.; et al. Effect of Selenium Nanoparticles and Mannan Oligosaccharide Supplementation on Growth Performance, Stress Indicators, and Intestinal Microarchitecture of Broilers Reared under High Stocking Density. *Animals* **2022**, *12*, 2910. [CrossRef]
34. Khajeh Bami, M.; Afsharmanesh, M.; Espahbodi, M.; Esmaeilzadeh, E. Effects of dietary nano-selenium supplementation on broiler chicken performance, meat selenium content, intestinal microflora, intestinal morphology, and immune response. *J. Trace Elem. Med. Biol.* **2022**, *69*, 126897. [CrossRef] [PubMed]
35. Quinteiro-Filho, W.M.; Ribeiro, A.; Ferraz-de-Paula, V.; Pinheiro, M.L.; Sakai, M.; Sá, L.R.; Ferreira, A.J.; Palermo-Neto, J. Heat stress impairs performance parameters, induces intestinal injury, and decreases macrophage activity in broiler chickens. *Poult. Sci.* **2010**, *89*, 1905–1914. [CrossRef]
36. He, X.; Lin, Y.; Lian, S.; Sun, D.; Guo, D.; Wang, J.; Wu, R. Selenium Deficiency in Chickens Induces Intestinal Mucosal Injury by Affecting the Mucosa Morphology, SIgA Secretion, and GSH-Px Activity. *Biol. Trace Elem. Res.* **2020**, *197*, 660–666. [CrossRef] [PubMed]
37. Muhammad, A.I.; Mohamed, D.A.; Chwen, L.T.; Akit, H.; Samsudin, A.A. Effect of Selenium Sources on Laying Performance, Egg Quality Characteristics, Intestinal Morphology, Microbial Population and Digesta Volatile Fatty Acids in Laying Hens. *Animals* **2021**, *11*, 1681. [CrossRef] [PubMed]
38. Dalia, A.M.; Loh, T.C.; Sazili, A.Q.; Samsudin, A.A. Influence of bacterial organic selenium on blood parameters, immune response, selenium retention and intestinal morphology of broiler chickens. *BMC Vet. Res.* **2020**, *16*, 365. [CrossRef]
39. Khambualai, O.; Yamauchi, K.; Tangtaweewipat, S.; Cheva-Isarakul, B. Growth performance and intestinal histology in broiler chickens fed with dietary chitosan. *Br. Poult. Sci.* **2009**, *50*, 592–597. [CrossRef]
40. Celi, P.; Verlhac, V.; Calvo, E.P.; Schmeisser, J.; Kluenter, A.-M. Biomarkers of gastrointestinal functionality in animal nutrition and health. *Anim. Feed Sci. Technol.* **2019**, *250*, 9–31. [CrossRef]
41. Sun, M.; He, C.; Cong, Y.; Liu, Z. Regulatory immune cells in regulation of intestinal inflammatory response to microbiota. *Mucosal Immunol.* **2015**, *8*, 969–978. [CrossRef]
42. Tang, Y.L.; Sim, T.S.; Tan, K.S. Oral streptococci subvert the host innate immune response through hydrogen peroxide. *Sci. Rep.* **2022**, *12*, 656. [CrossRef]

43. Groux, H.; O'Garra, A.; Bigler, M.; Rouleau, M.; Antonenko, S.; de Vries, J.E.; Roncarolo, M.G. A CD4+ T-cell subset inhibits antigen-specific T-cell responses and prevents colitis. *Nature* **1997**, *389*, 737–742. [CrossRef]
44. McNamee, E.N.; Masterson, J.C.; Jedlicka, P.; McManus, M.; Grenz, A.; Collins, C.B.; Nold, M.F.; Nold-Petry, C.; Bufler, P.; Dinarello, C.A.; et al. Interleukin 37 expression protects mice from colitis. *Proc. Natl. Acad. Sci. USA* **2011**, *108*, 16711–16716. [CrossRef] [PubMed]
45. Sabat, R.; Grütz, G.; Warszawska, K.; Kirsch, S.; Witte, E.; Wolk, K.; Geginat, J. Biology of interleukin-10. *Cytokine Growth Factor Rev.* **2010**, *21*, 331–344. [CrossRef]
46. Rusetskaya, N.Y.; Fedotov, I.V.; Koftina, V.A.; Borodulin, V.B. Selenium compounds in redox regulation of inflammation and apoptosis. *Biochem. Moscow Suppl. Ser. B* **2019**, *13*, 277–292. [CrossRef]
47. Lu, J.; An, Y.; Wang, X.; Zhang, C.; Guo, S.; Ma, Y.; Qiu, Y.; Wang, S. Alleviating effect of chlorogenic acid on oxidative damage caused by hydrogen peroxide in bovine intestinal epithelial cells. *J. Vet. Med. Sci.* **2024**, *86*, 1016–1026. [CrossRef]
48. Li, Z.; Huang, Z.; Jia, G.; Zhao, H.; Liu, G.; Chen, X. L-theanine attenuates H_2O_2-induced inflammation and apoptosis in IPEC-J2 cells via inhibiting p38 MAPK signaling pathway. *Food Chem. Toxicol.* **2024**, *186*, 114561. [CrossRef] [PubMed]
49. Yuan, Z.; Yang, M.; Liang, Z.; Yang, C.; Kong, X.; Wu, Y.; Wang, S.; Fan, H.; Ning, C.; Xiao, W.; et al. PI3K/AKT/mTOR, NF-κB and ERS pathway participated in the attenuation of H_2O_2-induced IPEC-J2 cell injury by koumine. *J. Ethnopharmacol.* **2023**, *304*, 116028. [CrossRef]
50. Yan, Y.; Shi, Z.; Zhang, Y. Hierarchical multi-task deep learning-assisted construction of human gut microbiota reactive oxygen species-scavenging enzymes database. *mSphere* **2024**, *9*, e0034624. [CrossRef]
51. Mitchell, J.P.; Carmody, R.J. NF-κB and the Transcriptional Control of Inflammation. *Int. Rev. Cell Mol. Biol.* **2018**, *335*, 41–84. [CrossRef]
52. Mao, H.; Zhao, X.; Sun, S.-c. NF-κB in inflammation and cancer. *Cell. Mol. Immunol.* **2025**, *22*, 811–839. [CrossRef]
53. Morgan, M.J.; Liu, Z.G. Crosstalk of reactive oxygen species and NF-κB signaling. *Cell Res.* **2011**, *21*, 103–115. [CrossRef] [PubMed]
54. He, Y.; Li, Z.; Xu, T.; Luo, D.; Chi, Q.; Zhang, Y.; Li, S. Polystyrene nanoplastics deteriorate LPS-modulated duodenal permeability and inflammation in mice via ROS drived-NF-κB/NLRP3 pathway. *Chemosphere* **2022**, *307*, 135662. [CrossRef] [PubMed]
55. Hayden, M.S.; West, A.P.; Ghosh, S. NF-κB and the immune response. *Oncogene* **2006**, *25*, 6758–6780. [CrossRef]
56. Li, H.; Che, H.; Xie, J.; Dong, X.; Song, L.; Xie, W.; Sun, J. Supplementary selenium in the form of selenylation α-D-1,6-glucan ameliorates dextran sulfate sodium induced colitis in vivo. *Int. J. Biol. Macromol.* **2022**, *195*, 67–74. [CrossRef] [PubMed]
57. Tang, J.; Cao, L.; Jia, G.; Liu, G.; Chen, X.; Tian, G.; Cai, J.; Shang, H.; Zhao, H. The protective effect of selenium from heat stress-induced porcine small intestinal epithelial cell line (IPEC-J2) injury is associated with regulation expression of selenoproteins. *Br. J. Nutr.* **2019**, *122*, 1081–1090. [CrossRef]
58. Kaur, R.; Thakur, S.; Rastogi, P.; Kaushal, N. Resolution of Cox mediated inflammation by Se supplementation in mouse experimental model of colitis. *PLoS ONE* **2018**, *13*, e0201356. [CrossRef]
59. Tirosh, O.; Levy, E.; Reifen, R. High selenium diet protects against TNBS-induced acute inflammation, mitochondrial dysfunction, and secondary necrosis in rat colon. *Nutrition* **2007**, *23*, 878–886. [CrossRef]
60. Alsulami, M.N.; El-Saadony, M.T. Supplementing broiler diets with bacterial selenium nanoparticles enhancing performance, carcass traits, blood indices, antioxidant status, and caecal microbiota of Eimeria tenella-infected broiler chickens. *Poult. Sci.* **2023**, *102*, 103111. [CrossRef]
61. Abdel-Gaber, R.; Hawsah, M.A.; Al-Otaibi, T.; Alojayri, G.; Al-Shaebi, E.M.; Mohammed, O.B.; Elkhadragy, M.F.; Al-Quraishy, S.; Dkhil, M.A. Biosynthesized selenium nanoparticles to rescue coccidiosis-mediated oxidative stress, apoptosis and inflammation in the jejunum of mice. *Front. Immunol.* **2023**, *14*, 1139899. [CrossRef]
62. Xu, Y.; Wang, X.C.; Jiang, W.; Chen, L.H.; Chen, T.; Wu, D.; Hu, J.N. Porphyra haitanensis polysaccharide-functionalized selenium nanoparticles for effective alleviation of ulcerative colitis. *Int. J. Biol. Macromol.* **2023**, *253*, 127570. [CrossRef] [PubMed]
63. Chen, Y.; Luo, C.; Li, S.; Liu, X.; Guo, Y.; Li, Y.; Wang, Y.; Yuan, J. Selenium nanoparticles promotes intestinal development in broilers by inhibiting intestinal inflammation and NLRP3 signaling pathway compared with other selenium sources. *Poult. Sci.* **2024**, *103*, 103958. [CrossRef] [PubMed]
64. Gao, X.; Zhang, Z.; Xing, H.; Yu, J.; Zhang, N.; Xu, S. Selenium Deficiency-Induced Inflammation and Increased Expression of Regulating Inflammatory Cytokines in the Chicken Gastrointestinal Tract. *Biol. Trace Elem. Res.* **2016**, *173*, 210–218. [CrossRef] [PubMed]
65. Lei, L.; Jing, M.; Yingce, Z.; Pei, Z.; Yun, L. Selenium deficiency causes oxidative stress and activates inflammation, apoptosis, and necroptosis in the intestine of weaned calves. *Metallomics* **2023**, *15*, mfad028. [CrossRef]
66. Barrett, C.W.; Singh, K.; Motley, A.K.; Lintel, M.K.; Matafonova, E.; Bradley, A.M.; Ning, W.; Poindexter, S.V.; Parang, B.; Reddy, V.K.; et al. Dietary selenium deficiency exacerbates DSS-induced epithelial injury and AOM/DSS-induced tumorigenesis. *PLoS ONE* **2013**, *8*, e67845. [CrossRef] [PubMed]

67. He, Y.; Peng, L.; Zhao, X.; Fan, X.; Tang, X.; Shi, G.; Li, S. Selenium Deficiency Induces Inflammatory Response and Decreased Antimicrobial Peptide Expression in Chicken Jejunum Through Oxidative Stress. *Biol. Trace Elem. Res.* **2023**, *201*, 3461–3473. [CrossRef]
68. Wang, G.; Jiang, Z.; Song, Y.; Xing, Y.; He, S.; Boomi, P. Gut microbiota contribution to selenium deficiency-induced gut-liver inflammation. *BioFactors* **2024**, *50*, 311–325. [CrossRef]
69. Speckmann, B.; Steinbrenner, H. Selenium and selenoproteins in inflammatory bowel diseases and experimental colitis. *Inflamm. Bowel Dis.* **2014**, *20*, 1110–1119. [CrossRef]
70. Bulteau, A.-L.; Chavatte, L. Update on selenoprotein biosynthesis. *Antioxid. Redox Signal.* **2015**, *23*, 775–794. [CrossRef]
71. Labunskyy, V.M.; Hatfield, D.L.; Gladyshev, V.N. Selenoproteins: Molecular pathways and physiological roles. *Physiol. Rev.* **2014**, *94*, 739–777. [CrossRef]
72. Kryukov, G.V.; Castellano, S.; Novoselov, S.V.; Lobanov, A.V.; Zehtab, O.; Guigó, R.; Gladyshev, V.N. Characterization of mammalian selenoproteomes. *Science* **2003**, *300*, 1439–1443. [CrossRef] [PubMed]
73. Prabhu, K.S.; Lei, X.G. Selenium. *Adv. Nutr.* **2016**, *7*, 415–417. [CrossRef]
74. Wickramasuriya, S.S.; Park, I.; Lee, Y.; Lillehoj, H.S. Effect of Dietary Organic Selenium on Growth Performance, Gut Health, and Coccidiosis Response in Broiler Chickens. *Animals* **2023**, *13*, 1560. [CrossRef]
75. Sunde, R.A.; Raines, A.M. Selenium regulation of the selenoprotein and nonselenoprotein transcriptomes in rodents. *Adv. Nutr.* **2011**, *2*, 138–150. [CrossRef]
76. Long, C.; Zhu, G.Y.; Sheng, X.H.; Xing, K.; Venema, K.; Wang, X.G.; Xiao, L.F.; Guo, Y.; Ni, H.M.; Zhu, N.H.; et al. Dietary supplementation with selenomethionine enhances antioxidant capacity and selenoprotein gene expression in layer breeder roosters. *Poult. Sci.* **2022**, *101*, 102113. [CrossRef] [PubMed]
77. Sun, H.; Zhao, L.; Xu, Z.J.; De Marco, M.; Briens, M.; Yan, X.H.; Sun, L.H. Hydroxy-Selenomethionine Improves the Selenium Status and Helps to Maintain Broiler Performances under a High Stocking Density and Heat Stress Conditions through a Better Redox and Immune Response. *Antioxidants* **2021**, *10*, 1542. [CrossRef]
78. Pardechi, A.; Tabeidian, S.A.; Habibian, M. Comparative assessment of sodium selenite, selenised yeast and nanosized elemental selenium on performance response, immunity and antioxidative function of broiler chickens. *Ital. J. Anim. Sci.* **2020**, *19*, 1108–1121. [CrossRef]
79. Kipp, A.; Banning, A.; van Schothorst, E.M.; Méplan, C.; Schomburg, L.; Evelo, C.; Coort, S.; Gaj, S.; Keijer, J.; Hesketh, J.; et al. Four selenoproteins, protein biosynthesis, and Wnt signalling are particularly sensitive to limited selenium intake in mouse colon. *Mol. Nutr. Food Res.* **2009**, *53*, 1561–1572. [CrossRef] [PubMed]
80. Malyar, R.M.; Li, H.; Liu, D.; Abdulrahim, Y.; Farid, R.A.; Gan, F.; Ali, W.; Enayatullah, H.; Banuree, S.A.H.; Huang, K.; et al. Selenium/Zinc-Enriched probiotics improve serum enzyme activity, antioxidant ability, inflammatory factors and related gene expression of Wistar rats inflated under heat stress. *Life Sci.* **2020**, *248*, 117464. [CrossRef]
81. Guevara Agudelo, F.A.; Leblanc, N.; Bourdeau-Julien, I.; St-Arnaud, G.; Lacroix, S.; Martin, C.; Flamand, N.; Veilleux, A.; Di Marzo, V.; Raymond, F. Impact of selenium on the intestinal microbiome-eCBome axis in the context of diet-related metabolic health in mice. *Front. Immunol.* **2022**, *13*, 1028412. [CrossRef]
82. Schomburg, L.; Schweizer, U. Hierarchical regulation of selenoprotein expression and sex-specific effects of selenium. *Biochim. et Biophys. Acta* **2009**, *1790*, 1453–1462. [CrossRef]
83. Carlson, B.A.; Xu, X.M.; Gladyshev, V.N.; Hatfield, D.L. Selective rescue of selenoprotein expression in mice lacking a highly specialized methyl group in selenocysteine tRNA. *J. Biol. Chem.* **2005**, *280*, 5542–5548. [CrossRef]
84. Gan, F.; Ren, F.; Chen, X.; Lv, C.; Pan, C.; Ye, G.; Shi, J.; Shi, X.; Zhou, H.; Shituleni, S.A.; et al. Effects of selenium-enriched probiotics on heat shock protein mRNA levels in piglet under heat stress conditions. *J. Agric. Food Chem.* **2013**, *61*, 2385–2391. [CrossRef]
85. Gan, F.; Chen, X.; Liao, S.F.; Lv, C.; Ren, F.; Ye, G.; Pan, C.; Huang, D.; Shi, J.; Shi, X.; et al. Selenium-enriched probiotics improve antioxidant status, immune function, and selenoprotein gene expression of piglets raised under high ambient temperature. *J. Agric. Food Chem.* **2014**, *62*, 4502–4508. [CrossRef] [PubMed]
86. Maseko, T.; Dunshea, F.R.; Howell, K.; Cho, H.J.; Rivera, L.R.; Furness, J.B.; Ng, K. Selenium-enriched Agaricus bisporus mushroom protects against increase in gut permeability ex vivo and up-regulates glutathione peroxidase 1 and 2 in hyperthermally-induced oxidative stress in rats. *Nutrients* **2014**, *6*, 2478–2492. [CrossRef] [PubMed]
87. Ye, R.; Guo, Q.; Huang, J.; Wang, Z.; Chen, Y.; Dong, Y. Eucommia ulmoides polysaccharide modified nano-selenium effectively alleviated DSS-induced colitis through enhancing intestinal mucosal barrier function and antioxidant capacity. *J. Nanobiotechnol.* **2023**, *21*, 222. [CrossRef] [PubMed]
88. Hosnedlova, B.; Kepinska, M.; Skalickova, S.; Fernandez, C.; Ruttkay-Nedecky, B.; Peng, Q.; Baron, M.; Melcova, M.; Opatrilova, R.; Zidkova, J.; et al. Nano-selenium and its nanomedicine applications: A critical review. *Int. J. Nanomed.* **2018**, *13*, 2107–2128. [CrossRef]

89. Te Velde, A.A.; Pronk, I.; de Kort, F.; Stokkers, P.C. Glutathione peroxidase 2 and aquaporin 8 as new markers for colonic inflammation in experimental colitis and inflammatory bowel diseases: An important role for H_2O_2? *Eur. J. Gastroenterol. Hepatol.* **2008**, *20*, 555–560. [CrossRef]
90. Sherif, A.H.; Zommara, M.A. Selenium Nanoparticles Ameliorate Adverse Impacts of Aflatoxin in Nile Tilapia with Special Reference to Streptococcus agalactiae Infection. *Biol. Trace Elem. Res.* **2024**, *202*, 4767–4777. [CrossRef]
91. He, Y.; Liu, Y.; Tang, J.; Jia, G.; Liu, G.; Tian, G.; Chen, X.; Cai, J.; Kang, B.; Zhao, H. Selenium exerts protective effects against heat stress-induced barrier disruption and inflammation response in jejunum of growing pigs. *J. Sci. Food Agric.* **2022**, *102*, 496–504. [CrossRef]
92. Hrdina, J.; Banning, A.; Kipp, A.; Loh, G.; Blaut, M.; Brigelius-Flohé, R. The gastrointestinal microbiota affects the selenium status and selenoprotein expression in mice. *J. Nutr. Biochem.* **2009**, *20*, 638–648. [CrossRef]
93. Kasaikina, M.V.; Kravtsova, M.A.; Lee, B.C.; Seravalli, J.; Peterson, D.A.; Walter, J.; Legge, R.; Benson, A.K.; Hatfield, D.L.; Gladyshev, V.N. Dietary selenium affects host selenoproteome expression by influencing the gut microbiota. *FASEB J.* **2011**, *25*, 2492–2499. [CrossRef]
94. Miao, L.P.; Zhou, M.Y.; Zhang, X.Y.; Yuan, C.; Dong, X.Y.; Zou, X.T. Effect of excess dietary fluoride on laying performance and antioxidant capacity of laying hens. *Poult. Sci.* **2017**, *96*, 2200–2205. [CrossRef]
95. Huang, D.; Ou, B.; Prior, R.L. The chemistry behind antioxidant capacity assays. *J. Agric. Food Chem.* **2005**, *53*, 1841–1856. [CrossRef]
96. Han, B.; Yoon, S.; Su, J.; Han, H.; Wang, M.; Qu, W.; Zhong, D. Effects of selenium, copper and magnesium on antioxidant enzymes and lipid peroxidation in bovine fluorosis. *Asian-Australas. J. Anim. Sci.* **2004**, *17*, 1695–1699. [CrossRef]
97. Unsal, V.; Dalkıran, T.; Çiçek, M.; Kölükçü, E. The Role of Natural Antioxidants Against Reactive Oxygen Species Produced by Cadmium Toxicity: A Review. *Adv. Pharm. Bull.* **2020**, *10*, 184–202. [CrossRef]
98. Li, J.L.; Zhang, L.; Yang, Z.Y.; Zhang, Z.Y.; Jiang, Y.; Gao, F.; Zhou, G.H. Effects of Different Selenium Sources on Growth Performance, Antioxidant Capacity and Meat Quality of Local Chinese Subei Chickens. *Biol. Trace Elem. Res.* **2018**, *181*, 340–346. [CrossRef]
99. Birben, E.; Sahiner, U.M.; Sackesen, C.; Erzurum, S.; Kalayci, O. Oxidative stress and antioxidant defense. *World Allergy Organ J.* **2012**, *5*, 9–19. [CrossRef]
100. Xiao, J.; Cao, H.; Guo, S.; Xiao, S.; Li, N.; Li, M.; Wu, Y.; Liu, H. Long-term administration of low-dose selenium nanoparticles with different sizes aggravated atherosclerotic lesions and exhibited toxicity in apolipoprotein E-deficient mice. *Chem. Biol. Interact.* **2021**, *347*, 109601. [CrossRef]
101. Bano, I.; Skalickova, S.; Arbab, S.; Urbankova, L.; Horky, P. Toxicological effects of nanoselenium in animals. *J. Anim. Sci. Biotechnol.* **2022**, *13*, 72. [CrossRef]
102. Fernandes, A.P.; Gandin, V. Selenium compounds as therapeutic agents in cancer. *Biochim. et Biophys. Acta* **2015**, *1850*, 1642–1660. [CrossRef] [PubMed]
103. Zhang, J.; Wang, H.; Yan, X.; Zhang, L. Comparison of short-term toxicity between Nano-Se and selenite in mice. *Life Sci.* **2005**, *76*, 1099–1109. [CrossRef]
104. Deng, S.; Hu, S.; Xue, J.; Yang, K.; Zhuo, R.; Xiao, Y.; Fang, R. Productive Performance, Serum Antioxidant Status, Tissue Selenium Deposition, and Gut Health Analysis of Broiler Chickens Supplemented with Selenium and Probiotics-A Pilot Study. *Animals* **2022**, *12*, 1086. [CrossRef] [PubMed]
105. Zhou, W.; Miao, S.; Zhu, M.; Dong, X.; Zou, X. Effect of Glycine Nano-Selenium Supplementation on Production Performance, Egg Quality, Serum Biochemistry, Oxidative Status, and the Intestinal Morphology and Absorption of Laying Hens. *Biol. Trace Elem. Res.* **2021**, *199*, 4273–4283. [CrossRef] [PubMed]

Disclaimer/Publisher's Note: The statements, opinions and data contained in all publications are solely those of the individual author(s) and contributor(s) and not of MDPI and/or the editor(s). MDPI and/or the editor(s) disclaim responsibility for any injury to people or property resulting from any ideas, methods, instructions or products referred to in the content.

antioxidants

MDPI

Article

Enhanced Anti-Inflammatory Effects of Rosemary (*Salvia rosmarinus*) Extracts Modified with *Pseudomonas shirazensis* Nanoparticles

Enrique Gutierrez-Albanchez [1], Elena Fuente-González [1], Svitlana Plokhovska [1,2], Francisco Javier Gutierrez-Mañero [1] and Beatriz Ramos-Solano [1,*]

[1] Faculty of Pharmacy, Universidad San Pablo-CEU Universities, 28040 Madrid, Spain; enrique.gutierrezalbanchez@ceu.es (E.G.-A.); e.fuente@usp.ceu.es (E.F.-G.); svetaplohovska@gmail.com (S.P.); jgutierrez.fcex@ceu.es (F.J.G.-M.)
[2] Institute of Food Biotechnology and Genomics, NAS of Ukraine, 01112 Kyiv, Ukraine
* Correspondence: bramsol@ceu.es

Abstract

Rosemary (*Salvia rosmarinus*) is renowned for its antioxidant, anti-inflammatory, and anti-hyperglycemic properties, largely attributed to its rich phytochemical profile. This study evaluates the potential of metabolites from *Pseudomonas shirazensis* NFV3, formulated in silver nanoparticles (AgNPs), to enhance the bioactivity of rosemary extracts in postharvest applications. Rosemary stems were treated with AgNPs coated with bacterial metabolites (NP), bacterial cells, or metabolites (LM), and the extracts' phytochemical composition and bioactivities were assessed. HPLC and HPLC–MS analyses revealed that the NP treatment induced significant metabolic remodeling, particularly upregulating rosmarinic acid and selected triterpenes (ursolic and betulinic acids), while reducing carnosic acid levels. NP-treated extracts exhibited significantly enhanced inhibition of cyclooxygenase (COX-1 and COX-2), indicating improved anti-inflammatory potential. The α-glucosidase inhibition and antioxidant activity (DPPH assay) of the extracts were not substantially altered, suggesting the selective enhancement of pharmacological functions. These findings demonstrate that nanoparticle-based elicitation selectively remodels secondary metabolism in rosemary, improving extract quality and bioactivity. This strategy offers a novel, sustainable tool for optimizing plant-based therapeutics in the phytopharmaceutical industry.

Keywords: *Salvia rosmarinus*; silver nanoparticles; secondary metabolism; beneficial bacteria

1. Introduction

Salvia rosmarinus (syn. *Rosmarinus officinals* L.) [1], commonly known as rosemary, is a perennial, aromatic shrub, belonging to the *Lamiaceae* family, and native to the Mediterranean region. Traditionally cultivated for both culinary and medicinal purposes, rosemary has been integrated into the daily lives of Mediterranean populations for centuries. Its historical applications span a variety of ailments, including digestive complaints, headaches, muscle pain, and memory enhancement, reflecting its broad therapeutic reputation in folk medicine [2,3]. The growing demand for natural, plant-based therapeutics has propelled rosemary extract-based products to the forefront of the nutraceutical and functional food markets. The global rosemary extract market was valued at approximately USD 260 million in 2024 and is projected to reach USD 377 million by 2032, with a compound annual growth rate (CAGR) of 5.9% [4]. This expansion is fueled by consumer preferences for clean-label,

natural ingredients and the recognition of rosemary's antioxidant and anti-inflammatory benefits across food, pharmaceutical, and personal care sectors.

The phytochemical richness of rosemary is central to its pharmacological potential. Its leaves are abundant in polyphenols, flavonoids, and terpenoids, with the presence of the phenolic diterpenes, carnosic acid and carnosol, standing out, as well as rosmarinic acid. These compounds are recognized for their potent antioxidant and anti-inflammatory properties, which are believed to underlie many of rosemary's health-promoting effects [5–7]. In addition, rosemary contains other bioactive constituents, such as triterpenes (e.g., ursolic acid, betulinic acid), phenolic acids, and volatile terpenoids (e.g., 1,8-cineole, α-pinene), which are major components of its essential oil fraction, further contributing to its therapeutic versatility [8]. Rosemary's role in the Mediterranean diet is not only culinary, but also therapeutic, as its regular consumption has been associated with reduced risk of chronic diseases that are prevalent in Mediterranean populations [9,10]. Pharmacological surveys have documented its use for metabolic, inflammatory, and neurocognitive disorders, supporting the scientific investigation of the traditional health claims related to its use [11,12].

Contemporary research has elucidated several mechanisms underlying the health-promoting properties of rosemary extracts, with particular emphasis on their anti-inflammatory, antihyperglycemic, and antioxidant effects. The anti-inflammatory activity of rosemary is primarily attributed to the modulation of key molecular pathways, including the inhibition of nuclear factor kappa B (NF-κB) activation, the downregulation of pro-inflammatory cytokines (e.g., TNF-α, IL-1β, IL-6), and the suppression of cyclooxygenase-2 (COX-2) and inducible nitric oxide synthase (iNOS) expression [5,13]. Notably, both carnosic acid and carnosol have demonstrated the capacity to attenuate inflammatory responses in vitro and in vivo, with evidence suggesting that whole rosemary extracts may exert synergistic effects beyond those of isolated compounds [7,14].

The antihyperglycemic properties of rosemary have been substantiated in several preclinical models of type 2 diabetes mellitus, wherein the administration of rosemary extracts or their polyphenolic constituents resulted in significant reductions in fasting plasma glucose, improved lipid profiles, and enhanced antioxidant defense systems. Mechanistically, these effects are linked to the inhibition of intestinal glucosidase enzymes, the enhancement of insulin sensitivity, and the upregulation of endogenous antioxidant enzymes [6,10]. Recent human studies, though limited, have indicated that rosemary tea consumption can lead to significant improvements in glycemic control among individuals with type 2 diabetes, supporting its potential use as a complementary metabolic regulator [9].

Rosemary's antioxidant capacity is largely ascribed to its high content of phenolic diterpenes and polyphenols, which act as free radical scavengers, metal ion chelators, and modulators of redox-sensitive signaling pathways, such as Nrf2 [15]. In vitro and in vivo studies have consistently demonstrated that rosemary extracts can inhibit lipid peroxidation, reduce oxidative stress markers, and enhance the activity of endogenous antioxidant enzymes, such as superoxide dismutase (SOD) and glutathione peroxidase (GPx) [5,10,16]. These findings have prompted the widespread application of rosemary extracts as natural antioxidants in the food industry and as potential therapeutic agents for oxidative stress-related disorders.

These pharmacologically active molecules are the plant's secondary metabolites, whose role is to aid the plant's adaptation to changing environmental conditions, and, therefore, they are inducible. Among the strategies to trigger plant secondary metabolism, beneficial bacterial strains and their metabolites have been used successfully [17,18]. Recent advances in nanotechnology have opened up new avenues for enhancing plant metabolism by formulating bacterial metabolites in nanoparticles, i.e., the metabolites are used as biore-

ductants of the metals, generating a nanoparticle coated with bacterial metabolites that have biological activity [19]. The biological synthesis of nanoparticles using bacterial metabolites or plant extracts (green synthesis) offers several advantages, including biocompatibility, reduced toxicity, and environmental sustainability, aligning with the growing demand for natural and safe therapeutic products [20,21]. A specific type of nanoparticles obtained by green synthesis was found to improve key phytochemical contents of rosemary, potentially amplifying their anti-inflammatory, antihyperglycemic, and antioxidant effects [22,23]. Bacterial metabolites act as reducing and capping agents during the synthesis of metallic or polymeric nanoparticles, enabling the development of hybrid systems that harness both the therapeutic potential of rosemary and the functional benefits of nanotechnology [24]. Preliminary in vitro and in vivo studies indicate that bacterial metabolite-loaded nanoparticles exhibit enhanced cellular uptake, with a consequent higher level of phytochemical modulation of the plant extract [20,23]. Unlike previous studies employing either silver nanoparticles or generic bacterial metabolites, this work uniquely demonstrates the selective remodeling of rosemary's secondary metabolism through the postharvest application of AgNPs coated with metabolites from *Pseudomonas shirazensis*, a strain not previously reported as being used for this purpose.

Among the beneficial strains, the genus *Pseudomonas* has a number of strains that are able to trigger plant metabolism [25]. Strain *Pseudomonas shirazensis* NFV3 has shown potential to stimulate the plant immune system [18], so we reasoned that it could stimulate rosemary metabolism, increasing the phytochemical concentration and, therefore, its antioxidant potential and health benefits. To reach this objective, the strain, its metabolites, and a formulation of these metabolites in silver nanoparticles were delivered to rosemary stems and, after metabolomic characterization, its ability to inhibit alfa-glucosidase, as an indicator of antihyperglycemic activity, and COX-1 and 2, as indicators of anti-inflammatory potential, were evaluated.

2. Materials and Methods

2.1. Biological Synthesis of Nanoparticles

Silver nanoparticles (AgNPs) were synthesized following the protocol described by Plokhovska [24]. Briefly, a 24 h culture of *Pseudomonas shirazensis* NFV3 (CECT 31128) was centrifuged on a (AFI LISA MultiLab Centrifuge, France), and the supernatant was filtered through a 0.25 μm membrane (VWR International, Radnor, PA, USA) to remove bacterial cells. The resulting filtrate was mixed with 1 mM $AgNO_3$ at a ratio of 2:4 (*v*/*v*) and incubated at 37 °C for 24 h. The synthesized AgNPs were characterized by UV–Vis spectroscopy (λ = 430 nm) on a SPECTROstar Nano spectrometer (BMG LABTECH, Ortenberg, Germany) and transmission electron microscopy (TEM a Thermo Fisher Scientific Prisma E and xT Microscope Control v16.2.2 software), revealing the occurrence of spherical nanoparticles with an average diameter of 20.71 ± 0.43 nm and an organic corona composed of bacterial metabolites. The AgNPs were lyophilized and resuspended in Milli-Q water to a stock concentration of 6000 μg/mL; a working solution of 60 μg/mL was prepared for the experiments (NP). The bacterial filtrate (ML) and corresponding cells were also used as treatments (LM, cells, respectively).

The datasets generated and/or analyzed during the current study are available from the Zenodo repository (https://doi.org/10.5281/zenodo.14051744).

2.2. Plant Material and Experimental Setup

A total of twelve (*Salvia rosmarinus*) plants, cultivated under homogeneous conditions, were selected for this study. From each plant, apical stem segments, measuring 15 cm in length, were randomly excised to ensure sample homogeneity.

Four different treatments were prepared, as a follows:

1. Control;
2. Cells (bacterial cells suspended in water);
3. LM (likely a liquid medium containing bacterial metabolites);
4. NP (bacterial metabolite LM formulated in silver nanoparticles).

Each treatment was applied to three independent rosemary branches (n = 3 per treatment). For the application, 5 mL of the corresponding solution was uniformly sprayed over the surface of each branch, using a fine-mist sprayer. An additional set of three untreated branches was collected to serve as the negative control group.

All the branches, treated and untreated, were air dried under controlled laboratory conditions until they reached a constant weight, ensuring complete desiccation.

2.3. Sample Processing and Extraction Procedure

After drying, each rosemary branch (previously treated and used as a replicate) was processed individually. The leaves were carefully separated from the stems and ground using a mortar and pestle in the presence of liquid nitrogen to facilitate sample pulverization.

The extraction protocol using 75% ethanol and overnight maceration was adapted from previous optimization studies involving rosemary [26,27], which demonstrated maximum polyphenol and flavonoid recovery under these conditions. To extract the bioactive compounds, 0.5 g of the powdered material from each replicate was subjected to maceration in 10 mL of 75% ethanol (v/v). The extraction was performed overnight at room temperature (22 °C) in dark conditions to minimize the photodegradation of sensitive metabolites. After maceration, the suspensions were centrifuged at 1100 rpm for 20 min. The supernatant was collected, and the pellet was discarded. This supernatant was then filtered through a 0.2 μm cellulose acetate membrane to remove particulate matter. The resulting filtrate was concentrated using a rotary evaporator (R210-Buchi Labortechnik AG, Flawil, Switzerland). until complete removal of the ethanol–water solvent phase was achieved.

The resulting dry extract was subsequently resuspended in the original volume (10 mL) of 100% ethanol to ensure concentration consistency across the replicates. A final filtration through a 0.2 μm cellulose acetate filter was performed to ensure extract purity. The extracts were stored at −20 °C in amber, airtight glass vials to protect them from light and oxidation until further use.

2.4. Quantification of Active Compounds Using HPLC

The chemical composition of the ethanolic extracts was analyzed using a modified version of the protocol described by Wellwood & Cole [26]. The analysis was carried out using an Agilent 1100 Series HPLC system, equipped with a G1315A diode array detector (DAD). Chromatographic separation was achieved using an Inertsil ODS-3V column (4.6 × 150 mm, 5 μm particle size, 100 Å pore size; GL Sciences, Eindoven, The Netherlands). The mobile phase consisted of the following:

1. Phase A: 840 mL Milli-Q water + 82.5 mL acetic acid + 150 mL acetonitrile;
2. Phase B: 100% methanol.

The gradient started at 90% of mobile phase A, gradually shifting to 0% over 30 min. Following the gradient, the column was re-equilibrated with 90% of mobile phase A for 10 min to ensure reproducibility and retention time stability across the injections. The flow rate was set at 1.5 mL/min, and the column temperature was maintained at 40 °C.

Detection was performed at 284 nm, with a ±30 nm bandwidth, while the full UV absorption spectra were recorded from 200 to 800 nm for each peak to support compound

identification. Active constituents were identified based on the retention times and spectral profiles, compared to authentic standards, and quantified using calibration curves, constructed from standard compounds.

Quantification was based on external calibration curves prepared using authentic standards (rosmarinic acid (Ref.536954), carnosic acid (Ref. PHR2208), and carnosol (Ref. C9617), Sigma Aldrich, Merck KGaA, Darmstadt, Germany). The linearity ($R^2 > 0.995$) of each curve is presented in Supplementary Figure S1.

2.5. Metabolic Profiling Using HPLC–MS Scan Mode

The metabolic profiling of *Salvia rosmarinus* extracts was carried out using high-performance liquid chromatography coupled to mass spectrometry (HPLC–MS). The analyses were conducted at the Structural Molecular Analysis Unit of the SIDI (Interdepartmental Research Service, Autonomous University of Madrid) (https://www.uam.es/uam/sidi/unidades-de-analisis/unidad-analisis-elemental-quimico-isotopico/cromatografia, accessed on 1 May 2025), following the protocol proposed by Sharma et al. [27]. In summary, chromatographic separation was performed using a Bruker UHPLC/MS Triple Quadrupole ELITE system, equipped with an HPG1300 binary pump, automatic degasser, column oven (maintained at 40 °C), and a thermostatted autosampler BR840, set at 4 °C. The mobile phase consisted of solvent A (Milli-Q water with 0.1% formic acid) and solvent B (acetonitrile with 0.1% formic acid), delivered at a constant flow rate of 0.5 mL/min. The following gradient program was applied: 0.00 min, 95% A/5% B; 6.00 min, 85% A/15% B; 21.00 min, 75% A/25% B; 23.00 min, 50% A/50% B; 24.10 min, 0% A/100% B; 28.10 min, 95% A/5% B; ending at 32.00 min with the initial conditions. Mass spectrometric detection was carried out using an ELITE triple quadrupole analyzer, equipped with HESI (Heated Electrospray Ionization) and APCI sources. For the HESI in negative ion mode, the following parameters were set: a spray voltage of 5000 V, a capillary (cone) temperature of 350 °C, a cone gas flow of 40 units, a heated probe temperature of 400 °C, a probe gas flow of 50 units, a nebulizer gas flow of 60 units, and the exhaust gas system was activated. The identification of compounds was conducted according to the respective retention times, as in [27].

2.6. Total Phenolic Content (TPC)

The total phenolic content was determined spectrophotometrically, using a Biomate-5 UV–visible spectrophotometer (a SPECTROstar Nano spectrometer (BMG LABTECH, Germany)). A volume of 50 µL of the previously prepared ethanolic extract was used for each analysis. The Folin–Ciocalteu method, adapted from Benvenuti [28] with slight modifications, was employed. Briefly, Folin–Ciocalteu reagent (Sigma Aldrich, Merck KGaA, Darmstadt, Germany) was added to the extract, followed by sodium carbonate (Na_2CO_3). After 30 min of incubation in the dark at room temperature, the absorbance was measured at 765 nm. The results were expressed as milligrams of gallic acid equivalent per gram of dry extract (mg GAE/g), based on a standard calibration curve of gallic acid.

2.7. Total Flavonol Content (TFC)

The total flavonol content was quantified according to the colorimetric method proposed by Zhishen [29], with modifications. For each sample, 1 mL of the ethanolic extract was reacted with aluminum chloride ($AlCl_3$) and sodium acetate under controlled conditions. Absorbance was measured at 510 nm, and quantification was based on a calibration curve prepared using catechin. The results were expressed as milligrams of catechin equivalent per gram of dry extract (mg CE/g).

2.8. Antioxidant Capacity (AC) Using DPPH Assay

The antioxidant capacity (TAC) of the extracts was assessed using the colorimetric DPPH assay described by Di Sotto [30], with some modifications, using 0.11 mM of DPPH solution and measuring the decrease in absorbance at 517 nm and using gallic acid as a positive control. The assay was performed in duplicate, using three replicates per sample. Gallic acid was used as positive control and the IC_{50} (g/mL) was calculated for each extract.

2.9. Inhibition of α-Glucosidase Activity

The inhibitory activity of the extracts on α-glucosidase was evaluated using a microplate-based assay. The assay utilizes the α-glucosidase enzyme from *Saccharomyces cerevisiae* (Sigma Aldrich, G5003-1KU, Merck KGaA, Darmstadt, Germany) and 4-nitrophenyl α-D-glucopyranoside (PNPG, Sigma Aldrich, N1377-1G, Merck KGaA, Darmstadt, Germany) as the substrate. Phosphate buffer (0.1 M, pH 7.5) was prepared using 0.144 g of KH_2PO_4, 9 g of NaCl, and 0.795 g of $Na_2HPO_4 \cdot 7H_2O$ per liter of distilled water.

Test samples were dissolved in dimethyl sulfoxide (DMSO). The enzyme solution was prepared at a concentration of 0.2 U/mL by dissolving 1 mg of α-glucosidase in 50 mL of Milli-Q water, which was diluted to a final concentration of 0.015 U/mL per well. The PNPG substrate was freshly prepared, with a concentration of 4 mM, and diluted to a final concentration of 1 mM in each well, with a total reaction volume of 200 µL.

All the reagents and equipment were preheated to 37 °C prior to use. In each well of a 96-well microplate, 125 µL of phosphate buffer, 10 µL of sample solution, 15 µL of enzyme solution, and 50 µL of PNPG substrate were added, sequentially. The reaction mixture was incubated at 37 °C, and the formation of p-nitrophenol was monitored by measuring the absorbance at 405 nm every 30 s for 35 min, using a microplate reader. The percentage inhibition of α-glucosidase activity was calculated for each sample concentration using the formula: % Inhibition = (Blank slope − Sample slope)/Blank slope) × 100, where the blank refers to wells without inhibitor. The IC_{50} value was determined from the plot of the sample concentration versus the percentage inhibition. All the measurements were performed in triplicate, and fresh substrate was prepared on the day of the experiment to ensure optimal results.

2.10. Inhibition of Cyclooxygenase Activity (COX)

Cyclooxygenase (COX) activity was assessed using the Cayman Chemical COX Activity Assay Kit (Item No. 760151), following the manufacturer's instructions, with minor adaptations as required. This colorimetric assay quantifies the peroxidase activity by monitoring the oxidation of N, N, N',N'-tetramethyl-p-phenylenediamine (TMPD), which results in a measurable color change at 590 nm.

All the reagents were equilibrated to room temperature before use. The assay was performed using a 96-well plate, with a final volume of 210 µL per well. Each sample was analyzed in triplicate, alongside background and standard controls. For the background determination, 150 µL of each sample was boiled for five minutes, centrifuged, and the supernatant was used as the background control. The plate was set up as follows: COX standard wells received 150 µL of assay buffer, 10 µL of hemin, and 10 µL of COX standard; background wells received 120 µL of assay buffer, 10 µL of Hemin, and 40 µL of boiled sample; sample wells received 120 µL of assay buffer, 10 µL of hemin, and 40 µL of sample; COX-1 or 2 specific inhibition wells received 110 µL of assay buffer, 10 µL of hemin, 40 µL of sample, and 10 µL of either DuP-697 (5-(4-Chlorophenyl)-1-(4-methoxyphenyl)-3-trifluoromethylpyrazole) or SC-560 (5-(4-Chlorophenyl)-1-(4-methoxyphenyl)-3-(trifluoromethyl)-1H-pyrazole). The plate was gently shaken and incubated for five minutes at 25 °C, after which 20 µL of colorimetric

substrate was added to each well. The reaction was initiated by adding 20 µL of arachidonic acid solution, followed by a five-minute incubation at 25 °C. Absorbance was measured at 590 nm, using a microplate reader.

Data analysis involved calculating the average absorbance for each set of replicates and subtracting the background values from the corresponding sample and inhibitor wells. The total COX activity was determined according to the kit's formula, accounting for the requirement of two TMPD (N,N,N′,N′-Tetramethyl-p-phenylenediamine) molecules to reduce PGG2 (Prostaglandin G_2) to PGH2 (Prostaglandin H_2). The percentage inhibition by each inhibitor was calculated to determine the relative proportions of COX-1 and COX-2 activity in the samples.

2.11. Data Processing and Statistical Analysis

All the extractions and quantifications were conducted in triplicate to ensure reproducibility and statistical reliability. Final values were expressed as the mean ± standard deviation (SD) from three independent measurements per treatment. A one-way ANOVA was performed to evaluate the differences among the groups. When the ANOVA indicated statistical significance ($p < 0.05$), Tukey's Honestly Significant Difference (HSD) post hoc test was applied to identify pairwise differences. All the statistical analyses were conducted using the JASP software (version 0.19.3) [JASP Team, University of Amsterdam, Amsterdam, The Netherlands].

3. Results

The quantification of the total phenolic content revealed that all the treatments significantly decreased the total phenols and total flavonols in the rosemary extracts (Figure 1).

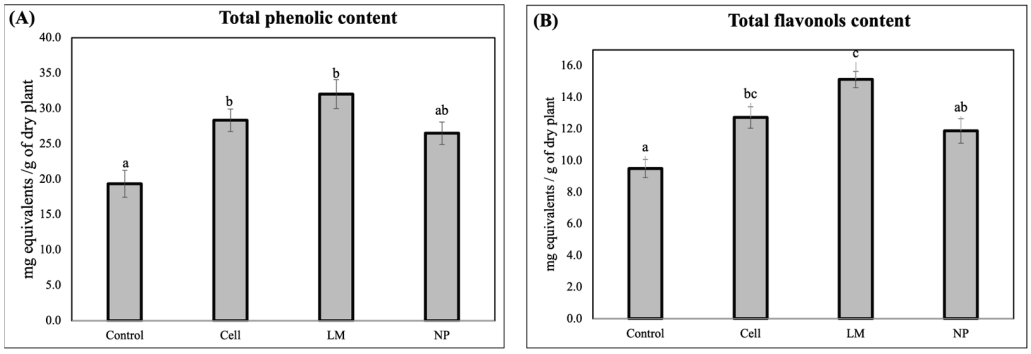


Figure 1. (**A**) Total phenols (mg of gallic acid equivalent per gram of dry extract) and (**B**) total flavonols (mg of catechin equivalent per gram of dry extract). Values correspond to the mean ± SD. Different letters (a, b, c) indicate statistically significant differences among treatments as determined by a one-way ANOVA, followed by Tukey's HSD post hoc test ($p < 0.05$).

The HPLC analysis revealed a significantly lower concentration of the diterpene, carnosol, in the LM and NP, while a significant increase in rosmarinic acid was detected in the NP treatments (Figure 2).

The HPLC–MS analysis in scan mode of the extracts revealed distinct variations in the metabolic profiles, specifically in the relative abundance of secondary metabolites among the control, cell-treated, LM-treated, and NP-treated plant extracts (Table 1) (Figure S2 in the Supplementary Materials). Notably, the NP-treated samples exhibited selective upregulation of several key compounds, particularly within the phenylpropanoid and flavonoid classes. For instance, rosmarinic acid and caffeic acid among the phenylpropanoid class, luteolin derivatives among the flavonoid class, carnosol in the diterpene class, and all of the triterpenes, except for asiatic acid. These changes suggest the targeted ac-

tivation of specific branches of secondary metabolism in response to nanoparticle treatment. Conversely, other compounds such as gallocatechin or syringic acid were downregulated, indicating a possible metabolic reallocation or competitive flux through biosynthetic pathways. The detailed distribution of relative changes in metabolite abundance is summarized in Table 1.

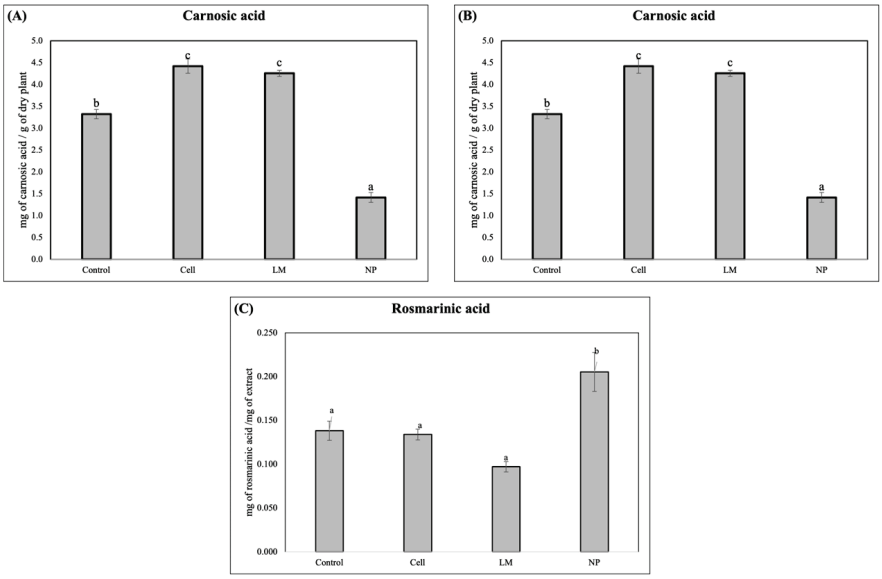


Figure 2. The total content of (**A**) carnosic acid, (**B**) carnosol, and (**C**) rosmarinic acid in rosemary plants after treatment are expressed as mg of active compound per mg of dry extract. Values correspond to the mean ± SD. Different letters (a, b, c) indicate statistically significant differences among treatments as determined by a one-way ANOVA, followed by Tukey's HSD post hoc test ($p < 0.05$).

Table 1. Relative (%) area of the different secondary metabolites identified in HPLC–MS in scan mode for control, cells, LM, and AgNP treatments. Metabolites with relevant increases in relative areas in response to the NP treatment are highlighted in blue.

	Compound	CONTROL	CELLS	LM	NP
S	Rosmarinic acid	7.87	6.69	7.65	10.72
S	Caffeic acid	2.76	3.01	2.83	4.23
S	Quinic acid	9.49	10.88	12.19	9.43
S	Syringic acid	1.19	1.32	1.16	0.77
S	Gallocatechin	12.85	15.10	13.41	5.44
	TOTAL PHENILPROPANOIDS	**34.16**	**36.99**	**37.24**	**30.59**
F	Luteolin	0.37	0.45	0.33	0.38
F	Hesperidin	0.45	0.37	0.32	0.52
F	6-Hydroxyluteolin-7-O-glucoside	0.59	0.59	0.46	0.54
F	Luteolin 7-O-rutinoside	0.32	0.32	0.25	0.33
F	Isorhamnetin-3-O-glucoside	2.92	2.66	2.66	3.64
F	Apigenin-7-O-glucoside	0.18	0.17	0.18	0.16
F	Isorhamnetin-3-O-rutinoside	0.09	0.08	0.08	0.10
F	Diosmin	0.40	0.48	0.41	0.55
F	Hispidulin-7-O-glucoside o Luteolin-7-O-	1.87	1.82	1.88	2.47

Table 1. *Cont.*

	Compound	CONTROL	CELLS	LM	NP
F	Isorhamnetin	0.42	0.56	0.39	0.45
F	Luteolin 3′-acetyl-O-glucuronide II	0.37	0.41	0.31	0.54
F	Diosmetin	0.57	0.78	0.67	0.76
F	Pectolinarigenin	1.57	2.10	1.76	1.55
F	Genkwanin	0.21	0.24	0.12	0.28
	TOTAL FLAVONOIDS	**10.33**	**11.03**	**9.83**	**12.27**
D	**Carnosic acid**	18.73	15.90	15.94	13.53
D	**Rosmanol isomer**	18.45	15.70	17.78	2.87
D	Carnosol	3.22	3.43	2.60	22.38
D	Rosmanol	7.33	8.43	7.94	8.28
D	Rosmadial	1.28	1.98	2.36	1.91
D	12-methoxy-carnosic acid	2.45	2.56	2.86	3.32
	TOTAL DITERPENS	**51.46**	**48.00**	**49.48**	**52.30**
T	Asiatic acid	0.91	0.85	0.62	0.82
T	Corosolic acid	0.94	0.83	0.79	1.04
T	Micromeric acid	0.56	0.61	0.47	0.85
T	Betulinic acid	0.76	0.76	0.62	0.99
T	Ursolic acid	0.89	0.93	0.96	1.15
	TOTAL TRITERPENS	**4.05**	**3.98**	**3.45**	**4.84**

The antioxidant capacity (AC) of the extracts, according to the DPPH Assay, is presented in Table 2. The IC_{50} values (expressed in μg/mL) indicated similar antioxidant activity across most of the treatments when compared to the control, suggesting that the overall free radical scavenging capacity remained largely unaffected. Specifically, the cells and LM extracts exhibited slightly higher IC_{50} values (58.00 and 54.53 μg/mL, respectively), which correspond to a modest reduction in antioxidant potency relative to the control. In contrast, the NP treatment demonstrated an IC_{50} value of 52.64 μg/mL, closely comparable to that of the control (52.81 μg/mL), indicating that the nanoparticle application maintained the antioxidant efficacy. These subtle variations may reflect differences in the qualitative composition of the antioxidant compounds rather than total antioxidant capacity, highlighting the need for further analysis of specific metabolite contributions to the observed activity.

Table 2. IC_{50} values of control, cells, LM, and NP extracts and positive controls in regard to the DPPH antioxidant assay. CL corresponds to confidence limits.

Treatment or Positive Control	IC_{50} (μg/mL)	CL (μg/mL)
Control	52.81	50.10–55.74
Cell	58.00	55.23–61.09
LM	54.53	50.58–58.81
NP	52.64	45.48–54.96
Gallic acid	0.96	8.54×10^{-7}–1.07×10^{-6}
Rosmarinic acid	5.14	5.04×10^{-6}–5.28×10^{-6}

The extracts' potential to inhibit α-glucosidase activity was calculated as the IC_{50} value (Figure 3). The cells and LM extracts increased the IC_{50} value as compared to the controls, therefore achieving worse results than the controls and NPs.

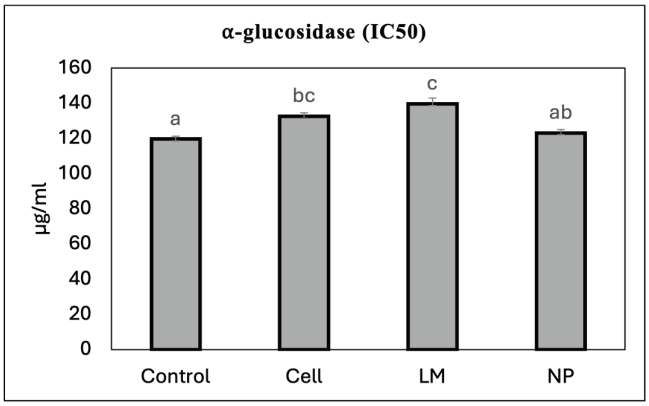


Figure 3. IC_{50} values (µg of extract/mL) for alpha-glucosidase inhibition of *Salvia rosmarinus* extracts. Values correspond to the mean ± SD. Different letters (a, b, c) indicate statistically significant differences among treatments as determined by a one-way ANOVA, followed by Tukey's HSD post hoc test ($p < 0.05$).

The extract's anti-inflammatory potential was evaluated based on the ability to inhibit cyclooxygenase (COX), evaluating COX-1, COX-2, and total COX (Figure 4).

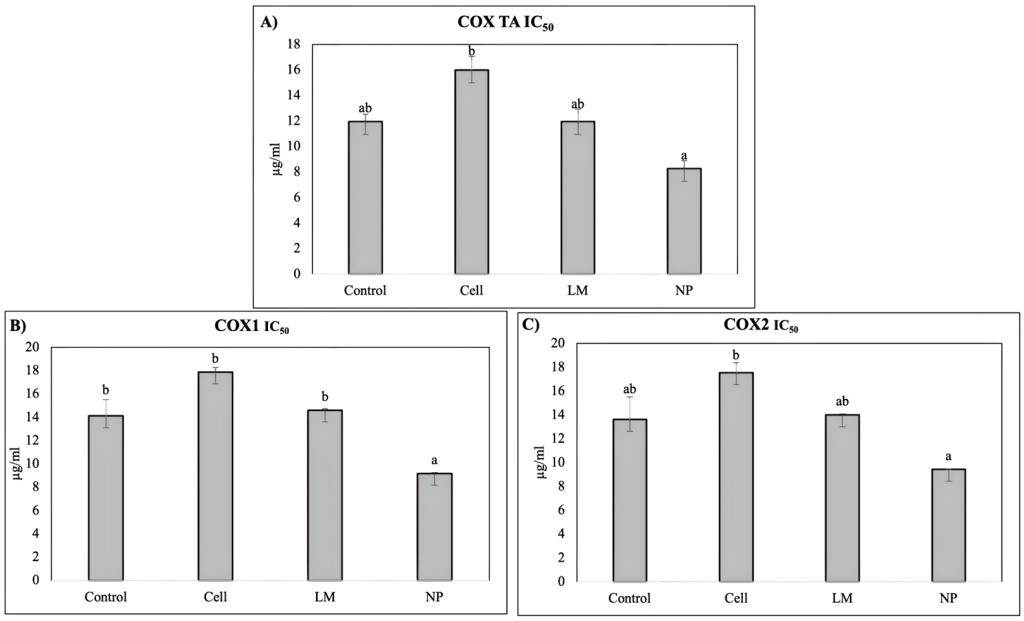


Figure 4. IC_{50} values (µg of extract/mL) for (**A**) total COX; (**B**) COX-1; and (**C**) COX-2 inhibition of *Salvia rosmarinus* extracts. Values correspond to the mean ± SD. Different letters (a, b) indicate statistically significant differences among treatments as determined by a one-way ANOVA, followed by Tukey's HSD post hoc test ($p < 0.05$).

The COX inhibition assays revealed a significant decrease in the IC_{50} values for rosemary extracts derived from NP-treated plants, indicating enhanced inhibitory potency against both cyclooxygenase isoforms, COX-1 and COX-2. This suggests that nanoparticle treatment effectively increased the concentration or bioavailability of active compounds capable of modulating inflammatory pathways. The improved inhibition of COX enzymes highlights the potential of NP-mediated metabolic induction to augment the anti-inflammatory properties of rosemary extracts.

4. Discussion

The ability of AgNPs coated with beneficial bacteria metabolites to trigger *Salvia rosmarinus* metabolism during the postharvest period has been shown to be a valuable biotechnological tool to improve the anti-inflammatory potential of rosemary extracts. AgNPs cause a different response to that of the original strain (cells) or the complex mixture of bacterial metabolites (LM), showing that the effects are attributed to the formulation of metabolites at the nanoscale, which enables deeper penetration and a concomitant more intense response. Despite the fact that the described effects are limited to rosemary in the present study, a wider effect on other plant species is anticipated as Pseudomonas strains are able to trigger many plant species [25]; more precisely, *Pseudomonas shirazensis* NFV3 is able to enhance plant growth and metabolism in different plant species like Arabidopsis [31], as well as tomato [32] and berries [18,25]

The HPLC and HPLC–MS analyses conducted in this study revealed a significant metabolic modification in the samples treated with AgNPs, demonstrated by the increased accumulation of rosmarinic acid and a decrease in carnosol (Figure 2). These metabolites are well-documented for their potent antioxidant and anti-inflammatory properties, contributing substantially to the pharmacological value of *Salvia rosmarinus* extracts [5–7]. The observed modification of these compounds indicates the robust activation of phenylpropanoids and the modification of diterpenoid biosynthetic pathways, which are typically involved in the plant's response to biotic and abiotic stimuli [10,12].

Interestingly, the NP treatment resulted in a markedly lower concentration of carnosol and carnosic acid compared to the control and the other treatments. This suggests the occurrence of a selective modulation or metabolic reallocation triggered by the nanoparticle formulation, potentially involving the differential regulation of key enzymes, such as geranylgeranyl diphosphate reductase or ferruginol synthase, which are crucial in the diterpenoid biosynthetic cascade [33]. Selective metabolic reprogramming in response to nanoparticles has been previously described in species such as *Arabidopsis* thaliana and *Medicago sativa*, wherein metallic and polymeric nanoparticles induced divergent transcriptomic responses and metabolite fluxes depending on the particle size, composition, and surface functionalization [20,21]. Such selective responses may be mediated by a combination of oxidative signaling, hormone crosstalk, and epigenetic reconfiguration, emphasizing the complexity of nanoparticle–plant interactions [24].

The dual effect observed, wherein some branches of the secondary metabolism are enhanced while others are downregulated, underscores the specificity and potential of NP-based elicitation to fine-tune metabolite profiles. This complexity highlights the necessity of integrating omics approaches (transcriptomics, proteomics, and metabolomics) to comprehensively elucidate the molecular mechanisms underpinning such metabolic plasticity [21,23]. Moreover, studies involving nanoparticle uptake, translocation, and subcellular localization would further clarify how these materials influence cellular metabolism at the biochemical level [20].

The HPLC–MS profiling further supported these findings, showing that all the rosemary extracts exhibited a similar profile, and all showed the same composition, despite the profiles from NP-treated plants showing increased relative peak areas compared to the controls (Table 1); interestingly, triterpenes were noticeably increased, specially betulinic and ursolic acid. This broad-spectrum metabolic activation implies that nanoparticle exposure may act as a general elicitor, potentially triggering multiple biosynthetic pathways through stress-induced signaling networks, such as ROS bursts, MAPK cascades, or jasmonate signaling [21,24]. These networks are known to orchestrate the transcriptional reprogramming of specialized metabolism genes, contributing to the activation of complex

metabolite assemblages that confer adaptive advantages to the plant, while simultaneously increasing extract bioactivity [5].

In pharmacological terms, this compositional remodeling translated into functional improvements in terms of anti-inflammatory potential, but not in regard to the hypoglycemic effects. Notably, the COX inhibition assays demonstrated a significant decrease in the IC_{50} values for the extracts derived from NP-treated plants, indicating enhanced inhibitory activity against both COX-1 and COX-2 isoforms. This increased potency correlates with the observed accumulation of specific anti-inflammatory compounds, such as rosmarinic acid, diosmetin, micromeric acid, and carnosol, all of which are known to interfere with eicosanoid synthesis or modulate NF-κB signaling [5,7,14]. This pharmacological enhancement occurred despite the absence of significant differences in the total phenolic content, emphasizing that it is the qualitative remodeling of the bioactive profile, not merely a quantitative increase, that defines extract potency and activity [10,23].

These findings indicate that nanoparticle treatment not only expands the overall metabolite pool, but also specifically modulates the composition and functional direction of the secondary metabolome to enhance its anti-inflammatory potential. This insight is particularly valuable for phytopharmaceutical applications, wherein the therapeutic efficacy of plant extracts often depends on the presence of synergistic combinations of bioactive compounds rather than high concentrations of a single molecule [5,9,34]. In this context, NP-mediated elicitation emerges as a promising tool in the field of plant metabolic engineering, enabling the controlled enhancement of targeted pharmacological properties [21,24].

In contrast to the highly specific metabolic remodeling observed in the NP-treated plants, the total phenolic quantification showed no significant differences between the NP and the control, suggesting that the overall pool of phenolic compounds remained relatively stable. However, both cells and LM treatments led to a statistically significant increase in the total phenolic content, reflecting a broader, non-selective stimulation of phenylpropanoid metabolism [6,12]. This observation indicates that while classical biotechnological tools, such as plant cell cultures or metabolic liquids, can upregulate entire pathways, nanoparticle formulations offer the advantage of selective pathway modulation [21,23].

The marked increase in flavonol content observed in the extracts from the LM-treated plants further supports this differential mode of action. It is plausible that LM contains endogenous or exogenously induced elicitors, such as signaling peptides or microbial metabolites, capable of activating transcription factors (e.g., MYB12, TTG1) involved in flavonoid biosynthesis [20,24] that are not able to reduce silver and, therefore, are not present in the organic crown of NP. Given the central role of flavonoids in oxidative stress protection, UV shielding, and hormone transport, such increases have physiological relevance beyond their pharmacological interest and may improve plant resilience and postharvest extract quality when delivered along the plant cycle [9,10].

Regarding antioxidant activity, the IC_{50} values from the DPPH assays showed only modest variations across the treatments, with the NP extracts exhibiting nearly identical antioxidant potency to the control samples. Although the cells and LM treatments yielded slightly higher IC_{50} values, suggesting marginally lower scavenging capacity, these changes are unlikely to be biologically significant. Rather, they likely reflect qualitative shifts in the antioxidant profile, wherein metabolites with high radical scavenging potential may be replaced by others with lower activity but greater relevance to anti-inflammatory or cytoprotective functions [5,7,10]. This further illustrates that antioxidant capacity is a multifactorial trait that is not governed solely by its phenolic abundance, but by the chemical nature, redox potential, and synergistic interactions of the constituent metabolites.

5. Conclusions

This study demonstrates that formulating *Pseudomonas shirazensis* bacterial metabolites in nanoparticles can effectively modulate the secondary metabolism of *Salvia rosmarinus*, leading to significant alterations in the metabolite composition and pharmacological activity, even when delivered during the postharvest period. Nanoparticle treatments offer a unique advantage by enabling targeted remodeling of metabolite profiles, enhancing specific anti-inflammatory compounds without indiscriminately increasing the total phenolic content. These findings open up new avenues for the application of nanotechnology in regard to phytopharmaceutical optimization and targeted metabolic engineering. Further work integrating transcriptomic and proteomic data, as well as in vivo pharmacological and toxicological assessments, will be essential to fully exploit the therapeutic potential of nanoparticle-enhanced medicinal plant extracts.

In summary, delivering NP to *Salvia rosmarinus* during the postharvest period represents a promising tool to further increase natural bioactives, improving their anti-inflammatory, antihyperglycemic, and antioxidant properties. This tool appears to be an excellent alternative for the plant extracts industry. However, further research is required to overcome current challenges related to standardization, mechanistic elucidation, and clinical efficacy.

6. Patents

A patent application has been filed with reference P202430961, entitled "*Pseudomonas shirazensis* NVF3 y sus metabolitos vehiculizados en nanopartículas de plata como promotores del crecimiento vegetal, estimulantes de la adaptación en situaciones de estrés hídrico y del metabolismo secundario de interés farmacológico y alimentario". The IET+OE has been published and recognizes patentability. It is not public yet.

Supplementary Materials: The following supporting information can be downloaded at: https://www.mdpi.com/article/10.3390/antiox14080931/s1, Figure S1. Supplementary Material. Calibration curves for quantification of phenolic compounds Using HPLC. (A) Rosmarinic acid calibration curve. (B) Carnosic acid calibration curve. (C) Carnosol calibration curve. Figure S2. Supplementary Material. HPLC–MS chromatogram of NP extracts.

Author Contributions: Conceptualization, B.R.-S. and F.J.G.-M.; methodology, E.F.-G. and E.G.-A.; validation, E.G.-A., F.J.G.-M. and B.R.-S.; formal analysis, S.P., E.F.-G. and E.G.-A.; investigation, S.P., E.F.-G. and E.G.-A.; resources, B.R.-S. and F.J.G.-M.; data curation, E.G.-A. and E.F.-G.; writing—original draft preparation, E.G.-A. and E.F.-G.; writing—review and editing, E.G.-A. and B.R.-S.; visualization, F.J.G.-M.; supervision, B.R.-S.; project administration, B.R.-S.; funding acquisition, B.R.-S. and F.J.G.-M. All authors have read and agreed to the published version of the manuscript.

Funding: This research was partially funded by Marie Skłodowska-Curie Actions fellowship (MSCA4Ukraine-project ID:101101923. The APC was funded by the International Seal award of University San Pablo CEU, to B.R-S.

Institutional Review Board Statement: Not applicable.

Informed Consent Statement: Not applicable.

Data Availability Statement: The data that support the findings of this study are stored on the computers at CEU San Pablo University and are available from the corresponding author upon reasonable request.

Acknowledgments: The authors received no specific support or assistance that needs to be declared.

Conflicts of Interest: The authors declare that there are no conflicts of interest.

Abbreviations

The following abbreviations are used in this manuscript:

Cell	*Pseudomonas shirazensis* NFV3 cells suspended in water
LM	Liquid medium containing *Pseudomonas shirazensis* NFV3 metabolites
NP	*Pseudomonas shirazensis* NFV3 metabolites (LM) formulated in silver nanoparticles

References

1. Drew, B.T.; González-Gallegos, J.G.; Xiang, C.L.; Kriebel, R.; Drummond, C.P.; Walked, J.B.; Sytsma, K.J. Salvia united: The greatest good for the greatest number. *Taxon* **2017**, *66*, 133–145. [CrossRef]
2. Begum, A.; Sandhya, S.; Ali, S.S.; Vinod, K.R.; Swapna, R.; Banji, D. An in-depth review on the medicinal flora *Salvia rosmarinus* (*Lamiaceae*). *Acta Sci. Pol. Technol. Aliment.* **2013**, *12*, 61–73.
3. de Oliveira, J.R.; Camargo, S.E.A.; de Oliveira, L.D. *Salvia rosmarinus* (rosemary): An ancient plant with uses in dentistry and medicine. *Br. J. Pharmacol.* **2019**, *176*, 1137–1150.
4. Rosemary Extract- Global Market Share and Ranking, Overall Sales and Demand Forecast 2025-2031. Available online: https://www.qyresearch.com/reports/3480301/rosemary-extract (accessed on 24 June 2025).
5. Habtemariam, S. Anti-Inflammatory Therapeutic Mechanisms of Natural Products: Insight from Rosemary Diterpenes, Carnosic Acid and Carnosol. *Biomedicines* **2023**, *11*, 545. [CrossRef] [PubMed]
6. Farhadi, F.; Baradaran Rahimi, V.; Mohamadi, N.; Askari, V.R. Effects of rosmarinic acid, carnosic acid, rosmanol, carnosol, and ursolic acid on the pathogenesis of respiratory diseases. *Biofactors* **2023**, *49*, 478–501. [CrossRef] [PubMed]
7. Tavares, W.R.; Seca, A.M.L.; Silva, A.M.S. Diterpenes from rosemary (*Salvia rosmarinus*): Defining their pharmacological activities. *Food Chem. Toxicol.* **2024**, *76*, 90–99.
8. Kurek-Górecka, A.; Górecki, M.; Rzepecka-Stojko, A.; Balwierz, R.; Stojko, J. *Salvia rosmarinus*: A Comprehensive Review of its Phytochemical Profile and Health-Promoting Properties. *Int. J. Pharm. Sci. Drug Res.* **2020**, *11*, 155–162.
9. Efenberger-Szmechtyk, M.; Nowak, A.; Kregiel, D. Rosemary (*Salvia rosmarinus*) as a functional ingredient. *Trends Food Sci. Technol.* **2021**, *61*, 68–82.
10. Noor, S.; Mohammad, T.; Rub, M.A.; Raza, A.; Azum, N.; Yadav, D.K.; Hassan, M.I.; Asiri, A.M. Biomedical features and therapeutic potential of rosmarinic acid. *Arch. Pharm. Res.* **2022**, *45*, 205–228. [CrossRef]
11. Al-Sereiti, M.R.; Abu-Amer, K.M.; Sen, P. Critical review on biological effect and mechanisms of diterpenoids from *Salvia rosmarinus*. *Front. Med. Chem.* **2025**, *3*, 112–130.
12. Rašković, A.; Milanović, I.; Pavlović, N.; Ćebović, T.; Vukmirović, S.; Mikov, M. Antioxidant activity of rosemary (*Salvia rosmarinus*) essential oil and its hepatoprotective potential. *BMC Complement. Altern. Med.* **2014**, *14*, 225. [CrossRef]
13. Wan, S.S.; Li, X.Y.; Liu, S.R.; Tang, S. The function of carnosic acid in lipopolysaccharides-induced hepatic and intestinal inflammation in poultry. *Poult. Sci.* **2024**, *103*, 103415. [CrossRef]
14. Fang, Z.; Lu, M.; Huang, R.; Wang, G.; Yushanjiang, F.; Jiang, X.; Li, J. Carnosol prevents cardiac remodeling and ventricular arrhythmias in pressure overload-induced heart failure mice. *Phytother. Res.* **2024**, *38*, 3763–3781. [CrossRef]
15. Tong, X.P.; Ma, Y.X.; Quan, D.N.; Zhang, L.; Yan, M.; Fan, X.R. Rosemary extracts upregulate Nrf2, Sestrin2, and MRP2 protein level in human hepatoma HepG2 cells. *Evid.-Based Complement. Altern. Med.* **2017**, *2017*, 7359806. [CrossRef]
16. El Kantar, S.; Yassin, A.; Nehmeh, B.; Labaki, L.; Mitri, S.; Aldine, F.N.; Hirko, A.; Caballero, S.; Monck, E.; Garcia-Maruniak, A.; et al. Deciphering the therapeutical potentials of rosmarinic acid. *Sci. Rep.* **2022**, *12*, 15489. [CrossRef]
17. Mehmood, N.; Saeed, M.; Zafarullah, S.; Hyder, S.; Rizvi, Z.F.; Gondal, A.S.; Jamil, N.; Iqbal, R.; Ali, B.; Ercisli, S.; et al. Multifaceted impacts of plant-beneficial *Pseudomonas* spp. in managing various plant diseases and crop yield improvement. *ACS Omega* **2023**, *8*, 22296–22315. [CrossRef] [PubMed]
18. Martin-Rivilla, H.; Garcia-Villaraco, A.; Ramos-Solano, B.; Gutierrez-Manero, F.J.; Lucas, J.A. Metabolic elicitors of *Pseudomonas fluorescens* N21.4 elicit flavonoid metabolism in blackberry fruit. *J. Sci. Food Agric.* **2021**, *101*, 205–214. [CrossRef] [PubMed]
19. Plokhovska, S.; García-Villaraco, A.; Lucas, J.A.; Gutiérrez-Mañero, F.J.; Ramos-Solano, B. *Pseudomonas* sp. N5. 12 Metabolites Formulated in AgNPs Enhance Plant Fitness and Metabolism Without Altering Soil Microbial Communities. *Plants* **2025**, *14*, 1655. [CrossRef] [PubMed]
20. Marslin, G.; Sheeba, C.J.; Franklin, G. Nanoparticles alter secondary metabolism in plants via ROS burst. *Front. Plant Sci.* **2017**, *8*, 832. [CrossRef]
21. Silva, S.; Dias, M.C.; Pinto, D.C.G.A.; Silva, A.M.S. Metabolomics as a Tool to Understand Nano-Plant Interactions: The Case Study of Metal-Based Nanoparticles. *Plants* **2023**, *12*, 491. [CrossRef]
22. Hadi Soltanabad, M.; Bagherieh-Najjar, M.B.; Mianabadi, M. Carnosic Acid Content Increased by Silver Nanoparticle Treatment in Rosemary (*Salvia rosmarinus*). *Appl. Biochem. Biotechnol.* **2020**, *191*, 482–495. [CrossRef] [PubMed]

23. Afrouz, M.; Ahmadi-Nouraldinvand, F.; Elias, S.G.; Alebrahim, M.T.; Tseng, T.M.; Zahedian, H. Green synthesis of spermine coated iron nanoparticles and its effect on biochemical properties of Salvia rosmarinus. *Sci. Rep.* **2023**, *13*, 775. [CrossRef] [PubMed]
24. Plokhovska, S.; García-Villaraco, A.; Lucas, J.A.; Gutierrez-Mañero, F.J.; Ramos-Solano, B. Silver nanoparticles coated with metabolites of *Pseudomonas* sp. N5.12 inhibit bacterial pathogens and fungal phytopathogens. *Sci. Rep.* **2025**, *15*, 1522. [CrossRef] [PubMed]
25. Gutierrez-Albanchez, E.; García-Villaraco, A.; Lucas, J.A.; Horche, I.; Ramos-Solano, B.; Gutierrez-Mañero, F.J. *Pseudomonas palmensis* sp. nov., a novel bacterium isolated from *Nicotiana glauca* microbiome: Draft genome analysis and biological potential for agriculture. *Front. Microbiol.* **2021**, *12*, 672751. [CrossRef]
26. Wellwood, C.R.; Cole, R.A. Relevance of carnosic acid concentrations to the selection of rosemary, *Rosmarinus officinalis* (L.), accessions for optimization of antioxidant yield. *J. Agric. Food Chem.* **2004**, *52*, 6101–6107. [CrossRef]
27. Sharma, Y.; Velamuri, R.; Fagan, J.; Schaefer, J. Full-spectrum analysis of bioactive compounds in rosemary (*Rosmarinus officinalis* L.) as influenced by different extraction methods. *Molecules* **2020**, *25*, 4599. [CrossRef]
28. Benvenuti, S.; Pellati, F.; Melegari, M.; Bertelli, D. Polyphenols, anthocyanins, ascorbic acid, and radical scavenging activity of Rubus, Ribes, and Aronia. *J. Food Sci.* **2004**, *69*, FCT164–FCT169. [CrossRef]
29. Jia, Z.; Tang, M.; Wu, J. The determination of flavonoid contents in mulberry and their scavenging effects on superoxide radicals. *Food Chem.* **1999**, *64*, 555–559. [CrossRef]
30. Di Sotto, A.; Di Giacomo, S.; Amatore, D.; Locatelli, M.; Vitalone, A.; Toniolo, C.; Nencioni, L. A polyphenol rich extract from *Solanum melongena* L. DR2 peel exhibits antioxidant properties and anti-herpes simplex virus type 1 activity in vitro. *Molecules* **2018**, *23*, 2066. [CrossRef]
31. Martin-Rivilla, H.; Garcia-Villaraco, A.; Ramos-Solano, B.; Gutierrez-Mañero, F.J.; Lucas, J.A. Extracts from cultures of *Pseudomonas fluorescens* induce defensive patterns of gene expression and enzyme activity while depressing visible injury and reactive oxygen species in *Arabidopsis thaliana* challenged with pathogenic *Pseudomonas syringae*. *AoB Plants* **2019**, *11*, plz049. [CrossRef]
32. Singh, V.K.; Singh, A.K.; Singh, P.P.; Kumar, A. Interaction of plant growth promoting bacteria with tomato under abiotic stress: A review. *Agric. Ecosyst. Environ.* **2018**, *267*, 129–140. [CrossRef]
33. Xia, J.; Lou, G.; Zhang, L.; Huang, Y.; Yang, J.; Guo, J.; Yang, D. Unveiling the spatial distribution and molecular mechanisms of terpenoid biosynthesis in *Salvia miltiorrhiza* and *S. grandifolia* using multi-omics and DESI–MSI. *Hortic. Res.* **2023**, *10*, uhad109. [CrossRef] [PubMed]
34. González-Vallinas, M.; Reglero, G.; Ramírez de Molina, A. Rosemary (*Salvia rosmarinus*) extract as a potential complementary agent in anticancer therapy. *Nutr. Cancer* **2015**, *67*, 1223–1231. [CrossRef] [PubMed]

Disclaimer/Publisher's Note: The statements, opinions and data contained in all publications are solely those of the individual author(s) and contributor(s) and not of MDPI and/or the editor(s). MDPI and/or the editor(s) disclaim responsibility for any injury to people or property resulting from any ideas, methods, instructions or products referred to in the content.

antioxidants

MDPI

Article

Chitosan Nanoparticle-Mediated Delivery of *Alstonia venenata* R.Br. Root Methanolic Extract: A Promising Strategy for Breast Cancer Therapy in DMBA-Induced Breast Cancer in Sprague Dawley Rats

Aarthi Jeganathan [1,†], Karuppusamy Arunachalam [2,†], Anju Byju [1], Anju Rani George [1], Sradha Sajeev [1], Kavimani Thangasamy [1] and Geetha Natesan [1,*]

[1] Department of Botany, Bharathiar University, Coimbatore 641046, TN, India; aarthij96@gmail.com (A.J.); anjubyju2014@gmail.com (A.B.); anju.rani.nx@gmail.com (A.R.G.); sajeevsradha@gmail.com (S.S.); kavieswari007@gmail.com (K.T.)

[2] Center for Studies in Stem Cells, Cellular Therapy and Toxicological Genetics (CeTroGen), Faculty of Medicine (FAMED), Federal University of Mato Grosso do Sul (UFMS), Campo Grande 79070-900, MS, Brazil; arunachalam04@gmail.com

* Correspondence: ngeethaptc@gmail.com

† These authors contributed equally to this work.

Abstract: *Alstonia venenata* R.Br., a plant native to the Western Ghats, is recognized for its diverse medicinal properties. The plant's extracts, particularly rich in alkaloids and other bioactive compounds, have shown potential anticancer activity. This study investigates the therapeutic potential of chitosan nanoparticles (CNPs) loaded with the root methanolic extract (RME) of *A. venenata* in combating breast cancer induced by dimethylbenz(a)anthracene (DMBA) in female Sprague Dawley rats. The RME-loaded chitosan nanoparticles (RME-EnCNPs) were synthesized and characterized, and their in vivo efficacy was evaluated. Treatment with RME-EnCNPs significantly inhibited tumor progression, which is evidenced by reduced tumor volume, burden, and incidence. Moreover, the nanoparticles demonstrated a sustained release of the active compounds, leading to marked improvements in various biochemical, enzymatic, and histopathological parameters. The study found that both RME and RME-EnCNPs effectively suppressed tumor growth, with RME-EnCNPs showing superior efficacy in modulating tumor progression. Antioxidant assays revealed that treatment with RME-EnCNPs (500 mg/kg) resulted in significant increases in total protein, superoxide dismutase (SOD), catalase, glutathione peroxidase (GPx), and glutathione (GSH) levels, alongside a marked reduction in lipid peroxidation (LPO) ($p < 0.001$). These findings suggest that RME-EnCNPs exert a potent antioxidant effect, mitigating oxidative stress within the tumor microenvironment. The root extract of *A. venenata* and its nanoparticle formulation hold promise as a potential therapeutic agent for breast cancer, warranting further investigation to isolate active bioactive compounds and elucidate their mechanisms of action.

Keywords: *Alstonia venenata*; chitosan nanoparticles; rats; dimethylbenz(a)anthracene; antioxidant activity; anticancer activity

1. Introduction

Cancer, a multifaceted spectrum of diseases, is characterized by the unchecked proliferation of abnormal cells with the potential to spread to different parts of the body—a process known as metastasis. According to the World Health Organization (WHO) in 2022, metastases were identified as the primary cause of cancer-related fatalities, contributing to approximately 10 million deaths in 2020 [1]. Among the various forms of cancer, breast cancer stands out as the most prevalent malignancy in women, exhibiting considerable molecular heterogeneity. In 2022, there were 2.3 million new breast cancer diagnoses in

women worldwide, and 670,000 women died from the disease. Breast cancer is the most prevalent cancer among Indian women, making up 28.2% of all cancer cases in the country [2]. Projections indicate a potential surge to 3.2 million new cases by 2040, underscoring the urgency for comprehensive research and therapeutic interventions [2]. The initiation of breast cancer in laboratory rodents, particularly Sprague Dawley and Wistar rats, often involves exposure to chemical carcinogens like DMBA and N-methyl nitrosourea [3]. Understanding the susceptibility of these rodents to carcinogens provides insights into the complex etiology of breast cancer. The development of chemopreventive medications has been instrumental in interrupting the carcinogenic cascade. These medications employ various mechanisms, including the enhancement of detoxifying enzymes, scavenging reactive oxygen species, and regulating apoptosis [4]. Despite significant therapeutic advancements, the treatments for breast cancer often come with a plethora of reactions that adversely impact the quality of life for patients.

Nanotechnology has recently emerged as a promising frontier in medical science, offering innovative solutions for bio-imaging, nucleic acid delivery, biosensors, and drug delivery. Nanoparticle-based drug delivery systems have garnered attention for their ability to improve pharmacokinetics, precisely target tumor cells, and mitigate drug resistance. Hybrid nanoparticle development has further enhanced the stability and performance of drug delivery systems by amalgamating the distinct features of various nanoparticles [5]. The potential of nanoparticle-based therapy to address multidrug resistance (MDR) in various cancer types, including breast cancer, has become a focal point of ongoing research [6]. The intersection of nanotechnology and medicine has ushered in a new era for cancer treatment, although further research is essential to fully comprehend the intricate dynamics between these two fields. This study seeks to consolidate fundamental concepts, address existing challenges, and outlining prospective research directions related to the utilization of nanocarrier systems in cancer therapy [7].

Chitosan, a derivative of chitin, has gained prominence as a potential material for drug carrier nanoparticles due to its biodegradability, biocompatibility, and low toxicity. The cationic composition of chitosan facilitates enhanced adherence to mucosal surfaces via electrostatic interactions, leading to improved drug absorption into targeted cells. Chitosan nanoparticles, utilizing encapsulation or direct attachment, have proven to be a robust, safe, and non-toxic alternative for drug delivery. Their ability to encapsulate various compounds has opened up avenues for applications in cancer therapy and other industries such as food, agriculture, cosmetics, and pharmaceuticals [8].

Alstonia venenata R.Br. a plant belonging to the Apocynaceae family, has gained prominence in various Indian systems of medicine. With 43 species in the genus Alstonia, *A. scholaris*, *A. boonei*, *A. congensis*, and *A. macrophylla* have demonstrated utility in treating various diseases, owing to their abundance in alkaloids, steroids, triterpenoids, and phenolic compounds [9]. A particular focus is placed on *A. venenata*, a medium-sized shrub endemic to Eastern and Southern India, known for its anti-venom properties. The plant has shown antibacterial efficacy, cytotoxicity against Dalton's lymphoma ascites (DLA) cells, antioxidant properties, and significant anticancer activity against Ehrlich Ascites carcinoma (EAC) cells, depending on the specific extracts utilized [10–12].

Plant-derived secondary metabolites have gained recognition for their potential in cancer treatment, offering natural, eco-friendly alternatives with fewer side effects. These compounds play a crucial role in the development of new anticancer drugs. Natural products, including essential oils and plant extracts, have been explored for their anticancer potential, creating nanoformulations that show preclinical promise. However, translating these findings into clinical applications is hindered by bioavailability challenges [13,14].

Despite the extensive research on natural products and their potential in cancer treatment, there is a notable gap concerning the breast cancer activity of *A. venenata* plant extract. This study seeks to fill that void by evaluating the anticancer potential of *A. venenata* extract loaded with chitosan nanoparticles. This novel approach aims to integrate the strengths of plant-derived compounds and nanotechnology, providing a potential

avenue for more effective and targeted breast cancer treatments. The complex interplay between nanocarriers and natural compounds, including the specific impact of chitosan nanoparticles on the efficacy of *A. venenata* extracts, requires further exploration for a comprehensive understanding of their synergistic potential in cancer therapy.

2. Materials and Methods

2.1. Chemicals

Tripolyphosphate (Cat. No. 7758-29-4, Mumbai, India), glacial acetic acid (Cat. No. 64-19-7, Mumbai, India), Chitosan (Cat. No. 9012-76-4 Mumbai, India), 7,12-dimethylbenz(a)anthracene (Cat No. 68141-56-0, Mumbai, India), ethylenediaminetetraacetic acid (Cat. No. 60-00-4, Mumbai, India), trichloroacetic acid (Cat. No. 76-03-9, Mumbai, India), disodium hydrogen phosphate (Cat. No. 7558-79-4, Mumbai, India), malondialdehyde (Cat. No. 100683-54-3, Mumbai, India), thiobarbituric acid (Cat. No. 504-17-6), magnesium chloride (Cat. No. 7791-18-6, Mumbai, India), sodium fluoride (Cat. No. 7681-49-4, Mumbai, India), hydrazine sulfate (Cat. No. 88491-70-7, Mumbai, India), sodium succinate (Cat. No. 6106-21-4), and potassium ferricyanide (Cat. No. 13746-66-2, Mumbai, India) were purchased from Sigma-Aldrich, Bangalore, India and stored at 4 °C.

2.2. Plant Material

The fresh roots of *A. venenata* were collected from Coonoor (GPS, Coordinates: 11°20′42″ N 76°47′42″ E), Tamil Nadu, India. The plant material was authenticated by the Botanical Survey of India, Coimbatore (voucher specimen No: BSI/SRC/5/23/2019/Tech, 3442). The plant samples were thoroughly washed with water, cut into small pieces, and shade-dried for two weeks. The dried samples were powdered using a Wiley mill and stored at 4 °C. The powdered samples were cold-extracted using methanol in the ratio of 1:10 (*w*/*v*) with an orbital shaker at 180 rpm for 24 h at room temperature. The filtrate was concentrated through evaporation at room temperature (20% of the extract yield) and dissolved in methanol to obtain a working solution of 10 mg/10 mL (*w*/*v*).

2.3. Preparation and Characterization of Root Methanolic Extract-Encapsulated Chitosan Nanoparticles (RME-ENCNPs)

In silico analysis and in vitro anticancer activity (MTT assay) confirmed the anticancer potential of the root methanolic extract (RME). Consequently, this extract was chosen for encapsulation with chitosan nanoparticles (CNPs) and subjected to characterization, as well as anticancer activity evaluation using an in vivo model.

2.3.1. Preparation of Chitosan Nanoparticles (CNPs)

TPP cross-linked nanochitosan was synthesized using the ionic gelation method [15]. Chitosan (low molecular weight, 0.5% *w*/*v*) was dissolved in 0.5% glacial acetic acid, agitated for 30 min, and left overnight at room temperature. The pH of the solution was set to 5.5 with 0.5 M NaOH. Subsequently, 0.5 mL of tripolyphosphate (0.5% TPP) was added dropwise to the above solution until the color changed to milky white, with stirring at 100 rpm. The nanoparticle suspension was then centrifuged at 10,000 rpm for 10 min at 4 °C temperature. The resulting pellet was collected, lyophilized, and stored at room temperature following the method outlined [16].

2.3.2. Preparation of RME-EnCNPS

Chitosan nanoparticles at five different concentrations (100, 200, 300, 400, and 500 µg/mL) were directly dissolved in root methanolic extract (RME-EnCNPs), followed by the gradual addition of TPP dropwise. The mixture was stirred on a magnetic stirrer for 40 min. Subsequently, it was centrifuged at 15,000 rpm for 10 min, and the resulting pellets were collected. The pellets were washed once or twice with deionized water and then dried at room temperature, following the methodology outlined [17].

2.3.3. Entrapment Efficiency

The encapsulation or entrapment efficiency of the nanoparticles was assessed by measuring the concentration of free RME. In a concise procedure, 2 mL of the RME-EnCNPs dispersion was subjected to ultracentrifugation at 15,000 rpm for 30 min. The supernatant obtained was collected and analyzed for RME-EnCNPs using a UV–visible spectrophotometer at a wavelength of 279 nm, as per the method described by Bagyalakshmi and Haritha [18]. All measurements were conducted in triplicate. The percentage of RME entrapped in the CNPs was calculated using the absorbance values, employing the following equation:

$$\text{Mass of initially added drug} - \text{Mass of free drug EE (\%)} = (\text{Mass of initially added drug} \times 100)$$

2.4. In Vitro Drug Release Study

In vitro release profiles of the optimized RME-EnCNPs were generated using the dialysis tube method with a molecular weight cutoff of 12,000–14,000. A known quantity of nanoparticles was dispersed in 2 mL of phosphate-buffered saline (pH 6.8). In addition, the membrane was washed with warm double-distilled water (70 °C) for 1 h and then rinsed thrice with water to eliminate glycerin. Approximately 5 mL of a suspension containing phosphate buffer (pH 6.8) was placed in the dialysis bag, sealed at both ends, and submerged in a beaker containing 100 mL of phosphate buffer (pH 6.8). The sample was stirred at 100 rpm using a magnetic stirrer at room temperature. At specific time intervals (0.5, 1, 1.5, 2, 2.5, and 3 h), a 2 mL aliquot was taken, and absorbance was measured at 450 nm. The spent aliquot was replaced in the dialysis membrane by an equal volume of fresh buffer, as per the method outlined [19].

The concentration of the drug present in the test sample was determined using the following equation, as described in [20]:

$$\text{Concentration of drug released Drug release [\%]} = (\text{Total concentration of drug} \times 100)$$

To theoretically understand the mechanism of RME release from CNPs, the in vitro drug release data were fitted into different mathematical models, including the zero order, first order, Higuchi model, and Korsmeyer–Peppas model [21].

2.4.1. Drug Release Kinetics

The in vitro dissolution test data were fitted into mathematical models representing (i) fero order, (ii) first order, (iii) Higuchi's, and (iv) Korsmeyer–Peppas model.

Equations were used to determine the release mechanism and the order of drug release.

2.4.2. Zero Order Kinetics

The zero order kinetics represent the drug release rate, which is independent from its concentration. The equation translating the zero order kinetics is as follows:

$$Q_t = Q_0 + k_{0t}$$

where Q_t is the quantity of RME or drug dissolved in time t, Q_0 is the initial concentration of the drug in the buffer solution, and K_{0t} is the zero order release constant, which was obtained from the slope of the linear plot of percentage drug release versus time.

2.4.3. First Order Kinetics

The first order kinetics represent the drug release from a system that is concentration-dependent and is expressed as follows:

$$\log C_t = \log C_0 - k_{1t}/2.303$$

where C_t is the concentration of drug released in time t, C_0 is the initial concentration of drug present in the nanoparticles, k_{1t} is the first order constant and it was calculated from the slope of the linear plot of the log values of the cumulative percentage of the drug remaining versus time.

2.4.4. Higuchi Model

The Higuchi model describes drug release from an insoluble matrix as the square root of a time-dependent process based on diffusion. The Higuchi model can be expressed as follows:

$$Q_t = k_H \times t0.5$$

where Q_t is the amount of drug released in time t, and k_H is constant, which was obtained from the slope of the linear plot of percentage drug (RME) release versus square root of time.

2.4.5. Korsmeyer–Peppas Model

The Korsmeyer–Peppas model explains drug release from a polymeric system, and can be expressed as follows:

$$Log_{Qt} = \log_{k} + n \times \log_{t}$$

where k is the kinetic constant and n is the diffusion exponent, a measure of the primary mechanism of drug release. Values of n and k were calculated from the slope and intercept of the linear plot of the log cumulative percentage drug release versus log time.

2.4.6. Correlation Coefficients Analysis (R^2)

R^2 analysis helps to determine the regression between selected items. Intercept and slope give the Y2-Y1/X2-X1 value. The R^2 value of the kinetic models clearly defines the influence of each factor % of drug release, log (cumulative frequency) CF%, and cumulative %.

2.5. Characterization of CNPs and RME-EnCNPs

Chitosan nanoparticles (CNPs) and root methanolic extract-encapsulated chitosan nanoparticles (RME-EnCNPs) were subjected to various spectroscopy characterization studies.

2.5.1. Ultraviolet–Visible Spectroscopy (UV–Vis)

To verify the formation of nanoparticles, the solution was scanned in the range of 200–800 nm in a spectrophotometer using a quartz cuvette with water as the reference.

2.5.2. Fourier Transform Infrared (FTIR) Spectroscopy

Fourier transform infrared spectroscopy (FTIR) is a technique used to obtain the infrared spectrum of absorption, emission, and photoconductivity in solids, liquids, and gasses. It is employed to detect various functional groups in a sample, and the spectrum corresponds to specific rotations around carbon atoms. FTIR analysis is performed to analyze the formation of CNPs and RME-EnCNPs. After preparing samples with KBr in pellet form, the spectra were recorded using FTIR at room temperature. The scan range was 4000 to 400 cm^{-1} at a resolution of 4 cm^{-1} [22].

2.5.3. X-Ray Diffraction

XRD analysis was conducted using a Cu Kα X-ray source (λ = 1.5406 Å). This technique is employed to investigate the crystalline nature of chitosan nanoparticles/encapsulated chitosan nanoparticles and to determine nanoparticle size. The analysis was performed within the scanning 2θ range of 20–80° with a scanning speed of 50 S^{-1}.

2.5.4. Scanning Electron Microscopy (SEM)

The topography of RME-EnCNPs was examined using a Quanta 400 ESEM/EDAX (FEI). Small amounts of vacuum-dried nanochitosan samples were placed on an SEM stub

using double-sided adhesive tape and subjected to sputter coating at 50 mA for 6 min. Subsequently, the stub containing the sample was positioned in the scanning electron microscopy (SEM) chamber, and a photomicrograph was captured at an acceleration voltage of 20 kV.

2.5.5. Zeta Potential

The zeta potential of RME and RME-EnCNPs was analyzed using a laser light scattering-based particle analyzer. The analysis was conducted in triplicate, and average values along with standard deviations were recorded.

2.6. Animals and Experimental Design

For the in vivo experiment, 21-day-old female Sprague Dawley rats weighing 120–140 g were utilized, and they were procured from the National Institute of Nutrition, Hyderabad, India. All the rats were housed at a room temperature of 22 ± 3 °C with a 12 h light/12 h dark cycle in the animal house. Throughout the study, the animals were provided with a commercial pellet diet and had free access to water, adhering to the guidelines of the Committee for the Purpose of Control and Supervision of Experiments on Animals (CPCSEA), New Delhi.

The experiment was conducted following the ethical guidelines and after obtaining clearance from the Institutional Animal Ethics Committee (IAEC) under IAEC No. KMCRET/ReRc/Ph.D/20/2021. The seven animal groups were separated, with each group being assigned eight animals. The animal treatment groups were as follows:

Group I Control rats given only saline (p.o.)
Group II Rats given DMBA only 25 mg/kg (i.p)
Group III Rats treated with DMBA + tamoxifen 10 mg/kg (standard control, p.o.)
Group IV Rats treated with DMBA + RME 250 mg/kg (p.o.)
Group V Rats treated with DMBA + RME 500 mg/kg (p.o.)
Group VI Rats treated with DMBA + RME-EnCNPs 250 mg/kg (p.o.)
Group VII Rats treated with DMBA + RME-EnCNPs 500 mg/kg (p.o.).

After completing the induction and treatment period, the animals were sacrificed and their tissues were collected for the evaluation of the estimation of the tumor parameters, enzymatic antioxidant and non-enzymatic antioxidant activities, glycolytic and non-glycolytic enzymes, estimation of mitochondrial TCA cycle enzymes, and histopathology analysis. The blood samples were used for biochemical analysis.

2.6.1. Acute Toxicity Study

To assess the safety of the plant extracts (RME and RME-EnCNPs), an acute oral toxicity analysis was conducted following the guidelines of the Organization for Economic Co-operation and Development (OECD) for testing chemicals [23]. The analysis received approval from the Institutional Animal Ethics Committee (IAEC). For this experiment, healthy female Sprague Dawley rats weighing between 120 and 140 g were selected and divided into 6 groups, with 3 animals in each group. The rats were housed in plastic cages under a 12 h light and dark period, with room temperature maintained at 22 ± 3 °C and humidity between 40 and 60%, ensuring proper ventilation. Oral doses of 500, 1000, and 2000 mg/kg of RME and RME-EnCNPs were administered to each group. Throughout a 14-day observation period, the animals were monitored for changes in behavior, function, and morphology. Observations included an assessment of toxicological symptoms such as alertness, grooming, touch response, torch response, pain response, tremors, convulsion, righting reflex, gripping strength, pinna reflex, corneal reflex, writhing, pupils, urination, salivation, and skin color [24].

2.6.2. Breast Cancer Induction by Chemical Carcinogen

In this study, 7,12-dimethylbenz(a)anthracene (DMBA) was employed to induce a chemical model of breast cancer in female rats. This model was utilized to investigate the

chemopreventive effects of RME and RME-EnCNPs, exploring their potential in treating and preventing breast cancer. DMBA, an aromatic pollutant, is recognized as a carcinogen capable of inducing cancer in humans and is commonly used to induce mammary gland tumors in rats [25].

Female Sprague Dawley rats, 30 days old and weighing approximately 120 to 140 g, were used for the induction of breast cancer by intra-peritoneal injection of DMBA (25 mg/mL dissolved in olive oil) over a 16-week period. After the development of breast tumors, the rats were treated with RME and RME-EnCNPs at 2 concentrations, 250 and 500 mg/kg body weight, administered orally for a duration of 4 weeks.

2.6.3. Estimation of Body Weight

Body weights were estimated for all the groups of animals at the end of 20 weeks using electrical balance [26].

2.6.4. Animal Sacrifice

At the end of the 20th week of treatment, all the rats were anesthetized with diethyl ether and euthanized by decapitation. The animals were subjected to overnight fasting before the sacrificial procedure. Blood was collected and transferred into tubes containing ethylenediaminetetraacetic acid (EDTA) for hematological parameters, while serum was separated by centrifugation at 3000 rpm for 15 min and stored at -20 °C for biochemical assays. Breast tumors were removed, counted, weighed, and measured using a 1 mm precision caliper. Additionally, the mammary gland, liver, kidney, and uterus were collected and immediately fixed in a 10% formalin solution.

2.6.5. Estimation of Tumor Parameters

The tumor volume was measured using the following formula: Tumor volume (cm^3) = Length $\times$ Weight $\times$ Height $\times$ $\pi/6$. The tumor weight was estimated for all the animal groups [27] using the formula: Tumor weight (g) = Length (cm) $\times$ Width (Cm^2)/2. The tumor burden was measured by the number of tumors formed in each animal [27], calculated using the following formula: Tumor burden (g) = Sum of the total relative tumor mass in a group. The tumor incidence percentage, calculated based on the presence of tumors, was determined by the following formula [27]: Tumor Incidence (%) = (Rat with tumors/Total number of rats) $\times$ 100. These parameters were utilized for the assessment of the effects of the treatments on tumor growth and incidence in accordance with the methodologies described [27].

2.6.6. Biochemical Assessment of Blood

A biochemical analysis of blood measures the amount of chemical substances released by body tissues during the metabolism of specific substances. This analysis provides valuable information about the function of organs such as the liver, kidneys, and others [27].

The separated serum from all seven groups of animals was used for the estimation of various parameters, including protein, bilirubin, serum glutamic oxaloacetic transaminase (SGOT), Serum Glutamic Pyruvic Transaminase (SGPT), alkaline phosphatase (ALP), estrogen hormone, progesterone hormone, total cholesterol, triglycerides, HDL-cholesterol, urea, uric acid, and creatinine. These analyses were performed using a semi-auto analyzer (RIELE Photometer 5010 V5+, RIELE, New Delhi, India), and standard enzymatic kits were procured from Piramal Healthcare Limited, Lab Diagnostic Division, Mumbai, India.

2.6.7. Enzymatic Antioxidant and Non-Enzymatic Antioxidant Activities

Estimation of Protein

The estimation of protein was conducted by using 0.1 mL of the homogenate mixed with 0.9 mL of water. Subsequently, 4.5 mL of the alkaline copper sulfate reagent was added, and the mixture was allowed to stand at room temperature for 10 min. To this solution, 0.5 mL of Folin's reagent was added. After 20 min, the color produced was

measured at 640 nm. The concentration of protein present was expressed as either mg/g tissue or mg/dL, following the methodology outlined [28].

Estimation of Superoxide Dismutase (SOD)

In this assay, 0.5 mL of supernatant tissue homogenate was added to a test tube. To this, 1.5 mL of carbonate buffer (pH 7.5), 0.5 mL of 0.1 mM EDTA, and 0.4 mL of epinephrine were added, and the absorbance reading was taken at 480 nm, following the procedure outlined [29]. The activity of SOD was expressed as units/min/mg protein, where one unit of the enzyme is defined as the amount that inhibits the rate of adrenaline autoxidation by 50%.

Estimation of Catalase

To analyze catalase activity, 1 mL portions of the reaction mixture were withdrawn and transferred to 2 mL of dichromate/acetic reagent at 1 min intervals. The mixture was then incubated for 30 min, and the optical density (OD) was measured at 570 nm. The activity of catalase was expressed as μmoles of H_2O_2 consumed per mg protein, following the method described [30].

Estimation of Glutathione Peroxidase (GPx)

To estimate GPx activity, a reaction mixture consisting of 0.2 mL each of EDTA, sodium azide and H_2O_2, 0.4 mL of phosphate buffer, and 0.1 mL homogenate/mitochondria was incubated at 37 °C at different time intervals. The reaction was halted by adding 0.5 mL of trichloroacetic acid (TCA), and the tubes were then centrifuged at 2000 rpm. To 0.5 mL of the supernatant, 4 mL of disodium hydrogen phosphate and 0.5 mL of DTNB were added, and the developed color was immediately measured at 420 nm. The activity of GPx was expressed as μmoles of glutathione oxidized per mg protein, following the method described [31].

Estimation of Reduced Glutathione (GSH)

The estimation of reduced glutathione (GSH) activity was carried out using 1 mL of the tissue homogenate, which was then treated with 1 mL of trichloroacetic acid (TCA) to precipitate proteins. The precipitate was removed by centrifugation. To 0.5 mL of the supernatant, 2 mL of DTNB was added, and the total volume was adjusted to 3 mL with phosphate buffer. The absorbance was read at 412 nm. The level of glutathione was expressed as μg/mg protein, following the methods outlined [32].

Lipid Peroxidation

In this method, malondialdehyde (MDA) and other thiobarbituric acid reactive substances (TBARS) were estimated by their reactivity with thiobarbituric acid (TBA) under acidic conditions to generate a pink-colored chromophore, which was then measured at 535 nm (pH 7.5). For the assay, 0.1 mL of tissue homogenate in Tris-HCl buffer (pH 7.5) was treated with 2 mL of TBA-HCl-TCA reagent in a 1:1:1 ratio (thiobarbituric acid 0.37%, 0.25 N HCl, and 15% TCA). The mixture was placed in a water bath for 15 min, then cooled. The absorbance of the clear supernatant was measured against a reference blank at 535 nm. The level of lipid peroxides was expressed in moles of MDA formed per mg protein [33].

2.6.8. Glycolytic and Non-Glycolytic Enzymes

The pooled samples from the seven groups of animals were subjected to assays for glycolytic enzymes (hexokinase and aldolase) and non-glycolytic enzymes (glucose 6-phosphate and fructose-1,6-diphosphatase) as described in [34].

Hexokinase

Hexokinase activity was measured based on the amount of glucose utilized after the addition of ATP. The incubation mixture consisted of 2.5 mL Tris-HCl buffer (pH 8.0),

1 mL of glucose, 0.5 mL ATP, 0.1 mL each of $MgCl_2$ and sodium fluoride, and 0.5 mL each of KH_2PO_4 and KCl. This mixture was pre-incubated at 37 °C for 5 min at room temperature. The reaction was initiated by adding 2 mL of glycolytic enzyme. At zero time, 1 mL aliquot of the reaction mixture was removed and added to tubes containing 1 mL of 10% trichloroacetic acid (TCA). After a 30 min incubation, another 1.0 mL aliquot of the reaction mixture was added to a separate set of tubes, and the reaction was stopped by the addition of 1.0 mL of TCA. After the samples were precipitated and centrifuged, the supernatants were used for the estimation of glucose by the ortho-toluidine method at 340 nm. The level of hexokinase was expressed as nmoles of glucose 6-phosphate per min per mg protein, following the method described [35].

Aldolase

For the aldolase assay, the incubation sample contained 0.25 mL of fructose-1,6-diphosphate, 0.25 mL of hydrazine sulfate, 1 mL of Tris-HCl buffer (pH 8.6), and the required amount of preparation to make it to 2 mL. This mixture was incubated at 37 °C for 15 min. The reaction was terminated by the addition of 10% trichloroacetic acid (TCA), and the tubes were centrifuged. An aliquot of the supernatant was transferred to tubes containing 1 mL of 0.75 N NaOH. The tubes were left at room temperature for 10 min. To this, 1 mL of dinitrophenyl hydrazine reagent was added, and the mixture was incubated at 37 °C for 60 min. The color developed after the addition of 7 mL of 0.75 N NaOH and the solution was read using a green filter at 540 nm. A color development curve was prepared with aliquots of a standard DL-glyceraldehyde solution by treating them in a similar manner. The enzyme activity was expressed as nmoles of glyceraldehyde formed per min per mg protein, following the method described [36].

Fructose-1,6-Diphosphatase

The assay medium, in a final volume, contained 1.2 mL of Tris-HCl buffer (pH 7.0), 0.1 mL of fructose-1,6-diphosphatase solution, 0.25 mL of MgCl2, 0.1 mL of KCl solution, 0.25 mL of EDTA solution, and 0.1 mL of enzyme. The incubation was carried out at 35 °C for 15 min, and the reaction was terminated by the addition of 1 mL of trichloroacetic acid (TCA). After centrifugation, the phosphorus content of the supernatant was estimated. The enzyme activity is expressed as nmoles of inorganic phosphate (Pi) liberated per minute per mg protein, following the method described [36].

Glucose-6-Phosphate

Glucose-6-phosphate was assayed according to the method described by King (1965b) [37]. The incubation mixture comprised 0.3 mL of citrate buffer (pH 6.5), 0.5 mL of glucose-6-phosphate, and 0.2 mL of enzyme solution. Incubation was carried out at 37 °C for 60 min. The reaction was terminated by the addition of 1 mL of 10% trichloroacetic acid (TCA) solution. After centrifugation, the phosphorus content in the supernatant was estimated by the method of Fiske and Subbarow [36]. The enzyme activity is expressed as nmoles of inorganic phosphate (Pi) liberated per minute per mg protein.

2.6.9. Assessment of Mitochondrial TCA Cycle Enzyme Activity

Isocitrate Dehydrogenase

The activity of isocitrate dehydrogenase was assayed according to the method outlined by King [37]. To 0.1 mL of Tris-HCl (pH 7.5), 0.2 mL of trisodiumisocitrate, 0.3 mL of manganese chloride, 0.2 mL of mitochondrial suspension, and 0.2 mL of NADP+ (0.2 mL of water for control) were added. After 60 min of incubation, 1 mL of 2,4-Dinitrophenylhydrazine was added followed by 0.5 mL of EDTA, and the mixture was kept at room temperature for 20 min. Then, 10 mL of NaOH was added, and the color developed was read at 390 nm. A standard containing α-ketoglutarate was run simultaneously. The isocitrate dehydrogenase activity was expressed as nmoles of α-ketoglutarate liberated per min per mg protein.

Succinate Dehydroganase

The activity of succinate dehydrogenase (SDH) in the heart mitochondrial fraction was assayed using the method outlined [38]. The reaction mixture contained 1.0 mL of phosphate buffer, 0.1 mL of EDTA, 0.1 mL of sodium cyanide, 0.1 mL of bovine serum albumin, 0.3 mL of sodium succinate, 0.2 mL of potassium ferricyanide, and was made up to 2.8 mL with distilled water. The reaction was initiated by the addition of 0.2 mL of mitochondrial fraction. The change in optical density was recorded at 15 s intervals for 5 min at 420 nm. The succinate dehydrogenase activity was expressed as nmoles of succinate oxidized per minute per mg protein.

Malate Dehydrogenase

The activity of malate dehydrogenase (MDH) in the heart mitochondrial fraction was assayed using the method described [39]. The reaction mixture consisted of 0.75 mL of phosphate buffer, 0.15 mL of reduced nicotinamide adenine dinucleotide (NADH), and 0.75 mL of oxaloacetate. The reaction was carried out at 25 °C and was initiated by the addition of 0.2 mL of mitochondrial fraction. The control tubes contained all reagents except NADH. The change in optical density at 340 nm was measured for 2 min at intervals of 15 s using a Systronics UV–visible spectrophotometer (Systronics, Ahmedabad, India). The enzyme activity was expressed as nmoles of NADH oxidized per minute per mg of total protein under the given incubation conditions.

Quantification of Hematological Parameters

Different hematological parameters were assessed using a Mindray BC-2800 Auto Hematology Analyzer from Shenzhen Mindray Bio-Medical Electronics Co., Ltd. (Shenzhen, China). After the treatment period, the animals were anesthetized with ketamine hydrochloride, and blood was collected from the retro-orbital sinus using a capillary tube into a centrifugation tube containing EDTA for hematological parameters. It was allowed to clot at room temperature, and serum was separated by centrifugation at 10,000 rpm for 10 min and utilized for hematological parameters such as red blood cell (RBC) count, white blood cell (WBC) count, hemoglobin, packed cell volume (PCV), polymorphs, lymphocytes, eosinophils, and mean corpuscular hemoglobin (MCH) [40].

2.6.10. Histopathology Analysis

Small pieces of rat breast tissues were fixed in 10% formalin for 24 h. Subsequently, the tissues underwent dehydration through ethanol, and then they were embedded in paraffin. Sections of 5 μm thickness were cut and stained with hematoxylin and eosin for histopathological investigation under a light microscope [41].

2.6.11. Statistical Analysis

The results were expressed as the mean ± SEM. The results obtained from the present study were analyzed by using one-way ANOVA followed by Dunnett's multiple comparison tests. Data were computed for statistical analysis by using GraphPad Prism version 5.00 for Windows, Graph Pad Software version 8, San Diego, CA, USA, www.graphpad.com (accessed on 15 March 2022) and compared with the vehicle control group. The p values ($p < 0.05$) were considered statistically significant.

3. Results

3.1. The Entrapment Efficiency (EE) of RME-EnCNPs

The entrapment efficiency (EE) of RME-EnCNPs was assessed with three replicates. The impact of different concentrations of RME on EE is presented in Figure 1. Chitosan nanoparticles exhibited an escalating trend in encapsulation effectiveness with the rise in RME concentrations. Among the various RME concentrations tested (100, 200, 300, 400, and 500 μg/mL), the highest entrapment efficiency (81.81%) was observed at 500 μg/mL (Figure 1).

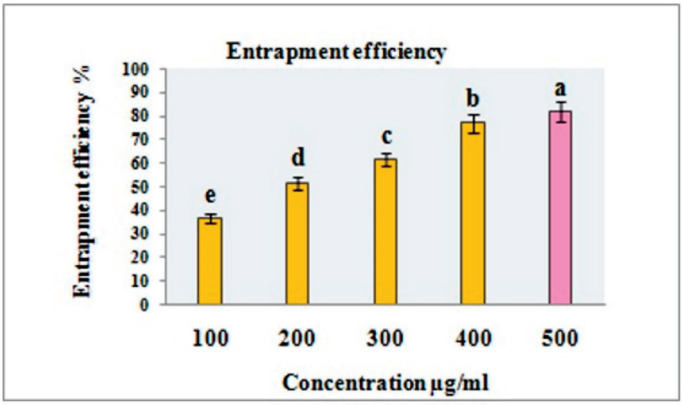


Figure 1. Entrapment efficiency of root methanolic extract-encapsulated chitosan nanoparticles (RME-EnCNPs). Effects a, b, c, d, and e were significant with consideration of probability $p < 0.05$. Values are means ± standard deviation of three replicates.

The in vitro drug release profile of the RME-EnCNPs demonstrated a slow and sustained release, with 50% of the drug being released within 2 h. Subsequently, after 5 h, 87.8% of the drug was released, as illustrated in Figure 2. The initial release observed within the first hours could be attributed to the release of drug molecules from the surface of chitosan nanoparticles. To comprehend the drug release mechanism, RME-EnCNPs underwent analysis using various mathematical models, including zero order, first order, Higuchi, and Korsmeyer–Peppas models.

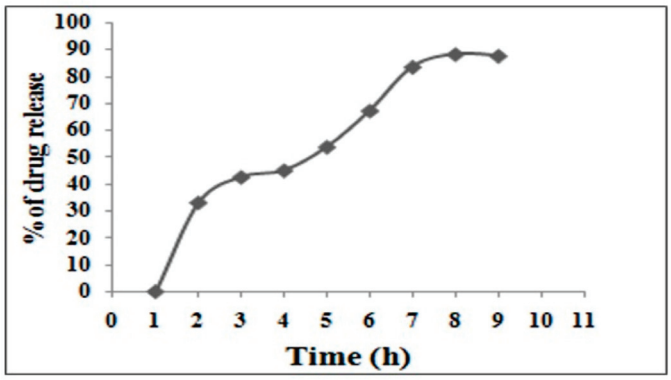


Figure 2. Drug release percentage of RME-EnCNPs.

The correlation coefficient values for these kinetic models are presented in Table 1; they help determine the most appropriate model for the slow and sustained drug release. In this study, the kinetic models of zero order, first order, Higuchi, and Korsmeyer–Peppas displayed good linearity, with R^2 values of 0.966, 0.942, 0.994, and 0.908, respectively. Notably, the Higuchi model exhibited the highest R^2 value of 0.994, confirming its suitability for describing the drug's delivery nature, as depicted in Figure 3.

Table 1. Correlation coefficients of different kinetics models for root methanolic extract-encapsulated chitosan nanoparticles (RME-EnCNPs).

Kinetic Models	Encapsulated Chitosan Nanoparticles		
	R^2	Slope	Intercept
Zero order kinetics	0.966	17.47	24.77
First order kinetics	0.942	0.398	16.47
Higuchi model	0.994	50.306	44.57
Korsmeyer–Peppas model	0.908	8.105	32.10

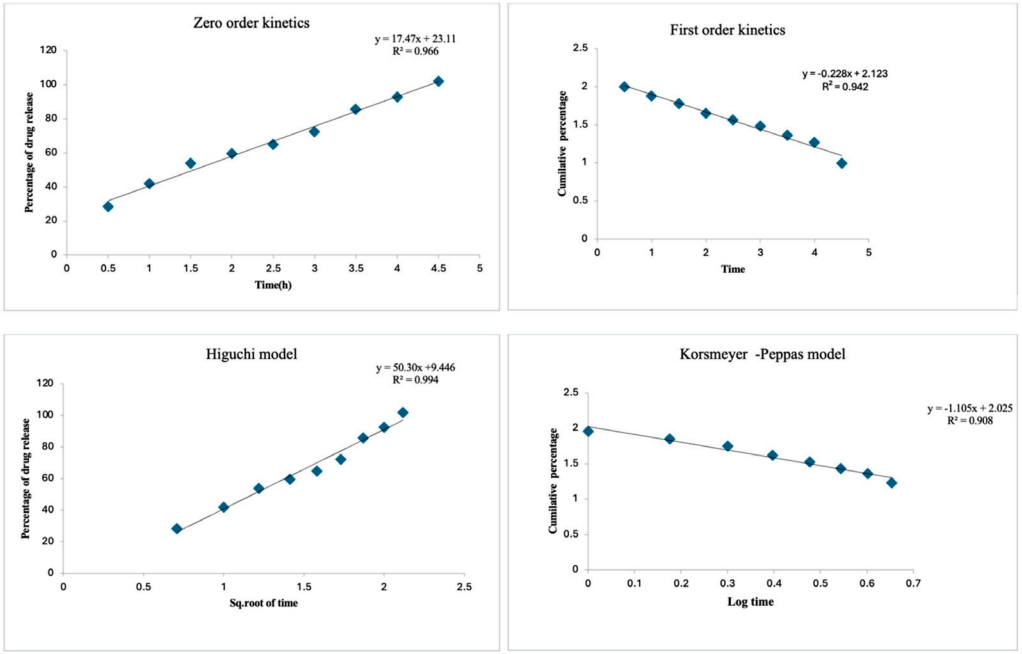


Figure 3. In vitro drug release kinetic models.

3.2. Characterization of RME-EnCNPs

3.2.1. Ultraviolet–Visible Spectroscopy (UV–Vis) Characterization

A concentration of 500 µg/mL of the RME-EnCNPs was chosen for comprehensive characterization studies. The encapsulation process of the RME-EnCNPs (500 µg/mL) and CSNPs was monitored and analyzed using a UV–vis spectrophotometer within the range of 200–800 nm (Figure 4). Both samples exhibited a single, broad, and sharp peak with a maximum absorbance wavelength at 250 nm. The consistent absorption maxima indicated that RME was effectively loaded within the chitosan nanoparticles (CNPs).

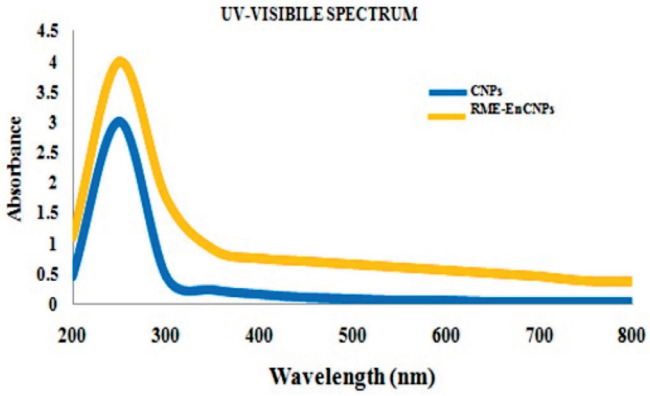


Figure 4. UV absorption spectra of chitosan nanoparticles (CNPs) and root methanolic extract-encapsulated chitosan nanoparticles (RME-EnCNPs).

3.2.2. Fourier Transform Infrared Spectroscopy (FTIR) Characterization

The FTIR spectrum (Figure 5) of chitosan displays characteristic bands attributed to the NH2 group's stretching vibration at the wavelength of 3390.24 cm^{-1}, C–O stretching at the wavelength of 1025.94 cm^{-1}, and the C-H vibration bond at the wavelength of 611.324 cm^{-1}. In the spectrum of the RME-EnCNPs (Figure 5), three distinctive bands unique to RME were observed: O-H in alcohols and phenols at 3423.03 cm^{-1}, C-W waging in alkyl halides at 1095.37 cm^{-1}, and stretching vibration of CH bend out of plane at 640.251 cm^{-1}.

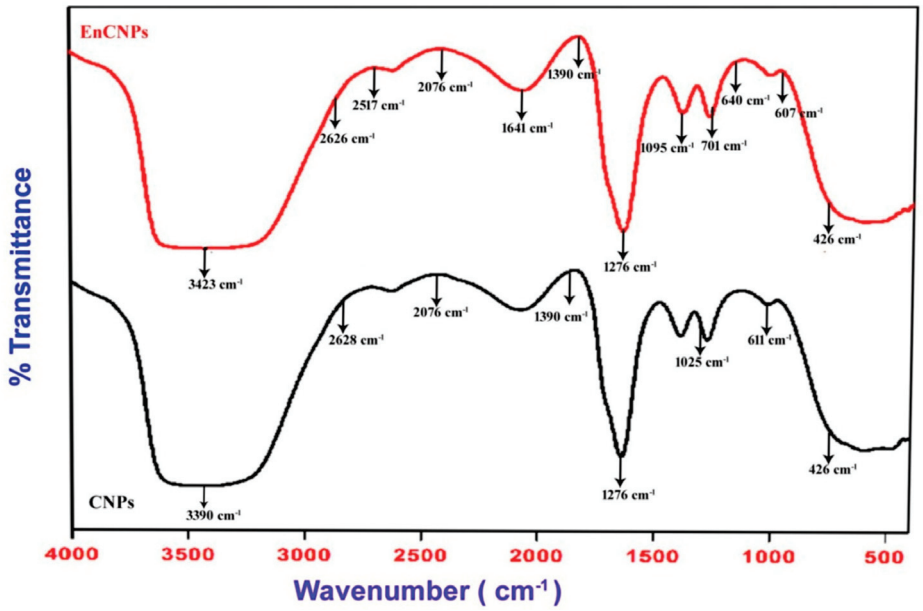


Figure 5. FTIR Spectra of chitosan nanoparticles (CNPs) and root methanolic extract-encapsulated chitosan nanoparticles (RME-EnCNPs).

3.2.3. XRD Analysis

The XRD patterns of the CNPs and RME-EnCNPs at 2θ in the range of 10–100° are depicted in Figures 6 and 7. The results indicate that RME-EnCNPs exhibit characteristics of both chitosan and RME. Both samples display an amorphous nature in their XRD patterns. The X-ray diffraction pattern of CNPs revealed prominent peaks in the 2θ range, corresponding to various crystal planes, including 20.49° (455), 22.50° (541), 27.50° (517), 30.50° (500), 35.50° (417), 37.49° (387), and 40.50° (355). In comparison, RME-EnCNPs exhibited crystal peaks at 22.50° (488), 24.49° (575), 28.49° (553), 31.50° (515), 36.48° (457), 39.50° (402), and 44.49° (375). Despite these crystalline peaks, both samples retained an amorphous nature in their XRD patterns. The broad diffraction peak observed in RME-EnCNPs is attributed to the loading of RME onto chitosan nanoparticles. The average size of CNPs and RME-EnCNPs was determined as 79 nm and 83 nm, respectively, utilizing the Debye–Scherrer equation. This size difference aligns with the successful loading of RME onto chitosan nanoparticles, contributing to the observed broad diffraction peak in the XRD pattern of the RME-EnCNPs.

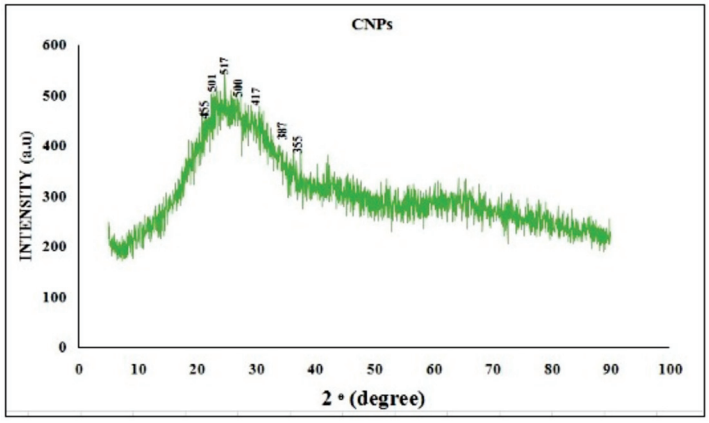


Figure 6. X-ray diffraction pattern of chitosan nanoparticles (CNPs) at 2θ (degree).

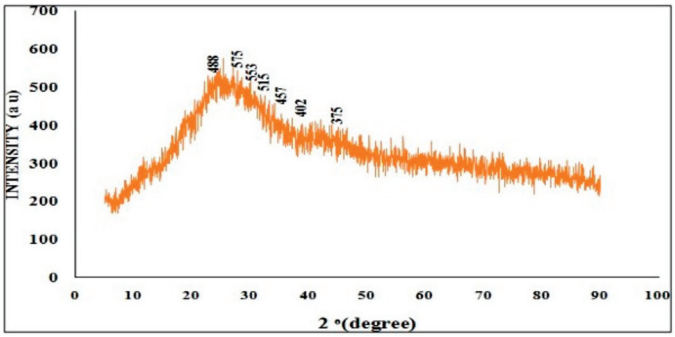


Figure 7. X-ray diffraction pattern of root methanolic extract-encapsulated chitosan nanoparticles (RME-EnCNPs) at 2θ (degree).

3.2.4. Scanning Electron Microscope (SEM) Analysis

Figure 8 depicts the SEM images of CNPs and RME-EnCNPs at a 10 µm scale bar. The SEM images confirm the successful formation of chitosan nanoparticles. In the SEM image of the CNPs, most particles appeared to be aggregated. However, in the SEM image of the RME-loaded CNPs, a uniform and spherical morphology was observed. The average size of the CNPs and RME-EnCNPs was measured as 79 nm and 83 nm, respectively. It is worth noting that the size of the nanoparticles increased after encapsulating RME onto chitosan nanoparticles.

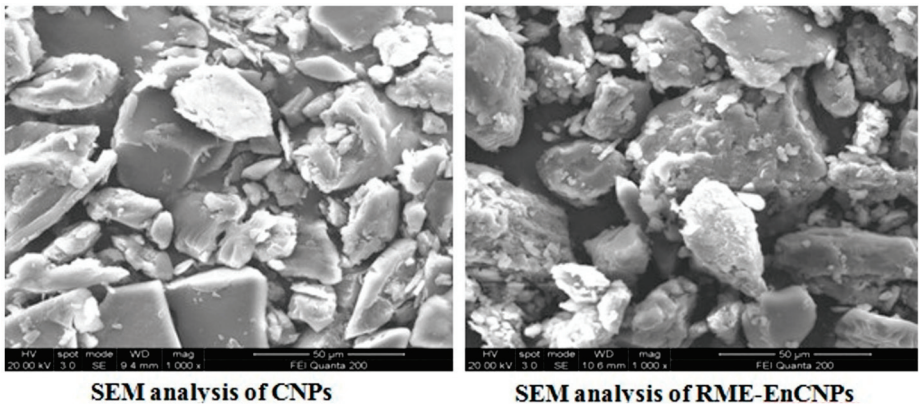


Figure 8. SEM images of chitosan nanoparticles (CNPs) and root methanolic extract-encapsulated chitosan nanoparticles (RME-EnCNPs).

3.2.5. Zeta Potential Analysis

The zeta potential values for CNPs and RME-EnCNPs are illustrated in Figure 9, with values of 33.5 mV and 40.6 mV, respectively.

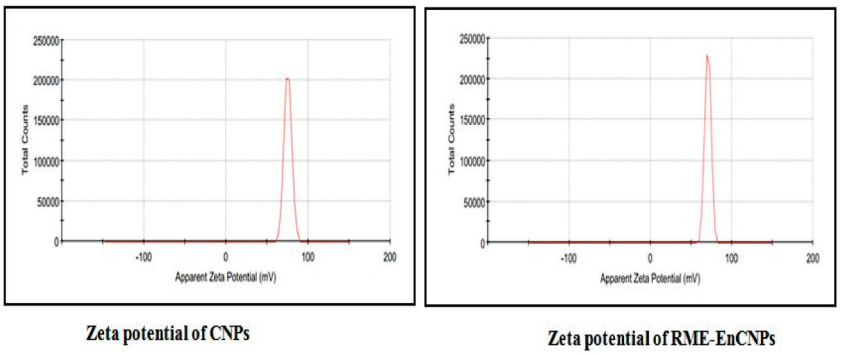


Figure 9. Zeta potential images of chitosan nanoparticles (CNPs) and root methanolic extract-encapsulated chitosan nanoparticles (RME-EnCNPs).

3.3. Evaluation of Acute Oral Toxicity

RME and RME-EnCNPs were utilized to assess acute toxicity. Visual parameters, including alertness, grooming, touch response, torch response, pain response, tremors, convulsions, righting reflex, gripping strength, pinna reflex, corneal reflex, writhing, pupils, urination, salivation, and skin color, were observed at specific intervals over a two-week period. Throughout the observation period, the rats did not exhibit any abnormal signs, behavioral changes, body weight fluctuations, or macroscopic findings. Furthermore, there were no instances of mortality recorded for the administered doses (500, 1000, 2000 mg/kg) at the conclusion of the 14-day observation period.

3.4. Assessment of Physical Parameters (Body Weight) of DMBA-Induced Mammary Cancer in Female Sprague Dawley Rats

In general, the body weight of the animals treated with RME and RME-EnCNPs showed an increase compared to DMBA (135 ± 1.0 g)-treated animals. Of the two doses of RME and RME-EnCNPs, the higher dose, i.e., 500 mg/kg, exhibited enhanced body weight (185 ± 1.9 g) (Table 2).

Table 2. Effect of root methanolic extract (RME) and root methanolic extract-encapsulated chitosan nanoparticles (RME-EnCNPs) on body weight of female Sprague Dawley rats.

Treatment	Initial Treatment of Body Weight (g) (4 Weeks Old)	Final Treatment of Body Weight (g) (20 Weeks Old)
Group I (Control)	125 ± 0.36	215 ± 1.3
Group II (DMBA 25 mg/kg)	131 ± 0.42	135 ± 1.0
Group III (DMBA + STD 10 mg/kg)	138 ± 0.46	190 ± 1.6 ***
Group IV (DMBA + RME 250 mg/kg)	130 ± 0.53	153 ± 1.3 **
Group V (DMBA + RME 500 mg/kg)	140 ± 0.56	166 ± 1.8 **
Group VI (DMBA + RME-EnCNPs 250 mg/kg)	142 ± 0.6	175 ± 1.7 **
Group VII (DMBA + RME-EnCNPs 500 mg/kg)	139 ± 0.59	185 ± 1.9 ***

Results expressed by triplicate means (n = 3) ± Standard error of mean (SEM). Statistical significance determined with Dunnett's t-distribution with probability value, *** $p < 0.001$, ** $p < 0.01$, calculated by comparing treated group with control group. DMBA-7, 12-Dimethylbenz[a]anthracene; STD, standard (tamoxifen); RME, root methanolic extract; RME-EnCNPs, root methanolic extract-encapsulated chitosan nanoparticles.

3.4.1. Analysis of Tumor Weight, Volume, Incidence, and Burden

During this period, a notable reduction ($p < 0.001$) in tumor weight (4.42 ± 0.878 mg/kg), volume (1.3 ± 0.024 mg/kg), burden (2.84 ± 0.577 mg/kg), and incidence (2.21 ± 0.333 mg/kg) was observed in Group VII (DMBA + RME-EnCNPs 500 mg/kg) in comparison to Group II (DMBA 25 mg/kg), as indicated in Table 3.

3.4.2. Biochemical Parameters

In the current study, a noteworthy reduction ($p < 0.001$) in total bilirubin (1.3 ± 0.289 mg/dL), SGOT (40 ± 4.04 u/L), SGPT (36.7 ± 0.82 u/L), and ALP (130 ± 4.62 u/L) was observed in Group VII (DMBA + RME-EnCNPs 500 mg/kg) during this period compared to Group II (DMBA 25 mg/kg). Additionally, hormonal analysis revealed an increase in the levels of estrogen and progesterone in DMBA-induced breast cancer rats (Group II).

These two hormones exhibited a decrease from Group III to Group VII, with a more significant reduction ($p < 0.001$) observed in RME-EnCNPs 500 mg/kg (estrogen: 50.1 ± 1.98 pg/mL; progesterone: 43.9 ± 0.39 ng/mL). A similar trend was observed for total cholesterol, where an increased level was noted in Group II (DMBA-induced breast

cancer rats: 215 ± 8.6 mg/dL). The total cholesterol levels decreased from Group III to Group VII, with a more significant reduction ($p < 0.001$) observed in RME-EnCNPs 500 mg/kg (151 ± 2.89 mg/dL). The same pattern was noted for total triglycerides in the treated animals, with an increased level observed in Group II (DMBA-induced breast cancer rats: 183 ± 3.7 mg/dL) (Table 4).

The total triglycerides exhibited a decrease from Group III to Group VII, with a more significant reduction ($p < 0.001$) observed in RME-EnCNPs 500 mg/kg (98 ± 2.34 mg/dL). Additionally, a significant increase ($p < 0.001$) in total HDL cholesterol was noted in Group VII (DMBA + RME-EnCNPs 500 mg/kg: 65.2 ± 0.318 mg/dL) during this period compared to Group II (DMBA 25 mg/kg) (Table 4).

In the present study, all three kidney markers (urea, uric acid, and creatinine) showed elevated levels in Group II (DMBA 25 mg/kg: 76 ± 4.07 mg/dL; 44.2 ± 0.34 mg/dL; 28.3 ± 0.52 mg/dL) compared to other groups treated with RME and RME-EnCNPs (200 and 500 mg/kg), as presented in Table 4.

Table 3. Effect of root methanolic extract (RME) and root methanolic extract-encapsulated chitosan nanoparticles (RME-EnCNPs) on tumor weight, volume, incidence, and burden of female Sprague Dawley rats.

Group	Group I	Group II Only	Group III	Group IV	Group V	Group VI	Group VII
	Control	DMBA- 25 mg/kg	DMBA + STD 10 mg/kg	DMBA + RME 250 mg/kg	DMBA + RME 500 mg/kg	DMBA + RME-EnCNPs 250 mg/kg	DMBA + RME-EnCNPs 500 mg/kg
Tumor Weight (mg/g)	----	20 ± 12.2 *	3.44 ± 0.59 ***	15.2 ± 3.96 **	8.04 ± 2.9 *	6.7 ± 2.9 **	4.42 ± 0.878 ***
Tumor Volume (cm^3)	----	5.3 ± 0.054 *	1.1 ± 0.045 ***	4.5 ± 0.169 *	3.3 ± 0.092 *	2.3 ± 0.049 **	1.3 ± 0.024 ***
Tumor Burden (g)	----	9.67 ± 0.882 *	2.33 ± 0.882 ***	7.33 ± 0.882 *	5.4 ± 0.882 **	3.2 ± 0.577 **	2.84 ± 0.577 ***
Tumor Incidence (%)	----	8.33 ± 0.333 *	2.17 ± 0.333 ***	6.67 ± 0.882 **	4.6 ±0.577 *	3.83 ± 0.882 **	2.21 ± 0.333 ***

Results are expressed by triplicate means ($n = 3$) ± Standard error of mean (SEM). In statistical significance determined with Dunnett's test-distribution with probability value, *** $p < 0.001$, ** $p < 0.01$, * $p < 0.05$ calculated by comparing DMBA-treated group with RME and RME-En CNPs-treated group. DMBA-7,12-Dimethyl benz[a]anthracene; STD, standard (tamoxifen); RME, root methanolic extract; RME-EnCNPs, root methanolic-extract-encapsulated chitosan nanoparticles.

Table 4. Effect of root methanolic extract (RME) and root methanolic extract-encapsulated chitosan nanoparticles (RME-EnCNPs) on bilirubin, serum glutamic oxaloacetic transaminase (SGOT), serum glutamate pyruvate transaminase (SGPT), alkaline phosphatase (ALP) total estrogen, progesterone, total cholesterol, triglycerides, high density level (HDL)-cholesterol, total urea, uric acid, and creatinine levels in female Sprague Dawley rats.

Group	Group I (Control)	Group II (Only DMBA 25 mg/kg)	Group III (DMBA + STD 10 mg/kg)	Group IV (DMBA + R ME 250 mg/kg)	Group V (DMBA + R ME 500 mg/kg)	Group VI (DMBA + R ME-EnCNPs (250 mg/kg)	Group VII (DMBA + R ME-EnCNPs (500 mg/kg)
Total Bilirubin (mg/dL),	2.35 ± 0.263	39.2 ± 0.346	2.15 ± 0.144 ***	30.1 ± 0.404 **	24.1 ± 0.231 **	12.6 ± 0.173 **	1.3 ± 0.289 ***
SGOT (u/L)	35 ± 2.89	139 ± 1.73	38 ± 1.73 ***	92 ± 2.31 **	75 ± 4.04 **	62.5 ± 0.866 **	40 ± 4.04 ***
SGPT (u/L)	33.3 ± 2.6	107 ± 5.2	34 ± 1.0 ***	84 ± 6.35 **	68.3 ± 2.6 **	57.7 ± 6.06 **	36.7 ± 0.82 ***
ALP (u/L)	125 ± 4.04	302 ± 31.2	128 ± 2.31 ***	190 ± 0.882 **	179 ± 5.77 **	155 ± 13.6 **	130 ± 4.62 ***
Est.H (Pg/mL)	62.8 ± 18.5	98 ± 4.7	58.6 ± 13.6 ***	89.9 ± 1.25 ***	75.2 ± 1.325 **	64.4 ± 1.28 **	50.1 ± 1.98 ***
Prog.H (ng/mL)	44.52 ± 0.36	92.52 ± 0.95	46.3 ± 1.63 ***	84.2 ± 0.652 **	72.9 ± 0.12 **	60.5 ± 0.165 **	43.9 ± 0.39 ***

Table 4. *Cont.*

Group	Group I (Control)	Group II (Only DMBA 25 mg/kg)	Group III (DMBA + STD 10 mg/kg)	Group IV (DMBA + R ME 250 mg/kg)	Group V (DMBA + R ME 500 mg/kg)	Group VI (DMBA + R ME-EnCNPs (250 mg/kg)	Group VII (DMBA + R ME-EnCNPs (500 mg/kg)
Total Cholesterol (mg/dL)	148 ± 1.44	215 ± 8.6	150 ± 5.77 ***	195 ± 37.5 **	186 ± 5.77 **	175 ± 14.4 *	151 ± 2.89 ***
Triglycerides (mg/dL)	95.3 ± 1.47	183 ± 3.7	96.2 ± 1.36 ***	179 ± 3.41 **	158 ± 0.202 *	122 ± 3.72 *	98 ± 2.34 ***
HDL-Cholesterol (mg/dL)	68.8 ± 1.67	22.9 ± 3.49	63.8 ± 0.635 ***	33.9 ± 5.17 **	46.1 ± 0.751 *	52.6 ± 2.14 **	65.2 ± 0.318 ***
Urea (mg/dL)	19.8 ± 1.67	76 ± 4.07	20.1 ± 3.18 ***	66.9 ± 2.34 **	55.3 ± 0.866 *	40.7 ± 3.41 *	20.7 ± 0.52 ***
Uric acid (mg/dL)	3.05 ± 0.26	44.2 ± 0.34	2.8 ± 0.231 ***	38.05 ± 0.43 **	26.1 ± 0.316 *	14.05 ± 0.144 *	2.3 ± 0.231 ***
Creatinine (mg/dL)	0.55 ± 0.144	28.3 ± 0.52	1.2 ± 0.23 ***	18.5 ± 0.202 **	11.8 ± 0.15 *	8.2 ± 0.346 *	1.6 ± 0.404 ***

Results expressed by triplicate means (n = 3) ± standard error of mean (SEM). Statistical significance determined with Dunnett's t-distribution with probability value, *** $p < 0.001$, ** $p < 0.01$, * $p < 0.05$ calculated by comparing treated group with control group. DMBA-7, 12-Dimethylbenz[a]anthracene; STD, standard (tamoxifen); RME, root methanolic extract; RME-EnCNPS, root methanolic extract-encapsulated chitosan nanoparticles.

3.4.3. In Vivo Antioxidant Activity

In the present study, DMBA-induced rats exhibited a significant reduction in total protein, SOD, catalase, GPx, and GSH (81.1 ± 0.06 mg/dL; 0.32 ± 0.06 Unit/min/mg protein; 1.01 ± 0.07 Unit/min/mg protein; 5.02 ± 0.46 nmol of glutathione peroxidase/min/mg protein and 0.36 ± 0.04 nmol of glutathione hydroxidase/min/mg protein), except for LPO, which significantly increased (23.41 ± 0.04 nmol of MDA/mg protein). The trend was found to be the inverse from Group III to Group VII. However, a more significant reduction ($p < 0.001$) was observed in Group VII (RME-EnCNPs 500 mg/kg treated animals), as shown in Table 5.

Table 5. Effect of root methanolic extract (RME) and root methanolic extract-encapsulated chitosan nanoparticles (RME-EnCNPs) on total protein, superoxide dismutase activity (SOD), catalase activity, glutathione peroxidase (GPX), glutathione content (GSH), and lipid peroxidation (LPO) levels in female Sprague Dawley rats.

Group	Group I Control	Group II Only DMBA25 mg/kg	Group III DMBA + STD	Group IV DMBA + RMEL.D	Group V DMBA + RMEH.D	Group VI DMBA + RME-	Group VII DMBA + RME-EnCNPs
			10 mg/kg	250 mg/kg	500 mg/kg	EnCNPsL.D 250 mg/kg	H.D500 mg/kg
Total Protein (mg/dL)	25.2 ± 0.09	8.1 ± 0.06	24.8 ± 0.05 ***	13.5 ± 0.08 **	15.7 ± 0.06 **	18.2± 0.07 *	23.3 ± 0.02 ***
SOD (Unit/min/mg protein)	9.27 ± 0.09	0.32 ± 0.06	10.25 ± 0.02 ***	3.282 ± 0.08 **	4.233 ± 0.07 **	6.21 ± 0.05 *	11.25 ± 0.06 ***
CATALASE (Unit /min/mg protein)	12.3 ± 0.04	1.01 ± 0.07	11.57 ± 0.04 ***	3.672 ± 0.08 **	8.529 ± 0.01 **	10.57 ± 0.04 **	16.51 ± 0.04 ***
GPX (nmol of Glutathione peroxidase/min/mg protein)	36.3 ± 0.82	5.02 ± 0.46	32.03 ± 0.26 ***	10.08 ± 0.15 **	15.53 ± 0.02 **	24.03 ± 0.03 *	35.1 ± 0.15 ***
GSH (nmol of Glutathione hyroxidase/min/mg protein)	37.35 ± 0.04	0.36 ± 0.04	35.09 ± 0.03 ***	5.76 ± 0.05 **	10.24 ± 0.02 **	25.41 ± 0.04 *	36.18 ± 0.08 ***
LPO (nmol of MDA/mg protein)	3.54 ± 0.03	23.41 ± 0.04	4.29 ± 0.73 ***	19.54 ± 0.93 **	14.24 ± 0.01 **	11.79 ± 0.01 *	5.26 ± 0.01 ***

Results expressed by triplicate means (n = 3) ± standard error of mean (SEM). Statistical significance determined with Dunnett's test-distribution with probability value, *** $p < 0.001$, ** $p < 0.01$, * $p < 0.05$ calculated by comparing treated group with control group. DMBA-7, 12-Dimethylbenz[a]anthracene; STD, standard (tamoxifen); RME, root methanolic extract; RME EnCNPs, root methanolic extract-encapsulated chitosan nanoparticles.

3.4.4. Enzymes Involved in Glycolysis and Non-Glycolytic Pathways

In the present study, glycolytic enzymes such as hexokinase and aldolase were found to be increased in the DMBA-induced breast cancer rats compared to RME and RME-EnCNPs (200 and 500 mg/kg treated rats). Conversely, the trend was the inverse for non-glycolytic enzymes such as glucose 6-phosphate and fructose 1,6-diphosphatase analyzed in DMBA breast cancer-induced rats and those treated with RME and RME-EnCNPs. However, there was a significant decrease ($p < 0.001$) observed in glucose 6-phosphatase (31.8 ± 0.32 µmoles of glucose 6-phosphatase/min/mg protein) and glyceraldehyde (32.1 ± 0.07 µmoles of glyceraldehyde's/min/mg protein) in Group VII (RME-EnCNPs 500 mg/kg treated animals). Simultaneously, an increase (53.9 ± 3.46 µmoles of glucose 6-phosphatase/min/mg protein; 51.3 ± 3.52 fructose 1,6-diphosphatase/min/mg protein) was observed for the same group, as depicted in Figure 10.

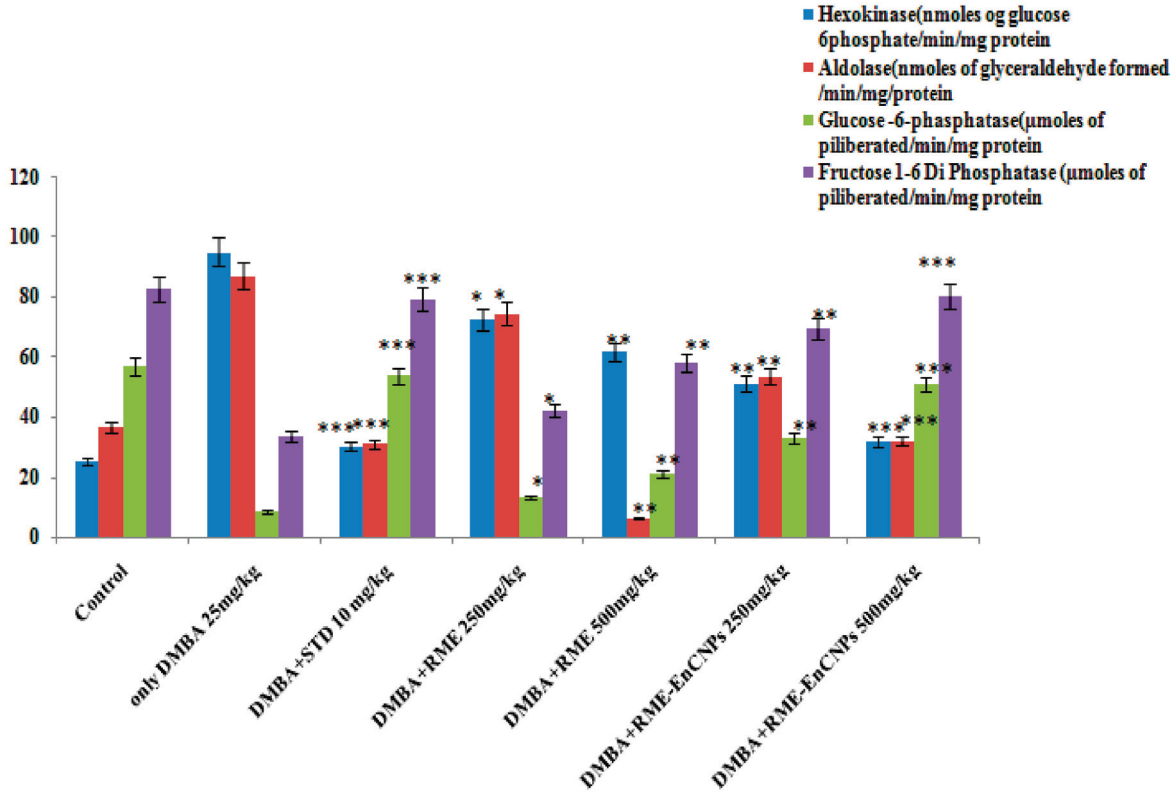


Figure 10. Effect of RME and RME-EnCNPs on hexokinase, aldolase, glucose-6-phosphatase, fructose 1-6-Di phosphatase levels in female Sprague Dawley rats. Results expressed by triplicate means ($n = 3$) ± standard error of mean (SEM). Statistical significance determined with Dunnett's t-distribution with probability value, *** $p < 0.001$, ** $p < 0.01$, * $p < 0.05$ calculated by comparing treated group with control group. DMBA-7, 12-Dimethylbenz[a]anthracene; STD, standard (tamoxifen); RME, root methanolic extract; RME-EnCNPs, root methanolic extract-encapsulated chitosan nanoparticles.

3.4.5. Estimation of Mitochondrial TCA Cycle Enzymes

In the present study, TCA cycle enzymes such as isocitrate dehydrogenase (IDH), succinate dehydrogenase (SDH), and malate dehydrogenase (MDH) were found to be decreased in the DMBA-induced breast cancer animals (585 ± 15.5 µmoles of α- ketoglutarate/min/mg protein; 35.4 ± 0.303 µmoles of succinate oxidized/min/mg protein; 213 ± 3.52 µmoles of NADH oxidized/min/mg protein). However, RME-EnCNPs 500 mg/kg treated animals showed a significant increase ($p < 0.001$) in IDH (817 ± 6.33 µmoles of α-ketoglutarate/min/mg protein), SDH (115.8 ± 0.641 µmoles of succinate oxidized/min/mg protein), and MDH (213 ± 3.52 µmoles of NADH oxidized/min/mg protein), as illustrated in Figure 11.

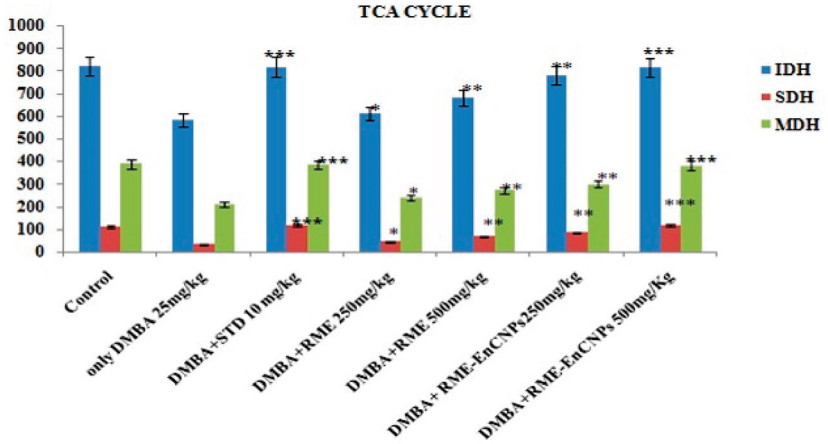


Figure 11. Effect of root methanolic extract (RME) and root methanolic extract-encapsulated chitosan nanoparticles (RME-EnCNPs) on isocitrate dehydrogenase (IDH), succinate dehydrogenase (SDH), and malate dehydrogenase (MDH) levels in female Sprague Dawley rats. Results expressed by triplicate means (n = 3) ± standard error of mean (SEM). Statistical significance determined with Dunnett's t-distribution with probability value, *** $p < 0.001$, ** $p < 0.01$, * $p < 0.05$ calculated by comparing treated group with control group. DMBA-7, 12-Dimethylbenz[a]anthracene; STD, standard (tamoxifen); RME, root methanolic extract; RME-EnCNPs, root methanolic extract-encapsulated chitosan nanoparticles.

3.4.6. Estimation of Hematological Parameters

The analysis of hematological parameters, including RBC, WBC, HB, PCV, polymorphs, lymphocytes, monocytes, eosinophils, and MCH, was conducted in the in rats with DMBA-induced mammary tumors. The results are presented in Table 6. A significant increase ($p < 0.001$) in RBC, HB, PCV, and MCH was observed in Group VII (DMBA + RME-EnCNPs 500 mg/kg: 16.07 ± 0.109; 14.3 ± 0.265; 37.3 ± 0.882; 32.6 ± 0.99) during this period compared to Group II (DMBA 25 mg/kg), which showed a decrease in these parameters (1.12 ± 0.139; 1.9 ± 0.491; 3.8 ± 1.23; 8.4 ± 1.07). Additionally, there was a significant decrease ($p < 0.001$) in lymphocytes, monocytes, and eosinophils in Group VII (DMBA + RME-EnCNPs 500 mg/kg: 88 ± 3.21; 54.3 ± 1.45; 38.7 ± 0.882) compared to Group II (DMBA 25 mg/kg: 52.7 ± 3.28; 6.67 ± 1.45; 8.4 ± 1.07), which exhibited decreased levels of these parameters.

Table 6. Effect of root methanolic extract (RME) and root methanolic extract-encapsulated chitosan nanoparticles (RME-EnCNPs) and hematological parameters in rats with DMBA–induced mammary tumors.

Group I	Group II Only DMBA	Group III DMBA + STD	Group IV DMBA + RMEL.D	Group V DMBA + RME	Group VI DMBA + RME-EnCNPs	Group VII DMBA + RME-EnCNPs
Group Control	25 mg/kg	10 mg/kg	250 mg/kg	500 mg/kg	250 mg/kg	500 mg/kg
RBC ($\times 10^6/\mu L$) 15.01 ± 0.10	1.12 ± 0.139	17.38 ± 0.237 ***	5.92 ± 0.397 *	8.57 ± 0.32 *	12.6 ± 0.283 **	16.07 ± 0.109 ***
WBC ($\times 10^3/\mu L$) 16.1 ± 0.896	61 ± 1.29	18.4 ± 0.503 ***	45.6 ± 0.867 *	37.9 ± 0.551 *	28.4 ± 1.38 *	17.3 ± 0.689 ***
HB (g/dL) 15.7 ± 0.669	1.9 ± 0.491	13.7 ± 1.06 ***	2.6 ± 0.788 *	4.6 ± 1.1 *	10.3 ± 0.29 **	14.3 ± 0.265 ***
PCV (%) 40.3 ± 1.92	3.8 ± 1.23	36.1 ± 3.34 ***	5.9 ± 2.28 *	18.3 ± 3.18 *	28.3 ± 1.48 *	37.3 ± 0.882 ***
Polymorphs (%) 12.7 ± 0.667	52 ± 1.53	13.2 ± 1.15 ***	47.3 ± 1.45 *	32.3 ± 0.882 *	21.3 ± 0.88 *	15.6 ± 1.45 ***
Lymphocytes (%) 1.3 ± 2.67	52.7 ± 3.28	87.3 ± 0.882 ***	51.3 ± 0.333 **	68.7 ± 0.667 *	79.3 ± 1.2 **	88 ± 3.21 ***
Monocytes (%) 59.33 ± 1.33	6.67 ± 1.45	58.7 ± 0.882 ***	26.3 ± 1.2 *	35.7 ± 0.333 *	42.7 ± 0.33 **	54.3 ± 1.45 ***
Eosinophils (%) 39.67 ± 0.66	6.67 ± 0.333	37 ± 0.577 ***	16.2 ± 0.577 *	24.4 ± 0.333 *	29.7 ± 0.33 *	38.7 ± 0.882 ***
MCH (Pg) 35.8 ± 1.15	8.4 ± 1.07	34.8 ± 0.767 ***	11.3 ± 0.794 *	18.5 ± 0.841 *	26 ± 0.695 *	32.6 ± 0.99 ***

Results expressed by triplicate means (n = 3) ± standard error of mean (SEM). Statistical significance determined with Dunnett's t-distribution with probability value, *** $p < 0.001$, ** $p < 0.01$, * $p < 0.05$ calculated by comparing treated group with control group. DMBA-7, 12-Dimethylbenz[a]anthracene; STD, standard (tamoxifen); RME, root methanolic extract; RME-EnCNPS, root methanolic extract-encapsulated chitosan nanoparticles.

3.4.7. Microscopic Histological Analysis

Histology of DMBA-Induced Mammary Tumor of Female Sprague Dawley Rats

Histopathological examinations of DMBA-induced mammary tissue sections from the experimental groups were conducted. The histomorphology of the mammary glands in the normal rat (Group I control) showed no evidence of malignancy, exhibiting normal ductal epithelial cells, nipple areola, and cytoplasm. In Group II (DMBA treatment), malignant epithelial cells with hyperchromasia and nuclear-cytoplasmic ratio, along with pleomorphism, were observed.

Group III (DMBA + standard—tamoxifen treatment) displayed nipple areola with hyperplastic glands, a reduction in tumor fibrosis, and the presence of elastosis with stroma and acinus. Group IV (DMBA + RME 250 mg/kg) exhibited neoplastic glands and fibrosis with myxoid degeneration, accompanied by individual cells of necrosis. Group V (DMBA + RME 500 mg/kg) showed non-neoplastic glands and acinus with fibrosis, and occasional areas of necrosis were seen.

In Group VI (DMBA + RME-EnCNPs 250 mg/kg), a single-layered non-neoplastic acinus was observed. Finally, Group VII (DMBA + RME-EnCNPs 500 mg/kg) showed a disappearance of tumor cells, and fibrosis was reduced (Figure 12).

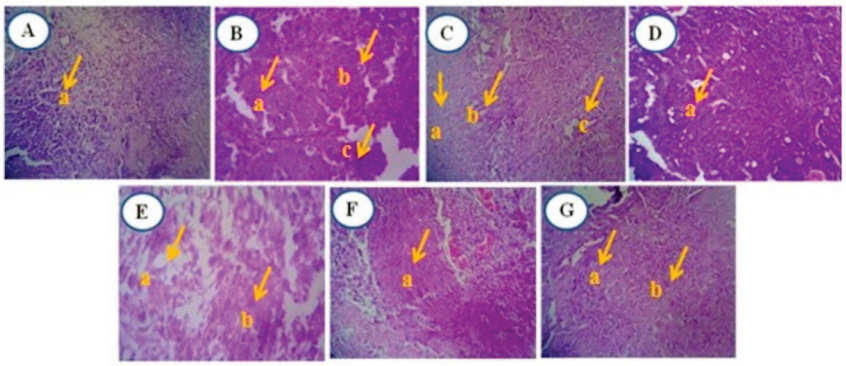


Figure 12. Histology of DMBA-induced mammary tumors of female Sprague Dawley rats. (**A**–**G**) Shows histopathological analysis of mammary tumors of control and experimental groups. Group (**A**): Control showed (a—arrow) normal architecture. Group (**B**): DMBA-induced cancer showed (a—arrow) malignant epithelial cells, (b—arrow) hyperchromasia, (c—arrow) nuclear cytoplasmic ratio and pleomorphism. Group (**C**): DMBA + standard (tamoxifen) treated animals showed (a—arrow) nipple areola complex, (b—arrow) hyperplastic glands and acinus, (c—arrow) areas of fibrosis and elastosis. Group (**D**): DMBA + RME 250 mg/kg treated animals showed (a—arrow) fibrosis with myxoid degeneration and individual cells of necrosis seen. Group (**E**): DMBA + RME 500 mg/kg showed (a—arrow) non-neoplastic glands and acinus, (b—arrow) fibrosis and occasional areas of necrosis seen. Group (**F**): VIDMBA + RME-EnCNPs 250 mg/kg treated animal shows (a—arrow) single layered non-neoplastic acinus. Group (**G**): DMBA + RME-EnCNPs 500 mg/kg treated animal shows (a—arrow) disappearance of tumor cells with no glands and acini noted, (b—arrow) fibrosis noted.

Histology of Liver of DMBA-Induced Mammary Tumor-Bearing Rats

The histomorphology of liver tissues in the control and experimental groups was examined. Group I (control animals) showed the normal architecture of hepatocytes. In Group II (DMBA-treated animals), an abnormal architecture was observed, with hepatocytes arranged in cords, and the portal tract appeared remarkable. Group III (DMBA + standard—tamoxifen) exhibited central veins with congestion. Group IV (DMBA + RME 250 mg/kg) showed sinusoidal dilatation. Group V (DMBA + RME 500 mg/kg) displayed normal hepatocytes with a portal tract. In Group VI (DMBA + RME-EnCNPs 250 mg/kg) treated animals, normal hepatocytes with a portal tract were observed. Finally, Group VII (DMBA + RME-EnCNPs 500 mg/kg) showed normal hepatocytes with central vein congestion (Figure 13).

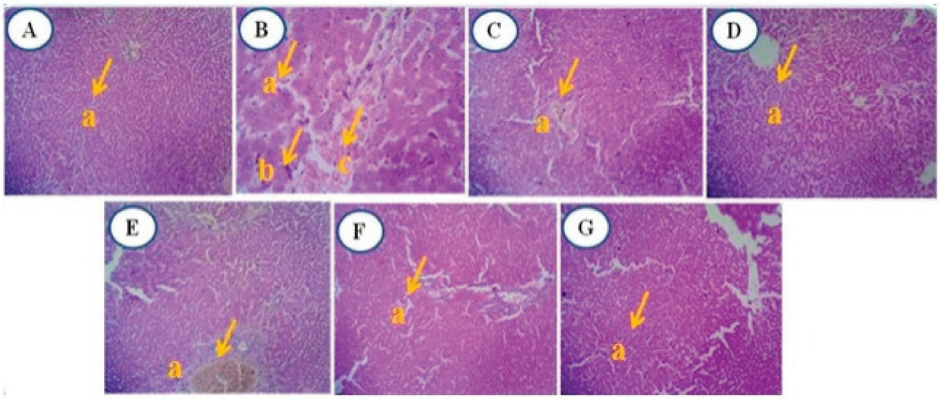


Figure 13. Histology of liver of DMBA-induced mammary tumor-bearing rats. (**A**–**G**) Shows histopathological analysis of liver tissue of control and experimental groups. Group (**A**): control showed normal architecture of hepatocytes (a—arrow) normal architecture. Group (**B**): DMBA-induced cancer bearing animal showed (a—arrow) abnormal architecture, (b—arrow) hepatocytes arranged in cords, (c—arrow) portal tract appears remarkable. Group (**C**): DMBA + standard (tamoxifen) treated animals showed (a—arrow) central veins with congestion. Group (**D**): DMBA + RME 250 mg/kg showed (a—arrow) sinusoidal dilatation. Group (**E**): DMBA + RME 500 mg/kg showed (a—arrow) normal hepatocytes with sinusoidal dilatation. Group (**F**): DMBA + RME-EnCNPs 250 mg/kg treated animals showed (a—arrow) normal hepatocytes with portal tract. Group (**G**): DMBA + RME-EnCNPs 500 mg/kg treated animals showed (a—arrow) normal hepatocytes with central vein congestion.

Histology of Kidney of DMBA-Induced Mammary Tumor-Bearing Rats

The histomorphology of kidney tissues in the control and experimental groups was examined. Group I (control animals) showed the normal architecture of kidney tissues. In Group II (DMBA-treated animals), glomeruli with loss of mesangial matrix expansion were observed. Group III (DMBA + standard—tamoxifen) displayed normal glomeruli.

Group IV (DMBA + RME 250 mg/kg) showed focal mild eosinophilic material seen within the lumen. Group V (DMBA + RME 500 mg/kg) showed no significant pathology of glomeruli, and the interstitium appeared normal. In Group VI (DMBA + RME-EnCNPs 250 mg/kg) treated animals, normal blood vessels with mild congestion were observed. Finally, Group VII (DMBA + RME-EnCNPs 500 mg/kg) showed normal interstitium and normal morphology (Figure 14).

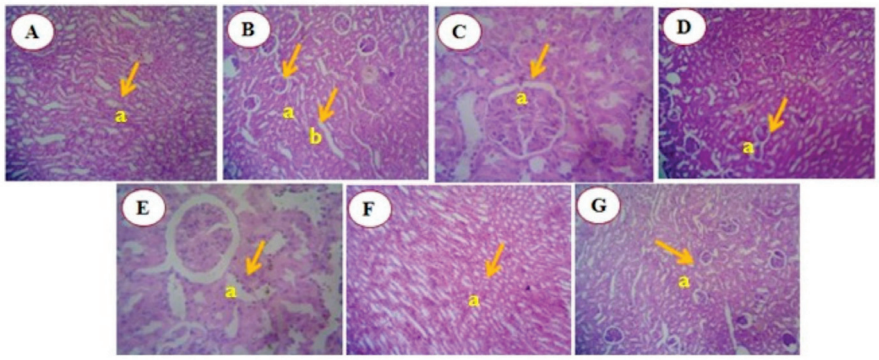


Figure 14. Histology of kidney of DMBA-induced mammary tumor-bearing rats. (**A**–**G**) Shows histopathological analysis of kidney tissue of control and experimental groups. Group (**A**): control showed (a—arrow) normal architecture. Group (**B**): DMBA-induced cancer bearing animals showed (a—arrow) glomeruli, (b—arrow) loss of mesangial matrix expansion. Group (**C**): DMBA + standard (tamoxifen) treated animals showed (a—arrow) normal glomeruli. Group (**D**): DMBA + RME 250 mg/kg showed (a—arrow) focal mild eosinophilic material in lumen. Group (**E**): DMBA + RME

500 mg/kg showed (a—arrow) no significant pathology in glomeruli. Interstitium showed normal. VI Group (**F**): DMBA + RME-EnCNPs 250 mg/kg treated animals showed (a—arrow) blood vessels with mild congestion. Group (**G**): DMBA + RME-EnCNPs 500 mg/kg treated animals showed (a—arrow) normal morphology in interstitium.

Histology of Uterus of DMBA-Induced Mammary Tumor-Bearing Rats

The histomorphology of uterus tissues in the control and experimental groups was examined. Group I (control animals) showed the normal architecture of uterus tissues. In Group II (DMBA-treated animals), abnormal epithelium with scattered inflammatory infiltrates was observed. Group III (DMBA + standard-tamoxifen) displayed glands with a circular and elongated shape.

Group IV (DMBA + RME 250 mg/kg) showed a stroma with scattered inflammatory infiltrates. Group V (DMBA + RME 500 mg/kg) showed normal mucosa. In Group VI (DMBA + RME-EnCNPs 250 mg/kg) treated animals, normal neutrophils and eosinophils were observed. Finally, Group VII (DMBA + RME-EnCNPs 500 mg/kg) showed normal endomyometrium with scattered infiltrates (Figure 15).

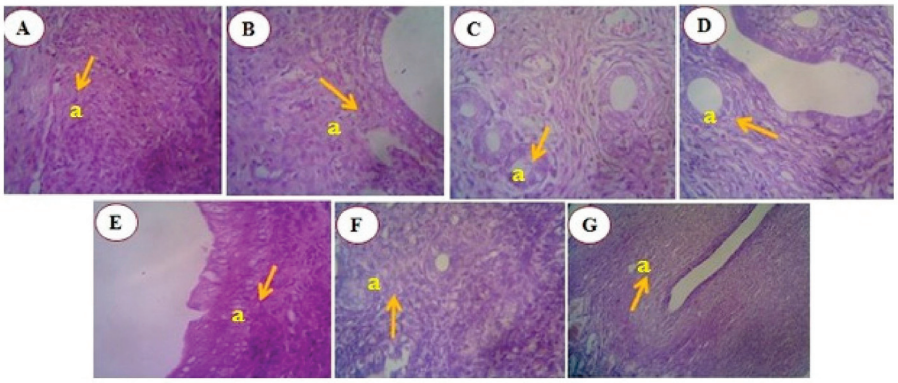


Figure 15. Histology of uterus of DMBA-induced mammary tumor-bearing rats. (**A**–**G**) Shows histopathological analysis of uterus tissue of control and experimental groups. Group (**A**): control showed (a—arrow) normal architecture. Group (**B**): DMBA-induced cancer bearing animals showed (a—arrow) abnormal epithelium with scattered inflammatory infiltrates. Group (**C**): DMBA + standard (tamoxifen) treated animals showed (a—arrow) glands with circular and elongated shape. Group (**D**): DMBA + RME 250 mg/kg showed (a—arrow) stroma with scattered inflammatory infiltrates. Group (**E**): DMBA + RME 500 mg/kg showed (a—arrow) normal mucosa. Group (**F**): DMBA + RME-EnCNPs 250 mg/kg treated animals showed (a—arrow) neutrophils and eosinophils. Group (**G**): DMBA + RME-EnCNPs 500 mg/kg treated animals showed (a—arrow) normal endomyometrium with scattered infiltrates.

4. Discussion

The biodegradable polymer chitosan has been widely employed in drug delivery applications. Chitosan (C), derived from the N-deacetylation of chitin, a natural polysaccharide, is primarily present in the exoskeletons of crustaceans, insects, and fungi [42]. Cross-linking chitosan with sodium tripolyphosphate (TPP) represents a mild and efficient method to produce chitosan nanoparticles (CNPs). These particles are primarily formed through the electrostatic interaction between the positively charged chitosan and the negatively charged TPP molecules. Chitosan nanocarriers have demonstrated significant potential for various challenging drug delivery applications. The ionic gelation method used for preparing chitosan-TPP nanoparticles involves the spontaneous aggregation of chitosan with TPP, facilitated by the formation of molecular linkages between TPPs and chitosan amino groups [43].

Encapsulation plays a crucial role in protecting bioactive compounds from degradation. Currently, there are two types of encapsulations: microencapsulation and nanoencapsulation. Nanoencapsulation is preferred over microencapsulation due to its nanoscale size.

Smaller particles not only enhance bioavailability but also allow for better control over their release [44]. Green chemistry strategies are favored for synthesizing nanomaterials replacing hazardous chemicals with eco-friendly biological materials during the synthesis of various therapeutic nanomaterials. This approach helps minimize the adverse impact of chemicals on human health [45].

In this study, the rise in drug entrapment efficiency with the escalation of plant extract concentration suggests that initially the nanoparticles were not saturated with the plant extract. The heightened concentration of the crude extract increased the drug's availability for encapsulation. Additionally, the size of the nanoparticles plays a role in encapsulation efficiency, where larger nanoparticles, with their increased volume, can accommodate a greater quantity of the drug. In our investigation, the size of the root methanolic extract-encapsulated nanoparticles (RME-EnCNPs) was determined to be 83 nm. Similar findings were reported in [46].

4.1. Charaterization of RME-EnCNPs

The characterization of the RME-EnCNPs in this study involved various techniques, including UV–visible spectroscopy, FTIR, XRD, SEM, and zeta potential. The UV–vis absorption peak observed for the RME-EnCNPs in the range of 200–800 nm indicated the presence of CO groups in the CNPs. The FTIR peaks shifting from 3390.24 cm^{-1}, 1025.94 cm^{-1}, and 611.324 cm^{-1} for the CNPs to 3423.03 cm^{-1}, 1095.37 cm^{-1}, and 701.96 cm^{-1} for the RME-EnCNPs suggested the successful loading of the root methanolic extract of A. venenata into the CNPs. The sizes of the CNPs and RME-EnCNPs were found to be 79 nm and 83 nm, respectively, with the interaction between the polymer and plant extract leading to an increase in RME-EnCNPs compared to CNPs [47]. SEM analysis revealed almost separated spherical-shaped NPs for both CNPs and RME-EnCNPs, as is consistent with previous findings [48,49].

The zeta potential analysis revealed a higher value for the RME-EnCNPs (40.6 mV) compared to the CNPs (33.5 mV), indicating the excellent stability of the encapsulated drug. Moving on to the in vitro drug release and kinetic models, the release profile of RME-EnCNPs was examined, demonstrating that 50% of the drug was released within 2 h in a rapid and sustained manner. By the 5th hour, 87.8% of the drug had been released. This release pattern aligns with the two common profiles observed in drug release from nanoparticles: an initial burst phase due to drug adsorption onto the NP surface, followed by a sustained release attributed to slow drug diffusion from the polymer matrix and carrier matrix breakdown [50].

The observed initial burst release of the drug within the first two hours is likely due to factors such as the high surface area of the drug particles, rapid dissolution of the drug, and the nature of the formulation matrix, which may allow for faster release at the surface compared to the core [50]. This burst phase is common in drug delivery systems and can be influenced by the solubility and physicochemical properties of the drug, as well as the release mechanism of the carrier [51]. Addressing this burst release in future formulations may involve optimizing drug encapsulation techniques, adjusting the matrix composition, or exploring alternative carriers to achieve a more controlled, sustained release profile [52].

Drug release profiles can be influenced by mechanisms like simple diffusion, erosion, degradation, and absorption activity [51]. To design pharmaceutical formulations effectively, researchers have introduced various mathematical models. Drug carriers exhibit variations in shape, dimension, drug dissolution properties, and functionality. Due to these diversities, developing a universal model for predicting release profiles is not feasible. Hence, it becomes crucial to carefully select the most appropriate model for each specific research case [52].

A comprehensive kinetic analysis of RME release from chitosan nanoparticles was conducted using four mathematical models: zero order (cumulative percentage of drug release vs. time), first order (logarithmic cumulative percent drug remaining vs. time), Higuchi (cumulative percentage of drug release vs. square root of time), and Korsmeyer–

Peppas (logarithmic cumulative percent drug release vs. log time) [53]. The zero order model indicated a gradual release of the drug, while the first order model described the absorption and/or elimination of the drug from the nanocarrier. The Higuchi model, which best fit the release profile with an R^2 value of 0.994, suggests a diffusion-controlled release mechanism. This indicates that RME is gradually released from the nanoparticles through diffusion, making it ideal for sustained drug delivery. Under physiological conditions, this diffusion-driven release ensures controlled drug release, maintaining therapeutic levels over time. Such sustained release is particularly beneficial for cancer treatment, where prolonged drug exposure is crucial for effective therapy and minimizing side effects. The Korsmeyer–Peppas model was used to assess the transport mechanisms involved in the release, whether by diffusion or swelling [54].

4.2. Acute Oral Toxicity Study

The outcomes of the acute toxicity analysis in the current study for both RME and RME-EnCNPs revealed no signs of toxicity or mortality in rats when administered orally at doses of 500, 1000, and 2000 mg/kg. Following the guidelines of the OECD (Organization for Economic Development, 2001) for the chemical labeling and classification of acute toxicity, RME and RME-EnCNPs would fall into category 5, considering their LD50 values greater than 2000–5000 mg/kg. This classification denotes the lowest toxicity class [55].

4.3. Assessment of Body Weight

DMBA, a known carcinogen, has been identified for its ability to induce mammary carcinoma in mice, particularly originating from the ductal elements of the mammary gland, by significantly increasing oxidative stress [56]. Throughout the 20-week study, a gradual increase in body weight was observed across all animal groups. Notably, a significant increase ($p < 0.001$) in body weight was observed in Group III (DMBA + STD) and Group VII (DMBA + RME-EnCNPs 500 mg/kg) during this period. Furthermore, rats administered RME at doses of 250 and 500 mg/kg exhibited a noteworthy increase ($p < 0.05$) in body weight at the end of the 20th week compared to Group II (DMBA 25 mg/kg). The injection of DMBA might have disrupted the body's normal biochemical processes, affecting the functioning of antioxidant enzymes, leading to epithelial cell death, elevated lipid peroxidation, and increased levels of free radicals, collectively contributing to cellular membrane damage. Consequently, these factors could have influenced the overall body weight. The findings align with previous studies [57–59].

4.4. Tumor Weight, Volume, Incidence, and Burden

Sprague Dawley rats are commonly employed in DMBA-induced carcinogenesis experiments to induce mammary tumors, with DMBA recognized as an efficient inducer of mammary carcinoma after a single dose administration [60]. In the current study, a single dose of DMBA (25 mg/kg) was administered to 30-day-old Sprague Dawley rats. Tumor weight, volume, incidence, and burden were assessed at the end of the 20th week. A significant decrease ($p < 0.001$) in tumor weight, volume, incidence, and burden was observed in Group VII (DMBA + RME-EnCNPs 500 mg/kg) during this period compared to Group III (DMBA + STD tamoxifen). Standard control tamoxifen, a selective estrogen receptor modulator, inhibits the effects of the reproductive hormone estrogen, which plays a crucial role in the growth and development of various breast cancers [61,62].

Inflammation within the tumor microenvironment is associated with increased invasiveness and poor prognosis in various cancers, including breast cancer. Critical mediators of the inflammatory response include cytokines like interleukin-6 (IL-6), tumor necrosis factor-alpha (TNFα), and interleukin-1 beta (IL-1β). Numerous studies have linked these cytokines to breast cancer progression [63].

4.5. Biochemical Parameters

Given the vital roles of the liver and kidneys in the body, any disturbance in their normal functions can significantly impede various metabolic processes, leading to increased overall body toxicity. The liver, being the primary organ responsible for metabolizing xenobiotic substances, is susceptible to damage from chemical agents. In the present study, the carcinogenic metabolites and reactive oxygen species (ROS) resulting from DMBA metabolism were implicated in liver degradation [64].

The rise in total serum protein concentration observed may be attributed to changes in albumin and other proteins, collectively known as globulins. Alterations in serum albumin concentration are known to occur under conditions of oxidative stress, such as that associated with cancer [64]. The majority of serum proteins produced in the liver serve as biomarkers for liver dysfunction. In this investigation, significantly higher levels of total bilirubin, SGOT, SGPT, and ALP were noted in DMBA-treated animals compared to the control group. These elevated levels indicate DMBA-induced hepatic impairment [65]. SGOT and SGPT are enzymes involved in liver function, and their increase suggests impaired liver function, possibly due to tumor invasion [66]. ALP activity is vital for membrane permeability, molecule transport, protein synthesis, and glycogen metabolism. The significant reduction in these parameters after treatment with RME and RME-EnCNPs (250 and 500 mg/kg) indicates the potential hepatoprotective effect of A. venenata methanolic root extract. Flavonoids present in the extract may contribute to this hepatoprotective activity by aiding in the restoration of damaged liver portions [67,68].

Obesity and high total cholesterol have long been associated with an increased incidence of tumors in breast carcinoma animal models. Cholesterol, susceptible to oxidation, produces more lipid peroxidation products during oxidative stress. Hypercholesterolemia and oxidative stress are subsequent effects of rising cholesterol levels, leading to the activation of cells and the formation of oxygen free radicals [69]. In the present investigation, increased levels of total cholesterol and triglycerides were observed in the DMBA-induced rats (Group II) compared to Groups III to VII. Low HDL-cholesterol levels are often associated with higher estrogen levels in obese or overweight women, representing a significant risk factor for breast cancer [68]. Group II (DMBA- induced breast cancer rats) and Group VII (500 mg/kg of RME-EnCNPs treated) exhibited decreased and increased levels of HDL-cholesterol, respectively, as is consistent with prior investigations [69].

The kidneys, responsible for excreting harmful metabolic waste products, are unable to escape the detrimental effects of DMBA's hazardous metabolic by-products. The present investigation noted significantly higher urea, uric acid, and creatinine levels in the DMBA-treated group compared to the control group, indicative of DMBA-induced renal impairment. However, after the administration of RME and RME-EnCNPs (250 and 500 mg/kg), a significant reduction in urea, uric acid, and creatinine levels was observed. This reduction in serum kidney biomarker levels suggests a renal protective effect of *A. venenata* root methanolic extract. The phenols and flavonoids present in this extract may contribute to the observed renal protective effect by aiding in the regeneration of damaged kidney components [70,71].

4.6. In Vivo Antioxidant Activity

In general, oxidative stress and the production of ROS have been connected to cancer progression. Compared to their normal cells, tumor cells show higher ROS levels and the tight regulation of REDOX homeostasis to maintain a low level of oxidative stress. Conventionally, several antioxidants have been extensively investigated to counteract breast carcinogenesis and tumor advancement as chemopreventive agents [72]. The total protein level in the rats administrated with DMBA was significantly decreased, in comparison with the rats treated with (200 and 500 mg/kg) RME and RME-EnCNPs. Similar results were reported in [73]. SODs use metal ions such as copper (Cu^{2+}), zinc (Zn^{2+}), manganese (Mn^{2+}), or iron (Fe^{2+}) as cofactors for catalyzing the dismutation of superoxide anion to oxygen and hydrogen peroxide. These metalloenzymes present in different compartments of the

eukaryotic and prokaryotic cells and are extremely specific in regulating coupled biological processes [74]. Catalase (CAT) assists the decomposition of hydrogen peroxide to water and oxygen. It is chiefly located in cytosol and the peroxisomes of eukaryotes [75]. GPX is a cytosolic enzyme that catalyzes the breakdown of hydrogen peroxide and organic hydroperoxides [76]. Glutathione also known as GSH is present in the liver and protects cells from oxidative stress by reducing disulfide bonds of cytoplasmic proteins to cysteines [77]. Many studies have indicated that lipid peroxidation may be involved in tumor progression because this process can produce reactive and toxic metabolites. Malondialdehyde (MDA) is one of the important aldehydes of lipid peroxidation, which can react with proteins, DNA, and other biomolecules and modify their structure and function. In recent years, the determination of the MDA of tissues and plasma has been extensively followed in various cancer studies including breast cancer. Several research reports indicate the possibility of a relation between lipid peroxidation and breast cancer [78].

This study explores the therapeutic potential of *A. venenata* root methanolic extract (RME) for counteracting oxidative stress in tumor cells. In rats with DMBA-induced breast cancer, elevated oxidative stress was indicated by increased LPO and decreased levels of antioxidant enzymes. Treatment with RME-EnCNPs (500 mg/kg) significantly reversed these alterations, improving levels of total protein, SOD, catalase, GPx, and GSH, while reducing LPO ($p < 0.001$). The nanoparticles not only enhance the bioavailability and targeted delivery of RME's bioactive compounds but also provide sustained antioxidant effects at the tumor site. By encapsulating RME in chitosan, a biopolymer with natural antioxidant properties, the nanoparticles facilitate continuous reactive oxygen species (ROS) scavenging, helping to neutralize oxidative damage [79–81]. This dual effect—enhanced drug delivery and ROS neutralization—reduced tumor growth and progression, highlighting the potential of RME-EnCNPs as a promising strategy for breast cancer treatment. Our findings supported the common observation that breast malignancies are connected to an increased level of SOD, catalase, GPx, and GSH and a decreased level of MDA [79–81].

4.7. Glycolytic and Non-Glycolytic Enzymes

Hexokinase, catalyzing the first step of glycolysis by phosphorylating glucose with ATP to produce glucose 6-phosphate, has four isoforms (HK1, HK2, HK3, and HK4) expressed in mammalian tissues. Cancer cells typically express high levels of HK2 compared to normal cells [82]. In the current study, DMBA-induced rats exhibited elevated levels of hexokinase, while RME-EnCNPs-treated animals showed reduced levels. Utilizing natural plant-derived secondary metabolites, which regulate glycolysis enzymes, holds promise for cancer treatment. For instance, physciosporin, a potent anticancer lichen compound, downregulates HK2 mRNA expression and inhibits breast cancer cell proliferation [83]. Similarly, morusin (flavonoid) and tanshinone IIA (diterpenoid) inhibit hepatocellular carcinoma and oral squamous cell carcinoma, respectively, with the suppression of HK2 enzyme [84,85].

Aldolase, a ubiquitous cytosolic enzyme in glycolysis, catalyzes the conversion of fructose 1-6-diphosphate to glyceraldehyde 3-phosphate and dihydroxyacetone phosphate. Classified into three groups (ALDOA, ALDOB, and ALDOC), ALDOA has been implicated in promoting tumor growth and metastasis in various cancers. The phosphorylation of ALDOA can enhance glucose metabolism in liver cancer cells, promoting their growth and tumor formation [86,87]. In the current study, aldolase levels were elevated in DMBA-induced rats and decreased in RME-EnCNPs-treated animals.

Glycogen has been linked to cancer cell survival, preventing glycogen breakdown, inducing apoptosis, and promoting early cell senescence in cancer cells. Glucose-6-phosphatase (encoded by G6PC) mediates the final step of gluconeogenesis, and its overexpression has been observed in glioblastomas. Fructose-1,6-bisphosphatase (FBPase), a key enzyme in gluconeogenesis, plays critical roles in tumor initiation and progression. Lower FBPase expression is associated with advanced tumor stages and worse prognoses

in cancer patients [88,89]. In the present study, G6PC and FBPase levels were reduced in DMBA-induced rats and RME-EnCNPs-treated animals.

4.8. Estimation of Mitochondrial TCA Cycle Enzymes

Mitochondria are central to cellular functions, including ATP production, metabolite generation, and the regulation of various cellular processes. They communicate with the cell through mechanisms such as cytochrome c release, AMP-activated protein kinase activation, reactive oxygen species (ROS) generation, and mitochondrial DNA release. Recently, the release of TCA cycle metabolites from mitochondria has been shown to influence cell function, macromolecule biosynthesis, and epigenetic modifications [90].

Key enzymes in the TCA cycle, such as isocitrate dehydrogenase (IDH), succinate dehydrogenase (SDH), and malate dehydrogenase (MDH), play critical roles in cellular metabolism. Mutations in IDH1 and IDH2 are common in cancers like gliomas and acute myeloid leukemia [91]. SDH deficiency is linked to tumor progression, with succinate accumulation stabilizing HIF-1α. Increased SDHA expression has been associated with reduced cell proliferation in ovarian cancer cells [92]. MDH is involved in regenerating cytosolic NAD+, a process essential for cancer cell proliferation [93].

In this study, the activities of TCA cycle enzymes (IDH, SDH, and MDH) were significantly reduced in DMBA-induced breast cancer animals, likely due to alterations in cell morphology, mitochondrial structure, and reduced mitochondrial numbers. This decline may also be related to deficiencies in the electron transport chain. Treatment with RME-EnCNPs led to a significant increase in the activities of these enzymes, suggesting a protective effect of the encapsulated root methanolic extract. These findings align with previous reports by Senthilnathan et al. [94], who observed decreased enzyme activities in lung cancer-bearing animals.

4.9. Estimation of Hematological Parameters

Red blood cell count, hemoglobin levels, and packed cell volume are key markers for anemia, which in cancer patients is associated with an increased risk of cardiovascular events and mortality [95]. Cancer-related anemia can be caused by bleeding, nutritional deficiencies, bone marrow damage, tumor invasion, or the malignancy itself. Low mean corpuscular hemoglobin concentration (MCHC) indicates insufficient hemoglobin in red blood cells [96]. In this study, animals treated with 500 mg/kg RME-EnCNPs showed improved levels of these parameters, while the DMBA-induced mammary tumor-bearing animals exhibited decreased levels. Cell cannibalism, where cancer cells phagocytose their own or other cells (e.g., neutrophils and lymphocytes), is another hallmark of cancer [96]. Low white blood cell (WBC) counts increase infection risk, while elevated WBC counts are linked to invasive breast cancer development [97]. In this study, the DMBA-induced tumor-bearing animals had higher WBC counts and polymorphonuclear cell percentages compared to those treated with RME-EnCNPs. These findings align with previous studies, showing significant decreases in hemoglobin and red blood cell indices, along with increased platelet and WBC counts in the DMBA-induced breast cancer-bearing animals compared to Ficus carica latex-treated groups [98].

4.10. Histological Analysis

The histopathological analysis of mammary tissues from the cancer-bearing animals revealed malignant epithelial cells with hyperchromasia, increased nuclear/cytoplasmic ratio, and pleomorphism. In contrast, animals treated with 500 mg/kg RME-EnCNPs showed the disappearance of tumor cells, with no glandular or acinar structures and areas of marked fibrosis. Examination of liver tissues in the cancer-bearing animals revealed abnormal architecture, with hepatocytes arranged in cords and prominent portal tracts, likely due to carcinogen-induced free radical damage to DNA [99]. In the RME-EnCNPs-treated animals, these changes were resolved, possibly due to the antioxidant properties of

the extract. The treated animals exhibited normal hepatocytes with central vein congestion, suggesting liver protection.

Kidney tissues from the cancer-bearing animals showed glomerular damage and tubular abnormalities, while the RME-EnCNPs-treated animals exhibited normal interstitial morphology, indicating preserved kidney function and detoxification processes [100]. The examination of uterine tissues in the cancer-bearing animals revealed abnormal epithelium and scattered inflammatory infiltrates. In contrast, the RME-EnCNPs-treated animals showed a normal endomyometrium with mild infiltrates.

4.11. Mechanism of Action and Molecular Pathways

The anticancer effects of RME-EnCNPs are likely driven by multiple mechanisms, primarily involving the generation of reactive oxygen species (ROS), which induces oxidative stress and leads to apoptosis in cancer cells. The bioactive compounds in *Alstonia venenata*, including alkaloids and flavonoids, are released from the chitosan nanoparticles in a sustained manner, enhancing the drug's stability, bioavailability, and therapeutic impact. These compounds may also modulate key signaling pathways, such as PI3K/Akt and MAPK/ERK, which are critical for cell survival and proliferation, contributing to tumor growth inhibition. Additionally, mitochondrial dysfunction, indicated by changes in TCA cycle enzyme activities, may further drive the anticancer effects of RME-EnCNPs.

Nanoparticle-based drug delivery systems have gained significant attention in cancer therapy due to their ability to enhance the stability, bioavailability, and targeted delivery of therapeutic agents. Studies by Yang et al. [101] and Zhang et al. [102] have demonstrated that chitosan nanoparticles loaded with anticancer drugs, such as doxorubicin and paclitaxel, significantly improve drug uptake and tumor targeting, resulting in reduced tumor growth and metastasis. These studies suggest that the anticancer effects of nanoparticle-loaded drugs are mediated by molecular mechanisms like ROS generation and apoptosis induction. Additionally, research on plant extracts, including *Alstonia venenata*, supports the notion that natural compounds can target multiple signaling pathways involved in cancer progression. Malik et al. [12] demonstrated that the ethanolic extract of *Alstonia venenata* leaves exhibits anticancer activity. In vitro studies showed cytotoxic effects on DLA, EAC, and normal splenocytes. The tumor-bearing animals treated with 100 mg/kg, 250 mg/kg, and 500 mg/kg doses of the extract had significant increases in survival, with the 500 mg dose extending lifespan by 30.79%. The results also indicated tumor growth inhibition, as reflected in changes in body weight, consistent with the findings in our study, where RME-EnCNPs effectively inhibited tumor growth and improved antioxidant activity [10–12].

Our results further align with studies on herbal extract-loaded nanoparticles, such as Patil et al. [101], who reported enhanced bioavailability and sustained drug release using chitosan nanoparticles. The diffusion-controlled release mechanism observed for RME-EnCNPs, as described by the Higuchi model, highlights the potential of chitosan-based systems for controlled, prolonged therapeutic effects. The anticancer activity of RME-EnCNPs likely involves a combination of ROS-induced oxidative stress, mitochondrial dysfunction, and the modulation of key signaling pathways like PI3K/Akt and MAPK/ERK. These findings underscore the advantages of the nanoparticle-mediated delivery of herbal extracts over conventional drug formulations, offering improved therapeutic outcomes with targeted delivery and reduced toxicity.

5. Conclusions

In this study, we evaluated the chemoprotective potential of RME-loaded chitosan nanoparticles (RME-EnCNPs) against DMBA-induced mammary gland tumors. Treatment with RME-EnCNPs demonstrated a dose-dependent effect, significantly reducing tumor markers, biochemical parameters, antioxidant levels, enzymatic activity, hematological parameters, and histopathological abnormalities. These results suggest that RME-EnCNPs have strong potential for preventing breast cancer.

Furthermore, the study highlights that RME-EnCNPs are more effective than free RME, providing enhanced tumor inhibition and sustained drug release. This positions RME-EnCNPs as a promising, less toxic alternative to conventional chemotherapy. However, to fully realize their clinical potential, further research is required, including toxicity assessments, long-term release studies, and an in-depth exploration of their mechanisms of action. Advanced preclinical models will also be crucial for evaluating the clinical feasibility of RME-EnCNPs.

Author Contributions: Conceptualization, A.J. and K.A.; methodology, A.J.; software, A.J.; validation, A.J., K.A. and G.N.; formal analysis, A.B.; investigation, A.J.; resources, A.J.; data curation, G.N.; writing—original draft preparation, A.J., K.A. and A.R.G.; writing—review and editing, S.S.; visualization, K.T.; supervision, G.N.; project administration, G.N.; funding acquisition, G.N. All authors have read and agreed to the published version of the manuscript.

Funding: This research was funded by RUSA 2.0—BCTRC (Bharathiar Cancer Theranostic Research Centre); Official memorandum (Grant No. BU/RUSA 2.0-BCTRC/2022/R7-R17/2314). K.A. thanks the Foundation to Support the Development of Education, Science and Technology of the State of Mato Grosso do Sul (Proc./No FUNDECT: 336/2022/No.FUNDECT:32338) and the Federal University of Mato Grosso do Sul (Proc. No. 135/2021-UFMS/PROPP/PROGEP) for the visiting professor grant.

Institutional Review Board Statement: The present study's animal experiments were conducted following the ethical guidelines and after obtaining clearance from the Institutional Animal Ethics Committee (IAEC) under IAEC No. KMCRET/ReRc/Ph.D/20/2021.

Informed Consent Statement: Not applicable.

Data Availability Statement: The raw data supporting the conclusions of this article will be made available by the authors on request.

Acknowledgments: We would like to express our gratitude to the Department of Botany, Bharathiar University, for providing the necessary facilities and support throughout the course of this research.

Conflicts of Interest: The authors declare no conflicts of interest.

References

1. Ferlay, J.; Colombet, M.; Soerjomataram, I.; Parkin, D.M.; Piñeros, M.; Znaor, A.; Bray, F.; Global Cancer Observatory: Cancer Today. [Internet] Lyon: International Agency for Research on Cancer. 2018. Available online: https://gco.iarc.fr/today/ (accessed on 1 June 2022).
2. Arnold, M.; Morgan, E.; Rumgay, H.; Mafra, A.; Singh, D.; Laversanne, M.; Vignat, J.; Gralow, J.R.; Cardoso, F.; Siesling, S.; et al. Current and future burden of breast cancer: Global statistics for 2020 and 2040. *Breast* **2022**, *66*, 15–23. [CrossRef] [PubMed]
3. Gullino, P.M.; Pettigrew, H.M.; Grantham, F.H. N-nitrosomethylurea as mammary gland carcinogen in rats. *J. Natl. Cancer Inst.* **1975**, *54*, 401–414. [CrossRef] [PubMed]
4. Anderson, M.E.; Meister, A. Transport and direct utilization of gamma-glutamylcyst (e) ine for glutathione synthesis. *Proc. Natl. Acad. Sci. USA* **1983**, *80*, 707–711. [CrossRef]
5. Mottaghitalab, F.; Farokhi, M.; Fatahi, Y.; Atyabi, F.; Dinarvand, R. New insights into designing hybrid nanoparticles for lung cancer: Diagnosis and treatment. *J. Control. Release* **2019**, *295*, 250–267. [CrossRef] [PubMed]
6. Almeida, P.V.; Shahbazi, M.A.; Mäkilä, E.; Kaasalainen, M.; Salonen, J.; Hirvonen, J.; Santos, H.A. Amine-modified hyaluronic acid-functionalized porous silicon nanoparticles for targeting breast cancer tumors. *Nanoscale* **2014**, *6*, 10377–10387. [CrossRef]
7. Yao, Y.; Zhou, Y.; Liu, L.; Xu, Y.; Chen, Q.; Wang, Y.; Wu, S.; Deng, Y.; Zhang, J.; Shao, A. Nanoparticle-based drug delivery in cancer therapy and its role in overcoming drug resistance. *Front. Mol. Biosci.* **2020**, *7*, 193. [CrossRef]
8. Detsi, A.; Kavetsou, E.; Kostopoulou, I.; Pitterou, I.; Pontillo, A.R.N.; Tzani, A.; Zoumpoulakis, P. Nanosystems for the encapsulation of natural products: The case of chitosan biopolymer as a matrix. *Pharmaceutics* **2020**, *12*, 669. [CrossRef]
9. Pratyush, K.; Misra, C.S.; James, J.; Dev, L.M.; Veettil, A.K.T.; Thankamani, V. Ethnobotanical and pharmacological study of Alstonia (Apocynaceae)—A review. *J. Pharm. Sci. Res.* **2011**, *3*, 1394.
10. Thomas, S.K.; George, R.E.; Kunjumon, M.; Thankamani, V. In-vitro antibacterial profile of Alstoniavenenata R. Br.—A comparative study. *Int. J. Curr. Pharm. Res.* **2015**, *7*, 86–88.
11. Bagheri, G.; Mirzaei, M.; Mehrabi, R.; Sharifi-Rad, J. Cytotoxic and antioxidant activities of Alstoniascholaris, Alstoniavenenata and Moringa oleifera plants from India. *Jundishapur J. Nat. Pharm. Prod.* **2016**, *3*, e31129. [CrossRef]
12. Malik, A.V.; Hedge, K. Evaluation of anti-cancer activity of the extract of Alstoniavenenata (Poison devil tree) leaves. *Int. J. Pharma Chem. Res.* **2018**, *4*, 125–130.

13. Taherian, A.; Esfandiari, N.; Rouhani, S. Breast cancer drug delivery by novel drug- loaded chitosan-coated magnetic nanoparticles. *Cancer Nanotechnol.* **2021**, *2*, 1–20. [CrossRef]
14. Yap, K.M.; Sekar, M.; Fuloria, S.; Wu, Y.S.; Gan, S.H.; Mat Rani, N.N.; Subramaniyan, V.; Kokare, C.; Lum, P.T.; Begum, M.Y.; et al. Drug delivery of natural products through nanocarriers for effective breast cancer therapy: A comprehensive review of literature. *Int. J. Nanosci.* **2021**, *16*, 7891–7941. [CrossRef]
15. Wu, Y.; Yang, W.; Wang, C.; Hu, J.; Fu, S. Chitosan nanoparticles as a novel delivery system forz mmonium glycyrrhizinate. *Int. J. Pharm.* **2005**, *295*, 235–245. [CrossRef]
16. Wani, T.U.; Raza, S.N.; Khan, N.A. Rosmarinic acid loaded chitosan nanoparticles for wound healing in rats. *Int. J. Pharm. Sci. Res.* **2019**, *10*, 1138–1147. [CrossRef]
17. Salim, C.J.; Liu, H.; Kennedy, J.F. Comparative study of the adsorption on chitosan beads of phthalate esters and their degradation products. *Carbohydr. Polym.* **2010**, *81*, 640–644. [CrossRef]
18. Bagyalakshmi, J.; Haritha, H. Green synthesis and characterization of silver nanoparticles using Pterocarpus marsupium and assessment of its in vitro Antidiabetic activity. *Am. J. Adv. Drug Deliv.* **2017**, *5*, 118–130. [CrossRef]
19. Chitravadivu, C.; Manian, S.; Kalaichelvi, K. Qualitative analysis of selected medicinal plants, Tamilnadu, India. *Middle East J. Sci. Res.* **2009**, *4*, 144–146.
20. Manne, B.K.; Denorme, F.; Middleton, E.A.; Portier, I.; Rowley, J.W.; Stubben, C.; Petrey, A.C.; Tolley, N.D.; Guo, L.; Cody, M.; et al. Platelet gene expression and function in patients with COVID-19. *Blood J. Am. Soc. Hemat.* **2020**, *136*, 1317–1329. [CrossRef] [PubMed]
21. Ritger, P.L.; Peppas, N.A. A simple equation for description of solute release II. Fickian and anomalous release from swellable devices. *J. Control. Release* **1987**, *5*, 37–42. [CrossRef]
22. Kaminski, P. The application of FTIR in situ spectroscopy combined with methanol adsorption to the study of mesoporous sieve SBA-15 with cerium-zirconium oxides modified with gold and copper species. *Arab. J. Chem.* **2020**, *13*, 851–862. [CrossRef]
23. OECD. *Annual Report 2001*; OECD Publishing: Paris, France, 2001. [CrossRef]
24. Botham, P.A. Acute systemic toxicity—Prospects for tiered testing strategies. *Toxicol. In Vitro* **2004**, *18*, 227–230. [CrossRef] [PubMed]
25. Hamza, A.A.; Khasawneh, M.A.; Elwy, H.M.; Hassanin, S.O.; Elhabal, S.F.; Fawzi, N.M. *Salvadora persica* attenuates DMBA-induced mammary cancer through downregulation oxidative stress, estrogen receptor expression and proliferation and augmenting apoptosis. *Biomed. Pharmacother.* **2022**, *147*, 112666. [CrossRef]
26. Faustino-Rocha, A.; Oliveira, P.A.; Pinho-Oliveira, J.; Teixeira-Guedes, C.; Soares-Maia, R.; Da Costa, R.G.; Colaco, B.; Pires, M.J.; Colaco, J.; Ferreira, R.; et al. Estimation of rat mammary tumor volume using caliper and ultrasonography measurements. *Lab. Anim.* **2013**, *42*, 217–224. [CrossRef]
27. Shreya, S.; Shekher, A.; Puneet, P.; Prasad, S.B.; Jain, B.P. Haematological and biochemical analysis of blood samples from early and late stage breast cancer patients in India. *Bioinformation* **2023**, *19*, 806. [CrossRef]
28. Lowry, O.; Rosebrough, N.; Farr, A.L. Protein measurement with the Folin phenol reagent. *J. Biol. Chem.* **1951**, *193*, 265–275. [CrossRef]
29. Kakkar, P.; Das, B.; Viswanathan, P.N. A modified spectrophotometric assay of superoxide dismutase. *Indian J. Biochem. Biophys.* **1984**, *21*, 130–132.
30. Sinha, A.K. Colorimetric assay of catalase. *Anal. Biochem.* **1972**, *47*, 389–394. [CrossRef] [PubMed]
31. Rotruck, J.T.; Pope, A.L.; Ganther, H.E.; Swanson, A.B.; Hafeman, D.G.; Hoekstra, W. Selenium: Biochemical role as a component of glutathione peroxidase. *Science* **1973**, *179*, 588–590. [CrossRef]
32. Moron, M.S.; Depierre, J.W.; Mannervik, B. Levels of glutathione, glutathione reductase and glutathione S-transferase activities in rat lung and liver. *Biochim. Biophys. Acta BBA Gen. Subj.* **1979**, *582*, 67–78. [CrossRef]
33. Ohkawa, H.; Ohishi, N.; Yagi, K. Assay for lipid peroxides in animal tissues by thiobarbituric acid reaction. *Anal. Biochem.* **1979**, *92*, 351–358. [CrossRef] [PubMed]
34. Venil, C.K.; Malathi, M.; Devi, P.R.; Ahmad, W.A. Chemo-preventive potential of flexirubin against human breast cancer: An in vitro, in vivo and in silico approach. *Mater. Today Proc.* **2021**, *47*, 2138–2147. [CrossRef]
35. Brandstrup, N.; Kirk, J.E.; Bruni, C. The hexokinase and phosphoglucoisomerase activities of aortic and pulmonary artery tissue in individuals of various ages. *J. Geron.* **1957**, *12*, 166–171. [CrossRef] [PubMed]
36. Gancedo, J.M.; Gancedo, C. Fructose-1, 6-diphosphatase, phosphofructokinase and glucose-6-phosphate dehydrogenase from fermenting and non fermenting yeasts. *Arch. Microbiol.* **1971**, *76*, 132–138. [CrossRef]
37. King, J. The transferases alanine and aspartate tranaminases. *Pract. Clin. Enzymol.* **1965**, *37*, 123–126.
38. Slater, E.C.; Borner, W.D. The effect of fluoride on the succinic oxidase system. *Biochem. J.* **1952**, *52*, 185–196. [CrossRef]
39. Mehler, A.H.; Kobnberg, A.; Gbisolia, S.; Ochoa, S. The enzymatic mechanism of oxidation-redactions between malate or isocitrate and pyravate. *J. Biol. Chem.* **1948**, *74*, 961–977. [CrossRef]
40. Divsalar, B.; Heydari, P.; Habibollah, G.; Kazemi, T.; Baghery, S.; Zeynali, M. Hematological Parameters Changes in Patients with Breast Cancer. *Clin. Lab.* **2021**, *67*, 1832–1840. [CrossRef]
41. Russo, J.; Gusterson, B.A.; Rogers, A.E.; Russo, I.H.; Wellings, S.R.; Van Zwieten, M.J. Comparative study of human and rat mammary tumorigenesis. *Pathol. Rev.* **1990**, *217*, 217–251.

42. Luo, Y.; Wang, Q. Recent development of chitosan-based polyelectrolyte complexes with natural polysaccharides for drug delivery. *Int. J. Biol. Macromol.* **2014**, *64*, 353–367. [CrossRef]
43. Zamora-Mora, V.; Fernández-Gutiérrez, M.; San Román, J.; Díaz, P.D.; Sánchez, M.; Rodríguez, J. Magnetic core–shell chitosan nanoparticles: Rheological characterization and hyperthermia application. *Carbohydr. Polym.* **2014**, *102*, 691–698. [CrossRef] [PubMed]
44. Moraru, C.; Mincea, M.; Menghiu, G.; Iovu, H.; Bârsan, M.; Popa, M. Understanding the factors influencing chitosan-based nanoparticles-protein corona interaction and drug delivery applications. *Molecules* **2020**, *25*, 4758. [CrossRef] [PubMed]
45. Gan, Q.; Wang, T. Chitosan nanoparticle as protein delivery carrier—Systematic examination of fabrication conditions for efficient loading and release. *Colloids Surf. B Biointerfaces* **2007**, *59*, 24–34. [CrossRef]
46. Lai, P.; Daear, W.; Löbenberg, R.; Alvarez, M.; Le, H.; Zhou, W. Overview of the preparation of organic polymeric nanoparticles for drug delivery based on gelatine, chitosan, poly (d, l-lactide-co-glycolic acid) and polyalkylcyanoacrylate. *Colloids Surf. B Biointerfaces* **2014**, *118*, 54–163. [CrossRef]
47. Kain, D.; Kumar, S. Synthesis and characterization of chitosan nanoparticles of *Achillea millefolium* L. and their activities. *F1000Research* **2020**, *9*, 1297. [CrossRef]
48. Khan, M.A.; Zafaryab, M.D.; Mehdi, S.H.; Ahmad, I.; Rizvi, M.M. Characterization and anti-proliferative activity of curcumin loaded chitosan nanoparticles in cervical cancer. *Int. J. Biol. Macromol.* **2019**, *93*, 242–253. [CrossRef]
49. Su, H.; Huang, C.; Liu, Y.; Kong, S.; Wang, J.; Huang, H.; Zhang, B. Preparation and characterization of cinnamomum essential oil–chitosan nanocomposites: Physical, structural, and antioxidant activities. *Processes* **2020**, *8*, 834. [CrossRef]
50. Soltanzadeh, M.; Peighambardoust, S.H.; Ghanbarzadeh, B.; Mohammadi, M.; Lorenzo, J.M. Chitosan nanoparticles as a promising nanomaterial for encapsulation of pomegranate (*Punica granatum* L.) peel extract as a natural source of antioxidants. *Nanomaterials* **2021**, *11*, 1439. [CrossRef]
51. Yang, W.; Fu, J.; Wang, T.; He, N. Chitosan/sodium tripolyphosphate nanoparticles: Preparation, characterization and application as drug carrier. *J. Biomed. Nanotechnol.* **2009**, *5*, 591–595. [CrossRef]
52. Nagaonkar, D.; Gaikwad, S.; Rai, M. Catharanthus roseus leaf extract-synthesized chitosan nanoparticles for controlled in vitro release of chloramphenicol and ketoconazole. *Colloid Polym. Sci.* **2015**, *293*, 1465–1473. [CrossRef]
53. Agarwal, U.P.; Ralph, S.A.; Reiner, R.S.; Hunt, C.G.; Baez, C.; Ibach, R.; Hirth, K.C. Production of high lignin-containing and lignin-free cellulose nanocrystals from wood. *Cellulose* **2018**, *25*, 5791–5805. [CrossRef]
54. Arifin, D.Y.; Lee, L.Y.; Wang, C.H. Mathematical modeling and simulation of drug release from microspheres: Implications to drug delivery systems. *Adv. Drug Deliv. Rev.* **2006**, *58*, 1274–1325. [CrossRef] [PubMed]
55. Ugwah-Oguejiofor, C.J.; Okoli, C.O.; Ugwah, M.O.; Umaru, M.L.; Ogbulie, C.S.; Mshelia, H.E.; Umar, M.; Njan, A.A. Acute and sub-acute toxicity of aqueous extract of aerial parts of Carallumadalzielii NE Brown in mice and rats. *Heliyon* **2019**, *5*, e01179. [CrossRef] [PubMed]
56. Barros, A.C.; Muranaka, E.N.; Mori, L.J.; Pelizon, C.H.; Iriya, K.; Giocondo, G.; Pinotti, J.A. Induction of experimental mammary carcinogenesis in rats with 7, 12- dimethylbenz (a) anthracene. *Rev. Hosp. Clín.* **2004**, *59*, 257–261. [CrossRef]
57. Karnam, K.C.; Ellutla, M.; Bodduluru, L.N.; Kasala, E.R.; Uppulapu, S.K.; Kalyankumarraju, M.; Lahkar, M. Preventive effect of berberine against DMBA- induced breast cancer in female Sprague Dawley rats. *Biomed. Pharmacother.* **2017**, *92*, 207–214. [CrossRef]
58. Rojas-Armas, J.P.; Arroyo-Acevedo, J.L.; Palomino-Pacheco, M.; Herrera-Calderón, O.; Ortiz-Sánchez, J.M.; Rojas-Armas, A.; Calva, J.; Castro-Luna, A.; Hilario-Vargas, J. The essential oil of Cymbopogon citratusstapt and carvacrol: An approach of the antitumor effect on 7, 12-dimethylbenz-[α]-anthracene (DMBA)-induced breast cancer in female rats. *Molecules* **2020**, *25*, 3284. [CrossRef]
59. Akhouri, V.; Kumari, M.; Kumar, A. Therapeutic effect of Aegle marmelos fruit extract against DMBA induced breast cancer in rats. *Sci. Rep.* **2020**, *10*, 18016. [CrossRef]
60. Emam, K.K.; Abdel Fattah, M.E.; El Rayes, S.M.; Hebishy, M.A.; Dessouki, A.A. Assessment of wheat germ oil role in the prevention of induced breast cancer in rats. *ACS Omega* **2022**, *7*, 13942–13952. [CrossRef]
61. Alvarado, A.; Faustino-Rocha, A.I.; Colaco, B.; Oliveira, P.A. Experimental mammary carcinogenesis—Rat models. *Life Sci.* **2017**, *173*, 116–134. [CrossRef]
62. Lopes, A.C.; Cova, T.F.; Pais, A.A.; Pereira, J.L.; Colaço, B.; Cabrita, A.M. Improving discrimination in the grading of rat mammary tumors using two- dimensional mapping of histopathological observations. *Exp. Toxicol. Pathol.* **2014**, *66*, 73–80. [CrossRef]
63. Esquivel-Velázquez, M.; Ostoa-Saloma, P.; Palacios-Arreola, M.I.; Nava-Castro, K.E.; Castro, J.I.; Morales-Montor, J. The role of cytokines in breast cancer development and progression. *J. Interferon Cytokine Res.* **2015**, *35*, 1–16. [CrossRef] [PubMed]
64. Dakrory, A.I.; Fahmy, S.R.; Soliman, A.M.; Mohamed, A.S.; Amer, S.A. Protective and curative effects of the sea cucumber Holothuriaatra extract against DMBA- induced hepatorenal diseases in rats. *Biomed Res. Int.* **2015**, *1*, 563652. [CrossRef]
65. Rajasekaran, C.; Kalaivani, T.; Ramya, S.; Jayakumararaj, R. Studies on hepatoprotective activity of ethanolic extracts of fruit pulp of Aegle *marmelos* (L.). *Corr. J. Pharm. Res.* **2009**, *2*, 1419–1423.
66. Arya, R.K.; Singh, A.; Yadav, N.K.; Cheruvu, S.H.; Hossain, Z.; Meena, S.; Maheshwari, S.; Singh, A.K.; Shahab, U.; Sharma, C.; et al. Anti-breast tumor activity of Eclipta extract in-vitro and in-vivo: Novel evidence of endoplasmic reticulum specific localization of Hsp60 during apoptosis. *Sci. Rep.* **2015**, *5*, 18457. [CrossRef] [PubMed]

67. Kulandaivelu, K.; Mandal, A.K.A. Positive regulation of biochemical parameters by tea polyphenol encapsulated solid lipid nanoparticles at in vitro and in vivo conditions. *IET Nanobiotechnol.* **2016**, *10*, 419–424. [CrossRef]
68. Lavudi, K.; Hemalatha, S.; Kokkanti, R.R.; Harika, G.V.; Patnaik, S. Anti-tumour efficacy of Musa paradisiaca flower extracts on DMBA induced mammary carcinogenesis in female wistar rats. *S. Afr. J. Bot.* **2022**, *151*, 200–207. [CrossRef]
69. Cedó, L.; Reddy, S.T.; Mato, E.; Blanco-Vaca, F.; Escolà-Gil, J.C. HDL and LDL: Potential new players in breast cancer development. *J. Clin. Med.* **2019**, *8*, 853. [CrossRef]
70. Rajakumar, T.; Pugalendhi, P.; Thilagavathi, S. Dose response chemopreventive potential of allyl isothiocyanate against 7, 12-dimethylbenz (a) anthracene induced mammary carcinogenesis in female Sprague-Dawley rats. *Chem. Biol. Interact.* **2015**, *231*, 35–43. [CrossRef]
71. Dwivedi, J.; Singh, M.; Sharma, S.; Sharma, S. Antioxidant and nephroprotective potential of Aegle marmelos leaves extract. *J. Herbs Spices Med. Plants* **2017**, *23*, 363–377. [CrossRef]
72. Griñan-Lison, C.; Blaya-Cánovas, J.L.; López-Tejada, A.; Ávalos-Moreno, M.; Navarro-Ocón, A.; Cara, F.E.; González-González, A.; Lorente, J.A.; Marchal, J.A.; Granados-Principal, S. Antioxidants for the treatment of breast cancer: Are we there yet? *Antioxidants* **2021**, *10*, 205. [CrossRef]
73. Shaban, N.Z.; El-Rashidy, F.H.; Adam, A.H.; Beltagy, D.M.; Ali, A.E.; Abde-Alaziz, A.A.; Talaat, I.M. Anticancer role of mango (*Mangifera indica* L.) peel and seed kernel extracts against 7, 12-dimethylbenz [a] anthracene-induced mammary carcinogenesis in female rats. *Sci. Rep.* **2023**, *13*, 7703. [CrossRef] [PubMed]
74. Copin, J.C.; Gasche, Y.; Chan, P.H. Overexpression of copper/zinc superoxide dismutase does not prevent neonatal lethality in mutant mice that lack manganese superoxide dismutase. *Free Radic. Biol. Med.* **2000**, *28*, 1571–1576. [CrossRef] [PubMed]
75. Hashimoto, F.; Hayash, H. Significance of catalase in peroxisomal fatty acyl-CoA β-oxidation: NADH oxidation by acetoacetyl-CoA and H_2O_2. *J. Biochem.* **1990**, *108*, 426–431. [CrossRef]
76. Brigelius-Flohé, R. Tissue-specific functions of individual glutathione peroxidases. *Free Radic. Biol. Med.* **1999**, *27*, 951–965. [CrossRef] [PubMed]
77. Braidy, N.; Zarka, M.; Jugder, B.E.; Welch, J.; Jayasena, T.; Chan, D.K.; Sachdev, P.; Bridge, W. The precursor to glutathione (GSH), γ-Glutamylcysteine (GGC), can ameliorate oxidative damage and neuroinflammation induced by Aβ40 oligomers in human astrocytes. *Front. Aging Neurosci.* **2019**, *11*, 177. [CrossRef]
78. Hauck, A.K.; Bernlohr, D.A. Oxidative stress and lipotoxicity. *J. Lipid Res.* **2016**, *57*, 1976–1986. [CrossRef]
79. Periyasamy, K.; Baskaran, K.; Ilakkia, A.; Vanitha, K.; Selvaraj, S.; Sakthisekaran, D. Antitumor efficacy of tangeretin by targeting the oxidative stress mediated on 7, 12-dimethylbenz (a) anthracene-induced proliferative breast cancer in Sprague–Dawley rats. *Cancer Chemother. Pharmacol.* **2015**, *75*, 263–272. [CrossRef]
80. Kumar, S.; Nandi, A.; Singh, S. Dll1+ quiescent tumor stem cells drive chemoresistance in breast cancer through NF-κB survival pathway. *Nat. Commun.* **2021**, *12*, 432. [CrossRef]
81. Fotsing, S.I.; Pambe, J.C.; Silihe, K.K.; Yembeau, N.L.; Choupo, A.; Njamen, D.; Pieme, C.A.; Zingue, S. Breast cancer cell growth arrest and chemopreventive effects of Passiflora edulis Sims (Passifloraceae) ethanolic leaves extract on a rat model of mammary carcinoma. *J. Ethnopharmacol.* **2023**, *311*, 116408. [CrossRef]
82. Maleki, N.; Eiteman, M.A. Recent progress in the microbial production of pyruvic acid. *Fermentation* **2017**, *3*, 8. [CrossRef]
83. Zhao, Y.; Chard Dunmall, L.S.; Cheng, Z.; Wang, Y.; Si, L. Natural products targeting glycolysis in cancer. *Front. Pharmacol.* **2022**, *13*, 4610. [CrossRef] [PubMed]
84. Taş, İ.; Varlı, M.; Son, Y.; Han, J.; Kwak, D.; Yang, Y.; Zhou, R.; Gamage, C.D.; Pulat, S.; Park, S.Y.; et al. Physciosporin suppresses mitochondrial respiration, aerobic glycolysis, and tumorigenesis in breast cancer. *Phytomedicine* **2021**, *91*, 153674. [CrossRef] [PubMed]
85. Cho, A.R.; Park, W.Y.; Lee, H.J.; Sim, D.Y.; Im, E.; Park, J.E.; Ahn, C.H.; Shim, B.S.; Kim, S.H. Antitumor effect of morusin via G1 arrest and antiglycolysis by AMPK activation in hepatocellular cancer. *Int. J. Mol. Sci.* **2021**, *22*, 10619. [CrossRef]
86. Saito, Y.; Takasawa, A.; Takasawa, K.; Aoyama, T.; Akimoto, T.; Ota, M.; Magara, K.; Murata, M.; Hirohashi, Y.; Hasegawa, T.; et al. Aldolase A promotes epithelial-mesenchymal transition to increase malignant potentials of cervical adenocarcinoma. *Cancer Sci.* **2020**, *111*, 3071–3081. [CrossRef]
87. Shen, Y.; Xu, J.; Pan, X.; Zhang, Y.; Weng, Y.; Zhou, D.; He, S. LncRNA KCNQ1OT1, sponges miR-34c-5p to promote osteosarcoma growth via ALDOA enhanced aerobic glycolysis. *Cell Death Dis.* **2020**, *11*, 278. [CrossRef]
88. Favaro, E.; Bensaad, K.; Chong, M.G.; Tennant, D.A.; Ferguson, D.J.; Snell, C.; Steers, G.; Turley, H.; Li, J.L.; Günther, U.L.; et al. Glucose utilization via glycogen phosphorylase sustains proliferation and prevents premature senescence in cancer cells. *Cell Metab.* **2012**, *16*, 751–764. [CrossRef] [PubMed]
89. Chen, M.; Zhang, J.; Li, N.; Qian, Z.; Zhu, M.; Li, Q.; Zheng, J.; Wang, X.; Shi, G. Promoter hypermethylation mediated downregulation of FBP1 in human hepatocellular carcinoma and colon cancer. *PLoS ONE* **2011**, *6*, e25564. [CrossRef]
90. Herzig, S.; Shaw, R.J. AMPK: Guardian of metabolism and mitochondrial homeostasis. *Nat. Rev. Mol. Cell Biol.* **2018**, *19*, 121–135. [CrossRef]
91. Ward, P.S.; Patel, J.; Wise, D.R.; Abdel-Wahab, O.; Bennett, B.D.; Coller, H.A.; Cross, J.R.; Fantin, V.R.; Hedvat, C.V.; Perl, A.E.; et al. The common feature of leukemia-associated IDH1 and IDH2 mutations is a neomorphic enzyme activity converting α-ketoglutarate to 2- hydroxyglutarate. *Cancer Cell* **2010**, *17*, 225–234. [CrossRef]

92. Amary, M.F.; Bacsi, K.; Maggiani, F.; Damato, S.; Halai, D.; Berisha, F.; Pollock, R.; O'Donnell, P.; Grigoriadis, A.; Diss, T.; et al. IDH1 and IDH2 mutations are frequent events in central chondrosarcoma and central and periosteal chondromas but not in other mesenchymal tumours. *J. Pathol.* **2011**, *224*, 334–343. [CrossRef]
93. Hanse, E.A.; Ruan, C.; Kachman, M.; Wang, D.; Lowman, X.H.; Kelekar, A. Cytosolic malate dehydrogenase activity helps support glycolysis in actively proliferating cells and cancer. *Oncogene* **2017**, *36*, 3915–3924. [CrossRef] [PubMed]
94. Senthilnathan, P.; Padmavathi, R.; Magesh, V.; Sakthisekaran, D. Modulation of TCA cycle enzymes and electron transport chain systems in experimental lung cancer. *Life Sci.* **2006**, *78*, 1010–1014. [CrossRef] [PubMed]
95. Arika, W.A.; Nyamai, D.W. Hematological markers of in vivo toxicity. *J. Hematol. Thromboembol. Dis.* **2016**, *4*, 2. [CrossRef]
96. Ali, L.O. Study effect of breast cancer on some hematological and biochemical parameters in Babylon Province, Iraq. *J. Pharm. Biol. Sci.* **2014**, *9*, 20–24. [CrossRef]
97. Qu, X.; Zhang, T.; Ma, H.; Sui, P.; Du, J. Lower mean corpuscular hemoglobin concentration is associated with unfavorable prognosis of resected lung cancer. *Future Oncol.* **2014**, *10*, 2149–2159. [CrossRef]
98. Ghandehari, F.; Fatemi, M. The effect of Ficus carica latex on 7, 12-dimethylbenz (a) anthracene-induced breast cancer in rats. *Avicenna J. Phytomed* **2018**, *8*, 286.
99. Ray, R.S.; Roy, S.; Ghosh, S.; Kumar, M.; Chatterjee, M. Suppression of cell proliferation, DNA protein cross-links, and induction of apoptosis by vanadium in chemical rat mammary carcinogenesis. *Biochim. Biophys. Acta BBA Gen. Subj.* **2004**, *1675*, 165–173. [CrossRef]
100. Langeswaran, K.; Selvaraj, J.; Ponnulakshmi, R.; Mathaiyan, M.; Vijayaprakash, S. Protective effect of Kaempferol on biochemical and histopathological changes in mercuric chloride induced nephrotoxicity in experimental rats. *J. Biol. Act. Prod. Nat.* **2018**, *8*, 125–136. [CrossRef]
101. Yang, H.; Sun, A.; Yang, J.; Cheng, H.; Yang, X.; Chen, H.; Huanfei, D.; Falahati, M. Development of doxorubicin-loaded chitosan–heparin nanoparticles with selective anticancer efficacy against gastric cancer cells in vitro through regulation of intrinsic apoptosis pathway. *Arab. J. Chem.* **2021**, *14*, 103266. [CrossRef]
102. Zhang, H.; Xue, Q.; Zhou, Z.; He, N.; Li, S.; Zhao, C. Co-delivery of doxorubicin and hydroxychloroquine via chitosan/alginate nanoparticles for blocking autophagy and enhancing chemotherapy in breast cancer therapy. *Front. Pharmacol.* **2023**, *14*, 1176232. [CrossRef]

Disclaimer/Publisher's Note: The statements, opinions and data contained in all publications are solely those of the individual author(s) and contributor(s) and not of MDPI and/or the editor(s). MDPI and/or the editor(s) disclaim responsibility for any injury to people or property resulting from any ideas, methods, instructions or products referred to in the content.

antioxidants

MDPI

Article

Antioxidant, Antitumoral, Antimicrobial, and Prebiotic Activity of Magnetite Nanoparticles Loaded with Bee Pollen/Bee Bread Extracts and 5-Fluorouracil

Cornelia-Ioana Ilie [1,2], Angela Spoiala [1,2,3], Cristina Chircov [1,2], Georgiana Dolete [1,2,3], Ovidiu-Cristian Oprea [4,5], Bogdan-Stefan Vasile [2,3,4], Simona Adriana Crainiceanu [1], Adrian-Ionut Nicoara [1,2], Ioana Cristina Marinas [6], Miruna Silvia Stan [6,7], Lia-Mara Ditu [6,8,*], Anton Ficai [1,2,4,*] and Eliza Oprea [8]

1 Department of Science and Engineering of Oxide Materials and Nanomaterials, Faculty of Chemical Engineering and Biotechnologies, National University of Science and Technology Politehnica Bucharest, 011061 Bucharest, Romania; cornelia_ioana.ilie@upb.ro (C.-I.I.); angela.spoiala@upb.ro (A.S.); cristina.chircov@upb.ro (C.C.); georgiana.dolete@upb.ro (G.D.); adriana.crainiceanu@upb.ro (S.A.C.); adrian.nicoara@upb.ro (A.-I.N.)
2 National Centre for Micro and Nanomaterials and National Centre for Food Safety, National University of Science and Technology Politehnica Bucharest, 060042 Bucharest, Romania; bogdan.vasile@upb.ro
3 Research Center for Advanced Materials, Products and Processes, National University of Science and Technology Politehnica Bucharest, 060042 Bucharest, Romania
4 Academy of Romanian Scientists, 010719 Bucharest, Romania; ovidiu.oprea@upb.ro
5 Department of Inorganic Chemistry, Physical Chemistry and Electrochemistry, Faculty of Chemical Engineering and Biotechnologies, National University of Science and Technology Politehnica Bucharest, 011061 Bucharest, Romania
6 The Research Institute, University of Bucharest, 050663 Bucharest, Romania; miruna.stan@bio.unibuc.ro (M.S.S.)
7 Department of Biochemistry, Faculty of Biology, University of Bucharest, 050095 Bucharest, Romania
8 Department of Botany and Microbiology, Faculty of Biology, University of Bucharest, 060101 Bucharest, Romania; eliza.oprea@g.unibuc.ro
* Correspondence: lia-mara.ditu@bio.unibuc.ro (L.-M.D.); anton.ficai@upb.ro (A.F.)

Abstract: The gut microbiota dysbiosis that often occurs in cancer therapy requires more efficient treatment options to be developed. In this concern, the present research approach is to develop drug delivery systems based on magnetite nanoparticles (MNPs) as nanocarriers for bioactive compounds. First, MNPs were synthesized through the spraying-assisted coprecipitation method, followed by loading bee pollen or bee bread extracts and an antitumoral drug (5-fluorouracil/5-FU). The loaded-MNPs were morphologically and structurally characterized through transmission electron microscopy (TEM), selected area electron diffraction (SAED), scanning electron microscopy (SEM), X-ray diffraction (XRD), Fourier transform infrared spectroscopy (FT-IR), Dynamic Light Scattering (DLS), and thermogravimetric analysis. UV-Vis spectroscopy was applied to establish the release profiles and antioxidant activity. Furthermore, the antibacterial and antitumoral activity of loaded-MNPs was assessed. The results demonstrate that MNPs with antioxidant, antibacterial, antiproliferative, and prebiotic properties are obtained. Moreover, the data highlight the improvement of 5-FU antibacterial activity by loading on the MNPs' surface and the synergistic effects between the anticancer drug and phenolic compounds (PCs). In addition, the prolonged release behavior of PCs for many hours (70–75 h) after the release of 5-FU from the developed nanocarriers is an advantage, at least from the point of view of the antioxidant activity of PCs. Considering the enhancement of *L. rhamnosus* MF9 growth and antitumoral activity, this study developed promising drug delivery alternatives for colorectal cancer therapy.

Keywords: bee bread; bee pollen; antioxidant; antitumoral and antibacterial agents; drug delivery systems

1. Introduction

Due to its unique structural, electrical, and magnetic properties, metal oxide nanoparticles such as magnetite nanoparticles (MNPs) are given tremendous attention. Over the past few decades, researchers and scientists have studied their applications in memory devices, data storage, water purification, bioprocessing, drug delivery, hyperthermia, magnetic resonance imaging, biosensors, electronic devices, aerospace, etc. [1,2].

Considering various nanoparticle synthesis approaches, chemical coprecipitation is the most used technique for synthesizing MNPs, mainly due to its eco-friendly precursors, cost-effectiveness, and easy procedure [3].

MNPs are used in several biomedical applications, especially for antimicrobial and anticancer therapies [4–7]. Also, due to their properties like precise targeting, low toxicity, biocompatibility, nanometric size, etc., MNPs can be internalized and guided with a magnetic field to the tissue/organ of interest [8,9]. Furthermore, MNPs can be functionalized/loaded with bioactive compounds (like antineoplastic drugs, antibiotics (ATBs), PCs, natural extracts, etc.) to develop multi-target drug delivery systems (DDS) [10–16].

Colorectal cancer (CRC) is a type of malignancy that affects the colon or rectum and, according to the World Health Organization, is the third most frequent cancer worldwide. Mainly, CRC affects older individuals and is the second leading cause of mortality rates, with the highest incidence rate in Australia and Europe [17,18]. It is estimated that in 2040, there will be an increase of 3.2 million new cases and 1.6 million deaths compared to 2020, when approximately 1.9 million new CRC cases and 930,000 deaths were reported [18]. However, gut microbiota dysbiosis may also play a key risk factor in promoting CRC by enhancing bacterial populations that stimulate tumorigenesis/exaggerated immune responses [19–22]. Recent studies suggest a strong correlation between gut microbiota imbalance and mechanisms of colorectal tumorigenesis. Moreover, since patients with CRC present a richness of procarcinogenic taxa (*Fusobacterium* sp., *Bacteroides* sp., *Porphyromonas* sp., and *Escherichia coli)* and less protective taxa, like *Roseburia* sp., gut microbiota may represent an important biomarker [21,23–25].

CRC treatments, such as radiotherapy and chemotherapy, can kill the tumor cells and significantly induce damage to the gut microbiota balance [26]. The related antineoplastic agents for CRC treatment are 5-fluorouracil (5-FU), oxaliplatin, irinotecan, capecitabine, cetuximab, etc., which generate dysbiosis, like diarrhea and intestinal mucositis [26–28]. Likewise, the gut microbiota composition is highly linked to the efficacity of antitumoral agents, and in general, during treatment, patients develop severe drug-resistant infections [29]. Additionally, some ATBs like ceftazidime, cefepime, vancomycin, imipenem, neomycin, and metronidazole diminished the 5-FU efficacity in CRC treatment [30,31]. Furthermore, recent studies have shown that exposure to ATB induces gut dysbiosis that is highly linked to CRC [32–34]. Consequently, current research approaches to developing multi-target systems could potentiate the effectiveness of chemotherapeutics and diminish the adverse effects by combining them with phytochemicals [35].

The adverse effects of antineoplastic agents on the gut can be reduced by using probiotics, prebiotic compounds, antioxidants, symbiotics, and postbiotics as adjuvants in cancer treatment [36]. PCs can represent a prebiotic substrate due to their resistance to host digestion, ability to be metabolized by microorganisms, and stimulation of the probiotic bacteria. Also, they possess antimicrobial, antioxidant, and antitumoral properties [37–40]. Additionally, other phytochemicals, such as carotenoids, organosulfur compounds, alkaloids, etc., present chemopreventive and antitumoral properties [41]. An excellent source rich in prebiotic compounds can be bee pollen (BP) and bee bread (BB), which can significantly stimulate the growth of probiotic bacteria and thus be considered a source of probiotics [42–47].

Antioxidants may act by reducing oxidative stress, modulating inflammation, and improving gut function to alleviate the adverse effects of chemotherapy on the gut microbiota. Some evidence suggests that using antioxidants may help reduce the adverse effects of chemotherapy on the gut microbiota in CRC [48].

Clinical trials in CRC patients have suggested that antioxidants [49–51], probiotics [52], and prebiotic supplements [53,54] may reduce the severity of chemotherapy-induced adverse effects and improve gut microbial diversity.

This study presents the development of magnetite-based drug delivery nanocarriers to improve the antitumoral activity of 5-FU and alleviate the adverse effects against gut microbiota. The MNPs were synthesized through a spray-assisted method and loaded with BP/BB extracts and 5-FU. The BPEs and BBEs were characterized in previous studies [42,43]. First, the loaded-MNPs were morphologically and structurally characterized through physical analysis. The bioactive agents' release behavior was evaluated for 5-FU and PCs, and their antioxidant activity was assessed through three assays. The aim of this research is based on using small concentrations of extracts and 5-FU in order to establish the influence of each bioactive compound and the effects against a selected bacteria with probiotic potential. Furthermore, this study's novelty involves enhancing the inhibitory activity of bacterial adhesion capacity to the inert substratum induced by the synthesized nanocarriers.

2. Materials and Methods

2.1. Materials

Iron chloride (97% reagent grade), sodium hydroxide (≥98%), silver nitrate (≥99.5% purity), 5-FU (≥99.9%, HPLC grade), Folin–Ciocalteu reagent, gallic acid (≥98.0%), sodium carbonate (≥99.5%), 2,2-diphenyl-1-picrylhydrazyl (DPPH), FRAP reagent, $CuCl_2$, neocuproin, Trolox (6-hydroxy-2,5,7,8-tetramethylchroman-2-carboxylic acid), ethanol (≥99.8%), methanol, Nutrient Broth No. 2 (NB), Sabouraud Glucose Agar (Sab) with chloramphenicol, Man-Rogosa-Sharpe (MRS), agar, acetic acid (AcA), and crystal violet (CV), were purchased from Sigma-Aldrich (Darmstadt, Germany). Ammonium iron sulfate crystallized hexahydrate with ≥98% purity was acquired from Roth (Karlsruhe, Germany), and the anhydrous trisodium citrate (99% purity) was from Alfa Aesar (Ward Hill, MA, USA). All chemicals were used without further purification. All strains tested in this paper were provided from the Microorganisms Collection of the Department of Microbiology, Faculty of Biology of the University of Bucharest.

2.2. Synthesis of Magnetic Nanoparticles and Loading with Bioactive Compounds

The Fe_3O_4 NPs stabilized with anhydrous trisodium citrate were synthesized by the spraying-assisted coprecipitation method using ammonium iron sulfate hexahydrate and iron chloride as precursors [55,56]. The obtained Fe_3O_4@citrate magnetic NPs (Figure 1) were dried and characterized to ensure that the obtained NPs presented the desired properties. After that, 1 g of the previously obtained Fe_3O_4@citrate magnetic NPs were loaded with 10 mL hydroethanolic bee pollen/bee bread extracts (BPEs/BBEs) by grinding until the solvent was evaporated. The BPEs and BBEs loaded on the surface of MNPs were previously characterized [42,43], and the samples with the highest concentration of PCs were used in this study. The anticancer drug (5-FU) was first solubilized in ethanol and loaded on the surface of the Fe_3O_4@BPEs/BBEs following the same method. Given that the bioactive compounds' loading method involves grinding the 5-FU/phenolic compound solutions with magnetite powders until the evaporation of the solvent, the drug loading efficiency is maximum [56].

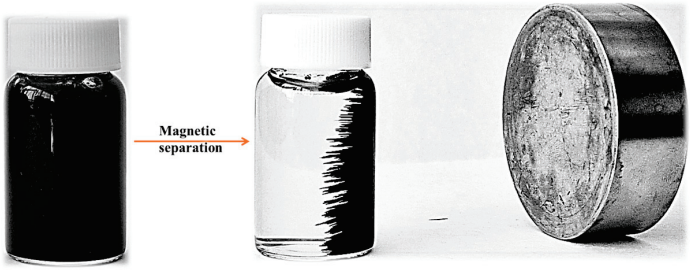


Figure 1. Fe_3O_4@citrate magnetic NPs suspension in water and the magnetic attraction.

2.3. Characterization of the Magnetic-Based Systems

The MNPs loaded with bioactive compounds were characterized using specific analysis that ensured the establishment of specific properties.

Transmission Electron Microscopy (TEM) and High-Resolution TEM (HR-TEM) images and SAED pattern were acquired on a high-resolution 80–200 TITAN THEMIS transmission microscope (purchased from FEI, Hillsboro, OR, USA). The microscope was equipped with a column EDXS detector and an image corrector, and it was operated in transmission mode at a voltage of 200 kV. In total, 10 μL deionized (DI) water were placed into a 400-mesh lacey carbon-coated copper grid. The size of the NPs was measured with the help of ImageJ software (version 1.8.0, National Institutes of Health, Madison, WI, USA) [4].

X-ray diffraction (XRD) was performed using a Shimadzu XRD-6000 diffractometer (Shimadzu Corporation, Kyoto, Japan) equipped with a Cu Kα radiation source. Scans were obtained between 20° and 80° 2θ with an acquisition step of 0.02. The crystallite sizes were calculated using the Scherrer equation.

The magnetic properties of the developed MNPs were evaluated with the vibrating sample magnetometer at 25 ± 2 °C using the 7400 Series VSM equipment manufactured by LakeShore (Lakeshore, CA, USA) [55].

The determination of the size, morphology, and elemental composition of MNPs were assessed using a Quanta Inspect F50 (FEI Company, Eindhoven, The Netherlands) scanning electron microscope equipped with a field emission gun electron (FEG) with 1.2 nm resolution and an Energy Dispersive X-ray spectrometer with a MnK resolution of 133 eV [55].

The Fourier Transform Infrared Spectroscopy (FT-IR) spectra were recorded at room temperature in ATR mode using a Nicolet iS50 spectrometer (Thermo Fischer Scientific, Waltham, MA, USA). The spectrum of each sample is an average of 64 scans, in the 400–4000 cm^{-1} range, at 4 cm^{-1} resolution [57].

Dynamic Light Scattering (DLS) measurements were performed after dispersing 5 mg of the developed MNPs in 15 mL of phosphate-buffer saline (PBS) 1× solution with a pH of 7.4 and dispersed using a Sonorex Digitec DT 514 ultrasonic bath (Bandelin, Berlin, Germany) for 10 min at 25 °C. A small amount of the dispersion was further introduced into the measurement cell and placed inside the DelsaMax Pro equipment (Backman Coulter, Brea, CA, USA). Three measurements were performed for each sample [4].

The thermogravimetric analysis (TG-DSC) was performed with a STA 449 F3 Jupiter equipment from Netzsch (Selb, Germany). About 10 mg of dry powder was placed in an alumina crucible and heated up to 900 °C with a 10 °C min^{-1} rate under a flow of 50 mL min^{-1} of dried air [58].

2.4. Antitumoral Agent Release Behavior

The 5-FU release profile was performed using the dialysis bag method [4,59]. Quantification of 5-FU was performed by plotting a calibration curve in the 0.1–10 μg/mL range. After that, 20 mg MNPs@5-FU 2%, respectively, 40 mg MNPs@5-FU 1%, were placed inside a dialysis bag, followed by immersion in 40 mL PBS 1× (pH = 7.4). The samples were slowly shaken in an orbital motion at 25 rpm for 48 h at 37 °C in a thermoshaker (Gerhardt GmbH & Co., Königswinter, Germany). At different time points, 500 μL of supernatant were collected and replaced with fresh PBS. The measurements were performed at 266 nm wavelength using a Thermo Evolution 600 double-beam UV-Vis Spectrophotometer (Thermo Fisher Scientific, Waltham, MA, USA) and a 1 cm optical path quartz cuvette. The 5-FU concentration was calculated using the calibration curve, and the cumulative release percentage (%) was determined with Equations (1) and (2), when P_{t-1} is the percentage release at the $t-1$ time point, and P_t is the percentage release at the t time point.

$$\text{Drug release}(\%) = \frac{\text{amount of drug in release medium}}{\text{amount of drug loaded on MNPs}} \times 100 \quad (1)$$

$$Cumulative\ drug\ release\ (\%) = \frac{volume\ of\ sample\ withdrawn}{volume\ of\ release\ medium} \times P_{t-1} + P_t \quad (2)$$

Table 1 presents the mathematical models that were performed to study the release kinetics of the 5-FU-loaded MNPs [60,61].

Table 1. Release kinetics models applied.

Release Kinetic	Equation
Zero-order	$C_t = C_0 + k_0 \cdot t$
First-order kinetics	$logC_t = logC_0 - k_1 \cdot \frac{t}{2.303}$
Higuchi model	$C_t = k_H \cdot t^{1/2}$
Hixson–Crowell model	$C_0^{1/3} - C_t^{1/3} = k_{HC} \cdot t$

C_t is the amount of drug released in time (t); C_0 is the initial amount of 5-FU in medium (usually is 0); k_0, k_1, k_H, and k_{HC} are the 5-FU release rate constants.

The drug release data results were performed using Microsoft Excel 365 (Microsoft Corporation, Redmond, OR, USA) and GraphPad Prism 10.2 (San Diego, CA, USA).

2.5. Phenolic Compounds Release Profiles

The PCs' release profile was performed using the dialysis bag method previously described. In total, 40 mg MNP were placed inside a dialysis bag followed by immersion in 40 mL PBS 1× (pH = 7.4), and the samples were slowly orbitally shaken at 25 rpm for 120 h at 37 °C. At different times, 250 µL of supernatant were collected and replaced with fresh PBS. The total phenol content (TPC) was achieved utilizing the Folin-Ciocalteu method [43,62]. A total of 125 µL of sample or standard (gallic acid), 1.25 mL of Folin-Ciocalteu reagent (diluted 10 times in DI), and 1 mL of 1 M of sodium carbonate were homogenized, and the absorbance was measured after 15 min (min) at 746 nm. A calibration curve was plotted with standard solutions of gallic acid with concentrations varying between 0.125 and 6 mg/L (R^2 = 0.9979). TPC was expressed as a cumulative percentage using Equations (1) and (2). Furthermore, the previously described mathematical models (Table 1) were performed to study the release kinetics of PCs.

2.6. Antioxidant Activity

2.6.1. Determination of Free-Radical Scavenging Capacity (DPPH)

Free radical scavenging activity of loaded MNPs was performed by using a spectrophotometric analysis [13,63]. DPPH (7 mg) was used as a free radical, which was dissolved in ethanol (30 mL) and vortexed until solubilization. Several concentrations of MNPs (1.25–10 mg/mL) were diluted in DI water, and in a 96-well plate were added 20 µL of MNPs suspension and 180 µL DPPH solution. The plate was incubated for 30 min in the dark, and spectrophotometric measurements were performed at 518 nm. Also, the DPPH assay was performed for extracts (20 µL BPEs/BBEs were mixed with 180 µL DPPH solution and performed the same method previously described). The experiment was performed in triplicate, and the percent of DPPH inhibition was calculated using Equation (3).

$$\text{DPPH Inhibition}(\%) = \frac{\text{A} - \text{B}}{\text{A}} \times 100 \quad (3)$$

A is represented by the absorbance of the oxidized solution in the absence of antioxidant agents (control—DPPH), and B is the absorbance of the oxidized solution in the presence of antioxidant agents. The concentration required to inhibit 50% of the DPPH radical (IC_{50}) was assessed using linear regression acquired using the plotting concentration vs DPPH inhibition (%).

2.6.2. Ferric Reducing Antioxidant Power (FRAP) Method

The reaction mixture included 50 µL of sample/standard and 950 µL of FRAP reagent [64]. A UV-VIS spectrophotometer (Mulsiskan FC instrument, Thermo Scientific,

Waltham, MA, USA) was used to detect the absorbance at λ = 593 nm after 25 min of dark incubation at 37 °C and 5 min of spinning at 7000 rpm. The calibration curve was plotted using 1 mM Trolox stock solution at concentrations ranging from 30 to 250 μM (R^2 = 0.9987).

2.6.3. Cupric Reducing Antioxidant Capacity (CUPRAC) Assay

The reaction mixture included 240 μL of sample/standard solutions of different concentrations, 200 μL $CuCl_2$ (10 mM), 200 μL neocuproin (7.5 mM), and 200 μL ammonium acetate buffer 1 M, pH = 7.00 [65]. After 30 min, the absorbance was measured at 450 nm. The concentrations used for the Trolox calibration curve ranged from 0.125 to 1.5 mM (R^2 = 0.9943).

2.7. Biological Activity of Magnetic-Based Systems

The biological properties of developed DDSs were assessed using standard Gram-positive and Gram-negative bacteria (*Enterococcus faecalis* ATCC 29212, *Staphylococcus aureus* ATCC 25923, *Escherichia coli* ATCC 25922, and *Pseudomonas aeruginosa* ATCC 27853), and a probiotic bacteria (*Lactobacillus rhamnosus* MF9) isolated from newborn feces. A cell viability assay was performed using a cell line specific for CRC (HT-29). To ensure the sterility of the experiments, MNP-based samples were sterilized for 30 min of UV radiation.

2.7.1. Qualitative Evaluation of Antibacterial Activity

The qualitative antibacterial activity was performed using an adapted spot diffusion method, according to the Clinical Laboratory Standards Institute [66,67]. The bacterial suspensions corresponding to 1.5×10^8 CFU/mL were prepared from 24 h cultures on NB with agar media. A stock of MNPs (100 mg/mL) suspension prepared with sterile physiological buffer saline (PBS) was used. Petri plates with NB media were seeded with inoculums, and 20 μL of each sample was spotted. After diffusion, the dishes were incubated at 37 °C for 24 h.

2.7.2. Quantitative Evaluation of Antibacterial Activity

The minimum inhibitory concentration (MIC) assay used an adapted binary serial microdilution standard assessment in NB medium [66]. In a 96-well plate, for each MNP sample, serial two-fold micro-dilutions were performed in 150 μL of broth medium seeded with the standard inoculum. The plates were incubated at 37 °C for 24 h. Visual and spectrophotometric analyses determined the MIC values by measuring the absorbance at 620 nm using the BIOTEK SYNERGY-HTX ELISA multi-mode reader (Winooski VT, USA) [66].

2.7.3. Semiquantitative Assessment of Microbial Adherence to the Inert Substratum

The biofilm development on the inert substratum was determined using the same serial two-fold microdilution method [66]. After 24 h of incubation and MIC measurements, the media from plates was removed, the walls were washed three times with PBS, and the bacterial cells adhered to the walls were fixed with methanol (5 min) and tinted with 1% CV (15 min). The dyed biofilm was resuspended with 33% AcA, and the absorbance was measured at 490 nm [66].

2.7.4. Evaluation of the Influence of the Magnetic-Based Systems on the Growth of a Microbial Strain with Probiotic Potential

The MNPs influence on the growth of *L. rhamnosus* MF9 was evaluated by following its growth and multiplication for 24 h using bacterial suspension, which corresponded to 1.5×10^8 CFU/mL and was prepared in PBS from fresh culture (24 h) [42]. The influence of MNPs against probiotic bacteria was evaluated in liquid media. In sterilized Eppendorf Safe-Lock tubes were performed binary-serial dilutions from 1000 to 125 μg/mL MNPs, followed by inoculation of *L. rhamnosus* MF9. The volumetric ratio between the volume of inoculated microbial suspension and of the broth media = 1:10. The tubes were incubated

at 37 °C in anaerobic conditions, and the growth was evaluated after 24 h of incubation. Serial dilutions from each sample were inoculated on a MRS agar plate in triplicate, and viable cell counts were assessed after 24 h incubation in anaerobic conditions at 37 °C, and are expressed as CFU/mL. Also, in 96-well plates were transferred 100 µL from tubes, and spectrophotometric measurements were performed at λ = 600 nm. The experiments were performed in triplicate. The results were expressed in percentages and calculated using Equation (4).

$$L.\ rhamnosus\ \text{MF9}(\%) = \frac{\text{A600 sample}}{\text{A600 control}} \times 100 \quad (4)$$

2.7.5. The Antiproliferative Assay

The HT-29 cells were cultured in Dulbecco's Modified Eagle's Medium (Gibco, Boston, MA, USA) supplemented with 10% fetal bovine serum (Gibco, Boston, MA, USA), 100 U/mL penicillin, and 100 µg/mL streptomycin, in a humidified atmosphere (with 5% CO_2) at 37 °C. The culture medium was changed every 2 days until cells reached confluence, and then the cells were detached with 0.25% trypsin–0.53 mM EDTA (Sigma-Aldrich, Darmstadt, Germany). For the experiments, cells were seeded at 5×10^4 cells/cm^2 and left overnight to adhere. Cellular viability was measured using the 3-(4,5-dimethylthiazol-2-yl)-2,5-diphenyltetrazolium bromide (MTT; Sigma-Aldrich, Darmstadt, Germany) assay. At the end of the incubation periods, the culture medium was removed, and the cells were incubated with 1 mg/mL MTT for 2 h at 37 °C. The purple formazan crystals formed in the viable cells were dissolved with 2-propanol (Sigma-Aldrich, Darmstadt, Germany), and the absorbance was measured at 595 nm using a plate multi-reader (FlexStation 3, San Jose, CA, USA) [68]. The cell viability of the samples was calculated using Equation (5).

$$\text{Cell viability}(\%) = \frac{\text{A595 sample}}{\text{A595 control}} \times 100 \quad (5)$$

2.8. Statistical Analysis

The data results were statistically analyzed using GraphPad Prism 10.2 from GraphPad Software (San Diego, CA, USA). The data results are expressed as ±SD (standard deviation) and analyzed using a one-way analysis of variance (one-way ANOVA) and Tukey's/Holm-Šídák's multiple comparisons test. The differences between samples were considered statistically significant when the *p*-value was < 0.05.

3. Results and Discussion

3.1. Magnetic-Based Systems Characterization

In the present study, the synthesized citrate-coated MNPs were first loaded with the BPEs and BBEs, which presented the highest concentration of PCs and antioxidant and antimicrobial properties determined previously [42,43]. Additionally, an antitumoral agent (5-FU) was loaded on the surface of Fe_3O_4@BPE and Fe_3O_4@BBE NPs to alleviate the adverse effects on the gut microbiota. In this approach, the developed nanocarriers were characterized using TEM, SEM, EDX, XRD, VSM, FT-IR, DLS, and thermal analyses.

3.1.1. Transmission Electron Microscopy

The morphology of the citrate-coated MNPs was evaluated using the TEM, HR-TEM, and SAED assessments (Figure 2). As can be observed, the NPs have a quasi-spherical shape and possess an increased tendency to agglomerate, probably due to the magnetic dipole moment interaction between particles. Moreover, these images were used to determine the size distributions of the MNPs. The distributions are considerably narrow, suggesting that the size of the MNPs is between 5 and 10 nm (average size particle of 7.0 ± 2 nm), which could further demonstrate their usability in the desired/targeted applications. Furthermore, the SAED results confirm that the patterns are linked with the Miller indices characteristic for Fe_3O_4 [69,70].

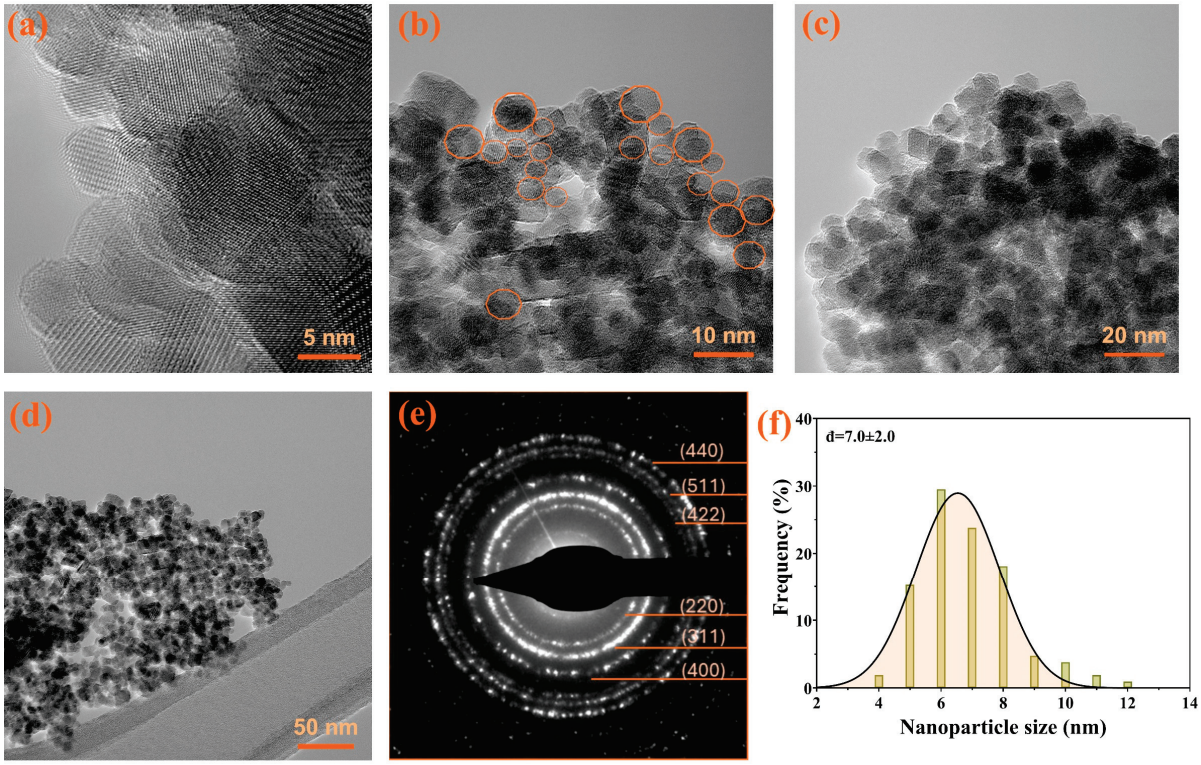


Figure 2. The TEM images, SAED pattern, and size distribution for citrate-coated Fe_3O_4 NPs. (**a**–**d**) HR-TEM, (**e**) SAED patterns, (**f**) size distributions. The quasi-spherical shapes were marked with orange circles in figure (**b**).

3.1.2. Scanning Electron Microscopy and Energy Dispersive X-ray Assay

The citrate-coated MNPs present a quasi-spherical shape with diameters less than 10 nm, and possess a tendency to agglomerate, probably due to the magnetic dipole moment interaction between particles (Figure 3). EDX confirms the stabilization of Fe_3O_4 NPs with citrate by the presence of the additional element on the MNPs' surface (C). Also, it is important to mention that the citrate shell leads to an overall negative charge (see also DLS data in Section 3.1.7) of the MNPs, while Na is present only in a small amount.

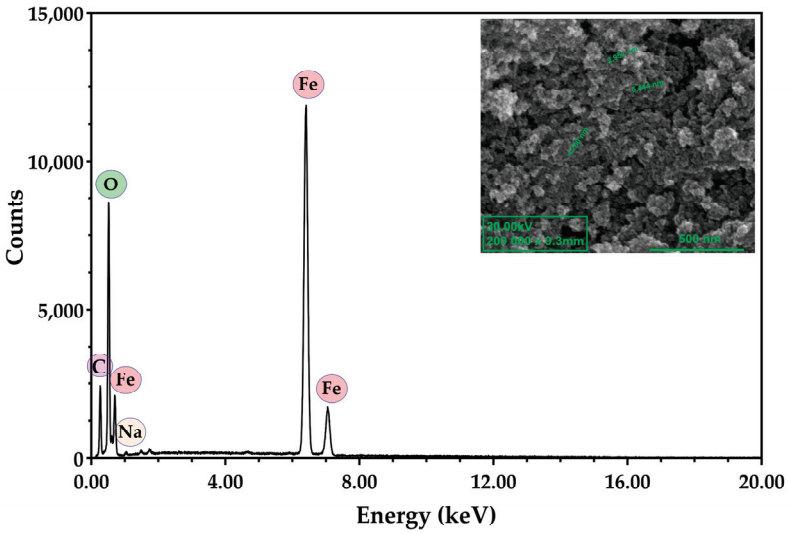


Figure 3. Representative SEM image and EDX analysis for citrate-coated Fe_3O_4 NPs.

3.1.3. VSM Analysis

The analysis of the degree of the magnetization indicates the characteristic magnetization curve that corresponds to citrate-coated MNPs (Figure 4).

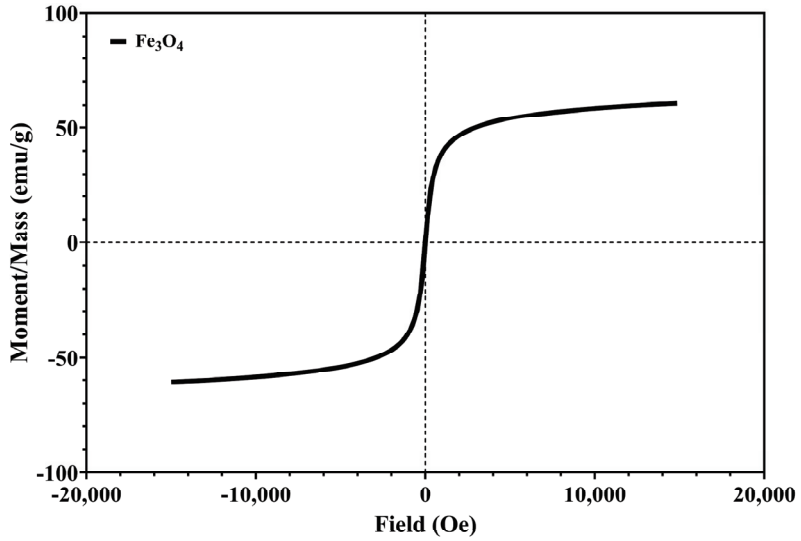


Figure 4. The magnetization/mass ratio for citrate-coated Fe_3O_4 NPs.

Figure 4 presents a symmetric hysteresis curve, and indicates the superparamagnetic behavior of citrate-coated MNPs. The coercivity (Hci) of the citrate-coated MNPs is 13.639 Oe and saturation magnetization (Ms) is 60.506 emu/g, which are correlated with other research with similar synthesis [71,72]. The Ms of bulk magnetite is around 90 emu/g, and a lower value is attributed to the small particle size effect and the sodium citrate layer [72].

3.1.4. X-ray Diffraction

The structure of the obtained nanocarriers was determined using X-ray diffraction, which confirmed the cubic structure of MNPs for all samples (Figure 5). Consequently, adding bioactive compounds from extracts and 5-FU does not conduct the formation of secondary iron oxides.

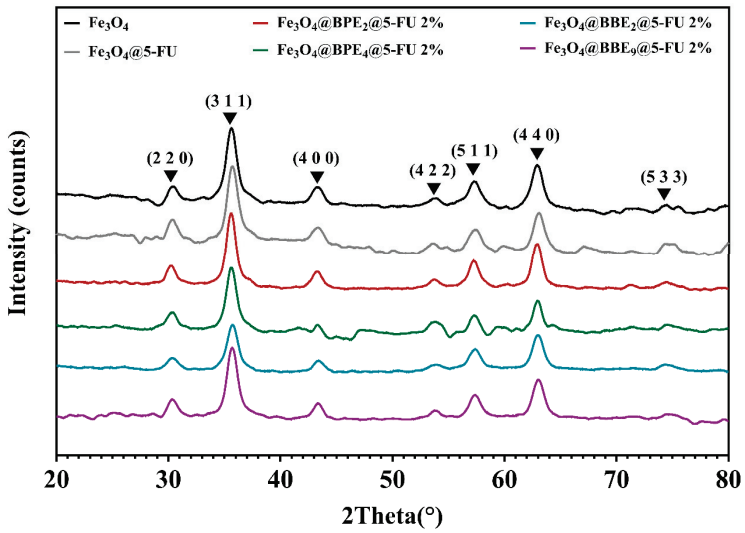


Figure 5. Diffractograms for magnetite and loaded MNPs.

Figure 5 displays the characteristics peaks of tetrahedral and polyhedral magnetite crystals as follows: 30.2°, 35.6°, 43.2°, 53.6°, 57.2°, 63°, and 74.3° [55,73]. Table 2 displays the crystallite size for the obtained MNPs, which are expressed as mean value ± standard deviation (SD).

Table 2. Crystallite size for obtained MNPs.

Sample	Average Crystallite Size ± SD (nm)
Fe_3O_4	7.05 ± 1.09
Fe_3O_4@5-FU 2%	6.52 ± 0.77
Fe_3O_4@BPE_2@5-FU 2%	7.29 ± 0.71
Fe_3O_4@BPE_4@5-FU 2%	8.31 ± 2.49
Fe_3O_4@BBE_2@5-FU 2%	6.19 ± 0.89
Fe_3O_4@BBE_9@5-FU 2%	6.78 ± 1.30

The crystallite sizes of developed MNPs range from 6.19 ± 0.89 to 8.31 ± 2.49 nm. Based on the presented results, it can be concluded that the ethanol used in the extract preparation and for 5-FU solubilization did not influence the magnetic structure of the MNPs.

3.1.5. FT-IR Spectroscopy

A FT-IR analysis was performed to establish the bonds and functional groups present within the obtained MNPs.

The FT-IR spectrum of the bare Fe_3O_4 sample (Figure 6a) exhibits distinctive peaks consistent with the molecular structure of magnetite (Fe_3O_4). The prominent absorption band at approximately 536 cm^{-1} indicates the Fe–O bond-stretching vibrations, a defining characteristic of magnetite. Moreover, the broad peak centered around 3400 cm^{-1} is attributed to O–H stretching vibrations, likely from absorbed water or hydroxyl groups on the sample's surface. Similar FT-IR patterns of bare Fe_3O_4 have been extensively reported in the literature, including prior studies conducted within our research group [4,55]. Fe_3O_4 NPs coated with BPEs and BBEs similarly displayed the characteristic peaks of Fe–O stretching vibrations at the same wavelengths. Nevertheless, the broad peaks attributed to O–H vibrations shifted to shorter wavenumbers, around 3180 cm^{-1}, and could be ascribed to O–H stretching vibrations from both the extracts and the residual water molecules on the surface of the NPs. By comparison, the respective peaks also changed their shape, becoming more pronounced and broader, possibly because of N-H stretching vibrations present in proteins [74]. Apart from the absorption bands corresponding to magnetite, the spectra are comparable to those obtained in our previous study [43], in which we evaluated bee bread extracts from a chemical and microbiological perspective. Precisely, additional peaks in the coated NPs arise from specific functional groups present in the bee pollen and bee bread extracts, such as at 2917 cm^{-1} and 2847 cm^{-1}, corresponding to the symmetric and asymmetric stretching of C–H groups present in carbohydrates and lipids or the large peak at 1030 cm^{-1} corresponding to C–O and C–OH vibrations in carbohydrates and PCs [75].

Concerning the samples loaded with 5-FU, Figure 6b shows the preservation of the above-mentioned signals, common to magnetite, BP, and BB extracts. Absorption bands at 1264 cm^{-1} and 812 cm^{-1}, corresponding to C–H stretching (in-plane) and C–F stretching in 5-FU [76], were observed in the magnetite sample loaded with the active substance (Fe_3O_4@5-FU). The signals were further distinguished for the drug-loaded samples coated with the extracts, and it was noticeable that the intensity of these bands varied with concentrations, visibly more intense in the case of samples loaded at higher concentrations of 5-FU (2% versus 1%).

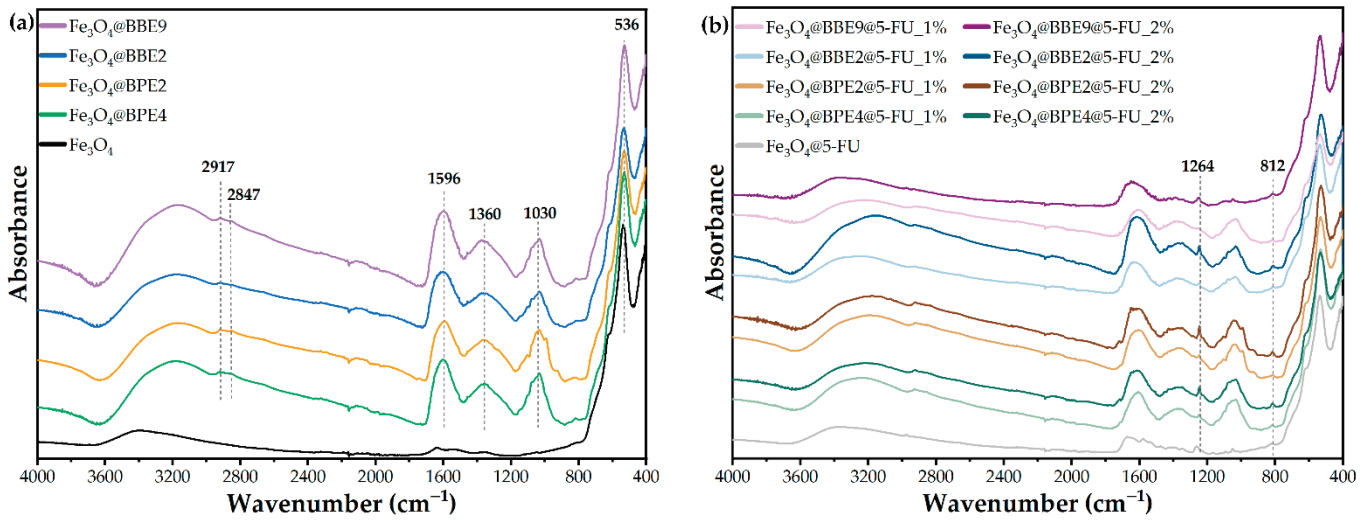


Figure 6. FT-IR spectra for magnetite and loaded MNPs. (**a**) MNPs with extracts and (**b**) MNPs with extracts, and antitumoral drug.

3.1.6. Thermal Analysis

The amount of loaded bioactive compounds was assessed using the TG-DSC assay (Table 3). In all MNP samples, under 200 °C, adsorbed water and volatile molecules are lost, with the associated effect on the DSC curve being endothermic. The organic compounds from bee product extracts loaded on the MNPs start to degrade, mainly by oxidation, after 100–150 °C, and Fe(II) is oxidized to Fe(III) when Fe_3O_4 is transformed to maghemite (γ-Fe_2O_3) [58,77]. The maximum exothermic effect on the DSC curve is around 223.1–233.1 °C, except Fe_3O_4@BBE_9@5-FU 2%, which occurs at 279.6 °C. The asymmetric shape of the effect indicates the existence of multiple oxidative processes up to 400 °C. The phase transformation of maghemite to hematite (α-Fe_2O_3) occurs around 550 °C, as indicated by the corresponding exothermic effect on the DSC curve. The residual mass, reddish-brown, consists of α-Fe_2O_3 [78,79]. The primary data from thermal analysis are presented in Figure 7 and Table 3.

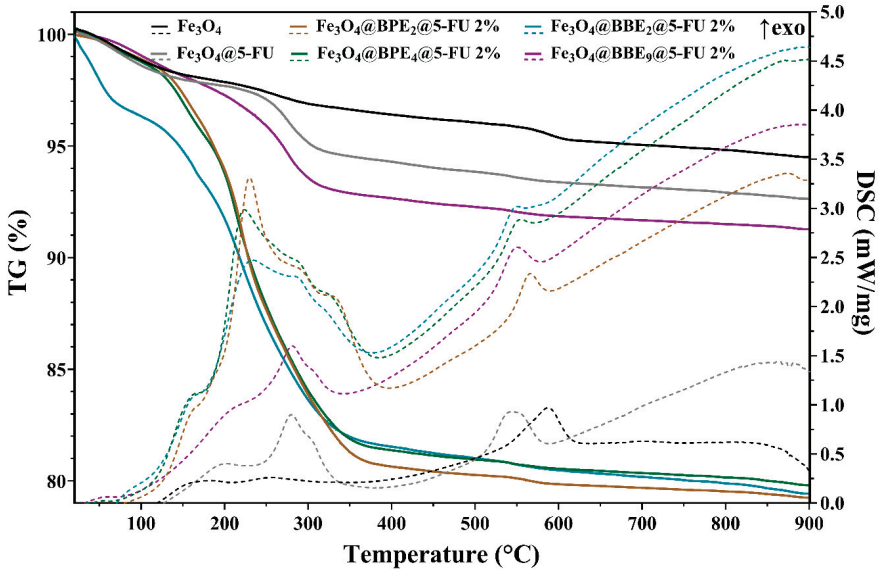


Figure 7. TG-DSC curves for obtained MNPs.

Table 3. The thermal effects, mass loss, and estimated load.

Sample	1st Mass Loss % (Water Loss)	2nd Mass Loss% (Organic Part Oxidation)	Exo (°C) γ-Fe_2O_3 to α-Fe_2O_3	Residual Mass (%) at 900 °C	Estimated Load % (α-Fe_2O_3)
Fe_3O_4	1.87%	1.72%	586.3 °C	94.51%	-
Fe_3O_4@5-FU 2%	2.31%	3.40%	542.6 °C	92.63%	1.99%
Fe_3O_4@BPE_2@5-FU 2%	1.75%	17.60%	565.0 °C	79.24%	16.16%
Fe_3O_4@BPE_4@5-FU 2%	1.98%	16.65%	552.5 °C	79.80%	15.56%
Fe_3O_4@BBE_2@5-FU 2%	3.55%	14.80%	550.7 °C	79.43%	15.96%
Fe_3O_4@BBE_9@5-FU 2%	1.86%	5.47%	549.4 °C	91.27%	3.43%

3.1.7. DLS Assay

The stability of the nanocarriers was evaluated through zeta potential, hydrodynamic diameter, and polydispersity index (PDI) measurements (Figure 8). The hydrodynamic diameter increases when it is loaded with 1% 5-FU, but decreases when it is added with a 2% anticancer agent. It can be assumed that the 5-FU is hydrophilic, and its addition at small concentrations increases the MNPs' hydrophilicity. In contrast, 5-FU overlaps the functional groups from BPEs/BBEs at higher concentrations and decreases the interaction with the solvent (PBS). For this reason, the Fe_3O_4@5-FU 2% sample presented a higher hydrodynamic diameter value. According to the zeta potential values for Fe_3O_4@5-FU 2%, Fe_3O_4@BBE_2@5-FU 1%, and Fe_3O_4@BBE_9@5-FU 1%, and to the higher hydrodynamic diameter, values may be due to the agglomeration of NPs. Considering the PDI values that are lower than 0.6, they indicate a thin/narrow particle distribution. The smaller PDI values indicate the long-term stability and uniformity [80–82].

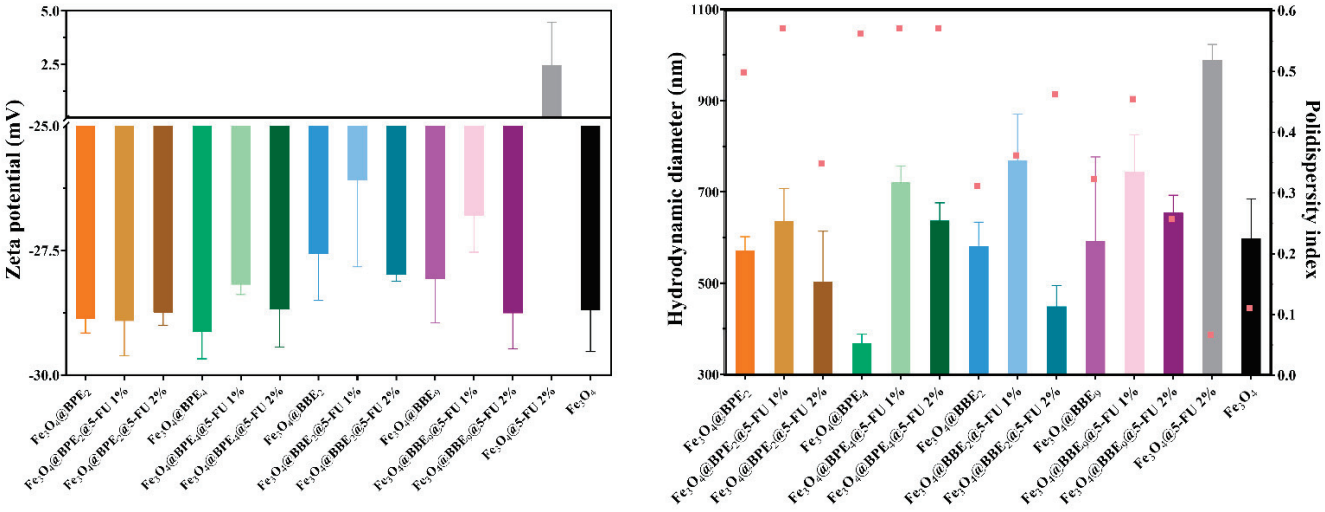


Figure 8. The zeta potential, hydrodynamic diameter (illustrated as columns), and the PDI (illustrated as pink dots) values for obtained MNPs.

3.2. Bioactive Agents' Release Behavior

5-FU, a pyrimidine-antineoplastic agent, inhibits the enzyme thymidylate synthase, deoxyribonucleic acid (DNA), and ribonucleic acid (RNA) synthesis, which may lead rapidly to cell death. According to the Food and Drug Administration (FDA) and the European Medicines Agency (EMEA), 5-FU should be administered intravenously [83,84]. Therefore, the drug and PCs release profiles (Figure 9) were assessed in PBS (pH = 7.4) at 37 °C.

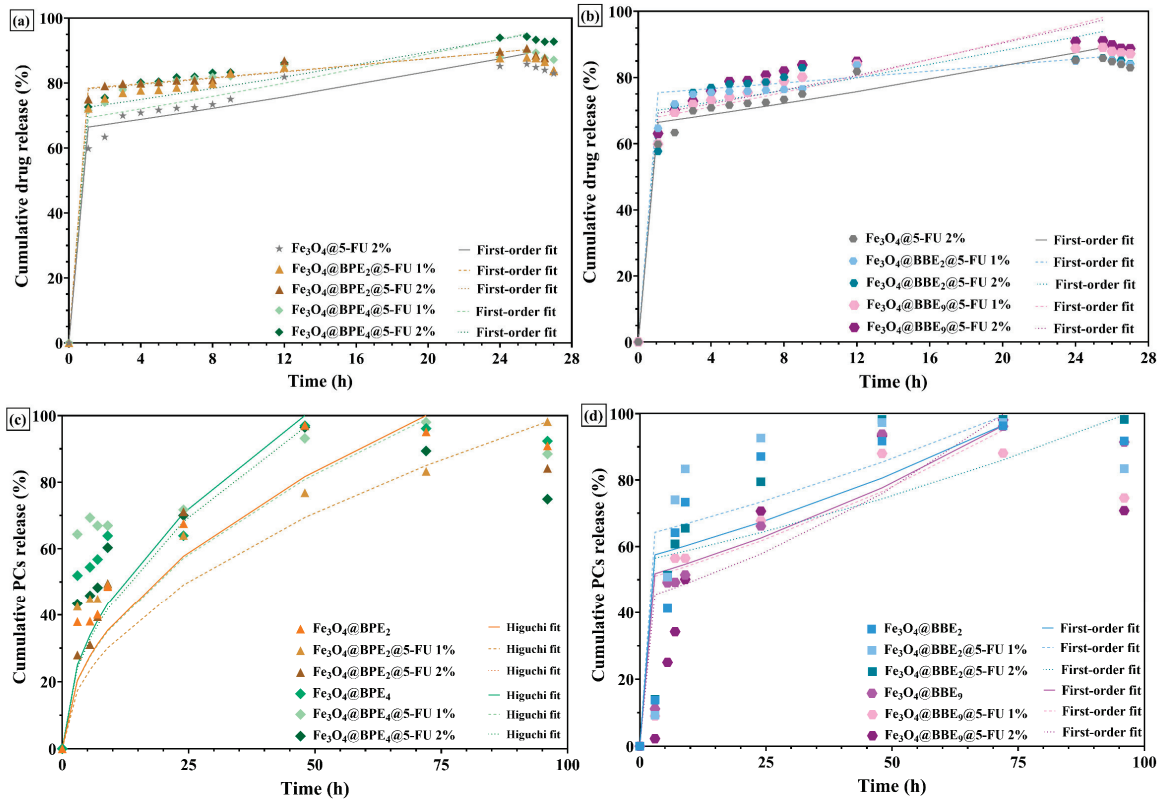


Figure 9. Antitumoral drugs' and PCs' release profiles of nanocarriers loaded with BPEs (**a**,**c**) and BBEs (**b**,**d**).

The 5-FU drug release profiles of nanocarriers loaded with BPEs and BBEs showed that the antitumoral drug releases rapidly in the first hour, but at a lower rate for samples without extracts (Figure 9a,b). Also, it can be observed that in two hours, the 5-FU has a maximum/fast release rate (~75% released), followed by a plateau. The nanocarriers with 5-FU and extracts showed a higher percentage of drug released after 24–25.5 h, and a slower release of drug molecules/degradation can be observed immediately. Likewise, Fe_3O_4@5-FU presented a similar profile/pattern, but with a smaller percentage released. It could be assumed that biomolecules from extracts facilitated the antitumoral drug to release in higher amounts in the first hours, which can be helpful for the death of tumoral cells [85,86]. Conversely, the PCs' release profiles (Figure 9c,d) illustrate similar patterns with prolonged release rates. In both cases, the PCs are gradually released from MNPs, reaching a plateau after 48 h, maintained up to 96 h, followed by a decrease that suggests the PCs' degradation. The higher release time of PCs compared to 5-FU is attributed to the flavonoids in extracts. These results are in agreement with another study [87], which reported similar prolonged release behavior for MNPs with quercetin. Moreover, since the surface of MNPs was firstly loaded with extracts and followed by 5-FU, the loading of the drug did not slow/affect the PCs' release.

In a recent study [60], magnetic nanocomposites were used as carriers for 5-FU and curcumin, and the release percentages for the anticancer drug in PBS ranged from 55 to 59% and 31 to 40% for curcumin in the first 24 h (at 37 °C). The shape of the release curves is similar to those obtained in our study, but the availability of 5-FU in the first 6 h from MNPs is higher. Also, the PCs' release rates are comparable to curcumin profiles, and from our knowledge, there are no literature data to confirm the release profiles of PCs, which are derived from BPEs/BBEs and are loaded on MNPs or another matrix.

Table 4 represents the kinetic parameters of four mathematical models applied to obtain the release data's best-fit mechanism/release profile.

Table 4. Release kinetic parameters.

5-FU Release Kinetics								
Sample	**Zero-Order Release Kinetics**		**First-Order Release Kinetics**		**Higuchi Release Kinetics**		**Hixson–Crowell Release Kinetics**	
	K_0	**R^2**	**K_1**	**R^2**	**K_H**	**R^2**	**K_{HC}**	**R^2**
Fe_3O_4@5-FU 2%	0.8241	0.8450	−0.0361	0.9225	5.2970	0.8670	−0.0323	0.9028
Fe_3O_4@BPE_2@5-FU 1%	0.5260	0.8886	−0.0298	0.9357	3.2880	0.8755	−0.0241	0.9289
Fe_3O_4@BPE_2@5-FU 2%	0.4837	0.8948	−0.0352	0.9521	2.9220	0.8315	−0.0269	0.9461
Fe_3O_4@BPE_4@5-FU 1%	0.5648	0.8433	−0.0341	0.9331	3.6550	0.8958	−0.0270	0.9153
Fe_3O_4@BPE_4@5-FU 2%	0.7443	0.9394	−0.0593	0.9888	4.7380	0.9177	−0.0436	0.9865
Fe_3O_4@BBE_2@5-FU 1%	0.5922	0.7906	−0.0286	0.8699	3.8280	0.8201	−0.0235	0.8606
Fe_3O_4@BBE_2@5-FU 2%	0.6153	0.5265	−0.0287	0.6962	4.2890	0.6641	−0.0235	0.6600
Fe_3O_4@BBE_9@5-FU 1%	0.8436	0.7935	−0.0433	0.9203	5.5080	0.8494	−0.0364	0.8875
Fe_3O_4@BBE_9@5-FU 2%	0.8094	0.7774	−0.0473	0.9213	5.2820	0.8436	−0.0412	0.8853
PCs Release Kinetics								
Sample	**Zero-Order Release Kinetics**		**First-Order Release Kinetics**		**Higuchi Release Kinetics**		**Hixson–Crowell Release Kinetics**	
	K_0	**R^2**	**K_1**	**R^2**	**K_H**	**R^2**	**K_{HC}**	**R^2**
Fe_3O_4@BPE_2	0.9470	0.9001	−0.0460	0.8509	119270	0.9790	−0.0395	0.8891
Fe_3O_4@BPE_2@5-FU 1%	0.6197	0.9482	−0.0186	0.9902	6.8219	0.9905	−0.0197	0.9786
Fe_3O_4@BPE_2@5-FU 2%	1.0660	0.8569	−0.0669	0.9858	11.4270	0.9877	−0.0497	0.9743
Fe_3O_4@BPE_4	0.6904	0.8967	−0.0430	0.8603	7.1410	0.9104	−0.0342	0.8799
Fe_3O_4@BPE_4@5-FU 1%	0.5092	0.9484	−0.0413	0.9545	11.6673	0.9636	−0.0299	0.9625
Fe_3O_4@BPE_4@5-FU 2%	0.7391	0.8316	−0.0332	0.6993	10.1680	0.9676	−0.0298	0.7750
Fe_3O_4@BBE_2	0.8498	0.5559	−0.0400	0.8894	9.6730	0.6837	−0.0347	0.7869
Fe_3O_4@BBE_2@5-FU 1%	0.7960	0.4252	−0.0464	0.7968	12.8670	0.5766	−0.0363	0.6749
Fe_3O_4@BBE_2@5-FU 2%	0.9048	0.6576	−0.0578	0.9191	10.0700	0.7736	−0.0433	0.8800
Fe_3O_4@BBE_9	0.9786	0.7716	−0.0444	0.9570	10.5900	0.8579	−0.0389	0.9252
Fe_3O_4@BBE_9@5-FU 1%	0.8135	0.6334	−0.0266	0.8646	9.0240	0.7399	−0.0270	0.8075
Fe_3O_4@BBE_9@5-FU 2%	1.2150	0.8028	−0.0552	0.9942	13.2500	0.9051	−0.0469	0.9609

The experimental data were subjected to four mathematical models (zero-order, first-order, Higuchi, and the Hixson–Crowell model). The zero-order kinetics describe that the constant release of 5-FU is independent of its concentration, and is considered the ideal model. Still, in our case, the regression coefficient (R^2) values are the smallest. According to Table 4 and the kinetic parameters for each model, the best-fit model for drug release is the first-order model, which is correlated with the hydrophilic molecules. However, the Fe_3O_4@BBE_2@5-FU 1% and Fe_3O_4@BBE_2@5-FU 2%, the R^2 values are less than 0.900, a fact that is unacceptable, and these samples are not suitable for pharmaceutical formulations and in vivo applications.

In the case of the PCs' release kinetics, the MNPs loaded with BPEs are linked to the Higuchi model, which is correlated to low solubility in the solid matrix, respectively, to a layer on the surface of the MNPs that prevents the release of the PCs rapidly over time [88]. Otherwise, the highest R^2 values of MNPs loaded with BBEs are associated with the first-order release, but for some samples, such as Fe_3O_4@BBE_2, Fe_3O_4@BBE_2@5-FU 1%, and Fe_3O_4@BBE_9@5-FU 1%, the regression coefficient values for all applied mathematical models are significantly lower.

3.3. Antioxidant Activity

The DPPH assay is a spectrophotometric assessment based on the antioxidants' capability to scavenge the chromogen radical. The formation of reduced DPPH radicals, due to radical reduction by hydrogen atom transfer from antioxidants, induces changes in the color of the solution from violet to light yellow [89]. Different concentrations of MNPs were assessed to establish the antioxidant concentration that scavenges 50% of the initial DPPH

radical, which is known as IC_{50} (Figure 10). The lower IC50 values correspond to higher antioxidant activity [90].

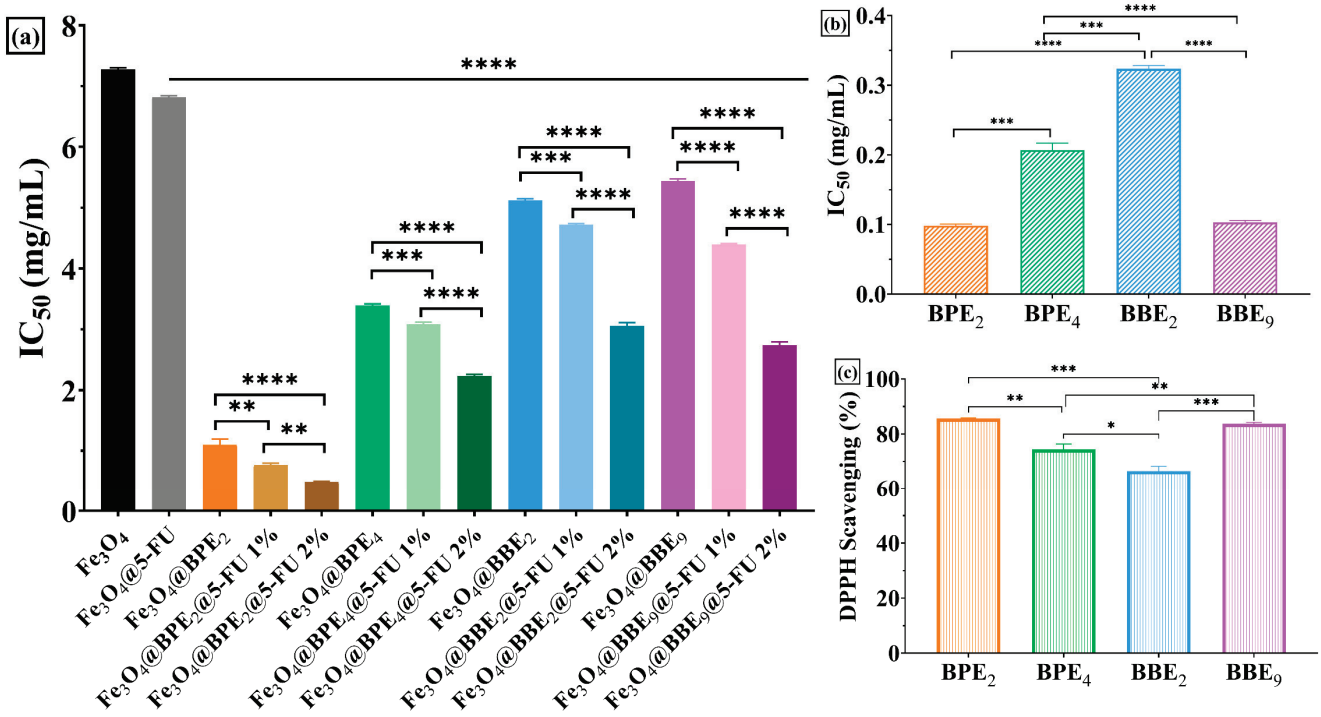


Figure 10. Antioxidant activity of developed MNPs using the DPPH assay. (**a**) IC_{50} values for nanocarriers, (**b**) IC_{50} values for extracts, and (**c**) DPPH% for extracts. The data results are considered statistically significant (* $p < 0.013$, ** $p < 0.07$, *** $p < 0.008$, **** $p < 0.0001$).

The developed MNPs presented the capacity to scavenge the DPPH radical, as expected, considering the previous studies on BPE and BBE antioxidant activity (TEAC method) [42,43]. Figure 10 highlights the lower IC_{50} values for MNPs loaded with BPEs and BBEs than Fe_3O_4@5-FU 2% or Fe_3O_4 samples. Moreover, it can be observed that a significant difference between samples with BPEs and BBEs and smaller IC_{50} values for MNPs loaded with BPE_2 indicate that the obtained nanocarriers are more potent antioxidants that could induce lower toxicity for patients [13]. The data results obtained using the DPPH assay confirmed the antioxidant activity of the extracts (Figure 10b,c), except MNPs loaded with BBE_9, which can scavenge the radical more than Fe_3O_4@5-FU 2%. The lower antioxidant activity for this sample could be explained by smaller amounts of bioactive compounds loaded on the MNPs' surface, according to thermal analysis results (Table 3). Additionally, Figure 10a displayed a decrease in IC_{50} values simultaneously with the concentration of 5-FU loaded on the MNPs, which implies a synergic effect between the antitumoral drug and PCs from extracts. Similar results are reported for Fe_3O_4 loaded with PCs (gallic acid, quercetin, and plant extracts) [13,63,91].

Furthermore, the antioxidant activity of synthesized MNPs was also evaluated using the FRAP and CUPRAC methods. Both the FRAP and CUPRAC assays are methods based on electron transfer (ET). CUPRAC offers different advantages over other ET-based tests, namely working conditions at physiological pH, the ability to quantify both hydrophilic and lipophilic antioxidants, selectivity oxidation of antioxidant compounds without interfering with sugars and citric acid, and it can quantify the SH-class antioxidants [92]. As a principle, the compound Cu(II) bis-neocuproine (Cu(II)Nc) reacts with the donor groups of electrons in the antioxidant molecule, and it is reduced to the complex Cu(I) Bis-neocuproin (Cu(I)NC) (the reduction potential of Cu(II)-NC/Cu(I)-NC is 0.6V) [93].

The antioxidant activity evaluated using the CUPRAC method highlighted that all MNPs with 5-FU 1% showed a better antioxidative activity compared to their coun-

terparts with 5-FU 2% and without the antitumoral agent, respectively, except for the Fe_3O_4@BPE_2@5-FU 1% /Fe_3O_4@BPE_2@5-FU 2% where the differences are insignificant ($p > 0.05$). It can be concluded that as the concentration of 5-FU increases, the antioxidant activity decreases. Among the groups tested, as shown in Figure 11a, the MNPs with BBE_2 showed the weakest activity, following the trend in the extract's activity (Figure 11b). All of the extracts' antioxidant activities were significantly higher than Fe_3O_4@ and Fe_3O_4@5-FU 2% ($p < 0.0001$) (Figure 11a).

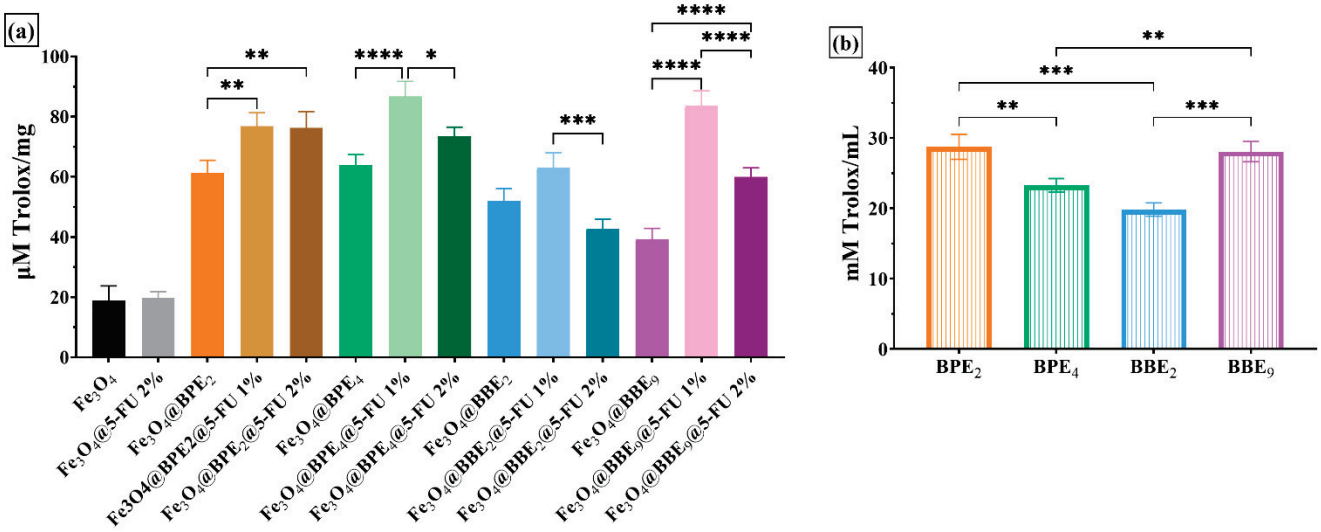


Figure 11. Antioxidant activity of developed MNPs using the CUPRAC assay for nanocarriers (**a**) and extracts (**b**). The data results are considered statistically significant (* $p < 0.05$, ** $p < 0.01$, *** $p < 0.001$, **** $p < 0.0001$).

FRAP evaluates hydrophilic antioxidants resistant to acid pH (pH = 3.6), which are not protein based (proteins precipitate at pH < pI) and do not have thiol groups [94]. In the FRAP method, the ET agent is the Fe^{3+}. The reduction potential of the redox couple Fe^{3+}/Fe^{2+} is 0.771V. At the time of the reaction, the Fe^{2+} ions form with TPTZ, a complex that can react with various oxidable groups [95].

The antioxidant activity evaluated using the FRAP method highlighted the same trend as the CUPRAC method, namely that all MNPs with 5-FU 1% showed a better antioxidant activity compared to their counterparts with 2-FU 2% and without the antitumoral agent, respectively, except for the Fe_3O_4@BPE_2@ 5-FU 1%/Fe_3O_4@BPE_2@5-FU 2%, where Fe_3O_4@BPE_2@5-FU 2% showed a better activity but were statistically insignificant ($p > 0.05$). Among the groups tested, it can be seen from Figure 12a that the group with BBE_2 presents lower activity in accordance with the trend in the extracts' activity (Figure 12b). The best activity was for the BPE_4 sample, although from Figure 12b, the activity was weaker compared to BPE_2 ($p < 0.001$) and BBE_9 ($p < 0.0001$).

Various methods were applied [13,63] to measure the total antioxidant capacity of magnetite nanocarriers, which mainly differ in their chemical reaction for producing different radicals and/or targeting molecules, as well as in measuring endpoints [96].

The combined use of DPPH, FRAP, and CUPRAC methods ensures a comprehensive analysis of the antioxidant capacity, providing detailed and relevant information for various potential applications. Thus, if the first method shows the ability to scavenge DPPH free radicals, CUPRAC details the chelating capacity of copper ions, while FRAP provides data on the metal-reducing capacity of MNPs. Applying these in vitro methods simultaneously closely reflects the in vivo action of MNPs' antioxidant capacity [97].

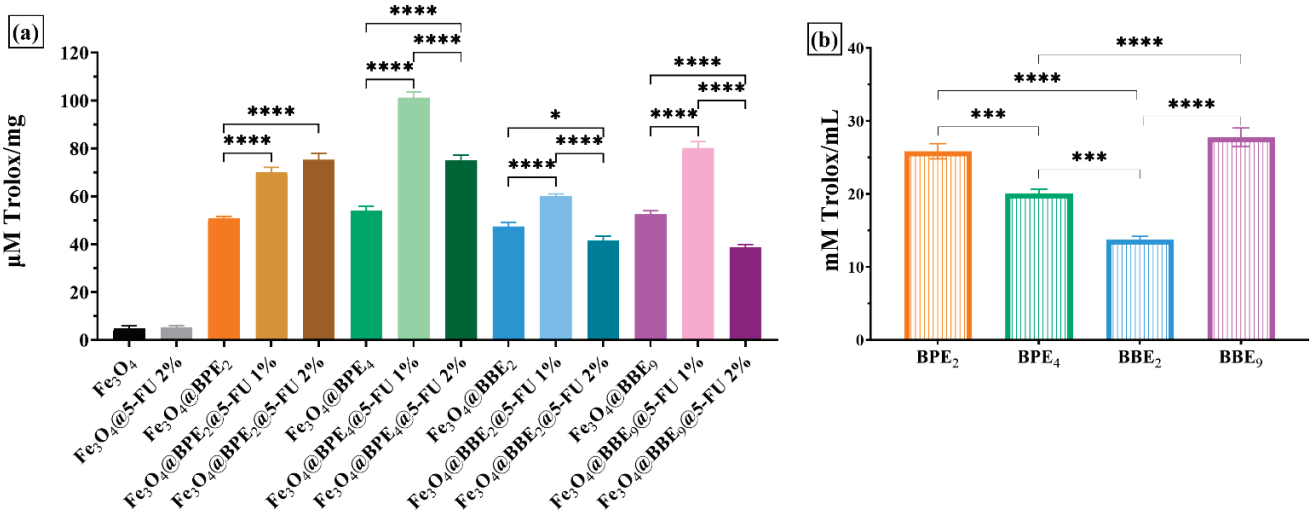


Figure 12. Antioxidant activity of developed MNPs using the FRAP assay for nanocarriers (**a**) and extracts (**b**). The data results are considered statistically significant (* $p < 0.05$, *** $p < 0.001$, **** $p < 0.0001$).

The antioxidant activity of the MNPs with BPE/BBE extracts is linked to the PC profiles previously established by UHPLC-DAD-ESI/MS [42,43]. Thus, BPE_2 contained high amounts of rutin, 4-hydroxybenzoic acid, and ferulic acid, while BPE_4 likewise contained a high content of rutin, chlorogenic acid, quercetin, and kaempferol. The antioxidant activity of BBE_2 and BBE_9 could mainly be attributed to quercetin, kaempferol, isorhamnetin, rutin, resveratrol, and caffeic acid. All PCs present strong antioxidant activity [98,99].

3.4. Antibacterial Activity

3.4.1. Qualitative Assessment

Firstly, the antibacterial properties of based MNPs were qualitatively evaluated by measuring the growth inhibition zone diameters (GIZDs) that developed near the spot, expressing them as mean values ±SD (Figure 13).

The antimicrobial profiles of developed MNPs highlight a significant inhibitory effect on the growth of tested Gram-positive and Gram-negative bacteria **(**Figure 13). The MNPs displayed the highest sensitivity on *E. faecalis*, *S. aureus*, and *E. coli*, followed by *P. aeruginosa*. Overall, the inhibitory effect increased with the quantity of bioactive compounds loaded on the surface of MNPs, and the highest inhibition was obtained for samples with 2% 5-FU. Moreover, the MNPs loaded with BPEs/BBEs and antitumoral drugs determined a higher sensitivity than MNPs loaded only with 5-FU (Fe_3O_4@5-FU 2%), which could be due to a synergistic effect between PCs from extracts and 5-FU. As well, recent research [60] reported the enhancement of the antibacterial activity of MNPs with 5-FU by adding curcumin.

The highest antibacterial activity on Gram-positive bacteria was for MNPs loaded with BPE_4, followed by BBE_9 and BPE_2. Also, the MNPs with BBE_2 presented significant inhibitory effects/properties. In the case of *E. coli* and *P. aeruginosa*, the MNPs showed similar antimicrobial profiles, but MNPs loaded with BPE_2 determined the highest sensitivity. The antibacterial activity of BPE-loaded MNPs is confirmed by the inhibitory effect of the extracts on the tested strains. *E. coli* and *P. aeruginosa* were the most sensitive strains on the influence of BPE_2, and likewise, *S. aureus* on BPE_4 [42]. Also, BBE_2 and BBE_9 presented higher GIZD values on Gram-positive and Gram-negative bacteria [43].

Gram-negative bacteria are more resistant to ATBs than Gram-positive bacteria due to their outer membrane [100], but iron oxide NPs can penetrate the outer and inner membrane of the cell wall due to the reactive oxidative species' (ROS) generation/excessive production, capacity to break mercapto, amino, and carboxyl groups of proteins, and inhibition of DNA replication [101]. In a research [102], various concentrations of Fe_3O_4 NPs (25–100 μg/mL) determined a significant inhibitory effect on *E. coli* and *Proteus vulgaris*,

with GIZD ranging from 11 to 21 mm. The MNPs have 33–40 nm size, and also inhibited *S. aureus* and *Xanthomonas* (8–11 mm).

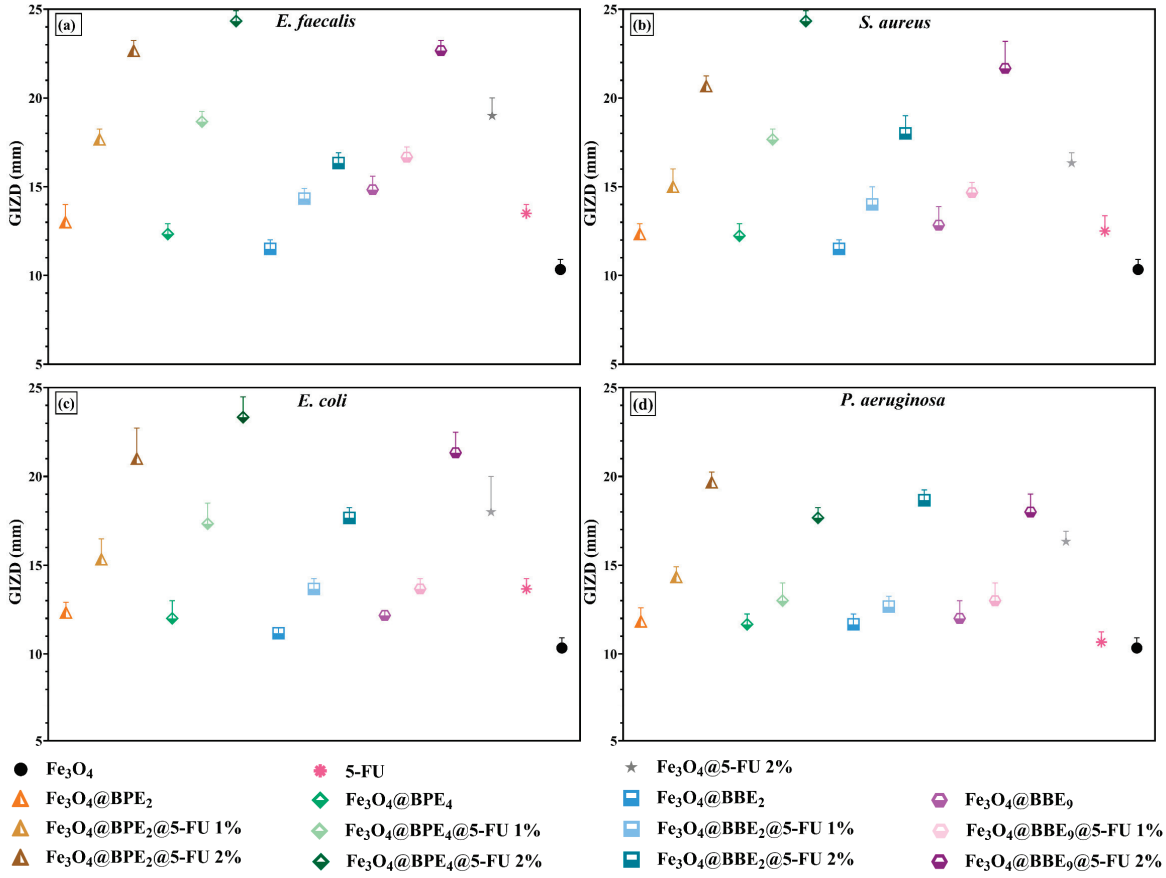


Figure 13. The representation of GIZDs: (**a**) *E. faecalis*, (**b**) *S. aureus*, (**c**) *E. coli*, and (**d**) *P. aeruginosa*. The differences between MNPs were statistically analyzed using the one-way ANOVA followed by Tukey's multiple comparisons tests, and the data were considered statistically significant.

3.4.2. Minimum Inhibitory Concentration Assay

Secondly, the qualitative antimicrobial assessment was continued using a qualitative assay by determining the MIC values (Figure 14), which are characterized by the smallest concentration of obtained MNPs that inhibit microbial growth.

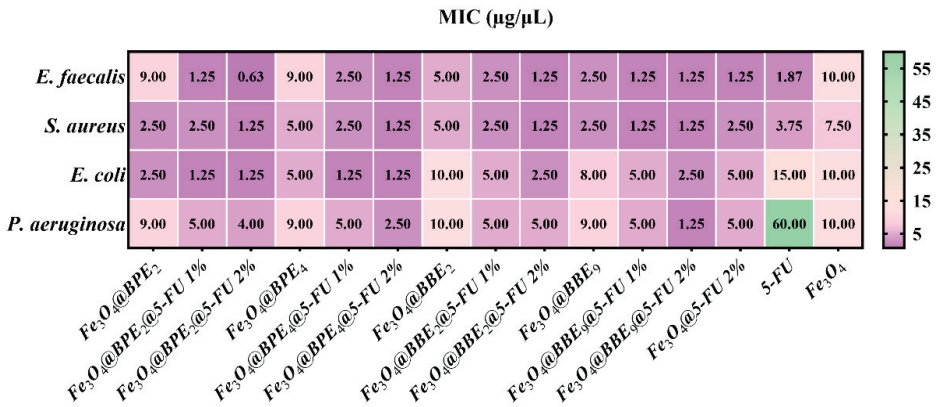


Figure 14. Heat map of MIC values. Data results marked in intense purple indicate the significantly lowest MIC values and highest sensitivity of strains. The scale bar shows the variations in the sensitivity of tested strains from the highest (purple) to the lowest (green).

The MIC assay confirmed the qualitative data, and the most sensitive strains were represented by Gram-positive bacteria. In the case of Gram-negative bacteria, the MNPs loaded with BPEs determined the highest sensitivity for *E. coli*. In contrast, MNPs with BBEs presented moderate inhibition of Gram-negative bacteria, and *P. aeruginosa* was the most resistant. Additionally, for most of the MNPs, the MIC values were lower than Fe_3O_4@5-FU 2% and 2% 5-FU. The addition of extracts significantly inhibited the development of the strains, which can be explained by the antioxidant activity of the BPEs and BBEs, and by the PCs' release behavior.

The lowest MIC value was obtained for Fe_3O_4@BPE_2@5-FU 2% (0.625 μg/mL) on *E. faecalis*. Also, the smallest MIC values were obtained for Fe_3O_4@BPE_4@5-FU 2% and Fe_3O_4@BPE_9@5-FU 2%, which range from 1.25 to 2.5 μg/mL for all strains. In contrast, the antitumoral drug determined less sensitivity of Gram-positive and Gram-negative bacteria than most MNPs. It is notable that at MIC of 0.625 μg/mL MNP, the contain of 5-FU is 0.012 μg/mL, which means a strong antibacterial activity of the drug when loaded on the MNP surface. The reduction of 5-FU dosage can possibly be improved due to the small dimensions of the synthesized MNPs (<10 nm), drug delivery efficiency (Figure 9), and antioxidant activity (Figures 10–12) [103–105]. Likewise, according to the IC_{50} values (Figure 10), a smaller quantity of MNPs is necessary to scavenge the DPPH radical, corresponding to the greatest antioxidant activity and significant inhibitory effects. Furthermore, a recent paper confirms our results regarding the antibacterial activity of the drug, and reported that MIC values for 5-FU are 2 μg/mL for *S. aureus* ATCC 25923, 16 μg/mL for *E. coli*, and 256 μg/mL for *P. aeruginosa* [106].

Otherwise, Spulber et al. [107] reported that Fe_3O_4 functionalized with *p*-aminobenzoic acid and BPEs with irregular shapes and 40–60 nm sizes exhibited inhibitory effects on *S. aureus* ATCC 29213 (MIC: 120–500 μg/mL), *E. faecalis* ATCC 29212 (250–500 μg/mL), *E. coli* ATCC ATCC 25922 (120–500 μg/mL), and *P. aeruginosa* ATCC 27853 (250–500 μg/mL). From our knowledge, there are no references to compare our results regarding the positive impact of MNPs on the antibacterial properties of antineoplastic agents, especially the synergic effects between extracts, 5-FU, and MNPs.

3.4.3. Semiquantitative Assay of the Bacterial Adherence to the Inert Substratum

Additionally, the influence of loaded MNPs on the pathogenic strains' adherence to the inert substratum was assessed. The minimal biofilm eradication concentration (MBEC) values are graphically represented in Figure 15.

The antibiofilm data confirms the qualitative (Figure 13) and quantitative/MIC results (Figure 14). Therefore, *S. aureus* and *E. faecalis* were the most sensitive strains in the presence of developed MNPs. Likewise, loaded MNPs significantly inhibited the adherence of *E. coli* and had moderate activity on *P. aeruginosa*.

The BPE-loaded MNPs presented similar antibacterial profiles, and the strongest antibiofilm activity was exhibited by MNPs loaded with BPE_4. The antibacterial activity of MNPs loaded with BPEs could be explained by the higher phenolic and flavonoid content and the greatest antioxidant activity. Moreover, PCs show inhibitory effects and induce a disturbance in biofilm development and architecture [108,109]. Otherwise, the MNPs trigger oxidative stress and cell lysis with ROS production, affecting H^+-fluxes through the bacterial membrane, DNA and ribosomal damage, inactivation of enzymes, and disrupting the cytoplasm and cell membrane [110–112]. Also, small sizes, long-term stability, and uniformity of the developed nanocarriers enable them to transport bioactive compounds to targeted tissues and penetrate the biofilms [113]. Regarding these MNPs' properties, it could be explained as the improvement of 5-FU anti-adherence activity. However, according to our knowledge, there are no reference data to compare our results on the enhancement of 5-FU antibacterial activity when is loaded on the MNPs' surface with BPEs or BBEs.

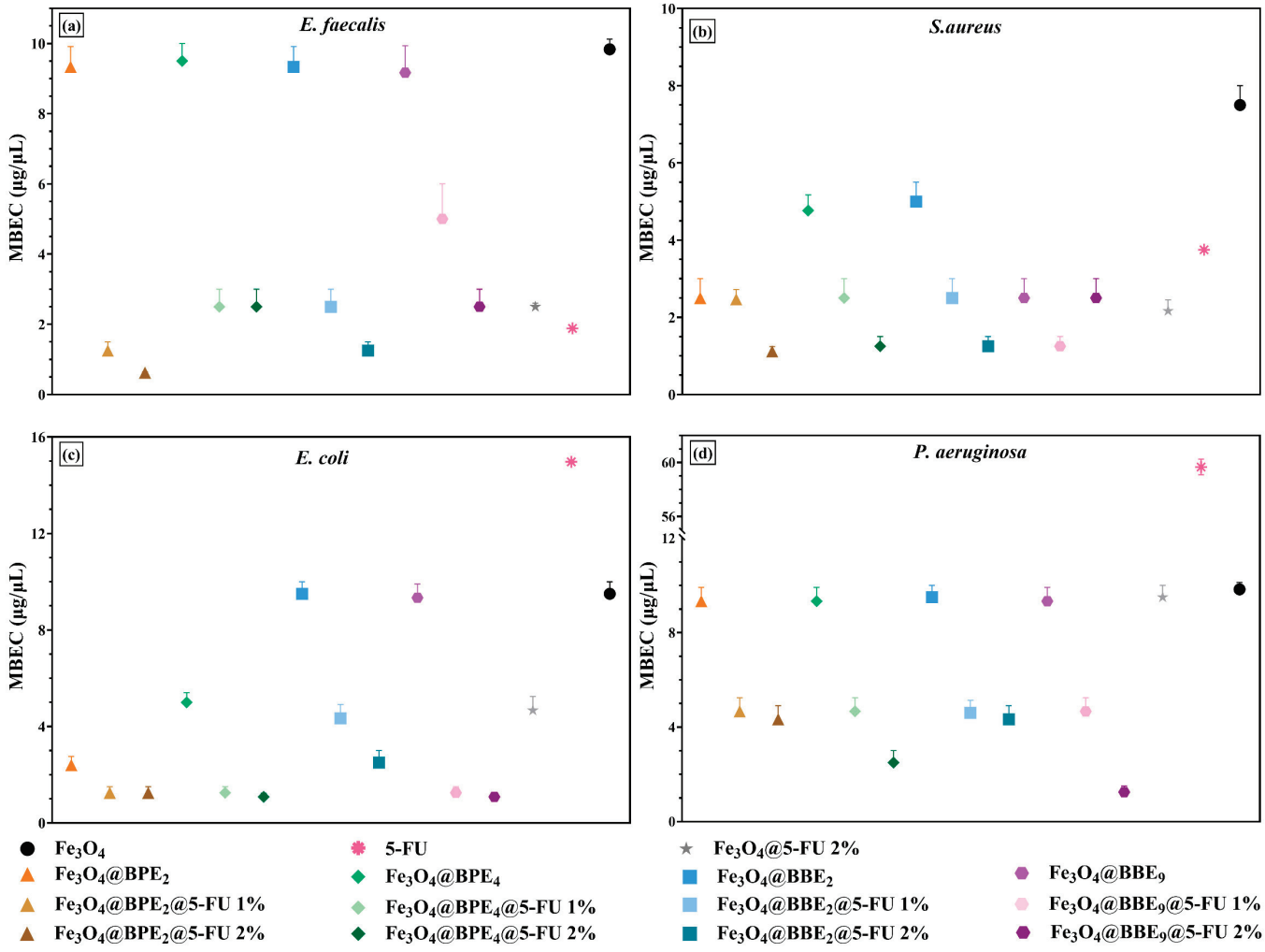


Figure 15. Graphical chart of MBEC values: (**a**) *E. faecalis*, (**b**) *S. aureus*, (**c**) *E. coli*, and (**d**) *P. aeruginosa*. The differences between MNPs were statistically analyzed using the one-way ANOVA followed by Tukey's multiple comparisons tests. The data results were considered statistically significant.

3.5. Influence of Bioactive Compounds against Probiotic Bacteria

The human gastrointestinal tract is characterized by complex microbial communities that generate many metabolites involved in numerous biological processes. The major challenge is to prevent dysbiosis that imbalances the REDOX equilibrium, which also damages the immune system by disrupting signaling and stimulating inflammatory responses [114]. Dietary antioxidants (PCs, fatty acids, vitamins, etc.) might prevent oxidative stress by regulating/restoring the gut microbiota [115,116]. The effect on the growth of *L. rhamnosus* MF9 under the influence of loaded MNPs after 24 h is represented in Figure 16.

The Fe_3O_4 NPs do not influence the growth of *L. rhamnosus* MF9, but are significantly stimulated (more than four logarithmic units) by all BPEs and BBE-loaded MNPs (Figure 16a). Otherwise, Figure 16b illustrates the impact of different concentrations of MNPs against *L. rhamnosus* MF9 growing. The negative influence of the antitumoral drug can be observed at concentrations between 250 and 1000 µg/mL. Also, Figure 16a confirms the impact of 5-FU on the probiotic bacteria' growth. At 125 µg/mL concentrations of MNPs, the *L. rhamnosus* MF9 growth was negatively influenced by the samples with 2% antineoplastic agent, less Fe_3O_4@BPE_2@5-FU 2%. The significant prebiotic potential of this sample is correlated with the prebiotic activity of their extract (BPE_2) and the antioxidant activity of loaded MNPs (Figures 10–12).

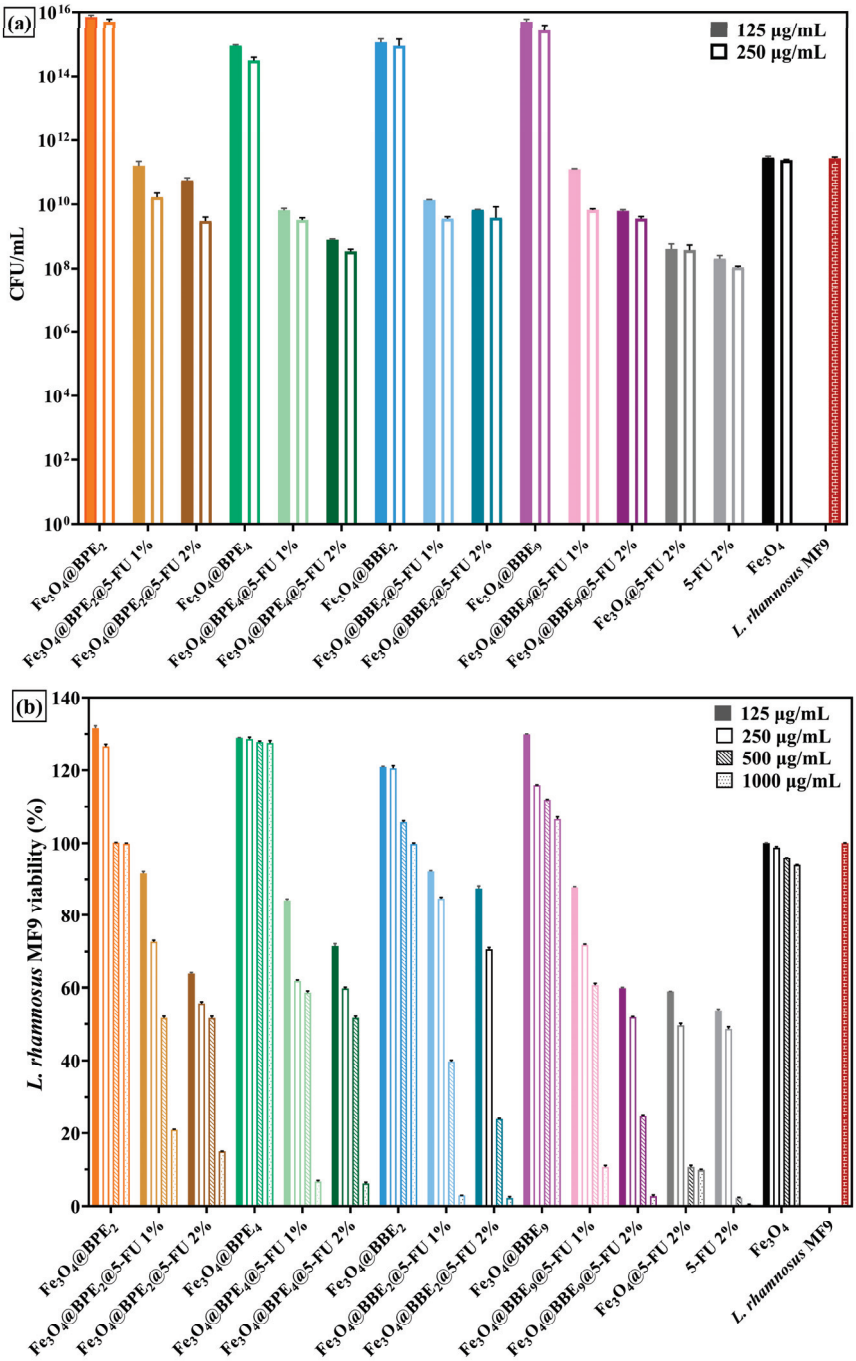


Figure 16. The influence of MNPs on the growth of *L. rhamnosus MF9* (after 24h). (**a**) Graphic representation of CFU/mL values. (**b**) A representation of the percentages of growth of probiotic bacteria viability under the influence of different concentrations of MNPs. The data results were considered statistically significant ($p < 0.001$).

According to the CUPRAC and FRAP results (Figures 11 and 12), the MNPs loaded with 5-FU 1% showed the highest antioxidant activity, and it could be correlated with the capacity of these samples to alleviate the oxidative stress induced by the anticancer drug against gut microbiota. Also, Figure 16a suggests that at 125 µg/mL MNPs, the growth of *L. rhamnosus* MF9 is not affected by the Fe_3O_4@BPE_2@5-FU 1% and Fe_3O_4@BPE_9@5-FU 1%. Previous studies [117,118] confirm the prebiotic effects of PCs on probiotic bacteria, and it could be assumed that bioactive compounds from extracts alleviate the adverse effects of 5-FU by protecting and enhancing the *L. rhamnosus* MF9 development.

The non-toxic properties of MNPs for probiotic strains are confirmed by Ghibaudo et al. [119], who synthesized MNPs coated with citrus pectin used as carriers for *L. plantarum*. The iron from NPs was non-toxic up to 1 mg/mL. In addition, the prolonged PCs' release profiles (Figure 9c,d) suggest an enhanced possibility of microbiota recovery. In addition, a high growth rate of probiotic bacteria does not affect the antitumoral effect of drugs [120].

3.6. The Antiproliferative Assay

The in vitro tumor cell viability and proliferation of HT-29 cells in the presence of synthesized MNPs were examined using the MTT assay (Figure 17). The cell viability of the colorectal tumoral cells was assessed at the lowest concentration of MNPs (62.5 µg/mL), which does not inhibit the growth of probiotic bacteria or affect the gut balance.

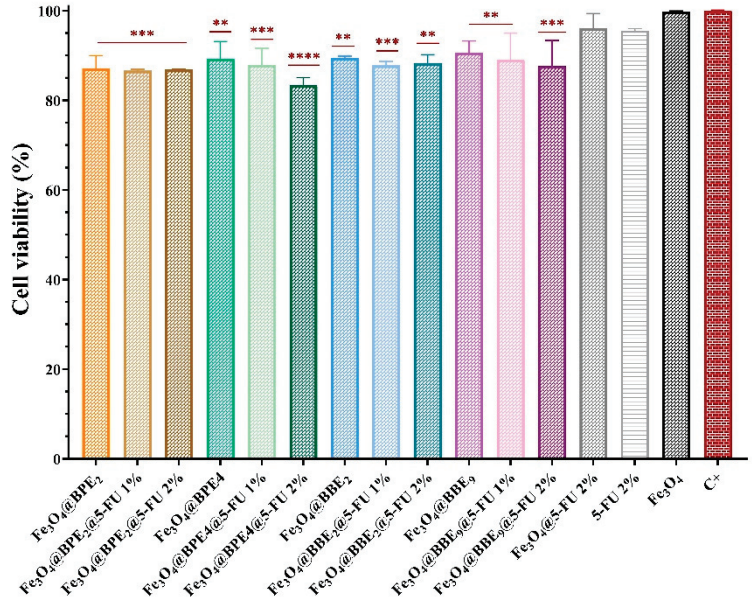


Figure 17. The influence of loaded-MNPs on the cell viability and proliferation of the colorectal tumoral cells (C+). The differences between the cell viability of HT-29 cells without MNPs (C+) and under MNPs' influence for the MTT assay were statistically analyzed using one-way ANOVA followed by Holm–Šídák's multiple comparisons tests (** $p \leq 0.005$; *** $p \leq 0.001$; **** $p < 0.0001$).

Figure 17 displays the significant differences between magnetite and loaded MNPs, and it reveals that the developed MNPs do not stimulate the proliferation of colorectal tumoral cells.

Fe_3O_4@BPE@5-FU/Fe_3O_4@BBE@5-FU and Fe_3O_4@BPE/Fe_3O_4@BBE samples present a lower cell viability than Fe3O4@5-FU 2%.

Likewise, adding 5-FU improves the inhibition of HT-29/tumoral cell proliferation, which could be explained by a synergic inhibitory effect between PCs from extracts and anticancer drug. Fe_3O_4@BPE_4@5-FU 2% presented the lowest percentage of cell viability (83.3%) and the highest inhibitory effect, respectively. Also, Fe_3O_4@BPE_2 with 1% and 2% 5-FU (~86.7%), Fe_3O_4@BBE_9@5-FU 2% (87.6%), and Fe_3O_4@BBE_2@5-FU 1% (87.8%) significantly inhibited the proliferation of tumoral cells. Otherwise, this study aimed to investigate the effects between 5-FU and extracts, especially the influence on gut microbiota, and for this reason it used small concentrations of 5-FU and MNPs and does not expect significant antitumoral activity.

The antitumoral activity of PCs present in high amounts in the BP/BB extracts has already been studied [40,121]. Akkoyunlu et al. [122] accomplished the BP antitumoral activity on the HCT116 cell line, and Uțoiu et al. [123] reported a moderate inhibitory

effect on Hep-2 cells and Caco-2 intestinal tumor cells of a fermented BP. In addition, the antitumoral activity of BB on CRC cell lines was reported [124].

The antitumoral properties of MNPs loaded with 5-FU are confirmed by another study [82], which reported that MNPs can play a role in improving 5-FU anticancer activity. Dextran-coated iron NPs loaded with 5-FU (1.5:1), with 30.19 ± 2 nm average particle size, also presented an antiproliferative effect on Caco-2 cells at 5–250 μg/mL NPs. Genc et al. [125] reported that spherical Fe_3O_4 NPs with 35 ± 5 nm average diameter do not inhibit the Caco-2-cells proliferation, but adding different concentrations of 5-FU enhanced the inhibitory effect. Moreover, the efficacy of loaded 5-FU on the chitosan-coated MNPs was improved by applying magnetic hyperthermia [126]. In our study, citrate-coated MNPs loaded with BPEs, BBEs, and/or lower/minor concentrations of 5-FU presented high stability, smaller particle sizes, lower IC50 values, and a high percentage of drugs released. Furthermore, the novelty of this study is represented by the development of the DDSs, which highlighted antibacterial, prebiotic, and antiproliferative activities.

Bacterial infections developed during the CRC treatment negatively impact the patient's survival [127], and the antimicrobial action of new MNPs on pathogen strains can only be beneficial. The biological properties of the developed (magnetic) nanocarriers improve gut homeostasis and could ensure a targeted delivery at the colon site.

4. Conclusions

The present study aimed to develop drug delivery systems based on citrate-stabilized MNPs, which act as nanocarriers for PCs from extracts and anticancer drugs. The results demonstrated the achievement of MNPs with narrow size distributions and an average NP size of ~10 nm. Moreover, it was shown that the antitumoral drug and PCs had fast release rates in the first 24 h from MNPs. Furthermore, the PCs exhibited prolonged release behavior (up to 96 h), and loading MNPs with extracts enhanced their antioxidant and antibacterial properties. Additionally, the non-toxic properties of magnetite and the prebiotic potential of the developed DDS on *L. rhamnosus* MF9 were demonstrated, underline the role of the antioxidants (PCs) in supporting gut microbiota. The moderate antiproliferative activity on a colorectal tumoral cell line at low concentrations of MNPs and 5-FU suggests the potential of DDS to alleviate the adverse effects of anticancer drugs and improve gut balance.

Author Contributions: Conceptualization, C.-I.I., E.O. and A.F.; methodology, C.-I.I., E.O., L.-M.D. and A.F.; validation, E.O., L.-M.D. and A.F.; formal analysis, C.-I.I., A.S., O.-C.O., B.-S.V., S.A.C., A.-I.N., C.C., G.D., I.C.M. and M.S.S.; investigation, C.-I.I., C.C., G.D., A.-I.N., E.O. and L.-M.D.; data curation, C.-I.I., O.-C.O., E.O., L.-M.D. and A.F.; writing—original draft preparation, C.-I.I., E.O., A.S., O.-C.O., C.C., G.D., A.-I.N., I.C.M., M.S.S. and L.-M.D.; writing—review and editing, C.-I.I., A.S., C.C., G.D., E.O., L.-M.D. and A.F.; visualization, E.O., L.-M.D. and A.F.; supervision, E.O. and A.F. All authors have read and agreed to the published version of the manuscript.

Funding: The APC was funded by the National University of Science and Technology POLITEHNICA Bucharest.

Institutional Review Board Statement: Not applicable.

Informed Consent Statement: Not applicable.

Data Availability Statement: Data are contained within the article.

Acknowledgments: This work was supported by the Romanian Government through the National Program "Installations and Strategic Objectives of National Interest" for access to research infrastructure National Research Center for Micro and Nanomaterials from the National University of Science and Technology Politehnica Bucharest and by a grant from the Romanian Ministry of Education and Research, CNCS-UEFISCDI, project number PN-III-P1-1.1-TE-2021-1342, Ctr. No 96TE/2022 (Intelligent controlled-release systems for treating cancer using a personalized approach-SmartAct).

Conflicts of Interest: The authors declare no conflicts of interest.

References

1. Revia, R.A.; Zhang, M. Magnetite nanoparticles for cancer diagnosis, treatment, and treatment monitoring: Recent advances. *Mater. Today* **2016**, *19*, 157–168. [CrossRef] [PubMed]
2. Poonam, L.; Jing, W. Magnetite Nanoparticles (Fe_3O_4) for Radio-Frequency and Microwave Applications. In *Iron Oxide Nanoparticles*; Huang, X.-L., Ed.; IntechOpen: Rijeka, Croatia, 2022; Chapter 5.
3. Campos, E.A.; Stockler Pinto, D.V.B.; Oliveira, J.I.S.d.; Mattos, E.D.C.; Dutra, R.D.C.L. Synthesis, Characterization and Applications of Iron Oxide Nanoparticles—A Short Review. *J. Aerosp. Technol. Manag.* **2015**, *7*, 267–276. [CrossRef]
4. Chircov, C.; Dumitru, I.A.; Vasile, B.S.; Oprea, O.C.; Holban, A.M.; Popescu, R.C. Microfluidic Synthesis of Magnetite Nanoparticles for the Controlled Release of Antibiotics. *Pharmaceutics* **2023**, *15*, 2215. [CrossRef] [PubMed]
5. Wlodarczyk, A.; Gorgon, S.; Radon, A.; Bajdak-Rusinek, K. Magnetite Nanoparticles in Magnetic Hyperthermia and Cancer Therapies: Challenges and Perspectives. *Nanomaterials* **2022**, *12*, 1807. [CrossRef] [PubMed]
6. Patel, N.N.; Mulla, N.R.; Khot, V.M.; Patil, R.S. Anticancer activity of surface functionalized magnetite (Fe_3O_4) nanoparticles—Effect of polymer coating. *Emergent Mater.* **2023**, *7*, 1071–1080. [CrossRef]
7. Rojas-Aguirre, Y.; Rizo, J.; Martínez-Aguilera, M.; Rodríguez-Hernández, A.; Díaz-Bello, B.; Vázquez-Victorio, G.; Domínguez, H.; Mendoza-Cruz, R.; Betancourt, I.; Ortega-Galindo, S.; et al. Facet-dependent magnetic properties of magnetite nanoparticles coated with dodecyl amine and their biological effect in hepatocarcinoma cell line. *J. Mater. Sci.* **2024**, *59*, 991–1009. [CrossRef]
8. Spoiala, A.; Ilie, C.I.; Motelica, L.; Ficai, D.; Semenescu, A.; Oprea, O.C.; Ficai, A. Smart Magnetic Drug Delivery Systems for the Treatment of Cancer. *Nanomaterials* **2023**, *13*, 876. [CrossRef] [PubMed]
9. Del Sol-Fernandez, S.; Martinez-Vicente, P.; Gomollon-Zueco, P.; Castro-Hinojosa, C.; Gutierrez, L.; Fratila, R.M.; Moros, M. Magnetogenetics: Remote activation of cellular functions triggered by magnetic switches. *Nanoscale* **2022**, *14*, 2091–2118. [CrossRef]
10. Shah, S.T.; Chowdhury, Z.Z.; Johan, M.R.B.; Badruddin, I.A.; Khaleed, H.M.T.; Kamangar, S.; Alrobei, H. Surface Functionalization of Magnetite Nanoparticles with Multipotent Antioxidant as Potential Magnetic Nanoantioxidants and Antimicrobial Agents. *Molecules* **2022**, *27*, 789. [CrossRef]
11. Chircov, C.; Petcu, M.-C.; Vasile, B.S.; Purcareanu, B.; Nicoara, A.I.; Oprea, O.C.; Popescu, R.C. Irinotecan-loaded magnetite-silica core-shell systems for colorectal cancer treatment. *Int. J. Pharm.* **2024**, *661*, 124420. [CrossRef]
12. El-Guendouz, S.; Lyoussi, B.; Lourenço, J.P.; Rosa da Costa, A.M.; Miguel, M.G.; Barrocas Dias, C.; Manhita, A.; Jordao, L.; Nogueira, I.; Faleiro, M.L. Magnetite nanoparticles functionalized with propolis against methicillin resistant strains of *Staphylococcus aureus*. *J. Taiwan. Inst. Chem. E* **2019**, *102*, 25–33. [CrossRef]
13. Ullah, M.; Kim, D.-S.; Hun Park, K. Evaluating antioxidant activity of phenolic mediated Fe_3O_4 nanoparticles using *Usnea Longissimma* methanol extract. *Results Chem.* **2022**, *4*, 100661. [CrossRef]
14. Matias-Reyes, A.E.; Alvarado-Noguez, M.L.; Perez-Gonzalez, M.; Carbajal-Tinoco, M.D.; Estrada-Muniz, E.; Fuentes-Garcia, J.A.; Vega-Loyo, L.; Tomas, S.A.; Goya, G.F.; Santoyo-Salazar, J. Direct Polyphenol Attachment on the Surfaces of Magnetite Nanoparticles, Using *Vitis vinifera*, *Vaccinium corymbosum*, or *Punica granatum*. *Nanomaterials* **2023**, *13*, 2450. [CrossRef] [PubMed]
15. Rosman, R.; Saifullah, B.; Maniam, S.; Dorniani, D.; Hussein, M.Z.; Fakurazi, S. Improved Anticancer Effect of Magnetite Nanocomposite Formulation of GALLIC Acid (Fe(3)O(4)-PEG-GA) Against Lung, Breast and Colon Cancer Cells. *Nanomaterials* **2018**, *8*, 83. [CrossRef] [PubMed]
16. Sagir, T.; Huysal, M.; Durmus, Z.; Kurt, B.Z.; Senel, M.; Isik, S. Preparation and in vitro evaluation of 5-flourouracil loaded magnetite-zeolite nanocomposite (5-FU-MZNC) for cancer drug delivery applications. *Biomed. Pharmacother.* **2016**, *77*, 182–190. [CrossRef] [PubMed]
17. World Health Organization. Colorectal Cancer. 2023. Available online: https://www.who.int/news-room/fact-sheets/detail/colorectal-cancer (accessed on 27 April 2024).
18. Morgan, E.A.-O.; Arnold, M.A.-O.; Gini, A.A.-O.; Lorenzoni, V.; Cabasag, C.J.; Laversanne, M.; Vignat, J.; Ferlay, J.; Murphy, N.A.-O.; Bray, F. Global burden of colorectal cancer in 2020 and 2040: Incidence and mortality estimates from GLOBOCAN, (1468–3288 (Electronic)). *Gut* **2023**, *72*, 338–344. [CrossRef] [PubMed]
19. Wu, S.; Rhee, K.J.; Albesiano, E.; Rabizadeh, S.; Wu, X.; Yen, H.R.; Huso, D.L.; Brancati, F.L.; Wick, E.; McAllister, F.; et al. A human colonic commensal promotes colon tumorigenesis via activation of T helper type 17 T cell responses. *Nat. Med.* **2009**, *15*, 1016–1022. [CrossRef] [PubMed]
20. Siddiqui, R.; Boghossian, A.; Alharbi, A.M.; Alfahemi, H.; Khan, N.A. The Pivotal Role of the Gut Microbiome in Colorectal Cancer. *Biology* **2022**, *11*, 1642. [CrossRef] [PubMed]
21. Liu, Y.; Lau, H.C.; Cheng, W.Y.; Yu, J. Gut Microbiome in Colorectal Cancer: Clinical Diagnosis and Treatment. *Genom. Proteom. Bioinform.* **2023**, *21*, 84–96. [CrossRef]
22. Lazar, V.; Ditu, L.M.; Pircalabioru, G.G.; Gheorghe, I.; Curutiu, C.; Holban, A.M.; Picu, A.; Petcu, L.; Chifiriuc, M.C. Aspects of Gut Microbiota and Immune System Interactions in Infectious Diseases, Immunopathology, and Cancer. *Front. Immunol.* **2018**, *9*, 1830. [CrossRef]
23. Wong, S.H.; Yu, J. Gut microbiota in colorectal cancer: Mechanisms of action and clinical applications. *Nat. Rev. Gastroenterol. Hepatol.* **2019**, *16*, 690–704. [CrossRef] [PubMed]

24. Zou, S.; Yang, C.; Zhang, J.; Zhong, D.; Meng, M.; Zhang, L.; Chen, H.; Fang, L. Multi-omic profiling reveals associations between the gut microbiome, host genome and transcriptome in patients with colorectal cancer. *J. Transl. Med.* **2024**, *22*, 175. [CrossRef] [PubMed]
25. Li, L.; Li, X.; Zhong, W.; Yang, M.; Xu, M.; Sun, Y.; Ma, J.; Liu, T.; Song, X.; Dong, W.; et al. Gut microbiota from colorectal cancer patients enhances the progression of intestinal adenoma in Apc(min/+) mice. *Ebiomedicine* **2019**, *48*, 301–315. [CrossRef] [PubMed]
26. Wan, L.; Li, H.; Sun, G.; Zhang, L.; Xu, H.; Su, F.; He, S.; Xiao, F. Mutational Pattern Induced by 5-Fluorouracil and Oxaliplatin in the Gut Microbiome. *Front. Microbiol.* **2022**, *13*, 841458. [CrossRef] [PubMed]
27. Lo, E.K.K.; Leung, H.K.M.; Zhang, F.; El-Nezami, H. Gut microbiota: Impact on 5-fluorouracil efficacy and toxicity. *Curr. Opin. Toxicol.* **2023**, *36*, 100423. [CrossRef]
28. Ashique, S.; Bhowmick, M.; Pal, R.; Khatoon, H.; Kumar, P.; Sharma, H.; Garg, A.; Kumar, S.; Das, U. Multi drug resistance in Colorectal Cancer- approaches to overcome, advancements and future success. *Adv. Cancer Biol. Metastasis* **2024**, *10*, 100114. [CrossRef]
29. Danielsen, A.S.; Franconeri, L.; Page, S.; Myhre, A.E.; Tornes, R.A.; Kacelnik, O.; Bjornholt, J.V. Clinical outcomes of antimicrobial resistance in cancer patients: A systematic review of multivariable models. *BMC Infect. Dis.* **2023**, *23*, 247. [CrossRef] [PubMed]
30. Pfab, C.; Abgaryan, A.; Danzer, B.; Mourtada, F.; Ali, W.; Gessner, A.; El-Najjar, N. Ceftazidime and cefepime antagonize 5-fluorouracil's effect in colon cancer cells. *BMC Cancer* **2022**, *22*, 125. [CrossRef] [PubMed]
31. Yuan, L.; Zhang, S.; Li, H.; Yang, F.; Mushtaq, N.; Ullah, S.; Shi, Y.; An, C.; Xu, J. The influence of gut microbiota dysbiosis to the efficacy of 5-Fluorouracil treatment on colorectal cancer. *Biomed. Pharmacother.* **2018**, *108*, 184–193. [CrossRef] [PubMed]
32. McDowell, R.; Perrott, S.; Murchie, P.; Cardwell, C.; Hughes, C.; Samuel, L. Oral antibiotic use and early-onset colorectal cancer: Findings from a case-control study using a national clinical database. *Br. J. Cancer* **2022**, *126*, 957–967. [CrossRef]
33. Simin, J.; Fornes, R.; Liu, Q.; Olsen, R.S.; Callens, S.; Engstrand, L.; Brusselaers, N. Antibiotic use and risk of colorectal cancer: A systematic review and dose-response meta-analysis. *Br. J. Cancer* **2020**, *123*, 1825–1832. [CrossRef] [PubMed]
34. Cheung, K.S.; Chan, E.W.; Tam, A.; Wong, I.O.L.; Seto, W.K.; Hung, I.F.N.; Wong, I.C.K.; Leung, W.K. Association between antibiotic consumption and colon and rectal cancer development in older individuals: A territory-wide study. *Cancer Med.* **2022**, *11*, 3863–3872. [CrossRef] [PubMed]
35. Gao, Q.; Feng, J.; Liu, W.; Wen, C.; Wu, Y.; Liao, Q.; Zou, L.; Sui, X.; Xie, T.; Zhang, J.; et al. Opportunities and challenges for co-delivery nanomedicines based on combination of phytochemicals with chemotherapeutic drugs in cancer treatment. *Adv. Drug Deliv. Rev.* **2022**, *188*, 114445. [CrossRef] [PubMed]
36. Constantin, M.; Chifiriuc, M.C.; Mihaescu, G.; Corcionivoschi, N.; Burlibasa, L.; Bleotu, C.; Tudorache, S.; Mitache, M.M.; Filip, R.; Munteanu, S.-G.; et al. Microbiome and cancer: From mechanistic implications in disease progression and treatment to development of novel antitumoral strategies. *Front. Immunol.* **2024**, *15*, 1373504. [CrossRef] [PubMed]
37. Plamada, D.; Vodnar, D.C. Polyphenols-Gut Microbiota Interrelationship: A Transition to a New Generation of Prebiotics. *Nutrients* **2021**, *14*, 137. [CrossRef] [PubMed]
38. Rodriguez-Daza, M.C.; Pulido-Mateos, E.C.; Lupien-Meilleur, J.; Guyonnet, D.; Desjardins, Y.; Roy, D. Polyphenol-Mediated Gut Microbiota Modulation: Toward Prebiotics and Further. *Front. Nutr.* **2021**, *8*, 689456. [CrossRef] [PubMed]
39. Chairez-Ramirez, M.H.; de la Cruz-Lopez, K.G.; Garcia-Carranca, A. Polyphenols as Antitumor Agents Targeting Key Players in Cancer-Driving Signaling Pathways. *Front. Pharmacol.* **2021**, *12*, 710304. [CrossRef] [PubMed]
40. Kim, K.H.; Ki, M.R.; Min, K.H.; Pack, S.P. Advanced Delivery System of Polyphenols for Effective Cancer Prevention and Therapy. *Antioxidants* **2023**, *12*, 1048. [CrossRef] [PubMed]
41. Rudzinska, A.; Juchaniuk, P.; Oberda, J.; Wisniewska, J.; Wojdan, W.; Szklener, K.; Mandziuk, S. Phytochemicals in Cancer Treatment and Cancer Prevention-Review on Epidemiological Data and Clinical Trials. *Nutrients* **2023**, *15*, 1896. [CrossRef] [PubMed]
42. Ilie, C.I.; Oprea, E.; Geana, E.I.; Spoiala, A.; Buleandra, M.; Gradisteanu Pircalabioru, G.; Badea, I.A.; Ficai, D.; Andronescu, E.; Ficai, A.; et al. Bee Pollen Extracts: Chemical Composition, Antioxidant Properties, and Effect on the Growth of Selected Probiotic and Pathogenic Bacteria. *Antioxidants* **2022**, *11*, 959. [CrossRef]
43. Ilie, C.I.; Spoiala, A.; Geana, E.I.; Chircov, C.; Ficai, A.; Ditu, L.M.; Oprea, E. Bee Bread: A Promising Source of Bioactive Compounds with Antioxidant Properties-First Report on Some Antimicrobial Features. *Antioxidants* **2024**, *13*, 353. [CrossRef]
44. Pelka, K.; Bin Hafeez, A.; Worobo, R.W.; Szweda, P. Probiotic potential of Isolates from Polish Bee Pollen and Bee Bread. *Probiotics Antimicrob. Proteins* **2023**.
45. Baky, M.H.; Abouelela, M.B.; Wang, K.; Farag, M.A. Bee Pollen and Bread as a Super-Food: A Comparative Review of Their Metabolome Composition and Quality Assessment in the Context of Best Recovery Conditions. *Molecules* **2023**, *28*, 715. [CrossRef]
46. Sawicki, T.; Starowicz, M.; Kłębukowska, L.; Hanus, P. The Profile of Polyphenolic Compounds, Contents of Total Phenolics and Flavonoids, and Antioxidant and Antimicrobial Properties of Bee Products. *Molecules* **2022**, *27*, 1301. [CrossRef]
47. Mohammad, S.M.; Mahmud-Ab-Rashid, N.-K.; Zawawi, N. Probiotic properties of bacteria isolated from bee bread of stingless bee *Heterotrigona itama*. *J. Apic. Res.* **2020**, *60*, 172–187. [CrossRef]
48. Singh, K.; Bhori, M.; Kasu, Y.A.; Bhat, G.; Marar, T. Antioxidants as precision weapons in war against cancer chemotherapy induced toxicity—Exploring the armoury of obscurity. *Saudi Pharm. J.* **2018**, *26*, 177–190. [CrossRef]

49. Dobani, S.; Latimer, C.; McDougall, G.J.; Allwood, J.W.; Pereira-Caro, G.; Moreno-Rojas, J.M.; Ternan, N.G.; Pourshahidi, L.K.; Lawther, R.; Tuohy, K.M.; et al. Ex vivo fecal fermentation of human ileal fluid collected after raspberry consumption modifies (poly)phenolics and modulates genoprotective effects in colonic epithelial cells. *Redox Biol.* **2021**, *40*, 101862. [CrossRef]
50. Wang, X.; Liu, Y.; Wu, Z.; Zhang, P.; Zhang, X. Tea Polyphenols: A Natural Antioxidant Regulates Gut Flora to Protect the Intestinal Mucosa and Prevent Chronic Diseases. *Antioxidants* **2022**, *11*, 253. [CrossRef]
51. Wang, Y.; Li, H. Gut microbiota modulation: A tool for the management of colorectal cancer. *J. Transl. Med.* **2022**, *20*, 178. [CrossRef] [PubMed]
52. Dikeocha, I.J.; Al-Kabsi, A.M.; Eid, E.E.M.; Hussin, S.; Alshawsh, M.A. Probiotics supplementation in patients with colorectal cancer: A systematic review of randomized controlled trials. *Nutr. Rev.* **2021**, *80*, 22–49. [CrossRef] [PubMed]
53. Lang, T.; Zhu, R.; Zhu, X.; Yan, W.; Li, Y.; Zhai, Y.; Wu, T.; Huang, X.; Yin, Q.; Li, Y. Combining gut microbiota modulation and chemotherapy by capecitabine-loaded prebiotic nanoparticle improves colorectal cancer therapy. *Nat. Commun.* **2023**, *14*, 4746. [CrossRef]
54. Yuan, X.; Xue, J.; Tan, Y.; Yang, Q.; Qin, Z.; Bao, X.; Li, S.; Pan, L.; Jiang, Z.; Wang, Y.; et al. Albuca Bracteate Polysaccharides Synergistically Enhance the Anti-Tumor Efficacy of 5-Fluorouracil Against Colorectal Cancer by Modulating beta-Catenin Signaling and Intestinal Flora. *Front. Pharmacol.* **2021**, *12*, 736627. [CrossRef]
55. Ilie, C.-I.; Spoiala, A.; Ficai, D.; Nicoara, A.-I.; Oprea, O.-C.; Surdu, V.-A.; Trusca, R.D.; Andronescu, E.; Ditu, L.-M.; Ficai, A. Magnetic platforms based on magnetite and polyphenols with antimicrobial activity. *UPB Sci. Bull. Ser. B* **2022**, *84*, 45–58.
56. Vlad, I.M.; Nuță, D.C.; Ancuceanu, R.V.; Caproiou, M.T.; Dumitrascu, F.; Marinas, I.C.; Chifiriuc, M.C.; Măruţescu, L.G.; Zarafu, I.; Papacocea, I.R.; et al. New O-Aryl-Carbamoyl-Oxymino-Fluorene Derivatives with MI-Crobicidal and Antibiofilm Activity Enhanced by Combination with Iron Oxide Nanoparticles. *Molecules* **2021**, *26*, 3002. [CrossRef]
57. Dolete, G.; Ilie, C.I.; Chircov, C.; Purcareanu, B.; Motelica, L.; Morosan, A.; Oprea, O.C.; Ficai, D.; Andronescu, E.; Ditu, L.M. Synergistic Antimicrobial Activity of Magnetite and Vancomycin-Loaded Mesoporous Silica Embedded in Alginate Films. *Gels* **2023**, *9*, 295. [CrossRef]
58. Spirescu, V.A.; Niculescu, A.G.; Slave, S.; Birca, A.C.; Dorcioman, G.; Grumezescu, V.; Holban, A.M.; Oprea, O.C.; Vasile, B.S.; Grumezescu, A.M.; et al. Anti-Biofilm Coatings Based on Chitosan and Lysozyme Functionalized Magnetite Nanoparticles. *Antibiotics* **2021**, *10*, 1269. [CrossRef]
59. Chircov, C.; Pirvulescu, D.C.; Birca, A.C.; Andronescu, E.; Grumezescu, A.M. Magnetite Microspheres for the Controlled Release of Rosmarinic Acid. *Pharmaceutics* **2022**, *14*, 2292. [CrossRef]
60. Bakr, E.A.; Gaber, M.; Saad, D.R.; Salahuddin, N. Comparative study between two different morphological structures based on polylactic acid, nanocellulose and magnetite for co-delivery of flurouracil and curcumin. *Int. J. Biol. Macromol.* **2023**, *230*, 123315.
61. Abali, S.O.; Ekenna, I.C. Comparison of the Use of Kinetic Model Plots and DD Solver Software to Evaluate the Drug Release from Griseofulvin Tablets. *J. Drug Deliv. Ther.* **2022**, *12*, 5–13.
62. Singleton, V.L.; Rossi, J.A. Colorimetry of Total Phenolics with Phosphomolybdic-Phosphotungstic Acid Reagents. *Am. J. Enol. Vitic.* **1965**, *16*, 144–158. [CrossRef]
63. Shah, S.T.; Yehye, W.A.; Chowdhury, Z.Z.; Simarani, K. Magnetically directed antioxidant and antimicrobial agent: Synthesis and surface functionalization of magnetite with quercetin. *Peerj* **2019**, *7*, e7651. [CrossRef]
64. Thaipong, K.; Boonprakob, U.; Crosby, K.; Cisneros-Zevallos, L.; Hawkins Byrne, D. Comparison of ABTS, DPPH, FRAP, and ORAC assays for estimating antioxidant activity from guava fruit extracts. *J. Food Compos. Anal.* **2006**, *19*, 669–675. [CrossRef]
65. Marinas, I.C.; Ignat, L.; Maurusa, I.E.; Gaboreanu, M.D.; Adina, C.; Popa, M.; Chifiriuc, M.C.; Angheloiu, M.; Georgescu, M.; Iacobescu, A.; et al. Insights into the physico-chemical and biological characterization of sodium lignosulfonate—Silver nanosystems designed for wound management. *Heliyon* **2024**, *10*, e26047. [CrossRef]
66. Spoiala, A.; Ilie, C.I.; Trusca, R.D.; Oprea, O.C.; Surdu, V.A.; Vasile, B.S.; Ficai, A.; Ficai, D.; Andronescu, E.; Ditu, L.M. Zinc Oxide Nanoparticles for Water Purification. *Materials* **2021**, *14*, 4747–4763. [CrossRef]
67. CLSI. *CLSI Supplemenent M100—Performance Standards for Antimicrobial Susceptibility Testing*; Clinical and Laboratory Standards Institute: Wayne, PA, USA, 2021; Volume 41, p. 352.
68. Geana, E.I.; Ciucure, C.T.; Tamaian, R.; Marinas, I.C.; Gaboreanu, D.M.; Stan, M.; Chitescu, C.L. Antioxidant and Wound Healing Bioactive Potential of Extracts Obtained from Bark and Needles of Softwood Species. *Antioxidants* **2023**, *12*, 1383. [CrossRef]
69. Sabur, M.A.; Gafur, M.A.; Wang, X. Crystallographic, Morphological, Magnetic, and Thermal Characterization of Superparamagnetic Magnetite Nanoparticles (Fe_3O_4) Synthesized by Chemical Coprecipitation Method and Calcined at 250 °C for 4 hr. *J. Nanomater.* **2024**, *2024*, 1–9. [CrossRef]
70. Niculescu, A.G.; Morosan, A.; Birca, A.C.; Gherasim, O.; Oprea, O.C.; Vasile, B.S.; Purcareanu, B.; Mihaiescu, D.E.; Radulescu, M.; Grumezescu, A.M. Microwave-Assisted Silanization of Magnetite Nanoparticles Pre-Synthesized by a 3D Microfluidic Platform. *Nanomaterials* **2023**, *13*, 2795. [CrossRef]
71. Wei, Y.; Han, B.; Hu, X.; Lin, Y.; Wang, X.; Deng, X. Synthesis of Fe_3O_4 Nanoparticles and their Magnetic Properties. *Procedia Eng.* **2012**, *27*, 632–637. [CrossRef]
72. Atrei, A.; Mahdizadeh, F.F.; Baratto, M.C.; Scala, A. Effect of Citrate on the Size and the Magnetic Properties of Primary Fe_3O_4 Nanoparticles and Their Aggregates. *Appl. Sci.* **2021**, *11*, 6974. [CrossRef]
73. Sato, J.; Kobayashi, M.; Kato, H.; Miyazaki, T.; Kakihana, M. Hydrothermal synthesis of magnetite particles with uncommon crystal facets. *J. Asian Ceram. Soc.* **2018**, *2*, 258–262. [CrossRef]

74. Prdun, S.; Svecnjak, L.; Valentic, M.; Marijanovic, Z.; Jerkovic, I. Characterization of Bee Pollen: Physico-Chemical Properties, Headspace Composition and FTIR Spectral Profiles. *Foods* **2021**, *10*, 2103. [CrossRef]
75. Dranca, F.; Ursachi, F.; Oroian, M. Bee Bread: Physicochemical Characterization and Phenolic Content Extraction Optimization. *Foods* **2020**, *9*, 1358. [CrossRef]
76. Cheralayikkal, S.; Manoj, K.; Safna Hussan, K.P. Formulation and evaluation of a smart drug delivery system of 5-fluorouracil for pH-sensitive chemotherapy. *Heliyon* **2022**, *8*, e09926. [CrossRef]
77. Puiu, R.A.; Balaure, P.C.; Constantinescu, E.; Grumezescu, A.M.; Andronescu, E.; Oprea, O.C.; Vasile, B.S.; Grumezescu, V.; Negut, I.; Nica, I.C.; et al. Anti-Cancer Nanopowders and MAPLE-Fabricated Thin Films Based on SPIONs Surface Modified with Paclitaxel Loaded beta-Cyclodextrin. *Pharmaceutics* **2021**, *13*, 1356. [CrossRef]
78. Caciandone, M.; Niculescu, A.G.; Rosu, A.R.; Grumezescu, V.; Negut, I.; Holban, A.M.; Oprea, O.; Vasile, B.S.; Birca, A.C.; Grumezescu, A.M.; et al. PEG-Functionalized Magnetite Nanoparticles for Modulation of Microbial Biofilms on Voice Prosthesis. *Antibiotics* **2022**, *11*, 39. [CrossRef]
79. Chircov, C.; Birca, A.C.; Grumezescu, A.M.; Vasile, B.S.; Oprea, O.; Nicoara, A.I.; Yang, C.H.; Huang, K.S.; Andronescu, E. Synthesis of Magnetite Nanoparticles through a Lab-On-Chip Device. *Materials* **2021**, *14*, 5906. [CrossRef]
80. Mudalige, T.; Qu, H.; Van Haute, D.; Ansar, S.M.; Paredes, A.; Ingle, T. Chapter 11—Characterization of Nanomaterials: Tools and Challenges. In *Nanomaterials for Food Applications*; López Rubio, A., Fabra Rovira, M.J., Martínez Sanz, M., Gómez-Mascaraque, L.G., Eds.; Elsevier: Amsterdam, The Netherlands, 2019; pp. 313–353.
81. Shimojo, A.A.M.; Fernandes, A.R.V.; Ferreira, N.R.E.; Sanchez-Lopez, E.; Santana, M.H.A.; Souto, E.B. Evaluation of the Influence of Process Parameters on the Properties of Resveratrol-Loaded NLC Using 2(2) Full Factorial Design. *Antioxidants* **2019**, *8*, 272. [CrossRef]
82. Predoi, D.; Balas, M.; Badea, M.A.; Ciobanu, S.C.; Buton, N.; Dinischiotu, A. Dextran-Coated Iron Oxide Nanoparticles Loaded with 5-Fluorouracil for Drug-Delivery Applications. *Nanomaterials* **2023**, *13*, 1811. [CrossRef] [PubMed]
83. FDA (Food and Drug Administration). *Fluorouracil Injection, for Intravenous Use*; Food and Drug Administration: Silver Spring, MD, USA, 2016; pp. 1–8.
84. EMEA. *Annex I, II, III- 5FU and Related Substances EMEA-H-A31-1481*; European Commision: Brussels, Belgium; pp. 1–48.
85. Ayyanaar, S.; Bhaskar, R.; Esthar, S.; Vadivel, M.; Rajesh, J.; Rajagopal, G. Design and development of 5-fluorouracil loaded biodegradable magnetic microspheres as site-specific drug delivery vehicle for cancer therapy. *J. Magn. Magn. Mater.* **2022**, *546*, 168853. [CrossRef]
86. Sanli, O.; Kahraman, A.; Solak, E.K.; Olukman, M. Preparation of magnetite-chitosan/methylcellulose nanospheres by entrapment and adsorption techniques for targeting the anti-cancer drug 5-fluorouracil. *Artif. Cell Nanomed. B* **2016**, *44*, 950–959.
87. Barreto, A.C.H.; Santiago, V.R.; Mazzetto, S.E.; Denardin, J.C.; Lavín, R.; Mele, G.; Ribeiro, M.E.N.P.; Vieira, I.G.P.; Gonçalves, T.; Ricardo, N.M.P.S.; et al. Magnetic nanoparticles for a new drug delivery system to control quercetin releasing for cancer chemotherapy. *J. Nanopart Res.* **2011**, *13*, 6545–6553. [CrossRef]
88. Ahmed, L.; Atif, R.; Eldeen, T.S.; Yahya, I.; Omara, A.; Eltayeb, M. Study the Using of Nanoparticles as Drug Delivery System Based on Mathematical Models for Controlled Release. *Int. J. Latest Technol. Eng. Manag. Appl. Sci.* **2019**, *VIII*, 52–56.
89. Gulcin, İ.; Alwasel, S.H. DPPH Radical Scavenging Assay. *Processes* **2023**, *11*, 2248. [CrossRef]
90. Martinez-Morales, F.; Alonso-Castro, A.J.; Zapata-Morales, J.R.; Carranza-Álvarez, C.; Aragon-Martinez, O.H. Use of standardized units for a correct interpretation of IC50 values obtained from the inhibition of the DPPH radical by natural antioxidants. *Chem. Pap.* **2020**, *74*, 3325–3334. [CrossRef]
91. Shah, S.T.; Yehya, W.A.; Saad, O.; Simarani, K.; Chowdhury, Z.; Alhadi, A.A.; Al-Ani, L.A. Surface Functionalization of Iron Oxide Nanoparticles with Gallic Acid as Potential Antioxidant and Antimicrobial Agents. *Nanomaterials* **2017**, *7*, 306. [CrossRef] [PubMed]
92. Apak, R.; Güçlü, K.; Demirata, B.; Özyürek, M.; Çelik, S.E.; Bektaşoğlu, B.; Berker, I.; Özyurt, D. Comparative Evaluation of Various Total Antioxidant Capacity Assays Applied to Phenolic Compounds with the CUPRAC Assay. *Molecules* **2007**, *12*, 1496–1547. [CrossRef]
93. Özyürek, M.; Güçlü, K.; Tütem, E.; Başkan, K.S.; Erçağ, E.; Esin Çelik, S.; Baki, S.; Yıldız, L.; Karaman, Ş.; Apak, R. A comprehensive review of CUPRAC methodology. *Anal. Methods* **2011**, *3*, 2439–2453. [CrossRef]
94. Chen, Y.; Lin, Q.; Wang, J.; Mu, J.; Liang, Y. Proteins, polysaccharides and their derivatives as macromolecular antioxidant supplements: A review of in vitro screening methods and strategies. *Int. J. Biol. Macromol.* **2023**, *224*, 958–971. [CrossRef]
95. Gupta, D. Methods for determination of antioxidant capacity: A review. *Int. J. Pharm. Sci. Res.* **2015**, *6*, 546–566.
96. Pellegrini, N.; Serafini, M.; Colombi, B.; Rio, D.D.; Salvatore, S.; Bianchi, M.; Brighenti, F. Total Antioxidant Capacity of Plant Foods, Beverages and Oils Consumed in Italy Assessed by Three Different In Vitro Assays. *J. Nutr.* **2003**, *133*, 2812–2819. [CrossRef]
97. Ronald, L.; Prior, X.W.; Schaich, K. Standardized Methods for the Determination of Antioxidant Capacity and Phenolics in Foods and Dietary Supplements. *J. Agric. Food Chem.* **2005**, *53*, 4290–4302.
98. Moazzen, A.; Oztinen, N.; Ak-Sakalli, E.; Kosar, M. Structure-antiradical activity relationships of 25 natural antioxidant phenolic compounds from different classes. *Heliyon* **2022**, *8*, e10467. [CrossRef] [PubMed]

99. Bononi, I.; Tedeschi, P.; Mantovani, V.; Maietti, A.; Mazzoni, E.; Pancaldi, C.; Brandolini, V.; Tognon, M. Antioxidant Activity of Resveratrol Diastereomeric Forms Assayed in Fluorescent-Engineered Human Keratinocytes. *Antioxidants* **2022**, *11*, 196. [CrossRef] [PubMed]
100. Breijyeh, Z.; Jubeh, B.; Karaman, R. Resistance of Gram-Negative Bacteria to Current Antibacterial Agents and Approaches to Resolve It. *Molecules* **2020**, *25*, 1340. [CrossRef]
101. Gudkov, S.V.; Burmistrov, D.E.; Serov, D.A.; Rebezov, M.B.; Semenova, A.A.; Lisitsyn, A.B. Do Iron Oxide Nanoparticles Have Significant Antibacterial Properties? *Antibiotics* **2021**, *10*, 884. [CrossRef]
102. Prabhu, Y.T.; Rao, K.V.; Kumari, B.S.; Kumar, V.S.S.; Pavani, T. Synthesis of Fe_3O_4 nanoparticles and its antibacterial application. *Int. Nano Lett.* **2015**, *5*, 85–92. [CrossRef]
103. Madhavi; Kumar, M.; Ansari, J.R.; Kumar, V.; Nagar, S.; Sharma, A. Fe_3O_4 Coated SiO_2 Magnetic Nanoparticles for Enhanced Antibacterial Activity and Electrochemical Sensing. *Metals* **2022**, *12*, 2145. [CrossRef]
104. Raam Dheep, G.; Ramachandran, K.; Shameer, M.; Natarajamoorthy, M.; Gaidi, M.; Daoudi, K.; Muthukumarasamy, A. Chapter 9—Functional magnetic nanomaterials with enhanced antimicrobial activity. In *Antimicrobial Nanosystems*; Hussain, C.M., Anand, K.V., Mallakpour, S., Eds.; Elsevier: Amsterdam, The Netherlands, 2023; pp. 191–211.
105. Rudrapal, M.; Khairnar, S.J.; Khan, J.; Dukhyil, A.B.; Ansari, M.A.; Alomary, M.N.; Alshabrmi, F.M.; Palai, S.; Deb, P.K.; Devi, R. Dietary Polyphenols and Their Role in Oxidative Stress-Induced Human Diseases: Insights Into Protective Effects, Antioxidant Potentials and Mechanism(s) of Action. *Front. Pharmacol.* **2022**, *13*, 806470. [CrossRef]
106. Patil, M.; Serhii, K.; Garzino, F.; Gobert, Q.; Giorgio, S.; Raimundo, J.M.; Bolla, J.M.; Camplo, M. Synthesis and antimicrobial testing of 5-fluorouracil derivatives. *Arch. Pharm.* **2023**, *356*, e2300103. [CrossRef]
107. Spulber, R.; Chifiriuc, C.; Fleancu, M.; Popa, O.; Babeanu, N. Antibacterial activity of magnetite nanoparticles coated with bee pollen extracts. In Proceedings of the Agriculture for Life, Life for Agriculture Conference, Bucharest, Romania, 7–9 June 2018; pp. 579–585.
108. Cui, S.; Ma, X.; Wang, X.; Zhang, T.-A.; Hu, J.; Tsang, Y.F.; Gao, M.-T. Phenolic acids derived from rice straw generate peroxides which reduce the viability of Staphylococcus aureus cells in biofilm. *Ind. Crop Prod.* **2019**, *140*, 111561. [CrossRef]
109. Lafay, S.; Gil-Izquierdo, A. Bioavailability of phenolic acids. *Phytochem. Rev.* **2007**, *7*, 301–311. [CrossRef]
110. Gabrielyan, L.; Hovhannisyan, A.; Gevorgyan, V.; Ananyan, M.; Trchounian, A. Antibacterial effects of iron oxide (Fe_3O_4) nanoparticles: Distinguishing concentration-dependent effects with different bacterial cells growth and membrane-associated mechanisms. *Appl. Microbiol. Biotechnol.* **2019**, *103*, 2773–2782. [CrossRef] [PubMed]
111. Gabrielyan, L.; Badalyan, H.; Gevorgyan, V.; Trchounian, A. Comparable antibacterial effects and action mechanisms of silver and iron oxide nanoparticles on *Escherichia coli* and *Salmonella typhimurium*. *Sci. Rep.* **2020**, *10*, 13145. [CrossRef] [PubMed]
112. Tasnim, N.T.; Ferdous, N.; Rumon, M.M.H.; Shakil, M.S. The Promise of Metal-Doped Iron Oxide Nanoparticles as Antimicrobial Agent. *Acs Omega* **2024**, *9*, 16–32. [CrossRef] [PubMed]
113. Yeh, Y.C.; Huang, T.H.; Yang, S.C.; Chen, C.C.; Fang, J.Y. Nano-Based Drug Delivery or Targeting to Eradicate Bacteria for Infection Mitigation: A Review of Recent Advances. *Front. Chem.* **2020**, *8*, 286. [CrossRef] [PubMed]
114. Kunst, C.; Schmid, S.; Michalski, M.; Tumen, D.; Buttenschon, J.; Muller, M.; Gulow, K. The Influence of Gut Microbiota on Oxidative Stress and the Immune System. *Biomedicines* **2023**, *11*, 1388. [CrossRef] [PubMed]
115. Riaz Rajoka, M.S.; Thirumdas, R.; Mehwish, H.M.; Umair, M.; Khurshid, M.; Hayat, H.F.; Phimolsiripol, Y.; Pallares, N.; Marti-Quijal, F.J.; Barba, F.J. Role of Food Antioxidants in Modulating Gut Microbial Communities: Novel Understandings in Intestinal Oxidative Stress Damage and Their Impact on Host Health. *Antioxidants* **2021**, *10*, 1563. [CrossRef]
116. Naliyadhara, N.; Kumar, A.; Kumar Gangwar, S.; Nair Devanarayanan, T.; Hegde, M.; Alqahtani, M.S.; Abbas, M.; Sethi, G.; Kunnumakkara, A. Interplay of dietary antioxidants and gut microbiome in human health: What has been learnt thus far? *J. Funct. Foods* **2023**, *100*, 105365. [CrossRef]
117. Milutinovic, M.; Dimitrijevic-Brankovic, S.; Rajilic-Stojanovic, M. Plant Extracts Rich in Polyphenols as Potent Modulators in the Growth of Probiotic and Pathogenic Intestinal Microorganisms. *Front. Nutr.* **2021**, *8*, 688843. [CrossRef]
118. Pacheco-Ordaz, R.; Wall-Medrano, A.; Goni, M.G.; Ramos-Clamont-Montfort, G.; Ayala-Zavala, J.F.; Gonzalez-Aguilar, G.A. Effect of phenolic compounds on the growth of selected probiotic and pathogenic bacteria. *Lett. Appl. Microbiol.* **2018**, *66*, 25–31. [CrossRef]
119. Ghibaudo, F.; Gerbino, E.; Copello, G.J.; Campo Dall' Orto, V.; Gomez-Zavaglia, A. Pectin-decorated magnetite nanoparticles as both iron delivery systems and protective matrices for probiotic bacteria. *Colloids Surf. B Biointerfaces* **2019**, *180*, 193–201. [CrossRef] [PubMed]
120. Chang, C.W.; Liu, C.Y.; Lee, H.C.; Huang, Y.H.; Li, L.H.; Chiau, J.C.; Wang, T.E.; Chu, C.H.; Shih, S.C.; Tsai, T.H.; et al. *Lactobacillus casei* Variety *rhamnosus* Probiotic Preventively Attenuates 5-Fluorouracil/Oxaliplatin-Induced Intestinal Injury in a Syngeneic Colorectal Cancer Model. *Front. Microbiol.* **2018**, *9*, 983. [CrossRef] [PubMed]
121. Sobral, F.; Calhelha, R.C.; Barros, L.; Duenas, M.; Tomas, A.; Santos-Buelga, C.; Vilas-Boas, M.; Ferreira, I.C. Flavonoid Composition and Antitumor Activity of Bee Bread Collected in Northeast Portugal. *Molecules* **2017**, *22*, 248. [CrossRef] [PubMed]
122. Akkoyunlu, A.; Dulger, G. Exploring the antibiofilm effects on *Escherichia coli* biofilm associated with colon cancer and anticancer activities on HCT116 cell line of bee products. *Biofouling* **2024**, *40*, 235–244. [CrossRef] [PubMed]

123. Utoiu, E.; Matei, F.; Toma, A.; Diguta, C.F.; Stefan, L.M.; Manoiu, S.; Vrajmasu, V.V.; Moraru, I.; Oancea, A.; Israel-Roming, F.; et al. Bee Collected Pollen with Enhanced Health Benefits, Produced by Fermentation with a *Kombucha* Consortium. *Nutrients* **2018**, *10*, 1365. [CrossRef] [PubMed]
124. Elsayed, N.; El-Din, H.S.; Altemimi, A.B.; Ahmed, H.Y.; Pratap-Singh, A.; Abedelmaksoud, T.G. In Vitro Antimicrobial, Antioxidant and Anticancer Activities of Egyptian *Citrus* Beebread. *Molecules* **2021**, *26*, 2433. [CrossRef] [PubMed]
125. Genc, S.; Taghizadehghalehjoughi, A.; Yeni, Y.; Jafarizad, A.; Hacimuftuoglu, A.; Nikitovic, D.; Docea, A.O.; Mezhuev, Y.; Tsatsakis, A. Fe(3)O(4) Nanoparticles in Combination with 5-FU Exert Antitumor Effects Superior to Those of the Active Drug in a Colon Cancer Cell Model. *Pharmaceutics* **2023**, *15*, 245. [CrossRef] [PubMed]
126. Dabaghi, M.; Rasa, S.M.M.; Cirri, E.; Ori, A.; Neri, F.; Quaas, R.; Hilger, I. Iron Oxide Nanoparticles Carrying 5-Fluorouracil in Combination with Magnetic Hyperthermia Induce Thrombogenic Collagen Fibers, Cellular Stress, and Immune Responses in Heterotopic Human Colon Cancer in Mice. *Pharmaceutics* **2021**, *13*, 1625. [CrossRef]
127. Attie, R.; Chinen, L.T.; Yoshioka, E.M.; Silva, M.C.; de Lima, V.C. Acute bacterial infection negatively impacts cancer specific survival of colorectal cancer patients. *World J. Gastroenterol.* **2014**, *20*, 13930–13935. [CrossRef]

Disclaimer/Publisher's Note: The statements, opinions and data contained in all publications are solely those of the individual author(s) and contributor(s) and not of MDPI and/or the editor(s). MDPI and/or the editor(s) disclaim responsibility for any injury to people or property resulting from any ideas, methods, instructions or products referred to in the content.

antioxidants

MDPI

Article

Rod-Shaped Mesoporous Zinc-Containing Bioactive Glass Nanoparticles: Structural, Physico-Chemical, Antioxidant, and Immuno-Regulation Properties

Xiuan Zhu [1,†], Wenjie Wen [1,†], Jingjing Yan [1], Yuran Wang [1], Rumeng Wang [1], Xiang Ma [1], Dandan Ren [1], Kai Zheng [2], Chao Deng [1,*] and Jue Zhang [1,*]

[1] Anhui Province Engineering Research Center for Dental Materials and Application, School of Stomatology, Binjiang Campus, Wannan Medical College, No. 22, West Wenchang Road, Yijiang District, Wuhu 241002, China; zhuxiuan@wnmc.edu.cn (X.Z.); 20230025@wnmc.edu.cn (W.W.); 20229566@stu.wnmc.edu.cn (J.Y.); 21105010120@stu.wnmc.edu.cn (Y.W.); 21105010119@stu.wnmc.edu.cn (R.W.); 20105010063@stu.wnmc.edu.cn (X.M.); 20230035@wnmc.edu.cn (D.R.)
[2] Jiangsu Province Engineering Research Center of Stomatological Translational Medicine, Nanjing Medical University, Nanjing 210029, China; kaizheng@njmu.edu.cn
* Correspondence: 20120015@wnmc.edu.cn (C.D.); 20210010@wnmc.edu.cn (J.Z.)
† These authors contributed equally to this work.

Abstract: Bioactive glass nanoparticles (BGNs) are applied widely in tissue regeneration. Varied micro/nanostructures and components of BGNs have been designed for different applications. In the present study, nanorod-shaped mesoporous zinc-containing bioactive glass nanoparticles (ZnRBGNs) were designed and developed to form the bioactive content of composite materials for hard/soft tissue repair and regeneration. The nanostructure and components of the ZnRBGNs were characterized, as were their cytocompatibility and radical-scavenging activity in the presence/absence of cells and their ability to modulate macrophage polarization. The ZnRBGNs possessed a uniform rod shape (length ≈ 500 nm; width ≈ 150 nm) with a mesoporous structure (diameter ≈ 2.4 nm). The leaching liquid of the nanorods at a concentration below 0.5 mg/mL resulted in no cytotoxicity. More significant improvements in the antioxidant and M1-polarization-inhibiting effects and the promotion of M2 polarization were found when culturing the cells with the ZnRBGNs compared to when culturing them with the RBGNs. The doping of the Zn element in RBGNs may lead to improved antioxidant and anti-inflammatory effects, which may be beneficial in tissue regeneration/repair.

Keywords: bioactive glass; rod-shaped nanoparticles; radical-scavenging activity; macrophage polarization

1. Introduction

Bioactive glass (BG) has been employed in clinics for more than 50 years since it was first prepared by Larry Hench and co-workers. It belongs to the SiO_2-Na_2O-CaO-P_2O_5 system [1]. Until now, BG with different components and micro/nanostructures has been prepared for different tissue regeneration/repair applications [2].

Mesoporous bioactive glass nanoparticles (MBGNs) with a uniform shape (sphere/rod) have attracted more attention due to their mesoporous structure, uniform shape, and high specific surface area compared with those of traditional BG [3]. The characteristics of the MBGNs mentioned above enable the efficient exchange of therapeutic ions and drugs/functional molecules loaded into Si-O-Si or the porous structure. Plenty of studies have used MBGNs as drug carriers, orthopedic implant coating materials, enhanced bioactive hydrogels, etc. [4,5].

All these materials usually show multifunctional biomedical properties, partly due to the ionic dissolution products of BG [6]. More and more researchers are showing that the ionic dissolution products of MBGNs during degradation stimulate biological functions,

such as osteogenesis, angiogenesis, and antibacterial and antioxidant processes, as well as impacting the immune system by inducing the release of specific growth factors or gene expression in different types of cells [7–9].

Some recent studies found that the immune system plays an important role in the tissue regeneration process [10,11]. Macrophages play a central role in inflammation. Different phenotypes may be displayed in response to different environmental stimuli [12,13]. The polarization of macrophages (M1 and M2 phenotypes) is very important throughout the regeneration process [14,15].

The release of reactive oxygen species (ROS) from cells also has beneficial effects on tissue repair [16]. A long-term and relatively large increase in the quantity of ROS induces damage to vital cellular macromolecules such as DNA, proteins, and lipids. Additionally, a range of reactive species can stimulate an intracellular signaling cascade that increases pro-inflammatory gene expression [17].

The ionic products from the dissolution of bioactive glass showed a great influence on macrophage polarization and strong antioxidant effects [18,19]. A previous study showed that Mg and Si ions dissolved from Mg-containing bioactive glass nanoparticles can regulate the polarization (from M1 to M2) of macrophages and promote osteogenesis [20]. Zinc (Zn) is an important element in the physiological environment. It is the key mediator of immune reactions, bone matrix mineralization, and bone regeneration [21]. A recent study showed that the incorporation of zinc into silicate-based bioglass evidently promoted osteogenesis in vitro while profoundly suppressing inflammatory reactions and osteoclastogenesis [22]. Yu's study found that Zn-coated scaffolds resulted in high M1 polarization at 6 h, triggering an M2 response after 24 h [23]. Another study also revealed that Zn can negatively regulate NF-κB signaling by inactivating PPAR-α, A20, IκB kinase-β (IKKβ), and phosphodiesterase (PDE); realize the conversion of M1 macrophages into M2 macrophages; and induce the secretion of a variety of cytokines, thereby regulating tissue regeneration [24]. Zinc is also widely accepted to be an effective antioxidant element [25]. Cerium-doped bioactive glass was regarded as a representative of the antioxidant series of bioactive glass, but few studies have focused on the antioxidant properties of Zn-doped bioactive glass [26].

The shape of particles is one of the factors influencing the mechanical properties, the ionic products/drug-dissolving process of the MBGN-based implant, the composite hydrogel, etc. [27]. Many studies have focused on the preparation and properties of spherical mesoporous bioactive glass nanoparticles. Recently, plenty of research has found that nanorods often seem to be more efficient in drug delivery to cancer cells compared to nanospheres [28,29]. Moreover, rod-shaped nanoparticle-reinforced nanocomposites showed better mechanical properties than those of spherical nanoparticles [30]. However, there has been less research on rod-shaped bioactive glass nanoparticles than on spherical ones. The fabrication methods, the immune-modulating functions, and the radical-scavenging activity of the rod-shaped Zn-containing bioactive glass nanoparticles still need to be explored.

In this study, rod-shaped zinc-containing mesoporous bioactive glass nanoparticles (ZnRBGNs) were synthesized via a sol–gel method. Zinc ions were doped onto a glass structure using a sintering method. BGNs with different contents of zinc ions were fabricated. The structure and composite of the particles were studied. The cytocompatibility of the particles was evaluated by co-culturing them with L929 cells. Furthermore, the macrophage polarization and radical-scavenging activity induced by the ZnRBGNs in the presence/absence of cells in vitro were explored.

2. Materials and Methods

2.1. Preparation of Zn-Containing Rod-Shaped Mesoporous Bioactive Glass Nanoparticles (ZnRBGNs)

The ZnRBGNs were fabricated using a sol–gel method according to previous studies [25]. Briefly, 0.15 g of cetyltrimethylammonium bromide (CTAB) was dissolved into 18 mL of ddH_2O at 60 °C. After the solution had been stirred for 20 min at 400 r/min, 1.5 mL

of aqueous ammonia (NH_3-H_2O) was dropped into the solution and left to react for 10 min. A total of 0.31 mL of tetraethyl orthosilicate (TEOS) was added to the abovementioned solution. After the reaction had proceeded for 4 h, the products were collected through centrifugation at 8000 rpm for 10 min and then washed with water twice and ethanol once. After drying in an air blast drying oven at 60 °C overnight, the products were dispersed into a zinc acetate solution (1M) and stirred at 300 rpm for 0 h, 2 h, 8 h, and 24 h. Then, the powder was collected through centrifugation at 8000 rpm for 10 min and then washed with water twice and ethanol once. After sintering in a muffle furnace at 700 °C for 4 h, samples named 0h-ZnRBGN, 2h-ZnRBGN, 8h-ZnRBGN, and 24h-ZnRBGN were obtained. All the chemicals were purchased from Shanghai Macklin Biochemical Technology Co., LTD. (Shanghai, China).

2.2. Characterization of the Physical and Chemical Properties of the Samples

The surface morphologies of 0h-ZnRBGN, 2h-ZnRBGN, 8h-ZnRBGN, and 24h-ZnRBGN were tested using a field emission scanning electron microscope (FE-SEM, Regulus 8100, Hitachi, Tokyo, Japan) at an accelerating voltage of 5 kV. Prior to SEM characterization, the nanoparticles were sputter-coated with gold for 30 s using a Quorum SC7640 high-resolution sputter coater to maintain an electrically conductive path. The nanostructure and composition of the different samples were observed using a transmission electron microscope (TEM, X-Max, Oxford Instrument, Abingdon, UK) equipped with an energy-dispersive spectrometer (EDS) at an accelerating voltage of 100 kV. The surface area and pore size of the samples were characterized using a volumetric adsorption analyzer (ASAP 2460, Micromeritics) based on the Brunauer–Emmett–Teller (BET) method. The specific surface area, pore size, and total pore volume were calculated using the Barrett–Joyner–Halenda (BJH) method using the desorption isotherm branch. The chemical structures of all the ZnRBGNs were characterized using a Fourier-transform infrared spectrometer (ATR-FTIR, TENSOR 27, Bruker, Billerica, MA, USA) at wavenumbers ranging from 400 to 2000 cm^{-1} with a resolution of 4 cm^{-1}. X-ray photoelectron spectroscopy (XPS, ESCALAB 250xi, Thermo Fisher Scientific, Waltham, MA, USA) was conducted to measure the composition and states of the Si, O, and Zn elements. The structure of the glass phase was determined using X-ray diffraction (XRD, Rigaku, Smartlab) with Cu Kα radiation (40 mA; 40 kV; 2θ range: 10−80°; scanning speed: 2°/min).

2.3. Cytocompatibility Evaluation In Vitro

2.3.1. Cell Culture

The cytocompatibility of the samples was evaluated by co-culturing them with L929 (American Type Culture Collection; Manassas, VA, USA). The effects on macrophage polarization were evaluated by co-culturing the samples with RAW 264.7 (American Type Culture Collection; Manassas, VA, USA). The cells were cultured in Dulbecco's Minimum Essential Medium (DMEM; Tianjin Songyang, China) supplemented with 10% fetal bovine serum (FBS) and 1% penicillin–streptomycin (Sigma-Aldrich, St. Louis, MI, USA) at 37 °C in a humidified 5% CO_2 incubator. The medium was changed every 2 days.

2.3.2. Preparation of Leaching Solution of Samples

The leaching solution of the samples was prepared to study the cytocompatibility and polarization of the macrophages. The leaching solutions were prepared by dispersing the 0h-ZnRBGN, 2h-ZnRBGN, 8h-ZnRBGN, and 24h-ZnRBGN samples in DMEM at 0.01 mg/mL, 0.1 mg/mL, 0.5 mg/mL, and 1 mg/mL at 37 °C with 200 rpm shaking for 24 h. After filtering with a 0.22-micron filter head, 10% FBS and 1% penicillin–streptomycin were added to the above solution for the following co-culture.

2.3.3. Cytotoxicity and Proliferation

The cytotoxicity and proliferation were evaluated according to a previous study [16]. Briefly, L929 cells were cultured on 24-well plates at 2×10^4 per well overnight for the

adhesion of cells. Then, the culture medium was changed to a leaching solution, and after 24 h of co-culturing, the medium was aspirated, and 300 μL of 10% CCK-8 solution was added. The plate was incubated at 37 °C for 2 h, and the OD value of the supernatant was determined using a microplate reader (Biotek, Cytation3, Rocklin, CA, USA) at 450 nm.

2.3.4. EdU Assay

The EdU cell proliferation kit (E-Click EdU Cell Proliferation Imaging Assay Kit, Elabscience Biotechnology Co., Ltd. Wuhan, China) was used to test cell proliferation. The experiment was conducted according to a previous study [31]. Briefly, the L929 cells seeded in 24-well plates (2×10^4 cells/well) were cultured for 24 h. Then, the cells were treated using an Edu solution; fixed with 4% paraformaldehyde, followed by a treatment with TritonX-100; and then stained using Dapi solution. The EdU-positive cell rate was analyzed using fluorescence microscopy (Olympus, IX73, Shinjuku, Japan) and Image J (version: 2.14.0).

2.3.5. Live–Dead Assay

The viability of L929 co-cultured with the leaching medium (0.1 mg/mL) was qualitatively evaluated using live–dead staining. The living cells were stained with calcein acetoxymethyl ester (calcein AM), while the dead cells were stained with propidium iodide (Shanghai ShengGong, Shanghai, China) according to a previous study [32]. Briefly, the cells were collected through centrifugation at 800 rpm after co-culturing them with the leaching medium for 24 h. Then, the samples were incubated with a staining solution containing 0.4% calcein AM and 0.5% propidium iodide in HBSS at 37 °C in a humidified 5% CO_2 incubator for 30 min. The stained samples were observed using a fluorescence microscope (Olympus, IX73, Shinjuku, Japan), and the data were analyzed using Image J (version: 2.14.0).

2.3.6. Flow Cytometry

Flow cytometry was used to identify the M1 (CD86) and M2 (CD206) macrophage surface markers according to a previous study [16]. The RAW 264.7 cells were plated (1×10^5 cells/well) and cultured with the leaching medium for 3 days. Then, the cells were gently scraped and centrifuged at 300× *g* for 5 min, followed by two rinses with PBS and blocking with 1% bovine serum albumin (BSA) for 30 min. Following this treatment, the cells were labeled with Brilliant Violet 421 (BV421)-conjugated CD206 and Alexa Fluor 647 (AF647)-conjugated CD86 (BD Pharminge, San Diego, CA, USA). A flow cytometer (BD, FACSVerse, San Diego, CA, USA) was used to analyze 500 μL suspensions of the cells.

2.4. Antioxidant Effect Evaluation

2.4.1. ROS (Reactive Oxygen Species) Generation Assay

The quantity of ROS in L929 was measured using the fluorogenic probe 2′,7′- dichlorofluorescein diacetate (DCFH-DA) in the ROS generation assay kit (UElandy Inc., Suzhou, China) [33]. In brief, 1×10^4 cells were seeded into a 96-well plate and incubated for 24 h. Subsequently, the medium was changed to a leaching medium. After incubation for 24 h, the cells were washed and exposed to DCFH-DA (30 μM) for 90 min. After being washed with PBS 3 times, the cells were re-suspended in DMEM without FBS. The cells cultured with a normal medium were the negative control. The cells were observed using a fluorescence microscope (Olympus, IX73, Japan), and the fluorescence intensity was analyzed using Image J (version: 2.14.0).

2.4.2. DPPH Assay

The radical-scavenging capacities of 0h-ZnRBGN and 8h-ZnRBGN were evaluated using the DPPH (1,1-Diphenyl-2-picrylhydrazyl radical 2,2-Diphenyl-1-(2,4,6-trinitrophenyl) hydrazyl) radical-scavenging method [34]. Concentrations of 5 mg/mL of 0h-ZnRBGN and 8h-ZnRBGN were dispersed into a DMSO solution of DPPH (200 μM, Sigma Aldrich) and

then incubated for 3 h; after this, the absorbance was recorded at 517 nm using a microplate reader (Biotek, Cytation3, USA).

All the results were calculated using the following formula.

$$\text{Radical-scavenging activity (\%)} = [1 - (Ae - Ag)/Ac] \times 100$$

Ac: Absorbance of DPPH solution in EtOH at 517 nm
Ag: Absorbance of the samples solutions in EtOH at 517 nm
Ae: Absorbance of DPPH and samples solution in EtOH at 517 nm

2.5. Statistical Analysis

All the experiments were performed using biological replicates, and the data are expressed as the mean ± standard deviation. One-way/two-way analysis of variance (ANOVA) was used to analyze the significance of the differences between the samples. Statistical analyses were performed using GraphPad Prism 9 software (GraphPad, Inc., La Jolla, CA, USA). p values < 0.05 were considered to indicate statistically significant results.

3. Results

3.1. Characterization of the Physical and Chemical Properties of the Samples

3.1.1. The Morphology and Composition of ZnRBGNs

In this study, rod-shaped zinc-containing mesoporous bioactive glass nanoparticles (ZnRBGNs) were prepared using the sol–gel method in an alkaline environment. Zn ions were incorporated into the structure using the immersing–sintering method. The micro/nanostructure of ZnRBGN was observed using TEM and SEM. According to the SEM results (Figure 1), the synthesized rod-shaped bioglass nanoparticles (ZnRBGNs) were monodispersed and showed a rod-shaped morphology, which is a typical feature of silica-based particles synthesized using the Stöber method under alkaline conditions. After doping the zinc element through immersion in a Zn solution for different durations (2 h, 8 h, and 24 h), the samples were still rod-shaped. The nanorods were about 500 nm in length and 150 nm in diameter, which is in accordance with the transmission electron microscopy results (TEM, Figure 2A). All the samples showed a similar rod-shaped morphology, indicating that the doping of Zn did not affect the structure of the bioglass nanoparticles.

Similar to the SEM results, the TEM images showed a rod-shaped morphology with a porous structure for all the ZnRBGNs, which is the typical morphology when using the template method of CTAB. The doping of the Zn element did not significantly change the porous structure. The energy spectrum was analyzed using TEM-EDS at the same time. The elemental distributions of Si and Zn were studied; the green parts reflect the distribution of Si, the red parts indicate O, and the blue parts denote the distribution of the Zn element. The results showed that the Zn composition was improved with the immersion time. The Zn composition of 2h-ZnRBGN could not be measured using TEM-EDS, which showed that the minimum reaction time should be more than 2 h. The Zn composition of 8h-ZnRBGN (Zn wt % = 8.8%) was similar to that of 24h-ZnRBGN (Zn wt % = 9.5%), which indicated that maximum reaction time was about 8 h for Zn doping. Based on the above results, the suitable immersion time in the Zn solution was 8 h. Additionally, the monodispersed nanorods were prepared, and the doping of zinc did not change the rods' morphology.

To study the structure and composition of the samples, XRD, FTIR, and XPS analyses were conducted. A broad peak from about 2theta = 15° to 25° can be seen in the XRD patterns (Figure 3A) of all the samples, which is a typical characteristic of amorphous silicate materials. No significant differences could be found in the XRD patterns of all the samples. The results indicated that the amorphous structure of glass was maintained with the doping of Zn ions, and no Zn crystalline phase developed. The FTIR spectra of the different ZnRBGNs showed the characteristic bands of silicate glass (Figure 3B). The wide band located in the range of 1000–1200 cm^{-1} is attributed to Si-O-Si symmetric stretching vibration. The bands at 806 and 474 cm^{-1} are ascribed to the symmetric stretching and

rocking of Si-O, respectively. All the above results indicate that the blending of Zn ions did not affect the amorphous silica glass structure.

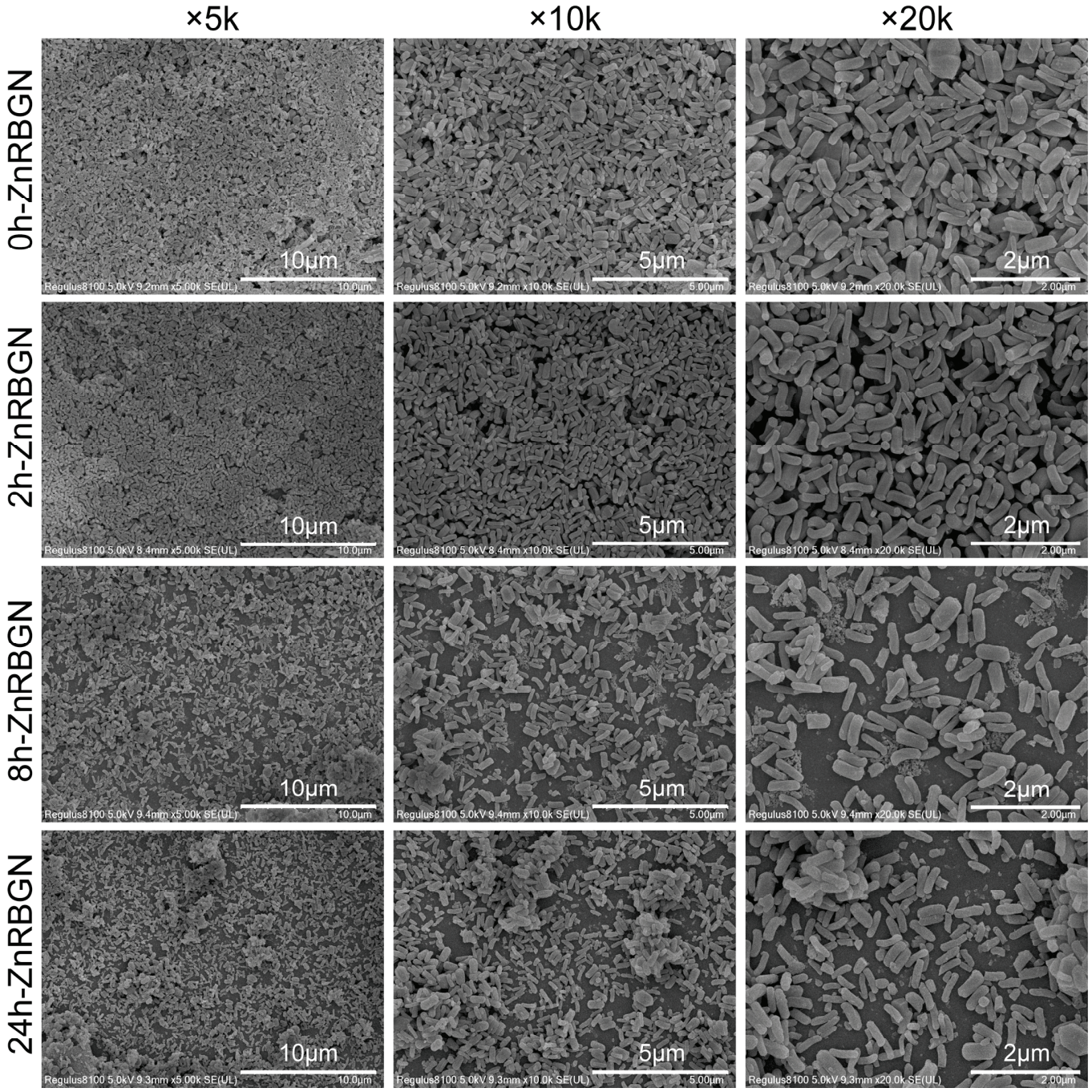


Figure 1. Scanning electron microscopy (SEM) images of 0h-ZnRBGN, 2h-ZnRBGN, 8h-ZnRBGN, and 24h-ZnRBGN (×5 k, ×10 k, and ×20 k).

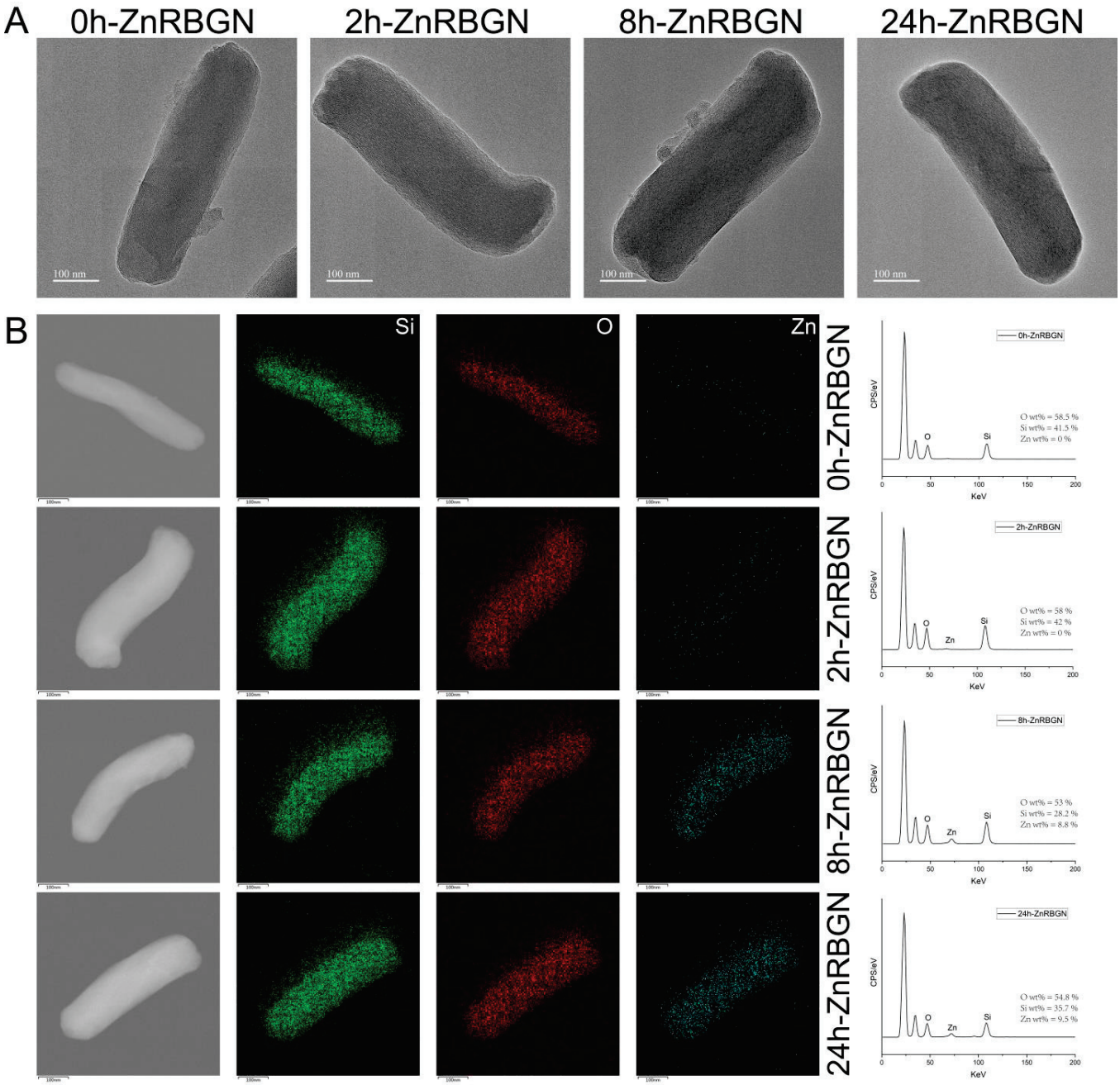


Figure 2. (**A**) Transmission electron microscope (TEM) images of 0h-ZnRBGN, 2h-ZnBGN, 8h-ZnRBGN, and 24h-ZnRBGN. (**B**) Energy spectrum analysis and element distribution (Green pots represented distribution of Si element, red for O and blue for Zn) of 0h-ZnRBGN, 2h-ZnRBGN, 8h-ZnRBGN, and 24h-ZnRBGN.

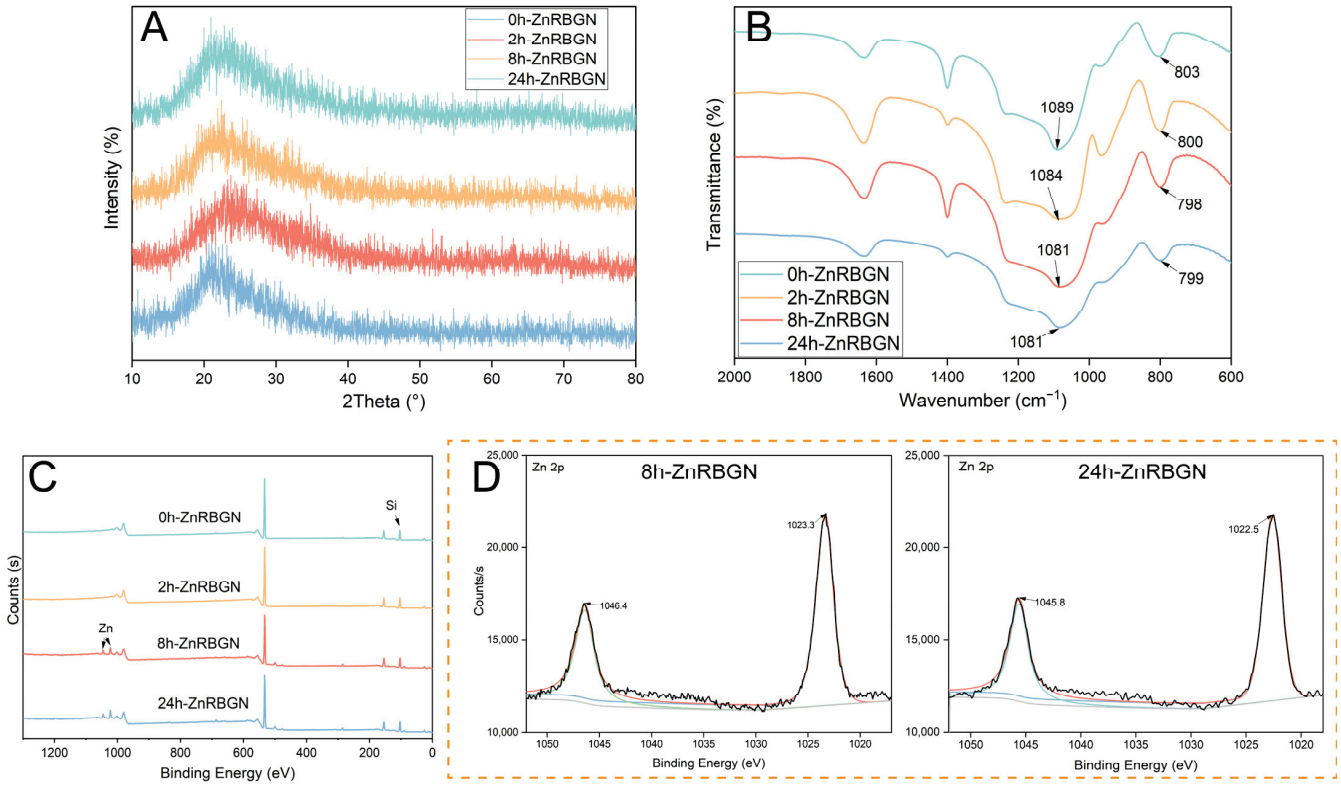


Figure 3. (**A**) XRD pattern, (**B**) FTIR, (**C**) XPS wide scan, and (**D**) narrow scan analyses of 0h-ZnRBGN, 2h-ZnBGN, 8h-ZnRBGN, and 24h-ZnRBGN.

XPS data for all the samples were obtained for the evaluation of the oxidation state of metals, the elemental composition, and the distribution of species (Figure 3C,D). The results showed that the elements distributed in the sample 0h-ZnRBGN were Si and O (Figure 3C), while the elements in 8h-ZnRBGN and 24h-ZnRBGN were Zn, Si, and O. Similar to the results of EDS, peaks corresponding to Zn in 2h-ZnRBGN were too weak to find. Two peaks appeared for 8h-ZnRBGN and 24h-RBGN (Figure 3D) at 1023 and 1046 eV as a result of the 2p orbital splitting of Zn^{2+} of ZnO. Moreover, the Zn 2p peaks are slightly higher, by 1 eV, than the peak of pure ZnO without a host, indicating that there was some Zn interaction with the Si atoms of the host [35]. The composition of Zn in the nanorods improved with immersion during the 8 h. The amorphous silicate structure was maintained after the doping of Zn.

3.1.2. The Mesoporous Structural Analysis of ZnRBGN

A classical type IV isotherm with an H1-type hysteresis can be seen in the N_2 isotherms of all the samples, corresponding to typical mesoporous materials according to the International Union of Pure and Applied Chemistry (IUPAC) classification (Figure 4A). The specific surface areas of 0h-ZnRBGN, 2h-ZnRBGN, 8h-ZnRBGN, and 24h-ZnRBGN were 710.19 m^2g^{-1}, 434.2 m^2g^{-1}, 443 m^2g^{-1}, and 452.74 m^2g^{-1}; the total pore volumes of 0h-ZnRBGN, 2h-ZnRBGN, 8h-ZnRBGN, and 24h-ZnRBGN were 0.46 cm^3g^{-1}, 0.26 cm^3g^{-1}, 0.26 cm^3g^{-1}, and 0.27 cm^3g^{-1} (Figure 4B). The decreases in the total pore volume and specific surface area may have been due to the immersion treatment. However, the treatment did not affect the average pore diameter (about 2.4 nm).

3.2. Cytocompatibility Evaluation In Vitro

The L929 cells were used to evaluate the cytotoxicity of 0h-ZnRBGN, 2h-ZnRBGN, 8h-ZnRBGN, and 24h-ZnRBGN and their effects on proliferation. Concentrations of 0.01 mg/mL, 0.1 mg/mL, 0.5 mg/mL, and 1 mg/mL leaching solution were co-cultured

with L929 for 24 h to evaluate the cytotoxicity of the samples. The results were as follows: (a) the extracts showed no significant cytotoxicity at 0.5 mg/mL; (b) all the 1 mg/mL extracts showed significantly more cytotoxicity than the control. The following co-culturing experiment was conducted with 0.1 mg/mL extracts of all the samples (Figure 5B).

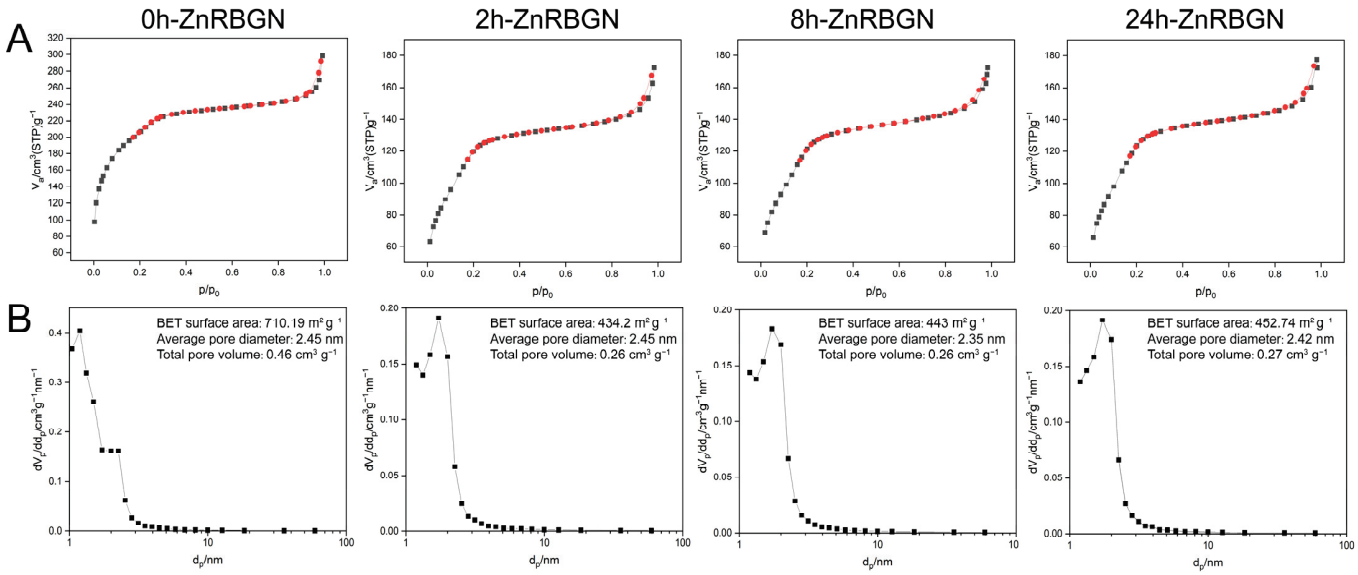


Figure 4. N_2 adsorption–desorption isotherms (**A**) and pore size distributions (**B**) of 0h-ZnRBGN, 2h-ZnRBGN, 8h-ZnRBGN, and 24h-ZnRBGN.

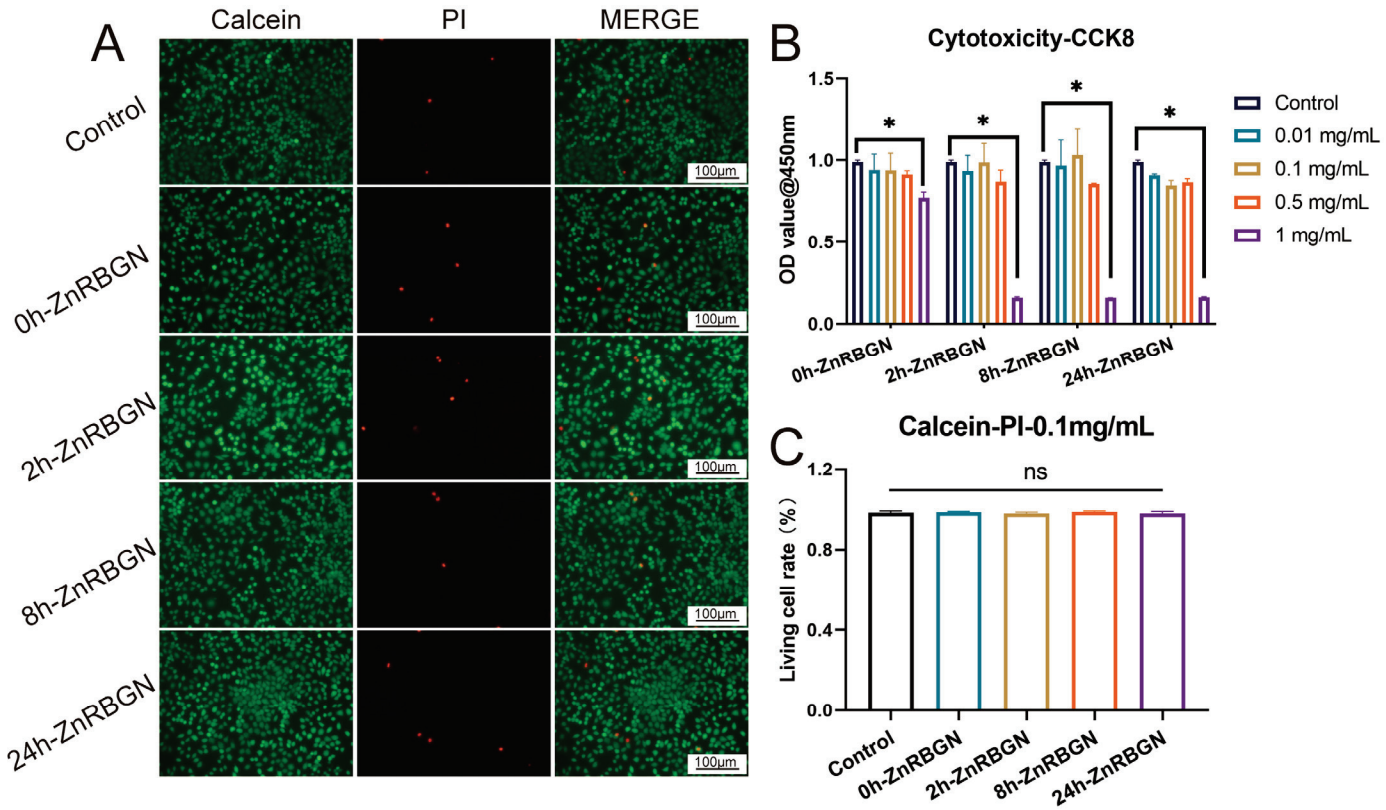


Figure 5. The cytotoxicity evaluation for 0h-ZnRBGN, 2h-ZnRBGN, 8h-ZnRBGN, and 24h-ZnRBGN. (**A**) Live and dead staining. Fluorescence imaging of calcein and PI staining of samples in 0.1 mg/mL. (**B**) OD value of L929 culture with extract of different samples in 0.01, 0.1, 0.5, and 1 mg/mL. (**C**) Quantitative evaluation of live and dead staining. * $p < 0.05$, "ns" means no significant difference.

Figure 5A shows live/dead staining images of L929s after 24 h of co-culturing with 0.1 mg/mL extracts of the different samples. Compared with the control, all the ZnRBGNs showed no significant toxicity (Figure 5A). The proportion of dead cells (marked in red) was about 2% in all the samples (Figure 5C).

The effect of 0h-ZnRBGN, 2h-ZnRBGN, 8h-ZnRBGN, and 24h-ZnRBGN on the proliferation of L929 cells was determined using CCK-8 and EDU assays (Figure 6). There was no significant difference in cell proliferation between the experimental and control groups on days 1 and 3. The results revealed that none of the 0.1 mg/mL extracts of the samples could promote the proliferation of L929 cells.

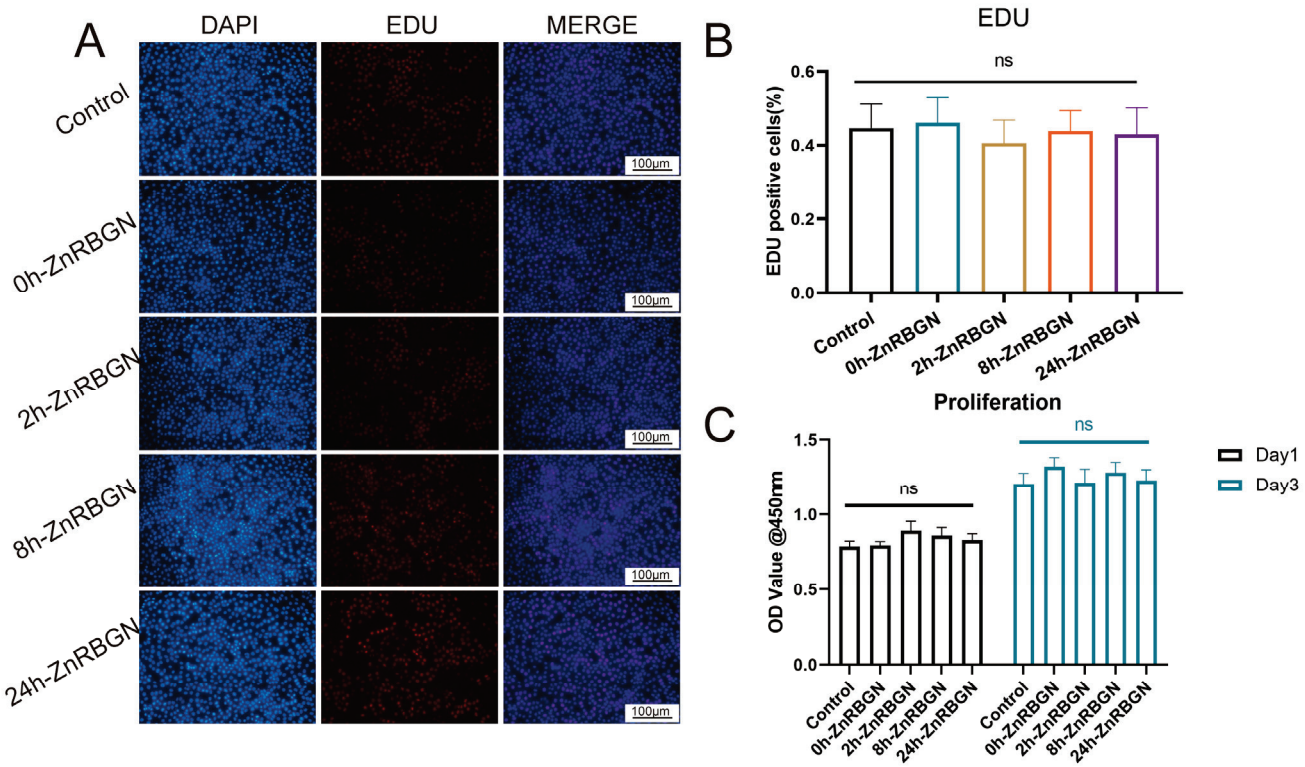


Figure 6. Evaluation of the effects of 0.1 mg/mL extracts of 0h-ZnRBGN, 2h-ZnRBGN, 8h-ZnRBGN, and 24h-ZnRBGN proliferation. (**A**) EDU and Dapi staining. The EDU fluorescence imaging and Dapi staining for the 0.1 mg/mL samples. (**B**) The quantitative evaluation of staining. (**C**) The OD values of the L929 culture with 0.1 mg/mL extracts of the different samples on days 1 and 3, "ns" means no significant difference.

To investigate the polarization of macrophages in response to the extracts of 0h-ZnRBGN, 2h-ZnRBGN, 8h-ZnRBGN, and 24h-ZnRBGN, the proportion of M1- and M2-polarized RAW 264.7 cells was examined using flow cytometry (Figure 7).

The fluorescence intensities of the M1 marker CD86 and the M2 marker CD206 were calculated (Figure 7C). The results revealed that 0h-ZnRBGN and 2h-ZnRBGN suppressed M1 polarization; this may have been due to the exit of the Si element, even though the Zn element promotes M1 polarization. Culturing with 2h-ZnRBGN, 8h-ZnRBGN, and 24h-ZnRBGN significantly promoted M2 polarization, while that with 0h-ZnRBGN did not result in a significant difference from the control. This may illustrate that the exit of Zn may facilitate the M2 polarization of RAW 264.7, while the exit of Si may have no effect on such polarization. Taken together, these results suggested that 2h-ZnRBGN had a more pronounced anti-inflammatory effect than that of the other group MBG, and 2h-ZnRBGN, 8h-ZnRBGN, and 24h-ZnRBGN promoted the conversion of RAW 264.7 to the M2 phenotype.

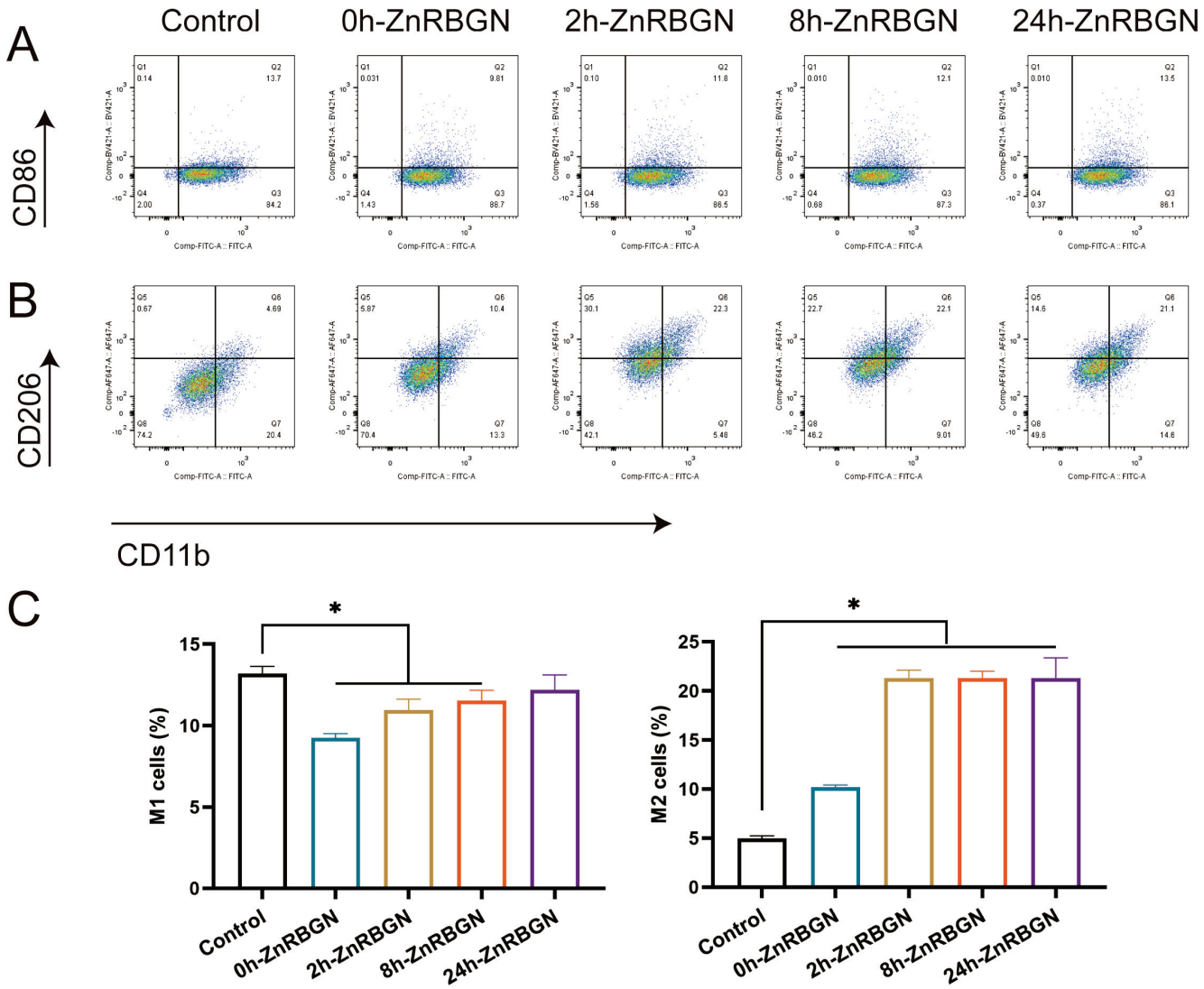


Figure 7. The flow cytometry analysis of macrophage surface marker expression; the fluorescence intensity of CD86 (**A**) and CD206 (**B**) of the RAW 264.7 cells cultured with 0h-ZnRBGN, 2h-ZnRBGN, 8h-ZnRBGN, and 24h-ZnRBGN. (**C**) The macrophage populations of M1 (CD86)- and M2-polarized (CD206) RAW 264.7 cells with 0h-ZnRBGN, 2h-ZnRBGN, 8h-ZnRBGN, and 24h-ZnRBGN. * $p < 0.05$.

3.3. Antioxidant Effect Evaluation

In this work, L929 cells were cultured to evaluate the capacity of rod-shaped nanoparticles to scavenge ROS. The control group showed the highest ROS level, the RBGNs without the Zn element showed a lower ROS level, and all the Zn-containing RBGNs showed the lowest ROS level. No significant differences among the groups of 2h-ZnRBGN, 8h-ZnRBGN, and 24h-ZnRBGN could be found (Figure 8A,B). A DPPH assay is generally used to measure non-enzymatic antioxidant activity. The ZnRBGNs do not have a direct scavenging capacity at 5 mg/mL (Figure 8C).

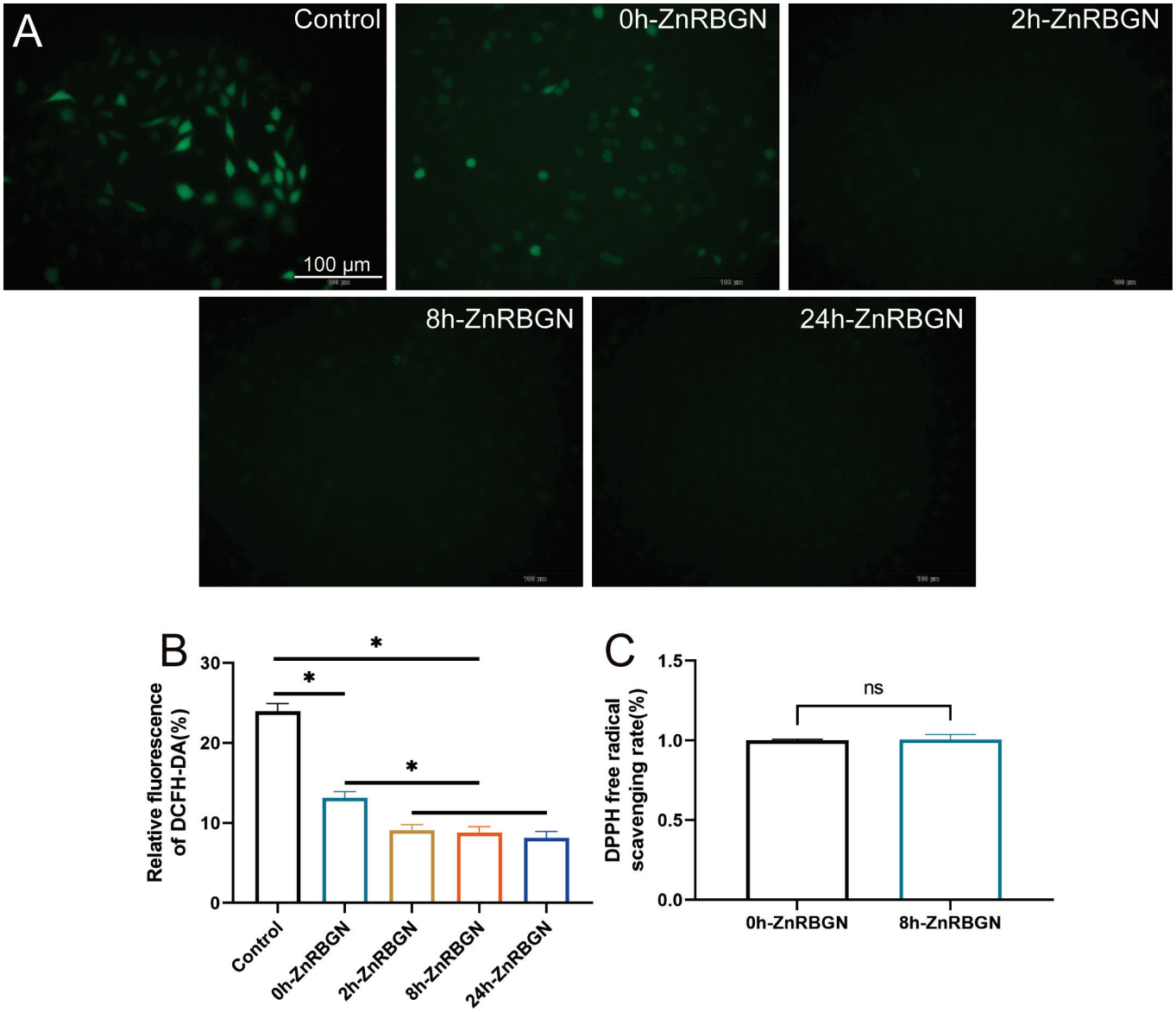


Figure 8. Antioxidant effect analysis. (**A**) ROS generation assay analysis. Images of the cells cultured with the leaching medium (green fluorescence represents ROS) and quantitative analysis (**B**). (**C**) The DPPH free radical-scavenging rates with 0h-ZnRBGN and 8h-ZnRBGN. * $p < 0.05$, "ns" means no significant difference.

4. Discussion

Usually, bioglass nanoparticles are formed into a composite with a polymer substrate to improve hydrophilicity, biocompatibility, osteogenesis, and immune modulation. Bioglass can establish a characteristic environment through the exchange of different types of ions. Different kinds of elements, such as Cu, Mg, Zn, and Ce, were incorporated into the amorphous structure [36]. These ions could be incorporated into the glass structure through the one-step [37] or two-step [38] molding of glass nanoparticles. In our research, the two-step molding process was used for the preparation of the rod-shaped zinc-doped bioactive glass nanoparticles due to the strong alkaline environment, which may have led to the changes in rod shape and mesoporous structure.

Most of the bioactive glass nanoparticles studied were prepared using the Stöber method and had a spherical shape. The rod-shaped mesoporous silica nanoparticles were more effective at delivering drugs to cancer cells than the spherical nanoparticles were. Moreover, the rod-shaped mesoporous silica nanoparticles had better mechanical properties

when used as composite materials compared with those of the spherical particles [39]. Considering the application of bioactive glass nanoparticles, rod-shaped bioactive glass nanoparticles also need to be more intensively researched.

This study successfully synthesized rod-shaped mesoporous zinc-containing bioactive glass nanoparticles (ZnRBGNs) and characterized their structure, cytocompatibility, antioxidant properties, and immune modulation capabilities. These findings highlight the significant potential of ZnRBGNs in biomedical applications, particularly in tissue regeneration. The ZnRBGNs retained a rod-shaped morphology with a uniform size distribution and mesoporous structure, which is essential for enhancing ion exchange and drug-delivery capabilities. However, interestingly, we observed a significant decrease in the BET surface area and total pore volume while the pore diameter was maintained. This may have been due to immersion in the zinc acetate solution; some pore structures of the nanoparticles could have been corroded by the environment.

However, the dispersibility of the nanorods must still be improved. We observed the aggregation of nanorods after dispersing them in the liquid environment. The search for new methods to fabricate new nanocomposites is ongoing.

The successful incorporation of zinc was confirmed by EDS and XPS analyses, indicating its homogeneous distribution within the silica matrix. Zinc can promote angiogenesis, cell proliferation, and migration, as well as the wound-healing process [40]. However, the application of Zn was limited by its toxicity [41]. The doping of Zn into the structure of bioactive glass could lead to the sustained and controlled release of Zn ions. This incorporation is crucial, as zinc ions play vital roles in various biological processes, including enzyme functions, protein synthesis, and cellular signaling.

The cytocompatibility assays demonstrated that the ZnRBGNs did not exhibit significant cytotoxicity at the tested concentrations, ensuring their safety for biomedical applications. The extracts of ZnRBGNs had no significant influence on the proliferation of L929 cells. The ZnRBGNs exhibited strong antioxidant properties, as evidenced by the significant reduction in intracellular ROS levels. The antioxidant capacity of ZnRBGNs is particularly beneficial in mitigating oxidative stress, which is a common challenge in tissue repair and regeneration. High-level oxidative stress can damage cellular components and impede the healing process. By scavenging ROS, ZnRBGNs can protect the cells from oxidative damage and create a healthier regenerative environment. The DPPH assay showed that the ZnRBGNs did not obtain antioxidant properties in the absence of cells. The ions of the extracts were not reducible.

The ability of ZnRBGNs to modulate macrophage polarization is the key finding of this study. The nanoparticles promoted the polarization of macrophages toward the M2 phenotype, which is associated with anti-inflammatory and tissue repair functions, while eliminating the M1 phenotype, which is associated with pro-inflammatory responses. This shift toward M2 polarization is crucial for creating a regenerative microenvironment, as M2 macrophages release anti-inflammatory cytokines and growth factors that support tissue healing and regeneration. The modulation of macrophage behavior by the ZnRBGNs underscores their potential in managing inflammation and enhancing the healing process. The unique combination of properties exhibited by the ZnRBGNs, e.g., toxicity, enhanced cell proliferation, strong antioxidant activity, and favorable immune modulation, makes them highly promising for applications in tissue regeneration. Their ability to simultaneously support cell growth, reduce oxidative stress, and modulate immune responses positions ZnRBGNs as multifunctional agents that can address several critical aspects of the regenerative process. Future research should focus on in vivo studies to further validate the efficacy of ZnRBGNs in tissue regeneration. Investigating the long-term effects and biodegradation profiles of these nanoparticles in living organisms will provide more comprehensive insights into their potential clinical application. Additionally, exploring the incorporation of other therapeutic ions or molecules into ZnRBGNs could enhance their multifunctionality and broaden their application scope.

5. Conclusions

In summary, the rod-shaped mesoporous zinc-containing bioactive glass nanoparticles developed in this study can be used for tissue regeneration applications. The doping of the zinc element did not change the mesoporous and rod-shaped structure of the nanoparticles. A suitable immersion time is about 8 h. ZnRBGNs' biocompatibility, antioxidant activity, and ability to modulate macrophage polarization highlight their therapeutic promise. These findings pave the way for further research and the development of ZnRBGNs as versatile and effective materials in regenerative medicine.

Author Contributions: Methodology, X.Z., W.W., R.W., Y.W. and J.Y.; software, W.W., X.Z., X.M. and C.D.; formal analysis, C.D., J.Z. and D.R.; writing, X.Z. and J.Z.; supervision, K.Z., J.Z. and C.D. All authors have read and agreed to the published version of the manuscript.

Funding: This study was supported by the Natural Science Key project of Anhui Education Department (2022AH051227), the Applied Basic Research Project of Wuhu Science and Technology Bureau (2022jc29, 2022jc30), the Program for Excellent Sci-tech Innovation Teams of Universities in Anhui Province (2023AH010073), the Natural Science Key project of Anhui Education Department (2023AH051741), and the young and middle-aged subjects of Wannan Medical College (WK202201).

Data Availability Statement: All the data sets collected and analyzed during this study are available from the corresponding author upon reasonable request.

Acknowledgments: We acknowledge the help from the students who were involved in the preparation of this manuscript and some suggestions from our colleague Yu Chen in the Anhui Province Engineering Research Center for Dental Materials and Application from Wannan Medical College.

Conflicts of Interest: The authors declare that they have no conflicts of interest.

References

1. Francesco, B.; Sepideh, H.; Saeid, K. Bioactive glasses: Where Are We and Where Are We Going. *J. Func. Biomater.* **2018**, *9*, 25. [CrossRef]
2. Denissen, H.W.; Groot, D.K.; Makkes, P.C.; Hooff, V.D.; Klopper, P.J. Tissue Response to Dense Apatite Implants in Rats. *J. Biomed. Mater. Res.* **1980**, *14*, 713–721. [CrossRef] [PubMed]
3. Vallet-Regi, M.; Salinas, A.J. Mesoporous Bioactive Glasses for Regenerative Medicine. *Mater. Today Bio.* **2021**, *11*, 100121. [CrossRef] [PubMed]
4. Charlotte, V.; Jean-Marie, N. Bioactive Glass Nanoparticles: From Synthesis to Materials Design for Biomedical Applications. *Materials* **2016**, *9*, 288. [CrossRef] [PubMed]
5. Kozon, D.; Zheng, K.; Boccardi, E.; Liu, Y.; Liverani, L.; Boccaccini, A.R. Synthesis of Monodispersed Ag-Doped Bioactive Glass Nanoparticles via Surface Modification. *Materials* **2016**, *9*, 225. [CrossRef] [PubMed]
6. Hoppe, A.; Cudal, N.S.; Boccaccini, A.R. A Review of the Biological Response to Ionic Dissolution Products from Bioactive Glasses and Glass-ceramics. *Biomaterials* **2011**, *32*, 2757–2774. [CrossRef] [PubMed]
7. Dai, Q.; Wang, Z.; Liu, C.; Chen, X.; Cao, X. High Performance Injectable Mg Doped Bioactive Glass Bone Cement for the Regulation of Osteogenic Immune Microenvironment. *Biomater. Adv.* **2024**, *160*, 213864. [CrossRef] [PubMed]
8. Baino, F.; Fiorilli, S.; Mortera, R.; Onida, B.; Vitale-Brovarone, C. Mesoporous Bioactive Glass as a Multifunctional System for Bone Regeneration and Controlled Drug Release. *J. Appl. Biomater. Func. Mater.* **2012**, *10*, 12. [CrossRef]
9. Mo, Y.; Zhao, F.; Lin, Z.; Cao, X.; Chen, D.; Chen, X. Local Delivery of Naringin in Beta-cyclodextrin Modified Mesoporous Bioactive Glass Promotes Bone Regeneration: From Anti-inflammatory to Synergistic Osteogenesis and Osteoclastogenesis. *Biomater. Sci.* **2022**, *10*, 1697–1712. [CrossRef]
10. Schlundt, C.; Fischer, H.; Bucher, C.H.; Rendenbach, C.; Duda, G.N.; SchmidtBleek, K. The Multifaceted Roles of Macrophages in Bone Regeneration: A Story of Polarization, Activation and Time. *Acta Biomater.* **2021**, *133*, 46–57. [CrossRef]
11. Wynn, T.; Chawla, A.; Pollard, J.W. Macrophage Biology in Development, Homeostasis and Disease. *Natural* **2013**, *496*, 445–455. [CrossRef] [PubMed]
12. Dziak, R. Osteoimmunology: Cross-talk between Bone and Immune Cells. *Immunol. Investig.* **2013**, *42*, 657–660. [CrossRef]
13. Walsh, M.C.; Takegahara, N.; Kim, H.; Choi, Y. Updating Osteoimmunology: Regulation of Bone Cells by Innate and Adaptive Immunity. *Nat. Rev. Rheumatol.* **2018**, *14*, 146–156. [CrossRef]
14. Liu, J.Y.; Chen, B.; Bao, J.; Zhang, Y.H.; Lei, L.; Yan, F.H. Macrophage Polarization in Periodontal Ligament Stem Cells Enhanced Periodontal Regeneration. *Stem Cell Res. Ther.* **2019**, *10*, 320. [CrossRef] [PubMed]

15. Zheng, K.; Niu, W.; Lei, B.; Boccaccini, A.R. Immunomodulatory Bioactive Glasses for Tissue Regeneration. *Acta Biomater.* **2021**, *133*, 168–186. [CrossRef] [PubMed]
16. Cerqueni, G.; Scalzone, A.; Licini, C.; Gentile, P.; Mattioli-Belmonte, M. Insights into Oxidative Stress in Bone Tissue and Novel Challenges for Biomaterials. *Mat. Sci. Eng. C Mater.* **2021**, *130*, 112433. [CrossRef] [PubMed]
17. Han, F.; Tu, Z.D.; Zhu, Z.; Liu, D.C.; Meng, Q.C.; Yu, Q.F.; Wang, Y.; Chen, J.Q.; Liu, T.; Han, F.X.; et al. Targeting Endogenous Reactive Oxygen Species Removal and Regulating Regenerative Microenvironment at Annulus Fibrosus Defects Promote Tissue Repair. *ACS Nano* **2023**, *17*, 7645–7661. [CrossRef]
18. Day, R.M.; Boccaccini, A.R. Effect of Particulate Bioactive Glasses on Human Macrophages and Monocytes in vitro. *J. Biomad. Mater. Res. B* **2005**, *73*, 73. [CrossRef] [PubMed]
19. Huang, Y.; Wu, C.T.; Zhang, X.; Chang, J.; Dai, K. Regulation of Immune Response by Bioactive Ions Released from Silicate Bioceramics for Bone Regeneration. *Acta Biomater.* **2018**, *66*, 81–92. [CrossRef]
20. Huo, S.; Wang, F.; Lyu, Z.; Hong, Q.; Nie, B.; Wei, J.; Wang, Y.; Zhang, J.; Yue, B. Dual-functional Polyetheretherketone Surface Modification for Regulating Immunity and Bone Metabolism. *Chem. Eng. J.* **2021**, *8*, 130806. [CrossRef]
21. Wu, D.; Lewis, E.D.; Pae, M.; Meydani, S. Nutritional Modulation of Immune Function: Analysis of Evidence Mechanisms, and Clinical Relevance. *Front. Immunol.* **2019**, *9*, 3160. [CrossRef]
22. Qian, G.; Lu, T.; Zhang, J.; Liu, R.; Wang, Z.; Yu, B.; Li, H.; Shi, H.; Ye, J. Promoting Bone Regeneration of Calcium Phosphate Cement by Addition of PLGA Microspheres and Zinc Silicate via Synergistic Effect of In-situ Pore Generation, Bioactive Ion Stimulation and Macrophage Immunomodulation. *Appl. Mater. Today* **2020**, *19*, 100615. [CrossRef]
23. Yu, D.; Li, B.; Yu, M.; Guo, S.; Guo, Z.; Han, Y. Cubic Multi-ions-doped Na_2TiO_3 Nanorod-like Coatings: Structure-stable, Highly Efficient Platform for Ions Exchanged Release to Immunomodulatory Promotion on Vascularized Bone Apposition. *Bioact. Mater.* **2022**, *18*, 72–90. [CrossRef]
24. Lin, P.H.; Sermersheim, M.; Li, H.; Lee, P.H.U.; Steinberg, S.M.; Ma, J. Zinc in Wound Healing Modulation. *Nutrients* **2017**, *10*, 16. [CrossRef] [PubMed]
25. Ananda, S.P. Zinc: An Antioxidant and Anti-inflammatory Agent: Role of Zinc in Degenerative Diorders of Aging. *J. Trace Elem. Med. Bio.* **2014**, *28*, 364–371. [CrossRef]
26. Kargozar, S.; Hooshmand, S.; Hosseini, S.A.; Gorgani, S.; Kermani, F.; Baino, F. Antioxidant Effects of Bioactive Glasses (BGs) and Their Significance in Tissue Engineering Strategies. *Molecule* **2022**, *27*, 6642. [CrossRef]
27. Liu, W.; Zhang, L.; Dong, Z.; Liu, K.; He, H.; Lu, Y.; Wu, W.; Qi, J. Rod-like Mesoporous Silica Nanoparticles Facilitate Oral Drug Delivery via Enhanced Permeation and Retention Effect in Mucus. *Nano Res.* **2022**, *15*, 9243–9252. [CrossRef]
28. Yang, G.; Gong, H.; Qian, X.; Tan, P.; Li, Z.; Teng, L.; Liu, J.; Li, Y.; Liu, Z. Mesoporous Silica Nanorods Intrinsically doped with Photosensitizers as a Multifunctional Drug Carrier for Combination Therapy of Cancer. *Nano Res.* **2015**, *8*, 751–764. [CrossRef]
29. Katunar, M.R.; Diaz, F.; Boccaccini, A.R.; Ballarre, J. SiO_2-CaO Rod-like Particles in Chitosan Matrix as Bioactive Coatings for Stainless Steel Implants. *Ceram. Int.* **2023**, *49*, 38535–38543. [CrossRef]
30. Boccacini, A.R.; Erol, M.; Stark, W.; Mohn, D.; Hong, Z.; Mano, J.F. Polymer/bioactive Glass Nanocomposites for Biomedical Applications: A Review. *Compos. Sci. Technol.* **2010**, *70*, 1764–1776. [CrossRef]
31. Lei, Y.; Wang, Y.; Shen, J.; Cai, Z.; Zhao, C.; Chen, H.; Luo, X.; Hu, N.; Cui, W.; Huang, W. Injectable Hydrogel Microspheres with Self-renewable Hydration Layers Alleviate Osteoarthritis. *Sci. Adv.* **2022**, *8*, 6449. [CrossRef] [PubMed]
32. Xu, D.; Liu, L.; Zhao, Y.; Yang, L.; Cheng, J.; Hua, R.; Zhang, Z.; Li, Q. Melatonin Protects Mouse Testes from Palmitic Acid-induced Lipotoxicity by Attenuating Oxidative Stress and DNA Damage in a SIRT1-dependent Manner. *J. Pineal Res.* **2020**, *69*, e12690. [CrossRef] [PubMed]
33. Wang, C.; Cheng, Y.T.; Li, B.; Qiu, X.; Hu, H.; Zhang, X.; Lu, Z.; Zheng, F. Transcriptional Characteristics and Functional Validation of Three Monocyte Subsets during Aging. *Immun. Ageing* **2023**, *20*, 50. [CrossRef] [PubMed]
34. Qin, Z.; Zou, Y.; Zhang, Y.; Wang, P.; Zhang, H. Electrospun Pullulan Nanofiber Loading Zanthoxylum Bungeanum Essential oil/β-cyclodextrin Inclusion Complexes for Active Packaging. *Int. J. Biol. Macromol.* **2022**, *210*, 465–474. [CrossRef] [PubMed]
35. Bera, S.; Prince, A.A.M.; Raghavan, P.S.; Gopalan, R.; Panneersevam, G.; Narasimhan, S.V. Formation of Zinc Ferrite by Solid-state Reaction and Its Characterization by XRD and XPS. *J. Mater. Sci.* **2001**, *36*, 5379–5384. [CrossRef]
36. Ege, D.; Lu, H.; Boccaccini, A.R. Bioactive Glass and Silica Particles for Skeletal and Cardiac Muscle Tissue Regeneration. *Tissue Eng. Part B Rev.* **2024**. [CrossRef] [PubMed]
37. Zambon, A.; Malavasi, G.; Pallini, A.; Fraulini, F.; Lusvardi, G. Cerium Containing Bioactive Glasses: A Review. *ACS Biomater-Sci. Eng.* **2021**, *7*, 4388–4401. [CrossRef]
38. Zhu, H.; Zheng, K.; Boccaccini, A.R. Multi-functional Silica-based Mesoporous Materials for Simultaneous Delivery of Biologically Active Ions and Therapeutic Biomolecules. *Acta Biomater.* **2021**, *129*, 1–17. [CrossRef]
39. Cong, V.T.; Gaus, K.; Tilley, R.D.; Gooding, J.J. Rod-shaped mesoporous silica nanoparticles for nanomedicine: Recent progress and perspectives. *Expert Opin. Drug Del.* **2018**, *15*, 881–892. [CrossRef]

40. Song, Y.; Wu, H.; Gao, Y.; Li, J.; Lin, K.; Liu, B.; Lei, X.; Cheng, P.; Zhang, S.; Wang, Y.; et al. Zinc silicate/nano-hydroxyapatite/collagen scaffolds promote angiogenesis and bone regeneration via the p38 MAPK pathway in activated monocytes. *ACS Appl. Mater. Interfaces* **2020**, *12*, 16058–16075. [CrossRef]
41. Chen, Z.; Duan, J.; Diao, Y.; Chen, Y.; Liang, X.; Li, H.; Miao, Y.; Gao, Q.; Gui, L.; Wang, X.; et al. ROS-responsive capsules engineered from EGCG-Zinc networks improve therapeutic angiogenesis in mouse limb ischemia. *Bioact. Mater.* **2021**, *6*, 1–11. [CrossRef] [PubMed]

Disclaimer/Publisher's Note: The statements, opinions and data contained in all publications are solely those of the individual author(s) and contributor(s) and not of MDPI and/or the editor(s). MDPI and/or the editor(s) disclaim responsibility for any injury to people or property resulting from any ideas, methods, instructions or products referred to in the content.

antioxidants

MDPI

Review

Applications of Antioxidant Nanoparticles in Immune-Mediated Inflammatory Diseases

Hong-Wei Shi [1,†], Bo-Cheng Yang [2,†], Yun-Qing Ren [3,*] and Yi Xue [3,*]

[1] Department of Radiology, The Children's Hospital, Zhejiang University School of Medicine, National Clinical Research Center for Child Health, Hangzhou 310058, China; 18846794048@163.com
[2] Department of Plastic Surgery, Zhongshan Hospital Affiliated to Xiamen University, School of Medicine, Xiamen University, Xiamen 361005, China
[3] Department of Dermatology, The Children's Hospital, Zhejiang University School of Medicine, National Clinical Research Center for Child Health, Hangzhou 310058, China
* Correspondence: yqren@zju.edu.cn (Y.-Q.R.); yxue@zju.edu.cn (Y.X.)
† These authors have contributed equally to this work.

Abstract

Immune-mediated inflammatory diseases (IMIDs) encompass a wide range of disorders, including autoimmune, acute, and chronic inflammatory conditions, which are often characterized by immune dysregulation and excessive oxidative stress. Oxidative stress plays a pivotal role in the initiation and progression of these diseases by promoting tissue damage and sustaining inflammation. However, conventional antioxidant therapies are limited by poor bioavailability, inadequate targeting, and short-lived efficacy. In recent years, nano-antioxidants have emerged as a promising therapeutic approach due to their enhanced stability, targeted delivery capabilities, and multifunctional therapeutic effects. This review provides a comprehensive overview of recent advances in the application of nano-antioxidants in the treatment of IMIDs. Their therapeutic roles are categorized into three major groups: autoimmune diseases, acute inflammatory diseases, and chronic inflammatory diseases. In autoimmune disorders such as alopecia areata and multiple sclerosis, nano-antioxidants have demonstrated the ability to reduce oxidative damage, modulate immune responses, and alleviate clinical symptoms. In acute inflammatory conditions, including acute kidney injury and acute liver injury, these nanomaterials exert protective effects by scavenging ROS, mitigating tissue injury, and restoring organ function. In chronic inflammatory diseases such as inflammatory bowel disease and ulcerative colitis, nano-antioxidants contribute to maintaining mucosal integrity, suppressing chronic inflammation, and improving therapeutic outcomes through localized delivery and sustained release. In summary, nano-antioxidants represent a novel and promising therapeutic strategy for the management of IMIDs. Their unique physicochemical properties offer significant advantages over traditional treatments. Further research is needed to optimize their delivery platforms, evaluate long-term safety, and facilitate clinical translation.

Keywords: antioxidant; immune; inflammatory; alopecia areata; multiple sclerosis

1. Introduction

Alopecia areata (AA), multiple sclerosis (MS), and other conditions—including inflammatory bowel disease (IBD), acute liver injury (ALI), acute kidney injury (AKI), and vitiligo—result from immune system dysregulation. Collectively termed immune-mediated inflammatory diseases (IMIDs), these disorders comprise autoimmune pathologies and

span both chronic and acute inflammatory processes [1]. Among the diverse pathogenic mechanisms involved, oxidative stress has emerged as a pivotal contributor to both disease onset and progression [2,3]. Oxidative stress, resulting from an imbalance between reactive oxygen/nitrogen species and intrinsic antioxidant systems, contributes to tissue dysfunction and cellular injury [4]. Accumulating evidence links oxidative stress to immune activation and tissue damage, while also implicating it in the amplification of inflammatory responses, thereby establishing a self-perpetuating pathogenic cycle.

Antioxidants, due to their capacity to counteract oxidative stress, have garnered considerable interest as therapeutic candidates for IMIDs. Conventional small-molecule antioxidants—such as vitamin C, vitamin E, and glutathione—exhibit limited clinical efficacy, primarily owing to low bioavailability, poor tissue specificity, and rapid systemic clearance [5,6]. Recent advances in nanotechnology have enabled new approaches for enhancing antioxidant therapy. Nano-antioxidants, constructed from nanomaterials with high surface-to-volume ratios, favorable biocompatibility, and modifiable surface chemistry, demonstrate improved physicochemical stability, enhanced biological targeting, and elevated therapeutic efficiency [7]. Notably, several nanomaterials possess intrinsic enzyme-mimetic properties. For instance, iron oxide- and manganese-based nanoparticles emulate the catalytic activities of endogenous antioxidant enzymes, including superoxide dismutase (SOD) and catalase (CAT), thereby facilitating efficient elimination of ROS and RNS [8,9]. Curcumin, a natural polyphenol derived from *Curcuma longa*, exhibits potent antioxidant and anti-inflammatory activities. However, its clinical application remains constrained by poor aqueous solubility, rapid metabolic degradation, and limited oral bioavailability. To overcome these barriers, various nanocarrier-based delivery platforms have been developed—such as liposomes, polymeric nanoparticles, solid lipid nanoparticles, and metal–organic frameworks [10]. These formulations significantly enhance curcumin's systemic stability and targeting efficiency, while simultaneously potentiating its antioxidative and immunomodulatory effects. Preclinical studies indicate that curcumin nanoformulations attenuate inflammation, mitigate tissue damage, and improve disease outcomes in autoimmune models such as MS, primarily through ROS scavenging [11]. Beyond curcumin, alternative nano-antioxidant systems exhibit therapeutic potential across multiple IMIDs. Gold nanoparticles (GNPs), owing to their superior biocompatibility and tunable physicochemical properties, have been widely investigated in MS and other immune-related conditions [12]. Experimental findings suggest that GNPs reduce oxidative damage and modulate inflammatory signaling, thereby limiting immune-mediated tissue injury [13,14]. In the context of acute inflammatory pathologies, nano-antioxidants also demonstrate promising efficacy. A recent study reported an ROS-responsive nanoplatform integrating mitochondrial-targeted cerium oxide nanoparticles with atorvastatin. This system enabled site-specific drug release in a septic AKI model, suppressed oxidative stress and inflammation, reduced tubular epithelial apoptosis, and preserved renal architecture [15]. In diseases like IBD, characterized by persistent inflammation, oxidative stress is deeply implicated in driving the pathological cascade leading to tissue damage. Nano-antioxidants have been shown to alleviate intestinal inflammation and reinforce epithelial barrier function by modulating ROS levels and regulating signaling cascades, including NF-κB and Nrf2. Furthermore, co-administration with probiotics enhances therapeutic effects through modulation of gut microbiota homeostasis [16]. Despite substantial progress, several obstacles impede the clinical translation of nano-antioxidants, including uncertainties regarding long-term biocompatibility, metabolic fate, and immunogenicity. Future efforts should emphasize the rational design of nanotherapeutic systems featuring controlled release, disease-specific targeting, and optimal safety profiles to accelerate their deployment in the management of IMIDs.

We summarize the current applications and mechanisms of nano-antioxidants in IMIDs in Tables 1–3. This review provides a comprehensive overview of recent advances in the application of nano-antioxidants in immune-mediated inflammatory diseases, with a particular focus on their roles in autoimmune, acute inflammatory, and chronic inflammatory conditions. The underlying mechanisms, therapeutic efficacy, and safety profiles of nano-antioxidants are critically examined, and future directions for their development and clinical translation are discussed.

Table 1. A brief summary of autoimmune disease treatment based on nano-antioxidant strategies.

Diseases	Active Ingredient	Nanomaterial	Side Effect	Benefit	Ref.
Alopecia areata (AA)	Minoxidil	Molybdenum nanoparticles (Mo NPs)	Mo-NPs may cause liver and kidney toxicity, oxidative imbalance, and potential inflammatory responses	Offering a novel direction and translational potential for antioxidant-based treatment of AA	[17]
Multiple Sclerosis (MS)	Curcumin	Dendritic nanocarriers (DNCs)	High doses (20 μM) reduce neural stem cell viability and increase oxidative stress, shifting differentiation toward astrocytes instead of oligodendrocytes	Enhancing remyelination capacity in vivo	[18]
	BBN-IONPs	Iron oxide nanoparticles	May not adequately reflect long-term effects, with the absence of human trials restricting therapeutic relevance	Elevated glutathione levels and total antioxidant capacity in brain tissues, reduced lipid peroxidation and inflammatory mediators	[19]
	MgH_2	Low-toxicity magnesium hydride nanoparticles (MgH_2)	Uncertainties remain regarding mechanism, brain region sensitivity, and variable microglial polarization effects	Significantly alleviating anxiety- and depression-like behaviors and attenuating inflammatory demyelinating lesions	[20]
	Clobetasol propionate (CP)	Double-layered nanoemulsion	Serious side effects include osteoporosis, glaucoma, and adrenal suppression	Improving brain-targeted delivery and reducing systemic toxicity	[21]
	Selenium and crocin	Crocin–selenium nanoparticles (Cor@SeNs)	Headache in two patients; no severe adverse events observed, generally well tolerated	Ameliorating MS-associated cognitive impairment	[22]
	Methylprednisolone neutrophil membranes	Biomimetic nanosystem (TFMN)	Negligible cytotoxicity up to 200 μg/mL; no severe adverse effects observed in vivo, but long-term safety unknown	Indicating excellent safety and therapeutic potential	[23]

Abbreviation: BBN-IONPs, BBN loaded within iron oxide nanoparticles.

Table 2. A brief summary of acute inflammatory disease treatment based on nano-antioxidant strategies.

Diseases	Active Ingredient	Nanomaterial	Side Effect	Benefit	Ref.
Acute kidney injury	Cerium and luteolin	Cerium–luteolin coordination nanocomposite (CeLutNCs)	Excellent biocompatibility with no significant toxicity or adverse effects in vitro and in vivo	Significantly improved organ function and reduced oxidative stress and inflammation	[24]
	L-serine	L-serine (Rh-Ser, 2–4 nm)	Rh-Ser showed no obvious adverse reactions or systemic toxicity in the experiment	Mimicked multiple antioxidant enzymes to efficiently eliminate RONS	[25]
	Tetrahedral framework nucleic acid (tFNA)	Nanodrug delivery system (TTC)	tFNAs showed good biocompatibility with no nephrotoxicity or significant side effects in vitro and in vivo	Significantly ameliorated renal injury and restored renal function, indicating promising antioxidant-mediated therapeutic effects	[26]
	Epigallocatechin gallate (EGCG) and 5-aminosalicylic acid (5-ASA)	pH-stable antioxidant nanoparticle system (EGA NPs)	EGCG shows poor stability in acidic environments, limiting oral bioavailability	Effectively scavenged ROS and mitigated oxidative stress	[27]
	ethyl caffeate and 4-hydroxybenzyl alcohol	Supramolecular nanoplatform (Ser-HPEC)	No significant systemic side effects in vivo in the experiment	Preserved renal structure and function	[28]
Acute liver injury	Polyphenol	Phlorotannin-based nanoparticles (PT NPs)	Traditional polyphenols face bioavailability and immunogenicity issues	Effectively alleviated oxidative and inflammatory damage	[29]
	Catechin	CCN150	CCN150 showed negligible acute toxicity, but potential long-term risks like	Reduced systemic inflammation driven by ROS	[30]
	NO	BSA-SNO NPs	No significant toxicity observed; potential risks include immune response, NO over-release, or thiol oxidation/cross-linking	Alleviated oxidative stress, improved hepatic microcirculation	[31]
	phenylboronic-acid-protected L-DOPA precursor (PAD)	Responsive biomimetic antioxidant nanoplatform (PADN)	Potential risks include batch variability, incomplete H_2O_2 scavenging, and reactive group-related off-target effects	Integrated efficient ROS scavenging, inflammation suppression, and hepatocyte protection	[32]

Abbreviation: CCN150, catechin-condensed nanotherapeutics; NO, nitric oxide; BSA, serum albumin; BSA-SNO NPs, self-sulfhydrated, nitro-fixed albumin nanoparticles.

Table 3. A brief summary of chronic inflammatory disease healing based on nano-antioxidant strategies.

Diseases	Active Ingredient	Nanomaterial	Side Effect	Benefit	Ref.
Periodontitis	quercetin	A mesoporous bioactive glass-based nanocarrier system	No significant toxicity observed; potential risks include initial burst release and uncertain long-term local effects.	Promoted both osteogenesis and angiogenesis in experimental periodontitis-related bone defects	[33]
	melatonin (MT)	melatonin-derived carbon dots (MT-CDs)	No significant side effects were observed during the experiment	Reduced alveolar bone resorption and osteoclast activity	[34]
	melanin	P/D-MNP-Ag	No significant organ inflammation observed in the experiment	Disrupted biofilms, attenuated inflammation, and reduced alveolar bone loss	[35]
	HAS, Mn^{2+}, $[Fe(CN)6]^{4-}$	HSA-MDSPB NPs	No significant side effects were observed during the experiment	Broadly scavenged ROS species	[36]
Ulcerative colitis (UC)	somatostatin (SST) and manno-oligosaccharide (MOS)	EUP-SeNPs	No obvious toxicity observed, potential risks include selenium accumulation	Improved oral stability and intestinal localization	[37]
	gallic acid	thiolated anionic nanoliposomes	No apparent toxicity observed	Prolonged drug residence time and enhanced local therapeutic effects	[38]
	curcumin	CMC	No obvious toxicity or systemic side effects were observed in this experiment	Effectively scavenged ROS, restored mucosal integrity, and regulated gut microbiota composition to mitigate UC pathology	[39]
	PSB	PSB@NP-FA	Minimized systemic toxicity compared to free DEX	Modulated dendritic cell function, promoted M2 polarization of macrophages, and regulated T cell infiltration	[40]
	TMCs and PEG	PMNFs	No significant side effects	Increased junction protein and MUC2 expression, thereby preserving intestinal barrier function	[41]
	pterostilbene	HA-L-Arg-CO_2@NPs	No significant side effects	Downregulated inflammatory mediators, restored barrier permeability, and effectively alleviated UC symptoms	[42]
	carbon dots	MML-CDs	No significant side effects were observed during the experiment	Demonstrated promising therapeutic efficacy	[43]

Abbreviation: P, phosphate group; D, 2-(Dimethylamino)ethyl methacrylate; MNP-Ag, melanin-Ag; HSA-MDSPB, human serum albumin-crosslinked, manganese-doped, self-assembling Prussian blue; CMC, carboxymethyl cellulose; PSB, pterostilbene; NP, nanoparticle; FA, folic acid; TMCs, transition metal chalcogenides; PEG, polyethylene glycol; PMNFs, PEG-modified Mo3Se4 nano flakes; HA-L-Arg-CO_2@NPs, hyaluronic acid (HA)-modified L-arginine CO_2 nanoparticles; MML-CDs, carbon dots derived from magnetite and medicated leaven.

2. Methods

Relevant studies discussing nano-antioxidants in IMIDs were identified through an extensive literature survey utilizing five core academic databases, including PubMed, Embase, Scopus, Web of Science, and Google Scholar, focusing on publications from January 2020 to June 2025. The literature search included publications available up to June 2025. Keywords and search phrases were carefully selected, including terms such as "nano-antioxidants", "autoimmune diseases", "acute inflammation", "chronic inflammatory diseases", "alopecia areata", "multiple sclerosis", "ulcerative colitis", "periodontitis", and "inflammatory bowel disease". The search strategy focused on identifying studies that explored the application, mechanism, or therapeutic efficacy of nano-antioxidants in immune-related inflammatory conditions. Studies meeting the following criteria were included: (1) investigations that evaluated nano-antioxidant therapies related to autoimmune, acute, or chronic inflammatory diseases; (2) research involving nanoformulations designed to improve antioxidant delivery or bioactivity; (3) preclinical or clinical studies with reproducible methodologies and consistent outcome measures; and (4) experimental studies—either in vitro or in vivo—examining the antioxidant capacity or immune-modulating effects of nanomaterials. Exclusion criteria were as follows: (1) studies with inconclusive evidence regarding the therapeutic benefit of nano-antioxidants; (2) publications lacking rigorous experimental protocols or clearly defined results; (3) non-randomized or observational studies without proper controls; (4) articles not published in English; and (5) narrative reviews, opinion pieces, or book chapters without primary research data.

3. Nano-Antioxidants for Autoimmune Diseases

3.1. Alopecia Areata

Characterized by patchy, non-scarring hair loss primarily on the scalp and other hairy areas, AA represents a T cell-mediated autoimmune inflammatory disorder [44]. Though the etiological framework of AA has not been fully delineated, the impairment of immune privilege within hair follicles continues to dominate current pathogenic models [45]. In addition, genetic predisposition, hypersensitivity, dysbiosis of skin and gut microbiota, and psychological stress are also recognized as important contributing factors to disease onset. Epidemiological data from the United States estimate the prevalence of AA to be approximately 0.1–0.2% [46]; however, this may be an underestimation due to underreporting and limited sample representativeness. AA significantly impairs patients' quality of life and remains a therapeutic challenge in clinical practice. In recent years, oxidative stress—defined as an imbalance between pro-oxidant and antioxidant defenses—has been increasingly implicated in the disruption of immune privilege, contributing significantly to the pathogenesis of AA [47].

AA patients exhibit elevated systemic oxidative stress, as evidenced by increased serum levels of advanced glycation end-products (AGEs) and advanced oxidation protein products, alongside decreased antioxidant indices such as ferric reducing antioxidant power (FRAP), paraoxonase-1, and lecithin–cholesterol acyltransferase. Notably, FRAP levels correlated positively with the extent of hair loss and negatively with C-reactive protein, indicating a close association between oxidative stress, inflammation, and disease severity [48]. Similarly, in a cohort of 40 patients with alopecia areata (AA), Sachdeva et al. [49] reported significantly elevated serum malondialdehyde (MDA) levels, indicative of heightened oxidative stress. Concurrently, both total antioxidant status (TAS) and SOD activity were markedly reduced compared to healthy controls, with the degree of reduction showing a clear correlation with disease severity. Moreover, impaired autophagy has been implicated in AA, as evidenced by reduced expression of autophagy-related proteins ATG5 and LC3B and increased expression of p62 in hair matrix tissues of AA patients.

Concurrently, oxidative stress biomarkers—including MDA, AGEs, and ischemia-modified albumin (IMA)—are significantly elevated in serum and lesional skin, suggesting potential diagnostic and monitoring value [50]. Taskin et al. [51] further demonstrated significantly increased serum levels of nitric oxide (NO·), peroxynitrite ($ONOO^-$), and nitric oxide synthase (NOS) activity in AA patients, indicating that nitrosative stress also contributes to AA pathophysiology. As $ONOO^-$ represents a convergence point between oxidative and nitrosative stress, it may exacerbate oxidative injury. These findings highlight NOS-related parameters as potential biomarkers. Accumulated evidence from observational studies over the past two decades (2000–2024) indicates that patients with AA consistently exhibit elevated oxidative stress markers (e.g., OSI, MDA) and reduced antioxidant enzyme activity, including SOD and glutathione peroxidase, suggesting a compromised antioxidant defense system. Collectively, these findings underscore the central role of oxidative stress in AA pathogenesis and provide a theoretical foundation for antioxidant-based therapeutic strategies [52].

Meanwhile, localized drug delivery approaches—particularly microneedle patches—have attracted increasing attention. A hydrogel-based microneedle immunomodulatory system has been developed to deliver regulatory T cell (Treg)-associated factors, such as CCL22 and interleukin-2 (IL-2), to effectively recruit and expand Tregs within lesional areas, thereby re-establishing local immune tolerance. IL-2 functions as a crucial survival and proliferation factor for regulatory T cells (Tregs) and has been widely utilized to selectively expand Tregs in both experimental and clinical settings. In AA mouse models, this system significantly enhanced Treg infiltration, suppressed inflammatory signaling pathways, and promoted hair regrowth [53]. Additionally, soluble microneedle array patches (S-MAPs) composed of hyaluronic acid have been employed for the transdermal delivery of the Janus kinase (JAK) inhibitor baricitinib in a painless and noninvasive manner, thereby avoiding systemic adverse effects. In AA models, this strategy achieved significantly higher hair regrowth rates (82% vs. 31%) compared to oral administration [54]. Although baricitinib is not a direct antioxidant, it exerts indirect antioxidant effects by downregulating pro-inflammatory cytokines such as IL-6, IFN-γ, and TNF-α via JAK/STAT pathway inhibition, thereby reducing oxidative enzyme activity and ROS production, contributing to a combined anti-inflammatory and antioxidant effect [55]. In the realm of nanomaterials, Xiao et al. [17] examined the effects of molybdenum nanoparticles (Mo NPs) on AA progression through the modulation of oxidative stress. As a novel nano-antioxidant, Mo NPs possess a multivalent electronic structure and can promote hair regrowth by eliminating ROS, alleviating oxidative stress, and activating hair follicle stem cells. Characterization studies revealed that Mo NPs had an average diameter of approximately 50 nm (TEM, Figure 1A) and exhibited characteristic Mo 3d multivalence peaks (XPS, Figure 1B). In vivo, mice treated with Mo NPs exhibited visible hair regrowth as early as day 7 (Figure 1C), and hair shaft length was significantly greater than in controls (Figure 1D,E), with synergistic effects observed when combined with minoxidil. Mechanistically, Mo NPs significantly downregulated the expression of the oxidative stress markers iNOS and COX2 in hair follicle tissue (Figure 1F–H), further supporting their hair-promoting effect via antioxidative pathways. In conclusion, Mo NPs demonstrate excellent antioxidant activity and can act synergistically with conventional therapies such as minoxidil, offering a novel direction and translational potential for antioxidant-based treatment of AA. Future studies should explore their long-term efficacy and safety to facilitate clinical application.

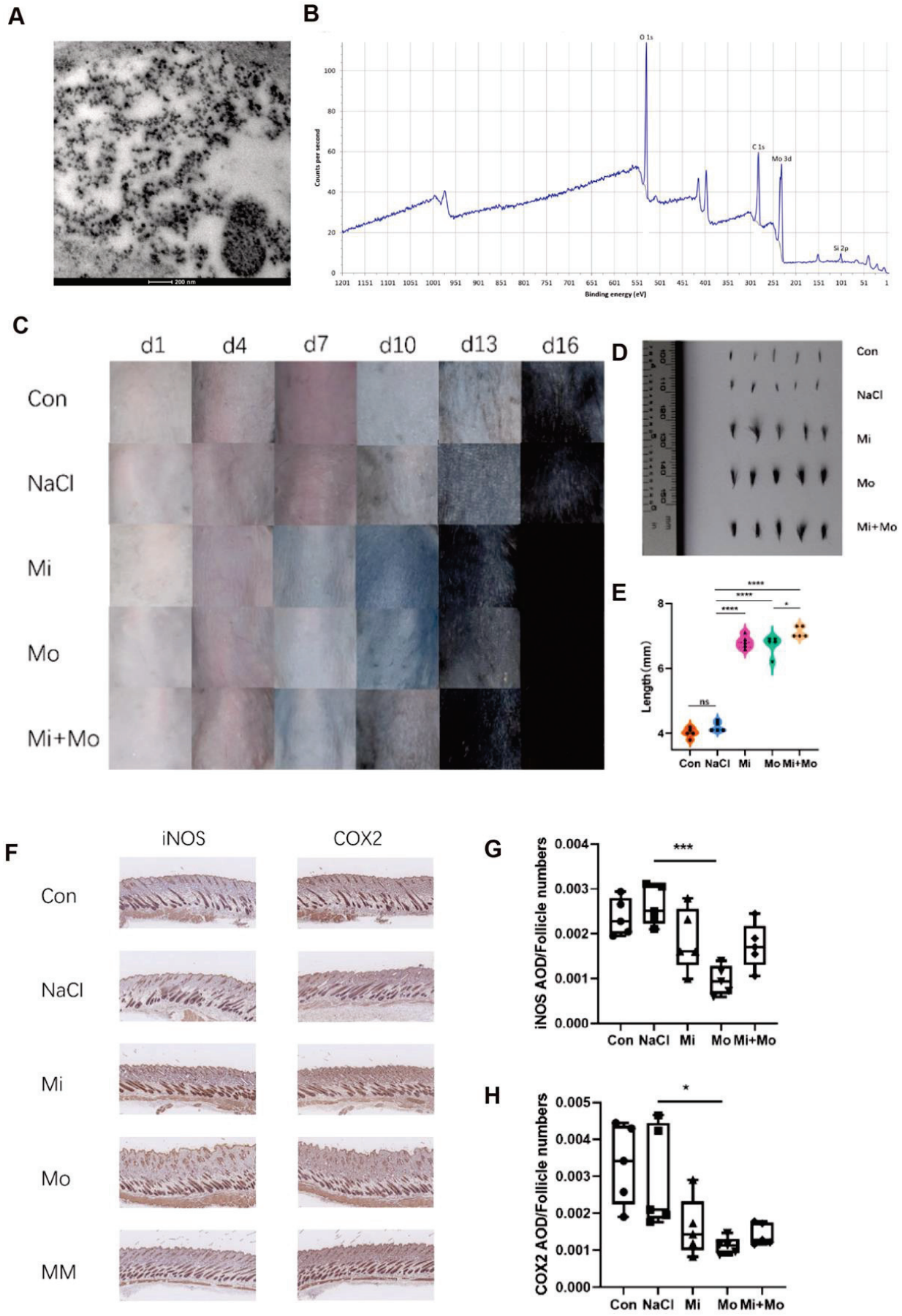


Figure 1. (**A**). TEM image showing Mo NPs distributed on mouse skin (scale bar: 200 nm). (**B**). XPS

spectrum of Mo NPs, with O, C, and Si peaks as references. (**C**). Representative dorsal skin images on days 1, 4, 7, 10, 13, and 16 across treatment groups. (**D**). Hair length assessment on day 16 via representative photos. (**E**). Comparison of hair length among five groups on day 16. (**F**). Immunohistochemical staining of iNOS and COX2 in skin tissues (10×, scale bar: 100 μm) from Con, NaCl, Mi, Mo, and MM groups. (**G**,**H**). Quantitative AOD analysis of iNOS and COX2 per follicle. Mean ± SD values were obtained from five mice in each group (n = 5). * $p < 0.05$; *** $p < 0.001$ indicate statistical significance. Copyright 2024 Elsevier GmbH.

3.2. Multiple Sclerosis

MS is characterized by immune-mediated damage targeting the central nervous system (CNS), leading to the formation of multifocal lesions in the brain and spinal cord, primarily involving demyelination and neuroinflammation. These lesions are predominantly located in the white matter and can be detected by magnetic resonance imaging. However, due to technical limitations, the identification of gray matter and cortical lesions remains challenging, posing a major difficulty in both diagnosis and treatment [56]. MS is frequently accompanied by psychiatric symptoms such as anxiety and depression, which significantly compromise patients' quality of life and adherence to treatment. Reports indicate that between 2015 and 2022, the age- and sex-standardized incidence of MS showed a slight declining trend, ranging from 17.46 per 100,000 population in 2016 (95% CI: 17.12–17.80) to 15.65 per 100,000 in 2019 (95% CI: 15.34–15.97) [57]. The pathogenesis of MS is closely associated with immune-mediated inflammation and oxidative stress, the latter of which induces neuronal damage through ROS-related signaling pathways [58]. Fluctuations in the redox environment can trigger cell type-specific stress responses, disrupt metabolic homeostasis, and exacerbate disease progression. Therefore, therapeutic strategies targeting oxidative stress, particularly low-toxicity and multi-targeted nano-antioxidants, have emerged as a research hotspot in MS therapy.

To improve its chemical stability and enhance absorption, curcumin—a natural antioxidant—has been integrated into a range of nanocarrier technologies [59]. For example, dendritic nanocarriers (DNCs) based on curcumin have been shown to dose-dependently promote the differentiation of neural stem cells (NSCs) and oligodendrocyte precursor cells (OPCs) into oligodendrocytes, thereby enhancing remyelination capacity in vivo. DNCs also improve the survival and differentiation efficiency of transplanted NSCs, synergistically facilitating myelin repair [18]. In addition, a high-density lipoprotein-mimicking peptide-phospholipid scaffold (HPPS) has been utilized to deliver curcumin (Cur-HPPS) in a targeted manner. This system exerts anti-inflammatory and antioxidant effects by inhibiting the NF-κB pathway and reducing the expression of key mediators involved in immune cell recruitment, offering a novel direction for the precision treatment of MS [60]. Another study developed a system of iron oxide nanoparticles loaded with berberine (BBN-IONPs), which demonstrated superior neuroprotective and antioxidant effects in MS animal models compared to free berberine. This nanoplatform improved CPZ-induced cognitive impairment, elevated glutathione levels and total antioxidant capacity in brain tissues, reduced lipid peroxidation and inflammatory mediators, and modulated the expression of the key molecules MBP and MMP-9 and other key effector molecules [19].

In recent years, antioxidant strategies based on nanotechnology have shown broad application prospects in autoimmune diseases of the CNS. Low-toxicity magnesium hydride nanoparticles (MgH_2) have also shown promising efficacy in MS mouse models, significantly alleviating anxiety- and depression-like behaviors and attenuating inflammatory demyelinating lesions [20]. The underlying mechanism may involve the promotion of M2-type microglial polarization, the inhibition of M1-type polarization, and the mitigation of oxidative stress and mitochondrial damage, suggesting their potential in treating MS-

related neuropsychiatric disorders. Sanadgol et al. [61] showed that metformin facilitates the maturation of oligodendrocyte progenitor cells via the activation of the AMPK/mTOR signaling pathway while enhancing Nrf2-mediated antioxidant responses, thereby facilitating remyelination. Abdelalim et al. [21] developed a double-layered nanoemulsion system using lactoferrin and chitosan to encapsulate clobetasol propionate (CP), improving brain-targeted delivery and reducing systemic toxicity. The prepared nanoparticles exhibited stable physicochemical properties (mean particle size: ~220 nm; zeta potential: +30.23 mV) and an antioxidant capacity equivalent to 9.8 μM of vitamin C. Rezaeimanesh et al. [22] were the first to evaluate the effects of crocin–selenium nanoparticles (Cor@SeNs) on cognitive function and oxidative stress status in patients with MS. In a triple-blind, randomized controlled trial, 60 MS patients treated with Cor@SeNs for 12 weeks showed a marked enhancement in total antioxidant capacity (TAC; $p = 0.01$) and marked improvements in several cognitive assessment scores, including CVLT-II, CVLT-II-delay, and SDMT (all $p < 0.01$), indicating its potential in ameliorating MS-associated cognitive impairment. Yang et al. [23] developed a biomimetic nanosystem (TFMN) camouflaged with neutrophil membranes, which demonstrated multiple therapeutic effects in MS models. TFMN demonstrated potent scavenging activity against key reactive oxygen species, including $O_2^{\bullet -}$, H_2O_2, and $^{\bullet}OH$ (Figure 2A), thereby reducing ROS-mediated neuronal injury, and significantly inhibited the migration of inflammatory cells across the blood–brain barrier (Figure 2B). In a PC12 cell oxidative injury model, TFMN significantly enhanced cell viability (Figure 2C–E), and in EAE mouse models, it lowered clinical scores, maintained stable body weight (Figure 2E,F), and mitigated inflammatory cell infiltration and demyelination in the brain and spinal cord (Figure 2G), indicating excellent safety and therapeutic potential. In summary, antioxidant strategies—particularly those based on multi-targeted nanomaterials—exhibit substantial advantages in the treatment of MS. These approaches not only alleviate inflammation and oxidative damage but also show potential in improving cognitive and psychiatric comorbidities, providing new perspectives and experimental foundations for the future development of individualized and precision therapies for MS.

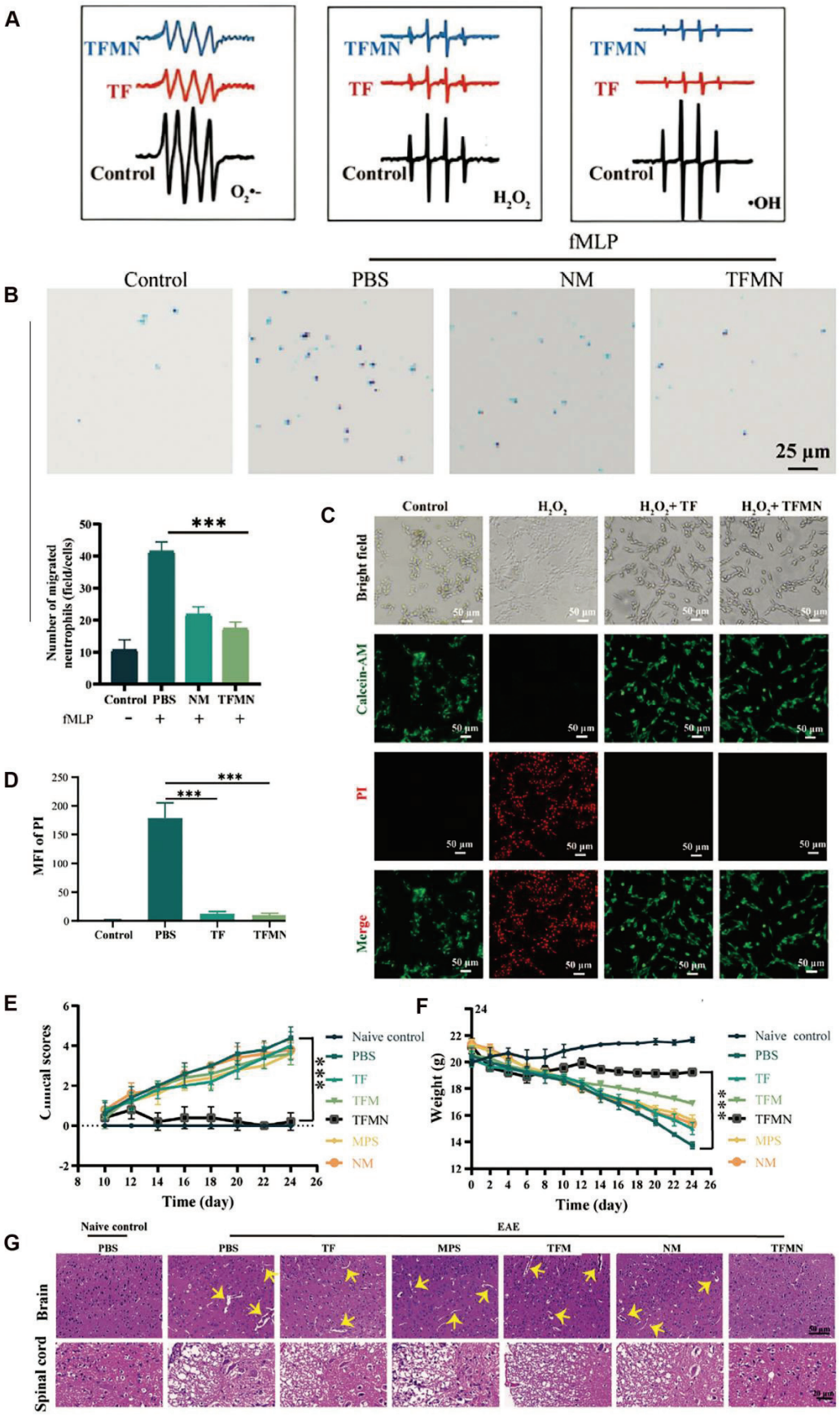


Figure 2. (**A**). Electron paramagnetic resonance (EPR) spectra of $O_2^{\bullet-}$, H_2O_2, and $^{\bullet}OH$ in various treatment groups, with 5,5-dimethyl-1-pyrroline N-oxide (DMPO) employed as the spin-trapping reagent. (**B**). Representative images and quantification of neutrophil migration ($n = 3$). Scale bar: 25 μm.

(**C**,**D**). Live/dead cell staining and corresponding quantification of propidium iodide (PI) fluorescence intensity in PC12 cells under different treatments. (**E**). Average clinical scores recorded for mice in each experimental group (n = 6). (**F**). Changes in body weight of EAE mice subjected to distinct treatment protocols (n = 6). (**G**). H&E-stained sections of brain and spinal cord tissues from EAE mice. Scale bars: 50 μm (brain) and 20 μm (spinal cord). Yellow arrows highlight areas of demyelination. Statistical significance assessed by one-way ANOVA followed by Tukey's post hoc test, *** $p < 0.001$. Copyright 2024 Wiley-VCHGmbH.

4. Nano-Antioxidants for Acute Inflammatory Diseases

4.1. Acute Kidney Injury

The kidneys play a critical role in maintaining systemic homeostasis due to their abundant blood perfusion and high oxygen consumption, enabling efficient clearance of metabolic waste. However, these same characteristics also make the kidneys more susceptible to exposure to toxic substances and hypoxic conditions [62]. In AKI, renal function declines rapidly within a limited period, often leading to systemic complications that carry high morbidity and mortality. In the 2017 study population, the age-standardized incidence rates of AKI varied across regions, ranging from 12.9 to 14.9 cases per 1000 person-years [63]. Currently, no specific clinical therapies are available for AKI, highlighting the urgent need to develop effective therapeutic strategies. Accumulating evidence indicates that the excessive accumulation of reactive oxygen and nitrogen species (RONS) at injury sites is a key driver of AKI progression. However, due to the structural complexity, cellular heterogeneity, and specialized physiology of the kidneys, conventional antioxidant and anti-inflammatory small-molecule drugs exhibit limited efficacy, primarily due to poor targeting capability and adverse side effects [64].

To address these limitations, various nanomedicine-based antioxidant strategies have emerged. Gu et al. [24] synthesized a cerium–luteolin coordination nanocomposite (CeLut-NCs), which effectively scavenges ROS, inhibits apoptosis, downregulates inflammatory cytokines, modulates macrophage activity, and suppresses NF-κB signaling. In both AKI models, CeLutNCs significantly improved organ function and reduced oxidative stress and inflammation, demonstrating strong therapeutic potential for ROS-related diseases. Zheng et al. [25] developed ultrasmall rhodium nanoparticles modified with L-serine (Rh-Ser, 2–4 nm), which mimic multiple antioxidant enzymes to efficiently eliminate RONS. Additionally, Rh-Ser generated oxygen at inflamed sites, alleviating hypoxia and suppressing inflammation, and increased the survival rate of AKI mice from 0% to 80%, outperforming traditional treatments. Yan et al. [26] designed a tetrahedral framework nucleic acid (tFNA)-based nanodrug delivery system (TTC), which specifically targets renal tubular cells and mitochondria, reduces oxidative stress, and suppresses apoptosis. In vitro and in vivo ischemia–reperfusion (I/R) models showed that TTC significantly ameliorated renal injury and restored renal function, indicating promising antioxidant-mediated therapeutic effects. Pan et al. [27] developed a pH-stable antioxidant nanoparticle system (EGA NPs), based on epigallocatechin gallate (EGCG) and 5-aminosalicylic acid (5-ASA). Through a "dissociation-reassembly" mechanism under acidic conditions, these particles self-assemble into stable nanoparticles with robust antioxidant and anti-inflammatory properties, suitable for both oral and intravenous administration. EGA NPs not only effectively scavenge ROS and mitigate oxidative stress but also serve as a drug delivery vehicle for anti-inflammatory agents such as curcumin, significantly enhancing their therapeutic efficacy in vivo. Jia et al. [28] proposed a supramolecular nanoplatform (Ser-HPEC) for AKI therapy, possessing ROS-responsive antioxidant capabilities. Leveraging a Kim-1-mediated targeting mechanism via L-serine, Ser-HPEC selectively accumulates at I/R-injured renal

sites and, under high ROS conditions, releases two antioxidant molecules—ethyl caffeate and 4-hydroxybenzyl alcohol. This results in efficient ROS scavenging, attenuation of oxidative stress and acute inflammation, and preservation of renal structure and function. Furthermore, a cerium-based nanozyme system with mitochondrial targeting capacity was successfully constructed. Transmission electron microscopy (TEM) images revealed that unmodified Ceria nanoparticles (Ceria NPs) [15] had a uniform spherical morphology with an average diameter of 7.74 ± 1.35 nm, while triphenylphosphine (TPP)-modified TCeria NPs exhibited a slightly larger diameter of 8.16 ± 1.98 nm, retaining good shape and dispersity (Figure 3A,B). Fourier-transform infrared spectroscopy (FT-IR) confirmed successful TPP modification, with characteristic absorption peaks at 1700–1900 cm^{-1} corresponding to the aromatic structure of TPP (Figure 3C). Mitochondrial membrane potential ($\Delta\psi m$) was assessed using JC-1 dye. In H_2O_2-treated cells, a significant reduction in the red/green fluorescence ratio indicated mitochondrial depolarization, whereas treatment with Atv/PTP-TCeria NPs restored $\Delta\psi m$ to near-normal levels (Figure 3D). Flow cytometry showed that this formulation significantly reduced H_2O_2-induced apoptosis (below 20%), outperforming both free drugs and empty carriers (Figure 3E). Quantitative fluorescence analysis further validated its mitochondrial protective effect (Figure 3F). In vivo imaging using near-infrared fluorescent dye (ICG)-labeled nanoparticles revealed sustained accumulation of Atv/PTP-TCeria NPs in the kidneys of AKI mice for over 36 h, indicating excellent passive targeting capability (Figure 3G). Quantitative analysis confirmed significantly higher fluorescence intensity in AKI kidneys compared to healthy controls, consistent with enhanced permeability and retention (EPR) effects (Figure 3H). Additionally, treatment with Atv/PTP-TCeria NPs significantly increased renal SOD activity, restoring redox homeostasis and demonstrating superior ROS-scavenging ability compared to free drugs and control groups (Figure 3I). In summary, the constructed Atv/PTP-TCeria NPs system possesses multiple advantages, including precise size control, effective mitochondrial targeting, ROS responsiveness, and synergistic drug release. These features enable it to significantly ameliorate AKI-associated pathological processes at both cellular and animal levels, offering a promising nanotherapeutic strategy for the treatment of AKI.

4.2. Acute Liver Injury

ALI is a clinically common and severe liver disorder that can be triggered by a wide range of etiologies, including drug overdose, viral infections, toxic exposures, pregnancy, autoimmune diseases, inherited metabolic disorders such as Wilson's disease, or vascular abnormalities such as Budd–Chiari syndrome. ALI is characterized by extensive hepatocellular necrosis and rapid deterioration of liver function. In certain cases, it may rapidly progress to acute liver failure (ALF), a life-threatening condition with a mortality rate of up to 80% [65]. Oxidative stress, particularly the excessive accumulation of ROS in hepatic tissue, is considered a key pathogenic mechanism in the onset and progression of ALI. Although broad-spectrum antioxidants such as N-acetylcysteine (NAC) have demonstrated partial therapeutic benefits, their limited targeting capacity, low clearance efficiency, and poor bioavailability severely hinder clinical outcomes. Therefore, there is an urgent need to develop more efficient, liver-targeted ROS-scavenging strategies to provide novel therapeutic approaches for ALI management [66].

Given the central role of oxidative stress in ALI pathogenesis, the development of nanomedicine-based antioxidant platforms with high ROS-scavenging efficiency and hepatic specificity has emerged as a promising research direction. Several studies have focused on integrating natural antioxidant molecules with functional nanomaterials to enhance therapeutic efficacy. Luo et al. [29] fabricated phlorotannin-based nanoparticles (PT NPs) from seaweed-derived polyphenols via a glycine-assisted Mannich reaction to improve

their stability and bioavailability. These nanoparticles exhibited robust ROS-scavenging activity in H_2O_2-induced HepG2 cell models and effectively alleviated oxidative. Similarly, Jang et al. [30] developed a catechin-based thermosensitive nanoformulation (CCN150), which significantly improved the solubility and stability of catechin while retaining its intracellular ROS-scavenging activity. CCN150 selectively accumulated at inflammation sites in vivo, attenuated systemic inflammation driven by ROS, and demonstrated excellent biocompatibility. In the context of acetaminophen (APAP)-induced liver injury, Song et al. [67] designed a carbon monoxide-releasing molecule, SMA/CORM2, which enhanced hepatic CO levels and suppressed oxidative stress. Mechanistically, SMA/CORM2 downregulated HIF-1α expression, promoted M2 polarization of macrophages, and activated the PI3K/Akt/mTOR pathway, thereby mitigating liver damage and facilitating tissue regeneration. Additionally, Mn_3O_4 nanozymes showed comparable efficacy to NAC at lower doses by simultaneously modulating the Nrf2 antioxidant axis and suppressing NF-κB-mediated inflammatory responses, offering synergistic antioxidative and anti-inflammatory effects [68].

Curcumin, a natural compound widely used in traditional Chinese medicine, has shown hepatoprotective potential in APAP-induced ALI through mechanisms involving ROS scavenging, inhibition of lipid peroxidation, restoration of glutathione levels, and anti-apoptotic effects. The incorporation of curcumin into nanocarriers can significantly enhance its bioavailability and therapeutic performance. Wang et al. [31] further developed BSA-SNO nanoparticles capable of stably releasing nitric oxide (NO). These nanoparticles alleviated oxidative stress, improved hepatic microcirculation, and increased survival rates in ischemia–reperfusion and endotoxin-induced ALI models. Hepatoprotection was achieved via Nrf2/HO-1 pathway activation and suppression of NF-κB-driven inflammation and mitochondrial apoptosis. A saponin–gallic acid conjugate-based nanodelivery system also demonstrated promising anti-inflammatory effects in CCl_4-induced ALI. By employing Zn/Ga@Gd-LDH as a pH-responsive carrier, the system enabled controlled drug release in the acidic microenvironment, suppressed p-p65 phosphorylation in the NF-κB pathway, and reduced CRP levels, exhibiting both in vitro and in vivo anti-inflammatory efficacy [69]. Yuan et al. [66] developed SeMC nanoparticles derived from the self-assembly of L-selenomethionine (SeMC), modified with glycyrrhizic acid for hepatic targeting. These nanoparticles significantly reduced lipid peroxidation, tissue vacuolation, and aminotransferase elevation in both APAP- and CCl_4-induced ALI models while enhancing endogenous antioxidant enzyme activity, showing favorable biocompatibility and liver-protective potential. Moreover, Zhao et al. [32] proposed a responsive biomimetic antioxidant nanoplatform (PADN) composed of PEGylated L-DOPA precursors protected by boronic acid groups. Upon exposure to oxidative stress, PADN undergoes deprotection to release PEG–L-DOPA, which subsequently undergoes a melanogenesis-like transformation into a high-molecular-weight melanin-like polymer with broad-spectrum ROS-scavenging capability. The self-assembled PADN exhibited a particle size of approximately 106.6 nm (Figure 4A) and maintained excellent colloidal stability for over three months under physiological conditions. It efficiently eliminated multiple ROS types, including H_2O_2, in a time- and dose-dependent manner (Figure 4B,C). At the cellular level, PADN significantly suppressed NO production and intracellular ROS accumulation in LPS-activated RAW264.7 macrophages (Figure 4D,E) and reduced TUNEL-positive hepatocytes in an H_2O_2-induced apoptosis model (Figure 4F). In vivo, PADN (50 mg/kg) effectively decreased serum ALT and AST levels in APAP-induced ALI mice, outperforming NAC in liver function recovery (Figure 4G–H). Histological analyses revealed reduced necrosis, inflammatory infiltration, and central venous congestion in PADN-treated mice, with the liver architecture approaching normal (Figure 4I). Additionally, PADN possessed photoacoustic imaging

capabilities, enabling real-time visualization of lesion sites. Collectively, PADN exemplifies an oxidative microenvironment-responsive nanoplatform capable of integrating efficient ROS scavenging, inflammation suppression, and hepatocyte protection. Its stable structure and biocompatibility make it a strong candidate for clinical translation of antioxidant nanotherapies in ALI treatment.

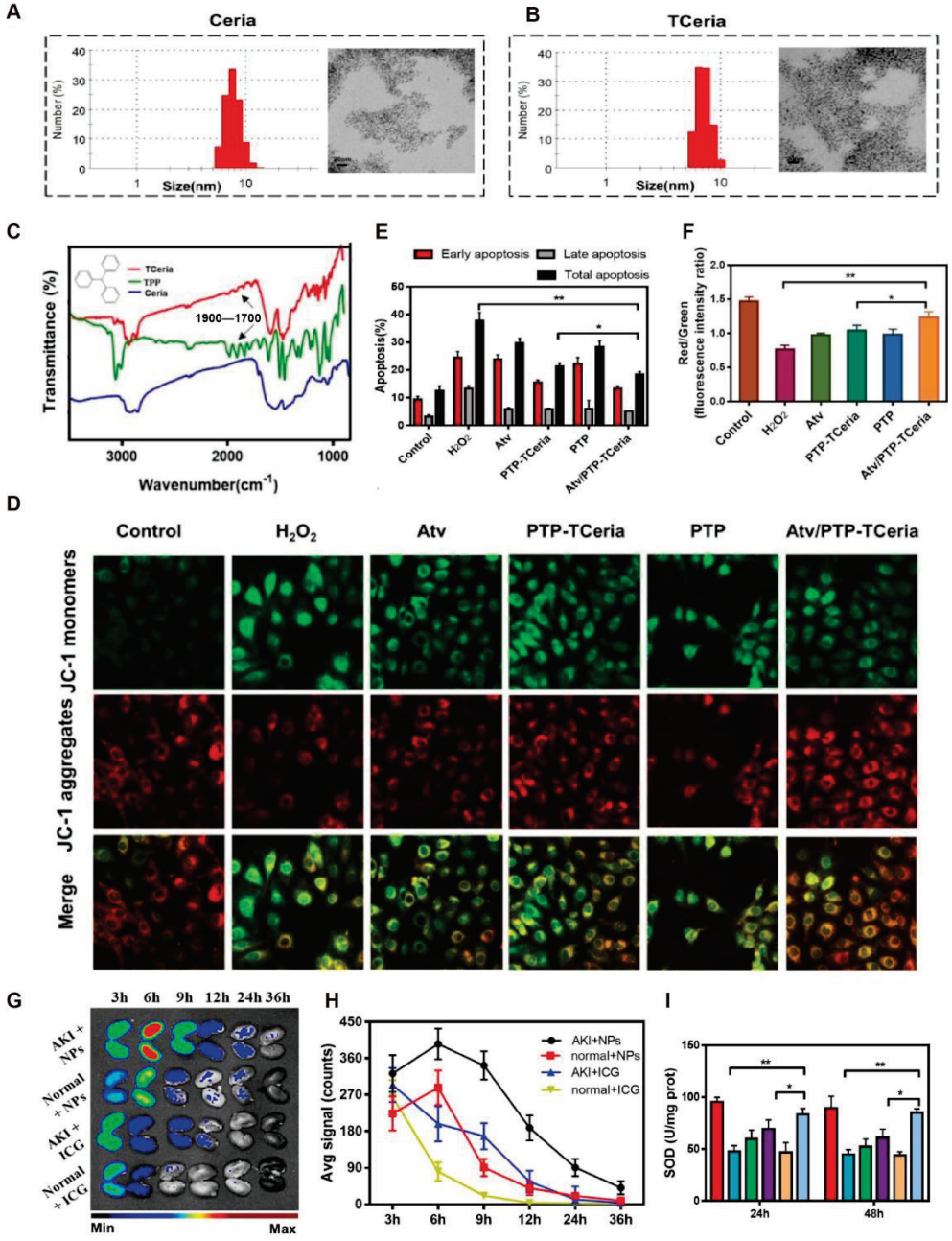


Figure 3. (**A**). Particle size distribution and transmission electron microscopy (TEM) images of Ceria NPs (scale bar: 20 nm). (**B**). Corresponding size distribution and TEM images of TCeria NPs (scale bar: 20 nm). (**C**). Fourier-transform infrared (FT-IR) spectra of TPP, Ceria NPs, and TCeria NPs. (**D**). Mitochondrial membrane potential (Δψm) assessed via confocal microscopy across treatment groups (scale bar: 20 μm). (**E**,**F**). Semi-quantitative analysis of Δψm alterations by flow cytometry and image-based quantification, respectively. Data are presented as mean ± SD (n = 3 per group). (**G**). Temporal changes in renal fluorescence intensity in AKI mice treated with ICG-loaded PTP-TCeria NPs versus free ICG. (**H**). Quantitative analysis of fluorescence intensity from panel. (**I**). Renal SOD levels measured at 24 and 48 h post-treatment. * $p < 0.05$, ** $p < 0.01$. CC BY 4.0.

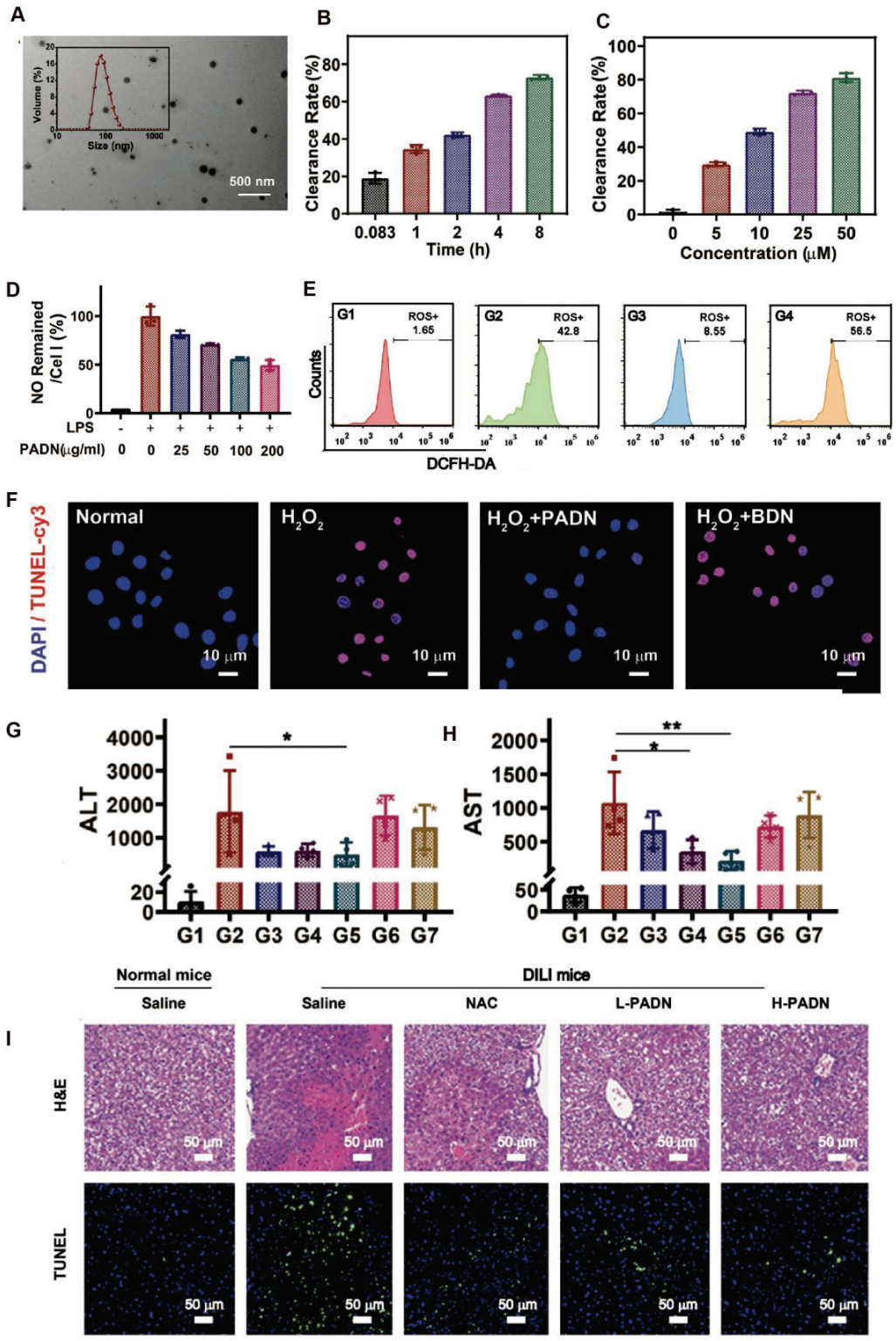


Figure 4. (**A**). TEM image and size distribution of PADN. (**B**). Time-dependent H_2O_2 scavenging activity of PADN. (**C**). Concentration-dependent H_2O_2 scavenging activity of PADN after 4 h incubation. (**D**). •NO levels in RAW 264.7 cells (LPS-stimulated) treated with varying concentrations of PADN. (**E**). Analysis of intracellular ROS in cells (RAW 264.7) under different treatments by flow cytometry (G1: normal + saline; G2: DILI + saline; G3: DILI + NAC; G4: DILI + L-PADN; G5: DILI + H-PADN; G6: DILI + L-BDN; G7: DILI + H-BDN). (**F**). CLSM images of L02 cells stained with DAPI (blue) and TUNEL-Cy3 (red) under different treatments. (**G**,**H**). Serum ALT (**G**) and AST (**H**) levels in DILI mice receiving different pretreatments. (**I**). H&E and TUNEL staining of liver sections from each group. *t*-test, $n = 4$; * $p < 0.05$, ** $p < 0.01$. Copyright 2021 Wiley-VCH GmbH.

5. Nano-Antioxidants for Chronic Inflammatory Diseases

5.1. Periodontitis

The global health impact of periodontitis, a chronic inflammatory condition affecting millions, has shown a consistent upward trend over recent years. Data from 2011 to 2020 indicate that approximately 62% of dentate individuals worldwide are affected, with over half of the cases classified as moderate to severe and nearly one-quarter as severe [70]. Compared with epidemiological data from 1990 to 2010, the prevalence of severe periodontitis increased from 10.8% to 23.6% [71]. By 2019, the global number of individuals affected had reached 1.1 billion [72].

Beyond being a prevalent oral disease, periodontitis is closely associated with a range of systemic conditions. While microbial plaque serves as the primary etiological factor, the progression of the disease—especially in its severe or refractory forms—is predominantly driven by the host immune response. Neutrophil-mediated mechanisms, notably the overproduction of ROS, play a pivotal role in tissue degradation. Oxidative stress, induced by intrinsic factors (e.g., metabolic disorders) and external triggers (e.g., smoking), creates a pro-inflammatory microenvironment that exacerbates periodontal damage. Thus, antioxidant-based therapies, such as those incorporating resveratrol, are being explored as promising strategies for periodontal intervention [73]. Li et al. [74] developed a novel bioactive glass-based microneedle system loaded with antioxidant agents for the treatment of diabetes-associated periodontitis. This system comprises Zn/V co-doped bioactive glass nanoparticles, gallic acid, and oxidized methacrylated hyaluronic acid, offering both antioxidative and antibacterial properties. By penetrating the mucosal barrier, the microneedles effectively deliver active agents into gingival tissues, enhancing retention and bioavailability. In diabetic periodontitis rat models, the system significantly promoted alveolar bone regeneration and alleviated local inflammation via suppression of the JAK-STAT and NF-κB signaling pathways. Yang et al. [33] constructed a mesoporous bioactive glass-based nanocarrier system for quercetin delivery, addressing its poor water solubility and limited bioavailability. This sustained-release platform promoted both osteogenesis and angiogenesis in experimental periodontitis-related bone defects. Additionally, it modulated the local immune microenvironment by regulating macrophage polarization. Mechanistically, quercetin acted through the miR-21a-5p/PDCD4/NF-κB axis to restore bone immune homeostasis. Similarly, Wang et al. [75] incorporated quercetin into octahedral nanoceria structures to enhance its antioxidative and immunomodulatory effects. The resulting nanocomposite effectively scavenged ROS, inhibited pro-inflammatory M1 macrophage polarization, and promoted the reparative M2 phenotype, enabling a smooth transition from inflammation to regeneration. This shift was evidenced by an increased M2/M1 polarization ratio, along with a rebalanced inflammatory profile in vivo, underscoring its therapeutic potential for managing periodontal inflammation.

To address oxidative stress-induced tissue injury in chronic periodontitis, Xin et al. [34] developed melatonin-derived carbon dots (MT-CDs) with excellent water solubility, biocompatibility, and ROS-scavenging capacity. MT-CDs stabilized mitochondrial function, mitigated oxidative cellular damage, and suppressed pro-inflammatory cytokine production. In a mouse model of periodontitis, MT-CDs reduced alveolar bone resorption and osteoclast activity. Cao et al. [35] designed a dual-polymer functionalized melanin-silver nanocomposite (P/D-MNP-Ag) with sequential therapeutic capabilities. One polymer becomes more cationic in acidic conditions to enhance membrane penetration, while the phosphate-rich polymer chelates Ca^{2+}, promoting adhesion to hydroxyapatite surfaces. Initially, the system enables Ag^{+}-mediated photothermal antibacterial activity; subsequently, as silver ions deplete, melanin's intrinsic antioxidative properties are restored, allowing ROS clearance in inflamed regions. Animal studies confirmed its ability to dis-

rupt biofilms, attenuate inflammation, and reduce alveolar bone loss. Moreover, Cao et al. [36] developed negatively charged human serum albumin-crosslinked, manganese-doped Prussian blue nanoparticles (HSA-MDSPB NPs) capable of broadly scavenging ROS species—including superoxide anions (O_2^-), hydroxyl radicals ($^\bullet OH$), hydrogen peroxide (H_2O_2), and singlet oxygen ($^1O_2$). As shown in Figure 5A–C, the nanoparticles exhibited strong radical-neutralizing capacity in DPPH and ABTS assays, achieving over 60% scavenging efficiency at 200 μg/mL. In vitro, they significantly reduced LPS-induced oxidative damage in periodontal cells: fluorescence analysis (Figure 5D,E) demonstrated decreased ROS levels in mouse gingival fibroblasts and bone marrow-derived macrophages (BMDMs). Additionally, HSA-MDSPB NPs facilitated macrophage repolarization, favoring an anti-inflammatory M2 profile over the pro-inflammatory M1 state (Figure 5F), thus promoting tissue repair. In vivo, using a ligature-induced periodontitis model (Figure 5G,H), these nanoparticles markedly reduced ROS accumulation, downregulated pro-inflammatory cytokines (e.g., IL-1β, TNF-α), and mitigated alveolar bone loss. In summary, by integrating ROS scavenging, immunomodulation, and osteogenesis promotion, HSA-MDSPB NPs—and related nanoplatforms—present a promising nanotherapeutic strategy for managing periodontitis, particularly under oxidative stress-driven pathological conditions.

5.2. Ulcerative Colitis

IBD, a chronic immune-driven condition targeting the gastrointestinal tract, primarily includes Crohn's disease (CD) and ulcerative colitis (UC). In 2021, the global age-standardized incidence rate among adolescents and young adults reached a notable level (4.08 per 100,000 population) [76]. Although the precise etiology of IBD remains unclear, dysregulation of intestinal immune responses is widely acknowledged as a central mechanism. The dysregulated production of ROS and RNS under oxidative stress conditions significantly accelerates IBD development [3]. These reactive species can compromise intestinal epithelial integrity and activate pro-inflammatory signaling pathways, thereby promoting the progression of inflammation.

UC, one of the most prevalent forms of IBD, is characterized by a complex pathogenesis, multifactorial etiology, and recurrent clinical course. Current treatment strategies face significant limitations, including suboptimal efficacy, adverse effects, and high relapse rates. Thus, the development of novel therapeutic approaches with high efficiency, targeted delivery, and minimal toxicity has become a research priority.

Recent advances highlight the therapeutic promise of nano-antioxidants in UC, attributed to their targeted delivery, high loading efficiency, and diverse bioactivities. For instance, Ye et al. [77] developed selenium nanoparticles modified with Eucommia ulmoides polysaccharides (EUP-SeNPs), which significantly alleviated DSS-induced UC in mice by restoring colonic histology, enhancing mucosal barrier function, reducing pro-inflammatory cytokines, and modulating gut microbiota. Moreover, EUP-SeNPs exerted anti-inflammatory effects via suppression of the TLR4/NF-κB signaling pathway and improved antioxidant capacity in colon tissues. In further studies, EUP-SeNPs were dually functionalized with somatostatin (SST) and manno-oligosaccharides (MOSs) for epithelial–macrophage dual-targeting and encapsulated within alginate-based microspheres (SA/SST/MOS@EUP-SeNPs) to improve oral stability and intestinal localization [37]. This system enabled targeted accumulation at inflamed sites, enhanced antioxidative and anti-inflammatory efficacy, promoted mucosal barrier repair, and effectively relieved UC symptoms. To address the limitations of traditional enema therapy—such as short retention time and systemic toxicity—thiolated anionic nanoliposomes were constructed to deliver the natural antioxidant gallic acid. This system exhibited enhanced mucosal adhesion at inflamed colonic sites, thereby prolonging drug residence time and

enhancing local therapeutic effects. In vivo experiments demonstrated that this nanocarrier significantly inhibited NF-κB, HIF-1α, and MMP-9 expression, reduced neutrophil infiltration, and promoted MUC2 expression and mucosal repair [38]. Another strategy utilized ROS-responsive nanocarriers based on diselenide-modified carboxymethyl cellulose (CMC) to deliver curcumin. This platform displayed excellent biocompatibility and ROS-triggered release. Through electrostatic interaction with cationic proteins in inflamed tissues, the system achieved targeted delivery and effectively scavenged ROS, restored mucosal integrity, and regulated gut microbiota composition to mitigate UC pathology [39].

To overcome the low bioavailability of the resveratrol analog pterostilbene (PSB), researchers developed folate-modified, ROS-responsive nanoparticles (PSB@NP-FA) with an average size of ~231 nm. In inflammatory environments, PSB was released in a controlled manner, allowing efficient uptake by macrophages and epithelial cells. This formulation modulated dendritic cell function, promoted M2 polarization of macrophages, and regulated T cell infiltration. When co-administered with dexamethasone, it showed synergistic therapeutic benefits [40]. In the field of nanozymes, researchers constructed a polyethylene glycol-modified 2D Mo_3Se_4 nanosheet nanozyme (PMNFs), which mimicked multiple enzymatic activities, including peroxidase, glutathione peroxidase, superoxide dismutase, and catalase. In DSS-induced UC models, PMNFs efficiently scavenged ROS and improved colonic tissue damage. Mechanistically, they activated the Nrf2–Keap1 antioxidant pathway, inhibited TLR4/NF-κB-mediated inflammation, and protected tight junction proteins and MUC2 expression, thereby preserving intestinal barrier function [41]. Wei et al. [42] designed a pH-responsive, hyaluronic acid-modified nanoplatform (HA-L-Arg-CO_2@NPs) for pterostilbene delivery. Upon encountering lysosomal acidic environments, the nanocarriers released CO_2 to generate a "nanobomb" effect, promoting cytosolic drug delivery and site-specific accumulation. This system exhibited favorable colonic targeting and biocompatibility, significantly downregulated inflammatory mediators, restored barrier permeability, and effectively alleviated UC symptoms. Inspired by traditional Chinese medicine, Wu et al. [43] developed a novel functional carbon dot (MML-CD) synthesized via hydrothermal treatment of magnetite and Medicated Leaven. These ultrasmall nanoparticles (~3.2 nm) possess Fe-rich surfaces, excellent gastrointestinal stability, potent ROS-scavenging capacity, and high biocompatibility. In a UC mouse model, MML-CDs demonstrated promising therapeutic efficacy. They maintained physicochemical stability in various solutions, simulated digestive environments (Figure 6A), and displayed dose-dependent antioxidant activity against $DPPH^{\bullet}$ and $ABTS+^{\bullet}$ (Figure 6B,C). MML-CDs significantly improved symptoms such as bloody diarrhea, restored colon length, and alleviated tissue damage and inflammation (Figure 6D). Furthermore, they promoted hemostasis, reduced bleeding time and volume and prolonged APTT and PT, indicating regulation of coagulation responses (Figure 6E–I). Collectively, these findings suggest that MML-CDs offer a novel oral nano-antioxidant strategy for UC treatment through multi-modal mechanisms including antioxidation, anti-inflammation, and hemostatic enhancement. In summary, nano-antioxidant strategies employing targeted delivery, functional modification, and responsive release show significant promise in UC therapy. These systems enable precise accumulation at inflamed sites, reinforce antioxidative and anti-inflammatory defenses, and modulate mucosal immunity and barrier function—offering new opportunities for effective clinical translation.

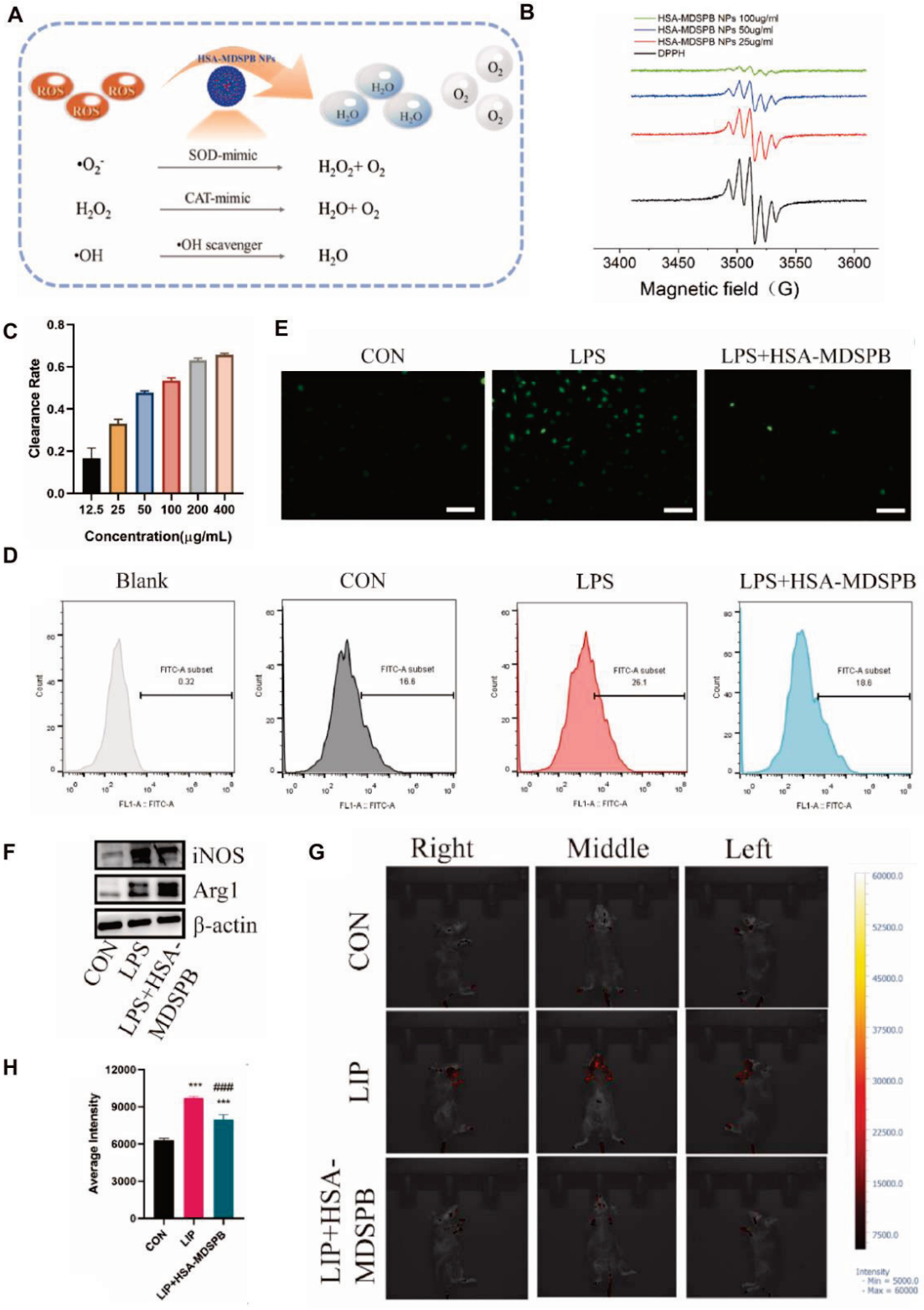


Figure 5. (**A**). Schematic diagram illustrating the antioxidative mechanism of HSA-MDSPB nanoparticles. (**B**,**C**). Assessment of the overall antioxidant activity of HSA-MDSPB NPs using DPPH and ABTS assays. (**D**). Fluorescence intensity analysis of MGF under different treatment conditions using DCFH-DA staining. (**E**). Representative fluorescence images of BMDMs stained with DCFH-DA (green) following various treatments (scale bar = 100 μm). (**F**). Western blot analysis showing protein expression in BMDMs under different treatment conditions. (**G**,**H**). In vivo imaging and quantitative evaluation of ROS levels in periodontal tissues on day 7 using the L012 probe. Statistical significance: $p < 0.05$, $p < 0.001$ (***, ###). CC BY 4.0.

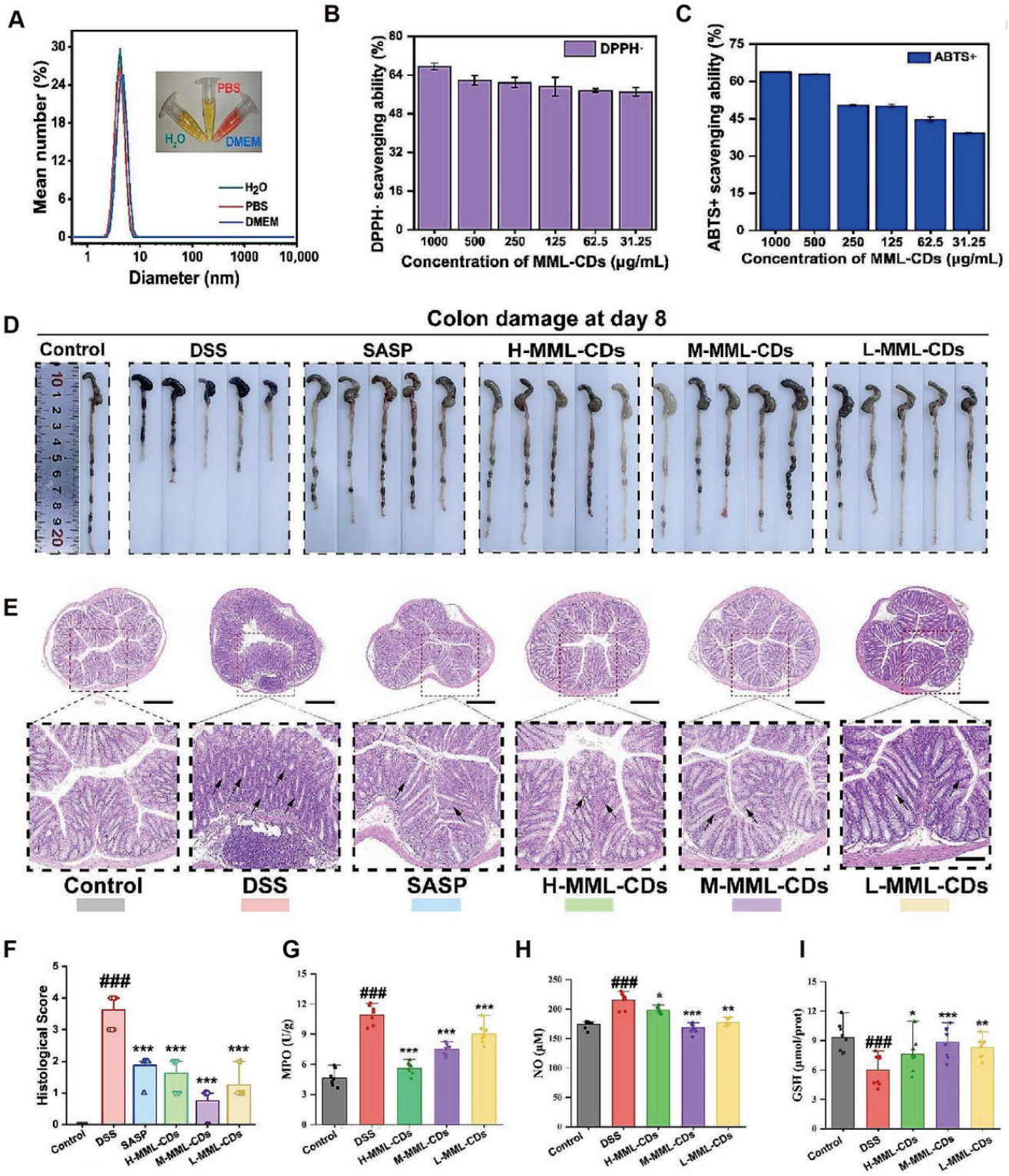


Figure 6. (**A**) DLS results of MML-CDs in different media (water, PBS, DMEM). (**B**,**C**) Free radical scavenging by MML-CDs (n = 6): (**B**) DPPH·; (**C**) $ABTS^{+}$. (**D**) Colon morphology in each treatment group. (**E**) Colon length measurements (n = 5) (top: 40×, scale bar: 1 cm; bottom: 400×, scale bar: 100 μm). (**F**) H&E-stained colon sections. (**G**–**I**) Oxidative stress markers after oral MML-CDs in UC mice: (**G**) MPO, (**H**) NO, and (**I**) GSH (n = 8). Data were analyzed using the Kruskal–Wallis test or one-way ANOVA with Tukey's correction. (### $p < 0.001$ vs. control; * $p < 0.05$, ** $p < 0.01$, *** $p < 0.001$ vs. DSS group). CC BY 4.0.

5.3. Crohn's Disease

CD is one of the major subtypes of IBD, and its global incidence has been steadily rising since 2000, with a prevalence of up to 1 in 200 individuals in Western countries. A prospective population-based cohort study conducted in Hungary between 2007 and 2018 reported an average annual incidence of CD at 9.9 per 100,000 population (95% CI: 9.0–10.9) [78]. CD can affect any part of the gastrointestinal tract and is characterized by segmental, chronic, relapsing, and transmural inflammation. Clinical manifestations include abdominal pain, diarrhea, bowel obstruction, and perianal lesions. While the exact cause of CD is not fully understood, substantial evidence points to the critical roles of genetic susceptibility, oxidative stress, immune dysregulation, and environmental stimuli in driving its onset and development [79]. Among these factors, oxidative stress plays a key role in IBD, especially in UC [80]. Multiple meta-analyses have confirmed the presence of significant oxidative damage in UC patients, particularly during active disease phases. This is characterized by elevated levels of lipid peroxidation products (e.g., MDA, 8-iso-prostaglandin F2α), and protein oxidation markers (e.g., advanced oxidation protein products) [81].

In this context, antioxidant-based therapeutic strategies have emerged as promising interventions for the prevention and treatment of CD. Crohn's disease develops through multifactorial interactions among genetic, immunological, microbial, and environmental influences, wherein oxidative stress caused by disrupted redox balance plays a central pathogenic role. Both endogenous and exogenous antioxidants can neutralize ROS and attenuate oxidative damage, thereby modulating intestinal inflammation and serving as important adjuvant approaches to mitigate disease progression and improve clinical outcomes [82]. Chen et al. [83] systematically investigated the associations between genetically predicted levels of antioxidants, minerals, and vitamins and the risk of Crohn's disease (CD) and ulcerative colitis (UC). Although not directly addressing immune metabolism, their findings revealed that specific micronutrient levels may influence disease susceptibility through oxidative stress and mitochondrial pathways. Furthermore, mechanistic studies highlighted the role of AFG3L2 in preserving mitochondrial integrity and enhancing antioxidant signaling via the PPARA/GPX4 axis, suggesting potential links between metabolic stress responses and intestinal inflammation [84].

Nanocarrier-based antioxidant therapies have emerged as a promising avenue for Crohn's disease treatment in recent years [85]. Ibrahim et al. [86] developed a multi-strain probiotic formulation encapsulated in a nanoparticle delivery system (BBLNPs), comprising *Bifidobacterium breve*, *Bacillus coagulans*, and *Lactobacillus plantarum*. This formulation significantly improved inflammation in mouse model. BBLNPs effectively reduced oxidative stress markers (e.g., MDA, ROS, H_2O_2) and enhanced the activity of antioxidant enzymes (SOD, CAT, GSH-Px), thereby exhibiting synergistic regulation of oxidative stress, inflammation, autophagy, and metabolic pathways and showing substantial therapeutic potential. Mohanbhai et al. [87] proposed a colon-targeted drug delivery system encapsulating melatonin within chitosan nanoparticles, further coated with Eudragit-S-100 to achieve colonic release upon oral administration. In an LPS-induced macrophage model, this system demonstrated strong nitric oxide-scavenging ability. In a CD mouse model, it alleviated tissue inflammation, protected mucosal structure, reduced goblet cell loss, and decreased immune cell infiltration, indicating both antioxidant and anti-inflammatory efficacy. Zhu et al. [88] designed a selenium-enriched Prussian blue nanozyme (Se-HMPB) with multi-enzyme mimetic activities, capable of efficiently scavenging ROS at inflammatory sites and exhibiting pronounced antioxidant effects. The selenium component endowed the nanozyme with glutathione peroxidase-like activity, enabling inhibition of ferroptosis and reduction in lipid peroxidation in intestinal epithelial cells. Furthermore, Se-HMPB

promoted intestinal barrier repair and regulated T cell differentiation, thereby strengthening immune barrier function and demonstrating favorable therapeutic efficacy in CD models. Shah et al. [89] synthesized a novel nitric oxide (NO)-releasing nano-antioxidant, S-nitrosoglutathione–alginate (SNA), constructed via conjugation and nitrosation of glutathione with alginate. This nanoformulation exhibited high NO loading capacity and sustained-release properties, offering a new antioxidant therapeutic option with potential for oral delivery in CD treatment.

Additionally, Fu et al. [90] developed a copper–flavonoid nanocomposite (CuL NCs) with multifunctional properties. The composite was synthesized through metal–polyphenol coordination self-assembly between luteolin and Cu^{2+} ions, forming uniformly sized nanoparticles (~7.58 ± 0.90 nm) with excellent dispersibility and colloidal stability in aqueous solution (Figure 7A,B). CuL NCs also exhibited strong free radical-scavenging capacity, particularly against superoxide anions ($O_2^{\bullet -}$), in a dose-dependent manner, outperforming individual components and their physical mixture (Figure 7C). In H_2O_2-induced oxidative stress cell models, CuL NCs significantly improved the viability of cells (RAW264.7; HT-29), fully restoring cell viability at 200 μg/mL and demonstrating robust cytoprotective effects (Figure 7D–F). In a TNBS-induced CD mouse model, CuL NCs markedly reduced MDA levels and MPO activity in colonic tissues while restoring CAT enzyme activity (Figure 7G–I), indicating effective mitigation of CD-associated oxidative injury. In summary, CuL NCs possess both SOD-like and CAT-like activities, efficiently scavenging ROS and ameliorating the oxidative microenvironment. Through a tri-modal mechanism encompassing antioxidant, anti-inflammatory, and barrier-protective actions, they exert multidimensional therapeutic effects in CD. These findings provide a strong theoretical foundation and emerging evidence for the application of nano-antioxidants in CD and other chronic inflammatory bowel diseases.

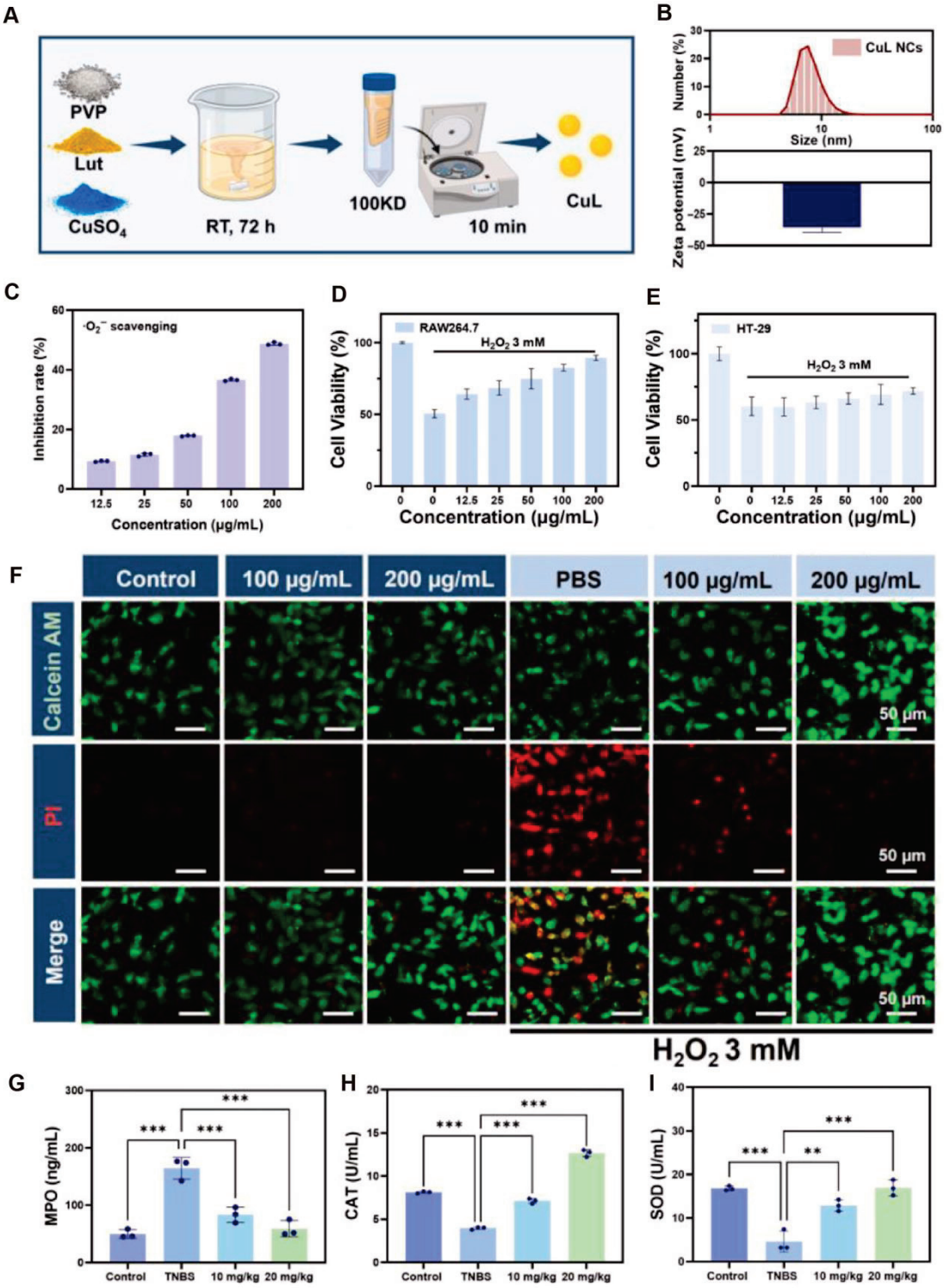


Figure 7. (**A**). Schematic illustration of the synthesis of CuL NCs. (**B**). Characterization of CuL NCs by dynamic light scattering (DLS) and zeta potential analysis. (**C**). Evaluation of concentration-dependent superoxide anion ($O_2^{\bullet -}$)-scavenging activity. (**D**,**E**). Assessment of cell viability in RAW264.7 and HT-29 cells under H_2O_2-induced oxidative stress after CuL NCs treatment. (**F**). Fluorescence imaging of cell viability following H_2O_2 exposure with or without CuL NC pretreatment. (**G**). Measurement of MDA levels in colonic tissues. (**H**). Detection of myeloperoxidase (MPO) activity in colonic tissues. (**I**). Analysis of CAT activity in colonic tissues. ** $p < 0.01$, *** $p < 0.001$. CC BY 4.0.

6. Others

In addition to their well-documented applications in autoimmune, acute, and chronic inflammatory diseases, antioxidants have also demonstrated significant therapeutic potential in a variety of dermatological conditions. As previously reviewed, antioxidants have shown promise in managing skin disorders such as atopic dermatitis and psoriasis [91]. Beyond their role in alopecia areata, we also explore their relevance in androgenetic alopecia, vitiligo, and rheumatoid arthritis.

Recent research has increasingly recognized oxidative stress as a key contributor to various forms of hair loss, especially androgenetic alopecia (AGA). Although conventional agents such as minoxidil can promote hair growth, they often exhibit slow onset, limited efficacy, and insufficient ability to mitigate oxidative stress-induced follicular damage. In this context, Xiao et al. [17] proposed the use of nanomolybdenum, a transition metal-based antioxidant material, as a novel therapeutic approach. Due to its excellent electron transfer capabilities, nanomolybdenum effectively modulates local redox homeostasis, promotes follicular regeneration, and downregulates the expression of iNOS, COX-2, and androgen receptors, thereby accelerating the hair regeneration process. Moreover, its combination with minoxidil produced a synergistic effect, suggesting a potential therapeutic approach for nanomaterial-based antioxidant therapy in alopecia. Zhang et al. [92] further emphasized the role of oxidative stress in AGA by employing machine learning techniques to identify an efficient SOD-mimicking nanomaterial—manganese thiophosphate ($MnPS_3$). This material exhibited a half-maximal inhibitory concentration (IC_{50}) of just 3.61 μg/mL, outperforming most reported SOD-like nanozymes. They also developed $MnPS_3$-loaded microneedle patches capable of penetrating the skin and targeting hair follicles, thereby effectively scavenging local ROS. Yang et al. [93] developed a multifunctional microneedle patch delivery system based on a curcumin–zinc metal–organic framework (ZnMOF-MN), which enables efficient transdermal delivery of Zn^{2+} and curcumin. This system exerts antioxidant, anti-apoptotic, and anti-androgenic effects, significantly enhancing dermal papilla cell activity and promoting hair follicle regeneration. Yang et al. [94] developed a quercetin–polydopamine-integrated nanoplatform (PDA@QLipo) designed to modulate the perfollicular microenvironment and stimulate follicle regeneration. This nanosystem not only exhibited potent ROS-scavenging activity but also promoted neovascularization, collectively contributing to a regenerative microenvironment favorable for hair growth. The pathogenesis of vitiligo involves oxidative stress as a major driving force behind melanocyte injury and programmed cell death. ROS (e.g., O_2^- and H_2O_2) generated during melanin synthesis render melanocytes particularly vulnerable to oxidative injury [95]. A disrupted antioxidant system is evident in the affected skin of vitiligo patients, marked by elevated antioxidant enzyme activity (e.g., SOD) and impaired hydrogen peroxide detoxification. This redox imbalance may perpetuate melanocyte degeneration in depigmented lesions. To address this, Li et al. [96] developed a microneedle-delivered antioxidant and immunomodulatory nanodrug (PDA-JAKi) for targeted vitiligo therapy. This system consists of polydopamine nanoparticles loaded with the JAK inhibitor tofacitinib. The nanodrug alleviated ROS-induced melanocyte apoptosis and suppressed the release of self-antigens and subsequent immune activation. In vivo studies demonstrated its ability to restore pigmentation, reduce ROS accumulation, and improve tissue integrity, underscoring its dual antioxidant and immunomodulatory efficacy. In rheumatoid arthritis (RA), Han et al. [97] synthesized ultrasmall iron–quercetin coordination nanoclusters (Fe-Qur NCNs) to mitigate oxidative and inflammatory responses associated with RA. These nanoparticles retained the ROS-scavenging properties of quercetin while improving its water solubility and biocompatibility. In addition, excessive ROS were effectively neutralized by Fe-Qur NCNs, inhibited pro-inflammatory macrophage polarization, and suppressed NF-κB path-

way activation, thereby reducing apoptosis and inflammatory cytokine release. In vivo, the nanodrug alleviated joint swelling and bone erosion, inhibited immune cell infiltration, promoted anti-inflammatory macrophage phenotypes, and attenuated osteoclast activity in RA mouse models. These results suggest that metal–natural product coordination nanoplatforms represent a promising strategy for managing RA and other oxidative stress-related diseases. In summary, oxidative stress contributes critically to the development of diverse cutaneous and immune-mediated inflammatory conditions. Nanomaterial-based antioxidant strategies, owing to their excellent targeting ability and biocompatibility, not only offer standalone therapeutic benefits but also demonstrate synergistic effects when combined with conventional treatments, highlighting their significant potential for clinical translation and further research.

7. Discussion

The treatment of IMIDs remains a significant challenge in both clinical and translational medicine, primarily due to their heterogeneous pathogenesis, chronic progression, and frequent systemic involvement [98]. IMIDs encompass a wide spectrum of disease types, including autoimmune disorders such as AA and MS, acute inflammatory injuries like AKI and ALI, and chronic inflammatory conditions such as IBD and periodontitis. A unifying pathological feature among these diseases is the excessive production of ROS, which not only directly damages tissues but also exacerbates immune dysregulation, thereby perpetuating a vicious cycle of inflammation [99,100]. Consequently, targeting oxidative stress has emerged as a theoretically grounded and promising therapeutic strategy.

However, the clinical efficacy of conventional antioxidant therapies remains limited, largely due to inherent shortcomings such as poor pharmacokinetics, inadequate tissue targeting, rapid metabolic degradation, and low intracellular retention. To address these limitations, recent research has increasingly focused on the development and application of nano-antioxidants. These nanomaterials or nano-delivery systems are engineered to exert direct or indirect antioxidative effects and demonstrate superior therapeutic performance. Nano-antioxidant platforms include metal oxide nanoparticles (e.g., zinc oxide, manganese dioxide), carbon-based nanomaterials (e.g., graphene oxide, fullerenes), polymeric nanoparticles, and lipid-based or exosome-mimetic delivery vehicles [101,102]. Compared to traditional antioxidants, these nanostructures offer several advantages, including enhanced stability in physiological environments, improved cellular uptake, targeted delivery to sites of inflammation or oxidative stress, and the ability to achieve sustained, localized drug release to maximize therapeutic efficacy. Furthermore, many nano-antioxidants possess intrinsic ROS-scavenging capabilities without the need for additional drug loading, thereby minimizing systemic exposure and reducing potential side effects [103]. Although nanoparticles or metallic nanoparticles (mNPs) are known to induce oxidative stress through excessive generation of ROS, recent advancements in nanoparticle engineering have demonstrated their potential to mitigate oxidative damage. Green-synthesized and surface-modified mNPs—such as plant-derived Cu and Pt nanoparticles—can scavenge free radicals via enzyme-mimetic activities resembling catalase or superoxide dismutase. These nano-antioxidants downregulate key pro-oxidant signaling pathways (e.g., NF-κB, JAK/STAT) and enhance cellular antioxidant defense mechanism [104]. Additionally, PEGylation and conjugation with natural antioxidants (e.g., flavonoids, polyphenols) offer effective strategies to reduce immune recognition and ROS-induced toxicity. Thus, depending on their composition and surface chemistry, mNPs can function either as pro-oxidant or antioxidant agents, providing a versatile platform for therapeutic modulation of oxidative stress [105].

An increasing body of evidence from in vitro studies, animal models, and early translational investigations suggests that nano-antioxidants can effectively alleviate inflammation, preserve tissue integrity, and modulate immune responses. For instance, in autoimmune diseases like AA, nano-antioxidants have been shown to mitigate inflammation by scavenging superoxide anions and hydrogen peroxide, offering a novel therapeutic avenue [17]. In MS models, polymeric nanoparticles loaded with antioxidants can traverse the blood–brain barrier and precisely deliver therapeutic agents to neuroinflammatory sites, thereby reducing demyelination and preserving neurological function [106]. In acute inflammatory conditions such as AKI, nano-antioxidants help alleviate renal oxidative stress, maintain mitochondrial function, and potentially enhance treatment outcomes [107]. Similarly, in chronic inflammatory diseases like IBD and ulcerative colitis, these agents promote mucosal healing, modulate gut microbiota composition, and reduce inflammatory cell infiltration in the colon [108].

8. Conclusions

Despite these encouraging preclinical findings, the clinical translation of nano-antioxidants remains in its infancy and faces several critical challenges. First, the biocompatibility and long-term safety of various nanomaterials are not yet fully understood, particularly under conditions of repeated or prolonged use. Second, the heterogeneity of IMIDs necessitates precision medicine approaches, as disease-specific redox pathways, immune activation patterns, and tissue microenvironments may significantly influence the efficacy and biodistribution of nano-antioxidants. Third, practical issues such as scalable manufacturing, regulatory approval, and cost-effectiveness must be systematically addressed. Moreover, nano-antioxidants must demonstrate therapeutic efficacy that is superior to—or at least non-inferior to—current standard treatments in rigorously designed randomized controlled clinical trials before widespread adoption can be recommended. Future research should prioritize the development of "smart" nano-antioxidant systems capable of responding to disease-specific microenvironmental cues (e.g., pH, ROS levels, enzymatic activity) to achieve precise and controlled drug release. Combining nano-antioxidant therapy with other modalities, such as immunomodulators, gene editing technologies (e.g., CRISPR/Cas9), or cell-based therapies, may further enhance therapeutic outcomes through synergistic effects. Additionally, personalized nanomedicine strategies—tailoring antioxidant interventions based on an individual's disease phenotype, genetic markers, and microbiome characteristics—hold promise for improving treatment precision and minimizing adverse effects. In summary, nano-antioxidants represent a highly promising and multifunctional therapeutic platform for the management of diverse IMIDs. By overcoming the limitations of traditional antioxidants and leveraging the unique properties of nanomaterials, this strategy offers novel avenues for the targeted and sustained regulation of redox balance and immune function. Although substantial progress has been made, multidisciplinary collaboration and robust clinical validation are essential to fully realize their clinical potential. If successfully translated, nano-antioxidant therapies may substantially transform the therapeutic landscape of IMIDs and bring new hope to affected patients.

Author Contributions: Y.X. and Y.-Q.R.: study conception and design. H.-W.S. and B.-C.Y.: organized the article's table section. Y.X. and H.-W.S.: organized the figures. Y.X. and H.-W.S.: copyright permission. H.-W.S. and B.-C.Y.: drafting the manuscripts. Y.X. and Y.-Q.R.: critical revision of the manuscript. All authors have read and agreed to the published version of the manuscript.

Funding: This work was supported by the Zhejiang Provincial Natural Science Foundation of China under grant LQN25H110001, the Key Research and Development Plan of Zhejiang Province (2025C02080), ZJU-GENSCI CHILDREN'S HEALTH RESEARCH & DEVELOPMENT CENTER (ZJU-

GENSCI2024YB004), Zhejiang Provincial Natural Science Foundation of China (LTGD23H110001), National Key R&D Program of China (Grant No.2022YFC2705300), and 2023 Xiamen Municipal Natural Science Foundation Project (3502Z202374016).

Institutional Review Board Statement: Not applicable.

Informed Consent Statement: Not applicable.

Data Availability Statement: No new data were created in this study. Permission for re-use of previously published figures has been obtained.

Acknowledgments: We thank Su-Zhuang Hong, Qi Chen, Ji-Peng Liu and Ke-Yi Ren for assistance with figure arrangement and Zheng-Ying Zhang, Yu-Xiang Yang, Can Lai and Xiao-Hui Ma for support in copyright permissions and organizing the article's table section.

Conflicts of Interest: The authors declare no conflicts of interest.

References

1. Luo, H. Global burden and cross-country inequalities in six major immune-mediated inflammatory diseases from 1990 to 2021: A systemic analysis of the Global Burden of Disease Study 2021. *Autoimmun. Rev.* **2024**, *23*, 103639. [CrossRef]
2. Dobrica, E.C.; Cozma, M.A.; Gaman, M.A.; Voiculescu, V.M.; Gaman, A.M. The Involvement of Oxidative Stress in Psoriasis: A Systematic Review. *Antioxidants* **2022**, *11*, 282. [CrossRef] [PubMed]
3. Muro, P.; Zhang, L.; Li, S.; Zhao, Z.; Jin, T.; Mao, F.; Mao, Z. The emerging role of oxidative stress in inflammatory bowel disease. *Front. Endocrinol.* **2024**, *15*, 1390351. [CrossRef]
4. Abot, A.; Fried, S.; Cani, P.D.; Knauf, C. Reactive Oxygen Species/Reactive Nitrogen Species as Messengers in the Gut: Impact on Physiology and Metabolic Disorders. *Antioxid. Redox Signal.* **2022**, *37*, 394–415. [CrossRef]
5. Lapenna, D. Glutathione and glutathione-dependent enzymes: From biochemistry to gerontology and successful aging. *Ageing Res. Rev.* **2023**, *92*, 102066. [CrossRef] [PubMed]
6. Zhang, J.; Ren, X.; Nie, Z.; You, Y.; Zhu, Y.; Chen, H.; Yu, H.; Mo, G.P.; Su, L.; Peng, Z.; et al. Dual-responsive renal injury cells targeting nanoparticles for vitamin E delivery to treat ischemia reperfusion-induced acute kidney injury. *J. Nanobiotechnol.* **2024**, *22*, 626. [CrossRef]
7. Akanchise, T.; Angelova, A. Potential of Nano-Antioxidants and Nanomedicine for Recovery from Neurological Disorders Linked to Long COVID Syndrome. *Antioxidants* **2023**, *12*, 393. [CrossRef] [PubMed]
8. Bardestani, A.; Ebrahimpour, S.; Esmaeili, A.; Esmaeili, A. Quercetin attenuates neurotoxicity induced by iron oxide nanoparticles. *J. Nanobiotechnol.* **2021**, *19*, 327. [CrossRef] [PubMed]
9. Chen, X.; Zhang, L.; Zeng, H.; Meng, W.; Liu, G.; Zhang, W.; Zhao, P.; Zhang, Q.; Chen, M.; Chen, J. Manganese-Based Immunomodulatory Nanocomposite with Catalase-Like Activity and Microwave-Enhanced ROS Elimination Ability for Efficient Rheumatoid Arthritis Therapy. *Small* **2023**, *19*, e2304610. [CrossRef]
10. Laurindo, L.F.; de Carvalho, G.M.; de Oliveira Zanuso, B.; Figueira, M.E.; Direito, R.; de Alvares Goulart, R.; Buglio, D.S.; Barbalho, S.M. Curcumin-Based Nanomedicines in the Treatment of Inflammatory and Immunomodulated Diseases: An Evidence-Based Comprehensive Review. *Pharmaceutics* **2023**, *15*, 229. [CrossRef]
11. Indriyani, N.; Nur'aeny, N. The Therapeutic Effects of Curcumin on Oral Disease: A Systematic Review. *Clin. Pharmacol.* **2025**, *17*, 13–24. [CrossRef]
12. Mohammadi, S.; Farjam, H.; Hosseini, S.; Larijani, K. Inhibitory effects of saffron compounds on multiple sclerosis: Molecular docking and dynamic, enhancing properties with gold nanoparticles and evaluating antioxidant, antibacterial, cytotoxicity. *Heliyon* **2025**, *11*, e42693. [CrossRef] [PubMed]
13. Bemidinezhad, A.; Mirzavi, F.; Gholamhosseinian, H.; Gheybi, F.; Soukhtanloo, M. Gold-containing liposomes and glucose-coated gold nanoparticles enhances the radiosensitivity of B16F0 melanoma cells via increasing apoptosis and ROS production. *Life Sci.* **2023**, *318*, 121495. [CrossRef]
14. Liu, X.; Ou, X.; Zhang, T.; Li, X.; Qiao, Q.; Jia, L.; Xu, Z.; Zhang, F.; Tian, T.; Lan, H.; et al. In situ neutrophil apoptosis and macrophage efferocytosis mediated by Glycyrrhiza protein nanoparticles for acute inflammation therapy. *J. Control. Release* **2024**, *369*, 215–230. [CrossRef] [PubMed]
15. Yu, H.; Jin, F.; Liu, D.; Shu, G.; Wang, X.; Qi, J.; Sun, M.; Yang, P.; Jiang, S.; Ying, X.; et al. ROS-responsive nano-drug delivery system combining mitochondria-targeting ceria nanoparticles with atorvastatin for acute kidney injury. *Theranostics* **2020**, *10*, 2342–2357. [CrossRef]
16. Hu, Q.; Li, J.; Wang, T.; Xu, X.; Duan, Y.; Jin, Y. Polyphenolic Nanoparticle-Modified Probiotics for Microenvironment Remodeling and Targeted Therapy of Inflammatory Bowel Disease. *ACS Nano* **2024**, *18*, 12917–12932. [CrossRef]

17. Xiao, Q.; Lu, Y.; Yao, W.; Gong, C.; Jia, C.; Gao, J.; Guo, J.; Qiu, T.; Jiang, Y.; Huang, M.; et al. Molybdenum nanoparticles as a potential topical medication for alopecia treatment through antioxidant pathways that differ from minoxidil. *J. Trace Elem. Med. Biol.* **2024**, *82*, 127368. [CrossRef]
18. Motavaf, M.; Sadeghizadeh, M.; Babashah, S.; Zare, L.; Javan, M. Dendrosomal nanocurcumin promotes remyelination through induction of oligodendrogenesis in experimental demyelination animal model. *J. Tissue Eng. Regen. Med.* **2020**, *14*, 1449–1464. [CrossRef]
19. Ibrahim Fouad, G.; Mabrouk, M.; El-Sayed, S.A.M.; Abdelhameed, M.F.; Rizk, M.Z.; Beherei, H.H. Berberine-loaded iron oxide nanoparticles alleviate cuprizone-induced astrocytic reactivity in a rat model of multiple sclerosis. *Biometals* **2025**, *38*, 203–229. [CrossRef]
20. Li, Z.; Chen, K.; Shao, Q.; Lu, H.; Zhang, X.; Pu, Y.; Sun, X.; He, H.; Cao, L. Nanoparticulate MgH(2) ameliorates anxiety/depression-like behaviors in a mouse model of multiple sclerosis by regulating microglial polarization and oxidative stress. *J. Neuroinflamm.* **2023**, *20*, 16. [CrossRef] [PubMed]
21. Abdelalim, L.R.; Elnaggar, Y.S.R.; Abdallah, O.Y. Lactoferrin, chitosan double-coated oleosomes loaded with clobetasol propionate for remyelination in multiple sclerosis: Physicochemical characterization and in-vivo assessment in a cuprizone-induced demyelination model. *Int. J. Biol. Macromol.* **2024**, *277 Pt 1*, 134144. [CrossRef] [PubMed]
22. Rezaeimanesh, N.; Rafiee, P.; Saeedi, R.; Khosravian, P.; Sahraian, M.A.; Eskandarieh, S.; Moghadasi, A.N.; Jahromi, S.R. The effect of crocin-selenium nanoparticles on the cognition and oxidative stress markers of multiple sclerosis patients: A randomized triple-blinded placebo-controlled clinical trial. *Biometals* **2024**, *37*, 305–319. [CrossRef] [PubMed]
23. Yang, Y.; Zhao, Y.; Liu, H.; Wu, X.; Guo, M.; Xie, L.; Wang, G.; Shi, J.; Yu, W.; Dong, G. Inflammation-Targeted Biomimetic Nano-Decoys via Inhibiting the Infiltration of Immune Cells and Effectively Delivering Glucocorticoids for Enhanced Multiple Sclerosis Treatment. *Adv. Healthc. Mater.* **2025**, *14*, e2402965. [CrossRef] [PubMed]
24. Gu, J.; Zhang, P.; Li, H.; Wang, Y.; Huang, Y.; Fan, L.; Ma, X.; Qian, X.; Xi, J. Cerium–Luteolin Nanocomplexes in Managing Inflammation-Related Diseases by Antioxidant and Immunoregulation. *ACS Nano* **2024**, *18*, 6229–6242. [CrossRef]
25. Zheng, Y.; Yi, H.; Zhan, Z.; Xue, S.S.; Tang, G.; Yu, X.; Zhang, D.Y. Reactive oxygen/nitrogen species scavenging and inflammatory regulation by renal-targeted bio-inspired rhodium nanozymes for acute kidney injury theranostics. *J. Colloid. Interface Sci.* **2024**, *662*, 413–425. [CrossRef]
26. Yan, R.; Cui, W.; Ma, W.; Li, J.; Liu, Z.; Lin, Y. Typhaneoside-Tetrahedral Framework Nucleic Acids System: Mitochondrial Recovery and Antioxidation for Acute Kidney Injury treatment. *ACS Nano* **2023**, *17*, 8767–8781. [CrossRef]
27. Pan, Q.; Xie, L.; Cai, P.; Wu, D.; Zhu, H.; Xu, L.; Liu, R.; Luo, K.; He, B.; Pu, Y. Acid-Resistant Nano-antioxidants Based on Epigallocatechin Gallate Alleviate Acute Intestinal and Kidney Inflammation. *ACS Appl. Mater. Interfaces* **2024**, *16*, 46090–46101. [CrossRef]
28. Jia, F.; Yu, B.; Li, J.; Cai, F.; Fu, G.; Jin, Q.; Ji, J. Supramolecular Nano-Assembly of Caffeate-Strengthened Phenylboronic Ester with Multistep ROS Scavenging Ability for Targeted Therapy of Acute Kidney Injury. *Adv. Healthc. Mater.* **2023**, *12*, e2301615. [CrossRef]
29. Luo, F.; Zhu, B.; Wu, D.; Xu, Y.; Chen, T.; Li, Y.; Hu, J. Construction of Phlorotannin-Based Nanoparticles for Alleviating Acute Liver Injury. *ACS Appl. Mater. Interfaces* **2023**, *15*, 47338–47349. [CrossRef]
30. Jang, D.; Choi, H.; Lee, J.; Chun, Y.; Heo, Y.H.; Lee, L.P.; Ahn, D.J.; Shin, I.S.; Kim, D.H.; Seo, Y.H.; et al. Inflamed Tissue-Targeting Polyphenol-Condensed Antioxidant Nanoparticles with Therapeutic Potential. *Adv. Healthc. Mater.* **2025**, *14*, e2500495. [CrossRef]
31. Wang, Y.; Liu, X.; Li, K.; Wang, X.; Zhang, X.; Qian, D.; Meng, X.; Yu, L.; Yan, X.; He, Z. Self-Sulfhydrated, Nitro-Fixed Albumin Nanoparticles as a Potent Therapeutic Agent for the Treatment of Acute Liver Injury. *ACS Nano* **2024**, *18*, 20772–20791. [CrossRef] [PubMed]
32. Zhao, C.; Li, Z.; Chen, J.; Su, L.; Wang, J.; Chen, D.S.; Ye, J.; Liao, N.; Yang, H.; Song, J.; et al. Site-Specific Biomimicry of Antioxidative Melanin Formation and Its Application for Acute Liver Injury Therapy and Imaging. *Adv. Mater.* **2021**, *33*, e2102391. [CrossRef] [PubMed]
33. Yang, S.Y.; Hu, Y.; Zhao, R.; Zhou, Y.N.; Zhuang, Y.; Zhu, Y.; Ge, X.L.; Lu, T.W.; Lin, K.L.; Xu, Y.J. Quercetin-loaded mesoporous nano-delivery system remodels osteoimmune microenvironment to regenerate alveolar bone in periodontitis via the miR-21a-5p/PDCD4/NF-kappaB pathway. *J. Nanobiotechnol.* **2024**, *22*, 94. [CrossRef]
34. Xin, X.; Liu, J.; Liu, X.; Xin, Y.; Hou, Y.; Xiang, X.; Deng, Y.; Yang, B.; Yu, W. Melatonin-Derived Carbon Dots with Free Radical Scavenging Property for Effective Periodontitis Treatment via the Nrf2/HO-1 Pathway. *ACS Nano* **2024**, *18*, 8307–8324. [CrossRef]
35. Cao, B.; Zhang, J.; Ma, Y.; Wang, Y.; Li, Y.; Wang, R.; Cao, D.; Yang, Y.; Zhang, R. Dual-Polymer Functionalized Melanin-AgNPs Nanocomposite with Hydroxyapatite Binding Ability to Penetrate and Retain in Biofilm Sequentially Treating Periodontitis. *Small* **2024**, *20*, e2400771. [CrossRef]
36. Cao, B.; Da, X.; Wu, W.; Xie, J.; Li, X.; Wang, X.; Xu, H.; Gao, J.; Yang, H.; Su, J. Multifunctional human serum albumin-crosslinked and self-assembling nanoparticles for therapy of periodontitis by anti-oxidation, anti-inflammation and osteogenesis. *Mater. Today Bio.* **2024**, *28*, 101163. [CrossRef]

37. Ye, R.; Guo, J.; Yang, Z.; Wang, Z.; Chen, Y.; Huang, J.; Dong, Y. Somatostatin and Mannooligosaccharide Modified Selenium Nanoparticles with Dual-Targeting for Ulcerative Colitis Treatment. *ACS Nano* **2025**, *19*, 14914–14930. [CrossRef]
38. Kanika; Ahmad, A.; Kumar, A.; Rahul; Mishra, R.K.; Ali, N.; Navik, U.; Parvez, S.; Khan, R. Leveraging thiol-functionalized biomucoadhesive hybrid nanoliposome for local therapy of ulcerative colitis. *Biomaterials* **2025**, *312*, 122747. [CrossRef]
39. Cai, W.Q.; Liang, W.; Li, D.; Dai, W.; Li, Z.; Wei, X.; Cheng, L.; Zhang, B.B.; Yang, Q. Reactive Oxygen Species-Responsive Polymer Drug Delivery System Targeted Oxidative Stressed Colon Cells to Ameliorate Colitis. *ACS Nano* **2025**, *19*, 17287–17308. [CrossRef] [PubMed]
40. Yan, X.; Meng, L.; Zhang, X.; Deng, Z.; Gao, B.; Zhang, Y.; Yang, M.; Ma, Y.; Zhang, Y.; Tu, K.; et al. Reactive oxygen species-responsive nanocarrier ameliorates murine colitis by intervening colonic innate and adaptive immune responses. *Mol. Ther.* **2023**, *31*, 1383–1401. [CrossRef]
41. Guo, H.; Guo, H.; Xie, Y.; Chen, Y.; Lu, C.; Yang, Z.; Zhu, Y.; Ouyang, Y.; Zhang, Y.; Wang, X. Mo_3Se_4 nanoparticle with ROS scavenging and multi-enzyme activity for the treatment of DSS-induced colitis in mice. *Redox Biol.* **2022**, *56*, 102441. [CrossRef] [PubMed]
42. Wei, W.; Zhang, Y.; Li, R.; Cao, Y.; Yan, X.; Ma, Y.; Zhang, Y.; Yang, M.; Zhang, M. Oral Delivery of Pterostilbene by L-Arginine-Mediated "Nano-Bomb" Carrier for the Treatment of Ulcerative Colitis. *Int. J. Nanomed.* **2022**, *17*, 603–616. [CrossRef]
43. Wu, T.; Bai, X.; Zhang, Y.; Dai, E.; Ma, J.; Yu, C.; He, C.; Li, Q.; Yang, Y.; Kong, H.; et al. Natural medicines-derived carbon dots as novel oral antioxidant administration strategy for ulcerative colitis therapy. *J. Nanobiotechnol.* **2024**, *22*, 511. [CrossRef] [PubMed]
44. Dai, Z.; Wang, E.H.C.; Petukhova, L.; Chang, Y.; Lee, E.Y.; Christiano, A.M. Blockade of IL-7 signaling suppresses inflammatory responses and reverses alopecia areata in C3H/HeJ mice. *Sci. Adv.* **2021**, *7*, eabd1866. [CrossRef]
45. Zhou, C.; Li, X.; Wang, C.; Zhang, J. Alopecia Areata: An Update on Etiopathogenesis, Diagnosis, and Management. *Clin. Rev. Allergy Immunol.* **2021**, *61*, 403–423. [CrossRef]
46. McMichael, A.J.; Roberson, M.L. Characterizing Epidemiology and Burden of Disease in Alopecia Areata-Making It Count. *JAMA Dermatol.* **2023**, *159*, 369–370. [CrossRef]
47. Ma, Y.Q.; Sun, Z.; Li, Y.M.; Xu, H. Oxidative stress and alopecia areata. *Front. Med.* **2023**, *10*, 1181572. [CrossRef]
48. Shakoei, S.; Mirmiranpoor, H.; Nakhjavani, M.; Nasimi, M.; Bakhshi, G.; Azizpour, A. Oxidative stress and antioxidant markers in patients with alopecia areata: A comparative cross-sectional study. *Indian J. Dermatol. Venereol. Leprol.* **2023**, *89*, 411–415. [CrossRef]
49. Sachdeva, S.; Khurana, A.; Goyal, P.; Sardana, K. Does oxidative stress correlate with disease activity and severity in alopecia areata? An analytical study. *J. Cosmet. Dermatol.* **2022**, *21*, 1629–1634. [CrossRef] [PubMed]
50. Peterle, L.; Sanfilippo, S.; Borgia, F.; Cicero, N.; Gangemi, S. Alopecia Areata: A Review of the Role of Oxidative Stress, Possible Biomarkers, and Potential Novel Therapeutic Approaches. *Antioxidants* **2023**, *12*, 135. [CrossRef]
51. Taskin, S.; Celik, H.; Cakirca, G.; Manav, V.; Taskin, A. Nitric oxide synthase activity: A novel potential biomarker for predicting Alopecia areata. *J. Cosmet. Dermatol.* **2022**, *21*, 7075–7080. [CrossRef]
52. Perlmutter, J.; Akouris, P.P.; Fremont, S.; Yang, B.; Toth, E.; Eze, M.; Wiseman, M. The Role of Reactive Oxygen Species in the Pathogenesis of Alopecia Areata: A Systematic Review and Meta-Analysis. *Skin. Pharmacol. Physiol.* **2025**, *38*, 59–67. [CrossRef]
53. Younis, N.; Puigmal, N.; El Kurdi, A.; Badaoui, A.; Zhang, D.; Morales-Garay, C.; Saad, A.; Cruz, D.; Al Rahy, N.; Daccache, A.; et al. Microneedle-Mediated Delivery of Immunomodulators Restores Immune Privilege in Hair Follicles and Reverses Immune-Mediated Alopecia. *Adv. Mater.* **2024**, *36*, e2312088. [CrossRef]
54. Jeong, D.I.; Lee, S.Y.; Kim, S.; Jo, S.-M.; Yang, H.; You, J.; Hwang, C.; Huh, J.W.; Choi, Y.E.; Jo, W.; et al. Baricitinib-loaded separable microneedle array patch (S-MAP) based on hyaluronic acid for alopecia areata therapy. *Carbohydr. Polym.* **2025**, *364*, 123789. [CrossRef]
55. Hindam, M.O.; Ahmed, L.A.; El Sayed, N.S.; Khattab, M.; Sallam, N.A. Repositioning of baricitinib for management of memory impairment in ovariectomized/D-galactose treated rats: A potential role of JAK2/STAT3-PI3K/AKT/mTOR signaling pathway. *Life Sci.* **2024**, *351*, 122838. [CrossRef]
56. McGinley, M.P.; Goldschmidt, C.H.; Rae-Grant, A.D. Diagnosis and Treatment of Multiple Sclerosis. *JAMA* **2021**, *325*, 765–779. [CrossRef]
57. Graf, J.; Akmatov, M.K.; Meuth, S.G.; Tremlett, H.; Holstiege, J. Updated Multiple Sclerosis Incidence, 2015–2022. *JAMA Neurol* **2024**, *81*, 1100–1102. [CrossRef] [PubMed]
58. Dash, U.C.; Bhol, N.K.; Swain, S.K.; Samal, R.R.; Nayak, P.K.; Raina, V.; Panda, S.K.; Kerry, R.G.; Duttaroy, A.K.; Jena, A.B. Oxidative stress and inflammation in the pathogenesis of neurological disorders: Mechanisms and implications. *Acta Pharm. Sin. B* **2025**, *15*, 15–34. [CrossRef]
59. Kasprzak-Drozd, K.; Nizinski, P.; Hawryl, A.; Gancarz, M.; Hawryl, D.; Oliwa, W.; Palka, M.; Markowska, J.; Oniszczuk, A. Potential of Curcumin in the Management of Skin Diseases. *Int. J. Mol. Sci.* **2024**, *25*, 3617. [CrossRef] [PubMed]

60. Lu, L.; Qi, S.; Chen, Y.; Luo, H.; Huang, S.; Yu, X.; Luo, Q.; Zhang, Z. Targeted immunomodulation of inflammatory monocytes across the blood-brain barrier by curcumin-loaded nanoparticles delays the progression of experimental autoimmune encephalomyelitis. *Biomaterials* **2020**, *245*, 119987. [CrossRef] [PubMed]
61. Sanadgol, N.; Barati, M.; Houshmand, F.; Hassani, S.; Clarner, T.; Shahlaei, M.; Golab, F. Metformin accelerates myelin recovery and ameliorates behavioral deficits in the animal model of multiple sclerosis via adjustment of AMPK/Nrf2/mTOR signaling and maintenance of endogenous oligodendrogenesis during brain self-repairing period. *Pharmacol. Rep.* **2020**, *72*, 641–658. [CrossRef] [PubMed]
62. Qin, W.; Huang, J.; Zhang, M.; Xu, M.; He, J.; Liu, Q. Nanotechnology-Based Drug Delivery Systems for Treating Acute Kidney Injury. *ACS Biomater. Sci. Eng.* **2024**, *10*, 6078–6096. [CrossRef]
63. Jensen, S.K.; Rasmussen, T.B.; Jacobsen, B.H.; Heide-Jørgensen, U.; Sawhney, S.; Gammelager, H.; Birn, H.; Johnsen, S.P.; Christiansen, C.F. Regional variation in incidence and prognosis of acute kidney injury. *Nephrol. Dial. Transpl.* **2024**, *39*, 1171–1180. [CrossRef]
64. Levey, A.S.; Eckardt, K.-U.; Dorman, N.M.; Christiansen, S.L.; Hoorn, E.J.; Ingelfinger, J.R.; Inker, L.A.; Levin, A.; Mehrotra, R.; Palevsky, P.M.; et al. Nomenclature for kidney function and disease: Report of a Kidney Disease: Improving Global Outcomes (KDIGO) Consensus Conference. *Kidney Int.* **2020**, *97*, 1117–1129. [CrossRef] [PubMed]
65. He, K.; Zhou, D.; Pu, Z.; Chen, S.; Shen, Y.; Zhao, S.; Qian, X.; Hu, Q.; Wu, X.; Xie, Z.; et al. Cellular Senescence in Acute Liver Injury: What Happens to the Young Liver? *Aging Dis.* **2024**, *16*, 1347–1362. [CrossRef]
66. Yuan, X.; Zhou, Y.; Sun, J.; Wang, S.; Hu, X.; Li, J.; Huang, J.; Chen, N. Preventing acute liver injury via hepatocyte-targeting nano-antioxidants. *Cell Prolif.* **2023**, *56*, e13494. [CrossRef]
67. Song, B.; Zhang, C.; Hu, W.; Guo, C.; Xia, Z.; Hu, W.; Qin, M.; Jiang, W.; Lv, J.; Xu, D.; et al. Nano-designed carbon monoxide donor SMA/CORM2 exhibits protective effect against acetaminophen induced liver injury through macrophage reprograming and promoting liver regeneration. *J. Control. Release* **2021**, *331*, 350–363. [CrossRef]
68. Liu, M.; Wu, H.; Li, Q.; Liu, H.; Chen, C.; Yin, F.; Wang, H.; Zha, Z.; Wang, F. Mn_3O_4 nanozymes prevent acetaminophen-induced acute liver injury by attenuating oxidative stress and countering inflammation. *J. Colloid Interface Sci.* **2024**, *654 Pt A*, 83–95. [CrossRef]
69. Aslam, M.; Fatima, B.; Batool, R.; Imran, M.; Hussain, D.; Najam-Ul-Haq, M.; Mehmood, R. Saponin Gallate-Loaded Gd-Doped Zinc-Gallium Layered Double Hydroxides (Zn/Ga@Gd-LDH) Nanocarrier for Attenuating NF-kappaB-Mediated Inflammation. *ACS Appl. Mater. Interfaces* **2025**, *17*, 26263–26281. [CrossRef]
70. Trindade, D.; Carvalho, R.; Machado, V.; Chambrone, L.; Mendes, J.J.; Botelho, J. Prevalence of periodontitis in dentate people between 2011 and 2020: A systematic review and meta-analysis of epidemiological studies. *J. Clin. Periodontol.* **2023**, *50*, 604–626. [CrossRef] [PubMed]
71. Kassebaum, N.J.; Bernabe, E.; Dahiya, M.; Bhandari, B.; Murray, C.J.; Marcenes, W. Global burden of severe periodontitis in 1990–2010: A systematic review and meta-regression. *J. Dent. Res.* **2014**, *93*, 1045–1053. [CrossRef] [PubMed]
72. Chen, M.X.; Zhong, Y.J.; Dong, Q.Q.; Wong, H.M.; Wen, Y.F. Global, regional, and national burden of severe periodontitis, 1990–2019: An analysis of the Global Burden of Disease Study 2019. *J. Clin. Periodontol.* **2021**, *48*, 1165–1188. [CrossRef]
73. Sczepanik, F.S.C.; Grossi, M.L.; Casati, M.; Goldberg, M.; Glogauer, M.; Fine, N.; Tenenbaum, H.C. Periodontitis is an inflammatory disease of oxidative stress: We should treat it that way. *Periodontol. 2000* **2020**, *84*, 45–68. [CrossRef]
74. Li, L.; Qin, W.; Ye, T.; Wang, C.; Qin, Z.; Ma, Y.; Mu, Z.; Jiao, K.; Tay, F.R.; Niu, W.; et al. Bioactive Zn-V-Si-Ca Glass Nanoparticle Hydrogel Microneedles with Antimicrobial and Antioxidant Properties for Bone Regeneration in Diabetic Periodontitis. *ACS Nano* **2025**, *19*, 7981–7995. [CrossRef]
75. Wang, Y.; Li, C.; Wan, Y.; Qi, M.; Chen, Q.; Sun, Y.; Sun, X.; Fang, J.; Fu, L.; Xu, L.; et al. Quercetin-Loaded Ceria Nanocomposite Potentiate Dual-Directional Immunoregulation via Macrophage Polarization against Periodontal Inflammation. *Small* **2021**, *17*, 2101505. [CrossRef]
76. Zhao, M.; Zhai, H.; Li, H.; Wei, F.; Ma, H.; Liu, Y.; Li, W.; Wei, P. Age-standardized incidence, prevalence, and mortality rates of autoimmune diseases in adolescents and young adults (15–39 years): An analysis based on the global burden of disease study 2021. *BMC Public Health* **2024**, *24*, 1800. [CrossRef]
77. Ye, R.; Guo, Q.; Huang, J.; Wang, Z.; Chen, Y.; Dong, Y. Eucommia ulmoides polysaccharide modified nano-selenium effectively alleviated DSS-induced colitis through enhancing intestinal mucosal barrier function and antioxidant capacity. *J. Nanobiotechnol.* **2023**, *21*, 222. [CrossRef]
78. Gonczi, L.; Lakatos, L.; Kurti, Z.; Golovics, P.A.; Pandur, T.; David, G.; Erdelyi, Z.; Szita, I.; Lakatos, P.L. Incidence, Prevalence, Disease Course, and Treatment Strategy of Crohn's Disease Patients from the Veszprem Cohort, Western Hungary: A Population-based Inception Cohort Study Between 2007 and 2018. *J. Crohns Colitis* **2023**, *17*, 240–248. [CrossRef] [PubMed]
79. Roda, G.; Chien Ng, S.; Kotze, P.G.; Argollo, M.; Panaccione, R.; Spinelli, A.; Kaser, A.; Peyrin-Biroulet, L.; Danese, S. Crohn's disease. *Nat. Rev. Dis. Primers* **2020**, *6*, 22. [CrossRef] [PubMed]

80. Xu, S.; Li, X.; Zhang, S.; Qi, C.; Zhang, Z.; Ma, R.; Xiang, L.; Chen, L.; Zhu, Y.; Tang, C.; et al. Oxidative stress gene expression, DNA methylation, and gut microbiota interaction trigger Crohn's disease: A multi-omics Mendelian randomization study. *BMC Med.* **2023**, *21*, 179. [CrossRef]
81. Tratensek, A.; Locatelli, I.; Grabnar, I.; Drobne, D.; Vovk, T. Oxidative stress-related biomarkers as promising indicators of inflammatory bowel disease activity: A systematic review and meta-analysis. *Redox Biol.* **2024**, *77*, 103380. [CrossRef]
82. Jarmakiewicz-Czaja, S.; Ferenc, K.; Filip, R. Antioxidants as Protection against Reactive Oxidative Stress in Inflammatory Bowel Disease. *Metabolites* **2023**, *13*, 573. [CrossRef] [PubMed]
83. Chen, J.; Ruan, X.; Yuan, S.; Deng, M.; Zhang, H.; Sun, J.; Yu, L.; Satsangi, J.; Larsson, S.C.; Therdoratou, E.; et al. Antioxidants, minerals and vitamins in relation to Crohn's disease and ulcerative colitis: A Mendelian randomization study. *Aliment. Pharmacol. Ther.* **2023**, *57*, 399–408. [CrossRef]
84. Chen, W.; Xu, Z.; Jiang, J.; Feng, W.; Li, B. Mitochondrial Protease AFG_3L_2 Inhibits Ferroptosis of Intestinal Epithelial Cells through PPARA/GPX_4 Signaling Pathway to Improve Experimental Enteritis. *Am. J. Pathol.* **2025**, *195*, 1443–1456. [CrossRef]
85. Zhong, H.; Luo, X.; Abdullah; Liu, X.; Hussain, M.; Guan, R. Nano-targeted delivery system: A promising strategy of anthocyanin encapsulation for treating intestinal inflammation. *Crit. Rev. Food Sci. Nutr.* **2025**, *online ahead of print*. [CrossRef]
86. Ibrahim, D.; Khater, S.I.; Sherkawy, H.S.; Elgamal, A.; Hasan, A.A.; Muhammed, A.A.; Farag, M.F.M.; Eissa, S.A.; Ismail, T.A.; Eissa, H.M.; et al. Protective Role of Nano-encapsulated Bifidobacterium breve, Bacilllus coagulans, and Lactobacillus plantarum in Colitis Model: Insights Toward Propagation of Short-Chain Fatty Acids and Reduction of Exaggerated Inflammatory and Oxidative Response. *Probiotics Antimicrob. Proteins* **2025**, *online ahead of print*. [CrossRef]
87. Mohanbhai, S.J.; Sardoiwala, M.N.; Gupta, S.; Shrimali, N.; Choudhury, S.R.; Sharma, S.S.; Guchhait, P.; Karmakar, S. Colon targeted chitosan-melatonin nanotherapy for preclinical Inflammatory Bowel Disease. *Biomater. Adv.* **2022**, *136*, 212796. [CrossRef]
88. Zhu, D.; Wu, H.; Jiang, K.; Xu, Y.; Miao, Z.; Wang, H.; Ma, Y. Zero-Valence Selenium-Enriched Prussian Blue Nanozymes Reconstruct Intestinal Barrier against Inflammatory Bowel Disease via Inhibiting Ferroptosis and T Cells Differentiation. *Adv. Healthc. Mater.* **2023**, *12*, e2203160. [CrossRef]
89. Shah, S.U.; Socha, M.; Fries, I.; Gibaud, S. Synthesis of S-nitrosoglutathione-alginate for prolonged delivery of nitric oxide in intestines. *Drug Deliv.* **2016**, *23*, 2927–2935. [CrossRef] [PubMed]
90. Fu, W.; Huang, Z.; Li, W.; Xu, L.; Yang, M.; Ma, Y.; Liu, H.; Qian, H.; Wang, W. Copper-luteolin nanocomplexes for Mediating multifaceted regulation of oxidative stress, intestinal barrier, and gut microbiota in inflammatory bowel disease. *Bioact. Mater.* **2025**, *46*, 118–133. [CrossRef] [PubMed]
91. Xue, Y.; Wang, T.; Liu, J.P.; Chen, Q.; Dai, X.L.; Su, M.; Cheng, Y.H.; Chu, C.C.; Ren, Y.Q. Recent Trends in the Development and Application of Nano-Antioxidants for Skin-Related Disease. *Antioxidants* **2024**, *14*, 27. [CrossRef]
92. Zhang, C.; Yu, Y.; Shi, S.; Liang, M.; Yang, D.; Sui, N.; Yu, W.W.; Wang, L.; Zhu, Z. Machine Learning Guided Discovery of Superoxide Dismutase Nanozymes for Androgenetic Alopecia. *Nano Lett.* **2022**, *22*, 8592–8600. [CrossRef]
93. Yang, Y.; Wang, P.; Gong, Y.; Yu, Z.; Gan, Y.; Li, P.; Liu, W.; Wang, X. Curcumin-zinc framework encapsulated microneedle patch for promoting hair growth. *Theranostics* **2023**, *13*, 3675–3688. [CrossRef]
94. Yang, W.; Lv, Y.; Wang, B.; Luo, S.; Le, Y.; Tang, M.; Zhao, R.; Li, Y.; Kong, X. Polydopamine Synergizes with Quercetin Nanosystem to Reshape the Perifollicular Microenvironment for Accelerating Hair Regrowth in Androgenetic Alopecia. *Nano Lett.* **2024**, *24*, 6174–6182. [CrossRef] [PubMed]
95. Speeckaert, R.; Bulat, V.; Speeckaert, M.M.; van Geel, N. The Impact of Antioxidants on Vitiligo and Melasma: A Scoping Review and Meta-Analysis. *Antioxidants* **2023**, *12*, 2082. [CrossRef]
96. Li, C.; Wang, W.; Shao, J.; Zhou, S.; Ji, X.; Xi, Y.; Xu, Q.; Huang, Y.; Wang, J.; Wan, Y.; et al. Biomimetic polydopamine loaded with janus kinase inhibitor for synergistic vitiligo therapy via hydrogel microneedles. *J. Nanobiotechnol.* **2025**, *23*, 63. [CrossRef] [PubMed]
97. Han, Z.; Gao, X.; Wang, Y.; Cheng, S.; Zhong, X.; Xu, Y.; Zhou, X.; Zhang, Z.; Liu, Z.; Cheng, L. Ultrasmall iron-quercetin metal natural product nanocomplex with antioxidant and macrophage regulation in rheumatoid arthritis. *Acta Pharm. Sin. B* **2023**, *13*, 1726–1739. [CrossRef]
98. McInnes, I.B.; Gravallese, E.M. Immune-mediated inflammatory disease therapeutics: Past, present and future. *Nat. Rev. Immunol.* **2021**, *21*, 680–686. [CrossRef]
99. Jing, W.; Liu, C.; Su, C.; Liu, L.; Chen, P.; Li, X.; Zhang, X.; Yuan, B.; Wang, H.; Du, X. Role of reactive oxygen species and mitochondrial damage in rheumatoid arthritis and targeted drugs. *Front. Immunol.* **2023**, *14*, 1107670. [CrossRef] [PubMed]
100. Bao, M.; Wang, K.; Li, J.; Li, Y.; Zhu, H.; Lu, M.; Zhang, Y.; Fan, Q.; Han, L.; Wang, K.; et al. ROS Scavenging and inflammation-directed polydopamine nanoparticles regulate gut immunity and flora therapy in inflammatory bowel disease. *Acta Biomater.* **2023**, *161*, 250–264. [CrossRef]
101. Asif, N.; Amir, M.; Fatma, T. Recent advances in the synthesis, characterization and biomedical applications of zinc oxide nanoparticles. *Bioprocess. Biosyst. Eng.* **2023**, *46*, 1377–1398. [CrossRef] [PubMed]

102. Jomova, K.; Alomar, S.Y.; Alwasel, S.H.; Nepovimova, E.; Kuca, K.; Valko, M. Several lines of antioxidant defense against oxidative stress: Antioxidant enzymes, nanomaterials with multiple enzyme-mimicking activities, and low-molecular-weight antioxidants. *Arch. Toxicol.* **2024**, *98*, 1323–1367. [CrossRef]
103. Kim, Y.G.; Lee, Y.; Lee, N.; Soh, M.; Kim, D.; Hyeon, T. Ceria-Based Therapeutic Antioxidants for Biomedical Applications. *Adv. Mater.* **2024**, *36*, e2210819. [CrossRef]
104. Awasthi, N.; Liongue, C.; Ward, A.C. STAT proteins: A kaleidoscope of canonical and non-canonical functions in immunity and cancer. *J. Hematol. Oncol.* **2021**, *14*, 198. [CrossRef]
105. Summer, M.; Ashraf, R.; Ali, S.; Bach, H.; Noor, S.; Noor, Q.; Riaz, S.; Khan, R.R.M. Inflammatory response of nanoparticles: Mechanisms, consequences, and strategies for mitigation. *Chemosphere* **2024**, *363*, 142826. [CrossRef] [PubMed]
106. Mohajeri, M.; Sadeghizadeh, M.; Najafi, F.; Javan, M. Polymerized nano-curcumin attenuates neurological symptoms in EAE model of multiple sclerosis through down regulation of inflammatory and oxidative processes and enhancing neuroprotection and myelin repair. *Neuropharmacology* **2015**, *99*, 156–167. [CrossRef]
107. Hou, J.; Wang, H.; Ge, Z.; Zuo, T.; Chen, Q.; Liu, X.; Mou, S.; Fan, C.; Xie, Y.; Wang, L. Treating Acute Kidney Injury with Antioxidative Black Phosphorus Nanosheets. *Nano Lett.* **2020**, *20*, 1447–1454. [CrossRef] [PubMed]
108. Cao, L.; Duan, D.; Peng, J.; Li, R.; Cao, Q.; Li, X.; Guo, Y.; Li, J.; Liu, K.; Li, Y.; et al. Oral enzyme-responsive nanoprobes for targeted theranostics of inflammatory bowel disease. *J. Nanobiotechnol.* **2024**, *22*, 484. [CrossRef]

Disclaimer/Publisher's Note: The statements, opinions and data contained in all publications are solely those of the individual author(s) and contributor(s) and not of MDPI and/or the editor(s). MDPI and/or the editor(s) disclaim responsibility for any injury to people or property resulting from any ideas, methods, instructions or products referred to in the content.

antioxidants

MDPI

Review

Cyclodextrin-Based Nanotransporters as a Versatile Tool to Manage Oxidative Stress-Induced Lung Diseases

Supandeep Singh Hallan [1], Francesca Ferrara [2], Maddalena Sguizzato [2,3] and Rita Cortesi [2,3,*]

[1] Department of Pharmaceutical Sciences and Natural Products, Central University of Punjab, Bathinda 151401, India; hllsnd@unife.it
[2] Department of Chemical, Pharmaceutical and Agricultural Sciences, University of Ferrara, I-44121 Ferrara, Italy; frrfnc3@unife.it (F.F.); sgzmdl@unife.it (M.S.)
[3] Biotechnology Interuniversity Consortium (C.I.B.), Ferrara Section, University of Ferrara, I-44121 Ferrara, Italy
* Correspondence: crt@unife.it

Abstract

Oxidative stress is one of the key elements in lung-related complications such as cystic fibrosis, acute lung injury, pulmonary hypertension, bronchopulmonary dysplasia, chronic airway diseases, lung cancer, COVID-19, and many others. Antioxidant and anti-inflammatory therapy can be considered as supportive alternatives in their management. However, most naturally derived antioxidants face issues with poor aqueous solubility and stability, which hinder their clinical utility. Remarkably, local pulmonary delivery circumvents the severe limitations of oral delivery, including hepatic first-pass metabolism and organ toxicity, and enables a higher drug payload in the lungs. Here, in this review, we present cyclodextrin as a potential drug carrier for pulmonary administration, exploring the possibilities of its surface modification, complexation with other drug transporters, and loading of cannabidiols, siRNA, and antibodies as future trends. However, the lack of a robust physiological model for assessing the efficacy of lung-oriented drug targeting is a significant concern in its path to clinical and commercial success.

Keywords: oxidative stress; polyphenols; cyclodextrins; pulmonary drug delivery; inflammation; solubility; inclusion complex; lungs; drug delivery

1. Introduction

Lungs are the organs exposed to a rich oxygen-containing environment, offering a large surface area and blood supply, which makes them susceptible to serious injuries caused by oxidative stress [1,2]. The inflammatory cells (neutrophils and macrophages), fibroblasts, endothelial, and epithelial cells liberate reactive oxygen species (ROS) as the end product of their metabolism [3,4]. In other words, oxidative stress is the result of an imbalance between the oxidants and antioxidants, as given in Figure 1, resulting in the overgeneration of free radicals or ROS or reactive nitrogen species (RNS) [5,6].

The major physiological events, for instance, inflammation, hypoxia, and hyperoxia, end up with oxidative stress which contributes to the rise in lung-related complications namely cystic fibrosis (CF), acute lung injury (ALI), pulmonary hypertension (PH), chronic obstructive pulmonary disease (COPD), bronchopulmonary dysplasia (BPD), and lung cancer (LC) along with compromised pulmonary hemodynamics and gas exchange [7]. Moreover, the sources of free radicals are either endogenous (mitochondria, NADPH, oxidases, xanthine oxidases, and endothelial nitric oxide synthase) or exogenous (UV and IR, air pollution, heavy metals, and cigarette smoking) [8–10]. The oxidative stress

originating from the ROS above further activates several inflammatory cascades, which can enhance the release of cytokines and inflammatory mediators; consequently, more complex lung injury can occur.

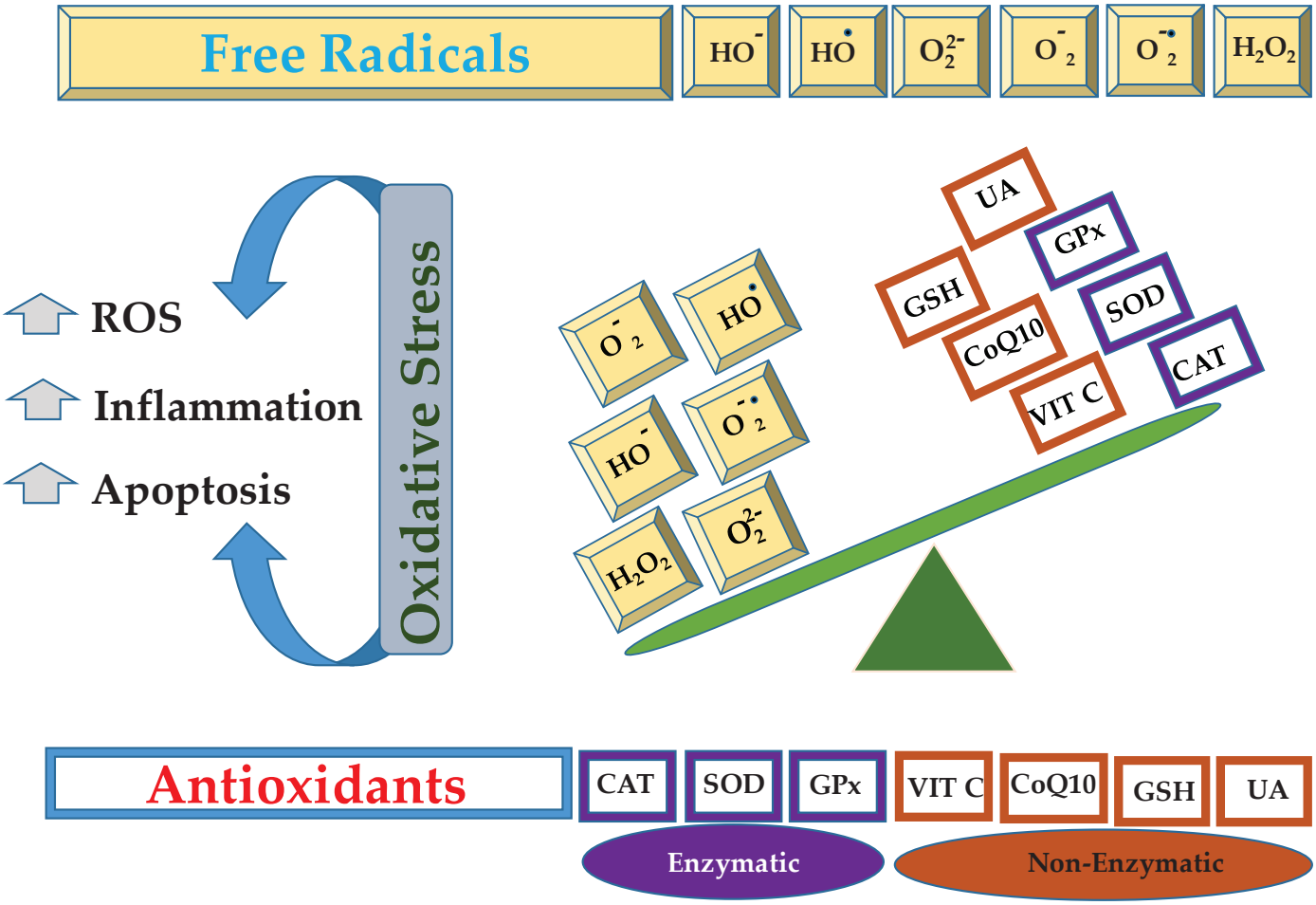


Figure 1. Schematic representation of imbalance between free radicals, such as hydroxide ion (HO^-), hydroxyl radical ($HO^•$), peroxide ion (O_2^{2-}), superoxide (O_2^-), superoxide anion ($O_2^{-•}$), hydrogen peroxide (H_2O_2), that can be neutralized by enzymatic (catalase, CAT; superoxide dismutase, SOD; glutathione peroxidase, GPx) or non enzymatic antioxidant mechanisms (vitamin C, VIT C; coenzyme Q10, CoQ10; reduced glutathione, GSH; uric acid, UA).

CF is classified as an autosomal recessive genetic disorder that results from a mutation of a gene on chromosome VII, which encodes the CF transmembrane conductance regulator (CFTR) [11,12]. In CF patients, the liberation of ROS, combined with the altered functioning of CFTR proteins, leads to an oxidative stress condition within the epithelial cells [13]. As of 4 July 2025, more than 2100 mutations have been listed in the CFTR mutation database [14].

ALI is defined as a hypoxic situation characterized by extensive lung weight gain due to edema and elevated pulmonary vascular permeability [15]. Despite the complex pathogenesis of ALI, the oxidative stress and initiation of inflammatory reactions (release of cytokines) are the key aspects of its development. In recent studies, a 20-fold increase in ROS levels has been reported in the lungs affected by ALI [16]. In ALI, pro-inflammatory cytokines are generally released from M1-like macrophages (a transformation of alveolar macrophages), and this entire event activates monocytes and neutrophils, which further liberate ROS to a great extent, killing pathogens. Consequently, the high production of ROS will elevate normal oxidative stress levels [17,18].

Among the ICU patients who are exposed to different viral infections, especially SARS-CoV-2, the immune reactions will trigger with a greater threshold, and a high mortality rate can be anticipated in this particular case [19]. Oxidative stress aberrantly activates the innate immune response and inflammatory cytokines, which are the major contributing factors responsible for multiple deaths [20]. Owing to exposure to COVID-19, the induced oxidative stress can collapse the pulmonary alveoli (pneumonia), followed by multiple organ dysfunction. Concerning this, the uptake of exogenous antioxidant therapy can neutralize the generated ROS and strengthen the immune system during COVID-19 [21,22].

PH is another complication, especially in the case of newborns, characterized by constriction and increased pressure in the pulmonary arteries, which undergo remodeling [23]. In this particular disease, the pulmonary vasoconstriction takes place due to an excessive release of ROS and RNS, which can inactivate various enzymes and vasodilators involved in nitric oxide pathways, consequently leading to persistent PH [24]. In this scenario, the elevated blood pressure exerts a burden on the right side of the heart, followed by right heart dysfunction, which puts the life of the patients in danger [25]. It is worth noting that there is no specific treatment for PH, and patients can temporarily rely on vasodilator agents. In addition, a median survival of three years after diagnosis was recorded in patients with PH, and, finally, lung transplantation was considered the definitive treatment, again with severe clinical complications [23,26].

Among PH, pulmonary arterial hypertension (PAH) has to be mentioned. Precisely, PAH is classified as WHO Group 1 PH, representing a distinct subtype within the broader category of PH. Group 1 PAH is characterized by a specific set of pathological changes in the pulmonary arteries, leading to increased pulmonary vascular resistance and elevated pulmonary artery pressure. PAH can be idiopathic (unknown cause), but also be inherited or associated with other conditions, including sickle cell anemia, connective tissue diseases, portal hypertension of the liver, HIV infection, and congenital heart disease. PAH can even occur after exposure to drugs and toxins and is occasionally related to pulmonary veno-occlusive disease or persistent PH of the newborn [27,28]. Furthermore, PH is associated with elevated oxidative stress, so it is important to emphasize that DNA damage and pulmonary vascular remodeling are significant concerns in the lungs of PAH patients. ROS and DNA are considered biomarkers of PAH susceptibility in various subgroups of PAH patients. Currently, there is no effective treatment for PAH [29].

LC occurs when the lungs are exposed to harmful carcinogens, as evidenced by genetic and epigenetic alterations [30]. The malignancies related to the lungs have also been a leading cause of the increase in death numbers in recent years. Squamous cell lung carcinoma and adenocarcinoma LC are more prominent, which are 30% and 40%, respectively, among non-small cell LC subtypes [31,32].

These elevated stress conditions within the cancerous tissues act as a strong driving factor responsible for shifting the free radical balance towards oxidative conditions, which further results in a reduced antioxidant threshold compared to non-cancerous or healthy tissues [33,34]. In this regard, an increase in the level of reactive aldehydes, oxidative modifications in DNA, and nuclear factor erythroid-2-related factor (NRF2) activity, along with a decline in fatty acid levels, has been monitored. Taking this into account, this study has emphasized the relationship between various lipid mediators and antioxidants in different types of LC [32].

BPD is a chronic lung disease primarily affecting premature infants and is a common cause of morbidity and mortality. It is characterized by lung damage and disrupted lung development, often stemming from the need for oxygen therapy and mechanical ventilation in babies with underdeveloped lungs. Therefore, BPD is a chronic disease persisting beyond hospital discharge and into adulthood. While BPD is not present at birth, it can develop

as a complication of other breathing problems, including respiratory distress syndrome (RDS), asthma, and emphysema. Furthermore, BPD is also involved in neurodevelopment, significantly affecting and delaying fine and gross motor skills and language [35–37]. In addition, infants with BPD are at high risk of cardiopulmonary sequelae, such as PH and systemic hypertension. The oxidative stress activates the inflammatory cells, especially granulocytes, which potentiates the inflammatory reactions. In this regard, the employment of antioxidants in preterm newborns predominantly exposed to oxidative stress and at risk for BPD represents a logical strategy to ameliorate injury caused by the presence of free radicals [37–39].

COPD is the third leading cause of death after stroke and cardiovascular disease, characterized by irreversible obstruction in the airflow [40]. Oxidative stress remains a leading concern in COPD, which affects various lung events, including the inactivation of anti-proteases, injury to alveolar epithelial architecture, remodeling, and ultimately, apoptosis. In addition, due to an upsurge in the levels of both oxidants and oxidative stress-related markers, patients experience chronic inflammation, fibrosis, and blood in the airways, which ultimately damages the lung parenchyma [10,41,42]. Researchers have reported that in COPD patients, an elevation in oxidative stress conditions and a decline in glutathione concentrations within the bronchoalveolar lavage fluid are present [43]. Considering that air pollutants represent one of the primary sources of oxidative stress, they are known to be involved in the development of many respiratory conditions, including COPD. The role of pollutants in the pathogenesis of COPD has been presented in Figure 2.

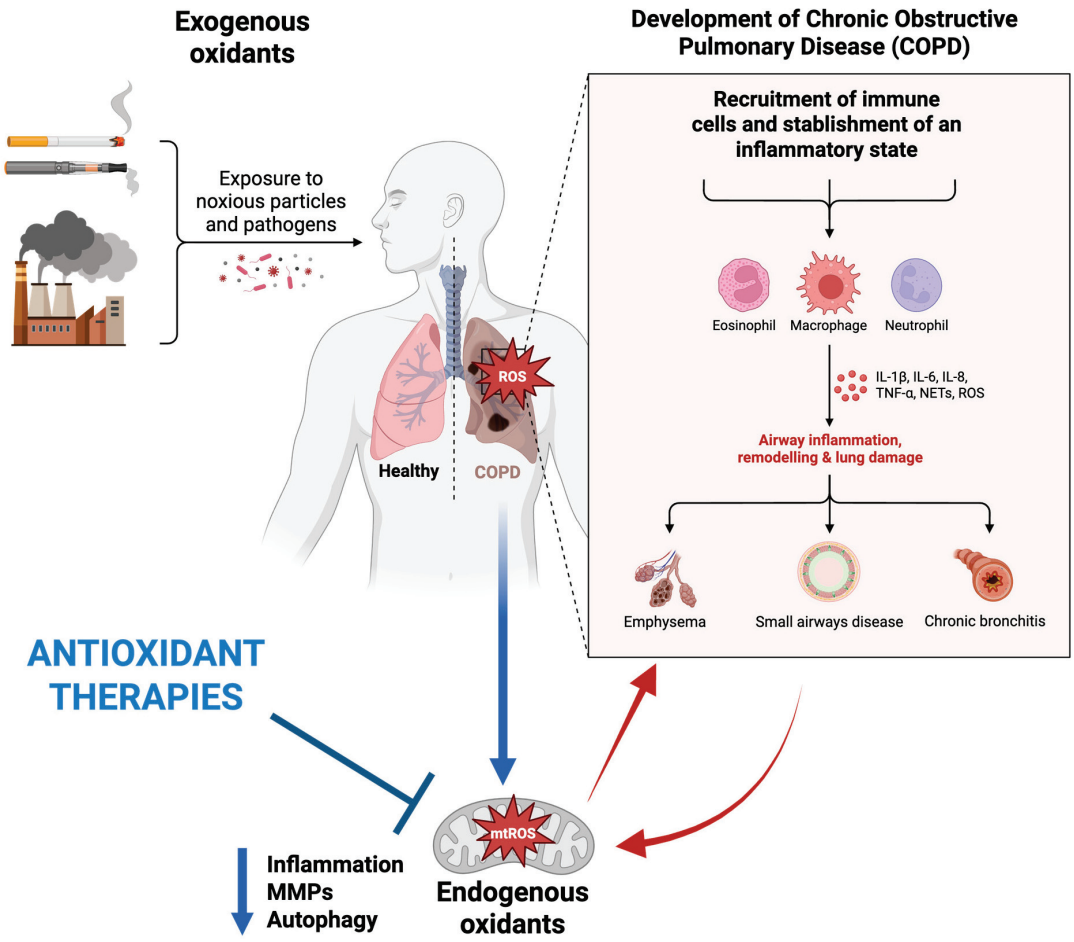


Figure 2. Schematic representation of factors influencing the pathogenesis of COPD and therapeutic effects of mitochondria-targeted antioxidants. Original figure created with www.BioRender.com (accessed on 30 June 2025).

It is a well-established fact that the intracellular level of ROS is stabilized by several enzyme or non-enzyme-linked cellular processes. The primary enzymes involved in the breakdown of oxidants are ascorbate peroxidase, glutathione peroxidase, metallothionein-3, ferritin heavy chain, catalase, and superoxide dismutase. Non-enzymes that destroy ROS by interrupting free radical chain formation through the building of a metal-protein complex [44,45].

The mitochondria are primarily engaged in the development of oxidative stress in all previously highlighted lung-related complications. When examining the cellular impact, ROS exert a more profound detrimental effect on mitochondrial DNA, the genetic material encoding mitochondrial proteins, than on nuclear DNA. The adverse effects observed include not only DNA damage but also impaired mitochondrial electron transport chain activity and altered membrane potential [46,47]. In addition, the hydroxyl ion is highly reactive towards lipids among the other ROS members, responsible for lipid peroxidation and protein fragmentation [48,49]. Moreover, this event can also influence the inflammatory and apoptotic pathways, with increased permeability of the outer mitochondrial membrane [50,51].

2. Role of Antioxidants in the Management of Lung-Related Complications

Taken together, both oxidative stress and impaired antioxidant mechanisms are key elements in the development of injury, which can permanently damage the lungs [18]. To minimize this ROS-induced lung destruction, the exogenous intake of antioxidants could potentially retard the deterioration of lung functioning [52].

Antioxidants are the moieties that exhibit remarkable radical scavenging potential, neutralizing ROS by donating an H-atom to free radicals. They can be employed as an effective therapy to address oxidative stress-induced lung complications [52,53]. As mentioned earlier, oxidative damage to lipids, proteins, and nucleic acids can be prevented by neutralizing free radical species with antioxidant substances [5,54,55].

The role of antioxidants in counteracting oxidative stress-related pathologies is summarized in Table 1.

Table 1. The exploitation of antioxidants in various lung diseases.

Disease	Antioxidants	Oxidative Stress Biomarker	In Vitro Model	In Vivo Model	Remarks	Ref.
PAH	Resveratrol	- SphK1-mediated NF-κB activation, - BMP/SMAD signaling pathway, - miR-638 and NR4A3/cyclin D1 pathway, - RhoA-ROCK signaling pathway.	--	Monocrotalin model in rats	- Resveratrol efficiently treated PAH via its action on signaling pathway, including interrupted proliferation of pulmonary arterial smooth muscle cells - Remodeling of right ventricle - The chemokine and cytokine-driven inflammatory response was reduced by controlling IL-6	[56]
BPD	Resveratrol	SIRT1 p53, Acetyl-p53 NLRP3 inflammasome IL-1β and IL-18 NF-κB		Neonate rats Model	- Assuaged hyperoxia-induced apoptosis in neonatal rats' lung tissue by reducing ROS and p53. - Induced SIRT1 upregulation and - Declining of acetyl-p53 - Induced SIRT1 mRNA and protein expression	[47,57]

Table 1. *Cont.*

Disease	Antioxidants	Oxidative Stress Biomarker	In Vitro Model	In Vivo Model	Remarks	Ref.
PAH	*Rhodiola crenulata* extract	PPARγ LC3B ATG7 p62 LKB1-AMPK	--	Rats with PAH	- The extract ameliorated PAH by inhibiting fatty acid oxidation and autophagy in PAH induced rats. - The extract also reversed the high level of decadienyl-L-carnitine by the modulation of metabolic enzyme CPT1A at mRNA and protein level in serum and lung in the rats having PAH	[58]
COPD	Fisetin	- Lowering NF-κB binding in the IL-8 promoter region in NCI-H292 lung epithelial cells, - Declined IL-8 release in response to TNF-α	Human lung epithelial cells NCI-H292 (CRL-1848) and HEK293T (CRL-3216) cells	--	- Effective in inhibiting the TNF-α/NF-κB signaling wordpathway by targeting protein kinase C. - Suppressed the inhibitor of IKK/NF-κB downstream signaling cascade	[59]
COPD	Resveratrol and genistein	NF-κB, TNF-α MMP-9	Isolated lymphocytes from healthy and COPD patients	--	- Increased level of TNF-α seen in MMP-9 and in COPD patients - Inhibitory mechanism against the translocation of NF-κB further reduces the concentration level of TNF-α and MMP	[60]
COPD	Crocin	NRF2	Assessment of cardiac parameters in COPD-induced rats by ECG under light anesthesia	Cigarette-induced lung injury model in rats	- Reduction in NRF2 - Cotinine concentration was increased - Protective effect against oxidative stress-induced lung injury - Cardiac abnormalities traced in electrocardiogram and hemodynamic parameters returned to normal range	[61]
LC	*Ilex latifolia* Thunb	Caspase-9 mRNA expression PI3K mTOR Bcl-2 NF-κB VEGF COX-2	Lung cancer A549 cell line Human normal lung epithelial cells BEAS-2B	--	- Conquer cancer by interrupting A549 cells' proliferation, followed by apoptosis - BEAS-2B proliferation remained unaffected - Increased the levels of lactate dehydrogenase and ROS, hence promoting apoptosis - The presence of rutin, kaempferol, isochlorogenic acid A, isochlorogenic acid B, and isochlorogenic acid C was confirmed by HPLC analyses	[62]
Asthma	Luteolin	IgE IFN-γ IL-4 IL-5 BALF	--	Mouse model (BALB/c male mice)	- Promisingly decreased the threshold of antigen-induced bronchoconstriction - Reduction in IgE and IL-4/IL-5 concentration - Significant increase IFN-γ, level in BALF	[63]

Table 1. *Cont.*

Disease	Antioxidants	Oxidative Stress Biomarker	In Vitro Model	In Vivo Model	Remarks	Ref.
CF	Olive Leaf Extract	CFTR F508del-CFTR	CFBE41o- HNE	--	- Avoided redox imbalance and inflammation - Declining in *P. aeruginosa* functioning - Synergism between extract and CFTR modulators has been established and can be employed as combinational therapy	[64]

BPD: Bronchopulmonary dysplasia, PAH: Pulmonary Arterial Hypertension, TNF: Tumor Necrosis Factor, NF-κB: Nuclear Factor-κB, MMP-9: Matrix Metalloproteinase-9, IgE: Immunoglobulin E, IFN-γ: Interferon Gamma, IL-Interleukin, BALF: Broncho-Alveolar Lavage Fluid, NRF2: Nuclear erythroid-related factor 2, PPARγ: Peroxisome Proliferator–activated Receptor γ, LKB1: Liver kinase B1, AMPK: Adenosine Monophosphate-activated Protein Kinase, ATG7: Autophagy Related Protein 7, LC3B: Microtubule-associated proteins light chain 3B, PI3K: Phosphatidylinositol 3-kinase, SIRT-1: Sirtuin-1, mTOR: Mammalian target of rapamycin, Bcl-2: B-cell lymphoma-2, VEGF: Vascular endothelial growth factor, COX-2: Cyclooxygenase-2, CFTR: Cystic fibrosis transmembrane conductance regulator, CFBE: CFBE41o- Human Cystic Fibrosis Bronchial Epithelial Cell, IKK/NF κB: Inhibitor of kappa B kinase.

Building on this, polyphenols are naturally derived, plant-based secondary bioactive compounds found abundantly in fruits, vegetables, grains, and herbs, known for their potent antioxidant and anti-inflammatory properties that offer therapeutic benefits in various lung diseases [65]. They help reduce oxidative stress and inflammation, which are key factors in lung conditions such as ALI, COPD, asthma, pulmonary fibrosis, PH, and LC [66]. These compounds work by neutralizing harmful free radicals, suppressing pro-inflammatory cytokines like TNF-α, IL-1, and IL-6, and blocking critical inflammatory signaling pathways such as NF-κB and mitogen-activated protein kinase (MAPK) [66]. For instance, flavonoids, such as kaempferol or pinocembrin, alleviate lung inflammation by inhibiting the phosphorylation of signaling molecules (ERK1/2, JNK, p38 MAPK) and reducing inflammatory cell infiltration in lung tissues [67].

In COPD patients, dietary polyphenols improve lung function parameters (e.g., FEV1/FVC ratio) and reduce oxidative damage by boosting antioxidant enzymes such as superoxide dismutase and glutathione, modulating gut microbiota, and activating pathways like 5′ adenosine monophosphate-activated protein kinase (AMPK) to prevent airway remodeling. Epidemiological and clinical studies endorse the lung-protective effects of diets rich in polyphenols. Meta-analyses reveal that higher consumption of fruit-derived polyphenols, including anthocyanins, correlates with enhanced pulmonary function (e.g., FVC, FEV1) and decreased inflammatory markers in both healthy individuals and patients with lung diseases [68,69]. Additionally, polyphenols help regulate immune cell recruitment and mitigate chronic lung inflammation, indicating their promise as complementary treatments for respiratory disorders driven by oxidative stress and inflammation [65]. Furthermore, polyphenols exhibit chemopreventive potential in LC by regulating phase I and II detoxifying enzymes, preventing DNA oxidative damage, and modulating cell survival pathways. Epidemiological research supports an inverse relationship between high polyphenol consumption and LC risk in at-risk populations, indicating their role in reducing carcinogenesis through antioxidant and antimutagenic mechanisms [30].

In particular, polyphenols were shown to exert beneficial effects against LC by regulating the expression of microRNAs via different mechanisms, especially by scavenging ROS production [64].

Studies show that several polyphenols, such as epigallocatechin gallate (EGCG), quercetin, resveratrol, and curcumin, can reduce the release of ROS involved in the dysregulation of miRNA regulatory pathways crucial for cell survival, proliferation, and apoptosis [70,71]. Notably, these polyphenols modulate the expression and activity of

molecules within ROS-mediated anticancer pathways. This is achieved by increasing the expression of tumor-suppressive miRNAs while simultaneously decreasing the expression of oncogenic miRNAs [72]. For example, quercetin has been demonstrated to upregulate miR-16, thereby contributing to the suppression of anti-apoptotic proteins such as Bcl-2. For instance, curcumin has been observed to elevate the levels of several tumor-suppressive miRNAs, including miR-34a and miR-101, concurrently downregulating the oncogenic miR-21. Furthermore, epigallocatechin gallate (EGCG) has been shown to increase miR-210, leading to the inhibition of LC cell proliferation [72,73]. Moreover, by modulating miRNAs, polyphenols can block pro-tumorigenic redox signaling pathways, such as PI3K/Akt, MAPK, and apoptosis-related cascades.

The polyphenols, namely quercetin and curcumin, exhibit numerous alterations in cellular processes after binding to microRNAs, which interrupts the invasion and migration of lung adenocarcinoma cells via the upregulation of microRNA-16 [70]. Other examples include the polyphenols Apigenin, thanks to its ability to induce apoptosis via the upregulation of microRNA-34a-5 [74], hesperidin, which inhibits cell proliferation by targeting microRNA-132 [75], and ailanthone, which induces autophagy by upregulating microRNA-195 [76]. Besides their ability to regulate miRNAs via an antioxidant mechanism, polyphenols can suppress cancer-promoting miRNAs or upregulate tumor-suppressor miRNAs via an epigenetic mechanism acting as inhibitors of DNA methyltransferase (DNMT) and histone deacetylase (HDAC) [77].

Firstly, even if the cause and pathogenesis of COPD are not fully understood, cigarette smoke has been reported as the primary etiologic factor in the progression of COPD [78]. The smoke produced from cigarettes can alter various mechanisms involved in inflammation, ultimately generating oxidant substances that can damage vital lung functioning [79]. To neutralize the oxidants, the potential of polyphenols available in apples has been investigated against oxidative stress-based ALI induced via exposure to cigarette smoke. Interestingly, the antioxidants significantly counteract lung injury by reducing oxidative stress and p-P38 expression levels [80].

Secondly, the pathogenesis of vascular aging and COPD is also associated with oxidative stress and is attributable to the deterioration of numerous anti-aging pathophysiological events. These mechanisms can promote the activation of sirtuin, which affects the Klotho protein-fibroblast growth factor (FGF) pathway as well as the induction of certain epigenetic modifications that collectively result in mitochondrial dysfunction [81].

Similarly, another subtype of RNA, known as non-coding RNA, also plays a significant role in regulating hypertension by expressing specific genes, such as through splicing, RNA editing, translational inhibition, and mRNA degradation. This subtype of RNA is responsible for controlling chromosome dynamics and is engaged in the expression of various diseases, especially hypertension. Interestingly, it has been found that polyphenols can target non-coding RNA and regulate its expression in hypertension [82].

3. Role of Nano-Scale Drug Delivery to Treat Lung Diseases

Interestingly, the therapeutic effects of natural and synthetic antioxidants have been demonstrated in animal model-based studies. Nonetheless, their reproducibility at the clinical level remains a considerable concern, which may be attributed to their limited absorption, concentration, and half-life [83].

The route of administration considerably impacts the efficacy and safety of the drug delivery. The parenteral route of administration remains a significant option for delivering biopharmaceuticals to the lungs for targeted delivery. Nonetheless, enduring therapy is often unable to maintain clinical suitability and patient adherence [84]. Apart from this,

drug targeting has numerous obstacles associated with poor bioavailability, low aqueous solubility, and degradation due to the hepatic first-pass effect [85].

Pulmonary delivery involves the direct transportation of actives to the lungs, where the drugs either accumulate or are used as a medium to treat local and systemic diseases. The lungs present a large surface area of thin epithelial membranes, which are smooth and facilitate the exchange of drug molecules between the air and blood, thereby allowing therapeutic moieties to reach the target site at the appropriate concentration without any deterrents [86,87]. Therefore, the airway route is an attractive approach for drug transportation, reflected in its non-invasive nature, which not only helps in managing damaged lung tissue but also enhances the systemic absorption of specific drug molecules directly from the lungs [88]. In addition, the first-pass metabolism, plasma binding, and systemic distribution can be avoided by adopting pulmonary-based drug delivery as a route of intake [89].

In addition, the instantaneous onset of action, along with higher efficacy, can be expected by avoiding systemic side effects at minimal doses compared to other routes of administration [90]. The drug molecules entering through the pulmonary route exhibit short-term action due to their immediate clearance; hence, prompt absorption is possible [91].

Concerning the translocation of drug moieties, it occurs via transcytosis into the epithelial cells and across the respiratory epithelia into the interstitium and then finally reaches to blood and lymph. It is worth highlighting that drugs reach the blood faster than other non-invasive modes of administration. In addition, short pulmonary exposure to inhaled medicines [92,93]. Furthermore, the small lipophilic drug molecules from the air lodge in the lining fluid of the lungs due to their significant miscibility with the fluid in the lung lining and are countered by lung surfactants first, which further facilitate the dissolution process, resulting in enhanced absorption. However, in the case of larger molecules, the absorption might be slower, but higher bioavailability can be anticipated from pulmonary delivery comparatively to non-invasive routes [94].

In the case of inhalation LC therapy, the biodistribution pattern of active molecules at the desired site can be modified to achieve higher accumulation. In this regard, the inhaled particles undergo lymphatic circulation and create a depot in the lymph nodes. It will allow the drug molecules to redistribute in the peripheral respiratory tract, allowing not only the uptake of poorly soluble drugs but also counteracting the cancerous cells that have metastasized to other neighboring organs [95,96]. Additionally, due to targeted delivery, the dose of anticancer agents can be minimized. At the same time, in the systemic application, high doses can toxicate the non-targeted organs as well [97].

Despite the numerous advantages, the lungs also present challenges, as the airway is fully equipped with defense mechanisms to prevent the entrance of exogenous particles into the respiratory tract, which limits pulmonary drug uptake. Therefore, the air-passage and clearance pathways are highly crucial elements that determine the availability of the drug molecules at the site of action [95,98]. For instance, inhaled particles are cleaned away in two ways. Firstly, cilia are present in the trachea and bronchi from the lungs along with mucus, and secondly, via phagocytosis of alveolar macrophages. In this manner, macrophages can adversely modify the fate of drug-carrying inhaled particles by triggering the immune response cascade. In other words, antigens taken up by macrophages are generally presented to the T lymphocytes, and co-factors in the lymph nodes may further activate or suppress the events related to humoral immunity [94,99].

Therefore, drug particles for pulmonary administration should be capable of overcoming these physiological barriers and reaching the desired site without losing their integrity [100]. Some of the crucial parameters affecting drug deposition and its metabolism

are presented in Figure 3. The major factors affecting drug deposition and metabolism generally depend on the diameter of particles, the solubility of the drugs, mucus-cilia clearance, the type of drug delivery system (DDS), the tendency of drug transporters toward alveolar macrophage uptake, and finally, cell specificity with the aid of a ligand approach.

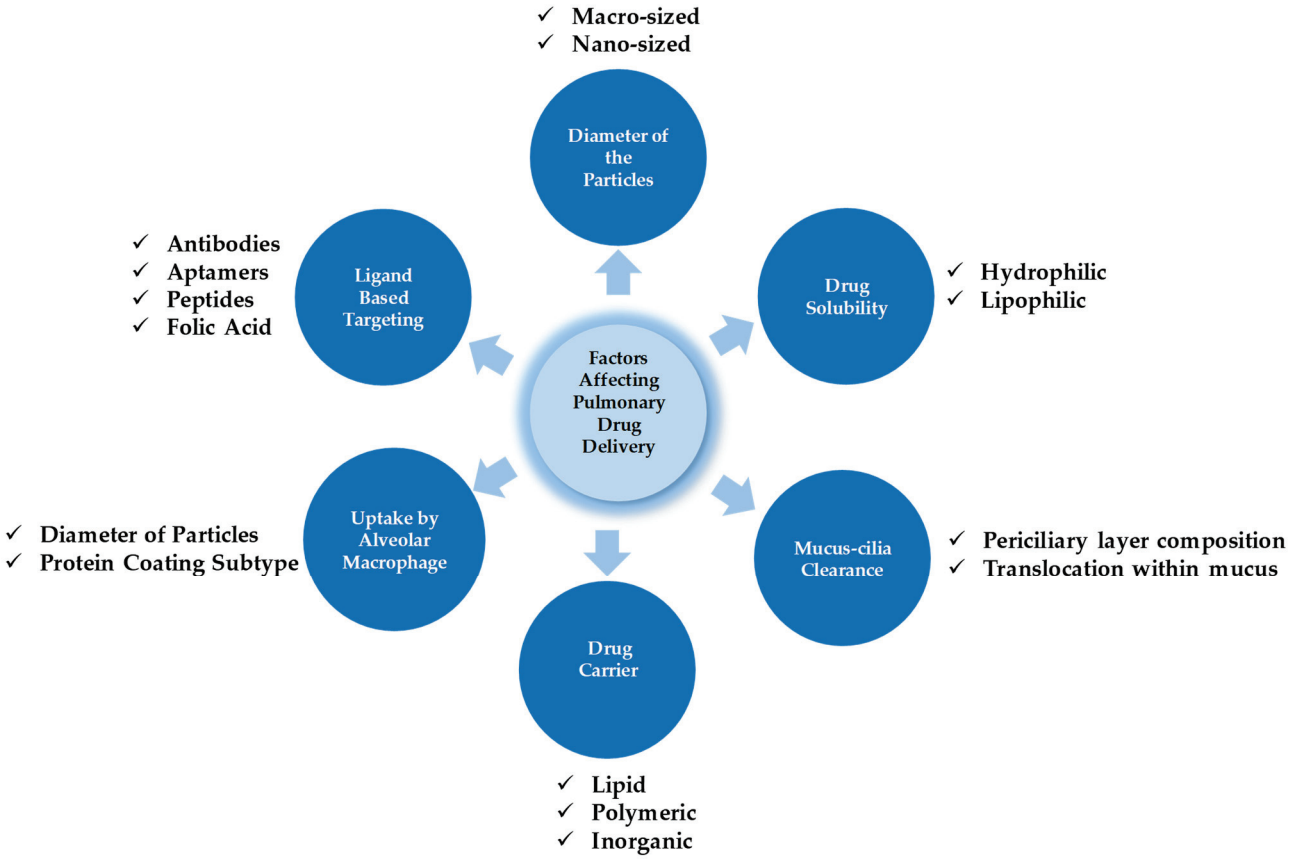


Figure 3. The interplay of factors dictating pulmonary drug targeting, retention, and biotransformation.

Moreover, another important barrier that needs to be overcome in the lungs is the pulmonary surfactant, a naturally occurring phospholipid–protein mixture that coats the alveolar surfaces in the lungs and plays a critical role in modulating the adsorption and fate of inhaled nanocarriers. Indeed, this surfactant is enriched with components such as dipalmitoylphosphatidylcholine (DPPC) and surfactant proteins (SP-A, SP-B), which can rapidly adsorb onto the nanoparticles' surface when they reach the alveolar space. As a consequence, a "surfactant corona" may be formed on the surface of nanoparticles, which changes the surface charge, hydrophobicity, and steric properties of the systems, thus affecting nanoparticle dispersion and aggregation [101,102].

Aggregation of nanoparticles can reduce their deposition and uptake by lung cells, and the interactions with surfactant may impact how deep the nanoparticles can travel within the lung [103,104].

To overcome the pulmonary surfactant barrier, pulmonary surfactant can be strategically utilized to improve drug delivery across the air–liquid interface of the lungs. Indeed, surfactant-mimicking modifications help particles remain at the air–liquid interface, enhancing local drug concentrations, and formulations that combine drugs with surfactant have been shown to enhance drug uptake into lung cells and reduce inflammation in models of lung injury [104,105].

Taken together, tough physiological barriers, lack of cell specificity, and the inability to reach the optimum drug concentration at the site are critical concerns associated with

the conventional mode of lung therapy, which can be addressed and avoided by adopting nanotechnological approaches in the area of drug delivery [106].

Nano-sized vehicles can deliver the therapeutic cargos to the lungs to cure both local and systemic diseases. These nano-sized carrier systems are fabricated from organic, inorganic, and/or hybrid materials and are not only capable of delivering natural/synthetic drug molecules but also can convey complex macromolecules, including DNA, proteins, and peptides, by targeting the desired site of action [107,108]. More precisely, nanostructure-enclosing therapeutic agents can achieve sustained release, active or passive drug targeting, uniform dose distribution, and multiple doses can be embedded in a single unit. The controllable diameter, modifiable surface charge, and properties make them very attractive candidates [107,109,110].

The success of nanotechnological products in terms of commercial viability, with promising results, is clearly evident from the already launched Abraxane® and Pazenirl®. These are FDA-approved nano-formulations employed to treat LC [111].

Particularly, in the case of lung delivery, the aerodynamic diameter of the particles plays a crucial role, as particles larger than 5 μm are likely to settle superficially. In comparison, smaller particles are taken up by macrophages and reach the deeper lung domains. It should be underlined that the rate of clearance is considerably higher than mucus-cilia clearance [112,113]. The nanostructures, once lodged in the lungs, undergo deep dissolution followed by immediate drug release, which directly depends on the low molecular weight and lipid solubility of the drug candidate [95,114]. However, the interaction of the nanomaterial with pulmonary surfactant and the different components of the lining fluids of the upper and lower respiratory tract would result in the formation of a protein corona that can affect the dispersion of the nanoparticle as described above. To overcome this problem, pulmonary surfactant can be used to enhance drug delivery across the air–liquid interface of the lungs [104,105].

Fascinatingly, the solubility profile of water-soluble drug molecules can also be amended by encapsulating them into respective nano-vectors. Therefore, apart from surface tuning, diameter reduction, and biocompatibility, nano-encapsulation of hydrophilic therapeutic moieties can also be achieved with the aid of nano-carriers [106,115].

Therefore, nano-sized particles can be an alternative approach to attain an effective pulmonary-based drug delivery. Moving further, apart from the diameter, charge properties on the surface of particles cannot be overlooked because the specific surface charge allows them to permeate through the lung tissues to a considerable extent. The negative charge on the cell membrane can be countered by applying a cationic charge to the surface of the drug particles. Nanotechnology offers the possibility of modifying the surface charge by employing suitable cationic surfactants to enhance uptake at the cytoplasmic level. However, their higher concentration may impart toxic effects, which need to be investigated thoroughly [114,116].

Despite the impressive success of nanomedicine in the domain of drug delivery, some targets remain to be accomplished. Specifically, in cancer treatment, the major obstacle still exists in terms of drug loss before reaching the target site. Only 0.7% of the injected dose in the form of nanoparticles reached the tumor cells, while a significant fraction is usually undergoing primary reticuloendothelial system (RES) clearance, primarily in the liver and spleen. Only a limited number of studies focusing on the endothelial-targeted antibody approach for avoiding undesired nanoparticle uptake and clearance have been published [117]. Table 2 summarizes the advantages and challenges of pulmonary delivery of nano-scale systems in the treatment of lung diseases.

Table 2. Overview of advantages and challenges of pulmonary delivery of nano-scale systems to treat lung diseases.

Advantages	Challenges	Ref.
Local or systemic lung treatment by delivering different drugs, such as natural, synthetic, macromolecules, DNA, proteins, peptides	Limited uptake and retention due to lung defense mechanisms, governed by ciliary clearance, macrophage phagocytosis, presence of mucus, and pulmonary surfactants	[94,95,98,99,108]
Enhanced solubility and bioavailability of hydrophilic compounds	Difficult targeting and undesired uptake	[95–97]
Size and surface modification using charged surfactants	Superficial deposition and high toxicity of cationic nanosystems	[107,109,110]
Avoidance of first-pass metabolism, sustained drug release, and reduced drug doses	Rapid clearance and immune responses onset	[89,90]
FDA-approved nano-formulations for lung cancer treatment (e.g., Abraxane®, Pazenirl®)	Difficult tumor site targeting and early drug loss due to reticuloendothelial system (RES) clearance	[111,117]

Taken together, nano-scale drug delivery can be auspicious and can overcome all the shortcomings related to conveying therapeutic active moieties by conventional methods. Moreover, nanotechnology offers numerous possibilities for treating lung diseases with minimal dose and toxicity.

4. Role of β-CD in Pulmonary Drug Delivery of Antioxidants

The donut-shaped cyclodextrins (CDs) are a series of macrocyclic units containing oligosaccharide units α-1,4-linked D (+)-glucopyranose, which act as molecular containers explored for biomedical applications by researchers globally. The CDs are mainly of three types, namely α-, β-, and γ-CDs, in which α-1,4 glycosidic bonds conjugate 6, 7, and 8 D-glucose units [118].

The water solubility of β-CDs is lower than that of all CDs, which is responsible for the strong internal Hydrogen Bonding in its crystal state. The chemical modifications are carried out on β-CDs to enhance water solubility, and examples of these modified products include hydroxypropyl-β-CDs, sulfobutylether-β-CDs, and epichlorohydrin-β-CDs. In addition, the melting points of all the aforementioned CD subtypes lie between 240 °C and 265 °C [119,120].

Interestingly, CDs are composed of both a hydrophilic surface and a hydrophobic central cavity, with the capability of enclosing poorly soluble drugs; hence, the solubility, stability, and bioavailability of the drugs can be improved upon loading onto CDs [15,121,122].

The chemistry of the CDs makes them very attractive as a drug transporter, as they possess two different types of hydroxyl groups (primary at position 6, while secondary at positions 2 and 3) located at the peripheral edge, which is responsible for providing a hydrophilic exterior. On the contrary, oxygen atoms in the glycosidic hemiacetals and C-H units comprise a hydrophobic core [123,124].

The possibility of adopting a CD-based drug delivery strategy in the lungs, as well as its involvement in the antioxidant mechanism and the inflammatory cascade, is illustrated in Figure 4. Moving ahead, the researchers have also explored the possibility of combining two different types of CDs, namely, α-CDs and 2-hydroxypropylβ-CDs (HP-β-CDs), to achieve a synergistic effect with enhanced solubility of cyclosporine. Similarly, the same trend was observed in the case of dexamethasone, where the additive impact of γ-CDs and HP-γ-CDs has been examined [118].

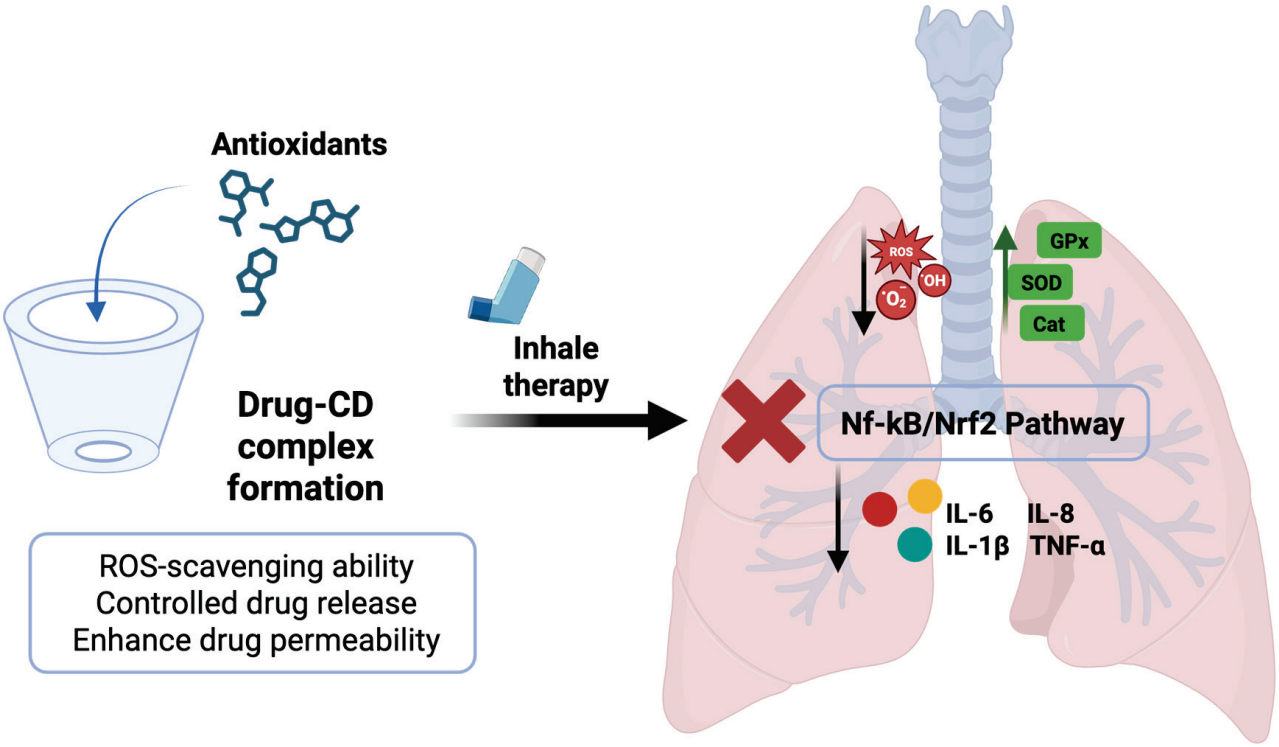


Figure 4. Scheme illustrating the formation of an antioxidant's inclusion complex and cyclodextrin frameworks with uniform inhalable particle size for the treatment of ALI. Original figure created with www.BioRender.com (accessed on 2 July 2025).

CDs are edible and usually safe for human consumption and are used commercially at a massive scale in pharmaceutical formulations. More precisely, hydroxypropyl-β-CDs (HP-β-CD) is an FDA-approved ingredient that possesses high solubility (>500 mg/mL) in aqueous medium and low toxicity toward biological membranes. HP-β-CDs and sulfobutylether-β-cyclodextrin are the most widely explored and researched CD-based drug delivery agents [125,126].

Numerous studies have been published in recent years, reflecting the promising potential of β-CDs in carrying antioxidants. Among all, there is research carried out on the β-CDs complex to treat ALI induced due to massive exposure of lungs to bombs and explosive material during army and firefighter operations. In an elaborative manner, bomb smoke is enriched with $ZnCl_2$, which affects the lungs badly on inhalation at high doses, giving rise to ALI followed by acute respiratory distress syndrome [127].

Resveratrol is a polyphenol explored for its role in managing oxidative stress, inflammation, and apoptosis, which is developed in response to various lung injuries; however, its poor solubility, stability, and bioavailability pose significant obstacles [56,128]. The encapsulation of resveratrol in β-CDs complex successfully improved the bio-profile of polyphenols in terms of healing pulmonary edema by maintaining blood vessel integrity and restoring respiratory function within a short time [129].

Pulmonary delivery of CDs results in rapid systemic absorption, broad extracellular distribution, and efficient renal clearance, minimizing tissue accumulation, including in the lungs. Animal studies report high bioavailability (up to 80% after lung instillation), confirming systemic circulation entry via pulmonary routes. CDs primarily distribute in extracellular fluids and are rapidly renally excreted [130]. Preclinical studies show minimal pulmonary toxicity of β-CD at therapeutic doses; for example, Yokohira et al. found only mild lung toxicity with no acute damage or fibrosis after intratracheal instillation in rats (2 mg/rat), supporting safety as a lung delivery excipient [131]. Nebulized

native and modified CDs were found not to cause acute lung toxicity at relevant drug-delivery concentrations, though mild lymphocyte increases in bronchoalveolar lavage fluid (BALF), suggesting low-grade immune activation without cytotoxicity or fibrosis. Moreover, while short-term inhalation of β-CDs or hydroxypropyl/γ-CD derivatives did not cause macrophage accumulation or histological lesions in murine models, higher doses or β-CD derivatives like methylated β-CD were found to increase cytotoxicity in vitro [131,132].

Pharmacokinetic studies in rabbits following intratracheal and intravenous administration found β-CD and derivatives with high systemic bioavailability (66–80%) after lung delivery, rapid absorption, renal elimination, and minimal tissue retention. For instance, HP-β-CD, despite its lower absorption from lungs, was efficiently transferred to systemic circulation and clearance with negligible organ retention [133]. Other studies confirm low tissue accumulation after parenteral (including pulmonary) delivery, with a renal excretion > 90% and near-complete elimination within 24 h [134]. Novel derivatives like thiolated HP-β-CD enhance local drug solubility, retention, and absorption without increasing systemic persistence despite mucoadhesive properties, as carriers remain rapidly cleared by absorption and renal excretion [135,136].

Beyond drug delivery, β-CD and modified CDs exhibit direct therapeutic effects in lung diseases, including anti-inflammatory and antioxidant properties, improved surfactant function, antiviral barrier, and anti-fibrotic activities, thus contributing to lung tissue stabilization [136]. For instance, modified β-CDs, notably HP-β-CD-SH, can form nanoaggregates that stabilize lung epithelium and reduce oxidative stress/inflammatory markers, whereas HP-β-CD formulations were found to reduce viral attachment and replication, serving as respiratory barriers. Recent 2024 studies, including SARS-CoV-2 models, show HP-β-CD lowers viral load and lung inflammation by disrupting viral entry, demonstrating direct antiviral and immunomodulatory effects [137,138].

Inhaled β-CD can reduce inflammation and fibrosis by regulating profibrotic proteins and collagen in pulmonary fibrosis models. Its anti-fibrotic effect is enhanced when combined with compounds like tetrandrine (as inclusion complexes), reducing hydroxyproline and improving survival in animals [139].

Studies of pulmonary surfactant dysfunction in CF, acute respiratory distress syndrome (ARDS), and bronchiolitis reveal impairment due to cholesterol and oxidized phospholipids. Methyl-β-CD restores surfactant function and exerts anti-inflammatory effects, supporting inhaled CDs' therapeutic potential for improving lung function and reducing inflammation across pulmonary diseases, enabling rapid deployment for acute injuries [140,141].

Another interesting approach for lung delivery of drugs is represented by CDs-based nanosponges (CD-NS). Recently, CDs-NS have been explored as a promising DDS for pulmonary administration, potentially improving the effectiveness and targeted delivery of drugs to the lungs. These macrostructures are crosslinked CDs characterized by a three-dimensional nanostructured network [142–144].

Notably, these complex macromolecular structures are composed of individual CD and nanochannels created between cross-linked CD units and cross-linkers. Therefore, CD-NS are colloidal carriers highly porous and able to maintain the properties of CDs, such as bioavailability, non-toxicity, biodegradability, and controlled release [145–147]. CD-NSs retain the ability to encapsulate poorly water-soluble drugs within their internal nanocavities, but also the possibility of achieving drug loading by forming non-inclusion complexes thanks to the presence of tiny mesh-like structures obtained through cross-linking [148].

As an example, the study of Abou Taleb and colleagues focused on the development of CD-NS for loading the flavonoid quercitrin to enhance, at the same time, the drug

solubility and its activity against LC as well as the SARS-CoV-2 virus. The results obtained confirmed the expectations, allowing the possible use of CD-NS as a basis for further animal studies [142].

4.1. β-CDs-Drug Conjugate Grafted Surface Modification

The performance of a CDs-based carrier system can be altered chemically, supporting better control over the drug release mechanism, mechanical characteristics, and response threshold to stimuli. The most significant result of these modifications is Cyclosert^{TM}, a linear CDs-DDS designed and launched commercially, which has been conjugated to the alkaloid camptothecin for anticancer therapy [122,149].

However, the toxicity associated with the design of β-CDs is a significant concern, which is one of the obstacles to their clinical transition. Concerning this, hydrophilic β-CDs, a toxicity-free derivative form of existing β-CDs, have been synthesized, wherein conjugation of hydroxypropyl groups of β-CDs has disrupted the intermolecular H-bonding in secondary hydroxyl groups of non-modified CDs, making possible the formation of H-bonds with the surrounding water molecules. This H-bonding has not only improved the aqueous solubility of the conjugate mentioned above but also minimized its toxicity [121].

It has been found that in many diseases, the misfolding of various proteins, along with impaired amyloid formation, can exhibit detrimental effects on different organs and tissues. The β-form CDs carrying β-amyloid have significantly reduced the aggregation of multiple proteins, including amyloid-β, insulin, recombinant human growth hormone, prion protein, transthyretin, and α-synuclein, as well as some multimeric enzymes, at very low concentrations in both in vitro and in vivo experiments. It is worth noting that α-, β-, and γ-CDs exhibit different anti-aggregant activities in various aromatic moieties [150,151]. Taking this further into account, different scaffolds containing hydroxyquinoline-cyclodextrin conjugates have been developed to establish synergism, supporting two mechanisms simultaneously: an antioxidant effect and a protective effect against amyloid-β-aggregation [151].

The mucus present in the nasal and lung cavities is composed of water, salts, and various glycoproteins, which protect the epithelium lining from external mechanical and enzymatic damage. It offers a formidable barrier to drug penetration [152]. To achieve improved mucoadhesive properties, thiolated HP-β-CDs have been fabricated, which can form disulfide bonds with cysteine-rich subdomains of a well-known glycoprotein; thus, pulmonary absorption can be enhanced. This strong affinity toward mucus will prolong the residence time of the drug moieties [123,152]. In the continuation, another complex named thiolated 2-methyl-β-CDs was employed in the fabrication of nanoaggregates enclosing dexamethasone. This complex was first synthesized via a microwave-assisted process, a straightforward method shown in Figure 5 [151].

Biofilms are the dispersion of immobile microbial colonies that produce polysaccharides, proteins, and nucleic acids based on a water-soluble matrix, which offers hindrances to the effectiveness of antibiotics due to poor permeability [153]. In CF, the risk of bacterial infection is significantly higher, which can subsequently lead to biofilm formation. This event is further taken up by the emission of quorum-sensing signals, which indicate the presence of bacterial strains. These different strains colonize to form biofilms, which a sputum test can confirm [154]. CDs can interrupt this Quorum Sensing inhibition (QSi) mechanism. To resolve this issue, long-chain alkylthio CD derivatives have shown an intensive inhibitory effect on the quorum-sensing system of *A. fischeri*. Hence, this modified CD system can interfere with QS signaling and control bacterial infections in CF [155].

Sulfobutyl ether-β-CDs (SBE-β-CDs) can enhance the aqueous solubility of lipophilic actives and are found to be safer compared to other derivative products of CDs. This complex was further conjugated with bedaquiline (FDA-approved anti-mycobacterial

moiety) and explored further for the treatment of non-small cell LC. This approach is a very effective inhalation therapy tool for inducing cytotoxicity in tumor cells [156].

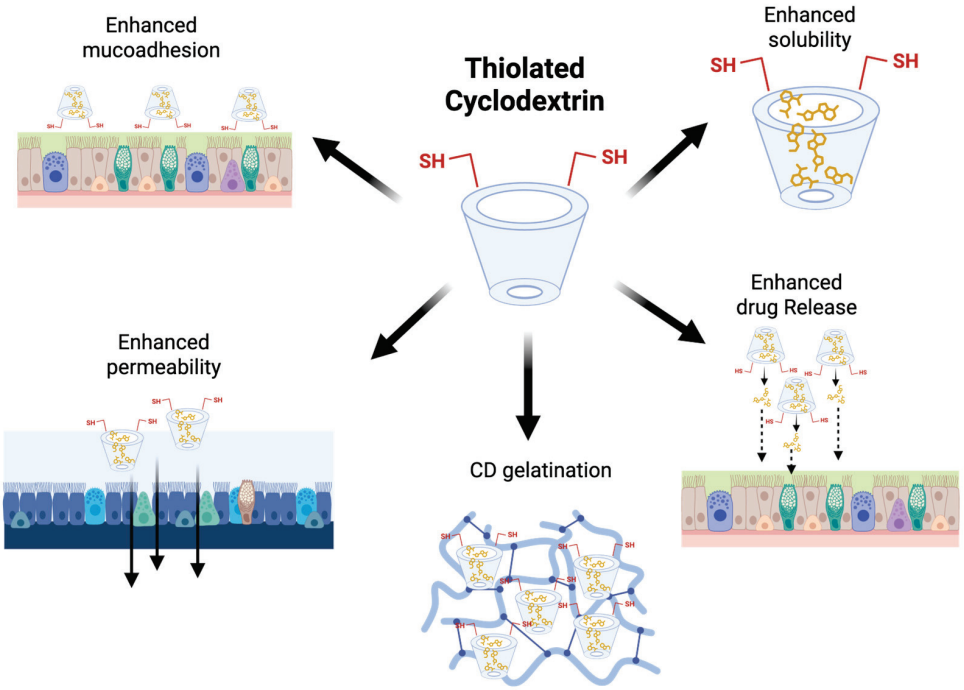


Figure 5. Schematic summary of the main properties of thiolated CDs. Original figure created with www.BioRender.com (accessed on 30 June 2025).

Following the COVID-19 pandemic, numerous targets have been achieved to combat respiratory viral infections, and it has been demonstrated through in situ RNA mapping that nasal susceptibility to viral infections is significantly higher than that of the lungs. The CD-based formulations allow us to block the attachment of viral moieties to the nasal lining. Taking this into account, two CDs, HP-β-CD and HP-γ-CD, were then investigated for their antiviral effects using SARS-CoV-2 pseudotypes. The significant reduction in viral load and inflammatory signaling in both Calu-3 cells and the K18-hACE2 murine model has been monitored [137].

Delamanid, an anti-tuberculosis medication, faces challenges such as poor solubility. Interestingly, solubility enhancement was 54-fold with HP-β-CDs, while 27-fold and 13-fold enhancements were achieved with SBE-β-CDs and HP-ɤ-CDs, respectively. In addition, the complex has shown significantly higher anti-bacterial activity against M. tuberculosis than a non-encapsulated drug solution alone [157].

Apart from drug delivery, chemically modified β-CDs are also helpful in radio-imaging for the early detection of cancer. A study emphasizing the diagnostic ability of CDs was conducted, in which randomly methylated β-CDs were conjugated with prostaglandin E2. It is a well-established fact that prostaglandin E2 is typically overexpressed in cancerous cells. The molecular dynamics-based docking tool has also confirmed the chemical affinity between β-CDs and various enzymes and proteins within the physiological environment [118,158].

By considering all the merits of CDs, it can be noted that the encapsulation of natural molecules in CDs could be an impressive approach, as most natural extracts face solubility issues and are prone to degradation due to non-enzymatic and enzymatic dioxygen oxidation. Therefore, all the capabilities of CDs can be leveraged to overcome these challenges [159]. Recent developments in CDs and their derivative-based antioxidant encapsulation are summarized in Table 3.

Table 3. Case studies of CD-based encapsulation of natural moieties.

Natural	Type of CDs	Target	Remarks	Ref.
Aurisin A	- β-CDs - (2,6-di-*O*-methyl-β-CDs) - HP-β-CDs	Anti-proliferative Activity against lung cancer cells	- Molecular dynamics simulations revealed that the stability and compactness of drug drug-conjugated complex were higher. - The introduction of drug is even responsible for enhancing the complex stability. - Upon encapsulation, the anti-proliferative activity of extract against A549 and H1975 lung cancer cells was significantly improved - High thermal stability achieved	[160]
Quercetin	- (2,6-di-*O*-methyl-β-CDs) - HP-β-CDs	Oxidative stress	- Both CDs have enhanced the pharmacological profile of Quercetin - In silico molecular dynamics confirmed various hydrogen bindings, supporting that both complexes can host quercetin - Calculations reflect that absolute binding free energies show that quercetin binds favorably to both CDs - Fluorescence spectroscopy shows moderate binding of quercetin in both CDs-based formulations	[159]
Olive leaf extracts and dexamethasone	- Thiolated HP-β-CDs	Oxidative stress in lungs	- The complex has promoted drug absorption while stabilizing nanoparticles against oxidative stress. - Promising for lung delivery, principally as stabilized nanoaggregates, proposing versatile administration for labile molecules like natural extracts.	[136]
Resveratrol	- SBE-β-CDs	Non-small Cell Lung Cancer	- Adequate drug deposition within lungs after nebulization of CDs based system - Enhanced the stability of resveratrol under physiological conditions - Significant cytotoxic effect was observed on five different Non-small Cell Lung Cancer cell lines	[129]
Resveratrol and Polydatin	- Polyvinylpyrrolidone/HP-β-CDs	Antioxidant and anti-inflammatory	- Immediate release of incorporated therapeutics - Penetration coefficients of both extracted molecules also increased - Antioxidant and anti-inflammatory activity against *P. cuspidati* extract was confirmed	[161]
Rosmarinic acid and Carvacrol.	- Maltodextrin	- Antioxidant, Anti-bacterial, Antifungal activities	- Encapsulation efficiency is more than 95% for both compounds of interest - Increased in vitro release of both the active compound	[162]
Curcumin	- α-, β-, and γ-CDs Polyethyleneglycol-Conjugated Gold Multifunctional Nanoparticles	Anticancer effect	- Amino-CDs conjugated with gold nanoparticles have been explored to achieve higher therapeutic effect of curcumin - Solubility of curcumin was improved, and remarkable high encapsulation efficiency was achieved - Proven in vitro cytotoxic effects on A549 cells were obtained	[163]
Hyperoside	- β-CDs - (2,6-di-O-methyl-β-CDs) - HP-β-CDs	Anti-microbial and anti-inflammatory effects	- Solubility was enhanced by 9-fold in the case of 2-hydroxypropyl-β-CD - Higher antioxidant activities in vitro and the H2O2–RAW264.7 cell model	[164]
Boswellia carterii	- HP-β-CDs - Epichlorohydrin-β-CDs	Inflammation	- The synergic effect of extract and formulation has been recorded - Reduction in level of ICAM-1, LTB4, and IL β 4 - Improved histopathologic profiles	[165]
Tetrandrine	- HP-β-CDs	Pulmonary fibrosis	- Alleviated inflammation and pulmonary fibrosis - Regulated protein expression in the development of pulmonary fibrosis - Improved post-operative survival. - Drug delivered via nebulization was chiefly found to be located in the lungs only; hence, more local effect was seen	[139]
Rutin	- HP-β-CDs	Dietary supplementation	- Greater encapsulation efficiency and stability of rutin, at least for 30 days - Rutin release approaches the plateau around the sixth hour - No toxicity was observed in HepG2 cells - Significant increase in glucose uptake	[126]
Ligustrazine	- ROS-sensitive cross-linked covalent CDs framework	ALI	- Excellent aerodynamic properties, along with prominent antioxidant and anti-inflammatory capacities - Alleviated the inflammation, oxidant stress, and lung damage in rat models - Shielded the lungs by regulating the NRF2/NF-κB signaling pathway	[16]

4.2. β-CDs-Based Hybrid Framework

It is worth mentioning that CDs, as a system, possess numerous qualities and yield auspicious results in physicochemical, in vitro, and in vivo evaluations. Fascinatingly, CDs also have great potential as a secondary carrier. This section of the review will explore the possibility of conjugating the primary vehicle (lipid, polymer, or inorganic-based nanosystem) with a CD's inclusion cage, where the combination of the two systems can lead to improved performance. Surprisingly, the tertiary system can also be introduced as a gel in the management of the wound-healing process [166].

Metal–organic frameworks technology is a combination of metal ions and organic ligands, seen as a promising tool for modulating the shape, dimensions, aggregation, and composition of particles. Wherein, multiple ligands can be conjugated with metal ions; interestingly, this conjugate can be further incorporated into the supermolecular β-CDs complex, which will hold both properties in one system. The combining effect will not only allow for higher drug loading with enhanced stability and bioavailability but also provide the possibility to attach ligand markers for cell-specific targeting [167,168].

The metal ions are biocompatible, and no toxicity concerns have been reported so far. The coordination of CDs with metal ions such as calcium, potassium, titanium, silver, iron, and yttrium has been reported [169]. It is worth mentioning here that among all the discussed CDs, the presence of –OCCO- in γ-CD makes it more suitable for interaction with metallic structures; it is also non-toxic and is considered as one of the first porous crystals that comprises the amphiphilic nanopores [170,171]. Furthermore, the employability of cetyl trimethyl ammonium bromide and polyethylene glycol 20000 is not only helpful in regulating the shape and size of the particles but also enhances the reproducibility of the synthesis process [172,173].

Topotecan, an anticancer drug, is highly effective against LC encapsulated in a metal–organic framework complex. Efficient loading, along with sustained release, was achieved at the local site, specifically in the lungs, after intravenous administration. The remarkable resistance to hydrolysis was monitored, which was significantly increased by many folds, thereby substantially extending the half-life of the drug. The complex has demonstrated noteworthy anticancer activity by inhibiting the migration and invasion of B16F10 cells [174].

The porogens, such as ammonium bicarbonate, poly (vinyl pyrrolidone), and Pluronic F127, are the agents utilized in the production of porous materials, which present inevitable obstacles to achieving uniformity in pores and batch-to-batch reproducibility. Moreover, the porogens need to be evaporated, which requires high-energy heat treatments that can further harm the thermolabile encapsulated therapeutics [175,176]. Yixian Zhou and team emphasized that the use of porogens can be avoided by considering CDs-based metal–organic frameworks (CD-MOFs) carrying ketoprofen prepared by the vapor diffusion method in the management of pulmonary inflammation. The proposed complex exhibits improved aerosol properties, a higher drug loading capacity, and enhanced lung deposition, as confirmed by the rat model [177].

Pulmonary function test was conducted on rats to evaluate the effects of intratracheal administration of CD-MOF, drug-loaded CD-MOF (CD-MOF-K), and a commercial formulation. A lung function system, coupled with a ventilator and plethysmograph, was used to assess lung resistance (RL) and dynamic lung compliance (Cdyn) at one and eight hours post-administration. The results showed no statistically significant differences in either RL or Cdyn between any of the treated groups and the untreated (blank) control group at either time point [177].

One step ahead, a biological cell can also be utilized as a drug carrier to solve numerous physiological obstacles. Following this point, the surface of endogenous macrophages

has been modified using β-CDs and has been explored as a drug carrier for the transportation of Adamantane-modified quercetin-loaded liposomes. Therefore, this involves the invagination of quercetin-loaded liposomes into CD-based modified macrophages that successfully activated the NRF2 pathway to inhibit plaque inflammation [178,179].

A recent study has been published, emphasizing the pulmonary delivery of Cyclosporine A based on γ-CDs metal–organic frameworks. The analysis exploits the vapor diffusion method and multiple modulators to achieve optimum aerosol properties and in vitro results. The results suggest that cubicle-shaped particles, along with reproducible thermal behavior and crystallinity, have been obtained. More precisely, in the case of polyethylene glycol 10000, the enhanced bioavailability has been recorded. The repeated dose also confirmed that no toxicity-related issues have been noted [180]. Xiaoxiao Hu and team have selected cholesterol and leucine as modulators in the case of pulmonary delivery of budesonide to increase the uniformity and flow properties of powders. The cholesterol has significantly improved flow properties with significantly higher encapsulation and minimal cytotoxicity. Furthermore, rhodamine B, used as a marker in fluorescence microscopy, confirmed the adequate deposition of this complex in the deeper portions of the lungs [132]. However, the careful selection of solvent and surfactant can be helpful in preparing a Dry Powder Inhaler (DPI) with controllable size and shape [172].

Nianxia Sun and co-authors have presented a study aimed at β- and γ-CDs metal–organic framework-based pulmonary delivery of allyl isothiocyanate. High drug loading and stable crystalline morphology have been achieved in this particular case. The diameter obtained ranged from 1 to 5 μm, and γ-CDs were found to be deposited effectively in the lungs (fluorescence signals have been recorded in a mouse model) and released 90% of the drug content within the first five minutes. It reflects good lung tolerance as no sign of toxicity has been observed [181].

Going further, the more multifaceted nature of the CD-based complex has been reported by the researchers in a timely manner. This statement can be supported by an example where pH-responsive hyaluronic acid-coated mesoporous silica nanoparticles are further loaded with chlorhexidine/β-CD complexes. This whole system was further put into a hybrid gelatin methacrylate (GelMA) system, which has managed to control the drug release for 12 days with considerable anti-bacterial activity. This gel-based composite has played a potential role in wound healing applications, and its design is shown in Figure 6 [166].

Similarly, the surface modification of gold nanoparticles has been achieved using polyethylene glycol and CDs (α, β, and γ) to encapsulate hydrophobic drugs. In this case, curcumin has been selected as a model drug owing to its poor water solubility. The combined effect of polyethylene glycol and β-CDs has shown the highest encapsulation and a prominent cytotoxic effect against a human LC cell line among all the CDs subtypes [163].

It has been well-explored by researchers that folic acid receptors are overexpressed in the cancer environment. Considering this argument in the treatment of lung and prostate cancer, authors have reported the design of a quantum dots-β-CDs hybrid system wherein a folate ligand has been attached for the cell-specific delivery of the anticancer compound. The complex conjugation was non-toxic and did not affect the performance of the anticancer compound in the encapsulated form. An increased uptake of the carrier has been observed through multiple endocytosis pathways. Hence, the proposed hybrid system possesses self-navigating properties within the physiological tumor environment [182,183].

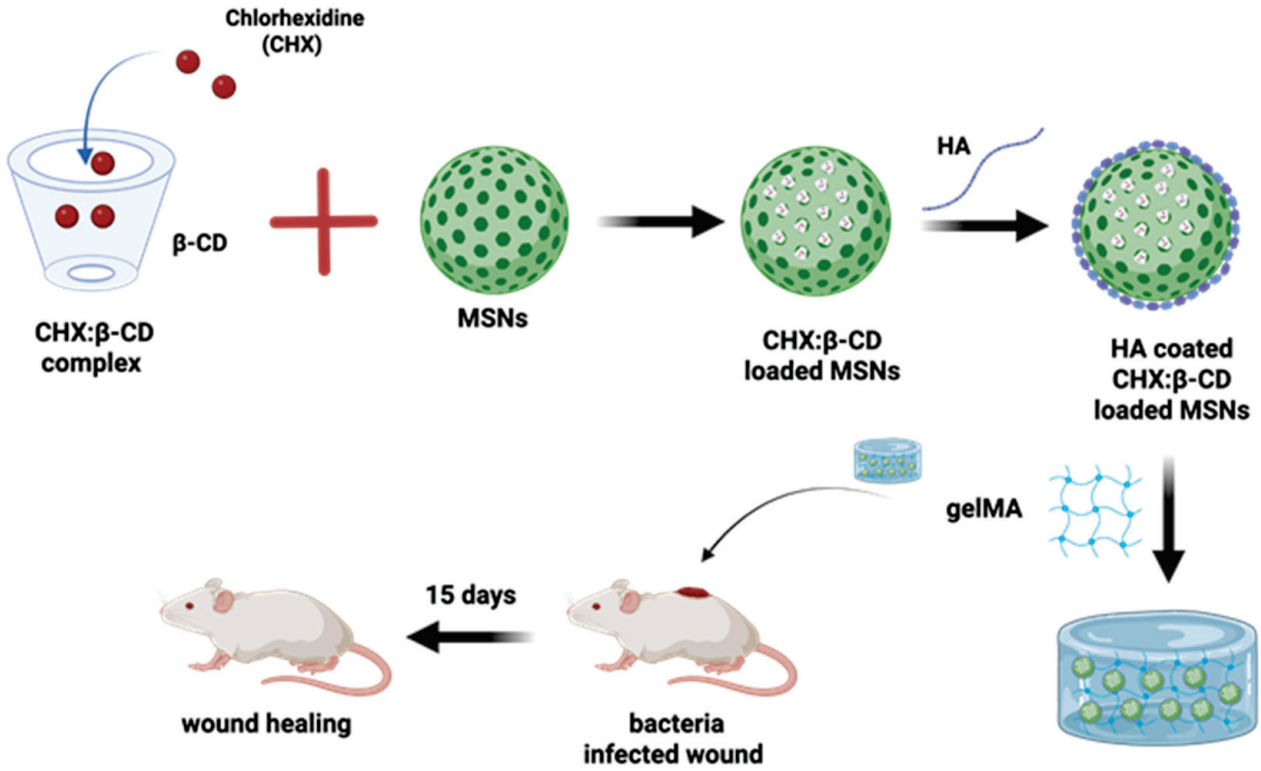


Figure 6. Schematic illustration of the preparation of a hybrid GelMA system combining hyaluronic acid (HA)-coated mesoporous silica nanoparticles (MSNs), which loaded complexes of chlorhexidine (CHX) with β-CDs for the bacteria-infected wound healing. Redrawn figure from reference [166] with BioRender.com.

4.3. Concept of Dual Therapy with CDs

Under the influence of serious complications, for example, LC, one regimen of anticancer drugs is sometimes not sufficient to elicit the desired effect. This gives rise to the need to develop a system that allows two drugs to be administered together to enhance their anticancer effect. Interestingly, it is worth stressing here that some of nanosystems (polymeric nanoparticles, micelles, dendrimers, nanocrystals, solid lipid nanoparticles, lipid nanostructured carriers, liposomes, mesoporous silica nanoparticles, etc.) give the possibility to encapsulate two drug moieties without affecting the overall effectiveness However, multi-drug loading onto a carrier still presents some serious flaws as it is very challenging to control drug ratios and their respective release pattern at the site of action owing to different physicochemical characteristics. Additionally, the simultaneous estimation of two drugs for chemical characterization is often a point of debate [184,185].

In this direction, some researchers have attempted to use CDs for combinational therapy. Especially in the case of tuberculosis, ethionamide is used as the second line of treatment; however, it has a low therapeutic index. To enhance the efficacy of this drug, a booster has been synthesized and co-encapsulated in the β-CDs inclusion complex to mitigate the issues of low solubility. The β-CDs managed to enhance the aqueous solubility of ethionamide and booster by 10- and 90-fold, respectively. The loaded drugs did not interfere with each other's performance [186]. Moving further, in tuberculosis, macrophages host the infection-causing microbes, and a strategic approach to target these macrophages could be beneficial. In this path, two tuberculosis drugs, namely rifampicin and levofloxacin, were complexed with CDs and further linked to curdlan nanoparticles. Curdlan is a glucan acquired from *Agrobacterium*, *Rhizobium*, and *Alcaligenes faecalis*, exhibiting remarkable immunomodulatory and anti-infective properties. With this, a high uptake of drugs has been observed, with major killing of *Mycobacterium smegmatis* residing

in macrophages within the four-hour timeframe. Therefore, this type of system can transport hydrophobic drugs into macrophages, providing essential insights into the area of TB-related drug delivery [187,188].

The surge in pulmonary fungal infections cannot be overlooked, as it imparts a significant burden on the healthcare system, with no effective treatment lines available so far. Salomé S. Celi and team workers have performed the co-encapsulation of two known antifungal therapeutic moieties, namely amphotericin B and itraconazole, in the γ-CDs framework. This complex was very effective against aspergillosis and reduced fungal infections in both the lung parenchyma and the upper respiratory tract by avoiding the serious effects associated with Amphotericin B [189].

A CD-based framework functionalized with RGD (a peptide that plays a crucial role in the adhesion of integrins expressed on lung tumor cells) has been proposed for the active targeting of low-molecular-weight heparin and doxorubicin to LC cells following intravenous administration. Therefore, the system will not only exhibit anticancer activity but also aid in the recognition of cancerous cells. The accountable effect has been achieved with five times lower doxorubicin (DOX) concentration; hence, organ-specific toxicity can be avoided with a reduced dose [190,191].

Moving further, working on the co-therapy of two individual drugs, it is also possible to encapsulate the entire extract, which carries multiple active molecules. An attempt has been made to encapsulate resveratrol and polydatin, derived from Polygoni Cuspidati *Radix* extract, for their antioxidant and anti-inflammatory properties. The Polyvinylpyrrolidone/CDs-based electrospun nanofibres managed to enhance the solubility by six-fold compared to the non-encapsulated form, and the activity of the whole extract was preserved [161,192]. Similarly, a blend of gum Arabic, Tween 20, and β-cyclodextrin was used in the embedding of Turkish Oregano Extract, achieving more than 95% encapsulation efficiency for the extract, which comprises rosmarinic acid and carvacrol [162].

The prodrug-based dual therapy has been projected to target colon cancer. 5-Aminosalicylic acid and butyric acid have been loaded into a carboxymethyl-β-CD inclusion complex, which inhibits cell proliferation against SW620 (colon cancer) cells. The long circulation time and high payload at the tumor site have been observed in nude mice bearing SW620 xenografts [193].

Cardiac fibrosis is a condition associated with chronic diabetes. Upon activation, cardiac myofibroblasts begin to accumulate in the extracellular matrix, which is responsible for cardiac dysfunction and ultimately leads to cardiac failure. In this regard, a Chrysin-based supramolecular CDs-calixarene complex has been designed for its anti-fibrotic activity, targeting the selective inhibition of galectin 1, which reduces the profibrotic cascade. In this, the CD complex has significantly enhanced the solubility and bioavailability of both moieties. The combination of both compounds boosts the antifibrotic activity in diabetic-induced rat cardiomyocytes [194,195].

In Sections 4.2 and 4.3, light has been shed on the possibility of combining two DDS comprising one primary (lipid, polymer, or inorganic-based nanosystem), one secondary (generally, a modified form of CDs) system carrying two different therapeutic cargos. Most of the studies conducted are based on modifications that are performed generally in the secondary system only. Notably, a more sophisticated model has been introduced in which both primary and secondary systems have been modified in a single approach to deliver two different drug molecules efficiently. This can be illustrated further by taking an example, where wheat germ agglutinin-conjugated liposomes with surface-grafted CDs have been utilized for loading two drugs, namely ciprofloxacin and betamethasone, to enhance oral bioadhesion. To mimic periodontal disease modal conditions, oral keratinocytes were

infected with *Aggregatibacter actinomycetemcomitans* (*A. actinomycetemcomitans*). Controlled drug delivery for 24 h in saliva, accompanied by a decline in inflammation and remarkable anti-bacterial activity, has been observed [196].

4.4. CDs-Based Miscellaneous Therapy Other than Antioxidants in the Pulmonary Complications

4.4.1. Cannabidiols

Cannabidiols are non-psychoactive plant-derived moieties obtained from *Cannabis sativa* that have multiple therapeutic effects, including anticonvulsant, sedative, hypnotic, antipsychotic, anticancer, anti-inflammatory, and neuroprotective properties.

Specifically, during acute cell injury, cannabidiols can decrease the production of inflammatory mediators. It has been suggested by many studies that cannabidiols can downregulate various COVID-19-related receptors and can be adopted as adjuvant therapy in the treatment of COVID-19 [197,198]. Apart from this, Cannabidiols are also helpful in relieving cancer-related pain and have anti-proliferative activity against cancer cells [199].

Besides their numerous merits, poor aqueous solubility is the main obstacle to their clinical applications. For this, a nano-spray solution composed of β-CDs and poloxamer 407 micelles carrying cannabidiol has been designed to reduce the production of cytokines in the inflammation induced by in vitro and ex vivo SARS-CoV-2. It has been concluded that the system was able to stabilize the drug for six months and release the entire loaded drug fraction within five minutes, exhibiting very high permeability across the nasal mucosa. Hence, it can be a promising approach in COVID-related inflammation [195].

4.4.2. siRNA

SiRNA (short interfering RNA containing 21–26 nucleotides) is an effective tool for gene silencing, successfully exploited in pulmonary diseases [200,201]. There is the possibility of introducing β-CDs as a carrier for siRNA, wherein two polycationic lipids, Lipofectamine 2000 and polycationic amphiphilic CDs, are used. The remarkable gene knockdown activity has been obtained from human glioblastoma cells (U87) and prostate cancer cells [202].

It is essential to note that surface charge plays a crucial role in designing the carrier for siRNA. As siRNA is negatively charged, a positively charged delivery system should be selected to ensure better cellular uptake and stability of the cargo. Regarding this, cationic-charged modified CD can be a suitable choice for gene delivery. Molecular dynamics computer simulations, in tandem with isothermal titration calorimetry, can be a beneficial strategy for high stability and minimal toxicity [203]. Furthermore, HP-β-CDs grafted with different grades of polyethylenimine have been selected for the pulmonary administration of insulin, calcitonin, 5(6)-carboxyfluorescein (CF), and fluorescein isothiocyanate dextrans. Considerable pulmonary uptake of these proteins without conferring any toxic effects has been achieved [135]. In continuation, a hybrid system can be proposed using low-molecular-weight polyethylenimine and pH-responsive CDs to load siRNA. This complex exhibits higher cell growth inhibition and apoptosis activation compared to a simple cationic vector [204].

4.4.3. Immunomodulation by Antibodies

It is also crucial to discuss new horizons in the treatment of lung-related diseases, primarily through antibody-based therapies, as they can effectively minimize the burden on the healthcare system [205]. WKS13 is a humanized monoclonal antibody that can counter the spread of SARS-CoV-2. The CDs conjugated to WKS13 have been proposed to target the nasal cavity. It can be effective against a broad range of respiratory viral infections [206]. Anti-human IL-4Rα are the antibodies that can enhance the stability of protein-based

moieties, and their biological activity can be a useful inhalation tool in asthma and other respiratory viral infections [207].

5. Challenges in Physiological Model Approach-Based Testing

The employability of animals in drug development remains crucial to understand the fate of inhaled actives. In this regard, numerous aspects should be considered, including cost, disease pathology, and immunological similarity to humans. However, the data obtained from pre-clinical studies is not always easy to handle due to dissimilarities in the nasal, tracheobronchial, and deep lung regions across species. Interestingly, rodents are unable to breath through the mouth, whilst humans prefer to breath through the nose and mouth. Therefore, lung deposition data is less relevant, and also, micron-sized particles may get trapped in the nasal–pharyngeal part of rodents; hence, lung profile may vary from that of human beings [208,209].

The respiratory tract has a very strong defensive mechanism, not only capable of pushing back the inhaled drug particles but also removing and inactivating their depots from the lungs. Therefore, the need for an ideal pulmonary DDS remains unmet and is badly affected by inadequate adherence due to mucociliary clearance and immune responses, along with the type of inhaler technique [210]. It is worth mentioning here that most of the investigations carried out to assess the protective effect of the antioxidant are based on murine and in vivo and/or clinical models and solely rely on dietary intake and/or systemic administration. Furthermore, the available literature also reflects that researchers explored only submerged cell lines and murine models without the aid of an inhalation technique, which overlooked many physiological aspects, too. Therefore, a more realistic model approach should be brought into practice so that the clinical transition can be more straightforward [211].

6. Conclusions

Although CD-based nano-sized drug delivery therapies focusing on lung deposition are still in the experimental phase, their potential in the areas of drug delivery, diagnosis, and gene knockdown cannot be ignored. Numerous derivatized CDs have been investigated for their physical, chemical, in vivo, and in vitro properties, which reveal that CDs can be utilized for antioxidant encapsulation in the management of oxidative stress-induced lung injuries. However, the concrete physiological testing model approach and inhalation devices are topics that warrant further exploration. Lastly, the biological fate of CDs and immunological response are also underexplored areas.

Author Contributions: Conceptualization, S.S.H. and R.C.; software, M.S. and F.F.; writing—original draft preparation, S.S.H.; writing—review and editing, R.C., M.S., and F.F.; supervision, R.C. All authors have read and agreed to the published version of the manuscript.

Funding: This research received no external funding.

Institutional Review Board Statement: Not applicable.

Informed Consent Statement: Not applicable.

Data Availability Statement: No new data were created.

Acknowledgments: We acknowledge University of Ferrara FIRD2023 and FAR2023 and are highly grateful to Central University of Punjab, for providing the necessary facilities.

Conflicts of Interest: The authors declare no conflicts of interest.

Abbreviations

The following abbreviations are used in this manuscript:

ROS	Reactive oxygen species
RNS	Reactive nitrogen species
IL-6	Interleukin 6
CS	Cystic Fibrosis
CFTR	Cystic Fibrosis Transmembrane Conductance Regulator
ALI	Acute Lung Injury
LC	Lung cancer
PH	Pulmonary Hypertension
COPD	Chronic Obstructive Pulmonary Disease
DDS	Drug Delivery System
CDs	Cyclodextrins
QS	Quorum Sensing
GelMA	Gelatin Methacrylate
BPD	Bronchopulmonary dysplasia

References

1. Pereira, A.C.; Martel, F. Oxidative stress in pregnancy and fertility pathologies. *Cell Biol. Toxicol.* **2014**, *30*, 301–312. [CrossRef] [PubMed]
2. Liu, X.; Chen, Z. The pathophysiological role of mitochondrial oxidative stress in lung diseases. *J. Transl. Med.* **2017**, *15*, 207. [CrossRef]
3. Hecker, L. Mechanisms and consequences of oxidative stress in lung disease: Therapeutic implications for an aging populace. *Am. J. Physiol. Lung Cell. Mol. Physiol.* **2018**, *314*, L642–L653. [CrossRef]
4. van der Vliet, A.; Janssen-Heininger, Y.M.W.; Anathy, V. Oxidative stress in chronic lung disease: From mitochondrial dysfunction to dysregulated redox signaling. *Mol. Aspects Med.* **2018**, *63*, 59–69. [CrossRef]
5. Hallan, S.S.; Ferrara, F.; Cortesi, R.; Sguizzato, M. Potential of the Nano-Encapsulation of Antioxidant Molecules in Wound Healing Applications: An Innovative Strategy to Enhance the Bio-Profile. *Molecules* **2025**, *30*, 641. [CrossRef]
6. Aranda-Rivera, A.K.; Cruz-Gregorio, A.; Arancibia-Hernández, Y.L.; Hernández-Cruz, E.Y.; Pedraza-Chaverri, J. RONS and Oxidative Stress: An Overview of Basic Concepts. *Oxygen* **2022**, *2*, 437–478. [CrossRef]
7. Perez, M.; Robbins, M.E.; Revhaug, C.; Saugstad, O.D. Oxygen radical disease in the newborn, revisited: Oxidative stress and disease in the newborn period. *Free Radic. Biol. Med.* **2019**, *142*, 61–72. [CrossRef] [PubMed]
8. Li, Y.R.; Trush, M. Defining ROS in Biology and Medicine. *React. Oxyg. Species* **2016**, *1*, 9–21. [CrossRef]
9. Sies, H.; Jones, D.P. Reactive oxygen species (ROS) as pleiotropic physiological signalling agents. *Nat. Rev. Mol. Cell Biol.* **2020**, *21*, 363–383. [CrossRef]
10. Barnes, P.J. Oxidative stress-based therapeutics in COPD. *Redox Biol.* **2020**, *33*, 101544. [CrossRef]
11. Castellani, C.; Assael, B.M. Cystic fibrosis: A clinical view. *Cell. Mol. Life Sci.* **2017**, *74*, 129–140. [CrossRef]
12. Sosnay, P.R.; Siklosi, K.R.; Van Goor, F.; Kaniecki, K.; Yu, H.; Sharma, N.; Ramalho, A.S.; Amaral, M.D.; Dorfman, R.; Zielenski, J.; et al. Defining the disease liability of variants in the cystic fibrosis transmembrane conductance regulator gene. *Nat. Genet.* **2013**, *45*, 1160–1167. [CrossRef]
13. Trotta, V.; Scalia, S. Pulmonary delivery systems for polyphenols. *Drug Dev. Ind. Pharm.* **2017**, *43*, 1043–1052. [CrossRef]
14. Cystic Fibrosis Mutation Database: Statistics. Available online: http://www.genet.sickkids.on.ca/ (accessed on 20 April 2025).
15. Dushianthan, A.; Grocott, M.P.W.; Postle, A.D.; Cusack, R. Acute respiratory distress syndrome and acute lung injury. *Postgrad. Med. J.* **2011**, *87*, 612–622. [CrossRef]
16. He, S.; Wu, L.; Sun, H.; Wu, D.; Wang, C.; Ren, X.; Shao, Q.; York, P.; Tong, J.; Zhu, J.; et al. Antioxidant Biodegradable Covalent Cyclodextrin Frameworks as Particulate Carriers for Inhalation Therapy against Acute Lung Injury. *ACS Appl. Mater. Interfaces* **2022**, *14*, 38421–38435. [CrossRef]
17. Zhai, Z.; Ouyang, W.; Yao, Y.; Zhang, Y.; Zhang, H.; Xu, F.; Gao, C. Dexamethasone-loaded ROS-responsive poly(thioketal) nanoparticles suppress inflammation and oxidative stress of acute lung injury. *Bioact. Mater.* **2022**, *14*, 430–442. [CrossRef]
18. Sánchez-Illana, Á.; Piñeiro-Ramos, J.D.; Ramos-Garcia, V.; Ten-Doménech, I.; Vento, M.; Kuligowski, J. Oxidative stress biomarkers in the preterm infant. In *Advances in Clinical Chemistry*; Elsevier: Amsterdam, The Netherlands, 2021; Volume 102, pp. 127–189, ISBN 978-0-12-824614-6.

19. Papageorgiou, S.T.; Damdoumis, S.; Goulis, D.; Tzikas, S.; Giannakoulas, G. The Effect of Pulmonary Hypertension on Mortality and Intensive Care Unit Admission in Patients with SARS-CoV-2 Infection: A Systematic Review and Meta-Analysis. *Heart Lung Circ.* **2024**, *33*, 1136–1146. [CrossRef]
20. Chernyak, B.V.; Popova, E.N.; Prikhodko, A.S.; Grebenchikov, O.A.; Zinovkina, L.A.; Zinovkin, R.A. COVID-19 and Oxidative Stress. *Biochem. Mosc.* **2020**, *85*, 1543–1553. [CrossRef] [PubMed]
21. Aisa-Alvarez, A.; Soto, M.E.; Guarner-Lans, V.; Camarena-Alejo, G.; Franco-Granillo, J.; Martínez-Rodríguez, E.A.; Gamboa Ávila, R.; Manzano Pech, L.; Pérez-Torres, I. Usefulness of Antioxidants as Adjuvant Therapy for Septic Shock: A Randomized Clinical Trial. *Medicina* **2020**, *56*, 619. [CrossRef] [PubMed]
22. Martín Giménez, V.M.; Inserra, F.; Tajer, C.D.; Mariani, J.; Ferder, L.; Reiter, R.J.; Manucha, W. Lungs as target of COVID-19 infection: Protective common molecular mechanisms of vitamin D and melatonin as a new potential synergistic treatment. *Life Sci.* **2020**, *254*, 117808. [CrossRef] [PubMed]
23. Pokharel, M.D.; Marciano, D.P.; Fu, P.; Franco, M.C.; Unwalla, H.; Tieu, K.; Fineman, J.R.; Wang, T.; Black, S.M. Metabolic reprogramming, oxidative stress, and pulmonary hypertension. *Redox Biol.* **2023**, *64*, 102797. [CrossRef]
24. Rawat, M.; Lakshminrusimha, S.; Vento, M. Pulmonary hypertension and oxidative stress: Where is the link? *Semin. Fetal. Neonatal Med.* **2022**, *27*, 101347. [CrossRef]
25. Schermuly, R.T.; Ghofrani, H.A.; Wilkins, M.R.; Grimminger, F. Mechanisms of disease: Pulmonary arterial hypertension. *Nat. Rev. Cardiol.* **2011**, *8*, 443–455. [CrossRef]
26. Friedlander, S.; Pogatchnik, B.; Furuya, Y.; Allen, T. Pulmonary transplant complications: A radiologic review. *J. Cardiothorac. Surg.* **2024**, *19*, 270. [CrossRef]
27. Lai, Y.-C.; Potoka, K.C.; Champion, H.C.; Mora, A.L.; Gladwin, M.T. Pulmonary Arterial Hypertension: The Clinical Syndrome. *Circ. Res.* **2014**, *115*, 115–130. [CrossRef]
28. Sharma, M.; Paudyal, V.; Syed, S.K.; Thapa, R.; Kassam, N.; Surani, S. Management of Pulmonary Arterial Hypertension: Current Strategies and Future Prospects. *Life* **2025**, *15*, 430. [CrossRef] [PubMed]
29. Xu, D.; Hu, Y.-H.; Gou, X.; Li, F.-Y.; Yang, X.-Y.-C.; Li, Y.-M.; Chen, F. Oxidative Stress and Antioxidative Therapy in Pulmonary Arterial Hypertension. *Molecules* **2022**, *27*, 3724. [CrossRef]
30. Amararathna, M.; Johnston, M.; Rupasinghe, H. Plant Polyphenols as Chemopreventive Agents for Lung Cancer. *Int. J. Mol. Sci.* **2016**, *17*, 1352. [CrossRef] [PubMed]
31. Ganti, A.K.; Klein, A.B.; Cotarla, I.; Seal, B.; Chou, E. Update of Incidence, Prevalence, Survival, and Initial Treatment in Patients With Non–Small Cell Lung Cancer in the US. *JAMA Oncol.* **2021**, *7*, 1824–1832. [CrossRef] [PubMed]
32. Gęgotek, A.; Nikliński, J.; Žarković, N.; Žarković, K.; Waeg, G.; Łuczaj, W.; Charkiewicz, R.; Skrzydlewska, E. Lipid mediators involved in the oxidative stress and antioxidant defence of human lung cancer cells. *Redox Biol.* **2016**, *9*, 210–219. [CrossRef]
33. Valavanidis, A.; Vlachogianni, T.; Fiotakis, K.; Loridas, S. Pulmonary Oxidative Stress, Inflammation and Cancer: Respirable Particulate Matter, Fibrous Dusts and Ozone as Major Causes of Lung Carcinogenesis through Reactive Oxygen Species Mechanisms. *Int. J. Environ. Res. Public Health* **2013**, *10*, 3886–3907. [CrossRef] [PubMed]
34. Milkovic, L.; Cipak Gasparovic, A.; Zarkovic, N. Overview on major lipid peroxidation bioactive factor 4-hydroxynonenal as pluripotent growth-regulating factor. *Free Radic. Res.* **2015**, *49*, 850–860. [CrossRef]
35. Anderson, P.J.; Doyle, L.W. Neurodevelopmental Outcome of Bronchopulmonary Dysplasia. *Semin. Perinatol.* **2006**, *30*, 227–232. [CrossRef] [PubMed]
36. Bhandari, A.; Bhandari, V. Pitfalls, Problems, and Progress in Bronchopulmonary Dysplasia. *Pediatrics* **2009**, *123*, 1562–1573. [CrossRef]
37. Kalikkot Thekkeveedu, R.; Guaman, M.C.; Shivanna, B. Bronchopulmonary dysplasia: A review of pathogenesis and pathophysiology. *Respir. Med.* **2017**, *132*, 170–177. [CrossRef]
38. Perrone, S.; Tataranno, M.; Buonocore, G. Oxidative stress and bronchopulmonary dysplasia. *J. Clin. Neonatol.* **2012**, *1*, 109–114. [CrossRef]
39. Ferrante, G.; Montante, C.; Notarbartolo, V.; Giuffrè, M. Antioxidants: Role the in prevention and treatment of bronchopulmonary dysplasia. *Paediatr. Respir. Rev.* **2022**, *42*, 53–58. [CrossRef]
40. Soriano, J.B.; Kendrick, P.J.; Paulson, K.R.; Gupta, V.; Abrams, E.M.; Adedoyin, R.A.; Adhikari, T.B.; Advani, S.M.; Agrawal, A.; Ahmadian, E.; et al. Prevalence and attributable health burden of chronic respiratory diseases, 1990–2017: A systematic analysis for the Global Burden of Disease Study 2017. *Lancet Respir. Med.* **2020**, *8*, 585–596. [CrossRef]
41. Singh, S.; Verma, S.K.; Kumar, S.; Ahmad, M.K.; Nischal, A.; Singh, S.K.; Dixit, R.K. Evaluation of Oxidative Stress and Antioxidant Status in Chronic Obstructive Pulmonary Disease. *Scand. J. Immunol.* **2017**, *85*, 130–137. [CrossRef] [PubMed]
42. Barnes, P.J.; Burney, P.G.J.; Silverman, E.K.; Celli, B.R.; Vestbo, J.; Wedzicha, J.A.; Wouters, E.F.M. Chronic obstructive pulmonary disease. *Nat. Rev. Dis. Primer* **2015**, *1*, 15076. [CrossRef]
43. Barnes, P.J. Oxidative Stress in Chronic Obstructive Pulmonary Disease. *Antioxidants* **2022**, *11*, 965. [CrossRef] [PubMed]

44. He, L.; He, T.; Farrar, S.; Ji, L.; Liu, T.; Ma, X. Antioxidants Maintain Cellular Redox Homeostasis by Elimination of Reactive Oxygen Species. *Cell. Physiol. Biochem.* **2017**, *44*, 532–553. [CrossRef] [PubMed]
45. Mirończuk-Chodakowska, I.; Witkowska, A.M.; Zujko, M.E. Endogenous non-enzymatic antioxidants in the human body. *Adv. Med. Sci.* **2018**, *63*, 68–78. [CrossRef]
46. Vedi, M.; Sabina, E.P. Assessment of hepatoprotective and nephroprotective potential of withaferin A on bromobenzene-induced injury in Swiss albino mice: Possible involvement of mitochondrial dysfunction and inflammation. *Cell Biol. Toxicol.* **2016**, *32*, 373–390. [CrossRef]
47. Zhu, L.; Hou, Y.; Zhao, M.; Yang, M.; Fu, X.; Sun, J.; Fu, X.; Shao, L.; Zhang, H.; Fan, C.; et al. Caudatin induces caspase-dependent apoptosis in human glioma cells with involvement of mitochondrial dysfunction and reactive oxygen species generation. *Cell Biol. Toxicol.* **2016**, *32*, 333–345. [CrossRef]
48. Shadyro, O.; Samovich, S.; Edimecheva, I. Free-radical and biochemical reactions involving polar part of glycerophospholipids. *Free Radic. Biol. Med.* **2019**, *144*, 6–15. [CrossRef] [PubMed]
49. Janciauskiene, S. The Beneficial Effects of Antioxidants in Health and Diseases. *Chronic Obstr. Pulm. Dis. J. COPD Found.* **2020**, *7*, 182–202. [CrossRef]
50. Ganta, K.K.; Mandal, A.; Chaubey, B. Depolarization of mitochondrial membrane potential is the initial event in non-nucleoside reverse transcriptase inhibitor efavirenz induced cytotoxicity. *Cell Biol. Toxicol.* **2017**, *33*, 69–82. [CrossRef] [PubMed]
51. Kenney, M.C.; Chwa, M.; Atilano, S.R.; Falatoonzadeh, P.; Ramirez, C.; Malik, D.; Tarek, M.; Caceres-del-Carpio, J.; Nesburn, A.B.; Boyer, D.S.; et al. Inherited mitochondrial DNA variants can affect complement, inflammation and apoptosis pathways: Insights into mitochondrial-nuclear interactions. *Hum. Mol. Genet.* **2014**, *23*, 3537–3551. [CrossRef] [PubMed]
52. Fen, F.; Zhang, J.; Wang, Z.; Wu, Q.; Zhou, X. Efficacy and safety of N-acetylcysteine therapy for idiopathic pulmonary fibrosis: An updated systematic review and meta-analysis. *Exp. Ther. Med.* **2019**, *18*, 802–816. [CrossRef]
53. Sguizzato, M.; Esposito, E.; Drechsler, M.; Hallan, S.S.; Cortesi, R. Monolein Aqueous Dispersions as a Tool to Increase Flavonoid Solubility: A Preliminary Study. In Proceedings of the 1st International Electronic Conference on Pharmaceutics, Virtual, 1–15 December 2020; p. 25.
54. Singh Hallan, S.; Sguizzato, M.; Pavoni, G.; Baldisserotto, A.; Drechsler, M.; Mariani, P.; Esposito, E.; Cortesi, R. Ellagic Acid Containing Nanostructured Lipid Carriers for Topical Application: A Preliminary Study. *Molecules* **2020**, *25*, 1449. [CrossRef]
55. Poyatos, P.; Gratacós, M.; Samuel, K.; Orriols, R.; Tura-Ceide, O. Oxidative Stress and Antioxidant Therapy in Pulmonary Hypertension. *Antioxidants* **2023**, *12*, 1006. [CrossRef] [PubMed]
56. Mirhadi, E.; Roufogalis, B.D.; Banach, M.; Barati, M.; Sahebkar, A. Resveratrol: Mechanistic and therapeutic perspectives in pulmonary arterial hypertension. *Pharmacol. Res.* **2021**, *163*, 105287. [CrossRef] [PubMed]
57. Jiang, L.; Zhang, L.; Kang, K.; Fei, D.; Gong, R.; Cao, Y.; Pan, S.; Zhao, M.; Zhao, M. Resveratrol ameliorates LPS-induced acute lung injury via NLRP3 inflammasome modulation. *Biomed. Pharmacother.* **2016**, *84*, 130–138. [CrossRef]
58. Ren, H.-H.; Niu, Z.; Guo, R.; Fu, M.; Li, H.-R.; Zhang, X.-Y.; Yao, L. Rhodiola crenulata extract decreases fatty acid oxidation and autophagy to ameliorate pulmonary arterial hypertension by targeting inhibition of acylcarnitine in rats. *Chin. J. Nat. Med.* **2021**, *19*, 120–133. [CrossRef]
59. Lee, S.; Ro, H.; In, H.J.; Choi, J.-H.; Kim, M.-O.; Lee, J.; Hong, S.-T.; Lee, S.U. Fisetin inhibits TNF-α/NF-κB-induced IL-8 expression by targeting PKCδ in human airway epithelial cells. *Cytokine* **2018**, *108*, 247–254. [CrossRef]
60. Liu, X.-J.; Bao, H.-R.; Zeng, X.-L.; Wei, J.-M. Effects of resveratrol and genistein on nuclear factor-κB, tumor necrosis factor-α and matrix metalloproteinase-9 in patients with chronic obstructive pulmonary disease. *Mol. Med. Rep.* **2016**, *13*, 4266–4272. [CrossRef] [PubMed]
61. Dianat, M.; Radan, M.; Badavi, M.; Mard, S.A.; Bayati, V.; Ahmadizadeh, M. Crocin attenuates cigarette smoke-induced lung injury and cardiac dysfunction by anti-oxidative effects: The role of Nrf2 antioxidant system in preventing oxidative stress. *Respir. Res.* **2018**, *19*, 58. [CrossRef]
62. Chen, J.; Du, Y.; Long, Y.; Tao, D.; Hu, M.; Jiang, Y.; Wan, Y.; Yang, D. Polyphenols in Ilex latifolia Thunb. inhibit human lung cancer cell line A549 by regulation of the PI3K-Akt signaling pathway. *BMC Complement. Med. Ther.* **2022**, *22*, 85. [CrossRef]
63. Ram, A.; Ghosh, B.; Das, M. Luteolin alleviates bronchoconstriction and airway hyperreactivity in ovalbumin sensitized mice. *Inflamm. Res.* **2003**, *52*, 101–106. [CrossRef]
64. Allegretta, C.; Difonzo, G.; Caponio, F.; Tamma, G.; Laselva, O. Olive Leaf Extract (OLE) as a Novel Antioxidant That Ameliorates the Inflammatory Response in Cystic Fibrosis. *Cells* **2023**, *12*, 1764. [CrossRef]
65. Emran, T.B.; Eva, T.A.; Zehravi, M.; Islam, F.; Khan, J.; Kareemulla, S.; Arjun, U.V.N.V.; Balakrishnan, A.; Taru, P.P.; Nainu, F.; et al. Polyphenols as Therapeutics in Respiratory Diseases: Moving from Preclinical Evidence to Potential Clinical Applications. *Int. J. Biol. Sci.* **2024**, *20*, 3236–3256. [CrossRef]
66. Wu, D.; Dong, Y.; Zhang, D.; Wang, T.; Ye, H.; Zhang, W. Efficacy and safety of dietary polyphenol supplements for COPD: A systematic review and meta-analysis. *Front. Immunol.* **2025**, *16*, 1617694. [CrossRef] [PubMed]

67. Impellizzeri, D.; Talero, E.; Siracusa, R.; Alcaide, A.; Cordaro, M.; Maria Zubelia, J.; Bruschetta, G.; Crupi, R.; Esposito, E.; Cuzzocrea, S.; et al. Protective effect of polyphenols in an inflammatory process associated with experimental pulmonary fibrosis in mice. *Br. J. Nutr.* **2015**, *114*, 853–865. [CrossRef]
68. Pounis, G.; Arcari, A.; Costanzo, S.; Di Castelnuovo, A.; Bonaccio, M.; Persichillo, M.; Donati, M.B.; de Gaetano, G.; Iacoviello, L. Favorable association of polyphenol-rich diets with lung function: Cross-sectional findings from the Moli-sani study. *Respir. Med.* **2018**, *136*, 48–57. [CrossRef]
69. Morton, L.; Braakhuis, A.J. The Effects of Fruit-Derived Polyphenols on Cognition and Lung Function in Healthy Adults: A Systematic Review and Meta-Analysis. *Nutrients* **2021**, *13*, 4273. [CrossRef]
70. Li, J.; Zhong, X.; Zhao, Y.; Shen, J.; Pilapong, C.; Xiao, Z. Polyphenols as Lung Cancer Chemopreventive Agents by Targeting microRNAs. *Molecules* **2022**, *27*, 5903. [CrossRef]
71. Mileo, A.M.; Miccadei, S. Polyphenols as Modulator of Oxidative Stress in Cancer Disease: New Therapeutic Strategies. *Oxid. Med. Cell. Longev.* **2016**, *2016*, 6475624. [CrossRef] [PubMed]
72. Yoshioka, Y.; Ohishi, T.; Nakamura, Y.; Fukutomi, R.; Miyoshi, N. Anti-Cancer Effects of Dietary Polyphenols via ROS-Mediated Pathway with Their Modulation of MicroRNAs. *Molecules* **2022**, *27*, 3816. [CrossRef] [PubMed]
73. Wang, H.; Bian, S.; Yang, C.S. Green tea polyphenol EGCG suppresses lung cancer cell growth through upregulating miR-210 expression caused by stabilizing HIF-1. *Carcinogenesis* **2011**, *32*, 1881–1889. [CrossRef]
74. Aida, R.; Hagiwara, K.; Okano, K.; Nakata, K.; Obata, Y.; Yamashita, T.; Yoshida, K.; Hagiwara, H. miR-34a-5p might have an important role for inducing apoptosis by down-regulation of SNAI1 in apigenin-treated lung cancer cells. *Mol. Biol. Rep.* **2021**, *48*, 2291–2297. [CrossRef] [PubMed]
75. Tan, S.; Dai, L.; Tan, P.; Liu, W.; Mu, Y.; Wang, J.; Huang, X.; Hou, A. Hesperidin administration suppresses the proliferation of lung cancer cells by promoting apoptosis via targeting the miR-132/ZEB2 signalling pathway. *Int. J. Mol. Med.* **2020**, *46*, 2069–2077. [CrossRef]
76. Bailly, C. Anticancer properties and mechanism of action of the quassinoid ailanthone. *Phytother. Res.* **2020**, *34*, 2203–2213. [CrossRef] [PubMed]
77. Singaravelan, N.; Tollefsbol, T.O. Polyphenol-Based Prevention and Treatment of Cancer Through Epigenetic and Combinatorial Mechanisms. *Nutrients* **2025**, *17*, 616. [CrossRef] [PubMed]
78. Tamimi, A.; Serdarevic, D.; Hanania, N.A. The effects of cigarette smoke on airway inflammation in asthma and COPD: Therapeutic implications. *Respir. Med.* **2012**, *106*, 319–328. [CrossRef]
79. Anthonisen, N.R. Effects of Smoking Intervention and the Use of an Inhaled Anticholinergic Bronchodilator on the Rate of Decline of FEV1: The Lung Health Study. *JAMA* **1994**, *272*, 1497–1505. [CrossRef]
80. Bao, M.-J.; Shen, J.; Jia, Y.-L.; Li, F.-F.; Ma, W.-J.; Shen, H.-J.; Shen, L.-L.; Lin, X.-X.; Zhang, L.-H.; Dong, X.-W.; et al. Apple polyphenol protects against cigarette smoke-induced acute lung injury. *Nutrition* **2013**, *29*, 235–243. [CrossRef]
81. Miklós, Z.; Horváth, I. The Role of Oxidative Stress and Antioxidants in Cardiovascular Comorbidities in COPD. *Antioxidants* **2023**, *12*, 1196. [CrossRef]
82. Shirazi-Tehrani, E.; Chamasemani, A.; Firouzabadi, N.; Mousaei, M. ncRNAs and polyphenols: New therapeutic strategies for hypertension. *RNA Biol.* **2022**, *19*, 575–587. [CrossRef]
83. Tavazzi, G.; Pozzi, M.; Mongodi, S.; Dammassa, V.; Romito, G.; Mojoli, F. Inhaled nitric oxide in patients admitted to intensive care unit with COVID-19 pneumonia. *Crit. Care* **2020**, *24*, 508. [CrossRef]
84. Alwani, S.; Wasan, E.K.; Badea, I. Solid Lipid Nanoparticles for Pulmonary Delivery of Biopharmaceuticals: A Review of Opportunities, Challenges, and Delivery Applications. *Mol. Pharm.* **2024**, *21*, 3084–3102. [CrossRef]
85. Premathilaka, R.; Rashidinejad, A.; Golding, M.; Singh, J. Oral delivery of hydrophobic flavonoids and their incorporation into functional foods: Opportunities and challenges. *Food Hydrocoll.* **2022**, *128*, 107567. [CrossRef]
86. Gerges, P.; Kfoury, M.; Landy, D.; Fourmentin, S.; Greige-Gerges, H. Cyclodextrin-based materials for pulmonary delivery: Insights and challenges. *Carbohydr. Polym.* **2025**, *363*, 123712. [CrossRef] [PubMed]
87. Wang, B.; Wang, L.; Yang, Q.; Zhang, Y.; Qinglai, T.; Yang, X.; Xiao, Z.; Lei, L.; Li, S. Pulmonary inhalation for disease treatment: Basic research and clinical translations. *Mater. Today Bio* **2024**, *25*, 100966. [CrossRef] [PubMed]
88. Walenga, R.L.; Longest, P.W. Current Inhalers Deliver Very Small Doses to the Lower Tracheobronchial Airways: Assessment of Healthy and Constricted Lungs. *J. Pharm. Sci.* **2016**, *105*, 147–159. [CrossRef]
89. Labiris, N.R.; Dolovich, M.B. Pulmonary drug delivery. Part I: Physiological factors affecting therapeutic effectiveness of aerosolized medications. *Br. J. Clin. Pharmacol.* **2003**, *56*, 588–599. [CrossRef]
90. Sorino, C.; Negri, S.; Spanevello, A.; Visca, D.; Scichilone, N. Inhalation therapy devices for the treatment of obstructive lung diseases: The history of inhalers towards the ideal inhaler. *Eur. J. Intern. Med.* **2020**, *75*, 15–18. [CrossRef]
91. Agnihotri, V.; Agrawal, Y.; Goyal, S.; Sharma, C.; Ojha, S. An Update on Advancements and Challenges in Inhalational Drug Delivery for Pulmonary Arterial Hypertension. *Molecules* **2022**, *27*, 3490. [CrossRef]

92. Tronde, A.; Nordén, B.o.; Marchner, H.; Wendel, A.; Lennernäs, H.; Bengtsson, U.H. Pulmonary Absorption Rate and Bioavailability of Drugs in Vivo in Rats: Structure–Absorption Relationships and Physicochemical Profiling of Inhaled Drugs. *J. Pharm. Sci.* **2003**, *92*, 1216–1233. [CrossRef]
93. Chaurasiya, B.; Zhao, Y.-Y. Dry Powder for Pulmonary Delivery: A Comprehensive Review. *Pharmaceutics* **2020**, *13*, 31. [CrossRef]
94. Guo, Y.; Bera, H.; Shi, C.; Zhang, L.; Cun, D.; Yang, M. Pharmaceutical strategies to extend pulmonary exposure of inhaled medicines. *Acta Pharm. Sin. B* **2021**, *11*, 2565–2584. [CrossRef] [PubMed]
95. Mangal, S.; Gao, W.; Li, T.; Zhou, Q. Pulmonary delivery of nanoparticle chemotherapy for the treatment of lung cancers: Challenges and opportunities. *Acta Pharmacol. Sin.* **2017**, *38*, 782–797. [CrossRef] [PubMed]
96. Tatsumura, T.; Koyama, S.; Tsujimoto, M.; Kitagawa, M.; Kagamimori, S. Further study of nebulisation chemotherapy, a new chemotherapeutic method in the treatment of lung carcinomas: Fundamental and clinical. *Br. J. Cancer* **1993**, *68*, 1146–1149. [CrossRef]
97. Wauthoz, N.; Rosière, R.; Amighi, K. Inhaled cytotoxic chemotherapy: Clinical challenges, recent developments, and future prospects. *Expert Opin. Drug Deliv.* **2021**, *18*, 333–354. [CrossRef]
98. Zoulikha, M.; Xiao, Q.; Boafo, G.F.; Sallam, M.A.; Chen, Z.; He, W. Pulmonary delivery of siRNA against acute lung injury/acute respiratory distress syndrome. *Acta Pharm. Sin. B* **2022**, *12*, 600–620. [CrossRef]
99. Bivasbenita, M.; Ottenhoff, T.; Junginger, H.; Borchard, G. Pulmonary DNA vaccination: Concepts, possibilities and perspectives. *J. Control. Release* **2005**, *107*, 1–29. [CrossRef]
100. Liu, J.; Wu, Z.; Liu, Y.; Zhan, Z.; Yang, L.; Wang, C.; Jiang, Q.; Ran, H.; Li, P.; Wang, Z. ROS-responsive liposomes as an inhaled drug delivery nanoplatform for idiopathic pulmonary fibrosis treatment via Nrf2 signaling. *J. Nanobiotechnol.* **2022**, *20*, 213. [CrossRef]
101. Schleh, C.; Rothen-Rutishauser, B.; Kreyling, W.G. The influence of pulmonary surfactant on nanoparticulate drug delivery systems. *Eur. J. Pharm. Biopharm.* **2011**, *77*, 350–352. [CrossRef]
102. Kapralov, A.A.; Feng, W.H.; Amoscato, A.A.; Yanamala, N.; Balasubramanian, K.; Winnica, D.E.; Kisin, E.R.; Kotchey, G.P.; Gou, P.; Sparvero, L.J.; et al. Adsorption of Surfactant Lipids by Single-Walled Carbon Nanotubes in Mouse Lung upon Pharyngeal Aspiration. *ACS Nano* **2012**, *6*, 4147–4156. [CrossRef] [PubMed]
103. Radiom, M.; Sarkis, M.; Brookes, O.; Oikonomou, E.K.; Baeza-Squiban, A.; Berret, J.-F. Pulmonary surfactant inhibition of nanoparticle uptake by alveolar epithelial cells. *Sci. Rep.* **2020**, *10*, 19436. [CrossRef] [PubMed]
104. Tang, K.; Cui, X. A Review on Investigating the Interactions between Nanoparticles and the Pulmonary Surfactant Monolayer with Coarse-Grained Molecular Dynamics Method. *Langmuir* **2024**, *40*, 11829–11842. [CrossRef]
105. Hidalgo, A.; Garcia-Mouton, C.; Autilio, C.; Carravilla, P.; Orellana, G.; Islam, M.N.; Bhattacharya, J.; Bhattacharya, S.; Cruz, A.; Pérez-Gil, J. Pulmonary surfactant and drug delivery: Vehiculization, release and targeting of surfactant/tacrolimus formulations. *J. Controlled Release* **2021**, *329*, 205–222. [CrossRef] [PubMed]
106. Deng, Z.; Kalin, G.T.; Shi, D.; Kalinichenko, V.V. Nanoparticle Delivery Systems with Cell-Specific Targeting for Pulmonary Diseases. *Am. J. Respir. Cell Mol. Biol.* **2021**, *64*, 292–307. [CrossRef] [PubMed]
107. Hallan, S.S.; Kaur, P.; Kaur, V.; Mishra, N.; Vaidya, B. Lipid polymer hybrid as emerging tool in nanocarriers for oral drug delivery. *Artif. Cells Nanomed. Biotechnol.* **2016**, *44*, 334–349. [CrossRef]
108. Mitchell, M.J.; Billingsley, M.M.; Haley, R.M.; Wechsler, M.E.; Peppas, N.A.; Langer, R. Engineering precision nanoparticles for drug delivery. *Nat. Rev. Drug Discov.* **2021**, *20*, 101–124. [CrossRef]
109. Pápay, Z.E.; Kósa, A.; Böddi, B.; Merchant, Z.; Saleem, I.Y.; Zariwala, M.G.; Klebovich, I.; Somavarapu, S.; Antal, I. Study on the Pulmonary Delivery System of Apigenin-Loaded Albumin Nanocarriers with Antioxidant Activity. *J. Aerosol Med. Pulm. Drug Deliv.* **2017**, *30*, 274–288. [CrossRef] [PubMed]
110. Qiao, Q.; Liu, X.; Yang, T.; Cui, K.; Kong, L.; Yang, C.; Zhang, Z. Nanomedicine for acute respiratory distress syndrome: The latest application, targeting strategy, and rational design. *Acta Pharm. Sin. B* **2021**, *11*, 3060–3091. [CrossRef]
111. Rodríguez, F.; Caruana, P.; De la Fuente, N.; Español, P.; Gámez, M.; Balart, J.; Llurba, E.; Rovira, R.; Ruiz, R.; Martín-Lorente, C.; et al. Nano-Based Approved Pharmaceuticals for Cancer Treatment: Present and Future Challenges. *Biomolecules* **2022**, *12*, 784. [CrossRef]
112. Silva, A.C.; Costa, M.P.; Zacaron, T.M.; Ferreira, K.C.B.; Braz, W.R.; Fabri, R.L.; Frézard, F.J.G.; Pittella, F.; Tavares, G.D. The Role of Inhaled Chitosan-Based Nanoparticles in Lung Cancer Therapy. *Pharmaceutics* **2024**, *16*, 969. [CrossRef]
113. ElKasabgy, N.A.; Adel, I.M.; Elmeligy, M.F. Respiratory Tract: Structure and Attractions for Drug Delivery Using Dry Powder Inhalers. *AAPS PharmSciTech* **2020**, *21*, 238. [CrossRef]
114. Yong, J.; Shu, H.; Zhang, X.; Yang, K.; Luo, G.; Yu, L.; Li, J.; Huang, H. Natural Products-Based Inhaled Formulations for Treating Pulmonary Diseases. *Int. J. Nanomed.* **2024**, *19*, 1723–1748. [CrossRef] [PubMed]
115. Liu, K.; Chen, W.; Yang, T.; Wen, B.; Ding, D.; Keidar, M.; Tang, J.; Zhang, W. Paclitaxel and quercetin nanoparticles co-loaded in microspheres to prolong retention time for pulmonary drug delivery. *Int. J. Nanomed.* **2017**, *12*, 8239–8255. [CrossRef]

116. Gulati, N.; Dua, K.; Dureja, H. Role of chitosan based nanomedicines in the treatment of chronic respiratory diseases. *Int. J. Biol. Macromol.* **2021**, *185*, 20–30. [CrossRef]
117. Zamora, M.E.; Essien, E.-O.; Bhamidipati, K.; Murthy, A.; Liu, J.; Kim, H.; Patel, M.N.; Nong, J.; Wang, Z.; Espy, C.; et al. Marginated Neutrophils in the Lungs Effectively Compete for Nanoparticles Targeted to the Endothelium, Serving as a Part of the Reticuloendothelial System. *ACS Nano* **2024**, *18*, 22275–22297. [CrossRef]
118. Inoue, Y.; Sekiya, N.; Yamamoto, M.; Iohara, D.; Hirayama, F.; Uekama, K. Formation of the Ternary Inclusion Complex of Limaprost with α- and β-Cyclodextrins in Aqueous Solution. *Chem. Pharm. Bull.* **2015**, *63*, 318–325. [CrossRef]
119. Loftsson, T.; Konrádsdóttir, F.; Másson, M. Development and evaluation of an artificial membrane for determination of drug availability. *Int. J. Pharm.* **2006**, *326*, 60–68. [CrossRef] [PubMed]
120. Abdellatif, A.A.; Ahmed, F.; Mohammed, A.M.; Alsharidah, M.; Al-Subaiyel, A.; Samman, W.A.; Alhaddad, A.A.; Al-Mijalli, S.H.; Amin, M.A.; Barakat, H.; et al. Recent Advances in the Pharmaceutical and Biomedical Applications of Cyclodextrin-Capped Gold Nanoparticles. *Int. J. Nanomed.* **2023**, *18*, 3247–3281. [CrossRef] [PubMed]
121. Liao, Y.; Zhang, X.; Li, C.; Huang, Y.; Lei, M.; Yan, M.; Zhou, Y.; Zhao, C. Inclusion complexes of HP-β-cyclodextrin with agomelatine: Preparation, characterization, mechanism study and in vivo evaluation. *Carbohydr. Polym.* **2016**, *147*, 415–425. [CrossRef]
122. Bognanni, N.; Bellia, F.; Viale, M.; Bertola, N.; Vecchio, G. Exploring Charged Polymeric Cyclodextrins for Biomedical Applications. *Molecules* **2021**, *26*, 1724. [CrossRef]
123. Hussain Asim, M.; Ijaz, M.; Rösch, A.C.; Bernkop-Schnürch, A. Thiolated cyclodextrins: New perspectives for old excipients. *Coord. Chem. Rev.* **2020**, *420*, 213433. [CrossRef]
124. Braga, S.S. Cyclodextrins: Emerging Medicines of the New Millennium. *Biomolecules* **2019**, *9*, 801. [CrossRef]
125. Motzwickler-Németh, A.; Körmendi, E.; Farkas, Á.; Csóka, I.; Ambrus, R. Nano-Spray-Drying of Cyclodextrin/Ibuprofen Complexes with Aerosolization-Enhancing Additives for Pulmonary Drug Delivery. *Int. J. Mol. Sci.* **2025**, *26*, 4320. [CrossRef]
126. Sguizzato, M.; Ferrara, F.; Sisto, M.; Drechsler, M.; Gallerani, E.; Nicoli, F.; Cortesi, R. Rutin-containing cyclodextrin nanosystems: A possible strategy for dietary supplementation in diabetics. *J. Drug Deliv. Sci. Technol.* **2025**, *110*, 107065. [CrossRef]
127. Mahboob, H.; Richeson III, R.; McCain, R. Zinc Chloride Smoke Inhalation Induced Severe Acute Respiratory Distress Syndrome: First Survival in the United States with Extended Duration (Five Weeks) Therapy with High Dose Corticosteroids in Combination with Lung Protective Ventilation. *Case Rep. Crit. Care* **2017**, *2017*, 7952782. [CrossRef]
128. Zhu, X.; Lei, X.; Wang, J.; Dong, W. Protective effects of resveratrol on hyperoxia-induced lung injury in neonatal rats by alleviating apoptosis and ROS production. *J. Matern. Fetal Neonatal Med.* **2020**, *33*, 4150–4158. [CrossRef]
129. Wang, W.; Liu, Y.; Pan, P.; Huang, Y.; Chen, T.; Yuan, T.; Ma, Y.; Han, G.; Li, J.; Jin, Y.; et al. Pulmonary delivery of resveratrol-*β* -cyclodextrin inclusion complexes for the prevention of zinc chloride smoke-induced acute lung injury. *Drug Deliv.* **2022**, *29*, 1122–1131. [CrossRef] [PubMed]
130. Evrard, B.; Bertholet, P.; Gueders, M.; Flament, M.-P.; Piel, G.; Delattre, L.; Gayot, A.; Leterme, P.; Foidart, J.-M.; Cataldo, D. Cyclodextrins as a potential carrier in drug nebulization. *J. Control. Release* **2004**, *96*, 403–410. [CrossRef]
131. Yokohira, M.; Kuno, T.; Yamakawa, K.; Hashimoto, N.; Ninomiya, F.; Suzuki, S.; Saoo, K.; Imaida, K. An Intratracheal Instillation Bioassay System for Detection of Lung Toxicity Due to Fine Particles in F344 Rats. *J. Toxicol. Pathol.* **2009**, *22*, 1–10. [CrossRef] [PubMed]
132. Matilainen, L.; Toropainen, T.; Vihola, H.; Hirvonen, J.; Järvinen, T.; Jarho, P.; Järvinen, K. In vitro toxicity and permeation of cyclodextrins in Calu-3 cells. *J. Controlled Release* **2008**, *126*, 10–16. [CrossRef]
133. Cabral Marques, H.M.; Hadgraft, J.; Kellaway, I.W.; Taylor, G. Studies of cyclodextrin inclusion complexes. III. The pulmonary absorption of β-, DM-β- and HP-β-cyclodextrins in rabbits. *Int. J. Pharm.* **1991**, *77*, 297–302. [CrossRef]
134. Neaz, S.; Alam, M.M.; Imran, A.B. Advancements in cyclodextrin-based controlled drug delivery: Insights into pharmacokinetic and pharmacodynamic profiles. *Heliyon* **2024**, *10*, e39917. [CrossRef]
135. Zhang, H.; Huang, X.; Sun, Y.; Lu, G.; Wang, K.; Wang, Z.; Xing, J.; Gao, Y. Improvement of pulmonary absorption of poorly absorbable macromolecules by hydroxypropyl-β-cyclodextrin grafted polyethylenimine (HP-β-CD-PEI) in rats. *Int. J. Pharm.* **2015**, *489*, 294–303. [CrossRef]
136. Cerri, L.; Migone, C.; Vizzoni, L.; Grassiri, B.; Fabiano, A.; Piras, A.M.; Zambito, Y. Cross-Linked Thiolated Hydroxypropil-β-Cyclodextrin for Pulmonary Drug Delivery. *Int. J. Mol. Sci.* **2024**, *25*, 9394. [CrossRef]
137. Lu, A.; Ebright, B.; Naik, A.; Tan, H.L.; Cohen, N.A.; Bouteiller, J.-M.C.; Lazzi, G.; Louie, S.G.; Humayun, M.S.; Asante, I. Hydroxypropyl-Beta Cyclodextrin Barrier Prevents Respiratory Viral Infections: A Preclinical Study. *Int. J. Mol. Sci.* **2024**, *25*, 2061. [CrossRef]
138. Pochet, A.; Brodin, P.; Gref, R.; Machelart, A. Beta-cyclodextrins in infectious disease therapy: A review of their function beyond simple drug carriers. *Carbohydr. Polym. Technol. Appl.* **2025**, *11*, 100921. [CrossRef]
139. Su, W.; Liang, Y.; Meng, Z.; Chen, X.; Lu, M.; Han, X.; Deng, X.; Zhang, Q.; Zhu, H.; Fu, T. Inhalation of Tetrandrine-hydroxypropyl-β-cyclodextrin Inclusion Complexes for Pulmonary Fibrosis Treatment. *Mol. Pharm.* **2020**, *17*, 1596–1607. [CrossRef]

140. Gunasekara, L.; Al-Saiedy, M.; Green, F.; Pratt, R.; Bjornson, C.; Yang, A.; Michael Schoel, W.; Mitchell, I.; Brindle, M.; Montgomery, M.; et al. Pulmonary surfactant dysfunction in pediatric cystic fibrosis: Mechanisms and reversal with a lipid-sequestering drug. *J. Cyst. Fibros.* **2017**, *16*, 565–572. [CrossRef] [PubMed]
141. Al-Saiedy, M.; Gunasekara, L.; Green, F.; Pratt, R.; Chiu, A.; Yang, A.; Dennis, J.; Pieron, C.; Bjornson, C.; Winston, B.; et al. Surfactant Dysfunction in ARDS and Bronchiolitis is Repaired with Cyclodextrins. *Mil. Med.* **2018**, *183*, 207–215. [CrossRef] [PubMed]
142. Abou Taleb, S.; Moatasim, Y.; GabAllah, M.; Asfour, M.H. Quercitrin loaded cyclodextrin based nanosponge as a promising approach for management of lung cancer and COVID-19. *J. Drug Deliv. Sci. Technol.* **2022**, *77*, 103921. [CrossRef]
143. Salem, Y.Y.; Hoti, G.; Sammour, R.M.F.; Caldera, F.; Cecone, C.; Matencio, A.; Shahiwala, A.F.; Trotta, F. Preparation and evaluation of βcyclodextrin-based nanosponges loaded with Budesonide for pulmonary delivery. *Int. J. Pharm.* **2023**, *647*, 123529. [CrossRef] [PubMed]
144. Pyrak, B.; Rogacka-Pyrak, K.; Gubica, T.; Szeleszczuk, Ł. Exploring Cyclodextrin-Based Nanosponges as Drug Delivery Systems: Understanding the Physicochemical Factors Influencing Drug Loading and Release Kinetics. *Int. J. Mol. Sci.* **2024**, *25*, 3527. [CrossRef]
145. Venuti, V.; Rossi, B.; Mele, A.; Melone, L.; Punta, C.; Majolino, D.; Masciovecchio, C.; Caldera, F.; Trotta, F. Tuning structural parameters for the optimization of drug delivery performance of cyclodextrin-based nanosponges. *Expert Opin. Drug Deliv.* **2017**, *14*, 331–340. [CrossRef]
146. Utzeri, G.; Matias, P.M.C.; Murtinho, D.; Valente, A.J.M. Cyclodextrin-Based Nanosponges: Overview and Opportunities. *Front. Chem.* **2022**, *10*, 859406. [CrossRef]
147. Ahmed, R.Z.; Patil, G.; Zaheer, Z. Nanosponges—A completely new nano-horizon: Pharmaceutical applications and recent advances. *Drug Dev. Ind. Pharm.* **2013**, *39*, 1263–1272. [CrossRef]
148. Pushpalatha, R.; Selvamuthukumar, S.; Kilimozhi, D. Cross-linked, cyclodextrin-based nanosponges for curcumin delivery—Physicochemical characterization, drug release, stability and cytotoxicity. *J. Drug Deliv. Sci. Technol.* **2018**, *45*, 45–53. [CrossRef]
149. McIlwain, C. Cyclosert-Camptothecin. In *xPharm: The Comprehensive Pharmacology Reference*; Elsevier: Amsterdam, The Netherlands, 2008; pp. 1–5, ISBN 978-0-08-055232-3.
150. Oliveri, V.; Vecchio, G. Cyclodextrins as Protective Agents of Protein Aggregation: An Overview. *Chem. Asian J.* **2016**, *11*, 1648–1657. [CrossRef] [PubMed]
151. Oliveri, V.; Bellia, F.; Pietropaolo, A.; Vecchio, G. Unusual Cyclodextrin Derivatives as a New Avenue to Modulate Self- and Metal-Induced Aβ Aggregation. *Chem. Eur. J.* **2015**, *21*, 14047–14059. [CrossRef] [PubMed]
152. Grassiri, B.; Cesari, A.; Balzano, F.; Migone, C.; Kali, G.; Bernkop-Schnürch, A.; Uccello-Barretta, G.; Zambito, Y.; Piras, A.M. Thiolated 2-Methyl-β-Cyclodextrin as a Mucoadhesive Excipient for Poorly Soluble Drugs: Synthesis and Characterization. *Polymers* **2022**, *14*, 3170. [CrossRef]
153. Hallan, S.S.; Marchetti, P.; Bortolotti, D.; Sguizzato, M.; Esposito, E.; Mariani, P.; Trapella, C.; Rizzo, R.; Cortesi, R. Design of Nanosystems for the Delivery of Quorum Sensing Inhibitors: A Preliminary Study. *Molecules* **2020**, *25*, 5655. [CrossRef] [PubMed]
154. Singh, P.K.; Schaefer, A.L.; Parsek, M.R.; Moninger, T.O.; Welsh, M.J.; Greenberg, E.P. Quorum-sensing signals indicate that cystic fibrosis lungs are infected with bacterial biofilms. *Nature* **2000**, *407*, 762–764. [CrossRef]
155. Fenyvesi, É.; Berkl, Z.; Ligethy, L.; Fekete-Kertész, I.; Csizmazia, M.; Malanga, M.; Puskás, I.; Szőcs, L.; Iványi, R.; Kese, I.; et al. Long-Chain Alkylthio Cyclodextrin Derivatives for Modulation of Quorum-Sensing-Based Bioluminescence in Aliivibrio fischeri Model System. *Int. J. Mol. Sci.* **2024**, *25*, 7139. [CrossRef] [PubMed]
156. Parvathaneni, V.; Elbatanony, R.S.; Goyal, M.; Chavan, T.; Vega, N.; Kolluru, S.; Muth, A.; Gupta, V.; Kunda, N.K. Repurposing Bedaquiline for Effective Non-Small Cell Lung Cancer (NSCLC) Therapy as Inhalable Cyclodextrin-Based Molecular Inclusion Complexes. *Int. J. Mol. Sci.* **2021**, *22*, 4783. [CrossRef] [PubMed]
157. Patil, S.M.; Barji, D.S.; Chavan, T.; Patel, K.; Collazo, A.J.; Prithipaul, V.; Muth, A.; Kunda, N.K. Solubility Enhancement and Inhalation Delivery of Cyclodextrin-Based Inclusion Complex of Delamanid for Pulmonary Tuberculosis Treatment. *AAPS PharmSciTech* **2023**, *24*, 49. [CrossRef]
158. Képes, Z.; Dénes, N.; Kertész, I.; Hajdu, I.; Trencsényi, G. Overview of Prostaglandin E2 (PGE2)-Targeting Radiolabelled Imaging Probes from Preclinical Perspective: Lessons Learned and Road Ahead. *Int. J. Mol. Sci.* **2023**, *24*, 6942. [CrossRef]
159. Vakali, V.; Papadourakis, M.; Georgiou, N.; Zoupanou, N.; Diamantis, D.A.; Javornik, U.; Papakyriakopoulou, P.; Plavec, J.; Valsami, G.; Tzakos, A.G.; et al. Comparative Interaction Studies of Quercetin with 2-Hydroxyl-propyl-β-cyclodextrin and 2,6-Methylated-β-cyclodextrin. *Molecules* **2022**, *27*, 5490. [CrossRef] [PubMed]
160. Charoenwongpaiboon, T.; Oo, A.; Nasoontorn, S.; Rungrotmongkol, T.; Kanokmedhakul, S.; Mahalapbutr, P. Aurisin A Complexed with 2,6-Di-O-methyl-β-cyclodextrin Enhances Aqueous Solubility, Thermal Stability, and Antiproliferative Activity against Lung Cancer Cells. *Int. J. Mol. Sci.* **2022**, *23*, 9776. [CrossRef]

161. Paczkowska-Walendowska, M.; Miklaszewski, A.; Cielecka-Piontek, J. Is It Possible to Improve the Bioavailability of Resveratrol and Polydatin Derived from Polygoni cuspidati Radix as a Result of Preparing Electrospun Nanofibers Based on Polyvinylpyrrolidone/Cyclodextrin? *Nutrients* **2022**, *14*, 3897. [CrossRef]
162. Baranauskaite, J.; Kopustinskiene, D.M.; Bernatoniene, J. Impact of Gelatin Supplemented with Gum Arabic, Tween 20, and β-Cyclodextrin on the Microencapsulation of Turkish Oregano Extract. *Molecules* **2019**, *24*, 176. [CrossRef]
163. Hoshikawa, A.; Nagira, M.; Tane, M.; Fukushige, K.; Tagami, T.; Ozeki, T. Preparation of Curcumin-Containing α-, β-, and γ-Cyclodextrin/Polyethyleneglycol-Conjugated Gold Multifunctional Nanoparticles and Their in Vitro Cytotoxic Effects on A549 Cells. *Biol. Pharm. Bull.* **2018**, *41*, 908–914. [CrossRef]
164. Zhang, X.; Su, J.; Wang, X.; Wang, X.; Liu, R.; Fu, X.; Li, Y.; Xue, J.; Li, X.; Zhang, R.; et al. Preparation and Properties of Cyclodextrin Inclusion Complexes of Hyperoside. *Molecules* **2022**, *27*, 2761. [CrossRef]
165. Ibrahim, B.M.M.; Darwish, A.B.; Taleb, S.A.; Mourad, R.M.; Yassen, N.N.; Hessin, A.F.; Gad, S.A.; Mohammed, M.A. Appraisal terpenoids rich Boswellia carterri ethyl acetate extract in binary cyclodextrin oligomer nano complex for improving respiratory distress. *Sci. Rep.* **2024**, *14*, 16779. [CrossRef] [PubMed]
166. Lin, J.; Shi, T.; Wang, Y.; He, Z.; Mu, Z.; Cai, X.; Deng, H.; Shen, J.; Liu, F. Hybrid Hydrogel Loaded with Chlorhexidine⊂β-CD-MSN Composites as Wound Dressing. *Int. J. Nanomed.* **2023**, *18*, 1725–1740. [CrossRef]
167. Rajamohan, R.; Ashokkumar, S.; Murali Krishnan, M.; Murugavel, K.; Murugan, M.; Lee, Y.R. Adenosine/β-Cyclodextrin-Based Metal–Organic Frameworks as a Potential Material for Cancer Therapy. *Biomolecules* **2023**, *13*, 1154. [CrossRef] [PubMed]
168. Yang, J.; Yang, Y. Metal–Organic Frameworks for Biomedical Applications. *Small* **2020**, *16*, 1906846. [CrossRef]
169. Sha, J.-Q.; Zhong, X.-H.; Wu, L.-H.; Liu, G.-D.; Sheng, N. Nontoxic and renewable metal–organic framework based on α-cyclodextrin with efficient drug delivery. *RSC Adv.* **2016**, *6*, 82977–82983. [CrossRef]
170. Rajkumar, T.; Kukkar, D.; Kim, K.-H.; Sohn, J.R.; Deep, A. Cyclodextrin-metal–organic framework (CD-MOF): From synthesis to applications. *J. Ind. Eng. Chem.* **2019**, *72*, 50–66. [CrossRef]
171. Smaldone, R.A.; Forgan, R.S.; Furukawa, H.; Gassensmith, J.J.; Slawin, A.M.Z.; Yaghi, O.M.; Stoddart, J.F. Metal–Organic Frameworks from Edible Natural Products. *Angew. Chem. Int. Ed.* **2010**, *49*, 8630–8634. [CrossRef]
172. Liu, B.; Li, H.; Xu, X.; Li, X.; Lv, N.; Singh, V.; Stoddart, J.F.; York, P.; Xu, X.; Gref, R.; et al. Optimized synthesis and crystalline stability of γ-cyclodextrin metal-organic frameworks for drug adsorption. *Int. J. Pharm.* **2016**, *514*, 212–219. [CrossRef]
173. Hu, X.; Wang, C.; Wang, L.; Liu, Z.; Wu, L.; Zhang, G.; Yu, L.; Ren, X.; York, P.; Sun, L.; et al. Nanoporous CD-MOF particles with uniform and inhalable size for pulmonary delivery of budesonide. *Int. J. Pharm.* **2019**, *564*, 153–161. [CrossRef]
174. Xiong, T.; Guo, T.; He, Y.; Cao, Z.; Xu, H.; Wu, W.; Wu, L.; Zhu, W.; Zhang, J. Lactone Stabilized by Crosslinked Cyclodextrin Metal-Organic Frameworks to Improve Local Bioavailability of Topotecan in Lung Cancer. *Pharmaceutics* **2022**, *15*, 142. [CrossRef]
175. Hou, A.; Li, L.; Huang, Y.; Singh, V.; Zhu, C.; Pan, X.; Quan, G.; Wu, C. Fragmented particles containing octreotide acetate prepared by spray drying technique for dry powder inhalation. *Drug Deliv. Transl. Res.* **2018**, *8*, 693–701. [CrossRef]
176. Yuan, W.; Cai, Y.; Chen, Y.; Hong, X.; Liu, Z. Porous microsphere and its applications. *Int. J. Nanomed.* **2013**, *8*, 1111–1120. [CrossRef] [PubMed]
177. Zhou, Y.; Niu, B.; Wu, B.; Luo, S.; Fu, J.; Zhao, Y.; Quan, G.; Pan, X.; Wu, C. A homogenous nanoporous pulmonary drug delivery system based on metal-organic frameworks with fine aerosolization performance and good compatibility. *Acta Pharm. Sin. B* **2020**, *10*, 2404–2416. [CrossRef]
178. Gao, C.; Liu, C.; Chen, Q.; Wang, Y.; Kwong, C.H.T.; Wang, Q.; Xie, B.; Lee, S.M.Y.; Wang, R. Cyclodextrin-mediated conjugation of macrophage and liposomes for treatment of atherosclerosis. *J. Control. Release* **2022**, *349*, 2–15. [CrossRef] [PubMed]
179. Klyachko, N.L.; Polak, R.; Haney, M.J.; Zhao, Y.; Gomes Neto, R.J.; Hill, M.C.; Kabanov, A.V.; Cohen, R.E.; Rubner, M.F.; Batrakova, E.V. Macrophages with cellular backpacks for targeted drug delivery to the brain. *Biomaterials* **2017**, *140*, 79–87. [CrossRef]
180. Huang, Y.; Tang, H.; Meng, X.; Liu, D.; Liu, Y.; Chen, B.; Zou, Z. γ-Cyclodextrin metal-organic frameworks as the promising carrier for pulmonary delivery of cyclosporine A. *Biomed. Pharmacother.* **2024**, *171*, 116174. [CrossRef] [PubMed]
181. Sun, N.; Zhang, M.; Zhu, W.; Song, P.; Dai, T.; Huang, P.; Han, Z.; Wang, D. Allyl isothiocyanate dry powder inhaler based on cyclodextrin-metal organic frameworks for pulmonary delivery. *iScience* **2023**, *26*, 105910. [CrossRef]
182. Yu, Y.; Wang, J.; Kaul, S.C.; Wadhwa, R.; Miyako, E. Folic Acid Receptor-Mediated Targeting Enhances the Cytotoxicity, Efficacy, and Selectivity of Withania somnifera Leaf Extract: In vitro and in vivo Evidence. *Front. Oncol.* **2019**, *9*, 602. [CrossRef]
183. Pilch, J.; Kowalik, P.; Kowalczyk, A.; Bujak, P.; Kasprzak, A.; Paluszkiewicz, E.; Augustin, E.; Nowicka, A.M. Foliate-Targeting Quantum Dots-β-Cyclodextrin Nanocarrier for Efficient Delivery of Unsymmetrical Bisacridines to Lung and Prostate Cancer Cells. *Int. J. Mol. Sci.* **2022**, *23*, 1261. [CrossRef]
184. Farooq, M.A.; Aquib, M.; Khan, D.H.; Ghayas, S.; Ahsan, A.; Ijaz, M.; Banerjee, P.; Khan, M.A.; Ahmad, M.M.; Wang, B. Nanocarrier-mediated co-delivery systems for lung cancer therapy: Recent developments and prospects. *Environ. Chem. Lett.* **2019**, *17*, 1565–1583. [CrossRef]
185. Wang, Y.; Zhang, H.; Hao, J.; Li, B.; Li, M.; Xiuwen, W. Lung cancer combination therapy: Co-delivery of paclitaxel and doxorubicin by nanostructured lipid carriers for synergistic effect. *Drug Deliv.* **2016**, *23*, 1398–1403. [CrossRef]

186. Salzano, G.; Wankar, J.; Ottani, S.; Villemagne, B.; Baulard, A.R.; Willand, N.; Brodin, P.; Manet, I.; Gref, R. Cyclodextrin-based nanocarriers containing a synergic drug combination: A potential formulation for pulmonary administration of antitubercular drugs. *Int. J. Pharm.* **2017**, *531*, 577–587. [CrossRef]
187. Tang, J.; Zhen, H.; Wang, N.; Yan, Q.; Jing, H.; Jiang, Z. Curdlan oligosaccharides having higher immunostimulatory activity than curdlan in mice treated with cyclophosphamide. *Carbohydr. Polym.* **2019**, *207*, 131–142. [CrossRef]
188. Yunus Basha, R.; Sampath Kumar, T.S.; Doble, M. Dual delivery of tuberculosis drugs via cyclodextrin conjugated curdlan nanoparticles to infected macrophages. *Carbohydr. Polym.* **2019**, *218*, 53–62. [CrossRef] [PubMed]
189. Celi, S.S.; Fernández-García, R.; Afonso-Urich, A.I.; Ballesteros, M.P.; Healy, A.M.; Serrano, D.R. Co-Delivery of a High Dose of Amphotericin B and Itraconazole by Means of a Dry Powder Inhaler Formulation for the Treatment of Severe Fungal Pulmonary Infections. *Pharmaceutics* **2023**, *15*, 2601. [CrossRef]
190. He, Y.; Xiong, T.; He, S.; Sun, H.; Huang, C.; Ren, X.; Wu, L.; Patterson, L.H.; Zhang, J. Pulmonary Targeting Crosslinked Cyclodextrin Metal–Organic Frameworks for Lung Cancer Therapy. *Adv. Funct. Mater.* **2021**, *31*, 2004550. [CrossRef]
191. Wang, F.; Li, Y.; Shen, Y.; Wang, A.; Wang, S.; Xie, T. The Functions and Applications of RGD in Tumor Therapy and Tissue Engineering. *Int. J. Mol. Sci.* **2013**, *14*, 13447–13462. [CrossRef]
192. Paczkowska-Walendowska, M.; Szymańska, E.; Winnicka, K.; Szwajgier, D.; Baranowska-Wójcik, E.; Ruchała, M.A.; Simon, M.; Cielecka-Piontek, J. Cyclodextrin as Functional Carrier in Development of Mucoadhesive Tablets Containing Polygoni cuspidati Extract with Potential for Dental Applications. *Pharmaceutics* **2021**, *13*, 1916. [CrossRef] [PubMed]
193. Chen, L.; Lin, Y.; Zhang, Z.; Yang, R.; Bai, X.; Liu, Z.; Luo, Z.; Zhou, M.; Zhong, Z. A novel dual-prodrug carried by cyclodextrin inclusion complex for the targeting treatment of colon cancer. *J. Nanobiotechnol.* **2021**, *19*, 329. [CrossRef] [PubMed]
194. Jiang, W.; Xiong, Y.; Li, X.; Yang, Y. Cardiac Fibrosis: Cellular Effectors, Molecular Pathways, and Exosomal Roles. *Front. Cardiovasc. Med.* **2021**, *8*, 715258. [CrossRef]
195. Trotta, M.C.; Herman, H.; Ciceu, A.; Mladin, B.; Rosu, M.; Lepre, C.C.; Russo, M.; Bácskay, I.; Fenyvesi, F.; Marfella, R.; et al. Chrysin-based supramolecular cyclodextrin-calixarene drug delivery system: A novel approach for attenuating cardiac fibrosis in chronic diabetes. *Front. Pharmacol.* **2023**, *14*, 1332212. [CrossRef]
196. Wijetunge, S.S.; Wen, J.; Yeh, C.-K.; Sun, Y. Wheat germ agglutinin liposomes with surface grafted cyclodextrins as bioadhesive dual-drug delivery nanocarriers to treat oral cells. *Colloids Surf. B Biointerfaces* **2020**, *185*, 110572. [CrossRef]
197. Esposito, G.; Pesce, M.; Seguella, L.; Sanseverino, W.; Lu, J.; Corpetti, C.; Sarnelli, G. The potential of cannabidiol in the COVID-19 pandemic. *Br. J. Pharmacol.* **2020**, *177*, 4967–4970. [CrossRef] [PubMed]
198. Wang, B.; Kovalchuk, A.; Li, D.; Ilnytskyy, Y.; Kovalchuk, I.; Kovalchuk, O. In Search of Preventative Strategies: Novel Anti-Inflammatory High-CBD Cannabis Sativa Extracts Modulate ACE2 Expression in COVID-19 Gateway Tissues. *Aging* **2020**, *12*, 22425–22444. [CrossRef] [PubMed]
199. Hatziagapiou, K.; Bethanis, K.; Koniari, E.; Christoforides, E.; Nikola, O.; Andreou, A.; Mantzou, A.; Chrousos, G.P.; Kanaka-Gantenbein, C.; Lambrou, G.I. Biophysical Studies and In Vitro Effects of Tumor Cell Lines of Cannabidiol and Its Cyclodextrin Inclusion Complexes. *Pharmaceutics* **2022**, *14*, 706. [CrossRef]
200. Changsan, N.; Sawatdee, S.; Suedee, R.; Chunhachaichana, C.; Srichana, T. Aqueous cannabidiol β-cyclodextrin complexed polymeric micelle nasal spray to attenuate in vitro and ex vivo SARS-CoV-2-induced cytokine storms. *Int. J. Pharm.* **2023**, *640*, 123035. [CrossRef] [PubMed]
201. Koli, U.; Krishnan, R.A.; Pofali, P.; Jain, R.; Dandekar, P. siRNA-Based Therapies for Pulmonary Diseases. *J. Biomed. Nanotechnol.* **2014**, *10*, 1953–1997. [CrossRef]
202. Malhotra, M.; Gooding, M.; Evans, J.C.; O'Driscoll, D.; Darcy, R.; O'Driscoll, C.M. Cyclodextrin-siRNA conjugates as versatile gene silencing agents. *Eur. J. Pharm. Sci.* **2018**, *114*, 30–37. [CrossRef]
203. Singh, R.P.; Hidalgo, T.; Cazade, P.-A.; Darcy, R.; Cronin, M.F.; Dorin, I.; O'Driscoll, C.M.; Thompson, D. Self-Assembled Cationic β-Cyclodextrin Nanostructures for siRNA Delivery. *Mol. Pharm.* **2019**, *16*, 1358–1366. [CrossRef]
204. Liu, X.; Wang, G.; You, Z.; Qian, P.; Chen, H.; Dou, Y.; Wei, Z.; Chen, Y.; Mao, C.; Zhang, J. Inhibition of hypoxia-induced proliferation of pulmonary arterial smooth muscle cells by a mTOR siRNA-loaded cyclodextrin nanovector. *Biomaterials* **2014**, *35*, 4401–4416. [CrossRef]
205. Beute, J.; KleinJan, A. Oral enoximone allows the reduction and discontinuation of inhaled steroids and beta2 agonists in asthmatic children. *Int. J. Pediatr. Adolesc. Med.* **2022**, *9*, 147–151. [CrossRef]
206. Seow, H.C.; Cai, J.-P.; Pan, H.W.; Luo, C.; Wen, K.; Situ, J.; Wang, K.; Cao, H.; Leung, S.W.S.; Yuan, S.; et al. Neutralisation of SARS-CoV-2 by monoclonal antibody through dual targeting powder formulation. *J. Control. Release* **2023**, *358*, 128–141. [CrossRef]
207. Pan, H.W.; Seow, H.C.; Lo, J.C.K.; Guo, J.; Zhu, L.; Leung, S.W.S.; Zhang, C.; Lam, J.K.W. Spray-Dried and Spray-Freeze-Dried Powder Formulations of an Anti-Interleukin-4Rα Antibody for Pulmonary Delivery. *Pharm. Res.* **2022**, *39*, 2291–2304. [CrossRef]
208. Price, D.N.; Kunda, N.K.; Muttil, P. Challenges Associated with the Pulmonary Delivery of Therapeutic Dry Powders for Preclinical Testing. *KONA Powder Part. J.* **2019**, *36*, 129–144. [CrossRef]

209. Fernandes, C.A.; Vanbever, R. Preclinical models for pulmonary drug delivery. *Expert Opin. Drug Deliv.* **2009**, *6*, 1231–1245. [CrossRef] [PubMed]
210. Newman, S.P. Drug Delivery to the lungs: Challenges and Opportunities. *Ther. Deliv.* **2017**, *8*, 647–661. [CrossRef] [PubMed]
211. Schichlein, K.D.; Smith, G.J.; Jaspers, I. Protective effects of inhaled antioxidants against air pollution-induced pathological responses. *Respir. Res.* **2023**, *24*, 187. [CrossRef] [PubMed]

Disclaimer/Publisher's Note: The statements, opinions and data contained in all publications are solely those of the individual author(s) and contributor(s) and not of MDPI and/or the editor(s). MDPI and/or the editor(s) disclaim responsibility for any injury to people or property resulting from any ideas, methods, instructions or products referred to in the content.

antioxidants

Review

Nanotechnological Approaches to Enhance the Potential of α-Lipoic Acid for Application in the Clinic

Chiara Bellini [1,†], Fabrizio Mancin [2], Emanuele Papini [1] and Regina Tavano [1,*]

[1] Department of Biomedical Sciences, University of Padova, Via U. Bassi 58/b, 35121 Padova, Italy; chiara.bellini@ttk.elte.hu (C.B.); emanuele.papini@unipd.it (E.P.)
[2] Department of Chemical Sciences, University of Padova, Via F. Marzolo 1, 35121 Padova, Italy; fabrizio.mancin@unipd.it
* Correspondence: regina.tavano@unipd.it
† Current address: Hevesy György PhD School of Chemistry, Eötvös Loránd University, Pázmány Péter Sétány 1/A, 1117 Budapest, Hungary.

Abstract: α-lipoic acid is a naturally occurring compound with potent antioxidant properties that helps protect cells and tissues from oxidative stress. Its incorporation into nanoplatforms can affect factors like bioavailability, stability, reactivity, and targeted delivery. Nanoformulations of α-lipoic acid can significantly enhance its solubility and absorption, making it more bioavailable. While α-lipoic acid can be prone to degradation in its free form, encapsulation within nanoparticles ensures its stability over time, and its release in a controlled and sustained manner to the targeted tissues and cells. In addition, α-lipoic acid can be combined with other compounds, such as other antioxidants, drugs, or nanomaterials, to create synergistic effects that enhance their overall therapeutic benefits or hinder their potential cytotoxicity. This review outlines the advantages and drawbacks associated with the use of α-lipoic acid, as well as various nanotechnological approaches employed to enhance its therapeutic effectiveness, whether alone or in combination with other bioactive agents. Furthermore, it describes the engineering of α-lipoic acid to produce poly(α-lipoic acid) nanoparticles, which hold promise as an effective drug delivery system.

Keywords: α-lipoic acid; nanoparticles; antioxidant; cytotoxicity; poly(α-lipoic acid)

1. Introduction

1.1. Chemical Structure of α-Lipoic Acid

α-lipoic acid, also known as thioctic acid, is a naturally occurring compound with potent antioxidant properties.

Structurally, it comprises three components: a five-atom dithiolate ring, an alkyl chain, and a terminal carboxylic acid (see Figure 1). The chiral centre at position C6 results in two enantiomers, R(+)-α-lipoic acid, the naturally available form, and S(-)-α-lipoic acid, which can be synthetically obtained [1].

R(+)-α-lipoic acid is generally recognized to exhibit superior activity compared to S(-)-α-lipoic acid [2–6], even as α-lipoic acid is usually marketed as a racemic mixture containing both enantiomers. To date, the extent to which each enantiomer contributes to α-lipoic acid pharmacological and toxicological effects is not fully understood. While it was proposed that S(-)-α-lipoic acid does not exhibit significant biological side effects [1–7], some studies indicated that it could potentially hinder the activity of the R(-)-enantiomer [8–10].

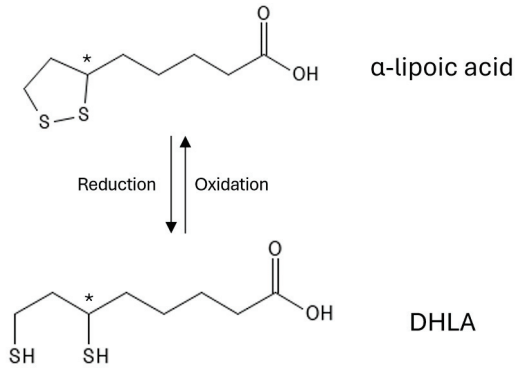


Figure 1. Structure of α-lipoic acid and its reduced form dihydrolipoic acid (DHLA). The asterisk (*) indicates the chiral center of α-lipoic acid and DHLA.

1.2. Antioxidant Activity of α-Lipoic Acid

The sulfur atoms within the α-lipoic acid ring play a crucial role in exerting antioxidant activity. The oxidised form (α-lipoic acid, ALA) and its reduced derivative (dihydrolipoic acid, DHLA) function as a potent redox couple, participating in different aspects of the antioxidant defence system (see Figure 1).

α-lipoic acid exerts its antioxidant activity through multiple mechanisms, including radical scavenging, the regeneration of other antioxidants, metal chelation, and signalling regulation.

ALA and DHLA can neutralise a variety of reactive oxygen species (ROS) and reactive nitrogen species (RNS), thereby reducing oxidative stress and damage. Different mechanisms have been proposed for the free-radical scavenging activity of α-lipoic acid [11]. ALA was suggested to work through a proton-loss electron transfer mechanism, while DHLA exhibits its activity by single electron transfer followed by proton transfer, or hydrogen atom transfer. In the latter, the ideal spacing between the sulfhydryl and carboxylate groups, determined by the optimal length of the alkyl chain, facilitates the efficient trapping of radicals and the transfer of hydrogen atoms [12].

Generally, antioxidants are categorised based on their solubility characteristics. Water-soluble antioxidants like vitamin C are effective in aqueous environments, while hydrophobic antioxidants like vitamin E prefer lipid-rich environments. Due to its amphiphilic nature, α-lipoic acid represents a unique universal antioxidant, exhibiting activity in aqueous and lipid-based environments, thus protecting a wide range of cellular structures and biomolecules.

The capacity of α-lipoic acid to form complexes with redox-active metals presents a dual benefit. On the one hand, it acts as a chelator for heavy metals like mercury, iron, cadmium, lead, and copper, mitigating their toxicity [13–15]. On the other hand, its ability to bind metals, especially gold, has been used to create innovative nanostructures for targeted drug delivery, imaging, and theranostic applications [16].

One distinctive feature of α-lipoic acid is its ability to regenerate the reduced form of either non-enzymatic antioxidants, such as vitamins C and E, glutathione and cysteine, or enzymatic antioxidants, like the coenzyme Q10 [17]. By recycling other antioxidants, α-lipoic acid actively contributes to maintaining the antioxidant network and the cellular redox equilibrium.

Moreover, α-lipoic acid acts as a modulator of proteins involved in cell signalling and transcription through the thiol/disulfide exchange mechanism [18–20]. As a result, it has been proposed to influence different aspects, including cell growth and death regulation, inflammatory responses, and glucose and lipid metabolism.

1.3. α-Lipoic Acid as a Therapeutic Agent

The extensive range of protective mechanisms exhibited by α-lipoic acid has attracted interest regarding its potential use as a therapeutic agent. Specifically, it has gained

particular attention in clinical conditions involving oxidative stress and inflammation, preserving various cell types and organs from oxidative damage.

Due to its role in contributing to cellular energy homeostasis, α-lipoic acid has proven beneficial against insulin resistance, metabolic syndrome, type 2 diabetes, and diabetes-related complications, such as diabetic neuropathy and nephropathy [21–26]. Notably, α-lipoic acid demonstrates nephroprotective effects and holds promise in liver disease prevention due to its rapid hepatic metabolism [27–33]. Several studies have described the cardiovascular benefits of α-lipoic acid administration [34–38]. Moreover, its ability to cross the blood–brain barrier has shown potential in protecting against neurodegenerative diseases, such as multiple sclerosis and Alzheimer's and Parkinson's diseases [39–41]. Also, α-lipoic acid has been suggested to have immunomodulatory activity on both innate and adaptive immune cells, down-regulating the proinflammatory markers and reducing the inflammatory response [11,42]. The topical application of α-lipoic acid has proved effective in skin-related conditions, such as ageing and wound healing, in which its antimicrobial properties may ensure a safe repair of skin damage [11,43–48]. The use of α-lipoic acid was also investigated in cancer research and it was described as having antiproliferative and antimetastatic activity in different cancer models [49–53].

The unique structure of α-lipoic acid not only makes it a versatile antioxidant but also a promising scaffold for derivatization, providing opportunities for the creation of novel therapeutic agents. From a chemical perspective, the dually modifiable structure of α-lipoic acid allows the functionalization of the dithiolane ring and the carboxylic acid. This feature enables the properties and activity of either the ligands or α-lipoic acid itself to be customised.

1.4. Limitations and Drawbacks in the Therapeutic Use of α-Lipoic Acid

While showing diverse beneficial effects, α-lipoic acid and its therapeutic usage exhibit some drawbacks.

α-lipoic acid is mainly administered orally in solid or liquid form. However, the oral administration of α-lipoic acid results in a limited pharmacokinetic profile, characterised by a short half-life, reaching the maximum plasma concentration in approximately 30 min, and reduced bioavailability (about 30%) [54–58]. This drawback becomes especially significant when administering α-lipoic acid as a racemic mixture. In fact, stereochemistry has been proved to notably affect the absorption, distribution, degradation, and elimination of lipoic acid enantiomers. R-(+)-α-lipoic acid has higher bioavailability than the S-(+) enantiomer, potentially because of the different mechanisms of absorption in the gastrointestinal tract [5,8,54–57,59,60]. The suboptimal pharmacokinetics of α-lipoic acid have been attributed to its reduced solubility in water and acidic environments and consequent limited gastric stability, and its high first-pass hepatic metabolism [8]. As a result, it needs appropriate formulation to optimise its therapeutic efficacy when used as a supplement or medication [59,61–63].

While the prolonged use of α-lipoic acid has been demonstrated to be well-tolerated among healthy individuals [64,65] and it is generally considered not toxic [66,67], registered adverse effects have been correlated with the use of high α-lipoic acid doses [68–70], such as gastrointestinal side effects such as stomach discomfort, nausea, or diarrhoea [71]. Moreover, α-lipoic acid at a high dosage negatively affected the liver enzyme activity and induced liver damage in mice and monkeys [66,72]. Also, its supplementation may lower blood sugar levels in genetically predisposed individuals, which can be problematic for diabetic individuals [73]. Finally, α-lipoic acid may interact with certain medications, including chemotherapy drugs, thyroid medications, and drugs that lower blood sugar levels.

Some in vitro and in vivo studies have indicated the pro-oxidant potential of α-lipoic acid, whether in the oxidised form or DHLA [73–75]. The result of this effect with either beneficial or detrimental outcomes depends on the specific physiological circumstances, although the pro-oxidant activity of α-lipoic acid has been associated with cardiovascular, renal, and liver damages [73–75].

From the chemical point of view, α-lipoic acid exhibits high sensitivity to various environmental factors. It gradually polymerizes, increasing the temperature, and forming an elastic compound [76,77]. Moreover, it is photosensitive, and exposure to UV light can impair the hindered dithiolane ring, leading to undesired polymerization [78]. α-lipoic acid is poorly soluble in water, but soluble in organic solvents. However, the drying process has been suggested to impact its stability. Specifically, Brown and Edwards [79] reported that solvents with easily extractable hydrogens or chlorine atoms minimise α-lipoic acid polymerization in solution. Thus, solvent evaporation at high temperatures and under reduced pressure could reduce the stabiliser effect of hydrogen/chlorine atoms.

Limitations and benefits of the use of α-lipoic acid are summarised in Figure 2.

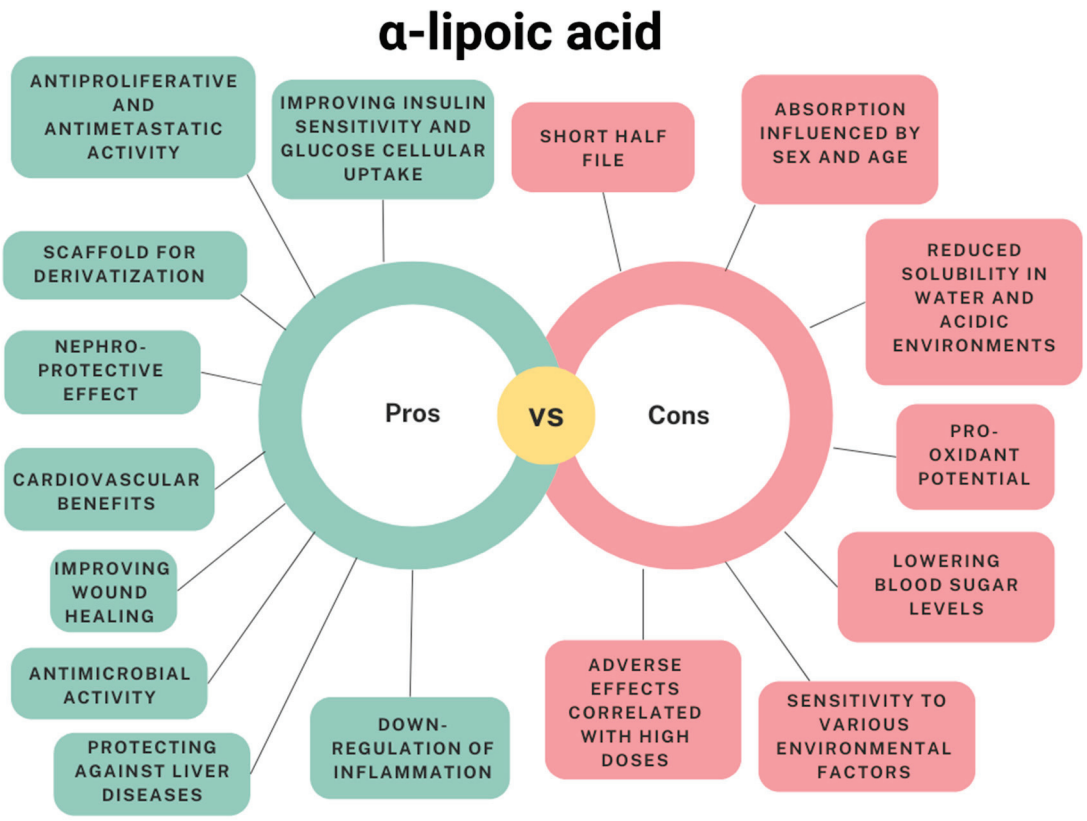


Figure 2. Beneficial aspects and limitations of α-lipoic acid.

1.5. Nanomedicine as a Strategy to Improve α-Lipoic Acid

Nanomedicine, the "application of nanotechnology for treatment, diagnosis, monitoring, and control of biological systems" [80–82], has raised great expectations [83]. Therapeutic and diagnostic nanoagents (nanotheranostics) may improve the pharmaceutical activity while reducing side effects [84], thanks to multiple functionalisations. Moreover, coating with polymers, like polyethylene glycol, reduces the binding of plasma opsonins, making nanoparticles invisible to macrophages' clearance [85–87].

Nanoparticles with antioxidant properties have recently emerged as possible therapeutic agents for controlling neurodegenerative diseases [88] and cardiovascular [89] and pulmonary diseases [90], and in wound healing [91] and the treatment of cancer [92].

This review aims to outline the application of α-lipoic acid to the nanomedicine field and to explore the advantages associated with its inclusion in nanoplatforms. Indeed, this work describes the strategies employed to increase the shelf life of α-lipoic acid through encapsulation in different nanocarriers, as well as studies utilising mixtures of α-lipoic acid and nanoparticles to enhance the biocompatibility or therapeutic activity of

the nanoparticles. Moreover, new frontiers of nanocomposites obtained with poly(α-lipoic acid) will be discussed.

2. Enhancement of α-Lipoic Acid Properties and Activity When Encapsulated in Nanoparticles

As described in the introduction, the primary challenges associated with the use of α-lipoic acid are its short half-life, limited bioavailability, and poor solubility. This section describes several strategies employed to address these drawbacks and improve α-lipoic acid properties by encapsulating the free molecule into different nanotechnological platforms [93]. The delivery systems established are visualised in Figure 3, while Table 1, at the end of this section, summarises the nanotechnological strategies described throughout the text.

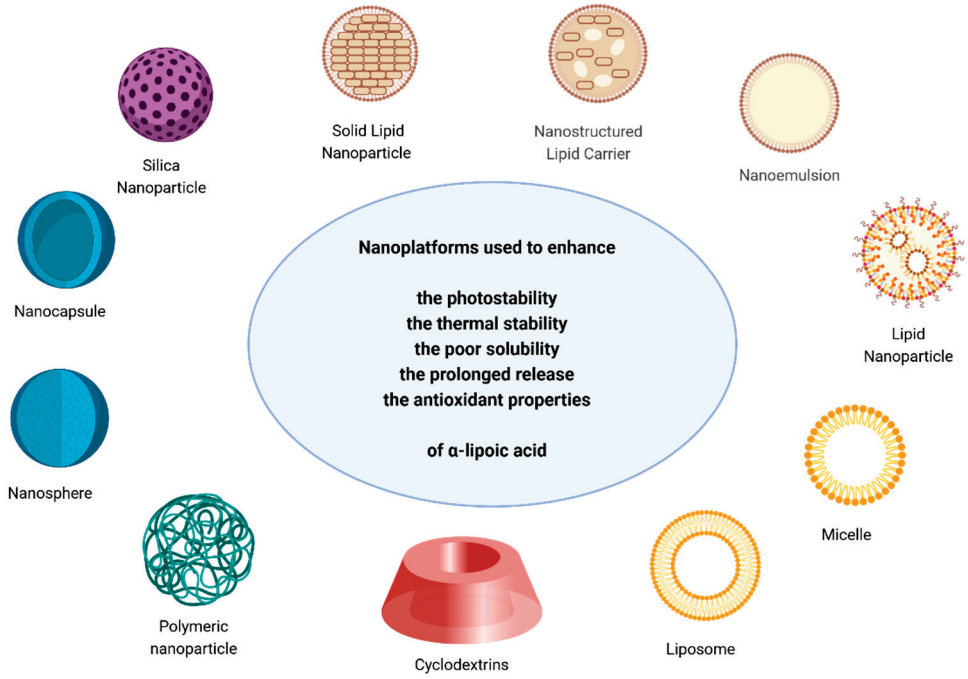


Figure 3. The different nanoplatforms used to encapsulate α-lipoic acid. Created with BioRender.com (accessed on 3 June 2024).

2.1. Silica Nanoparticles

Silica nanoparticles represent suitable candidates to overcome several challenges faced by bioactive compounds, including hydrolysis, solubility concerns, and susceptibility to light and heat degradation [92].

To enhance the α-lipoic acid photo- and thermal stability, Dolinina et al. synthesised novel mesoporous silica-based nanocomposites using the widely applied sol–gel method [93]. Two different final products were proposed for α-lipoic acid thermal- and photodegradation, namely polymeric α-lipoic acid and DHLA, respectively. α-lipoic acid was stabilised by the interaction with the silica matrices through H-bonds and electrostatic and hydrophobic forces. As a result, its thermal degradation decreased when compared to the free molecule. As regards UV-induced degradation, the photodegradation rates were comparable to the free α-lipoic acid. The authors suggested that the significant amount of water contained in the nanocomposites, being a suitable hydrogen atom source, favoured the formation of DHLA. Also, the stability of the nanocomposites and the release of α-lipoic acid was investigated, mimicking the pH of digestive fluids. The silica-based composites displayed a release behaviour close to the zero-order kinetic, sustained a plasma concentration of α-lipoic acid comparable to clinically available oral formulations, and preserved its antioxidant activity at all pH values for up to 24 h [94].

2.2. Lipid-Based Nanoparticles (Lipid Carriers, Solid Lipid Nanoparticles, Nanoemulsions, Liposomes, Micelles)

Encapsulation into lipid nanoparticles can overcome the poor solubility of compounds in aqueous media, and their susceptibility to degradation when exposed to oxygen in water. Moreover, lipid nanoparticles have been shown to sustain the release of different drugs, increasing the therapeutic effect and bioavailability and enhancing their biocompatibility.

Platforms belonging to this category include nanostructured lipid carriers, solid lipid nanoparticles, nanoemulsions, liposomes, lipid nanocapsules, and micelles. They are composed of lipids comprising fatty acids, fatty alcohols, glycerides, and waxes, along with stabilising agents like surfactants or polymeric coatings [95].

While solid lipid nanoparticles are formed from solid lipids stabilised by surfactants, nanostructured lipid carriers include both solid and liquid lipids in their matrix. They represent the next generation lipid nanoparticles, designed to overcome the limitations of conventional colloidal carriers, like emulsions, liposomes, and polymeric nanoparticles [96,97].

Indeed, when α-lipoic acid was formulated into nanostructured lipid carriers, solid lipid nanoparticles, and nanoemulsions, the former two displayed a prolonged release of α-lipoic acid compared to nanoemulsions. They also proved high entrapment efficiency and stability over time, and exhibited antioxidant activity comparable to pure α-lipoic acid [98].

Conjugation with stearylamine was used to stabilise α-lipoic acid and synthesise solid lipid nanoparticles, and was then investigated as a delivery system for the chemotherapeutic tamoxifen. The formulation was proved to stabilise α-lipoic acid, which exerted its antioxidant activity, restoring the antioxidant protein network. Moreover, it efficiently enhanced the bioavailability of tamoxifen [99]. Also, solid lipid nanoparticles, co-delivering docetaxel and α-lipoic acid, were demonstrated to have enhanced efficacy against murine mammary carcinoma cells and human breast adenocarcinoma cells. The nanoformulation containing the chemotherapeutic agent and the antioxidant molecule showed increasing cytotoxic effects and significantly higher uptake efficiency compared to free drugs or single drug-loaded solid lipid nanoparticles [100].

Wang et al. synthesised nanostructured lipid carriers using the biodegradable components phosphatidylcholine, stearic acid, oleic acid, and glyceryl monostearate, with the aim of incorporating α-lipoic acid and improving its stability and solubility. The authors found that the obtained lipid carriers were not cytotoxic in vitro, retained α-lipoic acid, and released it within 72 h [101].

Phosphatidylcholine was also employed in the formulation of both nanoemulsions and liposomes containing α-lipoic acid. While both nanosystems efficiently entrapped α-lipoic acid, nanoemulsions exhibited a slower release of α-lipoic acid compared to phosphatidylcholine liposomes. The authors proposed that the slower release from nanoemulsions could be attributed to their multiple-layer structure, whereas liposomes, being primarily single-layered particles, facilitated a faster release. Thus, nanoemulsions might represent a more suitable formulation for α-lipoic acid, prolonging the drug's action [102].

Different oil-in-water nanoemulsions were also investigated for the co-delivery of α-lipoic acid and vitamin B. Specifically, the influence of using different oils (castor oil and sunflower oil) and agitation methods on the properties of the obtained emulsions was evaluated, including metrics of colloidal stability, encapsulation efficiency and drug release. The formulation prepared by the widely applied solvent displacement method and using castor oil under magnetic stirring resulted in the best colloidal properties, highest thermal and pH stability, and higher encapsulation and release rates [103]. In another study, pumpkin oil was used to solubilize α-lipoic acid and develop a self-nanoemulsifying drug delivery system, stabilised by Tween 80 polyethylene glycol 200. The formulation demonstrates higher protective effects against gastric ulcer models compared to the free α-lipoic acid [104].

Phophatidylcholine-based liposomes were prepared to improve the stability and absorption of α-lipoic acid. The formulation proved to be stable, enhanced the oral absorption and bioavailability of α-lipoic acid, and improved hepatoprotection in hepatic injury model rats [105]. Other authors have synthesised new liposomes, consisting of phosphatidylcholine and curcumin, in which α-lipoic acid has been encapsulated; using these liposomes, they demonstrated a high encapsulation efficiency of lipoic acid and its slow release, which countered cisplatin-induced toxicity in HEI-OC1 cells, a cell line utilised as a model for auditory cells [106].

Polymers can be used to stabilise different platforms, including emulsions, liposomes, and micelles. Huang et al. developed an advance system for preparing a multilayer emulsion. A primary oil-in-water emulsion, stabilised by Tween 20 and phosphatidylcholine, was used to encapsulate α-lipoic acid and linseed oil. Subsequently, a chitosan coating was applied to improve the thermostability of the oil droplets and to address the limited capacity of emulsions to counteract oxidative stress, which could potentially affect the stability of both encapsulated molecules. The system demonstrated a higher thermal stability than the primary emulsion and limited lipolysis of linseed oil in vivo, and inhibited the degradation of α-lipoic acid [107]. The use of a chitosan coating also proved efficient in stabilising liposomes co-encapsulating α-lipoic acid and Coenzyme Q10 with the purpose of improving the solubility and stability of both molecules for transdermal application. It was found that chitosan interacted with α-lipoic acid and Coenzyme Q10 via H-bonds and ionic forces, promoting the permeation and accumulation of both molecules in rabbit skin. Moreover, the system demonstrated higher scavenging activity compared to free α-lipoic acid and Coenzyme Q10 [108]. α-lipoic acid was also incorporated into micelles composed of a copolymer (methoxypoly(ethylene glycol) and poly(caprolactone)). This incorporation led to an enhanced loading capacity of the micelles for IR780, a near-infrared dye for imaging and photothermal therapy, while also preserving their loading capacity for docetaxel, a chemotherapeutic agent [109]. Pluronic nanoparticles were prepared by the oil-in-water emulsion method, encapsulating α-lipoic acid into a soybean oil core and using Pluronic F127 to form the hydrophilic shell. When administered in the mouse middle ear cavity, the system was demonstrated to preserve hearing ability after ototoxicity induction, and could be delivered in a more effective way with respect to free α-lipoic acid [110].

2.3. Nanocapsules and Nanospheres

Nanocapsules are composed of a polymeric shell surrounding an oily core, in which the drug may either dissolve within the core or adhere to the polymeric wall. In contrast, nanospheres lack an oily component and instead constitute a polymeric matrix, in which the drug can be uniformly distributed or adsorbed.

α-lipoic acid was encapsulated in lipid-core nanocapsules with triglycerides of capric and caprylic acid, sorbitan monostearate, and poly (ε-caprolactone) as main components, and stabilised by polysorbate 80. The encapsulation counteracted α-lipoic acid's undesired pro-oxidant activity, and contributed to the wound healing process, although to a lesser extent than lipoic acid alone [43]. Also, Xia et al. encapsulated α-lipoic acid into lipid nanocapsules containing triglycerides of capric and caprylic acids and phosphatidylcholine as a surfactant. The capsules proved to be stable and have high encapsulation efficiency and drug loading. Moreover, antioxidant activity remained intact within the nanocapsules, and sustained release of α-lipoic acid was achieved [111]. Interestingly, a dual stabilising effect of α-lipoic acid and the antioxidant resveratrol was observed when co-encapsulated into lipid-core nanocapsules. The co-encapsulation was shown to enhance the stability, photostability, and antioxidant properties of both compounds. When α-lipoic acid was encapsulated alone, it exhibited rapid release, consistent with previous findings [112]; however, when co-encapsulated with resveratrol, the release rates of both compounds decreased [113].

Nishiura et al. exploited the self-assembly properties of α-lipoic acid, along with the non-ionic surfactant polyoxyethylene (20) stearylether, to create a nanosphere matrix

encapsulating α-lipoic acid. The encapsulation improved the stability and bioavailability of α-lipoic acid by placing its hydrophobic moiety inside the nanocapsule, thereby protecting the unstable disulfide bond from degradation [77]. The same method was used to encapsulate α-lipoic acid and test its antitumor effects in a mouse model of Ehrlich solid tumour. Both free and encapsulated α-lipoic acid significantly reduced oxidative stress, but encapsulated α-lipoic acid remained stable and in circulation for longer periods of time [114]. Also, EL-Gebaly et al.'s approach was used to investigate the beneficial effects of encapsulated α-lipoic acid against 99mTc-MIBI-induced injury, showing significant protective effects and suggesting its efficacy as a radioprotector [115]. Kubota and collaborators used a similar approach by mixing α-lipoic acid with the polyoxyethylene (20) stearylether to improve its skin permeation. The results confirmed that nanoencapsulation is a suitable method for the efficient topical administration of α-lipoic acid [116].

2.4. Polymeric Nanoparticles

Natural polymers have frequently been used to develop biodegradable and biocompatible delivery systems.

Gogoi et al. co-loaded α-lipoic acid and curcumin into chitosan nanoparticles to improve the limited solubility and bioavailability of both drugs. They investigated the in vitro activity of the nanosystem in a breast cancer cell model, highlighting the synergistic activity of curcumin and α-lipoic acid in inhibiting tumour cell growth and inducing tumour cell death [117]. Also, the bioavailability and stability of α-lipoic acid formulated into chitosan nanoparticles and solid lipid nanoparticles was compared [118]. Both systems encapsulated α-lipoic acid effectively, demonstrated high stability, and counteracted the oxidative stress and neurotoxicity induced by aluminium chloride in rats. However, as expected, the effect was superior when α-lipoic acid was loaded into solid lipid nanoparticles compared to chitosan nanoparticles.

To improve its skin delivery, α-lipoic acid was loaded into liquid crystalline nanoparticles. The surface of the platform was modified by lipopolymers composed of Polyethylene glycol (PEG) and 1,2-dioleoyl-sn-glycero-3-phosphoethanolamine, and functionalized with the epidermal growth-factor-receptor-targeting D4 peptide, and the HIV-1-derived TAT cell-penetrating peptide. The system demonstrated a high drug encapsulation rate and released the α-lipoic acid into the deepest layers of the epidermis, where it counteracted the oxidative stress and inflammation after exposure to UVB light [119].

The use of α-lipoic acid is also interesting in suppressing appetite. Traditional formulations (salt or micronized crystals) had poor absorption and a short plasma half-life, not sufficient to suppress appetite. Park and collaborators introduce a novel α-lipoic acid nanoparticulate formulation developed through nano-comminution, employing different polymeric stabilisers (hydroxypropyl cellulose, Pluronic® F127, and polyvinylpyrrolidone). Interestingly, they found that nanoparticle powder formulations, when compared to nanosuspension formulations, were endowed with an improved efficacy in reducing food intake [120].

2.5. Cyclodextrins

Cyclodextrins (CDs) are cyclic oligosaccharides derived from the enzymatic degradation of starch which typically comprise six (α-), seven (β-), or eight (γ-) glucose units linked through α-1,4 glycosidic bonds. They have a toroidal-like shape characterised by a hydrophilic outer surface and a more hydrophobic central cavity. This distinctive arrangement enables them to interact with molecules of appropriate size and geometry, and form complexes with the entire molecule or part of it. They are frequently used as excipients in pharmaceutical formulations to increase the aqueous solubility of poorly soluble active substances, improving the stability and bioavailability of drugs [121–123].

α-lipoic acid has been proven to be complexed by α-, β-, and γ-CDs [124,125], and in particular the R-(+)-α-lipoic acid complex with γ-CD exhibited biocompatibility and stability towards heat, humidity, and low pH [76]. γ-CD significantly improved the

bioavailability of R-(+)-α-lipoic acid in rats by enhancing its intestinal absorption [126]. As a result, the R-(+)-α-lipoic acid/γ-CD complex exhibited a 2.2 times higher plasma concentration compared to free α-lipoic acid, after oral administration. This evidence was confirmed by a recent clinical trial in healthy volunteers, where the bioavailability of the R-(+)-α-lipoic acid/γ-CD complex demonstrated results 2.5 higher than the non-complexed R-(+)-α-lipoic acid [127].

Table 1. Nanotechnological strategies used to improve α-lipoic acid characteristics and efficacy.

Nanoplatform	Goal	Reference
Silica nanoparticles	Stabilise	[93,94]
Lipid-based nanoparticles	Prolong the release	[98,100–103,106,108,110]
	Stabilise	[99,103,107,110]
	Improve solubility	[104]
	Improve bioavailability	[105]
	Improve antioxidant activity	[108]
Nanocapsules and nanospheres	Counteract pro-oxidant activity	[43]
	Preserve antioxidant activity	[111]
	Improve the stability	[114]
	Prolong the release	[111,113,114]
Polymeric nanoparticle	Improve the solubility and bioavailability	[118–120]
	Improve the release	[120]
Cyclodextrins	Improve the stability and bioavailability	[76,126,127]

3. Exploring the Role of α-Lipoic Acid in Therapeutic Nanoplatforms

α-lipoic acid has been studied in numerous works in combination with several types of nanoparticles. The formulations have been shown to enhance either the effects of nanoparticles or α-lipoic acid antioxidant properties, both in cellular systems and in mouse models of different pathologies.

3.1. Renewing Tissues: Nanoparticles and α-Lipoic Acid in Regenerative Medicine

The application of nanotechnology to non-healing wounds aims to facilitate healing and tissue repair and avoid complications like infections.

The potential benefits of therapies based on a mixture of nanoparticles and antioxidant agents on tissue regeneration have been demonstrated by Leu et al. The topical application of a mixture containing gold nanoparticles, the antioxidant epigallocatechin gallate, and α-lipoic acid significantly enhanced the proliferation and migration of skin cells and accelerated wound healing in mice [128]. The same combination was also investigated in the treatment of diabetic ulcers, reducing the expression of the receptor for advanced glycation end-products, enhancing angiogenesis, and exerting anti-inflammatory effects [129].

Moreover, wound healing was improved by the treatment with α-lipoic acid conjugated with hexagonal boron nitride and boron carbide nanoparticles, exhibiting regenerative and antioxidant properties. α-lipoic acid has also been demonstrated to improve the antimicrobial properties of boron nitride and boron carbide nanoparticles against *Staphylococcus aureus* and *Escherichia coli* strains [130].

Finally, α-lipoic acid-capped silver nanoparticles introduced into alginate-based aerogels demonstrated improved biological properties, including higher antioxidant capacity and anti-inflammatory activity, compared to a commercial dressing made of alginate containing colloidal silver [131].

3.2. Exploring the Use of α-Lipoic Acid-Containing Nanoparticles in Tumour Fighting

In cancer nanomedicine, α-lipoic acid has found application in three primary aspects: (1) the exploitation of its intrinsic antitumor activity when nanoformulated; (2) the development of tumour environment-responsive nanoparticles, taking advantage of the characteristics of its disulfide bond; (3) its action as a linker to enhance the binding strength of tumour-targeting ligands on the surface of nanoparticles.

As reviewed elsewhere, α-lipoic acid has different powerful effects against cancer cells, such as inducing apoptosis and suppressing proliferation, and cancer stemness. Moreover, it shows potential in mitigating chemotherapy-induced side-effects and overcoming chemoresistance [49,132].

α-lipoic acid can be nanoformulated and investigated for its potential effects against tumour cells. For example, Usama et al. proposed the synergistic activity of α-lipoic acid with simvastatin, a statin with direct cytotoxic activity against different types of tumour cells. The synthesised α-lipoic acid-simvastatin nanoparticles demonstrated a significant increase in the cellular uptake and cytotoxicity of the statin in breast carcinoma cells [133].

The disulfide bond of α-lipoic acid can be exploited to prepare stimuli-responsive nanoparticles, specifically systems that respond to the reducing environment found in tumour cells. In fact, it is well known that the concentration of glutathione in its reduced form (GSH) is significantly higher in cancer cells, and it can trigger the reduction of the α-lipoic acid dithiolane ring, facilitating the release of the chemotherapeutics.

For example, α-lipoic acid was esterified to phosphatidylcholine to produce stimuli-responsive cross-linked liposomes for the intracellular delivery of doxorubicin. The system demonstrated a high serum stability and reduced-responsive drug release, resulting in an in vitro anticancer activity comparable to the free doxorubicin. Moreover, the liposomal formulation improved the pharmacokinetic profile of doxorubicin, which was maintained in the blood circulation for a longer time [134]. Also, α-lipoic acid was conjugated to a tocopheryl moiety to produce stimuli-responsive nanovesicles designed for the delivery of doxorubicin. The nanovesicles efficiently encapsulated doxorubicin, and released it in a glutathione-responsive manner. Moreover, the system proved to be biocompatible and to have an anticancer activity superior to doxorubicin alone in drug-resistant cancer cells [135]. Also, α-lipoic acid was conjugated to xylan to produce redox-sensitive nanoparticles aimed to deliver the anticancer drug niclosamide. The platform exhibited good stability and biocompatibility as well as higher anticancer activity compared to the free drug [136].

Additionally, dual targeting delivery systems have been developed, combining the stimuli-responsive behaviour of α-lipoic acid and other tumour-specific targets or tumour-specific environmental conditions (see Table 2). In this category, several works exploit the concept of charge-reversible nanoplatforms, capable of adjusting their surface charge according to the surrounding environment [137]. They exhibit either a negative or a neutral charge under physiological pH conditions to prevent adsorption to serum proteins that can induce opsonization, complement activation, and rapid clearance. To achieve this feature, specific functional groups, such as the imidazole moiety and maleic anhydride [138–141], or coatings like polyethylene glycol, have been introduced [138,141,142]. Consequently, charge-reversible nanosystems exhibit enhanced plasma stability and can accumulate in tumour tissues. Once it has reached the tumour microenvironment, the acidic pH triggers the charge switch and the positively charged surface facilitates the cellular internalisation of the delivery platform.

In other works, tumour-specific ligands were introduced to improve the targeting of the delivery systems, such as binders of the tumour-overexpressed receptors [138,143–148].

After internalisation, drug release was achieved by the activity of high glutathione intracellular concentration on α-lipoic acid.

Table 2. α-lipoic acid-based dual responsive drug delivery systems in cancer treatment.

Tumour Target	Molecule	Nanoplatform	Goal	Reference
Acidic pH and Overexpressed ASGPR *	Dimethylmaleic acid—PEG and lactobionic acid	Polymeric nanoparticle	Delivery of Doxorubicin	[138]
Overexpressed ASGPR and folate receptor	Pullulan and folic acid	Polymeric nanoparticle	Delivery of Paclitaxel	[148]
Overexpressed folate receptor	Folic acid	Silica hybrid Magnetic nanoparticles	Delivery of Doxorubicin	[143]
Acidic pH	Histidine	Polymeric nanoparticle	Delivery of Doxorubicin	[139]
	Dimethylmaleic anhydride	Polymeric nanoparticle	Delivery of Doxorubicin	[140]
	Histidine—PEG	Liposomes	Delivery of VEGF *** siRNA and Etoposide	[141]
	PEG	Albumin-based nanocarrier	Delivery of Doxorubicin	[142]
CD44 receptor overexpression	Hyaluronic acid	Polymeric nanoparticle	Delivery 17α-Methyltestosterone	[134]
	Hyaluronic acid	Polymeric nanoparticle	Delivery of Doxorubicin	[135]
Tumour esterase overexpression	Chlorambucil	Polymeric nanoparticle	Delivery of Doxorubicin and Chlorambucil	[136]
αvβ3 receptor overexpression	cRGD peptide **	Micelle	Delivery of Doxorubicin	[137]

* asialoglycoprotein receptor; ** cyclic arginyl-glycyl-aspartic acid peptide; *** vascular endothelial growth factor.

Thiols are commonly used as ligands for attaching drugs to the surface of nanoparticles, such as gold nanoparticles. Using linkers with multiple thiols, such as α-lipoic acid, increases the binding strength between the nanoparticles' surface and the ligands. Also, α-lipoic acid's carboxylic group can be directly functionalised with chemotherapeutics, spacers, and tumour-specific targets. The following works, mainly focused on the functionalisation of gold nanoparticles, describe the use of α-lipoic acid for these purposes. Ghorbani et al. used α-lipoic acid as a linker to attach curcumin to the surface of Fe_3O_4, resulting in a novel, particularly potent medicinal compound with increased cytotoxicity compared to curcumin alone [149]. Also, promising antimetastatic activity was shown by linking a tumour-associated carbohydrate antigen to gold nanoparticles through an analogue of α-lipoic acid, the iso-α-lipoic acid. Moreover, the advantage of having an achiral linker as iso-α-lipoic acid lies in the simplified design, synthesis, and characterisation of the nanosystem [150]. α-lipoic acid was used to link folic acid and doxorubicin to the surface of gold nanoparticles to obtain a targeted delivery system for the chemotherapeutic drug. The approach resulted in enhanced cell penetration and the prolonged release of doxorubicin [151]. α-lipoic acid was used in the development of gold tumour-targeting nanoparticles capable of responding to the acidic intracellular environment and aggregating to amplify nanoparticle retention within tumour cells. Specifically, in the work of Cheng, α-lipoic acid was used to link a biotin-end-derived PEG moiety to the gold surface. As a result, the nanoplatform exhibited stealth properties and active targeting ability [152]. A similar approach was used to conjugate doxorubicin and anti-PD-L1 antibody on the gold nanoparticle surface, through an α-lipoic acid-PEG-*N*-hydroxysuccinimide linker. The thiol groups of α-lipoic acid interacted with the gold surface, while it formed an amide bond with the *N*-hydroxysuccinimide moiety binding the cancer-targeting ligands [153].

Wang and collaborators modified star poly(lactic-co-glycolic acid) ends with α-lipoic acid to obtain a new nanoparticle with enhanced loading capacity, reduced drug leakage, and efficient uptake in melanoma cells [154,155].

3.3. Exploring Miscellaneous Applications of Nanoparticles and α-Lipoic Acid

The combination of α-lipoic with nanomaterials, including metal and polymeric nanoparticles, was also investigated in other therapeutic areas.

Indeed, Tudose et al. covalently immobilised α-lipoic acid onto the surface of silver nanoparticles–decorated silica nanoparticles, and they evaluated the antioxidant, cytotoxic, and antimicrobial activities of these new nanoparticles. They found that the functionalisation of silver nanoparticles–decorated silica nanoparticles with α-lipoic acid enhanced the specificity of the interaction with mammalian cell lines and antioxidant activity, while reducing cytotoxicity, suggesting its potential for modulating the cell cycle to achieve desired therapeutic effects [156].

The mixture of α-lipoic acid with gold nanoparticles showed a superior neuroprotective effect compared to each compound alone in vivo, with the inhibition of brain damage induced by radiation in rats [157]. The combination of α-lipoic acid with PEGylated gold nanoparticles proved to counteract oxidative stress in osteoporosis development. α-lipoic acid-gold nanoparticles were biocompatible, and effectively removed reactive oxygen species and promoted osteoblast proliferation [158].

The impact of α-lipoic acid in combination with caffeine-loaded chitosan nanoparticles was evaluated against obesity and its hepatic and renal complications in rats. The treatment was shown to mitigate weight gain and improve hepatic and renal function, reducing biochemical markers and histopathological alterations [159]. The same nanosystem was also tested for its ability to mitigate cardiovascular complications induced by obesity in rats. Treatment with α-lipoic acid and caffeine-loaded chitosan nanoparticles alleviated cardiac complications and the cardioprotective effect of the combined treatment, was more evident than that of the two agents used individually [160]. A nanosphere matrix made of zein (a water-insoluble plant protein derived from maize) and α-lipoic acid was employed to encapsulate Vardenafil, a medication used for the treatment of erectile dysfunction [161]. α-lipoic acid has indeed previously been shown to significantly improve sexual function and quality of life in both animals and human investigations [162]. In the work of Ahmed [161], α-lipoic acid was stabilised by the interaction with the zein polymer; moreover, the bioavailability, delivery, and effects of Vardenafil were improved thanks to the nanoformulation.

4. Protective Role of α-Lipoic Acid against Nanoparticle Cytotoxicity

Different studies have shown that α-lipoic acid can inhibit the intrinsic cytotoxicity of various types of nanoparticles. Two strategies have been used by researchers: on one hand, directly conjugating α-lipoic acid to the surface of the nanoparticle, and on the other hand, mixing α-lipoic acid with the nanoparticles before application. Using α-lipoic acid in conjunction with various types of nanoparticles has been demonstrated to limit many of the cytotoxic effects induced by the nanoparticles themselves (see Figure 4).

4.1. α-Lipoic Acid and Silver Nanoparticle Cytotoxicity

As is already known, silver nanoparticles possess potent antimicrobial activity, but they can exert cytotoxic effects [163,164]. Hajtuch et al., comparing uncoated silver nanoparticles with α-lipoic acid silver nanoparticles, found that silver nanoparticles coated with α-lipoic acid maintained their antimicrobial properties, while improving their biosafety. In fact, α-lipoic acid silver nanoparticles were found to be biocompatible with Huvec cells, red blood cells, and platelets [165]. Also, Cotton and collaborators mitigated silver nanoparticles' toxic effects by capping them with α-lipoic acid. The protective effect of α-lipoic acid was investigated on human gingival fibroblasts in comparison to ionic silver and clinical antiseptics (chlorhexidine and silver diamine fluoride). The authors found that α-lipoic acid-capped silver nanoparticles exhibited notably lower toxicity than the clinically utilised controls, while keeping their antimicrobial properties intact [166]. In another study, the damage induced on rat testes by silver nanoparticles was attenuated by mixing them with α-lipoic acid [167]. The authors demonstrated that the co-treatment mitigated the

biochemical, oxidative, and apoptotic changes induced by silver nanoparticles. These kinds of nanoparticles, when administered, can damage the blood–brain barrier function and induce neurotoxicity; the co-treatment with α-lipoic acid was demonstrated to be favourable in ameliorating the neurotoxic side effects of silver nanoparticles by reducing the induced apoptosis, inflammation, and oxidative stress [168]. The co-treatment with α-lipoic acid and silver nanoparticles was also used to mitigate adverse effects of these nanoparticles in the treatment of pancreatic ductal adenocarcinoma. α-lipoic acid, in fact, reduced the production of reactive oxygen species (ROS) induced by the silver nanoparticles themselves, protecting non-malignant cells from oxidative stress [169].

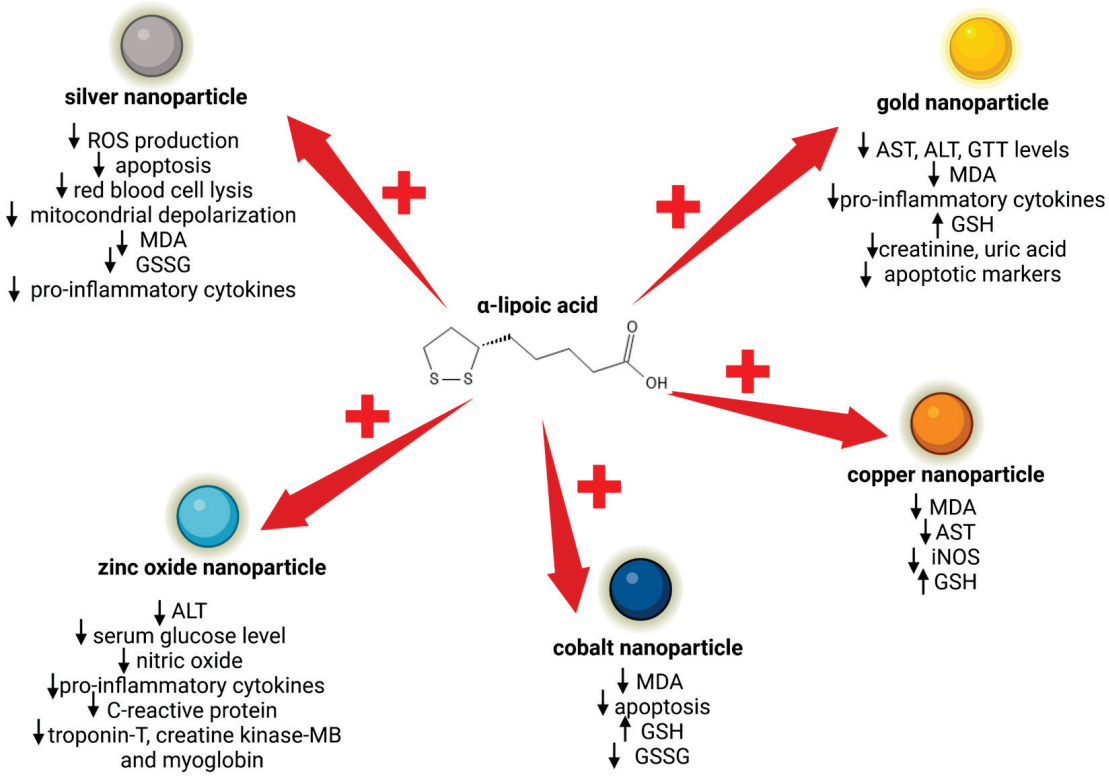


Figure 4. The impact of α-lipoic acid on mitigating the cytotoxic effects induced by various metal nanoparticles. ALT: alanine aminotransferase; AST: aspartate transaminase; MDA: malondialdehyde; GSSG: glutathione disulfide; GSH: glutathione; iNOS: inducible nitric oxide synthase. Created with BioRender.com (accessed on 3 June 2024).

4.2. α-Lipoic Acid and Gold Nanoparticle Renal and Hepatic Toxicity

Exposure to gold nanoparticles can induce hepatic oxidative damage and toxicities; it has been shown that the co-administration of α-lipoic acid with gold nanoparticles has protective effects, suppressing oxidative stress and inflammation [170]. Gold nanoparticles can also have nephrotoxic effects: α-lipoic acid has been demonstrated to reduce nanoparticle kidney damage, suggesting that combining natural antioxidants with gold nanoparticles may offer a potential strategy to prevent nanoparticle-induced toxicity [170–172].

4.3. α-Lipoic Acid and the Inhibition of Toxicity Induced by Other Types of Nanoparticles

α-lipoic acid exhibited hepatoprotective functions against zinc oxide nanoparticle toxicity, decreasing liver damage and the expression of metabolic disorder markers, which were up-regulated by the treatment with zinc oxide nanoparticles [173]. The co-administration of α-lipoic acid also significantly mitigated the cardiotoxic effects of zinc oxide nanoparticles by reducing serum cardiac injury markers, pro-inflammatory biomarkers, nitric oxide, and vascular endothelial growth factor levels, as well as cardiac calcium concentration and oxidative DNA damage, indicating its potential as s protective agent against ZnO-NP-

induced cardiac tissue injury [174]. Moreover, α-lipoic acid displayed a therapeutic role after the exposure to lead and zinc oxide nanoparticles, attenuating the biochemical alterations in neurological, immunological, and male reproductive organs of rats, suggesting its potential as a protective agent against their adverse effects [175]. Cobalt nanoparticles can be generated from cobalt-containing implants and they can induce ferroptosis-like cell death through, among other things, increasing intracellular reactive oxygen species. Cobalt nanoparticle adverse effects have been mitigated by the co-administration of α-lipoic acid, which effectively counteracts the adverse effects induced by CoNPs, thus stabilising the cell's antioxidant capacity and preventing ferroptosis-like cell death [176]. α-lipoic acid was also shown to be a promising hepatoprotective agent against copper-nanoparticle-induced oxidative damage; its administration mitigated hepatic damage, maintaining an antioxidant status [177].

5. Poly(α-Lipoic Acid)-Based Polymeric Nanoparticles: Insights and Perspectives

The 1,2-dithiolane ring contained in α-lipoic acid can undergo ring-opening polymerization (ROP) to produce poly(disulfide)s [178]. ROP [179] is the approach most used to propagate α-lipoic acid polymerization and obtain its cross-linking. ROP can be achieved by using different methods: elevated temperatures, photo-initiated radical polymerization, and thiolate compounds (see Figure 5).

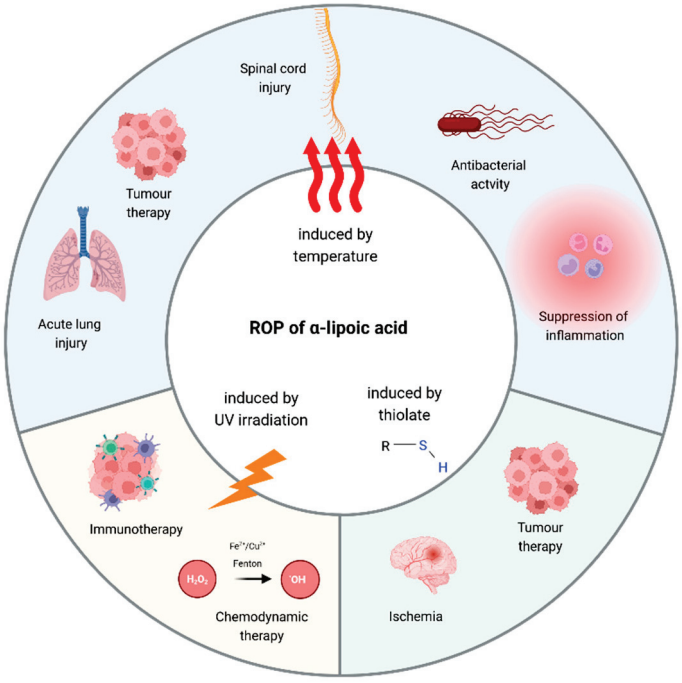


Figure 5. ROP of α-lipoic acid can be obtained thanks to three different strategies; by temperature, by irradiation, and by thiolate initiation. All these protocols were used to prepare poly(α-lipoic acid) nanoparticles, which were then tested for their abilities to fight various pathologies or pathological environments, and to enhance different types of therapies. Created with BioRender.com (accessed on 3 June 2024).

All these approaches have been used to produce nanoparticles based on the polymerization of α-lipoic acid.

It is interesting to note how heat and light are often listed as factors that destabilise α-lipoic acid (see Introduction), but if used properly, they are good alternatives for achieving polymerization. On the other hand, ROP initiated using a thiolate monomer represents a promising approach due to the mild conditions it requires and the better control of the polymerization process [180]. The advantages and limitations of each strategy are summarised in Table 3.

Table 3. Advantages and limitations of the most common methods used to synthesise poly(α-lipoic acid) nanoparticles [181].

Method	Mechanism	Advantages	Limitations
Thermal polymerization	Free radical polymerization	• Solvent-free bulk conditions • Rapid above the melting point	• Potential degradation • Uncontrollable (often results in a mixture of poly(α-lipoic acid) and cyclic monomers)
Thiolate-initiated polymerization	Thiol–disulfide exchange	• Mild conditions • Controllable (homogeneity) • Rapid	• Stability of the thiolate initiator • Control of temperature and light exposure
Photo-initiated polymerization	Free radical polymerization	• Mild conditions	• Potential degradation • Uncontrollable (often results in a mixture of poly(α-lipoic acid) and cyclic monomers)

5.1. Poly(α-Lipoic Acid) Nanoparticles Obtained by Thermal Polymerization

Poly(α-lipoic acid) nanoparticles, synthesised via thermal polymerization, were employed alongside various drugs to augment their anticancer efficacy. The general method applied in the studies outlined in this section involves polymerizing α-lipoic acid at a temperature above its melting point, then utilising the resulting poly(α-lipoic acid) to create the desired nanoparticles.

For instance, Yang et al. synthesised a PEGylated poly(α-lipoic acid) copolymer and assembled it into nanoparticles in aqueous solution. The nanoparticles showed the ability to load doxorubicin with high efficiency, and the doxorubicin-loaded nanoparticles were efficiently internalised in 4T1 cancer cells, where doxorubicin was released, displaying its antiproliferation ability. Moreover, these nanoparticles exhibited improved antitumoral efficacy in a mouse model, while causing fewer toxic effects on healthy organs [182]. The same nanoparticles were co-loaded with paclitaxel and doxorubicin and both were studied in a cellular and an animal model for osteosarcoma. The authors found that the dual-drug-loaded nanoparticles were effectively taken up by osteosarcoma cells, releasing drugs intracellularly in response to an acidic pH and the reductive environment of cancer cells. Moreover, the co-loaded nanoparticles exhibited improved biodistribution into the tumour in mice, resulting in a more effective inhibition of tumour growth compared to free drugs [183]. A similar strategy was used to develop pH-responsive nanovesicles from a PEGylated poly(α-lipoic acid) copolymer to deliver the chemotherapeutics doxorubicin and gefitinib for the treatment of ovarian cancer. The drugs were efficiently encapsulated and released intracellularly in a pH-responsive manner, inducing the apoptosis of cancer cells [184]. Liu and collaborators conjugated poly(α-lipoic) nanoparticles to combretastatin A4, a potent vascular disrupting agent, resulting in a specific accumulation of combretastatin A4 in tumour cells and in a prolonged apoptosis of cancer cells because of its long retention time [185]. Also, they used the same approach with the cytotoxic drug honokiol and another vascular disrupting agent, 5,6-dimethylxanthenone-4-acetic acid, obtaining a nanoparticle with high antitumor potency against a murine model of breast tumour [186].

Poly(α-lipoic acid) nanoparticles obtained thanks to elevated temperatures were also tested for their potential ability to treat spinal cord injury. The antibiotic minocycline was encapsulated in polymeric nanoparticles, and loaded with methylprednisolone, a drug used to inhibit inflammation after traumatic spinal cord injury. The combined nanoparticle was biocompatible and exhibited a potent anti-inflammatory activity, able to inhibit proinflammatory cytokine release in a microglia cell line treated with LPS [187].

The encapsulation of Venetoclax, a Bcl2 inhibitor, in polymeric nanoparticles has been demonstrated to enhance its effects when administered freely. It inhibits the production of pro-inflammatory cytokines in a murine model of lung injury by inducing the apoptosis of infiltrated neutrophils [188]. Also, the antioxidant properties of the natural compound quercetin were enhanced through encapsulation in polymeric nanoparticles. This encapsulation favoured its chemical stability and slow release, and the antioxidants properties of encapsulated quercetin have been shown to be improved with respect to its crystalline form in a rat model of acute liver injury [189].

Rhein (an anthraquinone with anti-inflammatory activity) and geraniol (a bioactive compound) were loaded onto poly(α-lipoic acid) acid nanoparticles, showing an enhanced antimicrobial activity against *Salmonella* infection, compared with free drugs. Additionally, co-loaded nanoparticles were also able to suppress the production of pro-inflammatory cytokines and to maintain the gut microbiota homeostasis [190]. With the aim of tackling *Salmonella* infection, characterised by the production of high levels of H_2S, PEGylated α-lipoic acid was thermally polymerized and polymeric nanoparticles were loaded with the antibiotic compound ciprofloxacin. The nanoplatform, besides demonstrating excellent stability in vitro and biocompatibility toward mammalian cells, selectively delivered the antibiotic to the inflammation site, thus improving its efficacy [191].

5.2. Poly(α-Lipoic Acid) Nanoparticles Obtained by Thiolate-Initiated Polymerization

Matile and colleagues examined the reactivity of cyclic disulfides in disulfide-exchange polymerization. They concluded that α-lipoic acid's disulfide bond length and the torsion angle of the thiolane ring exhibited the optimal reactivity to achieve optimal and controlled polymerization [192]. In most of the studies detailed in this paragraph, the process begins with the formation of nanoparticles containing α-lipoic acid, followed by the induction of polymerization using a thiolate initiator to yield poly(α-lipoic acid) nanoparticles.

Cross-linked α-lipoic acid nanocapsules using 1,4-dithiothreitol (DTT) thiolate have been employed to encapsulate two precursors of combretastatin (a compound displaying strong inhibitory activity on tumour cell growth) and a copper catalyst. Encapsulation ensured that the prodrug was not prematurely activated. Within the tumour tissue, the high concentration of GSH induces the breakdown of poly(α-lipoic acid) nanoparticles, releasing prodrugs and catalysts and inducing the death of only tumour cells [193]. The polymerization of α-lipoic acid was used to project nanoparticles based on a conjugate of lipoic acid and hyaluronic acid; these cross-linked nanoparticles were used to encapsulate and then deliver doxorubicin specifically to breast cancer and myeloma and leukaemia cells [194]. DTT was also used to induce the polymerization of α-lipoic acid contained in a dimeric surfactant-like amphiphilic molecule: this molecule can form nanoaggregates, due to the hydrophobic head of α-lipoic acid and the hydrophilic tail of gemini surfactant. Nanoaggregates were then stabilised thanks to α-lipoic acid polymerization and loaded with doxorubicin: the nanonetwork was selectively cytotoxic against cancer cells with respect to normal cells [195].

Mancin and collaborators showed that α-lipoic acid polymerization could be realised through a single-step synthesis using 1-octanethiol as initiator, producing cross-linked poly(α-lipoic acid) nanoparticles loaded with dye and protected by PEG directly from small molecule precursors [196]. Interestingly, they conducted a comparison on the long-term stability of nanoparticles synthesised with a thiolate initiator versus those formed without any initiators. The results highlighted that nanoparticles produced through thiol-initiated ROP resulted in the formation of more rigid and stable nanoparticles. Also, α-lipoic acid preserved its antioxidant activity within the nanoformulation, demonstrating in vitro efficacy in mitigating damages caused by post-ischemic reperfusion [197]. The potential of these nanoparticles as cardiomyocyte-targeted drug was validated in rats, revealing their specific accumulation in the heart without inducing any toxicity in cardiomyocytes. Furthermore, the nanoparticles were tested in vitro as a delivery system for nucleic acids

in cardiomyocytes, demonstrating their ability to enter this specific cell type and release their cargo in the perinuclear area [198].

Conversely to the previous works described in this section, Gu et al. first induced the polymerization of α-lipoic acid using cysteine hydrochloride, and then prepared poly(α-lipoic acid) nanoparticles through ultrasonic emulsification. The newly obtained nanoplatform was employed for the delivery of docetaxel, demonstrating specific drug targeting in cancer cells and preventing unspecific drug release [199].

5.3. Poly(α-Lipoic Acid) Nanoparticles Obtained by UV light

In the case of irradiation-induced polymerization, as well, the majority of studies first involve the synthesis of nanoparticles containing α-lipoic acid, followed by its polymerization.

A new pH-responsive nanodrug based on a form of camptothecin (an inhibitor of topoisomerase) was loaded into cross-linked R(+)-α-lipoic acid nanoparticles, enhancing the anticancer activity of camptothecin, stabilising the drug, and achieving a higher drug concentration in the HT29 tumour cells [200].

UV cross-linked R(+)-α-lipoic acid nanoparticles were used to anchor quaternary ammonium salts provided with long alkyl chains, which have the ability to destabilise cell membranes. Their link to α-lipoic acid nanoparticles ensured that their activity occurs only within the cell, following the dissolution of the nanocontainer due to the cytosolic redox environment. As a result, they exerted a selective cytotoxic activity only to the tumour environment [201].

Two α-lipoic acid monomers were modified, one with a disulfide Zn-coordinated dipicolylamine analogue, known to boost protein transfection efficiency, and the other with a guanidinium side chain, mimicking the structure of cell-penetrating peptides. The modified monomers were then polymerized by irradiation, and the new compound showed enhanced delivery efficacy for nucleic acids compared to commercial transfection reagents, demonstrating potential for both gene therapy and immunotherapy applications [202].

Chemodynamic therapy is a kind of therapy based on inducing high concentrations of hydroxyl radical (one of the most toxic radicals) from hydrogen peroxide through the Fenton or Fenton-like reaction which can be catalysed by iron-containing compounds. The high concentration of hydroxyl ions in turn induces lipid peroxidation and consequent cell death through ferroptosis. This type of therapy is highly specific but requires high concentrations of iron, which is toxic to non-tumour cells [203]. With the aim of specifically delivering iron into tumour cells, an iron-doped cross-linked α-lipoic acid nano-aggregate was developed. Inside the tumour cells the new nanocompound was able to self-supply H_2O_2 and accelerate Fe^{3+}/Fe^{2+} conversion, thus increasing ROS levels [204]. For the same purpose, UV cross-linked α-lipoic acid nanoparticles were utilised to anchor copper, which can catalyse the Fenton reaction even at neutral or slightly acidic pH levels. By conjugating copper to α-lipoic acid nanoparticles, the authors achieved a nanoplatform capable of consuming less copper, facilitated by the ability of dihydrolipoic acid to reduce Cu^{2+} to Cu^{+}, thus maintaining the production of hydroxyl radicals for a longer period compared to iron [205].

In another study, PSMA (prostate-specific membrane antigen) was cross-linked to poly α-lipoic acid nanoparticles, with a *trans*-cyclooctene functionalized lysine linker also added. In this way, the authors obtained a nanoplatform specific for prostate cancer cells, with pro-apoptotic activity given by the α-lipoic acid's ability to inhibit Bcl2 and equipped with pre-targeting for tetrazine (which can selectively conjugate with *trans*-cyclooctene), thus enabling radiotherapy, suggesting a promising therapeutic approach for metastatic castration-resistant prostate cancer [206].

Poly(α-lipoic acid) nanoparticles were also employed to load indole-3-methanol, a natural compound capable of activating Phosphatase and tensin homolog (PTEN). PTEN is a well-known tumour suppressor, whose expression is found to be three times lower in triple-negative breast cancer cells. The designed nanoplatform delivered indole-3-methanol

to tumour cells, where its PTEN-activating ability was enhanced by the co-presence of α-lipoic acid, leading to the specific apoptosis of tumour cells [207].

Interestingly enough, the polymerization of α-lipoic acid induced by irradiation has also been used to stabilise and finely control the size of gold nanoparticles. In this case, Cely-Pinto and co-authors first induced the polymerization of α-lipoic acid through irradiation; then, they mixed poly(α-lipoic acid) with tetralone (a photoinitiator for gold reduction) and $HAuCl_4$, and irradiated the solution again; this way, they obtained stabilised gold nanoparticles with a diameter of 20–40 nm [208].

5.4. Harnessing Poly(α-Lipoic Acid) in Hydrogel Engineering

Hydrogels are three-dimensional networks of hydrophilic polymers capable of retaining large amounts of water within their structure. These materials exhibit a unique combination of properties, including high water content, softness, and flexibility, resembling natural tissues [209,210]. Hydrogels can be synthesised from a variety of polymers, including α-lipoic acid.

For example, both a coenzyme salt polymer (poly(sodium α-lipoate)) and a poly(α-lipoic acid) were incorporated in an elastomer adhesive patch. The patch had hydrogen bonding cross-links between poly(α-lipoic acid) and poly(sodium α-lipoate), which prevented poly(α-lipoic acid) depolymerization. This design enabled the sustainable delivery of bioactive α-lipoic acid and provided durable adhesion to oral mucosal wounds due to the adhesive action of poly(sodium α-lipoate). In mouse and mini-pig models of oral ulcers, the adhesive patch showed promising therapeutic effects. In fact, it accelerated ulcer healing by regulating the inflammatory environment of damaged tissue, maintaining oral microbiota stability, and promoting faster re-epithelialization and angiogenesis, showing promising therapeutic properties for treating oral ulcers [211]. Qi et al. projected an elastic patch made of methacrylated gelatin in combination with a poly(α-lipoic acid). Also, in this case, the crosslinking between poly(α-lipoic acid) and the methacrylated gelatin prevented poly(α-lipoic acid) depolymerization and slowed down its dissociation in water, enabling durable adhesion to oral periodontal tissue and the continuous release of bioactive small molecules in periodontitis wounds [212]. Hydrogels of poly(α-lipoic acid-*co*-sodium lipoate) were obtained by inducing the polymerization of the α-lipoic acid by heating in the presence of sodium bicarbonate. These green hydrogels maintained the ROS scavenging ability and they have been demonstrated to reduce inflammation in a rat spinal injury model, promoting the functional recovery of the spinal cord [213]. Hydrogels comprising poly(α-lipoic acid) and poly(ethylene glycol) were utilised as drug delivery vehicles to encapsulate doxorubicin, which was shown to be selectively released within the tumour microenvironment due to the presence of disulfide bonds in the hydrogel and the reducing conditions found in the tumour [214]. Additionally, a multifunctional supramolecular polymer hydrogel was engineered by merging gold nanostars with insulin through the ring-opening polymerization of α-lipoic acid. This hydrogel demonstrated the capacity to expedite the healing process of diabetic wounds infected by *S. aureus*, showcasing remarkable antibacterial efficacy under near-infrared irradiation (attributed to gold nanostars) and redox balance regulation (attributed to α-lipoic acid) [215].

Pluronic F127 has gained attention in the development of wound healing hydrogel due to the possibility of easily adjusting the phase transition temperature. In fact, F127 undergoes a sol–gel thermo-reversible transition within the range of room temperature to physiological temperatures. However, F127 hydrogel rapidly dissolves in physiological conditions, thereby limiting their efficacy. The functionalization of the copolymer was investigated as a strategy to target this drawback.

For instance, the thiol/disulfide exchange reaction was employed to produce an injectable self-healing cross-linked hydrogel. α-lipoic acid-functionalized PEG reacted with thiol-modified F127 to form a dynamic thermoresponsive hydrogel with a rapid sol–gel transition ability at body temperature [216]. Also, α-lipoic acid was linked to Pluronic F127, resulting in a co-polymer that self-assembled in micelles. Subsequently, the hydrogel

formation was obtained by the photo-induced cross-linking of α-lipoic acid. The hydrogel exhibited biocompatibility, optimal mechanical properties, and temperature-dependent swelling properties, and provided the release of bovine serum albumin in a reducing environment [217]. A similar approach was used by Wang et al., who conjugated α-lipoic acid to Pluronic F127 to create an injectable tissue-adhesive hydrogel. The exposure of the hydrophobic dithiolane ring of α-lipoic acid facilitated the formation of bigger micelles compared to F127 alone, promoting the hydrophobic aggregation. Moreover, α-lipoic acid was used to enhance the biocompatibility by preventing the potential toxicity of the aldehyde groups of F127. The micelles were combined with Ce^{3+}/tannic acid/ulinastatin nanoparticles with LPS- and ROS-scavenging activity to obtain a wound-healing-promoting hydrogel. The nanohydrogel demonstrated excellent injectability and tissue adherence at physiological temperatures. Moreover, upon UV irradiation, the initially semisolid hydrogel solidified, providing tight tissue adherence. The application of the nanohydrogel on wounds suppressed inflammation and facilitated the healing process [218]. Eventually, an injectable hydrogel with near-infrared, antioxidant, and antiinflammatory properties was developed, incorporating α-lipoic acid-modified palladium nanoparticles into a sodium alginate hydrogel crosslinked with calcium ions [219].

6. Conclusions and Future Perspectives

α-lipoic acid has been extensively studied as a dietary supplement, with a current high impact and growing market. Moreover, it has been investigated in different therapeutic contexts, showing encouraging outcomes in both preclinical and clinical studies.

However, α-lipoic acid use has faced challenges, such as sensitivity to external factors, instability, and poor bioavailability, which affect its pharmacokinetic and pharmacological profile. Nevertheless, certain fundamental aspects are still debated and poorly understood, such as the impact of each enantiomer in the therapeutic activity and the paradoxical pro-oxidant activity despite its being a well-established antioxidant. Thus, additional investigation should be undertaken to elucidate these issues.

Nanotechnology has emerged as a promising strategy to target these limitations and offers the possibility of an efficient formulation of α-lipoic acid. Furthermore, α-lipoic acid represents a promising scaffold for derivatisation and is used in the design of delivery nanoplatforms for different drugs and therapeutic areas. This review highlights numerous ways in which research on α-lipoic acid and nanotechnology has sought to address some of the challenges encountered when working with this compound. Although nanotechnological platforms incorporating α-lipoic acid have shown promise, many studies have focused solely on investigating the effects of nanoformulated α-lipoic acid at low concentrations or short exposure times, not considering the side effects observed with prolonged exposure to α-lipoic acid alone. Furthermore, the potential long-term side effects of the materials used to encapsulate α-lipoic acid (such as surfactants and copolymers) have often not been considered, and few studies provide data on the pharmacokinetic and pharmacodynamic properties of the new nanoplatforms. Further data also need to be obtained regarding the chemical degradation of the new nanoplatforms once in circulation and how they are eliminated from the body. Finally, many studies have been conducted using cellular models, while few studies utilise disease models in small animals, highlighting the need for further studies, including clinical trials testing nanoformulations of α-lipoic acid, to validate their effectiveness as formulations and delivery systems for α-lipoic acid.

Author Contributions: All authors contributed to the writing of this article. All authors have read and agreed to the published version of the manuscript.

Funding: This research was funded by the EU—NRRP Next Generation EU—Mission 4, Component C2, Investment 1.4, project CN00000041 "National Center for Gene Therapy and Drugs based on RNA Technology".

Acknowledgments: We thank Giulio Fracasso for the critical reading of the manuscript.

Conflicts of Interest: The authors declare no conflicts of interest.

References

1. Wang, J.-Q.; Ling, X.; Wang, H.-J.; Chen, F.-E. α-Lipoic Acid Chemistry: The Past 70 Years. *RSC Adv.* **2023**, *13*, 36346–36363. [CrossRef] [PubMed]
2. Liu, Q.; Li, W.; Huang, S.; Zhao, L.; Zhang, J.; Ji, C.; Ma, Q. R- Is Superior to S-Form of α-Lipoic Acid in Anti-Inflammatory and Antioxidant Effects in Laying Hens. *Antioxidants* **2022**, *11*, 1530. [CrossRef] [PubMed]
3. Lechner, S.; Steimbach, R.R.; Wang, L.; Deline, M.L.; Chang, Y.-C.; Fromme, T.; Klingenspor, M.; Matthias, P.; Miller, A.K.; Médard, G.; et al. Chemoproteomic Target Deconvolution Reveals Histone Deacetylases as Targets of (R)-Lipoic Acid. *Nat. Commun.* **2023**, *14*, 3548. [CrossRef] [PubMed]
4. Pacini, A.; Tomassoni, D.; Trallori, E.; Micheli, L.; Amenta, F.; Ghelardini, C.; Di Cesare Mannelli, L.; Traini, E. Comparative Assessment of the Activity of Racemic and Dextrorotatory Forms of Thioctic (Alpha-Lipoic) Acid in Low Back Pain: Preclinical Results and Clinical Evidences From an Open Randomized Trial. *Front. Pharmacol.* **2021**, *12*, 607572. [CrossRef] [PubMed]
5. Uchida, R.; Okamoto, H.; Ikuta, N.; Terao, K.; Hirota, T. Investigation of Enantioselective Membrane Permeability of α-Lipoic Acid in Caco-2 and MDCKII Cell. *Int. J. Mol. Sci.* **2016**, *17*, 155. [CrossRef] [PubMed]
6. Smith, J.R.; Thiagaraj, H.V.; Seaver, B.; Parker, K.K. Differential Activity of Lipoic Acid Enantiomers in Cell Culture. *J. Herb. Pharmacother.* **2005**, *5*, 43–54. [CrossRef] [PubMed]
7. Shay, K.P.; Moreau, R.F.; Smith, E.J.; Smith, A.R.; Hagen, T.M. Alpha-Lipoic Acid as a Dietary Supplement: Molecular Mechanisms and Therapeutic Potential. *Biochim. Biophys. Acta (BBA) Gen. Subj.* **2009**, *1790*, 1149–1160. [CrossRef] [PubMed]
8. Salehi, B.; Berkay Yılmaz, Y.; Antika, G.; Boyunegmez Tumer, T.; Fawzi Mahomoodally, M.; Lobine, D.; Akram, M.; Riaz, M.; Capanoglu, E.; Sharopov, F.; et al. Insights on the Use of α-Lipoic Acid for Therapeutic Purposes. *Biomolecules* **2019**, *9*, 356. [CrossRef]
9. Amenta, F.; Buccioni, M.; Ben, D.D.; Lambertucci, C.; Navia, A.M.; Ngouadjeu Ngnintedem, M.A.; Ricciutelli, M.; Spinaci, A.; Volpini, R.; Marucci, G. Ex-Vivo Absorption Study of Lysine R-Lipoate Salt, a New Pharmaceutical Form of R-ALA. *Eur. J. Pharm. Sci.* **2018**, *118*, 200–207. [CrossRef]
10. Lucarini, E.; Trallori, E.; Tomassoni, D.; Amenta, F.; Ghelardini, C.; Pacini, A.; Di Cesare Mannelli, L. Toxicological Profile of the Pain-Relieving Antioxidant Compound Thioctic Acid in Its Racemic and Enantiomeric Forms. *Antioxidants* **2020**, *9*, 749. [CrossRef]
11. Tripathi, A.K.; Ray, A.K.; Mishra, S.K.; Bishen, S.M.; Mishra, H.; Khurana, A. Molecular and Therapeutic Insights of Alpha-Lipoic Acid as a Potential Molecule for Disease Prevention. *Rev. Bras. Farmacogn.* **2023**, *33*, 272–287. [CrossRef] [PubMed]
12. Castañeda-Arriaga, R.; Alvarez-Idaboy, J.R. Lipoic Acid and Dihydrolipoic Acid. A Comprehensive Theoretical Study of Their Antioxidant Activity Supported by Available Experimental Kinetic Data. *J. Chem. Inf. Model.* **2014**, *54*, 1642–1652. [CrossRef] [PubMed]
13. Bjørklund, G.; Aaseth, J.; Crisponi, G.; Rahman, M.; Chirumbolo, S. Insights on Alpha Lipoic and Dihydrolipoic Acids as Promising Scavengers of Oxidative Stress and Possible Chelators in Mercury Toxicology. *J. Inorg. Biochem.* **2019**, *195*, 111–119. [CrossRef]
14. Gurer, H.; Ozgunes, H.; Oztezcan, S.; Ercal, N. Antioxidant Role of α-Lipoic Acid in Lead Toxicity. *Free Radic. Biol. Med.* **1999**, *27*, 75–81. [CrossRef]
15. Ou, P.; Tritschler, H.J.; Wolff, S.P. Thioctic (Lipoic) Acid: A Therapeutic Metal-Chelating Antioxidant? *Biochem. Pharmacol.* **1995**, *50*, 123–126. [CrossRef] [PubMed]
16. Koufaki, M.; Detsi, A.; Kiziridi, C. Multifunctional Lipoic Acid Conjugates. *CMC* **2009**, *16*, 4728–4742. [CrossRef] [PubMed]
17. Gorąca, A.; Huk-Kolega, H.; Piechota, A.; Kleniewska, P.; Ciejka, E.; Skibska, B. Lipoic Acid—Biological Activity and Therapeutic Potential. *Pharmacol. Rep.* **2011**, *63*, 849–858. [CrossRef]
18. Packer, L.; Cadenas, E. Lipoic Acid: Energy Metabolism and Redox Regulation of Transcription and Cell Signaling. *J. Clin. Biochem. Nutr.* **2010**, *48*, 26–32. [CrossRef]
19. Smith, A.R.; Shenvi, S.V.; Widlansky, M.; Suh, J.H.; Hagen, T.M. Lipoic Acid as a Potential Therapy for Chronic Diseases Associated with Oxidative Stress. *Curr. Med. Chem.* **2004**, *11*, 1135–1146. [CrossRef]
20. Tibullo, D.; Li Volti, G.; Giallongo, C.; Grasso, S.; Tomassoni, D.; Anfuso, C.D.; Lupo, G.; Amenta, F.; Avola, R.; Bramanti, V. Biochemical and Clinical Relevance of Alpha Lipoic Acid: Antioxidant and Anti-Inflammatory Activity, Molecular Pathways and Therapeutic Potential. *Inflamm. Res.* **2017**, *66*, 947–959. [CrossRef]
21. Namazi, N.; Larijani, B.; Azadbakht, L. Alpha-Lipoic Acid Supplement in Obesity Treatment: A Systematic Review and Meta-Analysis of Clinical Trials. *Clin. Nutr.* **2018**, *37*, 419–428. [CrossRef] [PubMed]
22. Bobe, G.; Michels, A.J.; Zhang, W.-J.; Purnell, J.Q.; Woffendin, C.; Pereira, C.; Vita, J.A.; Thomas, N.O.; Traber, M.G.; Frei, B.; et al. A Randomized Controlled Trial of Long-Term (R)-α-Lipoic Acid Supplementation Promotes Weight Loss in Overweight or Obese Adults without Altering Baseline Elevated Plasma Triglyceride Concentrations. *J. Nutr.* **2020**, *150*, 2336–2345. [CrossRef] [PubMed]
23. Golbidi, S.; Badran, M.; Laher, I. Diabetes and Alpha Lipoic Acid. *Front. Pharmacol.* **2011**, *2*, 69. [CrossRef]
24. Ziegler, D. Pathogenetic Treatments for Diabetic Peripheral Neuropathy. *Diabetes Res. Clin. Pract.* **2023**, *206*, 110764. [CrossRef] [PubMed]

25. Derosa, G.; D'Angelo, A.; Romano, D.; Maffioli, P. A Clinical Trial about a Food Supplement Containing α-Lipoic Acid on Oxidative Stress Markers in Type 2 Diabetic Patients. *Int. J. Mol. Sci.* **2016**, *17*, 1802. [CrossRef] [PubMed]
26. Capece, U.; Moffa, S.; Improta, I.; Di Giuseppe, G.; Nista, E.C.; Cefalo, C.M.A.; Cinti, F.; Pontecorvi, A.; Gasbarrini, A.; Giaccari, A.; et al. Alpha-Lipoic Acid and Glucose Metabolism: A Comprehensive Update on Biochemical and Therapeutic Features. *Nutrients* **2022**, *15*, 18. [CrossRef] [PubMed]
27. Kamt, S.F.; Liu, J.; Yan, L.-J. Renal-Protective Roles of Lipoic Acid in Kidney Disease. *Nutrients* **2023**, *15*, 1732. [CrossRef]
28. Basu, P.P.; Shah, N.J.; Aloysius, M.M.; Brown, R.S., Jr. Effect of Vitamin E and Alpha Lipoic Acid in Nonalcoholic Fatty Liver Disease: A Randomized, Placebo-Controlled, Open-Label, Prospective Clinical Trial (VAIN Trial). *OJGas* **2014**, *4*, 199–207. [CrossRef]
29. Kaya-Dagistanli, F.; Tanriverdi, G.; Altinok, A.; Ozyazgan, S.; Ozturk, M. The Effects of Alpha Lipoic Acid on Liver Cells Damages and Apoptosis Induced by Polyunsaturated Fatty Acids. *Food Chem. Toxicol.* **2013**, *53*, 84–93. [CrossRef]
30. Longhitano, L.; Distefano, A.; Musso, N.; Bonacci, P.; Orlando, L.; Giallongo, S.; Tibullo, D.; Denaro, S.; Lazzarino, G.; Ferrigno, J.; et al. (+)-Lipoic Acid Reduces Mitochondrial Unfolded Protein Response and Attenuates Oxidative Stress and Aging in an in Vitro Model of Non-Alcoholic Fatty Liver Disease. *J. Transl. Med.* **2024**, *22*, 82. [CrossRef]
31. Uskoković, A.; Dinić, S.; Jovanović, J.A.; Poznanović, G.; Vidaković, M.; Mihailović, M. Liver Diseases: Epigenetic Mechanisms, Oxidative Stress and Use of Alpha-Lipoic Acid. In *Handbook of Nutrition, Diet, and Epigenetics*; Patel, V., Preedy, V., Eds.; Springer International Publishing: Cham, Switzerland, 2018; pp. 1–21. ISBN 978-3-319-31143-2.
32. Bustamante, J. α-Lipoic Acid in Liver Metabolism and Disease. *Free Radic. Biol. Med.* **1998**, *24*, 1023–1039. [CrossRef] [PubMed]
33. El-Maadawy, W.; Hammam, O.; Seif el-Din, S.; El-Lakkany, N. α-Lipoic Acid Modulates Liver Fibrosis: A Cross Talk between TGF-B1, Autophagy, and Apoptosis. *Hum. Exp. Toxicol.* **2020**, *39*, 440–450. [CrossRef] [PubMed]
34. Hu, Q.-F.; Sun, A.-J. Cardioprotective Effect of Alpha-Lipoic Acid and Its Mechanisms. *Cardiol. Plus* **2020**, *5*, 109–117. [CrossRef]
35. Wollin, S.D.; Jones, P.J.H. α-Lipoic Acid and Cardiovascular Disease. *J. Nutr.* **2003**, *133*, 3327–3330. [CrossRef] [PubMed]
36. Skibska, B.; Goraca, A. The Protective Effect of Lipoic Acid on Selected Cardiovascular Diseases Caused by Age-Related Oxidative Stress. *Oxidative Med. Cell. Longev.* **2015**, *2015*, 313021. [CrossRef] [PubMed]
37. Hajizadeh-Sharafabad, F.; Sharifi Zahabi, E. Role of Alpha-Lipoic Acid in Vascular Function: A Systematic Review of Human Intervention Studies. *Crit. Rev. Food Sci. Nutr.* **2022**, *62*, 2928–2941. [CrossRef] [PubMed]
38. Rochette, L.; Ghibu, S. Mechanics Insights of Alpha-Lipoic Acid against Cardiovascular Diseases during COVID-19 Infection. *Int. J. Mol. Sci.* **2021**, *22*, 7979. [CrossRef] [PubMed]
39. Khan, H.; Singh, T.G.; Dahiya, R.S.; Abdel-Daim, M.M. α-Lipoic Acid, an Organosulfur Biomolecule a Novel Therapeutic Agent for Neurodegenerative Disorders: An Mechanistic Perspective. *Neurochem. Res.* **2022**, *47*, 1853–1864. [CrossRef] [PubMed]
40. Kaur, D.; Behl, T.; Sehgal, A.; Singh, S.; Sharma, N.; Chigurupati, S.; Alhowail, A.; Abdeen, A.; Ibrahim, S.F.; Vargas-De-La-Cruz, C.; et al. Decrypting the Potential Role of α-Lipoic Acid in Alzheimer's Disease. *Life Sci.* **2021**, *284*, 119899. [CrossRef]
41. Xie, H.; Yang, X.; Cao, Y.; Long, X.; Shang, H.; Jia, Z. Role of Lipoic Acid in Multiple Sclerosis. *CNS Neurosci. Ther.* **2022**, *28*, 319–331. [CrossRef]
42. Liu, W.; Shi, L.; Li, S. The Immunomodulatory Effect of Alpha-Lipoic Acid in Autoimmune Diseases. *BioMed Res. Int.* **2019**, *2019*, 1–11. [CrossRef] [PubMed]
43. Külkamp-Guerreiro, I.C.; Souza, M.N.; Bianchin, M.D.; Isoppo, M.; Freitas, J.S.; Alves, J.A.; Piovezan, A.P.; Pohlmann, A.R.; Guterres, S.S. Evaluation of Lipoic Acid Topical Application on Rats Skin Wound Healing. *Acta Cir. Bras.* **2013**, *28*, 708–715. [CrossRef] [PubMed]
44. Lateef, H.; Aslam, M.N.; Stevens, M.J.; Varani, J. Pretreatment of Diabetic Rats with Lipoic Acid Improves Healing of Subsequently-Induced Abrasion Wounds. *Arch. Dermatol. Res.* **2005**, *297*, 75–83. [CrossRef] [PubMed]
45. Yang, Y.; Xiao, Y.; Jiang, Y.; Luo, J.; Yuan, J.; Yan, J.; Tong, Q. Alpha-Lipoic Acid Promotes Intestinal Epithelial Injury Repair by Regulating MAPK Signaling Pathways. *Mediat. Inflamm.* **2022**, *2022*, 1894379. [CrossRef] [PubMed]
46. Fernandes, A.; Rodrigues, P.M.; Pintado, M.; Tavaria, F.K. A Systematic Review of Natural Products for Skin Applications: Targeting Inflammation, Wound Healing, and Photo-Aging. *Phytomedicine* **2023**, *115*, 154824. [CrossRef] [PubMed]
47. De Bengy, A.-F.; Decorps, J.; Martin, L.S.; Pagnon, A.; Chevalier, F.P.; Sigaudo-Roussel, D.; Fromy, B. Alpha-Lipoic Acid Supplementation Restores Early Age-Related Sensory and Endothelial Dysfunction in the Skin. *Biomedicines* **2022**, *10*, 2887. [CrossRef] [PubMed]
48. Beitner, H. Randomized, Placebo-Controlled, Double Blind Study on the Clinical Efficacy of a Cream Containing 5%alpha-Lipoic Acid Related to Photoageing of Facial Skin. *Br. J. Dermatol.* **2003**, *149*, 841–849. [CrossRef] [PubMed]
49. Farhat, D.; Lincet, H. Lipoic Acid a Multi-Level Molecular Inhibitor of Tumorigenesis. *Biochim. Biophys. Acta (BBA) Rev. Cancer* **2020**, *1873*, 188317. [CrossRef] [PubMed]
50. Abdullah, K.M.; Sharma, G.; Takkar, S.; Kaushal, J.B.; Pothuraju, R.; Chakravarti, B.; Batra, S.K.; Siddiqui, J.A. α-Lipoic Acid Modulates Prostate Cancer Cell Growth and Bone Cell Differentiation. *Sci. Rep.* **2024**, *14*, 4404. [CrossRef]
51. Chakravarti, B.; Rajput, S.; Raza, S.; Rajak, S.; Tewari, A.; Gupta, P.; Upadhyay, A.; Chattopadhyay, N.; Sinha, R.A. Lipoic Acid Blocks Autophagic Flux and Impairs Cellular Bioenergetics in Breast Cancer and Reduces Stemness. *Biochim. Biophys. Acta (BBA) Mol. Basis Dis.* **2022**, *1868*, 166455. [CrossRef]
52. Peng, P.; Zhang, X.; Qi, T.; Cheng, H.; Kong, Q.; Liu, L.; Cao, X.; Ding, Z. Alpha-lipoic Acid Inhibits Lung Cancer Growth via mTOR-mediated Autophagy Inhibition. *FEBS Open Bio* **2020**, *10*, 607–618. [CrossRef] [PubMed]

53. Bossio, S.; Perri, A.; Gallo, R.; De Bartolo, A.; Rago, V.; La Russa, D.; Di Dio, M.; La Vignera, S.; Calogero, A.E.; Vitale, G.; et al. Alpha-Lipoic Acid Reduces Cell Growth, Inhibits Autophagy, and Counteracts Prostate Cancer Cell Migration and Invasion: Evidence from In Vitro Studies. *Int. J. Mol. Sci.* **2023**, *24*, 17111. [CrossRef] [PubMed]
54. Hermann, R.; Mungo, J.; Cnota, P.J.; Ziegler, D. Enantiomer-Selective Pharmacokinetics, Oral Bioavailability, and Sex Effects of Various Alpha-Lipoic Acid Dosage Forms. *CPAA* **2014**, *6*, 195–204. [CrossRef] [PubMed]
55. Hermann, R.; Niebch, G.; Borbe, H.O.; Fieger-Büschges, H.; Ruus, P.; Nowak, H.; Riethmüller-Winzen, H.; Peukert, M.; Blume, H. Enantioselective Pharmacokinetics and Bioavailability of Different Racemic α-Lipoic Acid Formulations in Healthy Volunteers. *Eur. J. Pharm. Sci.* **1996**, *4*, 167–174. [CrossRef]
56. Gleiter, C.H.; Schug, B.S.; Hermann, R.; Elze, M.; Blume, H.H.; Gundert-Remy, U. Influence of Food Intake on the Bioavailability of Thioctic Acid Enantiomers. *Eur. J. Clin. Pharmacol.* **1996**, *50*, 513–514. [CrossRef] [PubMed]
57. Breithaupt-Grögler, K.; Niebch, G.; Schneider, E.; Erb, K.; Hermann, R.; Blume, H.H.; Schug, B.S.; Belz, G.G. Dose-Proportionality of Oral Thioctic Acid—Coincidence of Assessments via Pooled Plasma and Individual Data. *Eur. J. Pharm. Sci.* **1999**, *8*, 57–65. [CrossRef] [PubMed]
58. Teichert, J.; Hermann, R.; Ruus, P.; Preiss, R. Plasma Kinetics, Metabolism, and Urinary Excretion of Alpha-Lipoic Acid Following Oral Administration in Healthy Volunteers. *J. Clin. Pharmacol.* **2003**, *43*, 1257–1267. [CrossRef] [PubMed]
59. Brufani, M.; Figliola, R. (R)-α-Lipoic Acid Oral Liquid Formulation: Pharmacokinetic Parameters and Therapeutic Efficacy. *Acta Biomed.* **2014**, *85*, 108–115.
60. Keith, D.J.; Butler, J.A.; Bemer, B.; Dixon, B.; Johnson, S.; Garrard, M.; Sudakin, D.L.; Christensen, J.M.; Pereira, C.; Hagen, T.M. Age and Gender Dependent Bioavailability of R- and R,S-α-Lipoic Acid: A Pilot Study. *Pharmacol. Res.* **2012**, *66*, 199–206. [CrossRef]
61. Lalić-Popović, M.N.; Vuković, M.M.; Jovičić-Bata, J.N.; Čanji-Panić, J.M.; Todorović, N.B. Comparison of Formulation Characteristics of Drugs and Dietary Supplements Containing Alpha-Lipoic Acid Relevant to Therapeutic Efficacy. *Eur. Rev. Med. Pharmacol. Sci.* **2023**, *27*, 3159–3170. [CrossRef]
62. Pop, A.; Crișan, S.; Bârcă, M.; Ciobanu, A.-M.; Varlas, V.; Pop, C.; Pali, M.-A.; Cauni, D.; Ozon, E.; Udeanu, D.; et al. Evaluation of Dissolution Profiles of a Newly Developed Solid Oral Immediate-Release Formula Containing Alpha-Lipoic Acid. *Processes* **2021**, *9*, 176. [CrossRef]
63. Di Martino, P. Human Bioavailability and Pharmacokinetic Profile of Different Formulations Delivering Alpha Lipoic Acid. *J. Clin. Cell. Immunol.* **2012**, *1*, 1–6. [CrossRef]
64. Derosa, G.; D'Angelo, A.; Preti, P.; Maffioli, P. Safety and Efficacy of Alpha Lipoic Acid During 4 Years of Observation: A Retrospective, Clinical Trial in Healthy Subjects in Primary Prevention. *DDDT* **2020**, *14*, 5367–5374. [CrossRef] [PubMed]
65. Parente, E.; Colannino, G.; Picconi, O.; Monastra, G. Safety of Oral Alpha-Lipoic Acid Treatment in Pregnant Women: A Retrospective Observational Study. *Eur. Rev. Med. Pharmacol. Sci.* **2017**, *21*, 4219–4227. [PubMed]
66. Cremer, D.R.; Rabeler, R.; Roberts, A.; Lynch, B. Safety Evaluation of α-Lipoic Acid (ALA). *Regul. Toxicol. Pharmacol.* **2006**, *46*, 29–41. [CrossRef] [PubMed]
67. Fogacci, F.; Rizzo, M.; Krogager, C.; Kennedy, C.; Georges, C.M.G.; Knežević, T.; Liberopoulos, E.; Vallée, A.; Pérez-Martínez, P.; Wenstedt, E.F.E.; et al. Safety Evaluation of α-Lipoic Acid Supplementation: A Systematic Review and Meta-Analysis of Randomized Placebo-Controlled Clinical Studies. *Antioxidants* **2020**, *9*, 1011. [CrossRef] [PubMed]
68. Moretti, R.; Angeletti, C.; Minora, S. Multiple Organ Failure and Shock Following Acute Alpha Lipoic Acid (ALA) Intoxication. *Clin. Toxicol.* **2019**, *57*, 749–751. [CrossRef] [PubMed]
69. Halabi, Z.; El Helou, C.; Al Balushi, H.; Gittinger, M.; Steck, A.R.; Kaakour, A.; Abu-Alfa, A.; El Zahran, T. Alpha Lipoic Acid Toxicity: The First Reported Mortality in an Adult Patient After Multiorgan Failure. *J. Emerg. Med.* **2023**, *64*, 190–194. [CrossRef] [PubMed]
70. Gatti, M.; Ippoliti, I.; Poluzzi, E.; Antonazzo, I.C.; Moro, P.A.; Moretti, U.; Menniti-Ippolito, F.; Mazzanti, G.; De Ponti, F.; Raschi, E. Assessment of Adverse Reactions to α-Lipoic Acid Containing Dietary Supplements through Spontaneous Reporting Systems. *Clin. Nutr.* **2021**, *40*, 1176–1185. [CrossRef]
71. Theodosis-Nobelos, P.; Papagiouvannis, G.; Tziona, P.; Rekka, E.A. Lipoic Acid. Kinetics and Pluripotent Biological Properties and Derivatives. *Mol. Biol. Rep.* **2021**, *48*, 6539–6550. [CrossRef]
72. Vigil, M.; Berkson, B.M.; Garcia, A.P. Adverse Effects of High Doses of Intravenous Alpha Lipoic Acid on Liver Mitochondria. *Glob. Adv. Health Med.* **2014**, *3*, 25–27. [CrossRef] [PubMed]
73. Usacheva, A.M.; Chernikov, A.V.; Karmanova, E.E.; Bruskov, V.I. Pharmacological Aspects of the Use of Lipoic Acid (Review). *Pharm. Chem. J.* **2022**, *55*, 1138–1146. [CrossRef]
74. Çakatay, U. Pro-Oxidant Actions of α-Lipoic Acid and Dihydrolipoic Acid. *Med. Hypotheses* **2006**, *66*, 110–117. [CrossRef] [PubMed]
75. Bhatti, F.; Mankhey, R.W.; Asico, L.; Quinn, M.T.; Welch, W.J.; Maric, C. Mechanisms of Antioxidant and Pro-Oxidant Effects of α-Lipoic Acid in the Diabetic and Nondiabetic Kidney. *Kidney Int.* **2005**, *67*, 1371–1380. [CrossRef]
76. Ikuta, N.; Sugiyama, H.; Shimosegawa, H.; Nakane, R.; Ishida, Y.; Uekaji, Y.; Nakata, D.; Pallauf, K.; Rimbach, G.; Terao, K.; et al. Analysis of the Enhanced Stability of R(+)-Alpha Lipoic Acid by the Complex Formation with Cyclodextrins. *Int. J. Mol. Sci.* **2013**, *14*, 3639–3655. [CrossRef] [PubMed]

77. Nishiura, H. A Novel Nano-Capsule of α-Lipoic Acid as a Template of Core-Shell Structure Constructed by Self-Assembly. *J. Nanomed. Nanotechnol.* **2012**, *4*, 2. [CrossRef]
78. Wada, N.; Wakami, H.; Konishi, T.; Matsugo, S. The Degradation and Regeneration of α-Lipoic Acid under the Irradiation of UV Light in the Existence of Homocysteine. *J. Clin. Biochem. Nutr.* **2009**, *44*, 218–222. [CrossRef] [PubMed]
79. Brown, P.R.; Edwards, J.O. Effect of Solvent on the Photolysis of .Alpha.-Lipoic Acid. *J. Org. Chem.* **1969**, *34*, 3131–3135. [CrossRef] [PubMed]
80. Moghimi, S.M.; Hunter, A.C.; Murray, J.C. Nanomedicine: Current Status and Future Prospects. *FASEB J.* **2005**, *19*, 311–330. [CrossRef]
81. Haleem, A.; Javaid, M.; Singh, R.P.; Rab, S.; Suman, R. Applications of Nanotechnology in Medical Field: A Brief Review. *Glob. Health J.* **2023**, *7*, 70–77. [CrossRef]
82. Malik, S.; Muhammad, K.; Waheed, Y. Emerging Applications of Nanotechnology in Healthcare and Medicine. *Molecules* **2023**, *28*, 6624. [CrossRef] [PubMed]
83. Ng, P.Q.; Ling, L.S.C.; Chellian, J.; Madheswaran, T.; Panneerselvam, J.; Kunnath, A.P.; Gupta, G.; Satija, S.; Mehta, M.; Hansbro, P.M.; et al. Applications of Nanocarriers as Drug Delivery Vehicles for Active Phytoconstituents. *CPD* **2020**, *26*, 4580–4590. [CrossRef] [PubMed]
84. Gupta, D.; Roy, P.; Sharma, R.; Kasana, R.; Rathore, P.; Gupta, T.K. Recent Nanotheranostic Approaches in Cancer Research. *Clin. Exp. Med.* **2024**, *24*, 8. [CrossRef] [PubMed]
85. Shafaei, N.; Khorshidi, S.; Karkhaneh, A. The Immune-Stealth Polymeric Coating on Drug Delivery Nanocarriers: In Vitro Engineering and in Vivo Fate. *J. Biomater. Appl.* **2023**, *38*, 159–178. [CrossRef] [PubMed]
86. Aljabali, A.A.; Obeid, M.A.; Bashatwah, R.M.; Serrano-Aroca, Á.; Mishra, V.; Mishra, Y.; El-Tanani, M.; Hromić-Jahjefendić, A.; Kapoor, D.N.; Goyal, R.; et al. Nanomaterials and Their Impact on the Immune System. *Int. J. Mol. Sci.* **2023**, *24*, 2008. [CrossRef] [PubMed]
87. Papini, E.; Tavano, R.; Mancin, F. Opsonins and Dysopsonins of Nanoparticles: Facts, Concepts, and Methodological Guidelines. *Front. Immunol.* **2020**, *11*, 567365. [CrossRef] [PubMed]
88. Fernandes, C.; Oliveira, C.; Benfeito, S.; Soares, P.; Garrido, J.; Borges, F. Nanotechnology and Antioxidant Therapy: An Emerging Approach for Neurodegenerative Diseases. *CMC* **2014**, *21*, 4311–4327. [CrossRef] [PubMed]
89. Cartaya, A.; Maiocchi, S.; Bahnson, E.M. Nanotherapies for Treatment of Cardiovascular Disease: A Case for Antioxidant Targeted Delivery. *Curr. Pathobiol. Rep.* **2019**, *7*, 47–60. [CrossRef] [PubMed]
90. Xu, Y.; Liu, H.; Song, L. Novel Drug Delivery Systems Targeting Oxidative Stress in Chronic Obstructive Pulmonary Disease: A Review. *J. Nanobiotechnol.* **2020**, *18*, 145. [CrossRef]
91. Zhu, X.; Yuan, W.; Li, Z.; Lin, Y.; Li, W.; Ji, L.; Wang, D.; Zhang, H.; Wang, Y. Progress of Research on Antioxidants and Carriers for Skin Wound Repair. *Processes* **2023**, *11*, 2069. [CrossRef]
92. Omran, B.; Baek, K.-H. Nanoantioxidants: Pioneer Types, Advantages, Limitations, and Future Insights. *Molecules* **2021**, *26*, 7031. [CrossRef] [PubMed]
93. Dolinina, E.S.; Akimsheva, E.Y.; Parfenyuk, E.V. Development of Novel Silica-Based Formulation of α-Lipoic Acid: Evaluation of Photo and Thermal Stability of the Encapsulated Drug. *Pharmaceutics* **2020**, *12*, 228. [CrossRef] [PubMed]
94. Dolinina, E.S.; Parfenyuk, E.V. Development of Novel Oral Formulations of Disulfide Antioxidants Based on Porous Silica for Controlled Release of the Drugs. *Materials* **2021**, *14*, 963. [CrossRef] [PubMed]
95. Tenchov, R.; Bird, R.; Curtze, A.E.; Zhou, Q. Lipid Nanoparticles–From Liposomes to mRNA Vaccine Delivery, a Landscape of Research Diversity and Advancement. *ACS Nano* **2021**, *15*, 16982–17015. [CrossRef] [PubMed]
96. Naseri, N.; Valizadeh, H.; Zakeri-Milani, P. Solid Lipid Nanoparticles and Nanostructured Lipid Carriers: Structure, Preparation and Application. *Adv. Pharm. Bull.* **2015**, *5*, 305–313. [CrossRef] [PubMed]
97. Viegas, C.; Patrício, A.B.; Prata, J.M.; Nadhman, A.; Chintamaneni, P.K.; Fonte, P. Solid Lipid Nanoparticles vs. Nanostructured Lipid Carriers: A Comparative Review. *Pharmaceutics* **2023**, *15*, 1593. [CrossRef] [PubMed]
98. Ruktanonchai, U.; Bejrapha, P.; Sakulkhu, U.; Opanasopit, P.; Bunyapraphatsara, N.; Junyaprasert, V.; Puttipipatkhachorn, S. Physicochemical Characteristics, Cytotoxicity, and Antioxidant Activity of Three Lipid Nanoparticulate Formulations of Alpha-Lipoic Acid. *AAPS PharmSciTech* **2009**, *10*, 227. [CrossRef] [PubMed]
99. Dhaundiyal, A.; Jena, S.K.; Samal, S.K.; Sonvane, B.; Chand, M.; Sangamwar, A.T. Alpha-Lipoic Acid–Stearylamine Conjugate-Based Solid Lipid Nanoparticles for Tamoxifen Delivery: Formulation, Optimization, in-Vivo Pharmacokinetic and Hepatotoxicity Study. *J. Pharm. Pharmacol.* **2016**, *68*, 1535–1550. [CrossRef] [PubMed]
100. Kothari, I.R.; Mazumdar, S.; Sharma, S.; Italiya, K.; Mittal, A.; Chitkara, D. Docetaxel and Alpha-Lipoic Acid Co-Loaded Nanoparticles for Cancer Therapy. *Ther. Deliv.* **2019**, *10*, 227–240. [CrossRef]
101. Wang, J.; Xia, Q. Alpha-Lipoic Acid-Loaded Nanostructured Lipid Carrier: Sustained Release and Biocompatibility to HaCaT Cells in Vitro. *Drug Deliv.* **2014**, *21*, 328–341. [CrossRef]
102. Shchelkonogov, V.A.; Alyaseva, S.O.; Lotosh, N.Y.; Baranova, O.A.; Chekanov, A.V.; Solov'eva, E.Y.; Kamyshinskii, R.A.; Vasilov, R.G.; Shastina, N.S.; Korepanova, E.A.; et al. Lipoic Acid Nanoforms Based on Phosphatidylcholine: Production and Characteristics. *Eur. Biophys. J.* **2020**, *49*, 95–103. [CrossRef] [PubMed]
103. Çoban, Ö.; Yıldırım, S.; Bakır, T. Alpha-Lipoic Acid and Cyanocobalamin Co-Loaded Nanoemulsions: Development, Characterization, and Evaluation of Stability. *J. Pharm. Innov.* **2022**, *17*, 510–520. [CrossRef]

104. Badr-Eldin, S.M.; Fahmy, U.A.; Aldawsari, H.M.; Ahmed, O.A.A.; Alhakamy, N.A.; Okbazghi, S.Z.; El-Moselhy, M.A.; Alghaith, A.F.; Anter, A.; Matouk, A.I.; et al. Optimized Self-Nanoemulsifying Delivery System Based on Plant-Derived Oil Augments Alpha-Lipoic Acid Protective Effects Against Experimentally Induced Gastric Lesions. *Dose-Response* **2021**, *19*, 155932582110012. [CrossRef] [PubMed]
105. Halder, S.; Mibe, Y.; Rikimura, S.; Kuromi, K.; Sato, H.; Onoue, S. Strategic Application of Liposomal System to R-α-Lipoic Acid for the Improvement of Nutraceutical Properties. *Drug Dev. Ind. Pharm.* **2022**, *48*, 239–246. [CrossRef] [PubMed]
106. Curcio, M.; Cirillo, G.; Amato, R.; Guidotti, L.; Amantea, D.; De Luca, M.; Nicoletta, F.P.; Iemma, F.; Garcia-Gil, M. Encapsulation of Alpha-Lipoic Acid in Functional Hybrid Liposomes: Promising Tool for the Reduction of Cisplatin-Induced Ototoxicity. *Pharmaceuticals* **2022**, *15*, 394. [CrossRef] [PubMed]
107. Huang, J.; Wang, Q.; Li, T.; Xia, N.; Xia, Q. Multilayer Emulsions as a Strategy for Linseed Oil and A-lipoic Acid Microencapsulation: Study on Preparation and In Vitro Characterization. *J. Sci. Food Agric.* **2018**, *98*, 3513–3523. [CrossRef]
108. Zhao, G.D.; Sun, R.; Ni, S.L.; Xia, Q. Development and Characterisation of a Novel Chitosan-Coated Antioxidant Liposome Containing Both Coenzyme Q10 and Alpha-Lipoic Acid. *J. Microencapsul.* **2015**, *32*, 157–165. [CrossRef]
109. Li, W.; Peng, J.; Yang, Q.; Chen, L.; Zhang, L.; Chen, X.; Qian, Z. α-Lipoic Acid Stabilized DTX/IR780 Micelles for Photoacoustic/Fluorescence Imaging Guided Photothermal Therapy/Chemotherapy of Breast Cancer. *Biomater. Sci.* **2018**, *6*, 1201–1216. [CrossRef]
110. Jung, S.Y.; Yoo, J.; Yang, K.-J.; Jang, S.; Yi, G.; Kim, D.-K.; Koo, H. Intratympanic Administration of Alpha-Lipoic Acid-Loaded Pluronic F-127 Nanoparticles Ameliorates Acute Hearing Loss. *Nanomed. Nanotechnol. Biol. Med.* **2021**, *32*, 102329. [CrossRef]
111. Xia, N.; Liu, T.; Wang, Q.; Xia, Q.; Bian, X. *In Vitro* Evaluation of α-Lipoic Acid-Loaded Lipid Nanocapsules for Topical Delivery. *J. Microencapsul.* **2017**, *34*, 571–581. [CrossRef]
112. Külkamp, I.C.; Rabelo, B.D.; Berlitz, S.J.; Isoppo, M.; Bianchin, M.D.; Schaffazick, S.R.; Pohlmann, A.R.; Guterres, S.S. Nanoencapsulation Improves the <I>In Vitro</I> Antioxidant Activity of Lipoic Acid. *J. Biomed. Nanotechnol.* **2011**, *7*, 598–607. [CrossRef] [PubMed]
113. Davies, S.; Contri, R.V.; Guterres, S.S.; Pohlmann, A.R.; Guerreiro, I.C.K. Simultaneous Nanoencapsulation of Lipoic Acid and Resveratrol with Improved Antioxidant Properties for the Skin. *Colloids Surf. B Biointerfaces* **2020**, *192*, 111023. [CrossRef] [PubMed]
114. Rageh, M.M.; El-Gebaly, R.H. Antioxidant Activities of α-Lipoic Acid Free and Nano-Capsule Inhibit the Growth of Ehrlich Carcinoma. *Mol. Biol. Rep.* **2019**, *46*, 3141–3148. [CrossRef] [PubMed]
115. EL-Gebaly, R.H.; Rageh, M.M.; Maamoun, I.K. Radio-Protective Potential of Lipoic Acid Free and Nano-Capsule against 99mTc-MIBI Induced Injury in Cardio Vascular Tissue. *XST* **2019**, *27*, 83–96. [CrossRef] [PubMed]
116. Kubota, Y.; Musashi, M.; Nagasawa, T.; Shimura, N.; Igarashi, R.; Yamaguchi, Y. Novel Nanocapsule of A-lipoic Acid Reveals Pigmentation Improvement: α-Lipoic Acid Stimulates the Proliferation and Differentiation of Keratinocyte in Murine Skin by Topical Application. *Exp. Dermatol.* **2019**, *28*, 55–63. [CrossRef] [PubMed]
117. Gogoi, P.; Dutta, A.; Ramteke, A.; Maji, T.K. Preparation, Characterization and Cytotoxic Applications of Curcumin-(±) α-LIPOIC Acid Coloaded Phosphorylated Chitosan Nanoparticles in MDA MB 231 Breast Cancer Cell Line. *Polym. Adv. Technol.* **2020**, *31*, 2827–2841. [CrossRef]
118. Metwaly, H.H.; Fathy, S.A.; Abdel Moneim, M.M.; Emam, M.A.; Soliman, A.F.; El-Naggar, M.E.; Omara, E.A.; El-Bana, M.A. Chitosan and Solid Lipid Nanoparticles Enhance the Efficiency of Alpha-Lipoic Acid against Experimental Neurotoxicity. *Toxicol. Mech. Methods* **2022**, *32*, 268–279. [CrossRef] [PubMed]
119. Campos, P.M.; Praça, F.G.; Mussi, S.V.; Figueiredo, S.A.; Fantini, M.C.D.A.; Fonseca, M.J.V.; Torchilin, V.P.; Bentley, M.V.L.B. Liquid Crystalline Nanodispersion Functionalized with Cell-Penetrating Peptides Improves Skin Penetration and Anti-Inflammatory Effect of Lipoic Acid after in Vivo Skin Exposure to UVB Radiation. *Drug Deliv. Transl. Res.* **2020**, *10*, 1810–1828. [CrossRef]
120. Park, C.H.; Lee, K.-U.; Park, J.-Y.; Koh, E.-H.; Kim, H.-S.; Lee, J. Lipoic Acid Nanoparticles: Effect of Polymeric Stabilizer on Appetite Suppression. *Pharmazie* **2010**, *65*, 580–584.
121. Del Valle, E.M.M. Cyclodextrins and Their Uses: A Review. *Process Biochem.* **2004**, *39*, 1033–1046. [CrossRef]
122. Muankaew, C.; Loftsson, T. Cyclodextrin-Based Formulations: A Non-Invasive Platform for Targeted Drug Delivery. *Basic Clin. Pharmacol. Toxicol.* **2018**, *122*, 46–55. [CrossRef] [PubMed]
123. Uekama, K.; Hirayama, F.; Arima, H. Recent Aspect of Cyclodextrin-Based Drug Delivery System. *J. Incl. Phenom. Macrocycl. Chem.* **2006**, *56*, 3–8. [CrossRef]
124. Ikuta, N.; Tanaka, A.; Otsubo, A.; Ogawa, N.; Yamamoto, H.; Mizukami, T.; Arai, S.; Okuno, M.; Terao, K.; Matsugo, S. Spectroscopic Studies of R(+)-α-Lipoic Acid—Cyclodextrin Complexes. *Int. J. Mol. Sci.* **2014**, *15*, 20469–20485. [CrossRef] [PubMed]
125. Ikuta, N.; Terao, K.; Matsugo, S. Stabilized R -α-Lipoic Acid by Encapsulation Using Cyclodextrins. In *Impact of Nanoscience in the Food Industry*; Elsevier: Amsterdam, The Netherlands, 2018; pp. 351–366, ISBN 978-0-12-811441-4.
126. Uchida, R.; Iwamoto, K.; Nagayama, S.; Miyajima, A.; Okamoto, H.; Ikuta, N.; Fukumi, H.; Terao, K.; Hirota, T. Effect of γ-Cyclodextrin Inclusion Complex on the Absorption of R-α-Lipoic Acid in Rats. *Int. J. Mol. Sci.* **2015**, *16*, 10105–10120. [CrossRef] [PubMed]
127. Ikuta, N.; Okamoto, H.; Furune, T.; Uekaji, Y.; Terao, K.; Uchida, R.; Iwamoto, K.; Miyajima, A.; Hirota, T.; Sakamoto, N. Bioavailability of an R-α-Lipoic Acid/γ-Cyclodextrin Complex in Healthy Volunteers. *Int. J. Mol. Sci.* **2016**, *17*, 949. [CrossRef]

128. Leu, J.-G.; Chen, S.-A.; Chen, H.-M.; Wu, W.-M.; Hung, C.-F.; Yao, Y.-D.; Tu, C.-S.; Liang, Y.-J. The Effects of Gold Nanoparticles in Wound Healing with Antioxidant Epigallocatechin Gallate and α-Lipoic Acid. *Nanomed. Nanotechnol. Biol. Med.* **2012**, *8*, 767–775. [CrossRef]
129. Chen, S.-A.; Chen, H.-M.; Yao, Y.-D.; Hung, C.-F.; Tu, C.-S.; Liang, Y.-J. Topical Treatment with Anti-Oxidants and Au Nanoparticles Promote Healing of Diabetic Wound through Receptor for Advance Glycation End-Products. *Eur. J. Pharm. Sci.* **2012**, *47*, 875–883. [CrossRef] [PubMed]
130. Türkez, H.; Yıldırım, Ö.Ç.; Öner, S.; Kadı, A.; Mete, A.; Arslan, M.E.; Şahin, İ.O.; Yapça, Ö.E.; Mardinoğlu, A. Lipoic Acid Conjugated Boron Hybrids Enhance Wound Healing and Antimicrobial Processes. *Pharmaceutics* **2022**, *15*, 149. [CrossRef]
131. Martínez-García, K.D.; Zertuche-Arias, T.; Bernáldez-Sarabia, J.; Iñiguez, E.; Kretzchmar, T.; Camacho-Villegas, T.A.; Lugo-Fabres, P.H.; Licea Navarro, A.F.; Bravo-Madrigal, J.; Castro-Ceseña, A.B. Radical Scavenging, Hemocompatibility, and Antibacterial Activity against MDR *Acinetobacter Baumannii* in Alginate-Based Aerogels Containing Lipoic Acid-Capped Silver Nanoparticles. *ACS Omega* **2024**, *9*, 2350–2361. [CrossRef]
132. Attia, M.; Essa, E.A.; Zaki, R.M.; Elkordy, A.A. An Overview of the Antioxidant Effects of Ascorbic Acid and Alpha Lipoic Acid (in Liposomal Forms) as Adjuvant in Cancer Treatment. *Antioxidants* **2020**, *9*, 359. [CrossRef]
133. Fahmy, U.A.; Aljaeid, B.M. Combined Strategy for Suppressing Breast Carcinoma MCF-7 Cell Lines by Loading Simvastatin on Alpha Lipoic Acid Nanoparticles. *Expert Opin. Drug Deliv.* **2016**, *13*, 1653–1660. [CrossRef]
134. Ling, L.; Ismail, M.; Du, Y.; Yao, C.; Li, X. Lipoic Acid-Derived Cross-Linked Liposomes for Reduction-Responsive Delivery of Anticancer Drug. *Int. J. Pharm.* **2019**, *560*, 246–260. [CrossRef]
135. Maiti, B.; Kumar, K.; Moitra, P.; Kondaiah, P.; Bhattacharya, S. Reduction Responsive Nanovesicles Derived from Novel α-Tocopheryl–Lipoic Acid Conjugates for Efficacious Drug Delivery to Sensitive and Drug Resistant Cancer Cells. *Bioconjug. Chem.* **2018**, *29*, 255–266. [CrossRef]
136. Sauraj; Kumar, A.; Kumar, B.; Kulshreshtha, A.; Negi, Y.S. Redox-Sensitive Nanoparticles Based on Xylan-Lipoic Acid Conjugate for Tumor Targeted Drug Delivery of Niclosamide in Cancer Therapy. *Carbohydr. Res.* **2021**, *499*, 108222. [CrossRef] [PubMed]
137. Veider, F.; Sanchez Armengol, E.; Bernkop-Schnürch, A. Charge-Reversible Nanoparticles: Advanced Delivery Systems for Therapy and Diagnosis. *Small* **2024**, *20*, 2304713. [CrossRef]
138. Chen, W.; Yang, S.; Li, F.; Qu, C.; Liu, Y.; Wang, Y.; Wang, D.; Zhang, X. Programmed pH/Reduction-Responsive Nanoparticles for Efficient Delivery of Antitumor Agents in Vivo. *Acta Biomater.* **2018**, *81*, 219–230. [CrossRef] [PubMed]
139. Li, F.; Chen, W.; You, B.; Liu, Y.; Yang, S.; Yuan, Z.; Zhu, W.; Li, J.; Qu, C.; Zhou, Y.; et al. Enhanced Cellular Internalization and On-Demand Intracellular Release of Doxorubicin by Stepwise pH-/Reduction-Responsive Nanoparticles. *ACS Appl. Mater. Interfaces* **2016**, *8*, 32146–32158. [CrossRef] [PubMed]
140. Yang, S.; Wang, Y.; Ren, Z.; Chen, M.; Chen, W.; Zhang, X. Stepwise pH/Reduction-Responsive Polymeric Conjugates for Enhanced Drug Delivery to Tumor. *Mater. Sci. Eng. C* **2018**, *82*, 234–243. [CrossRef]
141. Li, F.; Wang, Y.; Chen, W.; Wang, D.; Zhou, Y.; You, B.; Liu, Y.; Qu, C.; Yang, S.; Chen, M.; et al. Co-Delivery of VEGF siRNA and Etoposide for Enhanced Anti-Angiogenesis and Anti-Proliferation Effect *via* Multi-Functional Nanoparticles for Orthotopic Non-Small Cell Lung Cancer Treatment. *Theranostics* **2019**, *9*, 5886–5898. [CrossRef]
142. Toosi Moghadam, F.; Mamashli, F.; Khoobi, M.; Ghasemi, A.; Pirhaghi, M.; Delavari, B.; Mahmoudi Aznaveh, H.; Nikkhah, M.; Saboury, A.A. A Dual Responsive Robust Human Serum Albumin-based Nanocarrier for Doxorubicin. *Biotechnol. App. Biochem.* **2022**, *69*, 2496–2506. [CrossRef]
143. Birlik Demirel, G.; Aygul, E.; Dag, A.; Atasoy, S.; Cimen, Z.; Cetin, B. Folic Acid-Conjugated pH and Redox-Sensitive Ellipsoidal Hybrid Magnetic Nanoparticles for Dual-Triggered Drug Release. *ACS Appl. Bio Mater.* **2020**, *3*, 4949–4961. [CrossRef] [PubMed]
144. Rezaei, S.; Kashanian, S.; Bahrami, Y.; Cruz, L.J.; Motiei, M. Redox-Sensitive and Hyaluronic Acid-Functionalized Nanoparticles for Improving Breast Cancer Treatment by Cytoplasmic 17α-Methyltestosterone Delivery. *Molecules* **2020**, *25*, 1181. [CrossRef] [PubMed]
145. Zhong, Y.; Meng, F.; Deng, C.; Mao, X.; Zhong, Z. Targeted Inhibition of Human Hematological Cancers *in Vivo* by Doxorubicin Encapsulated in Smart Lipoic Acid-Crosslinked Hyaluronic Acid Nanoparticles. *Drug Deliv.* **2017**, *24*, 1482–1490. [CrossRef] [PubMed]
146. Poursani, E.; Cirillo, G.; Curcio, M.; Vittorio, O.; De Luca, M.; Leggio, A.; Nicoletta, F.P.; Iemma, F. Dual-Responsive Chondroitin Sulfate Self-Assembling Nanoparticles for Combination Therapy in Metastatic Cancer Cells. *Int. J. Pharm. X* **2024**, *7*, 100235. [CrossRef] [PubMed]
147. Chen, T.; Qiu, M.; Zhang, J.; Sun, H.; Deng, C.; Zhong, Z. Integrated Multifunctional Micelles Co-Self-Assembled from Polypeptides Conjugated with Natural Ferulic Acid and Lipoic Acid for Doxorubicin Delivery. *ChemPhysChem* **2018**, *19*, 2070–2077. [CrossRef] [PubMed]
148. Huang, L.; Chaurasiya, B.; Wu, D.; Wang, H.; Du, Y.; Tu, J.; Webster, T.J.; Sun, C. Versatile Redox-Sensitive Pullulan Nanoparticles for Enhanced Liver Targeting and Efficient Cancer Therapy. *Nanomed. Nanotechnol. Biol. Med.* **2018**, *14*, 1005–1017. [CrossRef] [PubMed]
149. Ghorbani, M.; Bigdeli, B.; Jalili-baleh, L.; Baharifar, H.; Akrami, M.; Dehghani, S.; Goliaei, B.; Amani, A.; Lotfabadi, A.; Rashedi, H.; et al. Curcumin-Lipoic Acid Conjugate as a Promising Anticancer Agent on the Surface of Gold-iron Oxide Nanocomposites: A pH-Sensitive Targeted Drug Delivery System for Brain Cancer Theranostics. *Eur. J. Pharm. Sci.* **2018**, *114*, 175–188. [CrossRef] [PubMed]

150. Mondal, A.; Das, S.; Ali, S.M.; Kolay, S.; Sengupta, A.; Molla, M.R. Bioderived Lipoic Acid-Based Dynamic Covalent Nanonetworks of Poly(Disulfide)s: Enhanced Encapsulation Stability and Cancer Cell-Selective Delivery of Drugs. *Bioconjug. Chem.* **2023**, *34*, 489–500. [CrossRef] [PubMed]
151. Dzwonek, M.; Załubiniak, D.; Piątek, P.; Cichowicz, G.; Męczynska-Wielgosz, S.; Stępkowski, T.; Kruszewski, M.; Więckowska, A.; Bilewicz, R. Towards Potent but Less Toxic Nanopharmaceuticals—Lipoic Acid Bioconjugates of Ultrasmall Gold Nanoparticles with an Anticancer Drug and Addressing Unit. *RSC Adv.* **2018**, *8*, 14947–14957. [CrossRef]
152. Cheng, M.; Zhang, Y.; Zhang, X.; Wang, W.; Yuan, Z. One-Pot Synthesis of Acid-Induced *in Situ* Aggregating Theranostic Gold Nanoparticles with Enhanced Retention in Tumor Cells. *Biomater. Sci.* **2019**, *7*, 2009–2022. [CrossRef]
153. Emami, F.; Banstola, A.; Vatanara, A.; Lee, S.; Kim, J.O.; Jeong, J.-H.; Yook, S. Doxorubicin and Anti-PD-L1 Antibody Conjugated Gold Nanoparticles for Colorectal Cancer Photochemotherapy. *Mol. Pharm.* **2019**, *16*, 1184–1199. [CrossRef] [PubMed]
154. Wang, X.; Cheng, R.; Cheng, L.; Zhong, Z. Lipoyl Ester Terminated Star PLGA as a Simple and Smart Material for Controlled Drug Delivery Application. *Biomacromolecules* **2018**, *19*, 1368–1373. [CrossRef] [PubMed]
155. Wang, X.; Qiu, M.; Deng, C.; Cheng, R.; Zhong, Z. Targeted and Reduction-Sensitive Cross-Linked PLGA Nanotherapeutics for Safer and Enhanced Chemotherapy of Malignant Melanoma. *ACS Biomater. Sci. Eng.* **2020**, *6*, 2621–2629. [CrossRef]
156. Tudose, M.; Culita, D.C.; Musuc, A.M.; Somacescu, S.; Ghica, C.; Chifiriuc, M.C.; Bleotu, C. Lipoic Acid Functionalized SiO2@Ag Nanoparticles. Synthesis, Characterization and Evaluation of Biological Activity. *Mater. Sci. Eng. C* **2017**, *79*, 499–506. [CrossRef]
157. Abdelkader, N.F.; El-Batal, A.I.; Amin, Y.M.; Hawas, A.M.; Hassan, S.H.M.; Eid, N.I. Neuroprotective Effect of Gold Nanoparticles and Alpha-Lipoic Acid Mixture against Radiation-Induced Brain Damage in Rats. *Int. J. Mol. Sci.* **2022**, *23*, 9640. [CrossRef]
158. Xi, Y.; Pan, W.; Liu, Y.; Liu, J.; Xu, G.; Su, Y.; Chen, D.; Ye, X. α-Lipoic Acid Loaded Hollow Gold Nanoparticles Designed for Osteoporosis Treatment: Preparation, Characterization and *in Vitro* Evaluation. *Artif. Cells Nanomed. Biotechnol.* **2023**, *51*, 131–138. [CrossRef]
159. Sawie, H.G.; Khadrawy, Y.A.; El-Gizawy, M.M.; Mourad, H.H.; Omara, E.A.; Hosny, E.N. Effect of Alpha-Lipoic Acid and Caffeine-Loaded Chitosan Nanoparticles on Obesity and Its Complications in Liver and Kidney in Rats. *Naunyn-Schmiedeberg's Arch. Pharmacol.* **2023**, *396*, 3017–3031. [CrossRef]
160. Hosny, E.N.; Sawie, H.G.; Abou-Seif, H.S.; Khadrawy, Y.A. Effect of Caffeine-Chitosan Nanoparticles and α-Lipoic Acid on the Cardiovascular Changes Induced in Rat Model of Obesity. *Int. Immunopharmacol.* **2024**, *129*, 111627. [CrossRef] [PubMed]
161. Ahmed, O.A.A. Development and Single Dose Clinical Pharmacokinetics Investigation of Novel Zein Assisted- Alpha Lipoic Acid Nanoencapsulation of Vardenafil. *Sci. Rep.* **2018**, *8*, 15802. [CrossRef]
162. Cai, J.; Chen, J.; Zeng, Q.; Liu, J.; Zhang, Y.; Cheng, H.; Yao, S.; Chen, Q. Assessment of the Efficacy of α-Lipoic Acid in Treatment of Diabetes Mellitus Patients with Erectile Dysfunction: A Protocol for Systematic Review and Meta-Analysis. *Medicine* **2020**, *99*, e22161. [CrossRef]
163. Bruna, T.; Maldonado-Bravo, F.; Jara, P.; Caro, N. Silver Nanoparticles and Their Antibacterial Applications. *Int. J. Mol. Sci.* **2021**, *22*, 7202. [CrossRef] [PubMed]
164. Ferdous, Z.; Nemmar, A. Health Impact of Silver Nanoparticles: A Review of the Biodistribution and Toxicity Following Various Routes of Exposure. *Int. J. Mol. Sci.* **2020**, *21*, 2375. [CrossRef] [PubMed]
165. Hajtuch, J.; Santos-Martinez, M.J.; Wojcik, M.; Tomczyk, E.; Jaskiewicz, M.; Kamysz, W.; Narajczyk, M.; Inkielewicz-Stepniak, I. Lipoic Acid-Coated Silver Nanoparticles: Biosafety Potential on the Vascular Microenvironment and Antibacterial Properties. *Front. Pharmacol.* **2022**, *12*, 733743. [CrossRef] [PubMed]
166. Cotton, G.C.; Gee, C.; Jude, A.; Duncan, W.J.; Abdelmoneim, D.; Coates, D.E. Efficacy and Safety of Alpha Lipoic Acid-Capped Silver Nanoparticles for Oral Applications. *RSC Adv.* **2019**, *9*, 6973–6985. [CrossRef] [PubMed]
167. Tohamy, H.G.; Lebda, M.A.; Sadek, K.M.; Elfeky, M.S.; El-Sayed, Y.S.; Samak, D.H.; Hamed, H.S.; Abouzed, T.K. Biochemical, Molecular and Cytological Impacts of Alpha-Lipoic Acid and Ginkgo Biloba in Ameliorating Testicular Dysfunctions Induced by Silver Nanoparticles in Rats. *Environ. Sci. Pollut. Res.* **2022**, *29*, 38198–38211. [CrossRef] [PubMed]
168. Lebda, M.A.; Sadek, K.M.; Tohamy, H.G.; Abouzed, T.K.; Shukry, M.; Umezawa, M.; El-Sayed, Y.S. Potential Role of α-Lipoic Acid and Ginkgo Biloba against Silver Nanoparticles-Induced Neuronal Apoptosis and Blood-Brain Barrier Impairments in Rats. *Life Sci.* **2018**, *212*, 251–260. [CrossRef] [PubMed]
169. An, X.; Liu, L.; Schaefer, M.; Yan, B.; Scholz, C.; Hillmer, S.; Wang, K.; Luo, Y.; Ji, H.; Gladkich, J.; et al. Alpha-Lipoic Acid Prevents Side Effects of Therapeutic Nanosilver without Compromising Cytotoxicity in Experimental Pancreatic Cancer. *Cancers* **2021**, *13*, 4770. [CrossRef] [PubMed]
170. Alshammari, G.M.; Al-Ayed, M.S.; Abdelhalim, M.A.; Al-Harbi, L.N.; Yahya, M.A. Effects of Antioxidant Combinations on the Renal Toxicity Induced Rats by Gold Nanoparticles. *Molecules* **2023**, *28*, 1879. [CrossRef] [PubMed]
171. Abdelhalim, M.A.K.; Qaid, H.A.Y.; Al-Mohy, Y.H.; Ghannam, M.M. The Protective Roles of Vitamin E and α-Lipoic Acid Against Nephrotoxicity, Lipid Peroxidation, and Inflammatory Damage Induced by Gold Nanoparticles. *IJN* **2020**, *15*, 729–734. [CrossRef]
172. Abdelhalim, M.; Moussa, S.; Qaid, H.; Al-Ayed, M. Potential Effects of Different Natural Antioxidants on Inflammatory Damage and Oxidative-Mediated Hepatotoxicity Induced by Gold Nanoparticles. *IJN* **2018**, *13*, 7931–7938. [CrossRef]
173. Al-Rasheed, N.M.; Al-Rasheed, N.M.; Abdel Baky, N.A.; Faddah, L.M.; Fatani, A.J.; Hasan, I.H.; Mohamad, R.A. Prophylactic Role of α-Lipoic Acid and Vitamin E against Zinc Oxide Nanoparticles Induced Metabolic and Immune Disorders in Rat's Liver. *Eur. Rev. Med. Pharmacol. Sci.* **2014**, *18*, 1813–1828.

174. Baky, N.A.; Faddah, L.; Al-Rasheed, N.; Al-Rasheed, N.; Fatani, A. Induction of Inflammation, DNA Damage and Apoptosis in Rat Heart after Oral Exposure to Zinc Oxide Nanoparticles and the Cardioprotective Role of α-lipoic Acid and Vitamin E. *Drug Res.* **2013**, *63*, 228–236. [CrossRef]
175. Deore, M.S.; S, K.; Naqvi, S.; Kumar, A.; Flora, S.J.S. Alpha-Lipoic Acid Protects Co-Exposure to Lead and Zinc Oxide Nanoparticles Induced Neuro, Immuno and Male Reproductive Toxicity in Rats. *Front. Pharmacol.* **2021**, *12*, 626238. [CrossRef]
176. Liu, Y.; Zhu, W.; Ni, D.; Zhou, Z.; Gu, J.; Zhang, W.; Sun, H.; Liu, F. Alpha Lipoic Acid Antagonizes Cytotoxicity of Cobalt Nanoparticles by Inhibiting Ferroptosis-like Cell Death. *J. Nanobiotechnol.* **2020**, *18*, 141. [CrossRef]
177. Khalaf, A.; Zaki, A.; Galal, M.; Ogaly, H.; Ibrahim, M.; Hassan, A. The Potential Protective Effect of α-Lipoic Acid against Nanocopper Particle–Induced Hepatotoxicity in Male Rats. *Hum. Exp. Toxicol.* **2017**, *36*, 881–891. [CrossRef] [PubMed]
178. Levkovskyi, I.O.; Mochizuki, S.; Zheng, A.; Zhang, X.; Zhang, F. Lipoic Acid-Based Poly(Disulfide)s: Synthesis and Biomedical Applications. *Nano Trans. Med.* **2023**, *2*, 100006. [CrossRef]
179. Nuyken, O.; Pask, S. Ring-Opening Polymerization—An Introductory Review. *Polymers* **2013**, *5*, 361–403. [CrossRef]
180. Bang, E.-K.; Lista, M.; Sforazzini, G.; Sakai, N.; Matile, S. Poly(Disulfide)s. *Chem. Sci.* **2012**, *3*, 1752. [CrossRef]
181. Yu, Q.; Fang, Z.; Luan, S.; Wang, L.; Shi, H. Biological Applications of Lipoic Acid-Based Polymers: An Old Material with New Promise. *J. Mater. Chem. B* **2024**, *12*, 4574–4583. [CrossRef]
182. Yang, H.; Shen, W.; Liu, W.; Chen, L.; Zhang, P.; Xiao, C.; Chen, X. PEGylated Poly(α-Lipoic Acid) Loaded with Doxorubicin as a pH and Reduction Dual Responsive Nanomedicine for Breast Cancer Therapy. *Biomacromolecules* **2018**, *19*, 4492–4503. [CrossRef]
183. Li, Y.; Hou, H.; Zhang, P.; Zhang, Z. Co-Delivery of Doxorubicin and Paclitaxel by Reduction/pH Dual Responsive Nanocarriers for Osteosarcoma Therapy. *Drug Deliv.* **2020**, *27*, 1044–1053. [CrossRef]
184. Zhang, H.; Yang, Y.; Chen, Y.; Zhang, X.; Chen, X. A Convergent Fabrication of Programmed pH/Reduction-Responsive Nanoparticles for Efficient Dual Anticancer Drugs Delivery for Ovarian Cancer Treatment. *J. Exp. Nanosci.* **2023**, *18*, 2193400. [CrossRef]
185. Liu, Z.; Shen, N.; Tang, Z.; Zhang, D.; Ma, L.; Yang, C.; Chen, X. An Eximious and Affordable GSH Stimulus-Responsive Poly(α-Lipoic Acid) Nanocarrier Bonding Combretastatin A4 for Tumor Therapy. *Biomater. Sci.* **2019**, *7*, 2803–2811. [CrossRef]
186. Liu, Z.; Tang, Z.; Zhang, D.; Wu, J.; Si, X.; Shen, N.; Chen, X. A Novel GSH Responsive Poly(Alpha-Lipoic Acid) Nanocarrier Bonding with the Honokiol-DMXAA Conjugate for Combination Therapy. *Sci. China Mater.* **2020**, *63*, 307–315. [CrossRef]
187. Lin, F.; Liu, Y.; Luo, W.; Liu, S.; Wang, Y.; Gu, R.; Liu, W.; Xiao, C. Minocycline-Loaded Poly(α-Lipoic Acid)–Methylprednisolone Prodrug Nanoparticles for the Combined Anti-Inflammatory Treatment of Spinal Cord Injury. *IJN* **2022**, *17*, 91–104. [CrossRef]
188. Su, R.; Wang, H.; Xiao, C.; Tao, Y.; Li, M.; Chen, Z. Venetoclax Nanomedicine Alleviates Acute Lung Injury via Increasing Neutrophil Apoptosis. *Biomater. Sci.* **2021**, *9*, 4746–4754. [CrossRef]
189. Banik, S.; Yamada, K.; Sato, H.; Onoue, S. Development of Poly(Lipoic Acid) Nanoparticles with Improved Oral Bioavailability and Hepatoprotective Effects of Quercetin. *Mol. Pharm.* **2022**, *19*, 1468–1476. [CrossRef]
190. Han, L.; Zang, T.; Tan, L.; Liang, D.; Long, T.; Liu, X.; Shen, X.; Ren, H.; Li, Z.; Lu, Z.; et al. Self-Assembly of H2S-Responsive Nanoprodrugs Based on Natural Rhein and Geraniol for Targeted Therapy against Salmonella Typhimurium. *J. Nanobiotechnol.* **2023**, *21*, 483. [CrossRef]
191. Han, L.; Liu, X.-W.; Zang, T.; Ren, H.; Liang, D.-S.; Bai, S.-C.; Li, C.; Liao, X.-P.; Liu, Y.-H.; Zhang, C.; et al. H2S Responsive PEGylated Poly (Lipoic Acid) with Ciprofloxacin for Targeted Therapy of Salmonella. *J. Control. Release* **2022**, *351*, 896–906. [CrossRef]
192. Carmine, A.; Domoto, Y.; Sakai, N.; Matile, S. Comparison of Lipoic and Asparagusic Acid for Surface-Initiated Disulfide-Exchange Polymerization. *Chem. Eur. J.* **2013**, *19*, 11558–11563. [CrossRef]
193. Wang, L.; Jing, P.; Tan, J.; Liao, C.; Chen, Y.; Yu, Y.; Zhang, S. "One-Stitch" Bioorthogonal Prodrug Activation Based on Cross-Linked Lipoic Acid Nanocapsules. *Biomaterials* **2021**, *273*, 120823. [CrossRef] [PubMed]
194. Zhong, Y.; Zhang, J.; Cheng, R.; Deng, C.; Meng, F.; Xie, F.; Zhong, Z. Reversibly Crosslinked Hyaluronic Acid Nanoparticles for Active Targeting and Intelligent Delivery of Doxorubicin to Drug Resistant CD44+ Human Breast Tumor Xenografts. *J. Control. Release* **2015**, *205*, 144–154. [CrossRef] [PubMed]
195. Mondal, U.K.; Barchi, J.J. Isolipoic Acid-Linked Gold Nanoparticles Bearing the Thomsen Friedenreich Tumor-Associated Carbohydrate Antigen: Stability and in Vitro Studies. *Front. Chem.* **2022**, *10*, 1002146. [CrossRef] [PubMed]
196. Trzciński, J.W.; Morillas-Becerril, L.; Scarpa, S.; Tannorella, M.; Muraca, F.; Rastrelli, F.; Castellani, C.; Fedrigo, M.; Angelini, A.; Tavano, R.; et al. Poly(Lipoic Acid)-Based Nanoparticles as Self-Organized, Biocompatible, and Corona-Free Nanovectors. *Biomacromolecules* **2021**, *22*, 467–480. [CrossRef] [PubMed]
197. Bellini, C.; Antonucci, S.; Morillas-Becerril, L.; Scarpa, S.; Tavano, R.; Mancin, F.; Di Lisa, F.; Papini, E. Nanoparticles Based on Cross-Linked Poly(Lipoic Acid) Protect Macrophages and Cardiomyocytes from Oxidative Stress and Ischemia Reperfusion Injury. *Antioxidants* **2022**, *11*, 907. [CrossRef] [PubMed]
198. Castellani, C.; Radu, C.M.; Morillas-Becerril, L.; Barison, I.; Menato, F.; Do Nascimento, T.M.; Fedrigo, M.; Giarraputo, A.; Virzì, G.M.; Simioni, P.; et al. Poly(Lipoic Acid)-Based Nanoparticles as a New Therapeutic Tool for Delivering Active Molecules. *Nanomed. Nanotechnol. Biol. Med.* **2022**, *45*, 102593. [CrossRef] [PubMed]
199. Gu, F.; Hu, C.; Tai, Z.; Yao, C.; Tian, J.; Zhang, L.; Xia, Q.; Gong, C.; Gao, Y.; Gao, S. Tumour Microenvironment-Responsive Lipoic Acid Nanoparticles for Targeted Delivery of Docetaxel to Lung Cancer. *Sci. Rep.* **2016**, *6*, 36281. [CrossRef] [PubMed]

200. Yang, F.; Chen, Y.; Zhang, J.; Liao, C.; Zhang, S. Cross-Linked (*R*)-(+)-Lipoic Acid Nanoparticles with Prodrug Loading for Synergistic Cancer Therapy. *J. Mater. Chem. B* **2021**, *9*, 1583–1591. [CrossRef] [PubMed]
201. Zhou, X.; Dai, X.; Tan, J.; Wu, X.; Zhou, X.; Liao, C.; Zhang, S. Quaternary Ammonium Salts Anchored on Cross-Linked (*R*)-(+)-Lipoic Acid Nanoparticles for Drug-Resistant Tumor Therapy. *ACS Appl. Mater. Interfaces* **2021**, *13*, 56850–56857. [CrossRef]
202. Hei, M.-W.; Zhan, Y.-R.; Chen, P.; Zhao, R.-M.; Tian, X.-L.; Yu, X.-Q.; Zhang, J. Lipoic Acid-Based Poly(Disulfide)s as Versatile Biomolecule Delivery Vectors and the Application in Tumor Immunotherapy. *Mol. Pharm.* **2023**, *20*, 3210–3222. [CrossRef]
203. Jia, C.; Guo, Y.; Wu, F. Chemodynamic Therapy via Fenton and Fenton-Like Nanomaterials: Strategies and Recent Advances. *Small* **2022**, *18*, 2103868. [CrossRef] [PubMed]
204. Tan, J.; Zhou, X.; Zhang, S. Iron-Doped Cross-Linked Lipoic Acid Nano-Aggregates for Ferroptosis-Mediated Cancer Treatment. *Acta Biomater.* **2023**, *159*, 289–299. [CrossRef] [PubMed]
205. Cui, R.; Li, B.; Liao, C.; Zhang, S. Copper-Mediated Chemodynamic Therapy with Ultra-Low Copper Consumption by Doping Cupric Ion on Cross-Linked (*R*)-(+)-Lipoic Acid Nanoparticles. *Regen. Biomater.* **2023**, *10*, rbad021. [CrossRef] [PubMed]
206. Dai, L.; Zhang, X.; Zhou, S.; Li, J.; Pan, L.; Liao, C.; Wang, Z.; Chen, Y.; Shen, G.; Li, L.; et al. Pretargeted Radiotherapy and Synergistic Treatment of Metastatic, Castration-Resistant Prostate Cancer Using Cross-Linked, PSMA-Targeted Lipoic Acid Nanoparticles. *J. Mater. Chem. B* **2024**, *12*, 2324–2333. [CrossRef] [PubMed]
207. Xiao, X.; Cui, R.; Liao, C.; Zhang, S. Cross-Linked Lipoic Acid Nanoparticles with Indole-3-Methanol Loading for the PTEN-Mediated TNBC Treatment. *J. Mater. Sci. Technol.* **2024**, *181*, 198–208. [CrossRef]
208. Cely-Pinto, M.; Wang, B.; Scaiano, J.C. Understanding α-Lipoic Acid Photochemistry Helps to Control the Synthesis of Plasmonic Gold Nanostructures. *Photochem. Photobiol. Sci.* **2023**, *22*, 1299–1307. [CrossRef] [PubMed]
209. Pourshahrestani, S.; Zeimaran, E.; Kadri, N.A.; Mutlu, N.; Boccaccini, A.R. Polymeric Hydrogel Systems as Emerging Biomaterial Platforms to Enable Hemostasis and Wound Healing. *Adv. Healthc. Mater.* **2020**, *9*, 2000905. [CrossRef] [PubMed]
210. Zhao, L.; Zhou, Y.; Zhang, J.; Liang, H.; Chen, X.; Tan, H. Natural Polymer-Based Hydrogels: From Polymer to Biomedical Applications. *Pharmaceutics* **2023**, *15*, 2514. [CrossRef] [PubMed]
211. Cui, C.; Mei, L.; Wang, D.; Jia, P.; Zhou, Q.; Liu, W. A Self-Stabilized and Water-Responsive Deliverable Coenzyme-Based Polymer Binary Elastomer Adhesive Patch for Treating Oral Ulcer. *Nat. Commun.* **2023**, *14*, 7707. [CrossRef]
212. Qi, Y.; Xu, C.; Zhang, Z.; Zhang, Q.; Xu, Z.; Zhao, X.; Zhao, Y.; Cui, C.; Liu, W. Wet Environment-Induced Adhesion and Softening of Coenzyme-Based Polymer Elastic Patch for Treating Periodontitis. *Bioact. Mater.* **2024**, *35*, 259–273. [CrossRef]
213. Du, J.; Wang, F.; Li, J.; Yang, Y.; Guo, D.; Zhang, Y.; Yang, A.; He, X.; Cheng, Y. Green Polymer Hydrogels from a Natural Monomer with Inherent Antioxidative Capability for Efficient Wound Healing and Spinal Cord Injury Treatment. *Biomater. Sci.* **2023**, *11*, 3683–3694. [CrossRef] [PubMed]
214. Liu, H.; Deng, Z.; Li, T.; Bu, J.; Wang, D.; Wang, J.; Liu, M.; Li, J.; Yang, Y.; Zhong, S. Fabrication, GSH-Responsive Drug Release, and Anticancer Properties of Thioctic Acid-Based Intelligent Hydrogels. *Colloids Surf. B Biointerfaces* **2022**, *217*, 112703. [CrossRef] [PubMed]
215. Wang, L.; Fan, G.; Zhu, L.; Zhang, Y.; Wang, X.; Qin, J.; Lu, K.; Hu, J.; Ma, J. A Lipoic Acid Supramolecular Polymer-Based Hydrogel with Self-Regulating ROS, Reduced Blood Sugar, and Antibacterial Ability for Improved Diabetic Wound Healing. *J. Sci. Adv. Mater. Devices* **2024**, *9*, 100677. [CrossRef]
216. Yu, H.; Wang, Y.; Yang, H.; Peng, K.; Zhang, X. Injectable Self-Healing Hydrogels Formed via Thiol/Disulfide Exchange of Thiol Functionalized F127 and Dithiolane Modified PEG. *J. Mater. Chem. B* **2017**, *5*, 4121–4127. [CrossRef] [PubMed]
217. Song, L.; Zhang, B.; Gao, G.; Xiao, C.; Li, G. Single Component Pluronic F127-Lipoic Acid Hydrogels with Self-Healing and Multi-Responsive Properties. *Eur. Polym. J.* **2019**, *115*, 346–355. [CrossRef]
218. Wang, T.; Fang, H.; Yalikun, S.; Li, J.; Pan, Y.; Zhang, K.; Yin, J.; Cui, H. Pluronic F127-Lipoic Acid Adhesive Nanohydrogel Combining with Ce^{3+} /Tannic Acid/Ulinastatin Nanoparticles for Promoting Wound Healing. *Biomacromolecules* **2024**, *25*, 924–940. [CrossRef]
219. Luo, Y.; Zhou, X.; Liu, C.; Lu, R.; Jia, M.; Li, P.; Zhang, S. Scavenging ROS and Inflammation Produced during Treatment to Enhance the Wound Repair Efficacy of Photothermal Injectable Hydrogel. *Biomater. Adv.* **2022**, *141*, 213096. [CrossRef]

Disclaimer/Publisher's Note: The statements, opinions and data contained in all publications are solely those of the individual author(s) and contributor(s) and not of MDPI and/or the editor(s). MDPI and/or the editor(s) disclaim responsibility for any injury to people or property resulting from any ideas, methods, instructions or products referred to in the content.

MDPI AG
Grosspeteranlage 5
4052 Basel
Switzerland
Tel.: +41 61 683 77 34

Antioxidants Editorial Office
E-mail: antioxidants@mdpi.com
www.mdpi.com/journal/antioxidants



Disclaimer/Publisher's Note: The title and front matter of this reprint are at the discretion of the Guest Editors. The publisher is not responsible for their content or any associated concerns. The statements, opinions and data contained in all individual articles are solely those of the individual Editors and contributors and not of MDPI. MDPI disclaims responsibility for any injury to people or property resulting from any ideas, methods, instructions or products referred to in the content.

MDPI

Academic Open
Access Publishing

mdpi.com

ISBN 978-3-7258-7333-3